Influence of mesoscale physical processes on planktonic ecosystems in the regional ocean: application to the Eastern Boundary Upwelling Systems.

Vincent Rossi

▶ **To cite this version:**

THÈSE

En vue de l'obtention du

DOCTORAT DE L'UNIVERSITÉ DE TOULOUSE

Délivré par *l'Université Toulouse III - Paul Sabatier*
Discipline ou spécialité : *Océanographie Physique et Biologique*

Présentée et soutenue par *Vincent ROSSI*
Le *15 Juin 2010*

Titre : *Influence des processus physiques à mésoéchelle sur l'écosystème planctonique :
application aux zones d'Upwelling de Bord Est.*

JURY
Serge Chauzy (Président)
Bruno Blanke (Rapporteur)
Nicolas Gruber (Rapporteur)
Hervé Claustre (Examinateur)
Pierre Fréon (Examinateur)
Véronique Garçon (Co-directrice)
Yves Morel (Co-directeur)

Ecole doctorale : *SDU2E (UPS/OMP)*
Unité de recherche : *Laboratoire d'Etudes en Géophysique et Océanographie Spatiales (UMR5566)*
Directeur(s) de Thèse : *Véronique Garçon et Yves Morel*
Rapporteurs : *Bruno Blanke et Nicolas Gruber.*

THÈSE

En vue de l'obtention du

DOCTORAT DE L'UNIVERSITÉ DE TOULOUSE

Délivré par *University of Toulouse III - Paul Sabatier*
Discipline ou spécialité : *Physical and Biological Oceanography*

Présentée et soutenue par *Vincent ROSSI*
Le *15th of June 2010*

Titre : *Influence of mesoscale physical processes on planktonic ecosystems in the regional ocean: application to the Eastern Boundary Upwelling Systems.*

JURY
Serge Chauzy (President)
Bruno Blanke (Referee)
Nicolas Gruber (Referee)
Hervé Claustre (Examiner)
Pierre Fréon (Examiner)
Véronique Garçon (PhD supervisor)
Yves Morel (PhD supervisor)

Ecole doctorale : *SDU2E (UPS/OMP)*
Unité de recherche : *Laboratoire d'Etudes en Géophysique et Océanographie Spatiales (UMR5566)*
Directeur(s) de Thèse : *Véronique Garçon and Yves Morel*
Rapporteurs : *Bruno Blanke and Nicolas Gruber.*

Remerciements

Ce manuscrit, bilan de ces années de thèse au sein du LEGOS, n'aurait pas pu voir le jour sans les nombreuses personnes que j'ai rencontré et qui ont su me former, me soutenir, m'encourager, voire me supporter, ou tout simplement partager un moment de cette tranche de vie. Qu'elles soient citées ou pas ci-dessous, toutes les personnes croisées pendant cette période ont contribué, à leur manière, à l'aboutissement de ce travail.

Mes premiers remerciements s'adressent naturellement à mes deux encadrants, Véronique Garçon et Yves Morel, qui m'ont introduit dans le monde de la recherche océanographique. En premier lieu, je leur suis grandement reconnaissant pour leurs nombreux et précieux conseils scientifiques prodigués tout au long de ma thèse. Ensuite, nous avons, je crois, partagé une vision commune de la science ce qui a facilité et enrichi notre travail en équipe. En plus d'une relation profes-sionnelle privilégiée grâce à la confiance qu'ils m'ont accordé, j'ai aussi réellement apprécié les relations personnelles que nous avons lié lors de ces années, notam-ment grâce à leurs grandes qualités humaines.

Je remercie ensuite mon jury de soutenance pour avoir associé un grand profes-sionnalisme à une chaleureuse ambiance lors de ma soutenance orale. Merci tout d'abord aux rapporteurs Nicolas Gruber et Bruno Blanke qui ont réalisé un travail important sur ce manuscrit, mais aussi aux autres membres du jury (Pierre Fréon, Hervé Claustre et Serge Chauzy) qui ont participé activement à ma soutenance.

Je souhaite également remercier les membres de l'équipe DYNBIO, notamment Guillaume Charria, Isabelle Dadou, Joël Sudre, Danièle Thouron pour les discus-sions et les projets scientifiques que l'on a pu aborder ensemble ; mais aussi Baris Salihoglu, Aurélien Paulmier et Elodie Gutknecht, avec qui j'ai tour à tour partagé le bureau 101. J'en profite pour adresser mes remerciements à tout le personnel du LEGOS que j'ai côtoyé pendant ces années, et plus particulièrement à l'équipe ad-ministrative qui a su gérer mes "nombreuses originalités administratives" (Nadine, Martine, Catherine et Brigitte) et à Yves Du-Penhoat, directeur du laboratoire, qui a pu suivre mon travail jusqu'à la fin, malgré un emploi du temps surchargé.

Du côté SHOM, j'adresse mes sincères remerciements à Rémy Baraille qui a patiemment initié le novice que j'étais à la modélisation 3D avec HYCOM, ce qui n'était pas une mince affaire. Une pensée est aussi dirigée vers l'équipe du SHOM Brest qui était embarquée sur le Pourquoi-Pas? lors de la campagne MOUTON 2007, et notamment un grand merci à Joëlle Tassel avec qui j'ai organisé les relevés biogéochimiques dans la bonne humeur.

Je suis particulièrement reconnaissant à Emilio Hernandez-García et Cristobal López tout d'abord pour m'avoir donné l'opportunité d'effectuer un séjour de recherche très enrichissant de 8 mois à l'IFISC à Palma de Mallorca. Mais je les remercie également pour leur encadrement scientifique irréprochable, leur curiosité pour des sujets connexes à leurs thématiques de recherche, et pour leur bonne humeur quotidienne. Je n'oublie pas aussi de mentionner tous les collègues de l'IFISC et de l'IMEDEA pour les nombreuses discussions scientifiques à l'interface de plusieurs disciplines qui ont stimulé ma curiosité.

De façon plus personnelle, mes pensées vont évidemment vers tous mes potes de "France et de Navarre", qui ont largement contribué à mon bon équilibre mental tout au long de ces trois années. Une mention spéciale pour les Toulousains et les Mallorquins, avec (sans aucun ordre) : Pédro, Rominou, Will, Kiki, Boutch, Marco, Fanfan, Guiche, Grenvez, Jean-Pat, An-so, Dinoune, SarahB, Pipatch, Isma, Boubou, Ainhoa, Isaac, Seb, Laureta... et j'en oublie énormément...

Certaines m'ont côtoyé d'encore plus près... Je pense à Aurélie qui m'a encouragé dans la phase d'initiation de ma thèse. Merci à Lucía qui partage une même passion pour la science et qui m'a largement soutenu lors d'une période charnière. Enfin, un grand merci à Emilia qui m'a encouragé, notamment durant la dernière ligne droite, mais aussi qui a su m'apaiser par sa grande sérénité.

Last but not least, je clôture ces remerciements avec de chaleureuses pensées pour ma famille qui m'a appuyé, orienté, soutenu, et tout simplement aimé avant, pendant et après cette thèse. Un "clin d'oeil" donc à Papou, Mamou, Caro, Annette, mais aussi à mes grands-parents (Pépé et Mémé du Beausset et de Nice), sans qui tout cela n'aurait pas été possible!

Contents

Chapter 1

General Introduction

The general objective of this thesis is the comprehension of coastal ecosystems functioning at regional to local scales. The need for a better monitoring of coastal ecosystems at small scales is obvious for economical (fisheries, aquaculture, recreational activities) or health (toxic algal blooms, pollution surveillance, water quality...) purposes. Moreover, ecosystems play an important role on the variability of the ocean/atmosphere physical state at climate timescales. Conversely, the effects of climate change and physical processes on ecosystems at regional scales are at the core of this manuscript.

After having presented the global context of this study, we will detail the current knowledge of the dynamics and evolution of physical and biogeochemical processes at mesoscale, in particular their coupling. Then we will briefly describe our areas of interest, the Eastern Boundary Upwelling Systems, followed by the detailed objectives and scientific questions of the thesis.

1.1   Global Climate change and Biogeochemistry.

Emissions of carbon dioxide, methane, nitrous oxide and of other reactive gases, which lead to the formation of secondary pollutants including aerosol particles and tropospheric ozone, have increased substantially in response to human activities. As biogeochemical cycles interact closely with the climate system over a variety of temporal and spatial scales, they have been perturbed significantly. Nonlinear interactions between the climate and biogeochemical systems could amplify (positive feedbacks) or attenuate (negative feedbacks) the disturbances produced by human

activities (*Denman et al.* [2007]). All models coupling the carbon cycle with climate change indicate a positive feedback effect with warming acting to suppress land and ocean uptake of CO_2, leading to larger atmospheric CO_2 increases and greater climate change for a given emission scenario, but the strength of this feedback effect varies markedly among models (*Solomon et al.* [2007]).

The place of the ocean in the complex global biogeochemical systems, as well as its role in the cycling and variability of CO_2, is detailed hereafter. The rapid increase in atmospheric carbon dioxide (CO_2) levels has stimulated a growing interest in understanding biogeochemical processes in the ocean and their interactions with the atmosphere. On millennial time scales, the ocean dictates the atmospheric concentration of CO_2. The upper portion of the water column is in overall equilibrium with the atmosphere at first order. This gradient is maintained by two carbon pumps (see figure 1.1).
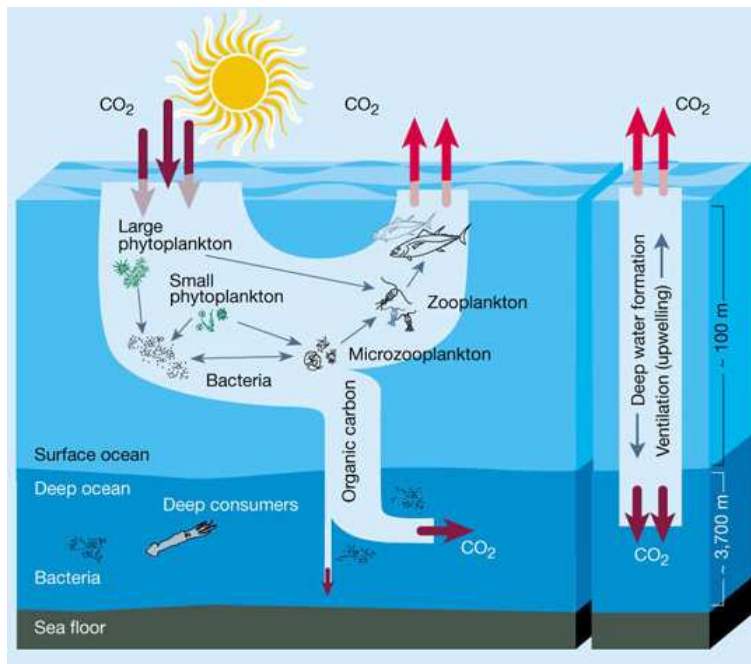
Figure 1.1: Schematic representation of the two oceanic carbon pumps: on the right hand side, the "solubility pump", which is driven by chemical and physical processes ; on the left hand side, the "biological pump" where planktonic ecosystems in the upper ocean play a key role (From *Chisholm* [2000]).

The chemical solubility pump depends on the fact that cold water holds more CO_2 than warm water. As a consequence, the net effect of sinking surface waters through thermohaline circulation is to enrich deeper waters in carbon. The second biological carbon pump begins with phytoplankton living in the upper or

2

euphotic layer of the ocean that takes up CO_2 and nutrients to form organic matter by photosynthesis (Primary Production PP). Although much of this organic matter is metabolized and recycled in the surface waters, a significant portion (roughly 10% to 20% but varying greatly over space and time) sinks into the deep ocean to be transformed in inorganic form via the metabolism of microorganisms (*Dickey* [2003]). Increasing atmospheric CO_2 concentrations lead also directly to increasing acidification of the surface ocean, that impacts directly marine ecosystem and organisms.

Understanding how mesoscale processes affect the biological carbon pump and planktonic ecosystems is also of great interest for global climate change issues.

1.2   Spatial and temporal scales in the Ocean.

Geosciences are an all-embracing term for the sciences related to the planet Earth. They include the study of the atmosphere, oceans and biosphere, as well as the solid earth. Typically Earth scientists will use tools from a variety of disciplines (physics, chemistry, biology, geology, mathematics, etc...) to build a quantitative understanding of how the Earth system works, and how it evolved to its current state. The main difficulty is to deal with the many spatial and temporal scales associated with this issue. A simple example, critical nowadays, is the global climate change. Opponents to the humans cause of global warming are claiming that it is difficult to distinguish a mean trend in observations over short time periods for which the signal is dominated by interannual variability. They also say that if we could look at temporal scales larger than a few decades, we would find some period in the geological time scale where global temperatures were similar to the observed current warming, suggesting that it might be a long-term natural cycle. The climate scientific community answered that some indirect records of temperature, ice cover, sea level, atmospherical carbon dioxide concentrations, etc... over very long time series (more than 10 millions years, going before the Quaternary period) show unambiguously through indirect measurements that the current global warming was never observed since humans discovered the use of fossil energy (*Solomon et al.* [2007]). This example stresses out the importance of scales in Geosciences, where a similar observation may be interpreted differently depending on the scale considered.
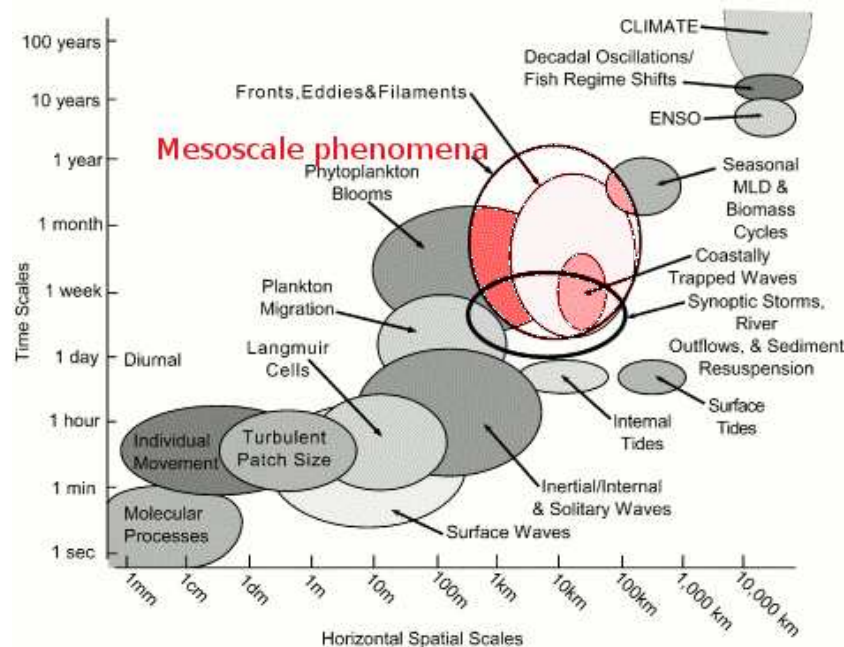
Figure 1.2: Spatial and temporal scales in the ocean and associated processes. Mesoscale processes, which range approximatively **from 1 km to 100 km and from 1 day to 1 year**, are highlighted in red (From *Dickey* [2003]). Energy cascades are observed from large scales to small ones and inversely.

In oceanography, we also have to be very careful with the temporal and spatial scales we are dealing with. Figure 1.2 is summarizing all spatial and temporal scales in the oceans, and their associated - known - processes. The oceans are naturally dynamic, with large-amplitude periodic and episodic variability that is confounded with small-scale high frequency variability. Recent studies (*Boffetta et al.* [2000]; *Capet et al.* [2008a]) suggested that a few powerful episodic small-scale events can be of far greater importance for local equilibrium than small-amplitude, slower long-term variations. Moreover, although it is obvious that large scales processes influence small scales ones by energy cascades, similar transfers of energy occur in the opposite direction. Understanding large scale phenomenon requires a comprehension of small scale processes and their interactions, since inverse energy cascades from small to large scales exist. All regions experience certain small- and mesoscale processes, especially over short time periods. But the effects of natural phenomena such as monsoons, equatorial longwaves, spring blooms, hurricanes and typhoons, deep convection, El Niño-Southern Oscillation, climatic oscillations vary greatly from one region to another. To answer many basic questions, large volumes of data are important to cover a wide range of time and space scales because of the vastness and complexity of the ocean (*Dickey* [2003]). For instance,

Paleo-oceanography is a science branch that is focussed on the past long-term climate variation of the global oceans and their associated biosphere changes. In fact paleo-oceanographers use some tools coming both from proper Oceanography and some from Geological sciences (*Jansen et al.* [2007]). Others may be interested in interannual variability as El Niño phenomenon and its decadal modulation.

In our case, we are interested in the evolution of regional marine ecosystems at high frequency (1 to 100 km and from day to several months). The mesoscale physical phenomena of interest, defined as a class of energetic phenomena of spatial scales ranging **from about one to several hundred kilometers and time scales ranging from a few days to several months**, are fronts, eddies, filaments, coastal waves, storms and high frequency dynamics of the mixed layer (see Fig. 1.2). Surface tides and internal tides can also have strong effects on the shelf circulation, impacting in turn coastal ecosystems. However this work is not concentrated on these processes since they are associated to time scale below 1 day (see Fig. 1.2) and because our areas of interest are not favouring significant tidal currents. Regional studies are then necessary to sample processes and to develop models to analyze the large influence of the hydrodynamical environment on marine ecosystems. The biology and biogeochemistry of the oceans are particularly sensitive to this class of small scale physical forcings since they are generally emphasized in the upper layers of the water column.

1.3 Mesoscale physical processes influence marine ecosystems.

As seen above, several spatio-temporal scales occur in the ocean. Here we focus on the mesoscale and submesoscale processes that have a tremendous importance in the current knowledge of the oceans. Mesoscale physical processes are consisting in eddies, filamental structures and frontal oceanic structure. Their forcing mechanisms are mainly instabilities from the large-scale circulation, interactions between currents and bathymetry, the direct effect of the atmosphere, in particular of the wind, and their interactions. In the ocean, the strength (in velocity and thermohaline signatures) of these mesoscale processes generally exceeds that of the mean flow by an order of magnitude or more. Most of the eddy kinetic energy is generated by instabilities of the mean flow, but fluctuating winds can also provide a direct forcing mechanism, which is particularly evident in low-eddy energy regions. Eddies can feed energy and momentum back into the mean flow and help

drive the deep ocean circulation (*Holland* [1978]; *Wunsch and Ferrari.* [2004]). Eddies also transport heat, salt, carbon, nutrients and oceanic non motile biota (as phytoplankton) as they propagate in the ocean (*Danabasoglu et al.* [1994]). Finally they are often associated with a strong hydrodynamic signature, especially vertical velocities, which are of importance for planktonic life in the ocean. Thus mesoscale processes play a significant role in the global budgets of these tracers, and have a strong impact on the ecosystem. For most operational oceanography applications (e.g. pollution monitoring, toxic algal bloom, coastal management, fisheries management, etc...) mesoscale structures need also to be documented and understood.

The impact of the vertical and horizontal exchanges of tracers due to mesoscale eddies has stimulated a large number of biogeochemical studies in the past decade. The quantification of these vertical exchanges (totally ignored in the past studies) indicates that they represent the second most important contribution to the annual nutrient requirement for phytoplankton on a global scale (*Garçon et al.* [2001]). There are a lot of observational as well as modelling evidences showing that mesoscale processes strongly modulate the functioning and the structure of marine planktonic ecosystem.

Horizontal transport, stirring and phytoplankton patchiness:

The observed patchy distribution of phytoplankton is subject to debate in the community: it is not clear whether it is the biological or physical processes which are responsible for this specific spatial structure. Biological processes by themselves, such as growth, grazing and behaviour, and the non-linear dynamics of ecosystems, all contribute to the spatial structure we see in plankton distributions. However, lateral advection and stirring by oceanic eddies and fronts at mesoscale are highly responsible for the observed patchiness distribution of phytoplankton in the surface ocean (see Fig. 1.3). Several processes such as shear effects, filamentation, patches formation, turbulent stirring, and diffusion are involved (*Abraham* [1998]; *Martin* [2003]). Academic modelling studies also reported the effect of horizontal stirring on tracer distribution. *López et al.* [2001] stressed the existence of a smooth-filamental transition in the plankton concentration patterns depending on the relative strength of the stirring by the chaotic flow and the relaxation properties of planktonic dynamical systems. More recently, *McKiver and Neufeld* [2009] showed the importance of the ratio between phytoplankton growth rate and the flow advection time scale. *Birch et al.* [2008] explained the small scale formation of plankton thin layers by shear and death by diffusion. Indeed all authors found dif-

ferent mechanisms to explain that lateral stirring and mixing can influence spatial structure in plankton distributions. *Martin* [2003] discussed the need to maintain the recent developments in sampling, instrumentation, image analysis and turbulence theory to obtain more data to determine which, if any, of these proposed mechanisms are the most important. *Martin* [2003] added that even though the emphasis is on lateral stirring and mixing, horizontal currents were also often strongly related to the vertical circulation (see Subsection below).
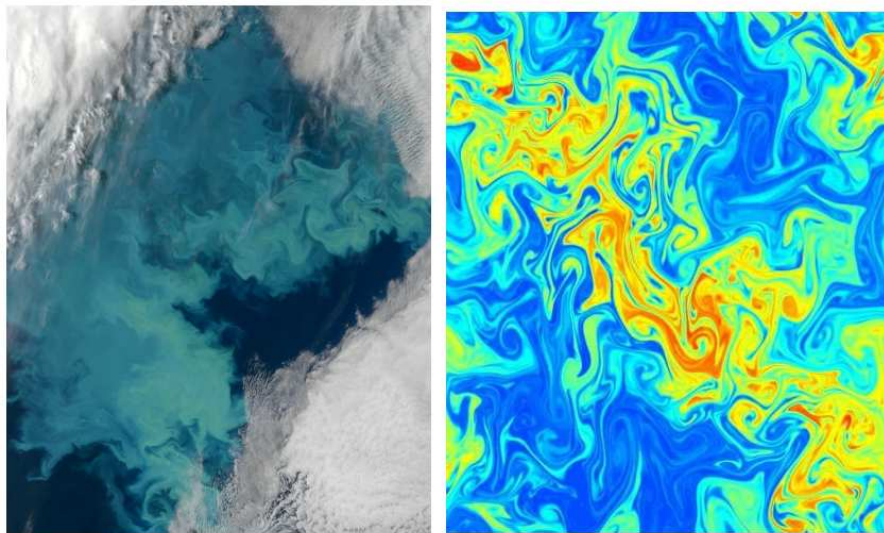
Figure 1.3: On the left, a MODIS Aqua image in true color mode showing a bloom of coccolithophorides in the Barent Sea (white areas are clouds). On the right, a simulated phytoplankton field by 2D modelling studies from *McKiver and Neufeld* [2009]. Similar small-scale structures are found in both pictures.

Eddies and filaments are also responsible for horizontal transport. They contain water masses with specific characteristics inside their core, relatively isolated from the surrounding ones, while moving in the surface ocean. The most notable transport is achieved when eddies or filaments develop in rich coastal areas and then move to oligotrophic offshore zones. *Moore et al.* [2007] studied eddies on the Western coast of Australia and found that anticyclonic eddies, formed adjacent to the shelf, entrain shelf waters with relatively high chlorophyll concentrations as they propagate westward, exporting coastal phytoplankton communities offshore. They suggest that sub-mesoscale injection of nutrients is associated with the eddy activity and displacement, developing at its boundary. *Alvarez-Salgado et al.* [2007] studied the impact of the horizontal transport within filaments. They found that transport by filaments accounts for 2.5 to 4.5 times the offshore carbon export driven by Ekman transport in an upwelling system. Since filaments are ubiquitous

features in all coastal transition zone systems, they must represent a significant flux of carbon to the open ocean, which should be considered in global biogeo-chemical models.

The interactions between the mean flow and islands is also a preferential source for creation of mesoscale eddies, that are then influencing greatly the ecosystem embedded inside. *Aristegui et al.* [1997] detailed two mechanisms: the first one is about nutrient pumping and vertical uplifting of the deep chlorophyll maximum by cyclonic eddies in the oligotrophic waters of the Canary region. The second deals with the incorporation into cyclonic eddies of water with high chlorophyll content, resulting from island stirring or local upwelling at the flanks of the islands, being subsequently transported downstream. More recently, *Sangra et al.* [2009] studied the 'Canary Eddy Corridor'. They suggested that constant formation of long-lived mesoscale eddies may stimulate the total PP through eddy pulsation along their route, being comparable to the PP of the northwest African upwelling system. These effects have been also studied in idealized settings by *Sandulescu et al.* [2008].

Horizontal turbulence plays a role on the spatial distribution of a single tracer, but it also strongly affects the competition between specific tracers, as it influences the community composition. *Karolyi et al.* [2000] argue that a peculiar small-scale, spatial heterogeneity generated by chaotic advection can lead to coexistence of several specific tracers. In open flows, this imperfect mixing lets the populations accumulate along fractal filaments, where competition occurs. They in fact provided an hydrodynamical explanation for the spatial and temporal heterogeneity of resources and populations in the presence of imperfect chaotic mixing. A recent coupled modelling study by *Perruche et al.* [2010] showed that a spatially extended and coupled system exhibits a wide range of ecosystem structures, allowing for instance coexistence between several phytoplankton species. They examined the physical and biological time scales and concluded on the likely coupling between ecosystem and ocean dynamics in three dimensions.

Vertical movements and velocities associated to mesoscales processes:

Examining the enhancement of production by a cyclonic eddy in the subtropical Pacific, *Falkowski et al.* [1991] were among the first ones to propose the eddy-pumping mechanism to markedly stimulate primary production. Then *McGillicuddy et al.* [1998] detailed the process involved and showed that mesoscale eddies and associated vertical movements in the water column lead to specific biological response. They documented from observation and models that vertical flux of nu-
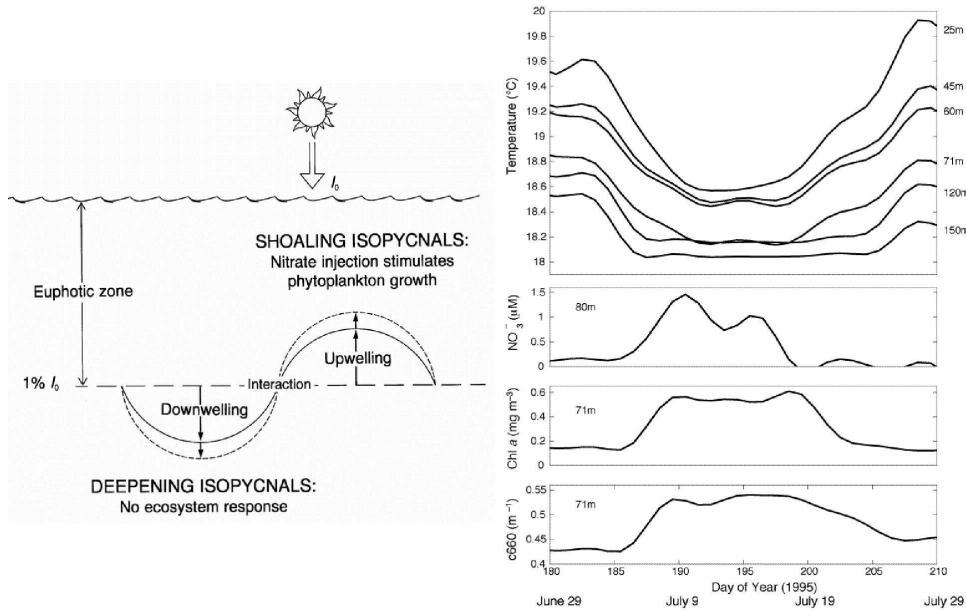
Figure 1.4: On the left, a schematic representation of the eddy-induced upwelling mechanism (for cyclonic - right - and anticyclonic - left - eddies). On the right, these are the results from the Bermuda Testbed Mooring third deployment during the summer of 1995 during the passage of a cyclonic eddy. From *McGillicuddy et al.* [1998].

trients induced by the dynamics of mesoscale eddies, the so-called eddy-pumping effect, is sufficient to balance the whole nutrient budget in the Sargasso Sea. They propose a simple mechanism: a surface cyclone (associated with a positive density anomaly) is doming the main pycnocline (positive vertical velocity inside the eddy) leading to a significant input of nutrient in the surface layer, followed by an increase of PP. On the other hand, a negative vertical velocity would occur in the case of anticyclonic eddies (see Fig. 1.4) without any response of the biology. It was stated since the mechanism of *McGillicuddy et al.* [1998] that it is the evolution of a vortical structure which create vertical velocities, but not the structure in equilibrium by itself.

Before these papers, coupled modelling studies at basin scale were under estimating these effects, resulting in an under estimation of the Primary Production. Realistic coupled physical-biogeochemical numerical simulations at basin scale (*Oschlies and Garçon* [1998]; *Oschlies* [2002]; *McGillicuddy et al.* [2003]), including mesoscale dynamics by altimetry data assimilation, took in account the eddy pumping mechanism. Their results indicate that mesoscale eddy activity accounts for about one-third of the total flux of nitrate into the euphotic zone (taken to represent new production) in the subtropics and at mid-latitudes. Mesoscale eddies

9

could then be the dominant mode of nutrient transport in the open ocean (*Oschlies* [2002]).
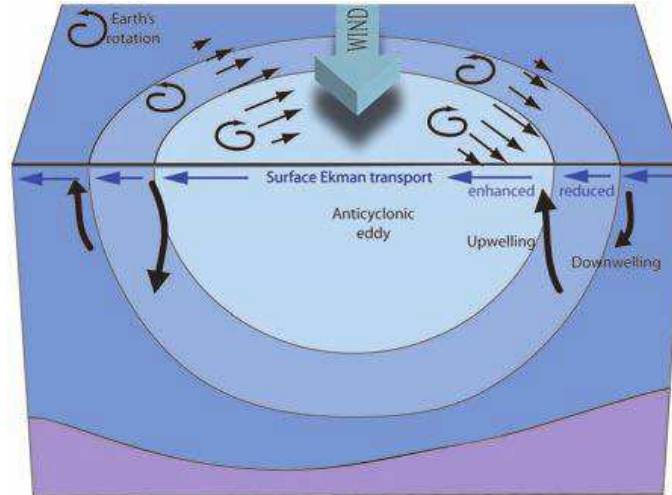
Figure 1.5: The nonlinear Ekman effect generates upwelling and downwelling in a Northern hemisphere anticyclonic eddy, as schematically depicted. From *Mahadevan et al.* [2008].

In another study by *Moore et al.* [2007], contrary to canonical ideas, it was observed low phytoplankton biomass in cyclonic eddies and high biomass in anticyclonic eddies. More recently, *McGillicuddy et al.* [2007] differentiate the types of eddies and their associated biological responses. The induced upwelling by mode-water eddies is being promoted from wind/eddy interactions, leading to a strong biological response in the surface water. On the other hand, wind effect on upwelling induced by cyclonic eddies is being dampened. This work was immediately criticized by *Mahadevan et al.* [2008] claiming that the effect of the wind on mesoscale eddies was much more complicated. They showed that the divergence/convergence of the Ekman transport drives both up/down motion in an eddy. The vertical motion associated with an anticyclonic eddy is greater than that with a cyclonic eddy of similar strength because decreasing the magnitude of the net rotation solicits a greater response than increasing it by the same amount (see Fig. 1.5).

The net effect of eddies on the water column and the associated response of the phytoplankton appear to be very complex, and different types of eddies, occurring in diverse environments, may have specific effects. However their global effect is strong and has to be assessed.

It appeared from previous modelling studies that it is very important to consider and represent mesoscale processes in coupled modelling to balance nutrients and phytoplankton budget (*Garçon et al.* [2001]; *Lévy et al.* [2001]; *Oschlies* [2002]). Sim-
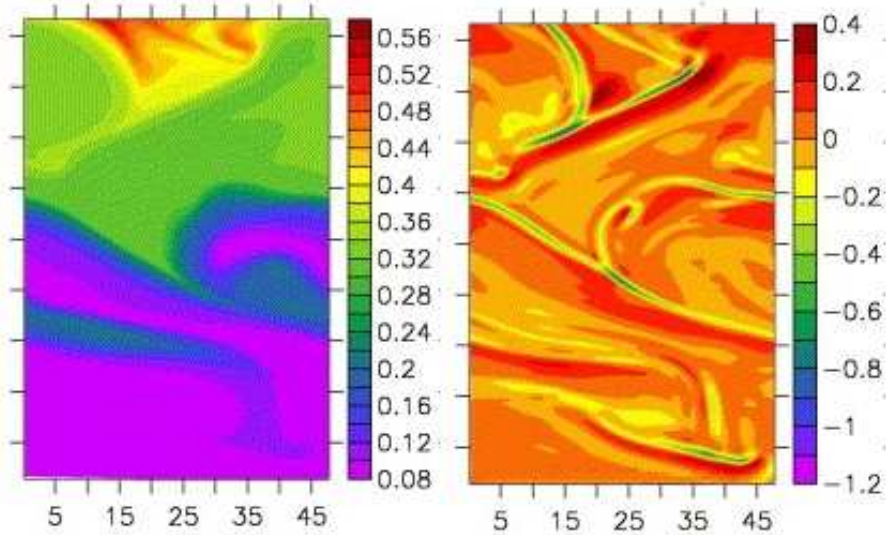
Figure 1.6: The density anomaly (in kg/m^3 - left panel) and vertical velocity fields w at 15 m (in mm/s - right panel) shown in plan view after 30 days of simulation. From *Mahadevan and Tandon* [2006].

ilar conclusions were made since increasing the spatial resolution of physical models reveals much larger vertical exchanges of tracers. This significant increase was principally due to the small scale vertical movements w. *Garçon et al.* [2001]; *Martin* [2003] pointed out the existence of small-scale upwelling or downwelling hot spots. They are associated with the mesoscale eddies and may have a significant impact on the biological dynamics at a global scale. In particular, the question of the existence of small-scale upwellings and downwellings (versus large-scale) within a turbulent eddy field has been addressed by *Lévy et al.* [2001]. They showed that using a higher spatial resolution (2 km instead of 6 km) produces very different w structures. High resolution leads to w structures with much smaller scales and a much larger amplitude, and characterized by either multipolar hot spots of large vertical fluxes or thin elongated patterns both within and outside the eddies. Frontal structures and frontogenesis are also associated to vertical movements. *Lapeyre and Klein* [2006] quantified the potential impact of the submesoscale structures (fronts, filaments) versus mesoscale eddies on the vertical nutrient fluxes on a global scale and suggested that their contribution is similar. They also showed that intermittent events, such as the encounter of an eddy with a stronger one, produce a very large number of small-scale filaments that trigger an intense vertical pump. Interactions between all these mesoscale structures in the real ocean (eddy-eddy or eddy-front or eddy-filament) create submesoscale variability and associated vertical movements.

Mahadevan and Tandon [2006] also showed that when a frontal region with horizontal density gradients is perturbed by the wind, a profusion of submesoscale (1 km), secondary circulation features develops in the upper 50 m. Narrow, elongated cells of intense up- and down-welling are found to occur close to the surface, overlying broader regions of weaker up- and down-welling associated with the mesoscale meanders of the baroclinically unstable front (see Fig. 1.6). In response to a production of small-scale density fronts at the surface, a vertical velocity field develops underneath. *Klein and Lapeyre* [2009] made a complete review of all mesoscale and submesoscale mechanisms that have been reported to influence the oceanic biological pump.

Bio-physical interactions at microscales.

Let us mention that such interactions between the physical environment and the biology occur also at smaller scale, of the order of centimeters to meters, strongly influencing planktonic communities. *Mitchell et al.* [2008] showed that driven by active physical turbulence, phytoplankton patches occur and may link large scale processes and microscale interactions, acting as fundamental components of marine ecosystems that influence grazing efficiency, taxonomic diversity, and the initiation of aggregation and subsequent carbon flux.

Another process to create vertical velocity at small scales is the homogeneization of upper ocean layer by vertical mixing induced by the wind. *Lewis et al.* [1984] already documented that vertical mixing and turbulence in the upper layer of the ocean transports algae through a light field that decreases exponentially from the sea surface, thus controling to a large degree the photosynthetic performance.

Mesoscale processes / ecosystem interactions in Upwelling areas.

From the three previous subsections, we emphasized the strong influence that have mesoscale processes on planktonic ecosystems, both in the horizontal or vertical dimensions. However, a quite high heterogeneity of the results has also been shown, depending on the oceanic region considered, on the sampled structure, on the type of coupled models chosen, etc... It reveals the complexity of the processes, both from biological and physical origins, involved in these observations. These issues were quite intensively studied in the Atlantic and Pacific ocean at the basin scale, but they have received much lower attention in coastal areas and more particularly in upwelling areas. The effect that these mesoscale structures have in the oligotrophic

environment as compared to the eutrophic zones such as upwelling is expected to be different, since the PP and ecosystem functioning do not rely on the same processes than those in the open ocean.

The Coastal Transition Zone program (*Brink and Cowles* [1991]) was designed to better assess the importance of mesoscale features in upwelling areas and to understand their implications. For instance in the Atlantic upwelling system, *Shillington et al.* [1992] documented the frontal region of the Benguela upwelling not as a smooth and unvarying line, but rather consisting of mesoscale plumes, jets and filaments. Long, narrow, cold, upwelling filaments have been observed to extend seaward of the Benguela frontal system and to be strongly linked to the biogeochemical variability. Later, *Joint et al.* [2001] (and references therein) performed a lagrangian study of the Iberian Peninsula Upwelling, following a filament offshore. They chose this strategy since these filamental structures are related to the observed variability of biogeochemical characteristics, as mentioned previously by *Castro et al.* [1997]. *Arístegui and Montero* [2005] observed a marked seasonal change in respiratory activity, plankton community structure, and the ratio of heterotrophic to autotrophic biomass, being largely explained by hydrographic changes at the mesoscale level. More recently, *Arístegui et al.* [2004] and *Sangra et al.* [2009] studied the interactions between the Canary island archipelago and the coastal upwelling, showing that both systems present numerous mesoscale structures that strongly interact and influence the biology. A few academic modelling studies also reported strong bio-physical interactions in upwelling areas, as the one by *Pasquero et al.* [2005]. They studied the dependence of PP on the spatial and temporal variability of the nutrient flux. PP was shown to strongly depend on the size and/or temporal duration of the upwelling events. *Sandulescu et al.* [2008] studied the planktonic biological activity in the wake of an island which is close to an upwelling region. They showed that the interplay between wake structures and biological growth leads to plankton blooms inside mesoscale hydrodynamic vortices that act as incubators of PP. One of the first high resolution coupled modelling studies of an upwelling area was performed by *Koné et al.* [2005] over the Benguela area and one year later by *Gruber et al.* [2006] over the Californian system. Among other findings, they globally stressed out the importance of the 3-D nature of circulation and mixing in a coastal upwelling system, that strongly influence the biological modelled components. More recently, *Capet et al.* [2008b] showed from a 3D high resolution physical model of the Californian upwelling that submesoscale features arises through surface frontogenesis growing off upwelled cold filaments that are pulled offshore and strained in between the mesoscale eddy centers. In turn, some submesoscale fronts become

unstable and develop submesoscale meanders and fragment into roll-up vortices. These recent realistic simulations reveal the very high occurrence of mesoscale structures in upwelling areas which are impacting the biology.

Mesoscale processes influence also higher trophic levels.

All these mesoscale processes also play a crucial role in the structuration of the whole oceanic ecosystem up to top marine predators. *Rykaczewski and Checkley* [2008] showed that the level of wind-stress curl has increased over the Californian upwelling system, and that the production of Pacific sardine varied with wind-stress curl over the past six decades. The size structure of plankton assemblages is related to the rate of wind-forced upwelling, and sardines feed efficiently on small planktonic species generated by slow upwelling. Eddy dynamics partly control the foraging behavior and the displacement of fishes and marine top predators, since they are also linked with accumulation of the lower trophic levels *TewKai et al.* [2009]. However, the impact of mesoscale activity on highier trophic levels is very hard to study since a decoupling in space and time of all levels of marine food chain occur. Understanding of the physical and biological mechanisms relating fisheries production to environmental variability at mesoscale is essential for designing a wise management of marine resources under a changing climate.

1.4 The Eastern Boundary Upwelling systems.

Eastern Boundary Upwelling Systems (EBUS) are some of the most productive marine ecosystems of the world oceans. Despite representing less than 1% of the world ocean area, their primary production accounts for about 10% of oceanic new production, and support up to 20% of the global fish catch (*Pauly and Christensen* [1995]).

The four main EBUSs, the Canary/Iberian, California, Humboldt and Benguela Currents (see Fig. 1.7) are narrow strips of the ocean that extend latitudinally over several thousands of kilometres and longitudinally to beyond the continental shelves whose widths range from 20 to 200 km. They are located on the western margin of the continents (eastern part of the oceans), on each side of the Equator (see Fig. 1.7). In these regions, intense trade winds combined with the earth's rotation generate coastal upwelling, bringing cold, nutrient-rich water from the deep ocean (of the order of 200 to 300 m) to the surface (see Fig. 1.8). These rich waters
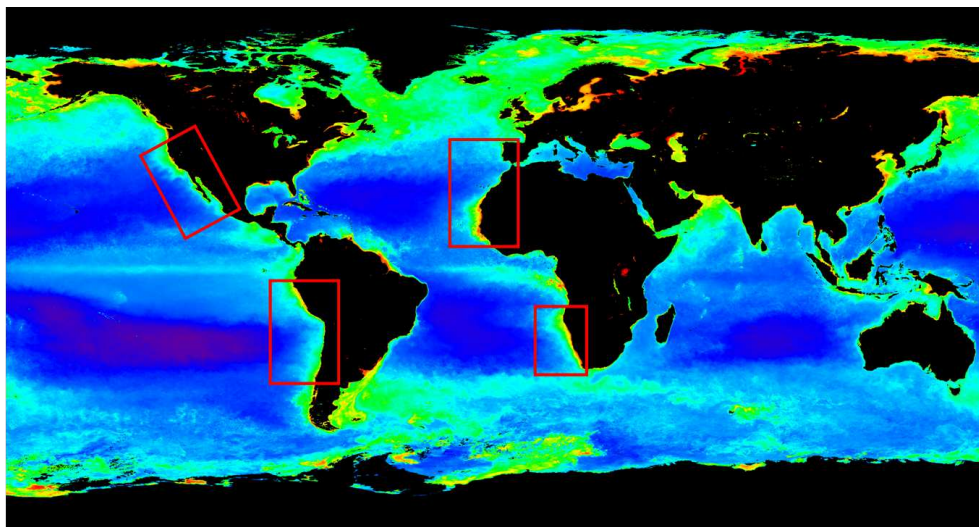
Figure 1.7: Localization of the 4 Eastern Boundary Upwelling Systems (EBUS) indicated on an annual averaged image of surface chlorophyll a concentration from SeaWiFS (rich area in green to red, poor area in blue). In the Atlantic Ocean (Pacific Ocean, respectively), we have the Canary/Iberian Upwelling system (California Upwelling system) in the northern hemisphere, and the Benguela Upwelling system (Humboldt Upwelling system) in the southern hemisphere.

reaching the euphotic layer fuel primary production (up to two orders-of-magnitude higher than in other coastal or open ocean regions), which supports a highly productive food web.

From more recent estimates (*Fréon et al.* [2009a]), EBUS provide $\sim 1/5$ of the marine fish global catch (see Tab. 1.1), thus contributing significantly to human food supply and playing a major socio-economical role in many adjacent countries.

EBUSs are characterized by a high abundance of a reduced number of small pelagic fish species that support large fisheries and a number of top predator populations. Because they are situated in the middle of the trophic food web, pelagic fish often play a central role in regulating the functioning of upwelling ecosystems, which are often described as wasp-waist ecosystems (see *Fréon et al.* [2009c]).

EBUS also contribute very significantly to gas exchange between the ocean and the atmosphere, particularly CO_2 and N_2O. From a biological point of view, EBUS would represent carbon sinks since in the long-term the high CO_2 fixation by phytoplankton production exceeds plankton community respiration. However, in spite of their high productivity, these areas usually behave as sources for CO_2 because cold upwelled water releases CO_2 when warmed at the surface (*Paulmier et al.* [2008]). The production of other greenhouse gases such as nitrogen dioxide, methane and
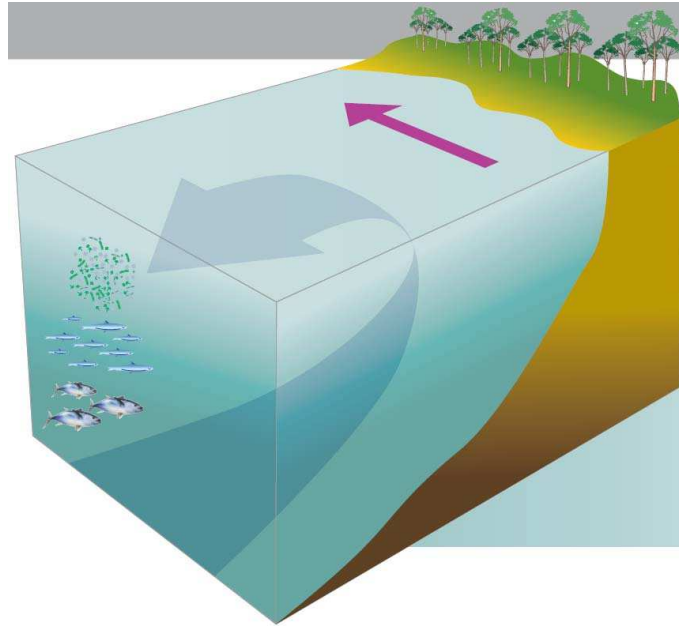
Figure 1.8: Schematic section of a coastal upwelling system in the southern hemisphere. Equatorwards trade winds are blowing almost all year along the coast, that create westward Ekman drift in the upper layer, and divergence at the coast, that is being compensated by upwelling of deep, cold, nutrient-rich waters.

other volatile gases has been recently considered significant in EBUS, potentially triggering further acidification of the ocean (*Checkley and Barth* [2009]). Certain phytoplankton groups are also known to contribute to increased fluxes of dimethyl-sulphide (*Franklin et al.* [2009]), a trace gas involved in the global biogeochemical cycling of sulphur, which influences climate by inducing aerosol and cloud formation in the atmosphere. Extended Oxygen Minimum Zones (OMZ) are also typical features of eastern tropical oceans and EBUS (*Paulmier and Ruiz-Pino.* [2009]). These OMZs are playing an essential role in the global nitrogen cycle, in which various chemical species (e.g. ammonium NH_4^+; nitrite NO_2^-; nitrate NO_3^-; nitrous oxide N_2O; dinitrogen, N_2) and different bacterial processes intervene (*Paulmier and Ruiz-Pino.* [2009]). Under oxic conditions, nitrification transforms NH_4^+, into NO_3^-. In O_2-deficient regions, bacterial denitrification converts NO_3^-, one of the main limiting nutrients in the ocean and upwelling, into gaseous nitrogen (N as N_2O or N_2) which is lost to the atmosphere. Recently, an additional process has been observed in sediments first and then in the water column of the OMZs. Anammox consists in the anaerobic oxidation of NH_4^+ using NO_2^-. Recent studies predict an expansion of OMZs with global warming (*Stramma et al.* [2008]; *Keeling et al.* [2010]), which might have tremendous effects on coastal upwelling regions, their biogeochemical cycling, and their ecosystem (mortality of fish due to hypoxia events). The processes

	Benguela	Canary	California	Humbolt	EBUS total	World total
Quantities (metric tons)	$1,308,300$	$2,232,005$	$1,277,672$	$12,021,549$	$16,839,525$	$92,056,118$
Percentage (per upwelling)	7.8	13.2	7.6	71.4	100	-
Percentage (global)	-	-	-	-	18.3	100

Table 1.1: Estimated average yearly catches (metric tons and percentage) by commercial fisheries in 4 EBUSs during the 2004 - 2007 period. Source: *Fréon et al.* [2009a] and FAO FishStat (see http://www.fao.org/fishery/statistics/en/).

in the sediments and at the sediment-water interface are clearly identified as critical components in the study of coastal upwelling biogeochemistry. However, the role of benthic processes at the boundary layer is poorly known, due to their complexity and spatio-temporal variability. Thus EBUS play a crucial role in the biogeochemical cycles (carbon, nitrogen, phosphorus, sulphur, oxygen...) in the ocean.

The geographical setting of each EBUS is important in determining the characteristics of each system. Trade winds play a significant role in modulating the intensity of upwelling processes and the depth of the thermocline, as well as the latitudinal location. Weather-driven mixing patterns in high latitudes and river discharges close to the equator are also observed. Consequently, each EBUS has 3-4 well-defined latitudinally distributed biomes.

Near shore areas (including gulfs, open lagoons, Rías, and estuaries) located in EBUS influence and modify the upwelling process, thus affecting the dynamics of EBUS ecosystems over a wide range of temporal and spatial scales. The coastal morphology and its influence on local wind patterns strongly influence the upwelling intensity and dynamics, leading to changes in biogeochemical processes. Coastal upwelling exchanges water and biogeochemical properties with the adjacent offshore regions, through the hydrographically complex Coastal Transition Zone (CTZ). In the past two decades, several multidisciplinary studies have addressed physical and biological processes in these highly dynamic boundary regions (*Brink and Cowles* [1991]; *Strub et al.* [1991]; *Barton et al.* [1998] and more recently by *Barton and Arístegui* [2004]; *Fréon et al.* [2009a] and references therein). It has been shown that mesoscale processes are ubiquitous features of these areas, related to the complex coastal circulation and its instabilites, as well as coastline irregularities. These mesoscale structures (filaments, eddies, fronts) that occur and travel in the transitional area between the productive shelf and the oligotrophic gyre are thus playing a key role in the CTZ exchange (*Alvarez-Salgado et al.* [2007]). This strong mesoscale variability also modulates the structure and dynamics of ecosys-

tems. Changes in patterns of distribution, of abundances and of plankton community structure, which concomitantly modify the carbon pathways within the food web, have been related to physical variability (*Gasol et al.* [2009]; *Rodríguez et al.* [2009]). Phytoplankton community growth and zooplankton grazing can explain a large fraction of the variability observed in the net changes of ambient chlorophyll *a* over small time scales of a few days. Spatio-temporal variation of upwelling intensity and circulation will affect nutrient delivery to shore and influence larval transport and patterns of recruitment along the shore.

Climate change has also been already identified as the cause of significant changes in the physical, biogeochemical or biological functioning of EBUS (*Bakun* [1990]; *Relvas et al.* [2009]; *Demarcq* [2009]). However it is not clear how the physical functioning of EBUSs and their ecosystem will clearly respond to these changes (see for instance a review by *Fréon et al.* [2009b]).

EBUSs appear to be very vulnerable from several aspects including climate change, physics of the ocean and atmosphere, biogeochemical cycling and greenhouse gases budget, ecosystem production, ecology, food web structure and dynamics, trophic interactions, and fisheries assessment and management. *Fréon et al.* [2009a,b] emphasize the crucial need to understand these regions, both in terms of the biogeochemical balance of the planet, and regarding the social and economic consequences of potential changes in global fish production. To sum-up this subsection, EBUSs constitute a natural laboratory to study the mesoscale physical processes and their influence on planktonic ecosystems.

1.5   Thesis objectives and plan.

Although the importance of mesoscale processes on open ocean ecosystems has been widely studied, and even though such interactions are known to occur in upwelling systems, the influence of mesoscale dynamics and their biological consequences on upwelling systems are still poorly understood. The aim of this study is **to assess and understand the effect of mesoscale physical processes on the planktonic ecosystem in upwelling areas**. As shown in the previous sections, it is highly relevant considering the high importance of these coastal areas both in terms of health or economical role.

To detail the global scientific objectives, we organized this manuscript as follow:

- Chapter 2 presents a brief overview of the **current tools** available to study mesoscale processes, both from a physical and biological point of view, that are being used in this work.

- Chapter 3 aims at studying jointly the **mesoscale spatio-temporal variability of both physical and biogeochemical properties of the Iberian Peninsula Upwelling System**. Based on a field survey designed to collect *in-situ* multi-disciplinary data, can we **explain the spatial variations of planktonic communities and their biogeochemical functioning in relation to the physical environment ?**

- The study of the effects of the physical processes on ecosystems first require a full knowledge of the physical part, which is the core of chapter 4. **Can we better understand the origin and characteristics of mesoscale processes typical of upwelling areas such as fronts, eddies and filaments ?**

- Chapter 5 presents a more global point of view. What is the relative importance of **Ekman transport versus mesoscale (filaments, eddies) processes in Upwelling areas (EBUS) ? Can we assess the eddy-induced horizontal mixing ? Can we have a better idea of which main factors drive the primary production in EBUS ?**

1.6   Résumé Introduction (français).

L'objectif général de cette thèse est de comprendre le fonctionnement des écosystèmes côtiers à une échelle régionale. Du fait des nombreuses activités que les zones côtières abritent, il est primordial de mieux connaître ces zones autant d'un point de vue économique (pêche, aquaculture, activités de loisirs...) que de santé publique (prolifération d'algues toxiques, surveillance de pollution, qualité de l'eau...).

Les cycles biogéochimiques, en particulier ceux des zones côtières qui sont très dynamiques, régulent à long terme l'interaction entre océan et atmosphère et ainsi le climat global. Plus du quart des émissions humaines de gaz carbonique, gaz qui contribue au réchauffement global de la Terre, serait absorbé par les océans. Deux processus fixateurs de carbone interviennent : la pompe physico-chimique qui consiste en une dissolution du CO_2 dans les couches océaniques superficielles mélangées, et la pompe biologique qui est liée à l'activité photosynthétique du phytoplancton en surface créant de la matière organique, puis sa transformation en

matière inorganique et son enfouissement dans le sédiment. En retour, on observe une forte influence des phénomènes physiques et climatiques de petites et grandes échelles sur les écosystèmes régionaux, qui en modifie leur productivité. Cependant les interactions entre phénomènes physiques et écosystèmes à petite échelle sont mal connues. Mieux connaître le fonctionnement des écosystèmes régionaux et de la pompe biologique est aussi un objectif important pour l'étude globale du climat futur.

Nous proposons dans ce travail d'analyser l'influence des processus physiques à petite échelle sur les écosystèmes planctoniques dans les zones d'upwelling de bord Est.

En océanographie, de nombreuses échelles spatio-temporelles et leur processus associés coexistent et interagissent. Si les cascades d'énergie des grandes vers les petites échelles sont bien documentées, les cascades inverses existent aussi et l'influence des petites échelles sur la dynamique à grande échelle et basse fréquence et un phénomène maintenant bien connu. Dans ce travail nous nous concentrons sur les processus océaniques à mésoéchelle (tourbillons, fronts, filaments,...) car ils représentent la source principale de variation d'origine physique pour les écosystèmes régionaux. Les échelles auxquelles on s'intéresse dans ce travail concernent donc des périodes typiques d'évolution temporelle allant de l'heure à plusieurs mois et des variations spatiales du kilomètre à quelques centaines de kilomètres.

De nombreuses études ont déjà démontré l'importance des processus à mésoéchelle sur l'écosystème de l'océan ouvert. Plusieurs approches ont permis de mettre en évidence divers phénomènes. Les tourbillons sont responsables de la distribution chaotique observée du phytoplancton dans l'océan. Le fort mélange horizontal dû à ces structures répartit les traceurs dans l'océan suivant des schémas complexes où des zones de convergence et divergence sont observées, résultant en une haute variabilité spatiale du plancton. Les tourbillons sont aussi responsables d'un transport horizontal en leur cœur : ils emprisonnent des eaux dans un environnement puis se déplace dans l'océan de surface vers d'autre zones advectant les eaux qu'ils contiennent. Cet effet est très significatif dans les zones d'upwelling qui présentent une forte occurrence de tourbillons et structures filamentaires qui exportent l'intense production côtière vers l'océan du large appauvri. Les structures à mésoéchelle influencent également la composition des écosystèmes planctoniques : il a été observé que les structures filamentaires favorisent la coexistence de plusieurs espèces à différents endroits du filament. Le deuxième effet très important de ces processus concerne l'induction de vitesses verticales, qui peuvent

enrichir la couche euphotique en nutriments et ainsi favoriser le développement de phytoplancton. Cet effet a été largement étudié et il a été montré que sa prise en compte sur des simulations à l'échelle d'un bassin permet de clore le budget de phytoplancton jusqu'ici non résolu. Plusieurs auteurs ont proposé des mécanismes qui expliquent la création de vitesses verticales associées à des tourbillons et des structures frontales à mésoéchelle. Malgré la diversité des mécanismes mis en évidence, il apparaît clairement que les processus à mésoéchelle ont une influence majeure sur l'évaluation de la production des écosystèmes planctoniques. L'effet de tous ces processus a été largement étudié dans l'océan ouvert, mais relativement peu dans les zones côtières, en particulier les upwellings. Des observations récoltées dans la zone de transition entre l'upwelling côtier et l'océan du large avaient suggéré l'impact des processus à mésoéchelle comme les filaments sur les échanges côte-large. Quelques études récentes de modélisation réaliste se sont focalisées sur l'écosystème planctonique, mais sans détailler l'effet ni les processus des interactions biologie/physique.

Il apparaît donc opportun de se focaliser sur la variabilité locale biogéochimique des upwelling côtiers, sur l'influence des processus physiques à mésoéchelle, et sur les facteurs qui régissent leur production.

Les systèmes d'upwellings de bord Est (EBUS pour Eastern Boundary Upwelling Systems) sont parmi les zones les plus productives de l'océan mondial et sont constitués des systèmes du Benguela et des Canaries/Péninsule Ibérique dans l'océan Atlantique, ainsi que de Californie et de Humboldt dans l'océan Pacifique. Bien qu'ils représentent moins de 1% de la surface de l'océan global, ils abritent environ 10% de la production primaire et environ 1/5 des pêcheries mondiales. Ils ont donc un rôle écologique et socio-économique primordial. Ces bandes côtières s'étendant au-delà du plateau continental et sur quelques milliers de kilomètres en latitude sont situées sur les bords Est des bassins océaniques, de part et d'autre de l'équateur. D'intenses vents dominants soufflant toute l'année créent, sous l'influence de la rotation de la Terre, la dérive d'Ekman des couches superficielles vers le large, remplacées à la côte par des remontées d'eau profonde, froide et riche en nutriments qui supportent une production biologique importante. Cette forte productivité profite à l'écosystème entier et ces zones sont caractérisées par la présence de nombreuses espèces de poissons pélagiques ainsi que de prédateurs marins supérieurs.

La position géographique des EBUS et des facteurs locaux (vents, relief de la côte,...) contrôlent l'intensité des différents upwellings. Ils sont souvent latitudi-

nalement divisés en plusieurs provinces ayant un fonctionnement biologique spécifique. La proximité de la côte, sa morphologie variable ainsi que la bathymétrie complexe induisent une forte variabilité de l'intensité au sein de l'upwelling et l'occurrence de nombreuses structures physique de méso-échelle qui interagissent avec l'écosystème. La zone de transition (Coastal Transition Zone) est une région très dynamique caractérisée par de nombreux tourbillons et filaments à méso et sub-mésoéchelle. Ces structures engendrent un transport vers le large des écosystèmes côtiers et influencent les communautés planctoniques présentes, mais aussi les populations de poissons, leurs larves, jusqu'au prédateurs supérieurs.

Les EBUS jouent un rôle crucial dans l'échange de gaz avec l'atmosphère, particulièrement de CO_2 et N_2O. Leur production biologique élevée souvent supérieure à la respiration globale favorise un comportement de puits de carbone. Cependant, les remontées d'eau profonde riches en CO2 à la surface entraînent un dégazage vers l'atmosphère résultant ainsi souvent en un comportement de source de carbone. Des études récentes ont mis en évidence la production par certains groupes de phytoplancton de diméthylsulphide, gaz impliqué dans le cycle du soufre également connu pour fortement influencer l'atmosphère. Les Zones de Minimum d'Oxygène (OMZ) typiques de l'océan tropical ont aussi été documentées dans les EBUS. Elles sont le siège de nombreux processus biogéochimiques complexes tels la nitrification, la dénitrification et plus récemment l'anammox dans les sédiments mais aussi dans la colonne d'eau. De manière générale, les processus ayant lieu à l'interface sédiment / colonne d'eau sont cruciaux pour la compréhension des cycles biogéochimiques dans les EBUS, bien qu'ils restent encore mal connus. L'expansion future des OMZ prévue par certaines études, ainsi que les fortes mortalités de biomasses halieutiques causées par des épisodes anoxiques, justifient l'intérêt grandissant pour ces problématiques. Siège de ces processus complexes, les EBUS jouent donc un rôle primordial dans les cycles biogéochimiques globaux.

Le but de ce travail est **de comprendre et d'estimer les effets des processus physiques à mésoéchelle sur l'écosystème planctonique dans les zones d'upwelling**. Pour répondre à cette problèmatique générale, le manuscrit a été organisé comme suit :

- Le chapitre 2 présente brièvement **les outils utilisés** dans ce travail pour étudier les processus physiques et biogéochimiques à mésoéchelle.

- Le chapitre 3 concerne **l'étude conjointe de la variabilité spatio-temporelle à mésoéchelle des propriétés physiques et biogéochim-**

iques de l'Upwelling de la Péninsule Ibérique. Basé sur une campagne océanographique multidisciplinaire, **peut-on expliquer les variations spatiales des communautés planctoniques en lien avec leur environnement physique ?**

- L'étude de l'impact des processus physiques sur la biologie requiert une bonne compréhension de la physique de l'océan côtier, coeur de ce chapitre 4. **Quelles sont les origines et les caractéristiques physiques des structures frontales et filamentaires couramment observées dans les upwellings ?**

- Le chapitre 5 reprend la thématique générale d'un point de vue comparatif entre les quatre EBUS. **Quelle est l'importance relative entre le transport d'Ekman et les processus à mésoéchelle sur l'activité biologique ? Quel est l'impact de la turbulence horizontale induite par les tourbillons ? Peut-on mieux comprendre les principaux facteurs qui gouvernent la production primaire des EBUS ?**

Chapter 2

Materials and Methods: a set of complementary tools to study the influence of physical processes on ecosystem dynamics at mesoscale.

In Oceanography, as well as in Geosciences in general, we are facing an important scale issue. How can we get a precise picture of the world ocean, with our human - tiny - point of view ? In the past decades, oceanographers were using ponctual measurements made from ship surveys, along with laboratory experiments, to extrapolate their results to larger scales. Then they increased the amount of data available by providing scientific sensors to commercial ships, allowing a better coverage of the world ocean, but only along commercial routes and at the surface.

Of course some people already thought of using aerial photography, that was developed for military monitoring and reconnaissance purposes during the World War I and the Cold War, but this stayed quite anecdotal. The development of satellites (initially for military purposes) in the second half of the 20th century (with a peak during the Cold War) allowed remote sensing to spread and progress to a global scale. Instrumentation onboard various Earth observing and weather satellites provided global measurements of various data for civil, research and military purposes.

Simultaneously to the satellite development, computing sciences were also benefiting from this huge military effort in the 20th century. Computer simulation was developed hand-in-hand with the rapid growth of computers, following their first large-scale deployment during World War II to model the process of nuclear detonation. Computer simulations are now used in a variety of domain, going from mathematical theory, physics, chemistry, through biological and ecological sciences, until social sciences.

This work is concentrated on mesoscale processes and oceanic turbulence, which cover spatio-temporal scales ranging from one to hundreds of kilometers and from hours to weeks, and which strongly modulate the structure, biomass and rates of marine ecosystems (see chapter 1). In this chapter, we present briefly a set of complementary tools, from satellite data to numerical models, that are being used to study mesoscale oceanic processes.

Contents

2.1 *In-situ* data from oceanographic surveys.

Oceanographic surveys are the most direct way to collect data of the ocean. The general sampling strategy (stations location and duration) of sea surveys is generally designed before the campaign itself. As a consequence, it is highly depending on the general *a priori* knowledge we have of the area. Another approach can be a lagrangian study, where the whole campaign is designed while following a water mass, tracked by drifters released at the beginning of the survey. In our case, the strategy was decided prior to the campaign itself (number and type of transects performed) but precise locations of stations and sections, as well as the sequence of events, were adjusted onboard twice a day, by using real-time acquisition of satellite data of Sea Surface Temperature (SST) and chlorophyll *a*. This strategy was a good compromise to obtain a nice data set on selected processes:

- North-South variability,

- Cross-shore gradient,

- Development of a filament,

- Diurnal cycle at selected location.

2.1.1 Data from CTD sensors.

Physical observations from MOUTON 2007 were made using a Conductivity-Temperature-Depth (CTD) instrument, a Lowered Acoustic Doppler Current Profiler (LADCP) functioning at $300 \, \mathrm{kHz}$, and also two Vessel Mounted Acoustic Doppler Current Profiler (VMADCP), functioning respectively at $38 \, \mathrm{kHz}$ and $150 \, \mathrm{kHz}$. A Seasoar was also onboard (see fig. 2.1), which allows high resolution coverage of hydrography, but data are not presented in this manuscript.

Simultaneously, a set of biogeochemical sensors were also deployed on the CTD-rosette (see fig. 2.2). We lowered two fluorometers (a Chelsea Aqua 3 for chlorophyll *a* and a Chelsea Aquatrack a for UV measurements, which can be converted to Colored Dissolved Organic Matter), a dissolved oxygen sensor SBE43 and a Turbidimeter CSS-631. There were also few optical sensors: a transmissiometer Wetlab for light transmission and attenuation, a Photosynthetically Active Radiation sensor (PAR) and a Surface PAR sensor. The sampling was adjusted to 24 scans per second and the lowering speed of the CTD was about $0.5 \, \mathrm{m/s}$. The CTD casts were

Figure 2.1: A picture of the Seasoar used onboard MOUTON 2007 survey. Towed behind the ship at 8 knots, it measures conductivity (salinity), temperature and pressure along a sinusoidal route in the water column.

limited to the upper 200 m (or above when the bathymetry was shallower) due to the maximum working depth of some biogeochemical sensors.

2.1.2 Data from water sample measurements and zooplankton net.

Seawater samples were collected at 1387 stations using a CTD-rosette system equipped with 12 ten litres Niskin bottles (see fig. 2.2). At each station, up to five depths in the water column were sampled: the surface (1 m), the upper thermocline, the deep chlorophyll maximum, the lower thermocline and an additional depth of interest. The conducting cable allowed us to monitor all measured variables during the descent and to determine at the same time our depths of interest. Then water samples were collected on the way up at the depths selected during the CTD descent. Although there was a small time-lag between the descent and the ascent, and although internal waves are known to be conspicuous in this area, the main structure were quite successfully sampled.

Nutrient analysis:
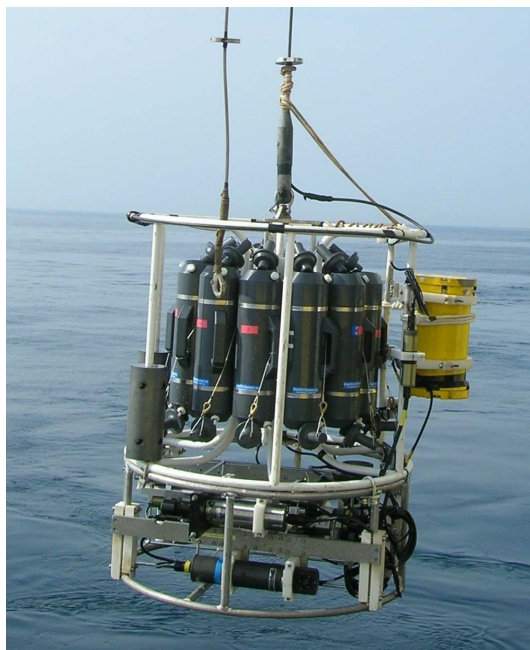
Figure 2.2: A picture of the CTD and rosette with Niskin bottles used onboard MOUTON 2007 survey. Grey containers are the Niskin bottles, yellow probe on the right is the LADCP, below are found all biogeochemical sensors.

To collect seawater for nutrient analysis, the container was first precautiously rinsed with the corresponding water and then samples were collected and identified. The 612 samples where then stored at $-20°$C for later analysis.

In the laboratory, the common nutrients concentrations - namely nitrate, silicate and phosphate - were determined by colorimetric methods, following *Aminot and Kerouel.* [2007]'s method. All solutions were prepared in Milli-Q water (Millipore Milli-Q water system) with reagent analytical grade salts. Artificial seawater for standards calibration, as well as for nitrate, silicate and phosphate samples, was prepared at a salinity of 34.7 g/l with sodium chloride (NaCl). All calibrations of working standards were prepared as described in the WOCE operation and method manual *Gordon et al.* [1995]. The automated procedure for the detection of nitrate and nitrite uses the procedure where nitrate is reduced to nitrite by a copper-cadmium reduction column. The nitrite then reacts with sulfanilamide under acidic conditions to form a diazo compound. This compound couples with N-1-naphthylethylene diamine dihydrochloride to form a purple azo dye, which is measured at 540 nm. The detection of soluble silicates (silicic acid) is based on the reduction of silicomolybdate in acidic solution to molybdenum blue by ascorbic acid. Oxalic acid is introduced in the sample stream before the addition of ascorbic acid to minimize interference from phosphates. The absorbance is then measured

at 820 nm. To measure ortho-phosphate, a blue color entity is formed by the re-action of ortho-phosphate, molybdate ion and antimony ion followed by reduction with ascorbic acid at a $pH < 1$. The reduced blue phospho-molybdenum complex is measured at 820 nm.

HPLC phytoplankton pigments analysis:

The water samples for pigment analysis were collected at 2 or 3 depths and then were vacuum filtered through 25 mm diameter Whatman GF/F glass fibre filters (0.7 μm particle retention size). Filtered volumes varied between 3 l in the offshore waters and less than 1 l for some stations inside the coastal upwelling zone. The filters were immediately stored in liquid nitrogen at $-80°$C until analysis on land. Among the total 219 samples, 16 were sampled in duplicate and then analyzed quasi-simultaneously by the SHOM Brest and by the Oceanography laboratory in Villefranche/Mer in order to perform a cross-validation between both laboratories.

In the laboratories, we determined phytoplankton pigments composition by HPLC methods. The filters were extracted at $20°$C in 3 ml methanol (100 %), dis-rupted by sonication and clarified one hour later by vacuum filtration through Whatman GF/F filters. The extracts were rapidly analyzed (within 24 h) by High Performance Liquid Chromatography (HPLC) with a complete Agilent Technologies system (comprising LC Chemstation software, a degasser, a binary pump, a refrig-erated autosampler, a column thermostat and a diode array detector). The pigments were separated and quantified following an adaptation of the method described by *Heukelem and Thomas.* [2001]. Modifications to this method allowed for increased sensitivity in the analysis of ultra-oligotrophic waters. The extraction used a nar-row reversed-phase C8 Zorbax Eclipse XDB column which was maintained at $60°$C and the separation was achieved within 28 min. A diode array detector allowed for the absorption of most pigments to be detected at 450 nm, while chlorophyll *a* and its derivatives were detected at 667 nm and bacteriochlorophyll *a* at 770 nm. The diode array absorption spectra of each peak were used for identification purposes. Pigment concentrations (in $mg.m^3$) were calculated from the peak areas with an in-ternal standard correction (Vitamin E acetate, Sigma) and external calibration. This method has proven to be satisfactory in terms of resolution, sensitivity, accuracy and precision *Ras et al.* [2008], with the detection of about 13 separate phytoplank-ton pigments with a lower limit of detection for chlorophyll *a* of 0.0001 $mg.m^3$ and with an injection precision of 0.4 %.

Dissolved oxygen titration:

The amount of dissolved oxygen is a measure of the biological activity of the water mass and results from the balance between respiration and PhotoSynthesis in the ocean. The oxygen probe mounted on the rosette was calibrated by independent sampling and Winkler titration following *Labasque et al.* [2004] (and references therein). Precautions must be taken to ensure the sample is not ventilated during collection and that no bubbles are trapped in the container. An excess of manganese (II) salt, iodide I^- and hydroxide HO^- ions are added to the seawater sample causing a white precipitate of $Mn(OH)_2$ to form. This precipitate is then oxidized by the dissolved oxygen in the water sample into a brown manganese precipitate. In the next step, a strong acid (either hydrochloric acid or sulfuric acid) is added to acidify the solution. The brown precipitate then converts the iodide ion I^- to Iodine. The concentration of dissolved oxygen is directly proportional to the titration of Iodine with a thiosulfate solution.

Zooplankton biomass analysis:

Zooplankton samples were collected during day and night at one CTD stations out of two or three, with the highest possible frequency. A WPII plankton net (mouth surface of 0.2552 m^2, see Fig. 2.3) mounted with 200 µm mesh size was used, and towed vertically at around 1 m/s over the water column from 5 m above the sea bottom, or 70 m depth, up to the surface. To consider the right volume of filtered water, the effective depth of the tow is confirmed by the cable meter onboard. Once onboard, the net is rinsed with seawater from outside and the sample is collected in a bucket. This solution is then splitted into two parts, using a motoda box *Motoda* [1959]. Half of the sample is directly preserved in formaldehyde for later analysis, whereas the other half is fixed on a pre-weighted filter (200 µm) and conserved at $-20°$C in individual sterile cases.

Zooplankton samples fixed in formaldehyde were digitized using the Zooscan imaging system (*Grosjean et al.* [2004]; *Gorsky et al.* [2010]). Image processing was performed by Image J software using the Zooprocess interface (www.zooscan.com), enabling fast and reliable enumeration and measurement of objects. Prior to digitization the samples were rinsed in freshwater to remove formaldehyde and allow a safe analysis. It is critical to scan no more than 1000 to 2000 objects at once, depending on size, to obtain good quality images and data (*Gorsky et al.* [2010]). Thus, a Motoda splitter (*Motoda* [1959]) was used for subsampling. For each sam-

Figure 2.3: A picture of the zooplankton WPII net used onboard MOUTON 2007 survey.

ple the objects were carefully separated on the scanning cell to avoid as much as possible touching objects. The digitization generates 16 bits, 15x24 cm, 2400 *dpi* raw images, (pixel width of 10.58 μm). A metadata form compiling various information relative to the sample is associated with each image. Image processing consists in 4 steps: (i) conversion to 8 bits and normalization to full grey scale range, (ii) background homogenization, (iii) segmentation (extraction of objects, threshold 243), (iv) measurements on objects. At present 54 parameters including shape, grey scale, size, and complexity of the shape parameters are measured on each object. The outputs of the image processing are (i) a set of vignettes and (ii) an associated *.pid* file compiling the measurements for each object and information on the processing. When enough samples were scanned and processed, a random subset of vignettes was manually sorted into coarse faunistical groups (e.g. Copepods, Chaetognaths, etc...). A learning set was generated, using the set of sorted vignettes and associated data, with the software Plankton Identifier (*Gasparini* [2007]). This learning set allowed the automatic sorting of unidentified vignettes into the previously defined groups (*Gorsky et al.* [2010] for detailed description of the machine learning process associated with the Zooscan techniques). The automatic sorting outputs were then checked and corrected if needed by a trained taxonomist. In this work, we will only separate living objects from the non-living objects (marine snow, particulate organic matter...) to only quantify zooplankton individuals without detrital matter. The biomass of organisms was computed following an estimation of the biovolume

based on size measurements. For Copepods the biovolume was estimated using the major and minor axes of the best fitting ellipse (*Vandromme et al.* [2010]). For other organisms the biovolume was estimated using Equivalent Spherical Diameter, computed from the exact surface of the object (*Gorsky et al.* [2010]). We finally defined two classes of size, the small and big individuals, separated by a volume limit of 1 mm^3.

Another estimation of zooplankton biomass is the dry-weight. All pre-weighted filters conserved at $-20°$C were dried in an oven during 24 h at 60°C. Similar treatments had been applied to the filter itself before pre-weighting. Then each filter containing stuck-on dried zooplankton was weighted using a high precision scale. The dry-weight of zooplankton biomass was then estimated by subtracting the initial weight of the filter to the latter.

2.1.3 Other data in marine sciences.

In the previous sections, we summed up all *in-situ* data that are going to be used in this work. However, other means exist for collecting data in the ocean, from autonomous drifters, platform and floats. These tools are being improved intensively due to the miniaturization of electronical materials and sensors, as well as to the recent advances in the power supply (battery). Among others, we can cite the Gliders which are able to measure physical as well as biogeochemical variables (*Johnson et al.* [2009]) and PROVOR, APEX and SOLO floats (measuring physical variables and dissolved oxygen in the next future, all participating in the ARGO international program), and diverse other drifters (that drift in the surface or subsurface layers).

Before ending this subsection, experimental data are also a very important part of oceanographic research. Several laboratories are specialyzed in these thematics and are generally located on the seashore to have a permanent supply of seawater. Among other studies, we are able to grow certain planktonic species under controled conditions in order to test their response to specific environmental changes (for instance ocean acidification, or higher atmospheric CO_2). Mesocosms constitute a transition between *in-situ* and laboratory data: they consists in a culture system (large enclosure) placed in a protected natural area as an embayment where a pelagic ecosystem is developed (phytoplankton, zooplankton...) and can be studied under different conditions.

A few last words just to mention one of the most recent progress in Oceanography, the use of genomics technics. Oceanographers realized about a decade ago the

paramount importance of the microbial life (viruses and bacteria) in the ocean. Because of its diversity and its implication in oceanic ecosystems, there is an urgent need to further study these organisms. Recent advances in Genomics tools allow us to unveil the large role of microbes in biogeochemical cycles (oxygen, carbon, nitrogen, phosphorus...), associated with their extreme sensitivity and adaptability to changing environmental conditions.

2.2   Satellite data

In this section, satellite data used in this work are briefly described. We first present the Ocean Color data that provide us a good estimate of the chlorophyll a content of the surface ocean, and then the Altimetry data that produce Sea Surface Height (SSH) fields. Associated with scatterometer data, altimetry data are derived to infer a surface velocity field, containing Geostrophic and Ekman currents. The computation applied to the raw data to obtain the velocity fied is also detailed.

2.2.1   Ocean Color.

It is said that the ocean reflects the color of the sky, but even on cloudless days the color of the ocean is not a consistent blue. All material, dissolved or suspended particles, present in a water mass will alter its color.

More generally, when an incident light reaches a surface, a part is absorbed by the surface, whereas another part is reflected, which provides its color. The Ocean Color uses passive teledetection principles to estimate the ocean color: the remote sensor measures the solar reflected light by terrestrial and oceanic surfaces. In a cloud free sky, the measured signal will be constituted by the ocean reflectance, but also by the atmospheric diffusion and reflectance. The signal has to be corrected to extract only the oceanic signal.

The color of the ocean is determined by the interactions of incident light with dissolved substances or particles present in the water. The most significant constituents are free-floating photosynthetic organisms (phytoplankton) and inorganic particles. Phytoplankton contain chlorophyll a (as well as other optically active pigments), which absorbs light at blue and red wavelengths and transmits in the green. Particulate matter as sediment load from coastal inputs, can reflect and absorb light, which reduces the clarity (light transmission) of the water. Substances

dissolved in the water, such as chemical emissions, can also affect its color. For instance *Ohde et al.* [2007] develop an algorithm applied to the medium resolution imaging spectrometer (MERIS, ocean color) Level-2 products to identify sulphur discoloration in the surface water off Namibia. Satellite instruments measure the amount of reflected light of different wavelengths. Ocean color being related to the presence of the constituents described above, it may therefore be used to calculate the concentrations of material in surface ocean waters and the level of biological activity. Ocean color observations made from space provide a global picture of biological activity in the world's oceans that is not accessible from ships or shore. In true color mode, very productive waters with a high concentration of plankton appear blue-green, whereas very pure waters appear deep-blue, almost black.

The measurements of ocean color are based on electromagnetic signal of 400-700 nm wavelength. This energy is emitted by the sun, transmitted through the atmosphere and reflected by the earth surface. Chlorophyll a is a primary source of green color. Semi-empirical equations can be used to estimate the concentration of chlorophyll a (and its degradation products) from satellite measurements of backscattered sunlight using several (typically two or three) wavebands centered in the blue and green regions of the spectrum. Sunlight backscattered by the atmosphere contributes 80-90 % of the radiance measured by a satellite sensor at these key wavelengths. Such scattering arises from dust particles and other aerosols, and from molecular (Rayleigh) scattering. However, the atmospheric contribution can be calculated and removed if additional measurements are made in the red and near-infrared spectral regions (e.g., 670 and 750 nm). Since blue ocean water reflects very little radiation at these longer wavelengths, the radiance measured is due almost entirely to scattering by the atmosphere. Long-wavelength measurements, combined with the predictions of models of atmospheric properties, can therefore be used to remove the contribution to the signal from aerosol and molecular scattering.

The equation below represents the total reflectance R_t measured at a certain wavelength λ by the satellite and its decomposition:

$$
\begin{aligned}
R_t(\lambda) &= \pi \frac{L_t(\lambda)}{F_0(\lambda)\cos(\theta_0)} \\
\text{where } R_t(\lambda) &\simeq R_r(\lambda) + R_a(\lambda) + R_{ra}(\lambda) + t(\lambda)R_{wc}(\lambda) + t(\lambda)R_{rsw}(\lambda)
\end{aligned}
$$

$$(2.1)$$
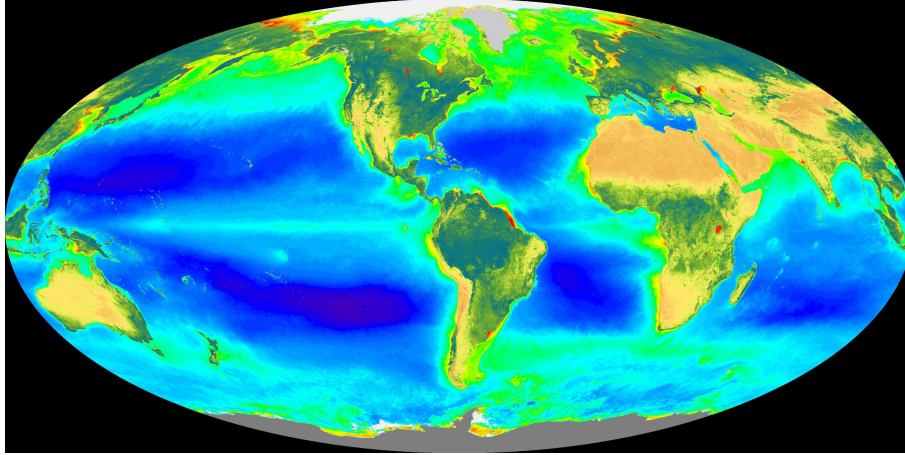
Figure 2.4: Earth planet with the continental and marine biosphere colored and averaged over one year of SeaWiFS sensor data. In the ocean, blue color indicates poor chlorophyll a concentrations (e.g. oligotrophic gyre), whereas green to red colors indicate high chlorophyll a concentrations (e.g. coastal areas, EBUS, high latitude spring bloom, equatorial upwelling...)

In the first equation, L_t is the total measured radiance, F_0 is the total extraterrestrial irradiance and θ_0 is the solar angle. Then, the total reflectance is decomposed into: R_r the Rayleigh diffusion contribution (air molecules), R_a due to multiple diffusion from aerosols, R_{ra} the interaction between Rayleigh and aerosols, R_{wc} the contribution of the whitecaps at the sea surface, and R_{rsw} the contribution of the sea water.

The satellite will measure the total radiance L_t (see equations 2.1) that contains all these signals. We are interested in the last contribution, the term R_{rsw}. To extract this information from the raw measurement, some corrections are applied to substract the effect of the atmosphere. Then a bio-optical algorithm is applied to this term to derive the chlorophyll a concentrations.

Additional methods were also developed to extract from ocean color other information about the planktonic life. Ocean color signal can be used to infer Particulate Organic Carbon (*Stramski et al.* [1999]), Primary Production (*Carr et al.* [2006]), Phytoplanktonic Functional Types (*Alvain et al.* [2006]; *Brewin et al.* [2010]; *Kostadinov et al.* [2010]), Coloured Dissolved Organic Matter (*Coble* [2007]) and phytoplankton physiological status (*Behrenfeld et al.* [2009].

In our studies, phytoplankton pigment concentrations are obtained from monthly SeaWiFS (Sea-viewing Wide Field-of-view Sensor) products of level 3 binned data, generated by the NASA Goddard Earth Science (GES)/ Distributed Active
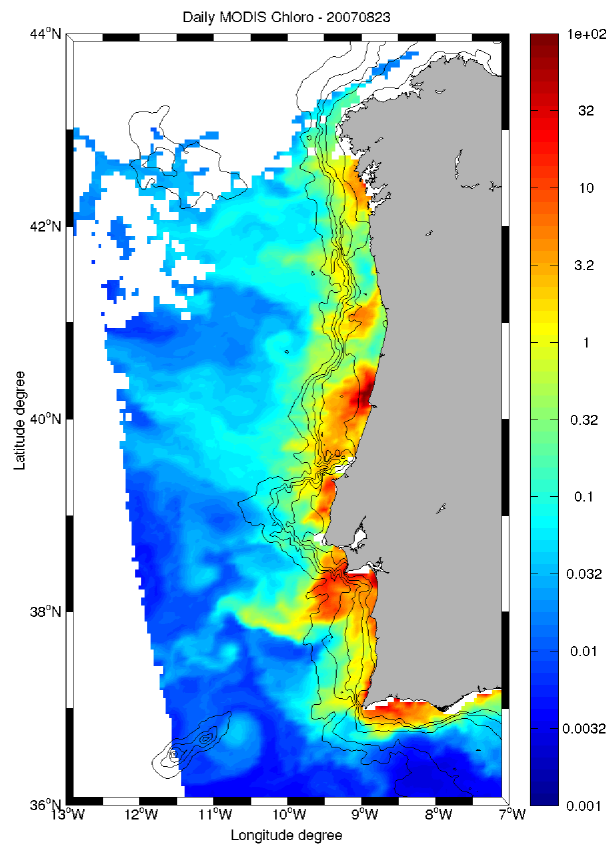
Figure 2.5: Chlorophyll-a in mg/m^3 from space (MODIS Aqua) for day 08/23/2007 over the Iberian Peninsula Upwelling System. White areas are clouds and black contouring represent the bathymetry.

Archive Center (DAAC) with reprocessing 5.1. The bins correspond to grid cells on a global grid, with each cell approximately 9 by 9 km. We also used MODerate resolution Imaging Spectroradiometer (MODIS) sensor on the Aqua satellite, which contains two radiometers. They acquire data in 36 spectral bands from 0.4 μm to 14.4 μm. Two bands are imaged at a nominal resolution of 250 m at nadir, with five bands at 500 m, and the remaining 29 bands at 1 km. The orbital travel provides global coverage every one to two days. In contrast to SeaWiFS, all MODIS data including high-resolution (1 km) data are processed to Level 2.

2.2.2 Ocean altimetry.

a - Generalities and basic principles:

Altimetry satellites basically determine the distance from the satellite to a target surface by measuring the satellite-to-surface round-trip time of a radar pulse. However, this is not the only measurement made in the process, and a lot of other information can be extracted from altimetry. The magnitude and shape of the echoes (or waveforms) also contain information about the characteristics of the surface which caused the reflection. The best results are obtained over the ocean, which is spatially homogeneous, and has a surface which conforms with known statistics. Surfaces which are not homogeneous and contain discontinuities or significant slopes, such as ice, rivers or land surfaces, make accurate interpretation more difficult.

Several different frequencies are used for radar altimeters. Each frequency band has its advantages and disadvantages : sensitivity to atmospheric perturbations for Ku-band, better observation of ice, rain, coastal zones, land masses... for Ka-band.

Radar altimeters permanently transmit signals to Earth, and receive the echo from the reflecting surface. The satellite orbit has to be accurately tracked (Doris system allows a very precise location of the satellite on its orbit) and its position is determined relative to an arbitrary reference surface, an ellipsoid. The sea surface height (SSH) is the deviation from the sea surface to a reference ellipsoid or a mean sea surface (see Fig. 2.6).

It is used today for a large panel of applications, going from large scale circulation, tides, mean sea level, continental water monitoring, and last but not least, the study of mesoscale circulation.
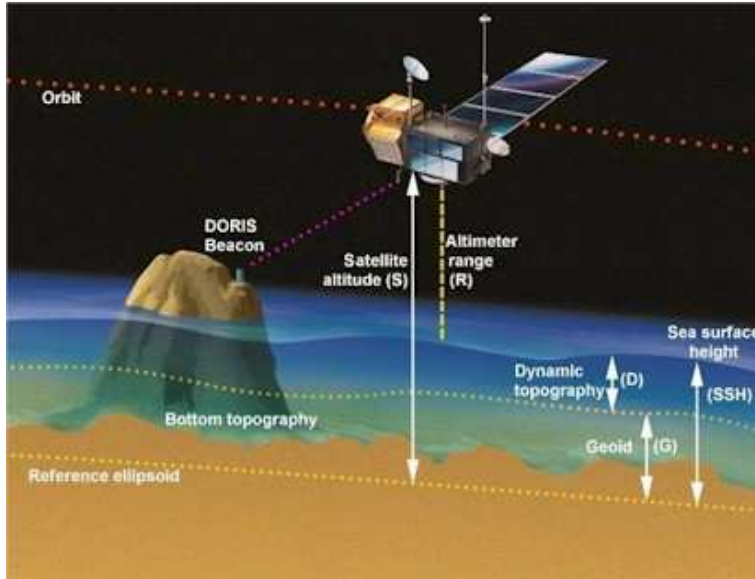
Figure 2.6: Cartoon showing the basic principle of Altimetry. The radar transmits and receives the echo from the ocean surface. The satellite orbit is tracked by GPS to determine its position relative to the ellipsoid. The Sea Surface Height is the distance from the measured sea surface to a reference ellipsoid.

The combination of several satellites enables high-precision altimetry and also allow a compromise between spatial resolution and temporal resolution. Topex/Poseidon-ERS and Jason-Envisat are fine examples of how altimetry satellites can operate together. After more than 15 years of progress in altimetry, data coming from at least two altimetry satellites in working order are needed to ensure a sufficient spatial resolution for mesoscale observation.

b - Sea Surface Height, Quikscat wind stress and derived geostrophic currents:

In this section, multi-satellite data are used to infer mesoscale velocity fields of the surface ocean in two dimensions.

The satellite surface currents we used, $U_t(u_t, v_t)$ in $m.s^{-1}$, are the sum of the gridded geostrophic velocities, $U_g(u_g, v_g)$ and the Ekman currents at 15 m depth, $U_e(u_e, v_e)$ (*Sudre and Morrow* [2008]).

The geostrophic currents are calculated from the a Sea Surface Height composite field. The Mapped Sea Level Anomaly (MSLA) from the Data Unification and Altimeter Combination System (DUACS) are combined with the mean dynamic topography RIO05 (*Rio et al.* [2005]) to obtain a time-variable sea surface height

(SSH) data product. The MSLA product for the 1999-2006 period merges altimetric measurements from five altimeter missions (Topex/Poseidon, ERS1 and 2, Geosat Follow-on, Envisat and Jason-1). The mean dynamic topography (MDT) is the mean sea surface height that is due to the permanent ocean circulation, with the marine geoid removed. The MDT product used hereafter is derived from the RIO05 product, which is based on multiple *in situ* and satellite data sets, including GRACE gravity data. We use the weekly DUACS SSH data that has a spatial resolution of $1/3°$ projected onto a Mercator grid. We convert this spatial resolution onto a $1/4°$ regular grid using a standard bilinear interpolation algorithm, which is more easily compared to other satellite data products (e.g. $1/4°$ resolution SST or Ocean Colour).

Firstly, we calculate the total SSH as the sum of the altimetric MSLA and the RIO05 MDT. The SSH gradients ($\frac{\partial h}{\partial y}, \frac{\partial h}{\partial x}$) are calculated linearly from the surrounding grid points using a finite difference formulation. Outside the equatorial band ($5°$S to $5°$N), the surface currents are calculated from these SSH gradients, assuming a geostrophic balance:

$$
\begin{aligned}
u_g &= -\frac{g}{f}\frac{\partial h}{\partial y} \\
v_g &= \frac{g}{f}\frac{\partial h}{\partial x}
\end{aligned}
$$

(2.2)

Where $f = 2\Omega\sin\varphi$ the Coriolis parameter depending on latitude, g is the acceleration due to gravity and h is the height of the sea surface above a level surface (SSH).

Ekman currents are coming from Quikscat wind stress fields. QuikSCAT was launched by the National Aeronautics and Space Administration on 19 June 1999 (http://winds.jpl.nasa.gov/missions/quikscat/index.cfm). The mission carries a Ku-band microwave scatterometer (SeaWinds) that measures near-surface wind stress and direction under all weather and cloud conditions, and has daily coverage over 92 % of the global ice-free oceans. We use the QuikSCAT mean wind field (QSCAT MWF) global $1/2°$ resolution product, which provides daily and weekly wind stress fields and is processed and distributed by the Centre ERS d'Archivage et de Traitement. The mean Ekman currents at 15 m are computed using the Ekman spiral

theory:

$$(u_e \; + \; i \; v_e) \quad = \quad B \; e^{i\theta} \; (\tau_x \; + \; i \; \tau_y)$$

(2.3)

The amplitude B is 0.3 $m.s^{-1}.Pa^{-1}$ and θ is the turning angle relative to the wind direction: $55°$ to the right (left) of the wind in the northern (southern) hemisphere at 15 m depth outside the equatorial band ($25°$N - $25°$S). Inside this equatorial band, B and θ vary with latitude as detailed by *Lagerloef et al.* [1999]. Wind stress (τ_x, τ_y) is in $N.m^{-2}$. As for the altimetric products, a bilinear interpolation is performed on the daily and weekly QuikSCAT MWF products to obtain a similar resolution on a $1/4°$ regular grid.

For both components, we have singularities near the equator because f vanishes for the geostrophic current calculation, whereas Ekman currents diverge, which require special attention. But in our case we used only velocity fields outside this equatorial band. Further details can be found in *Lagerloef et al.* [1999]; *Sudre and Morrow* [2008].

Finally, $U_t(u_t, v_t)$ in $m.s^{-1}$ (see fig. 2.7) are obtained by a simple sum:

$$\begin{aligned} u_t &= u_g \; + \; u_e \\ v_t &= v_g \; + \; v_e \end{aligned}$$

(2.4)

This current product was validated by *Sudre and Morrow* [2008] with different types of *in situ* data such as Lagrangian buoys, ADCP, and current-meter float data. In all areas where they will be used, zonal and meridional components show an average correlation between 0.54 and 0.8 when comparing with *in situ* data. The position and strenght of dynamical structures such as fronts and eddies are also generally in good agreement with available observations.

2.3 The Finite-Size Lyapunov Exponents: a lagrangian powerful tool.

In this thesis, we used the computation of Finite-Size Lyapunov Exponents (FSLE) that allow us to reveal mesoscale structures such as fronts and eddies in a
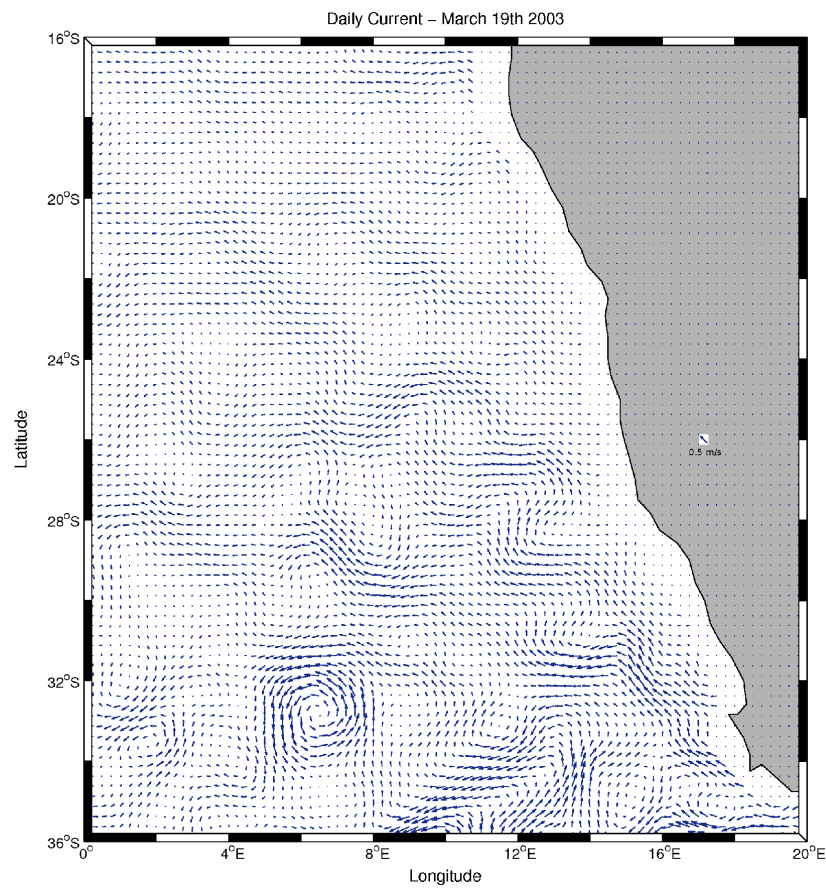
Figure 2.7: A snapshot of the surface current $U_t(u_t, v_t)$ for the Benguela area derived from satellite altimetry and scatterometry for day March 19, 2003. Mesoscale eddies are clearly visible, especially in the southern area.

2D flow. They are also used to characterize transport by these structures in surface layers as well as to measure the horizontal mixing in a given spatial area.

In this chapter we first introduce the general concepts and tools, inspired from the theory of nonlinear dynamical systems, which will be used to understand the global geometry of fluid flows. Then we describe how it allows a quantitative analysis of transport and mixing in oceanic process.

2.3.1 Eulerian / Lagrangian description.

The description of fluid motion can be addressed following two different ways: one can evaluate the velocity, pressure and density fields at fixed spatial locations in the fluid, or either follow the trajectory of each fluid particle. The first approach is called *Eulerian* and the second one *Lagrangian*. In principle both are equivalent, and if we denote by $v(x, t)$ the Eulerian velocity field, providing us the value of the fluid velocity at any space-time point (x, t), then the motion of a fluid particle with initial localization $x(0)$ is given by:

$$\frac{dx}{dt} = v(x, t).$$
(2.5)

This expression establishes the physical connection between the Eulerian and Lagrangian description. It clearly says that when a particular fluid particle is known to be at a specific space-time point, its Lagrangian velocity must be equal to the Eulerian field value at that space-time point.

2.3.2 Dynamical systems and manifolds.

A dynamical system of general form is often expressed by

$$\frac{dx}{dt} = v(x(t), t)$$
(2.6)

$$x(t_0) = x_0$$
(2.7)

In the differential Eqs. (2.6), (2.7), t represents time and it is the independent variable, and the dependent variable, $x(t)$, represents the state of the system at time t. The vector function $v(x, t)$ typically satisfies some level of continuity.

As time evolves, solutions of Eqs. (2.6), (2.7) trace out curves. In dynamical systems terminology, solutions flow along their trajectory. Numerical solutions of Eqs. (2.6), (2.7) can almost always be found by numerical integration of v, however such solutions are not convenient for general analysis. While the exact solution of Eqs. (2.6), (2.7) would be ideal, the analytic solution of Eqs. (2.6), (2.7) can not be calculated in general.

If v is independent of time t, the system is known as time-independent, or autonomous, and there are a number of standard techniques for analyzing such systems. The global flow geometry can be understood by studying invariant manifolds of the fixed points of Eqs. (2.6), (2.7), in particular stable and unstable manifolds often play a central role.

A fixed point of v is a point x^c such that $v(x^c) = 0$. The stable manifolds of a fixed point x^c are all trajectories which asymptote to x^c when $t \to \infty$. Similarly, the unstable manifolds of x^c are all trajectories which asymptote to x^c when $t \to -\infty$. Often, stable and unstable manifolds separate distinct regions with different flow geometry. The stable and unstable manifolds can help uncover the global flow geometry of a dynamical system (see Fig. 2.8). The notion of stable and unstable manifolds becomes ambiguous for time-dependent systems, which are the most relevant for us. Such systems rarely even have fixed points in the traditional sense. Many dynamical systems of practical importance are time-dependent, especially in cases where the dynamical system represents the motion of a geophysical fluid. These time-dependent dynamical systems typically have regions of dynamically distinct behavior which can be thought of as being divided by separatrices. However, for such systems these regions change over time, and hence so do the separatrices. We consider a generic hyperbolic point and its associated stable and unstable manifolds (see Fig. 2.8).

If we integrate two points that are initially on either side of a stable manifold forward in time, then these points will eventually diverge from each other. Likewise, if we started with two points on either side of an unstable manifold, then these points would quickly diverge from each other if integrated backward in time. This is why these manifolds are often called separatrices, since they separate trajectories. We would like to define such structures by looking at the divergence or stretching between trajectories. To find separatrices that are analogous to stable manifolds, we measure stretching forward in time and to find separatrices that are analogous to unstable manifolds, we measure stretching backward in time (Fig. 2.8). However, the analogy between these separatrices and traditional definitions of stable and
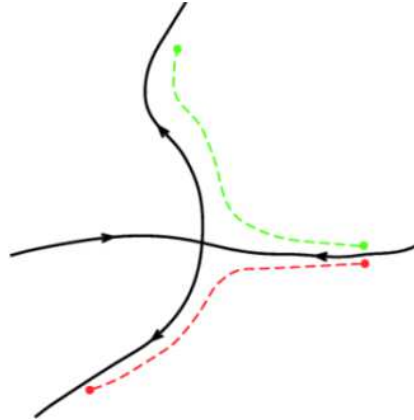
Figure 2.8: Two points on either side of a separatrice will diverge from each other. The quasi vertical separatrice is equivalent to the unstable manifold, whereas the quasi horizontal separatrice represents the stable manifold. The intersection between the two black lines is the hyperbolic point.

unstable manifolds is not straightforward. For time-dependent flows, we refer to theses separatrices as Lagrangian Coherent Structures (LCS), a common name in fluid mechanics that will be defined in the following. While there are numerous ways to measure stretching, we have found that the Local Lyapunov Exponent (Finite-Time Lyapunov Exponent and Finite-Size Lyapunov Exponent) provides the best measure when trying to understand the flow geometry of general time-dependent systems.

2.3.3 The non asymptotic Finite-Size Lyapunov Exponents.

The existence of chaotic behavior systems was first introduced by the French mathematician Henri Poincaré in the 1890s in a paper on the stability of the Solar System. Some time later, other scientists found additional chaotic systems and they developed new mathematics and theories (Kovalevska, Hopf, Kolmogorov, Lorentz among others). Chaos is a motion irregular in time, unpredictable in the long term, hyper-sensitive to initial conditions and complex, but ordered, in the phase space: it is associated with a fractal structure. In present day literature, a system is said to be chaotic if small (i.e. infinitesimal) perturbations grow exponentially with time, which is connected to a positive Lyapunov exponent.

The classical Lyapunov exponent is defined as the exponential rate of separation, averaged over infinite time, of particle trajectories initially separated infinitesimally. Consider $x(t_0)$ and $x(t) = x(t_0) + \delta x(t)$ the position of two particle separated

initially by a distance $\delta x(t_0)$. The global Lyapunov exponent is defined by

$$\lambda = \lim_{t \to \infty} \lim_{\delta x(t_0) \to 0} \frac{1}{t} \ln \frac{|\delta x(t)|}{|\delta x(t_0)|}, \tag{2.8}$$

The Lyapunov exponent is quite useful in the study of time-independent dynamical systems. The seminal work of *Lyapunov* [1992] was very important in laying the theory of Lyapunov exponent for time-independent systems. Then the manuscript by *Barreira and Pesin* [2002] contains a good modern and comprehensive treatment of the subject. However, many dynamical systems of practical importance, especially in the realm of fluids, are time-dependent and only known over a finite interval of time and space. Because of its asymptotic nature, the classical Lyapunov exponent is not suited for analyzing these dynamical systems. The infinite-time limit in Eq.(2.8) makes the Lyapunov exponent of limited practical use when dealing with experimental data. A generalization of the Lyapunov exponent, called the Local Lyapunov exponent (LLE), has been proposed to study the growth of non-infinitesimal perturbations (distance between trajectories) in dynamical systems. Recently the concept of a LLE has been applied to study dispersion in turbulent flow fields.

The LLE is a scalar value which characterizes the amount of stretching about the trajectory of point x over a time interval. The LLE varies as a function of space and time. The LLE is not an instantaneous separation rate, but rather measures the average, or integrated, separation between trajectories. This distinction is important because in time-dependent flows, the instantaneous velocity field is often not revealing much about actual trajectories, that is, instantaneous streamlines can quickly diverge from actual particle trajectories. However the LLE accounts for the integrated effect of the flow because it is derived from particle trajectories, and is thus more indicative of the actual transport behavior. Depending on which asymptotic character is eliminated, there are two non-asymptotic Lyapunov exponents: finite-time (FTLE) and finite-size (FSLE) Lyapunov exponents, that are very similar.

Here we will detail only the Finite-Size Lyapunov Exponent (FSLE) which is a measure for the growth rate of a perturbation.

In our study, we quantify horizontal transport processes by the Lagrangian technique of the Finite Size Lyapunov Exponents (FSLEs) (*Aurell et al.* [1997]), which is specially suited to study the stretching and contraction properties of transport in
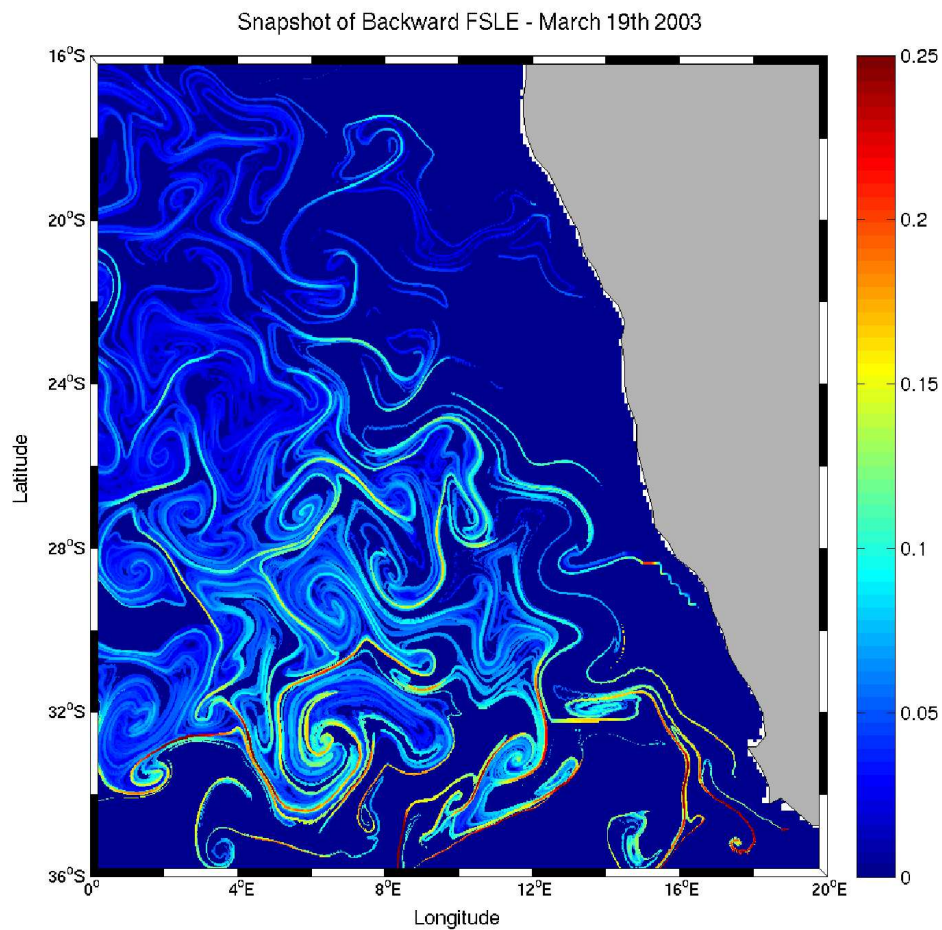
Figure 2.9: A snapshot of the backward FSLE computed for the Benguela current, on the day March 19, 2003. Unity is day^{-1}. One can observe ridges in the FSLE field that are called LCS (FSLE $> 0.15\ day^{-1}$).

geophysical data (*d'Ovidio et al.* [2004]). The calculation of the FSLE is based on the evaluation of the time, τ, after which two tracers, initially separated by a distance δ_0, reach a final separation distance δ_f, following their trajectories in a 2 D velocity field. At position x and time t the FSLE λ is then defined by:

$$\lambda(x, t, \delta_0, \delta_f) = \frac{1}{|\tau|} \ln \frac{\delta_f}{\delta_0}, \tag{2.9}$$

FSLEs depend critically on the choice of the two length scales: the initial separation δ_0 and the final one δ_f. We can then analyze oceanic structures at different sizes using different δ_f values. *d'Ovidio et al.* [2004] argued that δ_0 has to be close to the intergrid spacing among the points x on which FSLEs will be computed, which is δ_0= 0.025˚. Since we are interested in mesoscale structures, δ_f is chosen equal to 1˚, implying a separation distance of about 110 km at the equator. For this choice, the FSLEs represent the inverse rate of dispersion (mixing rate) of fluid parcels beyond the characteristic scales of eddies in prescribed areas. Choosing slightly different values for δ_f does not alter qualitatively our results, the main pattern and averages remain the same. For further information about the sensitivity of this measurement, see *Hernández-Carrasco et al.* [2010].

In this work, we chose to compute FSLE on all points of a latitude-longitude grid with a spacing of δ_0 = 0.025˚. Numerically, we follow the trajectories for 300 days, so that if τ gets larger than 300 days, we define λ = 0. The time integration of the particle trajectories can be performed in two different ways: forward or backward in time. In a typical snapshot of the backward-in-time dynamics (see Fig. 2.9), the maximum values of FSLE organize in lines which are a good approximation for the areas of maximal convergence. On the other hand, FSLE calculated with the forward-in-time integration exhibit large values in the regions of maximal divergence. The line-shaped regions of maximal convergence, divergence respectively, approximate the so-called unstable, stable respectively, manifolds of the hyperbolic points in the flow (*Boffetta et al.* [2001]; *Koh and Legras* [2002]; *d'Ovidio et al.* [2004]).

We focus in this work on the backward-in-time dynamics since FSLEs' lines have a clear interpretation as fronts of passive scalars advected by the flow *d'Ovidio et al.* [2009]. In a different set of papers (*d'Ovidio et al.* [2004, 2009]; *Lehahn et al.* [2007]; *Rossi et al.* [2008, 2009]), the adequacy of FSLE to characterize horizontal mixing and transport by structures in the marine surface layers, has been demonstrated as well as its usefulness when correlating with tracer fields like temperature or

chlorophyll. In addition, spatial averages of FSLEs can define a measure of horizontal mixing in a given spatial area, the larger this spatial average the larger the mixing activity. Following these studies, we will use in this work the FSLE as an analysis tool of the horizontal mixing activity of the surface ocean.

2.3.4 Lagrangian Coherent Structures (LCS) as ridges in the FSLE field

For highly time-dependent systems, the FSLE fields admit analogous ridges or separatrices similar to manifolds that divide dynamically different regions, and these structures are themselves time-dependent. As stated above, notions of manifolds are well defined for time-independent flows, but for general time-dependent flows they are becoming ambiguous. However, using FSLE computation, we are studying a time-dependent flow in terms of LCS as the analog of studying a time-independent flow in terms of stable and unstable manifolds. LCS are defined as ridges of maximum separation or convergence rates (see Fig. 2.9). The selected threshold depends on the average intensity of the horizontal mixing from FSLE field in the area of interest.

The properties of the LCS are:

- For well-defined LCS, which are obtained from FSLE field with a sufficient integration time, the flux of matter across such structures is expected to be very small.

- The FSLE measures the integrated effect of the flow, so if time integration is sufficient, the FSLE is indicative of Lagrangian behavior.

- LCS (at least those clearly visible in the FSLE fields) are invariant manifolds for all practical purposes.

As a consequence, these LCSs move with the flow as if they were material lines and thus delineate fluid domains with quite distinct origin and characteristics. Such lines strongly modulate the fluid motion since when reaching maximum values, they act as transport barriers for particle trajectories thus constituting a powerful tool for predicting fronts generated by passive advection, eddy boundaries, material filaments, etc... These LCS will be used in a study presented in Annex B (*TewKai et al.* [2009]).

2.4 Academic and realistic numerical modelling.

2.4.1 Interests and principles.

Data from satellites or field surveys allow to observe the real ocean, at different scales. Several issues can be addressed using these data, but the sensitivity of the evolution of a system to specific processes or parameters is generally impossible to assess. The tools to do so are numerical models.

A numerical model is a computer program that attempts to simulate an abstract model of a particular complex natural system. It is generally based on a system of simplified equations, that are discretized in time and space and then resolved using computers. Because numerical model have a lot of error sources, their results must be cautiously extrapolated to the real ocean. However, lots of progress have been achieved in recent years, especially in the hydrodynamical part, and physical numerical models are now generally able to represent, at least qualitatively, realistic evolutions. They are thus reliable tools for sensitivity studies. A biological system might be more difficult to model, especially biogeochemical models since a lot of processes are not yet well understood and quantified. I would like here to insist on the need to define very carefully the scientific question and then to build the numerical model that will answer the question. A very complex model is nothing else than a model. Nature is a billion times much more complicated than any of the human-built model and will not be - ever - modelled!

2.4.2 Hydrodynamical and biological models.

A very few general concepts of coupled modelling are introduced here.

Hydrodynamical part:

Within the field of ocean general circulation modelling, all models resolve very similar equations (primitive equations) but differ by their choice of spatial discretization (finite difference, finite element, finite volume) and vertical coordinate (geopotential, isopycnic, sigma, hybrid).

The primitive equations are based on the Navier-Stokes equations on a rotating sphere with thermodynamic terms for various energy sources (radiation, latent
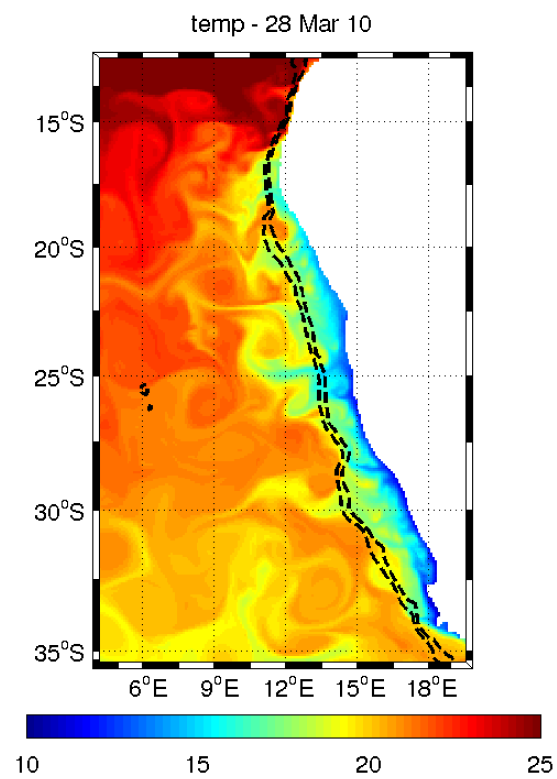
Figure 2.10: A snapshot of the sea surface temperature from ROMS model for the Benguela upwelling, averaged on 3 days. Black dotted lines are 500 m and 100 m bathymetric contours.

heat, etc...). These equations are the basis for complex computer programs commonly used for simulating the evolution of the atmosphere or the ocean. They are three-dimensional (x,y and z) models that discretize the equations for fluid motion and integrate them forward in time (time is the fourth dimension). They also contain parametrizations for processes such as convection, or turbulence that occur on scales too small to be resolved directly. To model a region of the ocean, fluxes from the frontiers such as the atmosphere, the coast, etc.. are imposed as external forcings. Most models include a software to diagnoze a wide range of output variables for comparison with observations or study of oceanic processes. As an example, Figure 2.10 presents an output of Sea Surface Temperature from the ROMS 3D model configuration for the Benguela area, being used in our group.

We consider the variables (u, v, w, p, ρ) where $U(u, v, w)$ is the three dimensional velocity field, p is the pression and ρ is the density of the fluid. Under the Boussinesq approximation, the primitive equations in three dimensions (x, y, z) are:

$$\frac{\partial u}{\partial t} + u\frac{\partial u}{\partial x} + v\frac{\partial u}{\partial y} + w\frac{\partial u}{\partial z} - fv = -\frac{1}{\rho_0}\frac{\partial p}{\partial x} + \frac{\partial}{\partial x}(A_U\frac{\partial u}{\partial x}) + \frac{\partial}{\partial y}(A_U\frac{\partial u}{\partial y})$$
$$+ \frac{\partial}{\partial z}(\kappa_U\frac{\partial u}{\partial z}) \qquad (2.10)$$

$$\frac{\partial v}{\partial t} + u\frac{\partial v}{\partial x} + v\frac{\partial v}{\partial y} + w\frac{\partial v}{\partial z} + fu = -\frac{1}{\rho_0}\frac{\partial p}{\partial y} + \frac{\partial}{\partial x}(A_U\frac{\partial v}{\partial x}) + \frac{\partial}{\partial y}(A_U\frac{\partial v}{\partial y})$$
$$+ \frac{\partial}{\partial z}(\kappa_U\frac{\partial v}{\partial z}) \qquad (2.11)$$

$$-\frac{\partial p}{\partial z} - \rho g = 0 \qquad (2.12)$$

$$\frac{\partial u}{\partial x} + \frac{\partial v}{\partial y} + \frac{\partial w}{\partial z} = 0 \qquad (2.13)$$

$$\frac{\partial T}{\partial t} + u\frac{\partial T}{\partial x} + v\frac{\partial T}{\partial y} + w\frac{\partial T}{\partial z} = \frac{\partial}{\partial x}(A_T\frac{\partial T}{\partial x}) + \frac{\partial}{\partial y}(A_T\frac{\partial T}{\partial y}) +$$
$$\frac{\partial}{\partial z}(\kappa_T\frac{\partial T}{\partial z}) + SMS_T \qquad (2.14)$$

$$\frac{\partial S}{\partial t} + u\frac{\partial S}{\partial x} + v\frac{\partial S}{\partial y} + w\frac{\partial S}{\partial z} = \frac{\partial}{\partial x}(A_S\frac{\partial S}{\partial x}) + \frac{\partial}{\partial y}(A_S\frac{\partial S}{\partial y}) +$$
$$\frac{\partial}{\partial z}(\kappa_S\frac{\partial S}{\partial z}) + SMS_S \qquad (2.15)$$

$$\rho = \rho\,(T, S, p) \qquad (2.16)$$

The three first equations 2.10, 2.11 and 2.12 are known as the *momentum equations*, the fourth one 2.13 is the *continuity equation*, Eqs. 2.14 and 2.15 are the *tracer equations* and Eq. 2.16 is the *equation of state*.

ρ_0 is the reference density, g is the gravitational acceleration, $f = 2\Omega\sin\varphi$ is the coriolis parameter, $A_{U,T,S}$ are the eddy viscosity, $\kappa_{U,T,S}$ are the vertical diffusion coefficients prescribed by a turbulent closure scheme. $SMS_{T,S}$ are the 'source-minus-sink' terms, which represent the external forcings (freshwater inputs, evaporation, heat fluxes...).

These equations are resolved numerically in Oceanic General Circulation Model, such as models like ROMS (for Regional Ocean Model System, see *Shchepetkin and McWilliams* [2005] and http://www.myroms.org/) or HYCOM (for HYbrid Coordinate Ocean Model, *Bleck* [2002] and see http://www.hycom.org/).

Biological part:

Ecosystem models have been developed to characterize the major dynamics of ecosystems, both to improve our understanding of such systems and to allow predictions of their behaviour (in general terms or in response to particular changes). Ecosystem models typically simplify the complex ecosystems they are being studied to a limited number of components. These may be particular species of interest, or may be broad functional types such as autotrophs/heterotrophs or grouping depending on the size, etc... In biogeochemistry, ecosystem models use functional types, usually including representations of non-living resources such as nutrients, which are consumed by (and may be depleted by) living components of the model. Since for planktonic marine organisms, many ecological traits, metabolic processes as well as predator-prey relationships are indeed mostly determined by size, ecological models can also be size structured or based on functional types, with subdivisions into size classes. Moreover, since planktonic marine organisms are highly dependent on their physical environment, they are generally modelled as a concentration of tracer (tracer phytoplankton, zooplankton, nitrogen, carbon, etc...) and not as Individual Based Model.

We consider a tracer C_i, that represents either all phytoplankton, or a specific group, a specific size of phytoplankton. The evolution of its concentration within a flow will be determined by the following equations:

$$\frac{\partial C_i}{\partial t} \quad = \quad -U\cdot\nabla(C_i) \; - \; A_C\nabla^2 C_i \; + \; \frac{\partial}{\partial z}(K_C\cdot\frac{\partial C_i}{\partial z}) \; + \; SMS_{C_i} \qquad (2.17)$$

With from right to left:

- The SMS for 'source-minus-sink' which represent exchange between model compartments, reproducing the ecosystem functioning (e.g. zooplankton grazing, natural death and growth...).

- The vertical mixing term, K_C is the turbulent diffusion coefficient for biological tracers.

- The horizontal diffusion term, A_C is the horizontal diffusion coefficient for biological tracers.

- The advection term ($U(u, v, w)$ is the velocity field).

The coupling between the hydrodynamical and biological models is performed by the advection and diffusion term coming from the physical model. These biological models exist in 0 dimension (a 'box') to 3D realistic configurations. A classical and simple type of biogeochemical model is the NPZD, reproducing the behavior of Nitrogen, Phytoplankton, Zooplankton and Detritus *Oschlies and Garçon* [1998, 1999].

Chapter 3

A mesoscale survey of the northern and central Iberian Peninsula Upwelling System: spatial variability and bio-physical interactions.

After having presented all tools that oceanographers can use to address such issues in the previous chapter, the MOUTON 2007 survey made over the Iberian Peninsula Upwelling is presented in the following part.

I was involved in the design of the research and the logistic organization prior to the cruise. More specifically, I was in charge with Joëlle Tassel of the biogeochemical sampling. Then my participation to the cruise itself consisted in several tasks. We refined the sampling strategy thanks to real-time acquisition of satellite images in close relation with the chief scientist, Yves Morel. I also organized the biogeochemical sampling and took part in it with the "biological team" onboard. I then performed the zooplankton sampling using a WPII net, followed by the preparation of all samples.

After the cruise, I gathered all physical and biological raw data that I finally carefully post-treated (organization and cleaning of the whole dataset). This dadataset, along with calculation and original display, allowed me to study the mesoscale vari-

ability of the Iberian Peninsula Upwelling ecosystem. This full research experience of an oceanographic survey was a very complete and constructive step of my PhD.

A detailed and descriptive study of the survey is performed in the first article[1].

Contents

---

[1]Readers: please note that sections *2.3 Sampling strategy and methods onboard* and *2.4.1 Laboratory measurements* of article 1 were already presented in similar shapes in Chapter 1. Please be aware that this descriptive article is about to be submitted in Progress in Oceanography very soon, in a more condensed form focussing on key results.

3.1 Article 1: A mesoscale survey of the northern and central Iberian Peninsula Upwelling System: spatial variability and bio-physical interactions, Rossi *et al.*, Progr. Oceanogr.

Reference : Rossi, V., Garçon V., J. Tassel, J.B. Romagnan, L. Stemmann, F. Jourdin, P. Morin and Y. Morel,. 2010, A mesoscale survey of the northern and central Iberian Peninsula Upwelling System: spatial variability and bio-physical interactions, to be submitted to Progress In Oceanography.

A mesoscale survey of the northern and central Iberian Peninsula Upwelling System: spatial variability and bio-physical interactions.

V. Rossi[*,a], V. Garçon[a], J. Tassel[b], J. B. Romagnan[c], L. Stemmann[c], F. Jourdin[b], P. Morin[d], Y. Morel[e]

[a]Laboratoire d'Études en Géophysique et Océanographie Spatiales, CNRS, 18 avenue Edouard Belin, 31401 Toulouse Cedex 9, France.
[b]EPSHOM/MGS/IES/LMCO 13, rue du Chatellier CS 30316, 29603 BREST CEDEX, France.
[c]Observatoire Ocanographique de Villefranche BP 28 06234 Villefranche/Mer, France.
[d]Station Biologique de Roscoff, Place Georges Teissier, BP74 29682 Roscoff Cedex, France.
[e]Service Hydrographique et Océanographique de la Marine, (SHOM), 42 av Gaspard Coriolis, 31057 Toulouse, France.

Abstract

Key words:

1. Introduction

Upwelling systems are characterized by high productivity of plankton and pelagic fish. Their contribution to the world ocean productivity, up to 17% of the global fish catch ([*Pauly and Christensen,* 1995]), while representing only 0.5% of the total surface of the world ocean, identifies them as major biological and socio-economical areas. Wind driven upwellings, and particularly the Eastern Boundary Upwelling systems, are regional processes mostly driven by the local wind stress: near a coast in the northern hemisphere, an along-shore wind oriented with the coast to its left produces offshore transport in the surface Ekman layer. Boundary conditions imply divergence of this current near the coast which generates an upwelling of rich nutrient water. These rich waters support a high primary productivity which in turn propagates along the whole trophic food web.

[*]Corresponding author (email: vincent.rossi@legos.obs-mip.fr ; tel: +33 561 333 007 ; fax: +33 561 253 205).

Email addresses: `vincent.rossi@legos.obs-mip.fr` (V. Rossi), `veronique.garcon@legos.obs-mip.fr` (V. Garçon), `yves.morel@shom.fr` (Y. Morel)

The MOUTON07 campaign at sea aimed at studying the physical and biogeo-
chemical properties of the Iberian Peninsula Upwelling System (IPUS). This area is
part of the four main wind-driven eastern boundary upwelling zones, the Canary-
Iberian upwelling. However, the Iberian region is quite distinct from the Canary
functioning and separated by a physical discontinuity: the entrance to the Mediter-
ranean Sea through the Gibraltar Strait. Another difference between the Canary and
Iberian regions is the temporal variability: although the Canary region shows inter-
and intra-annual variability, the trade winds which favor upwelling are present all
year round. On the other hand, the IPUS shows a strong seasonality mainly due to
the annual cycle of the atmospheric system, and we observe roughly a winter regime
and a summer fall regime, with superimposed smaller scales variability. The Iberian
shelf is then known as an important wind-driven eastern boundary upwelling area,
characterized by intense seasonal upwelling conditions and high biological produc-
tivity. It then constitutes a natural laboratory to study the influence of the physical
environment on the biological and biogeochemical variables.

An along-shore southward wind stress establishes during late spring / summer
[*Wooster et al.,* 1976, *Fiúza et al.,* 1982] and creates a surface Ekman current di-
rected to the west (offshore), generating a strong upwelling of cold rich-nutrient
waters at the coast, supporting biological productivity (see Figure 3). The effects
of upwelling on the western Iberian pelagic ecosystem are intense, since the nutrient
inputs are relatively high at those latitudes. [*Joint et al.,* 2002] estimated that up-
welling results in an increase of about 50 % of the total primary production. During
upwelling, a dynamical food web based on new nutrients from the upwelling (as ni-
trate) would be expected. [*Castro et al.,* 2000] detailed the biogeochemical response
of the IPUS from two contrasting upwelling events. They insisted on the impor-
tance of the wind intensity and also the type of upwelled waters off Northern IPUS.
[*Alvarez-Salgado et al.,* 2002] also confirmed that the production in the IPUS and its
inter-annual and seasonal variability are mainly driven by the Ekman offshore trans-
port variability. During an upwelling event, [*Cermeno et al.,* 2006] observed that
microphytoplankton dominates the assemblage but both nano- and picophytoplank-
ton have a significant impact in these waters, confirmed by [*Joint et al.,* 2001b].
[*Joint et al.,* 2002] added that these pico- and nanophytoplankton populations are
strongly controled by microzooplankton grazing. Some authors concentrated on the
remineralization process and [*Castro et al.,* 2006] observed its maximum in sum-
mer/autumn coinciding with the upwelling period. They suggested that secondary
cycling of nutrients helps to maintain high nutrient levels over the shelf between up-
welling pulses. [*Tilstone et al.,* 2003, *Lorenzo et al.,* 2005] described the shelf phy-
toplankton communities as diatoms and dinoflagellate dominated, whereas mainly

2

cyanobacteria are found in the oceanic waters. [*Lorenzo et al.,* 2005] added that in between upwelling events, cyanobacteria are significantly present over the shelf. [*Barbosa et al.,* 2001] studied the bacterioplankton production and found that it is around 15 % of the plankton community over the shelf, whereas it can reach about 40 % under the more oligotrophic conditions in a filament. They also mentionned a close coupling between bacteria and phytoplankton in their biogeochemical functioning. More recently, [*Resende et al.,* 2007] suggest that phytoplankton assemblage are mostly driven by the temperature gradient, in relation with the nutrient content and also the intrinsic temperature optima of species.

During this favourable upwelling season, the Portugal Current (PC) establishes and is composed of a south-west surface drift, associated with a coastal jet flowing equatorward. It is sometimes associated with a poleward counter-current, namely Iberian Poleward Current (IPC), thought to be density gradient driven, just above the slope during most of the year, intensified in winter [*Peliz et al.,* 2005]. The upwelling front also reveals small scale instabilities, where mesoscale processes as filaments and eddies are very commonly observed. They mainly occur from July to October (upwelling favourable season) and several papers concentrate on the theories of filament formation [*Haynes et al.,* 1993, *Roed and Shi,* 1999, *Batteen et al.,* 2007, *Sanchez et al.,* 2008, *Meunier et al.,* 2010]. Large filaments were often closely related with capes and coast irregularities, but it was noted the repeated occurrence of a few large filaments at different locations corresponding with a straight coastline. Different processes have then been studied and among others, we can cite the capes effect, front and flow instabilities resulting in meander formation, and lately the creation of vorticity anomalies by upwelling current/topography interactions [*Meunier et al.,* 2010]. Other authors concentrated on their biological role and showed they are responsible of important cross-shelf exchange of biological material while feeding the oligotrophic offshore waters with nutrients and organic materials [*Alvarez-Salgado et al.,* 2001, *Alvarez-Salgado et al.,* 2007]. They also constitute ecological niches by themselves, where changes in biological process rates [*Alvarez-Salgado et al.,* 2001, *Fileman and Burkill,* 2001], phytoplankton [*Joint et al.,* 2001a] and zooplankton populations [*Batten et al.,* 2001, *Halvorsen et al.,* 2001] occur along the offshore physical drift of the filament. [*Borges and Frankignoulle,* 2001] claimed that upwelling filaments are an important feature of the inorganic carbon cycle, controlling partly the partial pressure of CO_2. Another physical important forcing at the northern tip of the IPUS is the occurrence of the Western Iberian Buoyant Plume (WIBP) [*Peliz et al.,* 2002] related to the freshwater discharge coming from the Galician Rias and Northern Portuguese rivers (the most significant discharges are from the Minho and Douro rivers). [*Otero et al.,* 2008] studied the dynamics

3

and extension of this low salinity lens, showing that it is highly influenced by the wind regime and the shelf circulation (i.e. IPC). It is confined to the coast when southerlies prevail, whereas it is exported offshore and southward under upwelling favourable northerlies. Few studies emphasized the crucial role this physical feature has on the biological activity, from plankton [*Ribeiro et al.,* 2005] to fish recruitment [*Santos et al.,* 2004, *Santos et al.,* 2007].

During winter, weak northerly winds occur rarely and are associated with localized and transient upwelling features. However winter is globally characterized by strong south - southwest winds, favouring coastal convergence and downwelling. In the absence of coastal upwelling, the surface circulation off the Iberian shelf is predominantly northward, partially driven by meridional alongshore density gradients and consists in a poleward jet (IPC) transporting higher salinity and warmer (subtropical) waters over the upper slope and shelf break [*Haynes and Barton,* 1990, *Peliz et al.,* 2005, *Relvas et al.,* 2007]. Its turbulent character leads to frontal instabilities and filaments - eddies formation at the shelf break. In the litterature, poleward flows observed in the area are sometimes refering to the slope poleward flow (IPC) or to a coastal counter-current at the inner shelf. The complex inner shelf circulation during winter is driven by the wind stress and its variability. Except transient short winter upwelling events, wind forced shelf currents are predominantly northward. However [*Relvas et al.,* 2007] claimed that the wind does not affect significantly the IPC over the slope, which was not the case in the modelling study by [*Otero et al.,* 2008]. The IPC has also some ecological implication and some studies showed the formation of retention areas or ecosystem partitioning [*Alvarez-Salgado et al.,* 2003, *Cabal et al.,* 2008] and poleward transport of planktonic communities [*Ribeiro et al.,* 2005] as well as fish larvae [*Santos et al.,* 2004, *Santos et al.,* 2007]. In downwelling favourable conditions (September to May), the IPC carries poor nutrient concentrations and isolates the moderately rich shelf waters (from coastal inputs and remineralisation processes) from the offshore ecosystem. Waters inside the poleward current display low plankton biomass, based on a microbial food web, constrasting with the enriched shelf waters. The occurrence of this poleward current during late spring and summer (upwelling season) is still subject to debate, although some evidences have already been documented [*Peliz et al.,* 2002].

During the transition from spring to summer, the wind forcing is highly variable with a time scale of 10 - 15 days, leading to repeated spin up and relaxation of upwelling. The circulation occurring during the transition between these two regimes was studied in details by [*Torres and Barton,* 2007]. In particular, the succession of the IPC and the equatorward surface current is discussed, along with the interactions with the WIBP.

4

All year round, the oceanic tides interact with the complex shelf topography and the existing stratification to create barotropic tide currents, intensified tidal ellipses over the shelf/slope, and high occurrence of non-linear internal tidal waves ([*Relvas et al.,* 2007] and references therein). Tide currents and internal waves are ubiquitous features of the IPUS, having some implication on the shelf stratification and on sediment resuspension processes [*Quaresma et al.,* 2007].

To sum-up, the Western Iberian circulation and hydrology reveal a high spatial and temporal variability. The strong seasonality is mainly linked with atmospheric forcings. [*Relvas et al.,* 2007] present a complete review of the general circulation patterns and their temporal variability. They also insisted on the numerous mesoscale features observed in the area and their large influence on the ecosystem, that has received a major attention in the literature. Spatial scales of 10 to 100 km are the most important ones when looking at the regional planktonic communities, since their transport, formation of retention areas and localized nutrient inputs depend on mesoscale physical features such as eddies, filaments, fronts, plumes and upwelling cells [*Queiroga et al.,* 2007, *Santos et al.,* 2007].

This paper presents a descriptive analysis of data collected from a multidisciplinary mesoscale survey of the central and northern IPUS, performed under upwelling favourable conditions. The first part of the paper presents the research survey plan and the data, both physical and biogeochemical, collected during August-September 2007 during which the meteorological conditions lead to a well developed upwelling. The second part explains the onboard sampling methods and the onland laboratory measurements. We selected a few sections to detail the spatial variability of the system. First a general study of the water masses and main circulation pattern is performed. Then we focus on the North-South variability of the central and northern IPUS and we define three sub-areas. Moreover we concentrate on the cross-shore variability between the coastal rich waters and the oligotrophic open ocean using two East-West sections. Finally, an upwelling filament was intensively sampled under calm conditions to study the export of coastal material offshore. Its physical structure is also discussed.

2. The MOUTON 2007 survey: a multidisciplinary study of the Iberian Peninsula Upwelling Zone.

2.1. General context.

The MOUTON07 cruise was conducted along the western coast of the Iberian Peninsula (mainly Portuguese coast), onboard the research vessel "Pourquoi-Pas?" (see Fig. 1). This survey aimed at studying the mesoscale variability both from a

5

physical and biogeochemical point of view the central and northern part of the Iberian Peninsula Upwelling System (IPUS) under favourable upwelling season. The cruise was divided in two legs during which the upwelling area north of Lisbon was surveyed: the leg one took place from August 11th to August 25th and leg 2 from August 30th to September 14th, 2007. Physical and biological data were gathered along East-West and North-South transects or repeatedly at fixed points from August 14th to August 25th and from August 30th to September 11th, 2007. The remaining periods of time correspond to transit time. The observational area extends from 38° to 42°N and from the coast to almost 3° offshore (until 11°W). The details of all CTD stations are displayed on Figure 1, superimposed with the local bathymetry.

After a general presentation of the whole dataset, the main water masses and the general circulation patterns, we will focus our analysis on a few particular features:

- the North-South variability,

- the cross-shore gradient, and

- a study of an upwelling filament.

Recently a particular feature, a secondary upwelling front above the continental margin, was observed along the section at 41°N and studied in details in [*Rossi et al., 2010*]. They documented for the first time this event in the IPUS and explained it using a numerical model. We refer to some of their findings, while adding some biological implication. The distribution of volatile halogenated organic compounds over the IPUS was simultaneously investigated and has been described, in relation with environmental conditions, in [*Raimund et al., 2010*]. Moreover, a complete description of the zooplankton data (biomass, species composition and size spectra) is currently being performed (Romagnan et al., 2010, in prep.).

2.2. Meteorological conditions.

Meteorological data were recorded from sensors onboard the vessel, simultaneously with the other physical and biogeochemical measurements. Data from the Quikscat scatterometer and on-board wind measurements (see Figure 2) reveal that upwelling favorable wind conditions occurred roughly from end of July to end of September. When looking in more detail, we have strong northern winds from July 20th to August 13th. These conditions result in well developed and intense upwelling of cold rich nutrient waters (temperature around 15°C) spreading around 1° offshore, with intense filaments formation reaching 1.5 to 2°W (see figure 3 a). Then we observe two days of moderate-strong southerly winds (15 m/s), from August 13th to the 15th, mid-day. After this short wind inversion, upwelling favourable wind conditions

6
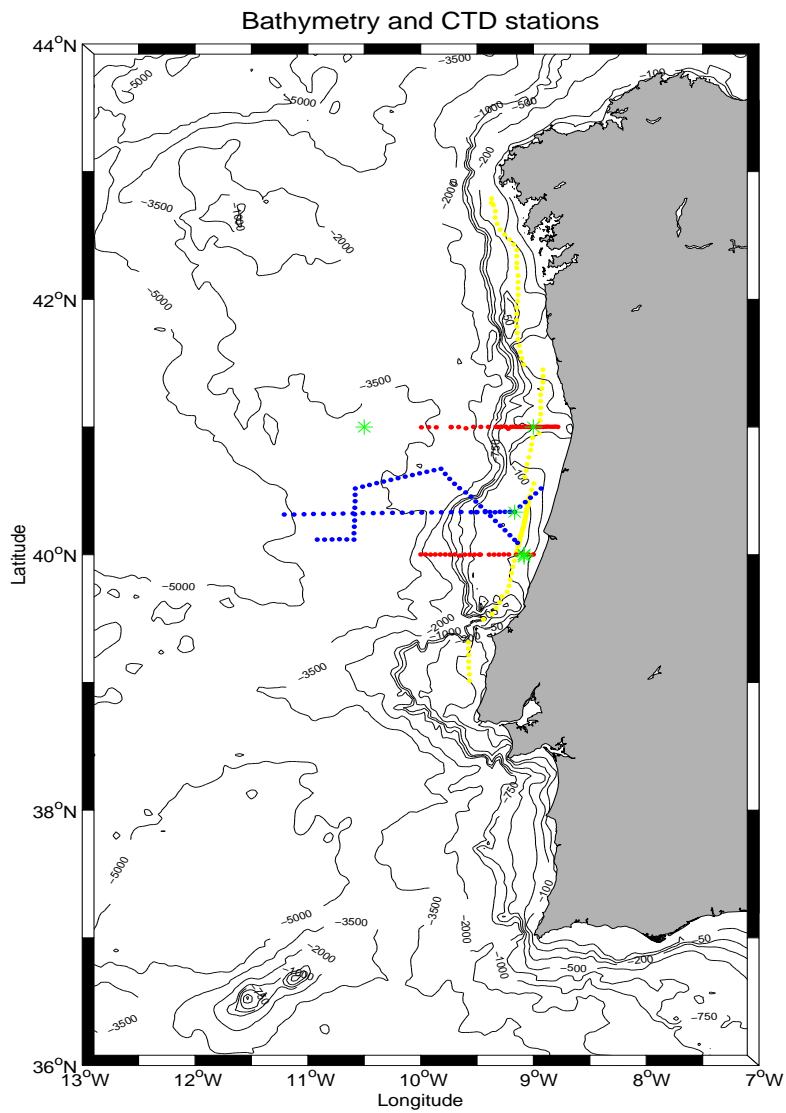
Figure 1: Overview of the MOUTON07 oceanographic campaign offshore the Iberian peninsula. Colored points represent the CTD stations (yellow for the NS section, red for the two EW sections, and blue for the filament network). Green crosses indicate the position of fixed point measurements. Contours represent the bathymetry (in m).
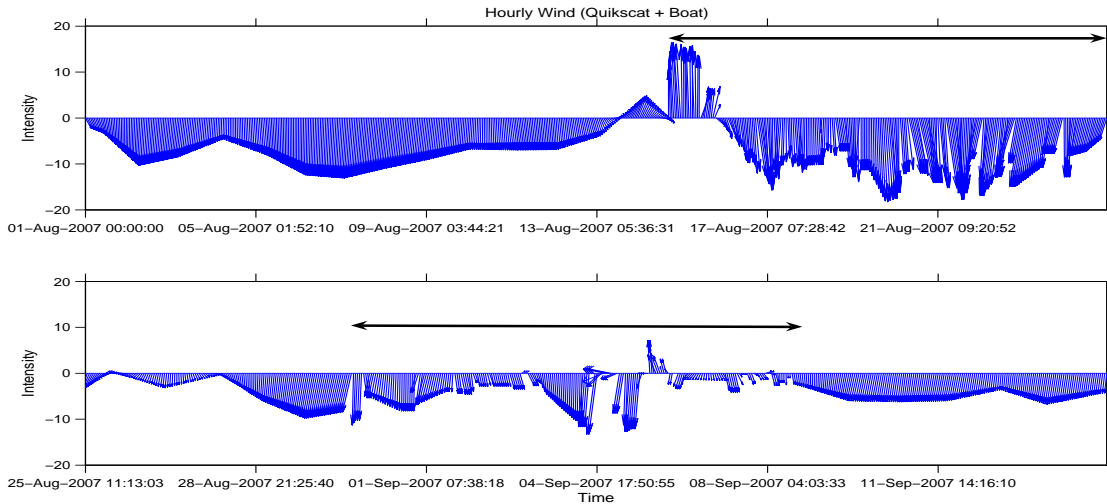
Figure 2: Wind (in m/s) vectors from Quikscat scatterometer (averaged over the surveyed area $39 - 43°N$ / $9 - 12°W$) and onboard measured wind during the 2 legs of the survey (indicated by the 2 black arrows).

prevailed during the first leg of the cruise with again intense northerlies (10 to 25 m/s) blowing during two weeks, from August, 15th to August, 30th with temperatures near the coast dropping to less than 13°C. Figure 3 b shows a satellite image of sea-surface temperature (SST) on 23th of August, where the upwelling is clearly visible. In this case, the westward extension of the main front is around 1.5°, with numerous filaments showing an extension maximum of around 3° offshore. From the 1st of September, the winds are again globally coming from the north but with intensity equal or below 10 m/s. We observed a transition from high mixed upwelling conditions to a relaxation period with increasing stratification. The upwelling strength decreased and the main upwelling front returned closer to the coast (less than 1° in average), while large filaments continued developing offshore.

2.3. Sampling strategy and methods onboard.

We focussed the survey on the study of the spatial and temporal variability of bio-physical processes occurring over the central/northern part of the IPUS area. The spatial variability was studied through a North-South transect roughly following the 100 m isobath along the coast when possible (avoiding navigation rails and fishing areas). The coast-offshore gradient was observed through two Est-West section, EW1 at 41°N and EW2 at 40°N (see Fig. 1). The export of coastal water masses to the

8
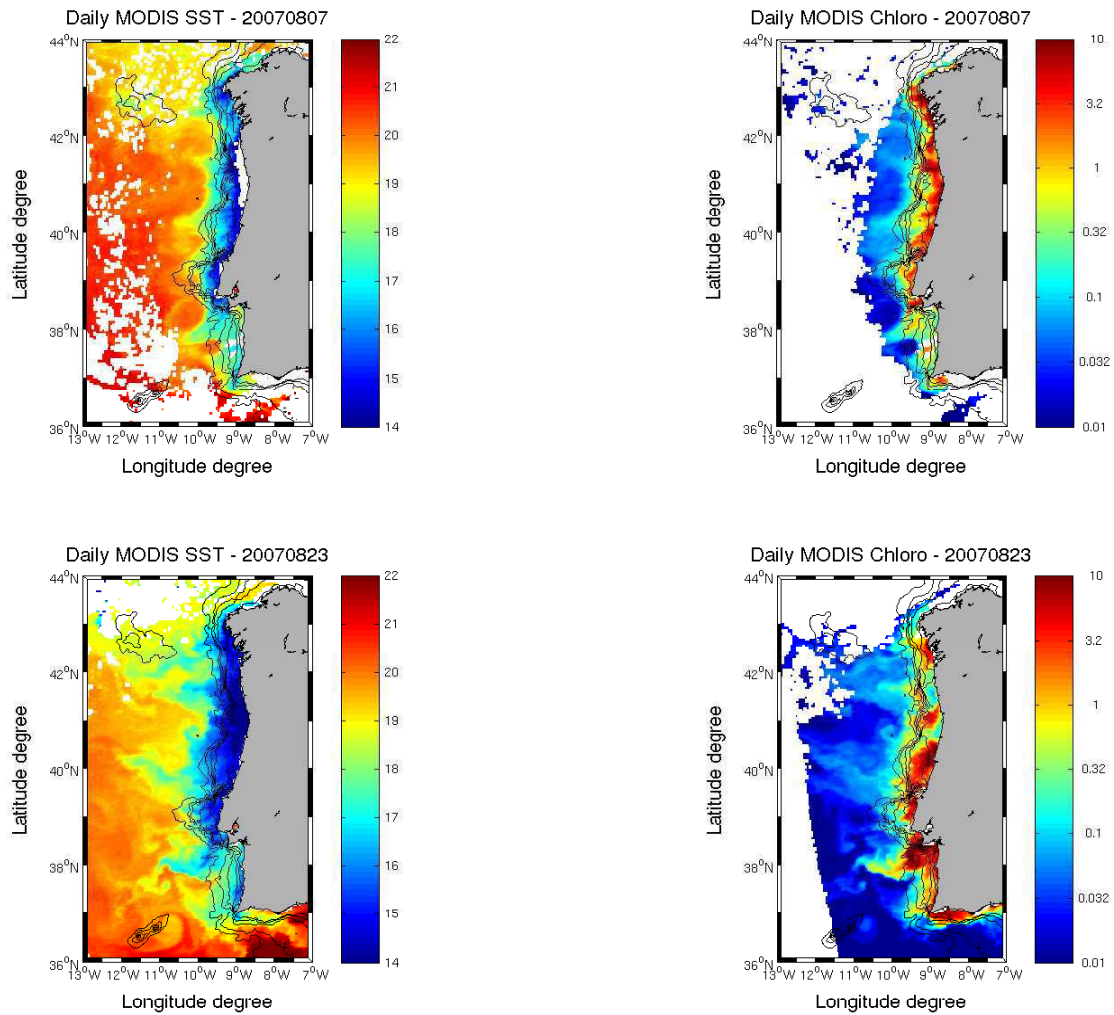
Figure 3: SST (°C) and Chlorophyll-a (mg chloro-a /m^3) from space (MODIS Aqua) for day 08/07/2007 (a) and 08/23/2007 (b). White areas are clouds and black contours represent the bathymetry.

open ocean via a filament was surveyed with a network of sections covering a selected filament at 40.3°N. Then measurements were continuously performed at three locations during 30 hours to observe the high frequency temporal variability. This fixed points sampling is not presented in this paper. This strategy was decided prior to the campaign itself but precise locations of stations and sections, as well as the sequence of events, were adjusted onboard twice a day, using real-time acquisition of satellite data of SST and chlorophyll *a*. This strategy, coupled with upwelling favourable meteorological conditions, led to a quite complete and nice dataset described here.

Physical observations were made using a Conductivity-Temperature-Depth (CTD) instrument, a Lowered Acoustic Doppler Current Profiler (LADCP) functioning at 300 kHz, and also two Vessel Mounted Acoustic Doppler Current Profiler (VMADCP), functioning at 38 kHz and 150 kHz, respectively. A Seasoar was also onboard, which allowed high resolution coverage of hydrography, but data are not presented here. Simultaneously, a set of biogeochemical sensors were also mounted onto the CTD-rosette. We lowered two fluorometers (a Chelsea Aqua 3 for chlorophyll *a* and a Chelsea Aquatrack a for UV measurements), an Oxygen sensor SBE43 and a Turbidimeter CSS-631. There were also optical sensors: a transmissiometer Wetlab for light transmission and attenuation, a Photosynthetically Active Radiation sensor (PAR) and a Surface PAR sensor. The sampling was adjusted to 24 scans per second and the lowering speed of the CTD was about 0.5 m/s. The CTD casts were limited to the upper 200 m (or above when the bathymetry was shallower) due to the maximum operation depth of some biogeochemical sensors. Data processing included removal of spurious values by low pass filtering.

Seawater samples were collected at 1387 stations (see Fig. 1) using a CTD-rosette system equipped with 12 ten litres Niskin bottles. At each station, up to five depths in the water column were sampled: the surface (1 m), the upper thermocline, the deep chlorophyll maximum, the lower thermocline and an additional depth of interest. The conducting cable allowed us to monitor all measured variables during the descent and to determine at the same time our depths of interest. Then water samples were collected along the way up thanks to the descent profiles. Although there was a small time lag between the descent and the ascent, and although internal waves are known to be conspicuous in this area, the main structures were quite successfully sampled.

The 612 samples of seawater, collected for nutrient analysis were stored at −20°C for later analysis. The water samples for pigment analysis were collected at 2 or 3 depths and then were vacuum filtered through 25 mm diameter Whatman GF/F glass fibre filters (0.7 µm particle retention size). Filtered volumes varied between 3 l in the offshore waters and less than 1 l for some stations inside the coastal upwelling zone. The filters were immediately stored in liquid nitrogen at −80°C until analysis

10

on land. Among the total 219 samples, 16 were sampled in duplicate and then analysed almost simultaneously by the SHOM Brest and by the Villefranche/Mer Oceanography Laboratory in order to perform a cross-validation between the two laboratories. The dissolved oxygen probe mounted on the rosette was calibrated by independent sampling and Winkler titration following [*Labasque et al.,* 2004] (and references therein).

Zooplankton samples were collected during day and night at one CTD stations out of two or three, with the highest possible frequency. A WPII plankton net (mouth surface of 0.2552 m^2) mounted with 200 μm mesh size was used, and towed vertically at around 1 m/s over the water column from 5 m above the sea bottom, or 70 m depth, up to the surface. To consider the proper volume of filtered water, the effective depth of the tow is confirmed by the cable meter onboard. Once onboard, the net is rinsed with seawater from outside and the sample is collected in a bucket. This solution is then splitted into two parts, using a motoda box [*Motoda,* 1959]. Half of the sample is directly preserved in formaldehyde for later analysis, whereas the other half is fixed on a pre-weighted filter (200 μm) and conserved at −20°C in individual sterile cases.

2.4. Samples treatments on land and data handling.

2.4.1. Laboratory measurements.

The common nutrients concentrations - namely nitrate, silicate and phosphate - were determined by colorimetric methods using an Autoanalyser II from Technicon, following [*Aminot and Kerouel.,* 2007]s method. All solutions were prepared in Milli-Q water (Millipore Milli-Q water system) with reagent analytical grade salts. Artificial seawater for standards calibration, as well as for nitrate, silicate and phosphate samples, was prepared at a salinity of 34.7 g/l with sodium chloride (NaCl). All working standards calibrations were prepared as described in the WOCE operation and method manual [*Gordon et al.,* 1995].

In the laboratories, we determined phytoplankton pigments composition by HPLC (High Performance Liquid Chromatography) methods. The filters were extracted at 20°C in 3 ml methanol (100 %), disrupted by sonication and clarified one hour later by vacuum filtration through Whatman GF/F filters. The extracts were rapidly analysed (within 24 h) by HPLC with a complete Agilent Technologies system. The pigments were separated and quantified following an adaptation of the method described by [*Van Heukelem and Thomas,* 2001]. Modifications to this method allowed for increased sensitivity in the analysis of ultra-oligotrophic waters. The extraction used a narrow reversed-phase C8 Zorbax Eclipse XDB column which was maintained at 60°C and the separation was achieved within 28 min. A diode array detector al-

11

lowed for the absorption of most pigments to be detected at 450 nm, while chlorophyll *a* and its derivatives were detected at 667 nm and bacteriochlorophyll *a* at 770 nm. The diode array absorption spectra of each peak were used for identification purposes. Pigment concentrations (in $mg.m^3$) were calculated from the peak areas with an internal standard correction (Vitamin E acetate, Sigma) and external calibration. This method has proven to be satisfactory in terms of resolution, sensitivity, accuracy and precision [*Ras et al.,* 2008], with the detection of about 13 separate phytoplankton pigments (see Tab. 1), with a lower limit of detection for chlorophyll *a* of 0.0001 $mg.m^3$ and with an injection precision of 0.4 %.

Net collected zooplankton samples were digitized using the Zooscan imaging system ([*Grosjean et al.,* 2004, *Gorsky et al.,* 2010]). Image processing was performed by Image J software using the Zooprocess interface (www.zooscan.com), enabling fast and reliable enumeration and measurement of objects. Prior to digitization the samples were rinsed in freshwater to remove formaldehyde and allow a safe analysis. It is critical to scan no more than 1000 to 2000 objects at once, depending on size, to obtain good quality images and data ([*Gorsky et al.,* 2010]). Thus, a Motoda splitter ([*Motoda,* 1959]) was used for subsampling. For each sample, the objects were carefully separated on the scanning cell to avoid as much as possible touching objects. The digitization generates 16 bits, 15x24 cm, 2400 *dpi* raw images, (pixel width of 10.58 μm). A metadata form compiling various information relative to the sample is associated with each image. Image processing consists in 4 steps: (i) conversion to 8 bits and normalization to full grey scale range, (ii) background homogenization, (iii) segmentation (extraction of objects, threshold 243), (iv) measurements on objects. At present 54 parameters including shape, grey scale, size, and complexity of the shape parameters are measured on each object. The outputs of the image process are (i) a set of vignettes and (ii) an associated *.pid* file compiling the measurements for each object and information on the process. When enough samples were scanned and processed, a random subset of vignettes was manually sorted into coarse faunistical groups (e.g. Copepods, Chaetognaths, etc.) In this study, we aimed at discriminating organisms from detrital matter. A learning set was generated, using the set of sorted vignettes and associated data, with the software Plankton Identifier ([*Gasparini,* 2007]). This learning set allowed the automatic sorting of unidentified vignettes into the previously defined groups (see [*Gorsky et al.,* 2010] for detailed description of the machine learning process associated with the Zooscan techniques). The automatic sorting outputs were then checked and corrected if needed by a trained taxonomist. In this work, we will only separate living objects from the non-living objects (marine snow, particulate organic matter...) to only quantify zooplankton individuals. The biomass of organisms was computed following an estimation of the

12

biovolume based on size measurements. For Copepods the biovolume was estimated using the major and minor axes of the best fitting ellipse ([*Vandromme et al.,* 2010]). For other organisms the biovolume was estimated using ESD, computed from the exact surface of the object ([*Gorsky et al.,* 2010]). We finally defined two classes of size, the small and big individuals, separated by a volume limit of 1 mm^3.

Another estimation of zooplankton biomass is the dry-weight. All pre-weighted were dried in an oven during 24 h at 60°C. Similar treatments have been applied to the filter itself before pre-weighting. Then each filter containing stuck-on dried zooplankton was weighted using a high precision scale. The dry-weight of zooplankton biomass was then estimated by subtracting the initial weight of the filter to the latter.

Visual counting and species identification were performed by expert planktonologists on a few samples of the survey. In particular, samples from the NS section, one EW section and the filament network were performed. Here we only describe very briefly the zooplankton community. As mentionned above, these data will be used in a paper focussing on the zooplankton data from the Zooscan, the detailed taxonomy and the dryweight estimations (Romagnan et al., 2010, in prep.).

2.4.2. Data handling.

While total chlorophyll *a* is the universal proxy for phytoplankton organisms, accessory pigments (chlorophylls-b and c, carotenoíds and others) are specific to phytoplankton groups (see Table 1), and their respective proportion to total chlorophyll *a* is a proxy of the community composition. Here we used the pigment grouping proposed by [*Ras et al.,* 2008]. Seven pigments are used as biomarkers of several phytoplankton taxa: fucoxanthin, peridinin, alloxanthin, 19-butanoyloxyfucoxanthin, 19-hexanoyloxyfucoxanthin, zeaxanthin, total chlorophyll-b. These taxa are then gathered into three size classes (micro- M, nano- N, and picophytoplankton P), according to the average size of the cells (M cell size > 20 µm, P size comprised between 2 and 20 µm, and N size < 2 µm). The fraction of each pigment-based size class with respect to the total phytoplankton biomass is calculated following [*Ras et al.,* 2008].

The fluorometer (chlorophyll *a* probe) from the rosette was calibrated using chlorophyll *a* concentration in mg/m^3 coming from the HPLC measurements. An average of a few fluorometer values (around 7 values of fluorescence) were selected, situated within a circle (radius = 30 cm) around the laboratory measurement, to calibrate while removing the high frequency noise. The regression line between HPLC measurements and fluorometer values fits quite well the scatterplots for concentration below 2 mg/m^3 . For higher concentrations, some dispersion exists. We obtain

13

HPLC measured pigments	Size classes	Taxonomic or biogeochemical significance
Chlorophyll a	All	All - except Prochlorophytes
Chlorophyll c2	All	Various
Chlorophyll c3	All	Prymnesiophytes, Chrysophytes
Chlorophyll b	P + N	**Green algae**
		(Chlorophytes, Prasinophytes)
Peridinin	M	**Dinoflagellates**
Fucoxanthin	M	**Diatoms**, Prymnesiophytes,
		and some Dinoflagellates
Zeaxanthin	P	**Cyanobacteria, Prochlorophytes**
Alloxanthin	P + N	**Cryptophytes**
Lutein	P + N	Chlorophytes
Diadinoxanthin	All	Various
19 − Butanoyloxyfucoxanthin	N	Prymnesiophytes, **Pelagophytes**
19 − Hexanoyloxyfucoxanthin	N	**Prymnesiophytes** (Haptophytes)
β Carotene	All	Various
Prasinoxanthin	P	Prasinophytes
Divinyl Chlorophyll a	P	Prochlorophytes
Chlorophyllide a	-	Senescent diatoms
Phaeophorbide a	-	Grazor fecal pellets

Table 1: List of the pigments used in this study and their taxonomic significance. We associate a few characteristic pigments (bold letters) to particular algal groups to describe the phytoplankton community, from [*Ras et al.,* 2008]. The last four pigments were additionally measured on a small subset of the total samples.

14
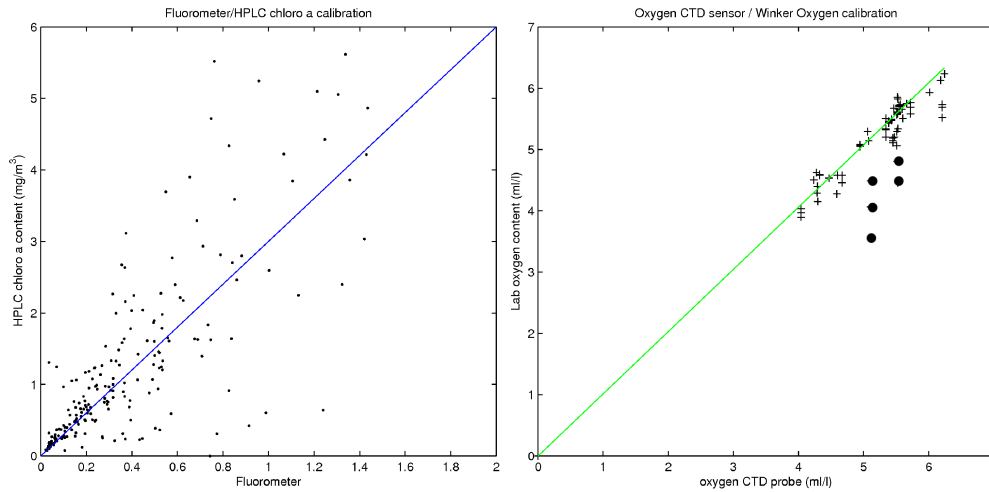
Figure 4: Calibration plots of CTD sensors. Left is for chlorophyll a with fluorometer values (x-axis) versus HPLC chlorophyll a content (y-axis); R^2 is 0.75 and regression factor is 3. Right is for dissolved oxygen, with CTD sensor values (x-axis) versus Winkler titration (y-axis); R^2 is 0.97 and regression factor is 1 (points displayed as black circles were disregarded to perform the regression).

the values of total chlorophyll a from the corresponding fluorescence by multiplying it by a factor of $\simeq 3$ (see Figure 4). The oxygen probe was calibrated using several Winkler titration performed on samples spread over the whole campaign to cover different biogeochemical environment. The correlation between dissolved oxygen values from Winkler titrations and from CTD probes is reasonable and the factor of the linear regression is 1 (figure 4). Note that a few measurements are far from the regression line. They all correspond to a subset that was analysed after a longer resting time (due to rough conditions at sea) than the protocol indications. They have been disregarded to calculate the regression factor and the R^2.

All continuous profiles coming from CTD sensors, ADCP or laboratory measurements presented in this paper were plotted using an optimal elliptic interpolation. For CTD and ADCP data, we set the vertical bin to 3 m and the horizontal bin to the mean spacing between casts, in order to remove the high frequency vertical variations of measured variables. Each original measurement was weighted sufficiently not to create any interpolated pattern. For the laboratory measurements, the bins were optimized depending on the vertical and horizontal resolution, while weighting the original measurement. Since the resolution was sometimes very variable, white areas may appear in the plot where no data were available (see for instance panels

15

384 of nutrients of Fig. 11).

385 We computed the Apparent Oxygen Utilization (AOU) according to [*Garcia and Gordon,* 1992].
386 It is the difference between the saturation value (that depends on the corresponding
387 temperature and salinity) and the measured dissolved oxygen. When the dissolved
388 oxygen is at its equilibrium, or saturation value, the water is only influenced by
389 the physic (advection, mixing, diffusion...). In this case, AOU will be $\simeq 0$. If the
390 AOU differs from 0, it means that the oceanic biota played a role in the measured
391 oxygen concentration. Oxygen can be either consumed by respiration or remineral-
392 ization processes, or produced by PhotoSynthesis (PS), making AOU a good proxy
393 for studying the biogeochemical functioning within a water mass. Indeed when pro-
394 duction is higher than consumption, we observe a negative AOU, whereas a positive
395 AOU is a sign of intense respiration/remineralization.

396 We also computed the Brunt-Väisälä Frequency, N^2. It was computed on each
397 interpolated profile using the following equation:

$$ N^2 \;=\; -\frac{g}{\rho_0}\frac{\partial \rho}{\partial z} \tag{1} $$

398 where N^2 is in rad^2/s^2, ρ_0 a reference potential density (mean of the vertical profile),
399 ρ the potential density σ_θ and z the depth. Each vertical profile was smoothed over
400 15 indices ($\simeq 4$ m) to filter out small scale structure or noise.

401 ## 3. Selected highlight: water masses analysis.

402 Figure 5 shows a T-S diagram of all CTD casts done during the survey. The
403 cloud of points above the isopycnal surface $\sigma_\theta \;=\; 27.1$ is composed of CTD casts
404 performed on the shelf and offshore using the bio-rosette limited at 200 m because of
405 the bearable depths of biological probes. The two lower branches come from two CTD
406 casts performed offshore the shelf using the phys-rosette (without any biogeochemical
407 probe that would not resist at these depths) which allowed us to record salinity and
408 temperature until 2000 m.

409 Dominant water masses can be identified, with the presence of North Atlantic
410 Deep Waters (NADW), the Mediterranean Waters (MW), North Atlantic Central
411 Waters (NACW) and Surface Atlantic Waters (SAW) mixed over the continental
412 margin with the Shelf Water (SW). When looking into details on the SW, we iden-
413 tify water masses coming from the Galician Rias and Portuguese northern river
414 which constitute the WIBP [*Peliz et al.,* 2002, *Otero et al.,* 2008], characterized by
415 low salinity (35.45 to 35.7 psu) and quite cold temperature ($12 - 16°$C) in upwelling
416 favourable conditions. These waters generally support very intense biological activity

16
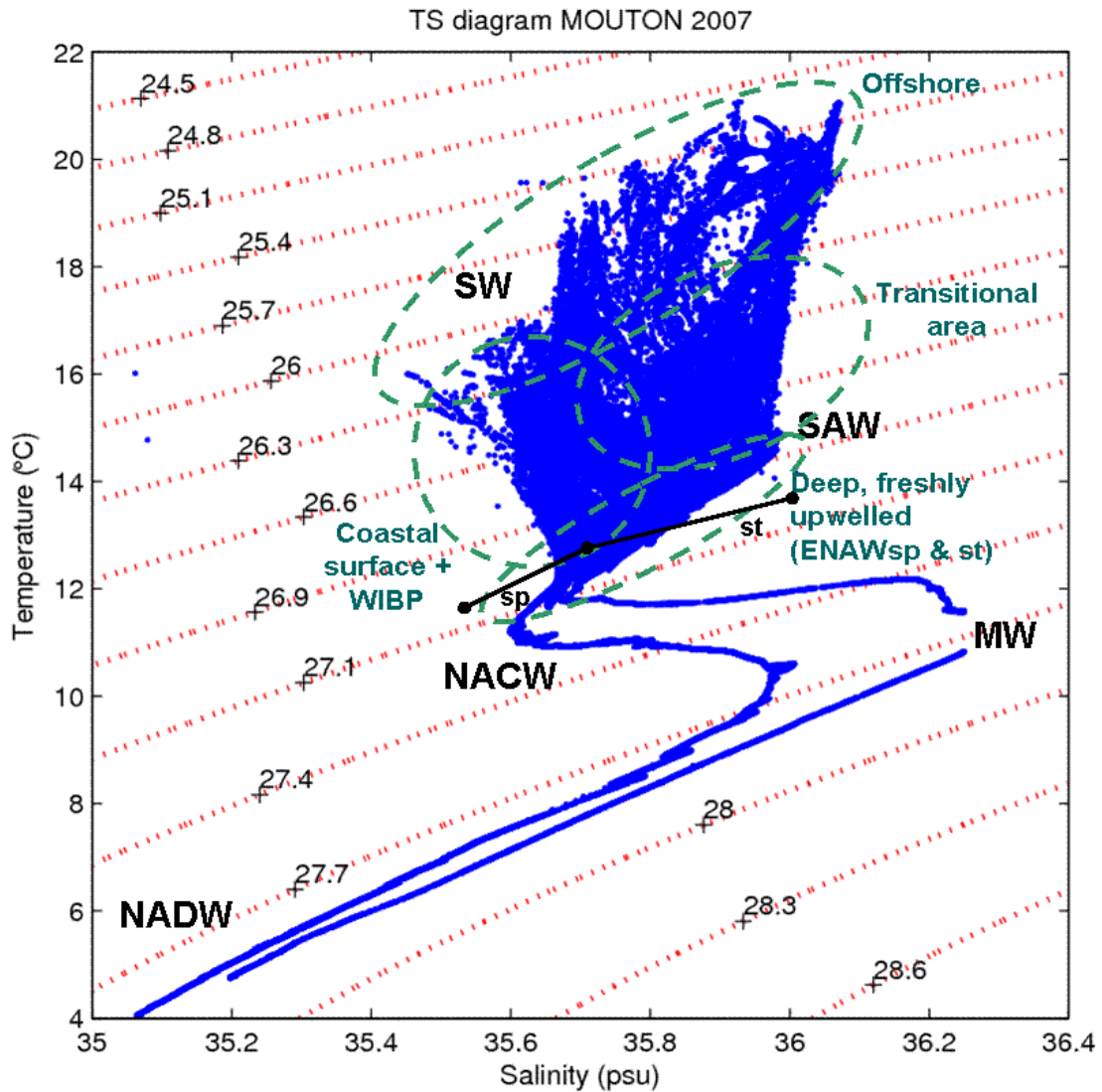
Figure 5: *In-situ* temperature (◦C) versus salinity (psu) diagram for the whole set of CTD casts. Red lines show isopycnals. The black straigh lines represent the separation between ENACWst and sp. TO BE ADDED: Coloring represents the Chlorophyll *a* concentration (in mg/m^3).

(high chlorophyll content) due to high nutrient levels once they reach the euphotic layer. Waters within the base of the parallelogram ($12 - 14°C$ from 35.6 to 36 psu) exhibit poor chlorophyll content and constitute the deep waters freshly upwelled onto the shelf that have not reached yet the euphotic layer. Waters within the top of the parallelogram are characterized by a similar salinity range but higher temperature ($17 - 22°C$) and low chlorophyll content. They represent the offshore water masses that were warmed up by solar radiation and depleted in nutrients by coastal biological activity. In between the base and top of the parallelogram, we found the waters of the transitional area between the very productive coastal upwelling and the oligotrophic ocean. They represent the filaments, eddies and other mesoscale structures that are characterized by intermediate chlorophyll content and a wide range of salinity and temperature (35.7 to 36 psu and $14 - 18°C$). On Fig. 5, the NACW are identified to be the source of the upwelled waters. [*Peliz et al.,* 2002] distinguished two type of central waters off the IPUS below the surface layer: the Eastern North Atlantic (Central) Water of subpolar origin (ENACWsp or ENAWsp, characterized by T $< 12.5°C$ and S < 35.7 psu) and Eastern North Atlantic (Central) Water of subtropical origin (ENACWst or ENAWst, warmer and saltier, 35.7 to 36 psu and $12.5 - 14°C$). The limit between ENAWsp and ENAWst is observed through a subsurface front characterized by intense convergence in the vicinity of Cape Finisterre, between $42°$ and $44°N$. Because of the wind driven Ekman pumping, these central waters are being upwelled over the shelf, mixed, warmed-up and transformed by biogeochemical processes to create the SW and SAW when reaching the coast and the surface. We then expect that ENAWsp are being upwelled in the extreme northern part of the IPUS whereas ENAWst are upwelled in the rest of the domain. On Fig. 5, we observe T $< 12.5°C$ at the base of the parallelogram (on the shelf) north of $41.5°N$, whereas other shelf waters south of $41.5°N$ are warmer than $12.5°C$. We can conclude that the latitudinal limit between ENAWsp and ENAWst during this cruise was located around $41.5°N$. [*Varela et al,* 2005] described all water masses in the Rías adjacent sea region and concluded that the limit between ENAWsp and ENAWst was located at around $43°N$. Our data suggest that this subsurface front may move southward until $41.5°N$ under very strong upwelling conditions. The Portugal southward Current (PC), which is intensified during upwelling events, may drag the subsurface front. Another explanation may be the southward advection over the shelf of waters that were originally upwelled further north.

We then tried to estimate the origins of the upwelled waters (sampled on the shelf) comparing the heaviest/coldest/less saline shelf waters against the few profiles performed offshore. [*Rossi et al.,* 2010] already used a similar approach on the East-West section which took place along $41°N$ on August, 21st, 2007. They roughly

18
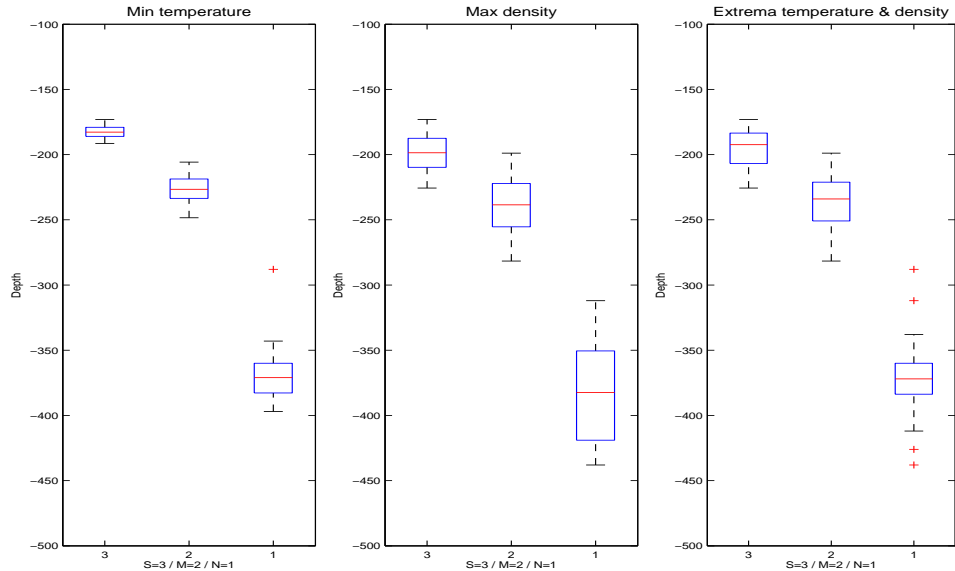
Figure 6: Boxplots representing all depths selected in appropriate offshore profiles depending on the extrema extracted from the NS section over the shelf. First left panel represents the selected depths using temperature alone, second is using the density alone, and third is using temperature and density together.

estimated the origin of upwelled waters along this section at around 200 m. We used here a similar approach along the whole NS section to analyse the spatial variability of the origins of the upwelled waters along the coast. This transect was performed within 3.5 days (quasi-synopticity, from 08/14/2007 at 8 a.m. to 08/17/2007 at 8 p.m.). We divided the section into 3 subsystems: 1 is north of 41.6°N, 2 is from 41.6°N to 40.3°N and 3 is south of 40.3°N (see also Section 5). We looked for the minimum of temperature sampled on the shelf (below 50 m), or the maximum of the density, in each area. In fact several tests were made to make sure that we were not selecting spurious values, and finally we averaged 100 extrema. In the northern subsystem 1, averaged extrema are 11.64°C and $\sigma_\theta = 27.17$; in the subsystem 2, they are 12.37°C and $\sigma_\theta = 27.05$; and finally for the southern area 3 we have 12.83°C and $\sigma_\theta = 27.05$.

We then selected among the offshore profiles all depths where such values (extrema) are found, only using temperature or density profiles alone, or both together (see Fig. 6). The offshore profiles used to estimate the origins of SW are two CTD casts made until 2000 m using the phys-rosette at 41°N / 10.5°W (08/22/2007) to be compared to subsystem 2, and at 39.45°N / 9.75°W (03/09/2010) to be compared to

19

subsystem 3. Because we did not have any deep CTD cast available for the northern subsystem 1, we used the values coming from 2 PROVOR drifters (42.1°N/11.5°W on 07/07/2007 and 43.3°N/10.6°W on 09/17/2007) and 3 XBTs (43°N/10.7°W on 08/14/2007, 43.4°N/11°W on 08/09/2007 and 42.6°N/11°W on 08/13/2007). We also looked into the World Ocean Atlas 2005 climatology to check the reliability of our extraction, using temperature, salinity and nutrient extrema. As expected, the climatology for August shows a clear north-south gradient of all variables symbolized by a slope for instance in the temperature isolines: the temperature of 13.5 °C is found at 75 m in front of the Rías (42.5°N), whereas it is approximately located at 150 m at 39.5°N. Another way to express this slope is to note that at 200 m below the sea level, there is a temperature difference of $\simeq$ 2°C between the Rías and the Nazare Canyon. In our data set, the mean bottom nitrate concentrations on the shelf of subsystem 1 (north) is 11.5 µmol/l whereas it is only 8.8 µmol/l for the subsystem 3 (south). The boxplot presented on Fig. 6 are composed of all depth values extracted from our different calculations to determine the origins of upwelled waters. The mean values indicated by the red line in the boxplot give a good approximation of the maximum depth where waters upwelled onto the shelf are coming from. As shown on the third panel of fig. 6, we found a significant difference in the origins of the upwelled waters between the 3 regions. In subsytem 1, the deepest upwelled waters are coming from around 375 m, whereas it is 235 m and 190 m for subsystems number 2 and 3, respectively. As mentionned before, the latitudinal gradient within the subsurface layer, below 150 m can not explain these differences since we used specific profiles in front of each subsystem. It may be linked to a stronger intensity of the upwelling, particularly due to the wind regime and also to the coast shape that might promote the Ekman pumping. [*Alvarez et al.,* 2008] studied the spatio-temporal evolution of the upwelling regime along the coast of the IPUS using Quikscat data. They found a positive Ekman pumping more intense during the whole year at Cape Finisterre than along the rest of the western coast of the IPUS. In particular, in late August/September, a patch of maximum of Ekman pumping intensity is present from 41° to 43°N. This may explain the deep origins of the waters, along with bathymetry effects which may drive the coastal deep flow within depressions or canyons. [*Joint et al.,* 2001a] considered that only ENAW at depths shallower than 150 - 200 m upwell over the Iberian shelf. Our new observations suggest that in the northern tip of the IPUS, waters may upwell from far below these limits, at least during an intense upwelling event. Waters being brought on the shelf from such depths have different physical characteristics and they also contain higher levels of nutrient. We then expect a strong response of the ecosystem in the euphotic zone.

20

We can also analyze the general biogeochemical functioning of water masses using Apparent Oxygen Utilization (AOU) versus a quasi-passive tracer (as temperature or salinity). On Figure 7 we plotted AOU versus salinity for all casts containing oxygen measurements, removing those made with the phys-rosette. On the upper panel, the large dark blue line centered on nul AOU constitutes saturated deep waters not - or poorly - affected by biology that are slowly being upwelled staying below the euphotic zone and the remineralization areas.

The negative values indicate surpersaturated waters. They coincide with the maximum chlorophyll contents and indicate very high photosynthesis and O_2 production by phytoplankton and autotroph microbes at the coast in the euphotic layer. Around 15 % of the total amount of measurements of the survey are found in negative AOU values, in between 0 and -3 ml/l (equivalent to 0 and -100 μmol/kg). The biogeochemical functioning during this upwelling event appears much more intense than other studies. For instance [Castro et al., 2000] or [Alvarez-Salgado et al., 2001] documented AOU maximum negative values around -30μmol/kg and -20μmol/kg respectively, under upwelling condition. Since our negative values come from surface or subsurface waters, we expect intense outgasing from the surface ocean to the atmosphere. [Borges and Frankignoulle, 2001] showed a tight correlation between the partial pressure of CO_2 and the dissolved oxygen saturation level. Their daily variations were controlled by the diurnal cycle of Primary Production (PP)/ respiration and the temperature variations that drive the air-sea exchange. They also described filaments as a net sink for atmospheric CO_2. Some methods described in [Minas et al., 1986] associated the percentage of oxygen supersaturation, along with nutrient data, to the intensity of the PP or Net Community Production. This kind of analysis may have been a simple way to roughly estimate the global PP of the IPUS, but are out of scope of the present manuscript.

The AOU positive values indicate undersaturated waters, where biological processes consume intensively oxygen. It can be due to respiration higher than PS but also to intense remineralization. In this case, it may be a combined effect of both since they coincide with subsurface waters but also with deep waters where only remineralization by the microbial loop plays a significant role. Note also the cloud of blue points (very low chlorophyll a content) located in the positive part of the plot ($0.5 <$ AOU < 1.8) and characterized by low salinity and temperature (waters deeper than 60 m). They correspond to freshly upwelled waters at the northern tip of the IPUS (north of 40.6°N) originally coming from ENAWsp that have been recently brought onto the shelf without chlorophyll. They present positive AOU due to their low initial oxygen content and ongoing remineralization processes. [Castro et al., 2006] observed a vertical fractionation of organic matter remineraliza-

21
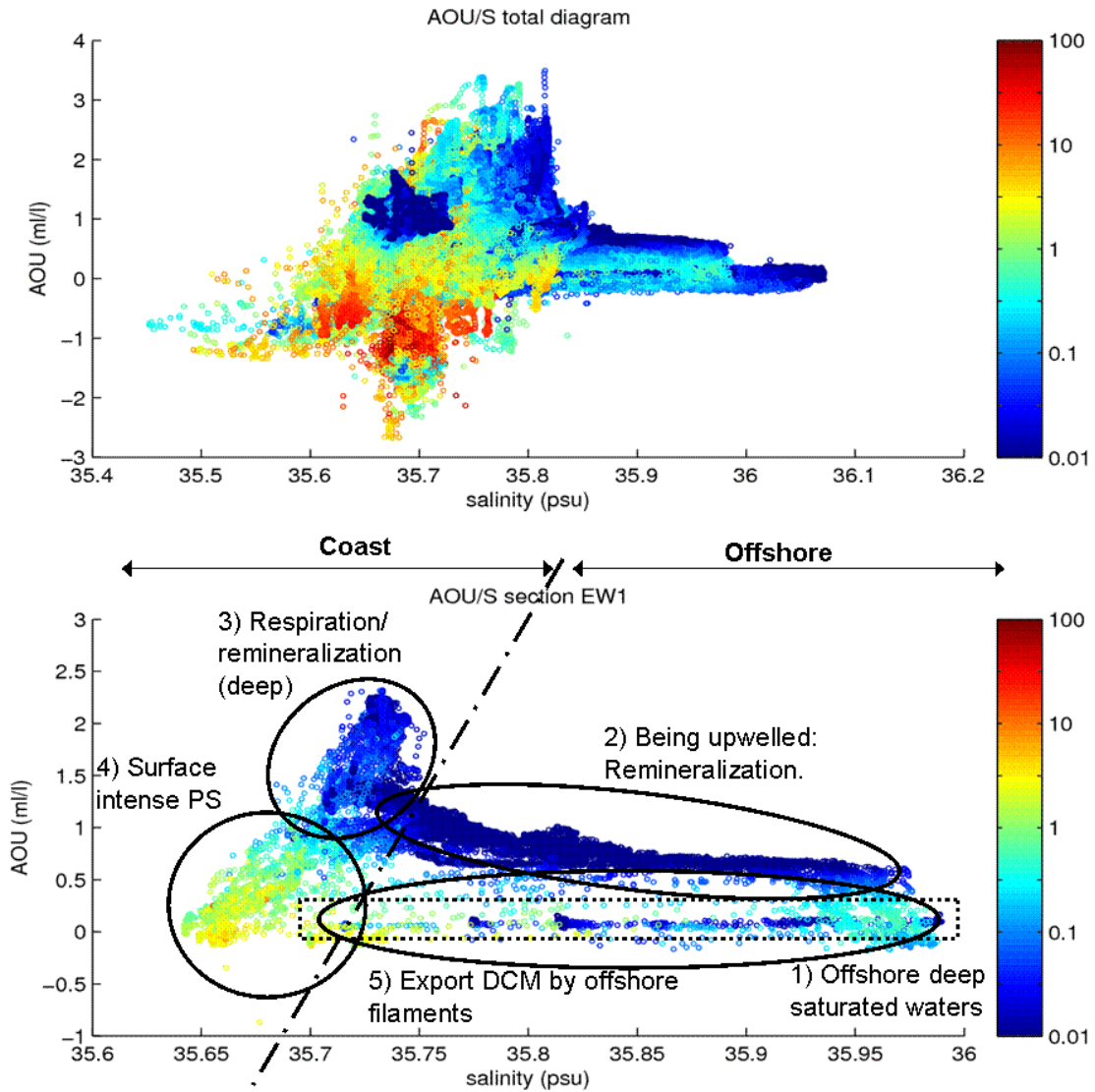
Figure 7: Apparent Oxygen Utilization versus Salinity diagram for all biological CTD casts (upper plot) and only for the east-west section along 41°N (lower plot). All points are colored depending on their chlorophyll *a* content (in mg/m^3).

22

tion in the water masses found off the Northern Iberian shelf. They also mentionned that at the northern tip of the IPUS, remineralization process intensity is responding to short-term upwelling events, as it was the case in our survey.

On the lower panel of Fig. 7, we plotted AOU versus salinity only for the EW1 transect. Analyzing this picture, we can reconstruct the water route under upwelling dynamics: from the deep ocean, to the offshore surface waters, going through the coastal surface upwelling. The quasi straight line of dark blue points centered on nul AOU corresponds to the offshore deep saturated waters. They are being upwelled forced by Ekman pumping on the bottom shelf, where microbial activity is starting to consume oxygen (AOU becomes slightly positive). Then they approach the surface and heterotrophic biological activity continues to consume oxygen, leading to even more positive AOU. When the rich nutrient waters reach the euphotic layer, autotrophic biological activity appears (moderate to high chlorophyll content) and AOU decreases forced by an intense PS (even becoming slightly negative for some areas). Finally these chlorophyll rich surface waters are advected offshore by the Ekman drift and filaments while the nutrient concentration decreases (AOU increases slightly, sign of a lower PS, whereas chlorophyll is still present).

4. General circulation: upwelling currents and mesoscale structures.

Data analyzed in this section are exclusively coming from the LADCP, although VMADCP 38 and 150 kHz were used for cross-validation. We estimate the errors around 5 cm/s for all current sections presented here. However we must mention that rough conditions occurred during leg 1 of the survey, due to intense northerlies (see Fig. 2) and to the presence of a strong swell (in average 3 m swell with a 10 s period). These rough conditions affected the ship navigation, especially offshore, as compared to the relatively protected shelf areas. This led to stronger errors offshore the shelf (VMADCP as well as LADCP). As a consequence the open ocean currents data have to be use cautiously.

The general circulation is typical of upwelling areas, especially during leg 1 when the favourable winds were very strong. On Figure 8 the along-shore velocities along EW1 and EW2 are mostly negative (southward), intensified at the surface (from -0.1 in the sub-surface to $\simeq -0.15$ m/s in the surface for section EW1); the cross-shore velocities are mostly positive (westward or offshore) at the surface ($\simeq 0.1$ m/s) and slightly negative (onshore) below ($\simeq -0.05$ m/s). We note also on EW1 the presence of a poleward jet around $0.3°$ offshore the shelf break in the subsurface waters, with values around 0.07 m/s. Since the northerlies were very strong during EW1, this feature may be related to the slope counter current observed in all major Eastern Boundary Upwelling Systems (EBUS) and it may be

23

80
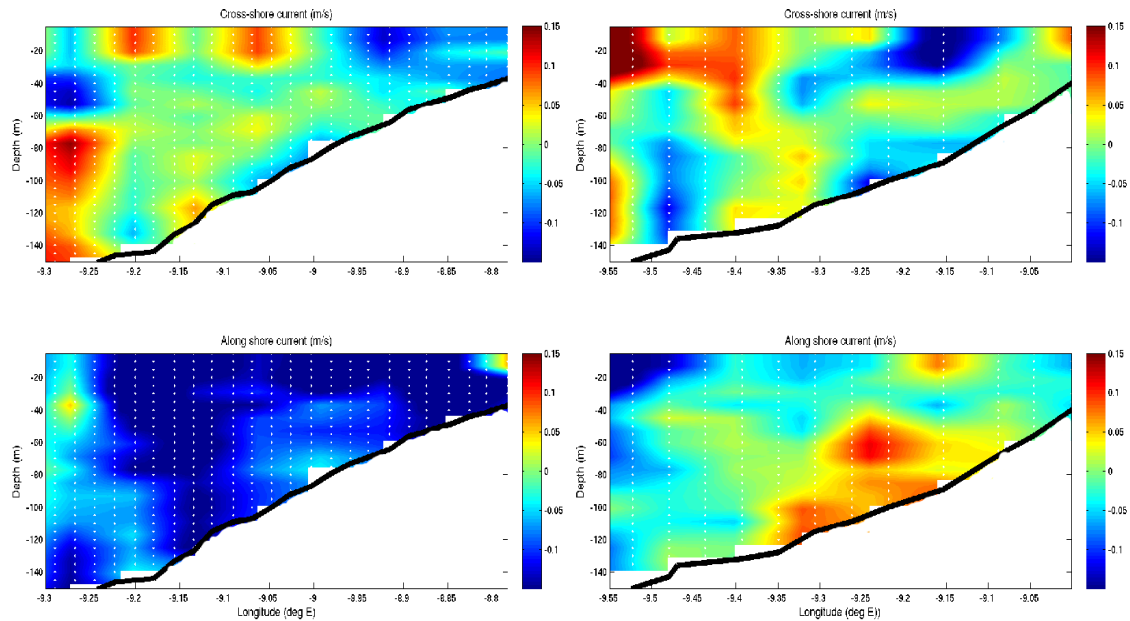
Figure 8: Cross-shore (upper panels) and along-shore (lower panels) velocities (m/s) from LADCP along the East-West transects numbered 1 at 41°N (left) and 2 at 40°N (right). On the upper panels red color indicates current directed to the west, while blue color to the east. On the lower panels, red color represents current to the north while yellow-green-blue colors to the south. The white dotted lines indicate the measurement positions; the thick black lines represent the observed bathymetry.

part of the upwelling circulation. Although controversial, it seems that the IPC well studied by [*Peliz et al.,* 2005] during winter, occurs also during the upwelling favourable season, at least for transient time periods. It has been already documented by [*Peliz et al.,* 2002, *Torres and Barton,* 2007] for the physical part and by [*Alvarez-Salgado et al.,* 2003] for its biological implication. On section EW2, upwelling relaxation occurred with lower northern winds. In this section, we observe a counter current on the shelf bottom waters (60 to 120 m) from 9.15 to 9.35°W with velocities around 0.1 m/s and a weak surface signature at 9.15°W. This counter coastal current may be the result of the wind relaxation, but [*Peliz et al.,* 2002] discussed different hypotheses. In their observations, the coastal counter current existed before the upwelling relaxation. They proposed that it responds to strong offshore deflection of upwelling currents and to the presence of the WIBP that influences stratification and the along-shore density gradient.

On the NS transect (Fig. 9), we can focus on the shelf circulation from August

24

14th to 18th. From 39° to 42.8°N the surface alongshore flow (0 to 25 m) is directed to the south. A few exceptions occur (positive values / northward circulation), associated with mesoscale features such as internal waves, meanders or eddies superimposing their signature on the mean flow driven by the wind (at 39.5°, 41.75° and 42.25°N). These structures will be analyzed below, focussing on the cross-shore component. Inside and north of Nazare canyon (39.5°N), several small scale structures are observed in the subsurface along-shore as well as in the cross-shore component of the ADCP velocities. It is likely that they are related to internal tidal waves and solitons, caused by the interaction between the semi-diurnal tidal currents, the shelf-break and other irregularities in the shelf topography with the existing stratification. Several papers ([*Relvas et al.,* 2007] and references therein) already documented the high occurrence of internal waves and solitons on the Portuguese margin, in particular in the Nazare Canyon [*Quaresma et al.,* 2007]. There is evidence of resuspension of the sediments and of formation of nepheloid layers, caused by solitons, that can have a significant effect on the biology.

The subsurface along-shore flow exhibits a much more complicated scheme. In some areas, a counter current (poleward) is observed: from 40.5° to 41.5°N and from 41.75° to 42.6°N. However inverse circulation (southward) is observed at $41.5 - 41.75°$N, between 39.6° and 40.5°N and north of 42.6°N. As mentionned by [*Relvas et al.,* 2007], the along-shore circulation on the shelf seems to be very sensitive to the wind regimes. We have observational evidences (section NS and EW2) that counter coastal flows constitute ubiquitous features of the area under upwelling favourable conditions. We believed that they are strongly linked with the local wind variations, the global imposed upwelling circulation, and the presence of the WIBP. Further observational as well as modelling studies are needed to better understand the variability of the shelf circulation under upwelling conditions.

The complex subsurface circulation leads to some areas of convergence at 42.6° and 41.5°N. At the latter location, the convergence area matches perfectly the initiation of a mesoscale filament that is indicated and clearly visible on the satellite image (right panel of fig. 9). The subsurface convergence at 42.5°N is also related to a filamental structure revealing a more complex picture. From 42.1° to 42.8°N, the SST shows an export of cold water mass offshore, with two colder veins at 42.25° and 42.6°N. The most northern vein seems to be related with the area of convergence at 42.6°N. Overall, subsurface areas of convergence may be related to a mechanism for filaments formation/maintenance, since the resulting cross-shore current may enhance offshore export of water masses. [*Sanchez et al.,* 2008] already discussed the fact that strong opposing subsurface flows will increase vertical shear, which is a source of baroclinic instability contributing to the generation of filaments.

25
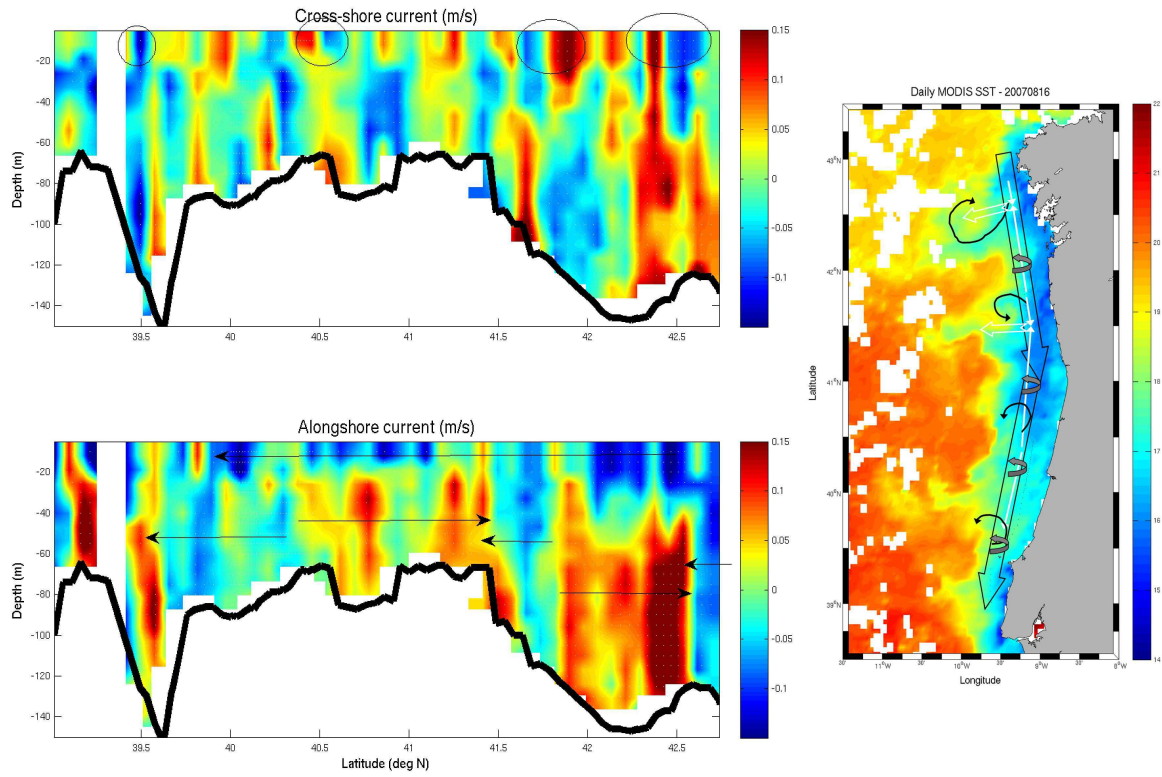
Figure 9: On the lefthand side, cross-shore (upper panel) and along-shore (lower panel) velocities (m/s) from LADCP along the North-South section. On the upper panel red color indicates current directed to the west, while blue color to the east. On the lower panel, red color represents current to the north while yellow-green-blue colors to the south. The thick black lines represent the observed bathymetry. On the righthand side, SST from MODIS Aqua with the main mesoscale structures annotated. Black wide arrows indicate the surface flow, whereas plain white thin arrows indicate subsurface circulation. Note the mesoscale eddies (black thin arrows) and the upwelling cells (grey curved arrows).

26

On the cross-shore component, the mesoscale circulation can be assessed, in particular, mesoscale eddies can be associated to dipole with positive and negative velocity patches within the surface layer. Their presence is then confirmed on the SST image. We found a strong anticyclonic eddy in between $42.2 - 42.7°$N which is reported on the SST map (diameter 50-60 km). This structure also feeds the complex filamental structure mentioned above. The westward flow coincide with the most southern cold vein at around 42.25°N. Characterized by an inverse dipole, a quite strong cyclonic eddy is centered around 41.75°N as indicated on the SST image. It presents a similar diameter ($\simeq 50$ km) than the previous eddy. Another small cyclonic eddy (diameter $\simeq$ 35-40 km) is characterized by a positive/negative dipole on the cross-shore velocities in the surface layer at 40.5°N. A last structure was observed at around 39.5°N (Nazare Canyon). It corresponds to a small cyclonic eddy, where divergence occurs (diameter of about 30-40 km). It seems to be related to the offshore drift of the above filament initiated at 40°N.

On Fig. 9 we also visualize active upwelling cells with intense negative bottom velocities (directed to the coast) over the shelf on the cross-shore components (local maxima), almost always associated to a divergence area in the along-shore component. There are located at $42, 40.8 - 41, 40 - 40.3$ and 39.5°N.

Globally, the main circulation is typical of any EBUS under favourable winds where several mesoscale structures are superimposed on a larger scale mean flow. The inner shelf circulation variability is also probably related to the complex hydrographic settings, the irregular shelf topography, and the small spatio-temporal scales of variation of the wind.

5. Selected highlight: North-South variability.

5.1. General physical analysis and subdivision.

We analyzed here the biogeochemical variability along the coast, using the North/South section performed from 39° to 42.75°N. Previous studies already documented the coastal domain of the Iberian Peninsula, but only focussing on smaller domain of $\simeq 1°$ in latitude (e.g. Rias only or a small area of the Portuguese coast). To our knowledge, it is one of the first quasi-synoptic survey spread along almost 4° of latitude in this area.

Figure 10 represents a few profiles of interest of CTD variable versus latitude and depth. All profiles (physical as well as biogeochemical) show very high vertical variations of the Mixed Layer Depth (MLD). The base of the thermocline on the temperature section, or the pycnocline on the density section, reveal vertical movements of more than 20 m, linked with the regular passages of internal waves that

27
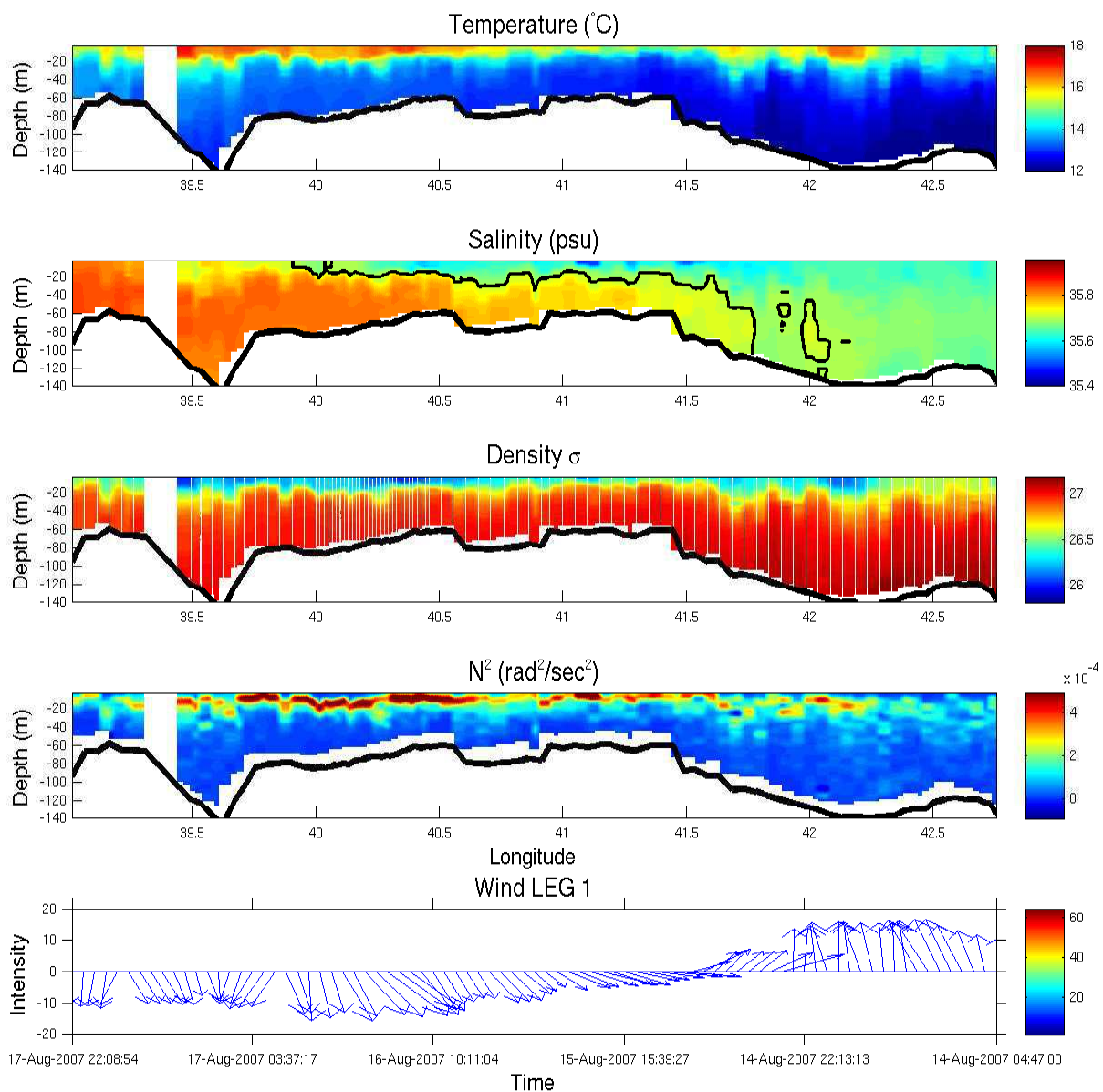
Figure 10: Latitude versus depth sections for NS transect from the CTD sensors: first panel is temperature (°C), second is salinity (psu or g salt /kg of water), third is density (σ_θ which is equivalent to grams per litre excess over one kg/m^3), fourth is buoyancy frequency, N^2 in rad^2/s^2(Brunt-Väisälä) and fifth is onboard measured wind. The white dotted lines on panel 3 indicate the measurement positions; the thick black lines represent the observed bathymetry.

28

deflected interfaces [*Relvas et al.,* 2007]. According to previous results (see Section 3), coldest and densest ENAWsp waters are found at the northern tip of the IPUS, north of 41.5°N on the temperature and density profiles. On the salinity plot, the WIBP is indicated with the isoline of salinity equal 35.7 psu [*Peliz et al.,* 2002]. It extends from 40°N to the northern end of the section (42.75°N). [*Peliz et al.,* 2002] present the WIBP as a surface layer of about 30 m occurring mainly in fall and winter, when the freshwater inputs are significant in this temperate climate. However during our cruise, the WIBP as defined by [*Peliz et al.,* 2002] is found in the whole water column, north of 41.75°N. It is in fact composed of the WIBP at the surface (since Rías and northern Portuguese rivers freshwater inputs are low but still present in August/September) and of the freshly upwelled ENAWsp (characterized by S < 35.7 psu, T < 12.5°C and density > 27). North of 41.75°N, an intense wind-driven mixing occurs (due to strong southerlies > 15 m/s) at the surface between WIBP waters and denser subsurface waters freshly upwelled. The low buoyancy frequency N^2 values (see Fig. 10) confirm the high mixing/low stability of the water column at the north of the section, related to opposite directions in the wind (northward) and the mean surface flow (southward). These ENAWsp upwelled waters are then mixed at the surface and warmed-up by solar heating in the euphotic zone. They are being transformed while advected by the south-west drift of the upwelling circulation. This $\simeq$ 30-40 m deep layer reaches 40°N sliding above denser waters continously upwelled. The southward advection of the WIBP was observed by [*Peliz et al.,* 2002] and studied in details by [*Otero et al.,* 2008]. From the south, more saline and warmer waters are advected by the counter subsurface current under the WIBP. [*Peliz et al.,* 2002] and [*Relvas et al.,* 2007] described a warm northward current at the inner shelf, separating colder upwelled waters from the coast, creating a double frontal system. This system is supposed to have high ecological implications for along-shore dispersion of species and coastal retention. From the physical characteristics, the subdivisions into three different subsystems already mentionned are derived: 1 is north of 41.6°N, composed of coldest, densest and less saline ENAWsp waters, being mixed with the surface WIBP. The transitional subsystem 2 stands from 41.6°N to 40.3°N and is composed of freshly upwelled ENAWst overlaid by the thin WIBP advected by the southward upwelling current. Finally south of 40.3°N we defined the subsystem 3 characterized by the most saline and less dense waters (ENAWst). As mentionned before, the upwelling process reveals variable intensity along the coast, detectable here with local minima of temperature, maxima of density, respectively, at $42.5, 42, 40.8 - 41, 40 - 40.2$ and 39.5°N. These upwelling cells are also visible on nutrients profiles with local maxima at the bottom (see Fig. 11). Water column stability, deduced from the buoyancy frequency N^2,

29

influences strongly the depth and characteristics of the ML. All maxima of buoyancy in the first 40 m (maximum of stability, linked with lower surface winds) are correlated with a maximum of temperature / minimum of density (see at $42.2, 41.2, 39.5$ to $40.6°N$). Daily winds appear to control the onset/offset of the uwpelling pulses, whereas short, transient, hourly winds drive the ML dynamics, which is also strongly influencing the ecosystem.

5.2. The Rías subsystem 1: north of $41.6°N$.

The chlorophyll *a* content deduced from the fluorometer reveals a complex horizontal and vertical repartition along the whole section (see Fig. 11). The highest concentrations are found north of $42.2°N$, in front of the Rías, where the upwelled waters are thought to be from the deepest origins (see fig. 6) and richest in nutrients. However, in our observations, nutrient concentrations are high at the north but the maximum values are found in the central area. The zone north of $42.2°N$ is also characterized by a high mixing revealed by the low buoyancy frequency: the first 40 m of the water column are very well mixed, exposing regularly to direct sunlight all cells evolving in this layer, meanwhile constantly updating the pool of available nutrients. In the surface mixed layer, all measured nutrients are depleted until 40 m, attesting the intense autotrophic planktonic activity. In this subsystem 1, the averaged nutrient concentrations below 50 m are around 11 µmol/l for nitrate, 0.8 µmol/l for phosphate and 6 µmol/l for silicate. These values confirmed the origin of the upwelled waters from ENAWsp and are consistent with previous observations [*Castro et al.,* 2000, *Alvarez-Salgado et al.,* 2002]. However they are among the highest concentrations recorded in this area, supporting the deeper origins of the upwelled waters. The AOU section (Fig. 11) indicates that remineralization in this subsystem is quite low (mainly < 50µmol/kg), except at two locations, 41.8 and $42.5°N$, where AOU reaches 75 µmol/kg. These two areas coincide with the highest nutrient concentrations originating from remineralization and being added to the upwelled pool. However, we also observe values of nutrients quite high outside those two remineralization hotspots. It supports the fact that high observed nutrient concentrations are mainly due to their source waters and poorly to remineralization processes.

The general repartition of size fractionated phytoplankton, estimated following [*Ras et al.,* 2008], is typical of an upwelling region (Fig. 13): coastal areas are dominated by microphytoplankton ($>$ 20 µm). Except 3 samples, all stations from the NS section contain roughly around 70 % of microphytoplankton. Then the next contributing fraction is the nanophytoplankton (size comprised between 2 and 20 µm) in the subsurface and surface waters (in average $\simeq$20 %). Finally the picophyto-

30
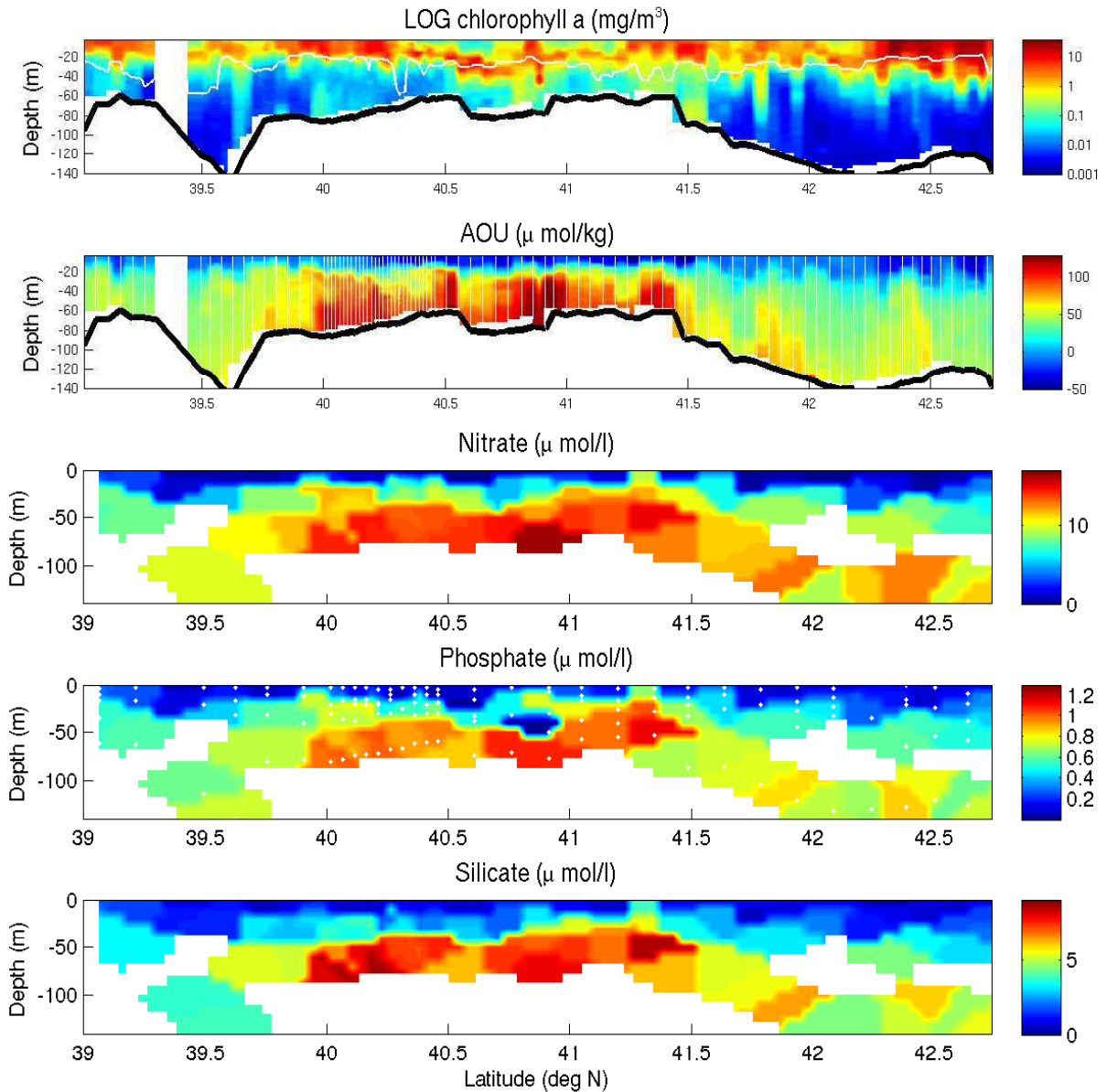
Figure 11: Latitude versus depth sections for NS transect from CTD sensors: first panel is chlorophyll a concentrations from the fluorometer (converted in mg/m^3), second is Apparent Oxygen Utilization (μ mol/kg). Last three panels are Nitrate, Phosphate and Silicate concentrations (μ mol/l). The white thick line of the first panel (chlorophyll a) shows the euphotic depth (1 % of PAR). The white lines or white markers indicate the measurement positions and the thick black lines represent the observed bathymetry.

31

748 plankton ($<$ 2 μm) is present with an average fraction of $\simeq 10$ %. Deeper samples
749 are also dominated by microphytoplankton ($\simeq 80$ %), picophytoplankton is around
750 20 %, whereas the nanophytoplankton decreases drastically. Although the model
751 from [*Ras et al.*, 2008] is not very reliable in specific eutrophic areas as upwelling
752 and for deep samples, it gives a general overview of the size fractionated communi-
753 ties along the coast of the IPUS. When moving slightly offshore (see further details
754 in the next Section 6), size repartition changes with a higher contribution of the
755 smaller cells, nano- and picophytoplankton. When focussing on the surface pigments
756 composition of the NS section (fig. 12), we clearly observe a dominance of the fu-
757 coxanthin, characterizing diatoms, associated with peaks of the total chlorophyll a
758 concentration from HPCL analysis. Other pigments present moderate concentrations
759 and attest (see table 1) the moderate presence of prymnesiophytes (or haptophytes,
760 as *Coccolithophores*), cyanobacteria (*Synechoccocus*) and prochlorophyte (nano- of
761 the type *Prochloroccocus Marinus*), as well as dinoflagellates (Peridinin). In fact,
762 the entire subdomain 1 is characterized by a dominance of diatoms and dinoflag-
763 ellates microphytoplankton, associated with moderate smaller species (roughly 15
764 % of nano- and 15 % of picophytoplankton). Following the discussion of upwelling
765 samples from [*Ras et al.*, 2008], a young nano- and picophytoplankton community
766 had quickly responded to a recent upwelling set-up, but the high constant inputs of
767 nutrients promote with a small time lag a diatom-dominated microplankton com-
768 munity. The surface waters are indeed completely depleted in nutrients despite the
769 constant inputs by upwelling and vertical mixing, attesting the presence of these very
770 efficient autotrophic cells.

771 The associated zooplankton populations are characterized by low biomass: abon-
772 dance $<$ 2000 individuals /m^3, low to moderate biovolume $<$ 900 mm^3/m^3 and
773 dryweight abundance $<$ 0.05 g/m^3 except one sample at 41.75°N. These populations
774 are however composed mainly of large individuals $>$ 1 mm^3/m^3 as shown on panel
775 7 of Fig. 12. Looking at their species composition (Fig. 13), it is dominated by
776 large Copepods, Doliolidae, large Chaetognaths and larvae of Crustaceans. In this
777 subsystem, low zooplankton biomass and the occurrence of mainly large individuals
778 (as compared to the southern domains) may be related to the very high mixing of
779 the region which decrease the encounter rate of grazers with their preys. The large
780 individuals having higher motility abilities take advantage of these environmental
781 conditions. A relatively low grazing pressure (globally low zooplankton biomass and
782 very low microzooplankton grazing pressure) is also in agreement with the highest
783 concentrations of chlorophyll a found in the region. Although the surface layer is
784 very productive, it seems that the export to the deep layer of organic materials, and
785 the expected associated remineralization processes that consume oxygen, are quite

32
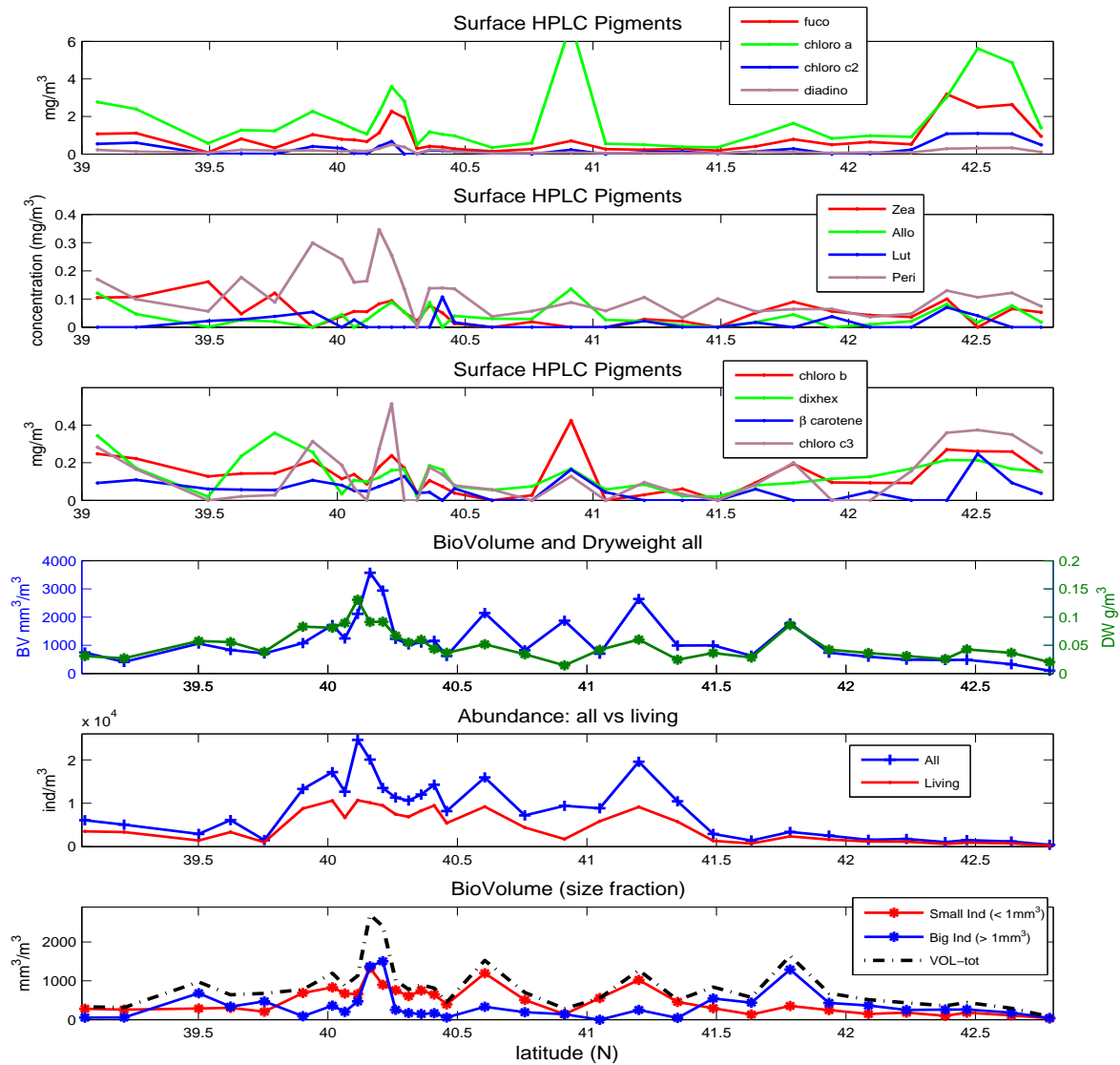
Figure 12: Phytoplankton pigments concentrations (from HPLC) on the three upper panels, and zooplankton biomass estimation (biovolume, dryweigth and abundance) on the three lower panels for the NS transect.

low (low AOU). It may be explained by the complex shelf circulation, composed of a surface upwelling current (southward) and a poleward under current which will advect in both direction all products of this intense biological activity in others zones. The angular coast-line, facing west then north, is related to an intensification of the circulation turning around Cape Finisterre. The presence of filaments and eddies may export these productive coastal ecosystems offshore in their core. Considering the phytoplankton assemblage observed, the low mineralization rate and the nutrient contents of shelf versus ENAWsp waters, we expect a higher new production than the regenerated production (i.e. a high f-ratio) in this area.

5.3. The central subsystem 2: from $41.6°N$ to $40.3°N$.

In subsystem 2, the vertical section of chlorophyll a is very different than in area 1 (Fig. 11). A Subsurface Chlorophyll Maximum (SCM) is observed, oscillating in between 20 and 40 m, with significant concentrations reaching the seabed. This vertical distribution is closely related to the high water column stability revealed by high values in the buoyancy frequency N^2, especially in the top 40 m. The wind decrease and inversion took place exactly at this period (see lower panel of Fig. 10) which led to a short stabilization and stratification of the water column. Nutrient values are the highest along the section: below 50 m, it is around $12 - 15$ µmol/l for nitrate, $0.9 - 1.1$ µmol/l for phosphate and $6 - 8$ µmol/l for silicate. The AOU values from the seabed to the thermocline are very high (> 75 µmol/kg up to 140 µmol/kg). It is the sign of intense remineralization processes that consume the dissolved oxygen present in the whole water column. First, it is related to an intense export of organic material from the surface layer to the seabed inside the water colum. This is confirmed when looking at the difference of abondance (from Zooscan) between all objects and living objects. The significant difference (in average 500 objects $/m^3$) from 40 to 41.5°N symbolize all particulate organic matter (POM) and marine snow that are being exported to the seabed. The maximum of remineralization processes have been found in summer autumn in a study by [*Castro et al.,* 2006]. Moreover, the highest values of nutrients found at the bottom, especially nitrate and silicate, associated to a shallow shelf (around 80 m for area 2), may suggest the release and resuspension of nutrients from the sediments in the nepheloid layers. This hypothesis is reinforced by a recent work of sediment resuspension under the influence of internal waves [*Quaresma et al.,* 2007]. Another source for resuspension is also the relatively strong tide currents that are observed in this shallow area (see the specific barotical tidal ellipses in [*Relvas et al.,* 2007] and reference therein). A recent work by [*Sharples et al.,* 2009] showed that a breaking internal tide at a shelf edge is a fundamental control on the structural and functional properties of ecosystems.

34

They mentionned that contrasts in vertical mixing of nitrate between the shelf and the open ocean correspond with horizontal and vertical changes in phytoplankton communities. We expect in this sub-area an important proportion of regenerated production as compared to the new production, i.e. a lower f-ratio. The surface phytoplankton community has evolved along the southward drift (Fig. 12) of the WIBP. This subsection is characterized by a slightly higher proportion of nano- and picophytoplankton, with the significant presence of cryptophytes (for instance of the type of *Cryptomonas*). The microphytoplankton community is now dominated by dinoflagellates (Peridinin) first and then diatoms (Fucoxanthin). Due to wind relaxation and restratification, surface waters are depleted (not fuelled) whereas significant nutrient concentrations are still found below. These large cells are concentrated at the SCM and smaller populations occur above. These observations have been already mentionned by [*Joint et al.,* 2001a]. They found small species mainly in the surface waters, just above the SCM where nutrient contents are low, and the larger ones at the SCM or even slightly below (higher nutrient contents). The varying concentration of nutrients through the whole water column is being used by a diverse and adaptative community of opportunists phytoplankton. [*Joint et al.,* 2001a] and [*Ras et al.,* 2008] discussed the possibility of having a flagellate biomass that develops rapidly after a recent upwelling set up, before being dominated by slower developing diatoms population. The zooplankton biomass is also very variable in subsystem 2. Using estimation from dry-weight or biovolume, moderate to high zooplankton biomass is found (300 to 1800 mm^3/m^3 and 0.025 to 0.075 g/m^3). Abundances vary significantly: from 2000 to 9000 individuals /m^3. This area is dominated by small individuals of zooplankton mainly composed of Copepods, Cladocera, Appendicularia and Bivalves whereas the large Crustaceans larvae become rare (Fig. 13). The most noticeable difference is the large apparition of Cladocera, which are related to more oligotrophic waters. However, since it is depth-integrated biomass estimation, it is hard to differentiate their origins. Numerous microzooplankton are present in this subarea, thus we expect to have a high grazing pressure. It may also explain that the surface waters are quite poor in phytoplankton because of an intense microzooplankton grazing, already mentionned by [*Cermeno et al.,* 2006]. When plotting chlorophyll *a* from CTD versus density (not shown), we found that in this area phytoplankton is present in a wide range of density layers. In this unique subsytem, the deepest and densest layer (density > 26.8) also contained chlorophyll *a*, whereas it was confined to the density < 26.7 along the whole section. It may be related to plankton migration patterns but also to the presence of two different populations. This transitional subsystem is clearly under the influence of two water masses. The surface WIBP advected from the north with its specifical plankton communities,

35
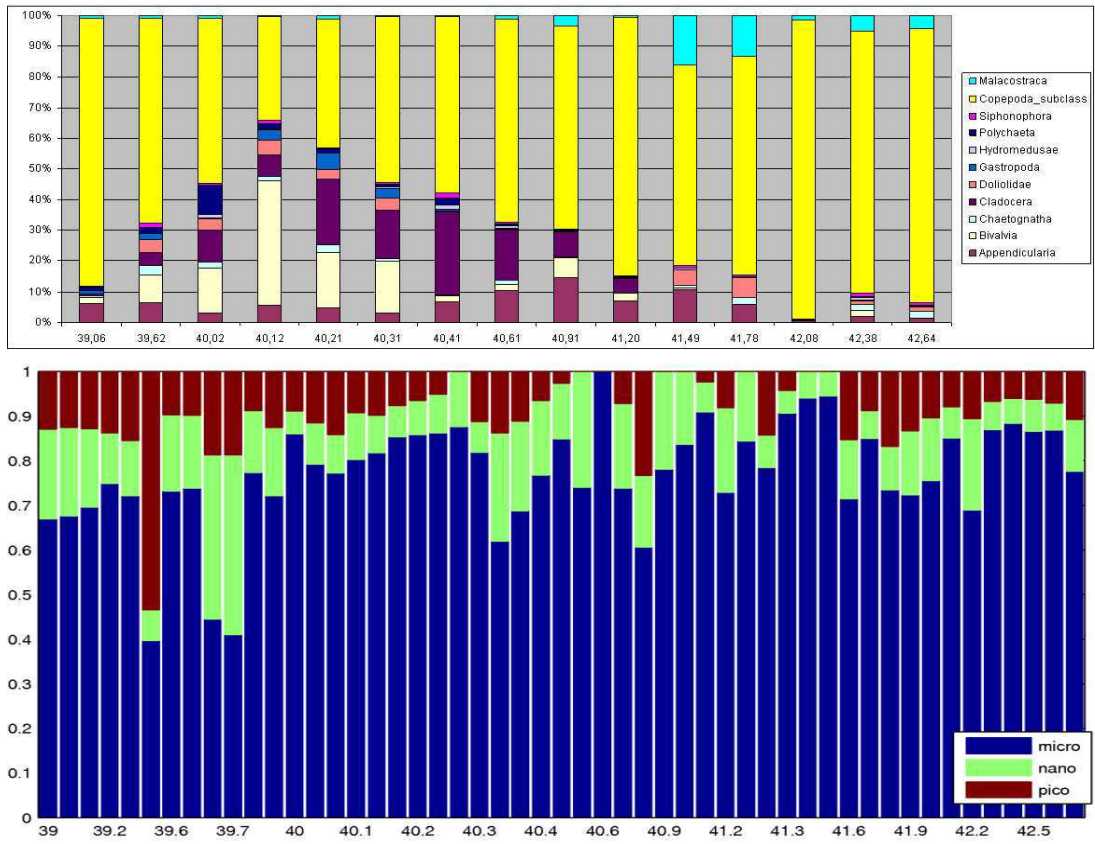
Figure 13: Zooplankton species composition for a few samples along the coast (upper plot) and phytoplankton size-fractionated along the NS transect (lower plot). X-axis are latitude.

861 and the subsurface layer coming from the south, containing more saline waters and
862 a different associated ecosystem.

863 *5.4. The southern subsystem 3: south of* 40.3°N.

864   The last subsystem 3 is characterized by cold, dense and rich nutrient waters in
865 the Nazare Canyon, whereas the rest of the subsystem has the highest temperature
866 and salinity (ENAWst), associated with the lowest nutrient. Nutrient concentra-
867 tions below 50 m are around 9 μmol/l for nitrate, 0.7 μmol/l for phosphate
868 and 3.5 μmol/l for silicate. These values are very similar to those reported by
869 [*Castro et al.,* 2000]. The chlorophyll *a* content is however moderate to high with
870 three surface local maxima, at 39.2, 39.9 and 40.25°N. From 39.8 to 40.25°N, we

36

observe a quite homogenous surface layer of about 35 m with chlorophyll a concentrations $> 1\text{mg/m}^3$. This coincides with one of the peaks in onboard measured winds (see lower panel of fig. 10). Looking back at the buoyancy frequency N^2, a subsurface line of very high values isolates a surface area where low values are found. It seems that a very high mixing occurs in the first 20 m(low values of N^2), whereas a stratified region appears to isolate this surface mixed layer (high values of N^2 at around 30 m). On Fig. 10, we observe that the surface layer is composed of the less saline waters being advected from the north (with slightly higher nutrient contents) above more saline waters. Their different physical properties may create strong stratification that isolates the surface mixed layer from subsurface waters. It generates a favourable window for phytoplankton growth, with moderate nutrients from the north. The AOU section reveals quite low values in the water column ($< 50\mu\text{mol/kg}$), symbolizing moderate to low remineralization processes. Conversely, a maximum of AOU is observed north of 40°N ($> 100\mu\text{mol/kg}$) that coincide with the previous chlorophyll a maximum. As it was the case in the previous subsystem 2, this AOU maximum indicates a strong export of POM, associated with intense remineralization along the water column as well as sediment resuspension processes. The phytoplankton community composition is globally again dominated by microphytoplankton, except 3 samples located above the Nazare Canyon (see Fig. 13), where we observe a SCM at 10 - 20 m. The local maximum from 39.8 to 40.25°N is characterized by a population of dinoflagellates indicated by the high values of peridinin. Significant values of fucoxanthine for diatoms are also found in this area, as well as haptophytes (19 Hex + chloro C3). We have in the surface waters a typical well developed upwelling ecosystem with large phytoplankton cells. Further south, diatoms and dinoflagellates are still present whereas small cells as cyanobacteria (*Synechoccocus*), prochlorophytes (type *Prochloroccocus Marinus*), haptophytes and cryptophytes are increasing (see Fig. 12). It seems we are in the transition between two ecosystems, a population dominated by large slowly but efficiently growing cells in the surface layer coming from the north, to a population dominated by small rapidly developing cells further south. Some evidence of very large and numerous cells of Ceratium (dinoflagellate) were clearly visible in some scanned images of the Zooscan, sometimes aggregated in chains. They were very abundant in almost all stations from subsystem 3, and a few of the most southern samples of subsystem 2 contained small quantities of Ceratium. They were reported before by [*Joint et al.,* 2001a] but they identified them as a typical species of oligotrophic open ocean waters. We hypothesize that this species was present in the subsurface layer (ENAWst saline waters), advected northward by a coastal current, and that was sampled by the zoo-net tow until 70 m. It confirmed that the subsystem 3, as well as southern subsurface waters of subsystem 2, are quite

37
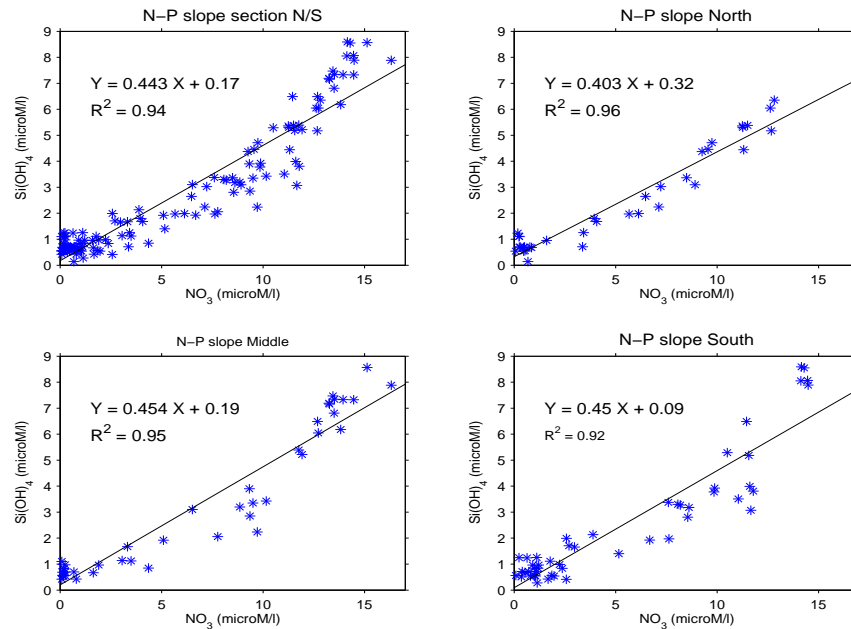
Figure 14: Silicate versus nitrate plots for the whole NS section (upper left) and separated in different subsystems 1 (upper right), 2 (lower left) and 3 (lower right). Black lines are the linear fitting to visualize the high Si uptake in the north (although a quadratic regression gave a better fitting).

far different from the northern IPUS.

Zooplankton biomass is heterogeneous in this subsystem. South of 39.8°N, we have moderate to low biomass (< 1200 mm^3/m^3 ; < 0.05 gm^3 and less than 5000 individuals /m^3) with similar proportion of small and large individuals. However, the 39.8 to 40.25°N area reveals the maximum of zooplankton biomass of the whole transect (from 1000 to 2900 mm^3/m^3 ; 0.06 to 0.13 g/m^3 and from 2000 to 10000 individuals /m^3). On each side of the maximum (40.2°N), these populations are dominated by small individuals whereas the 2 central stations are dominated by large individuals. This coincides with a local minimum of chlorophyll a, under grazing pressure, surrounded by two local maxima. This small area is a hot spot for biological productivity, with larvae of Crustaceans and Gastropodes, Doliolidae and Chaetognaths that represent the big individuals typical of rich ecosystems. The species found south of this hot spot are different from the northern areas, with less Copepods, more Cladocera, few Appendicularia. The most remarkable difference is a relatively high presence of Cladocera, Bivalves and Doliolidae.

38

On Figure 14, we plotted the ratio silicate - nitrate for the NS section, and then for each subsystem. The linear regressions of nitrate with phosphate (not shown) and silicate give an indication of the stoichiometry of the net consumption of nutrients during the coastal upwelling event. It seems that the nitrate utilization was different between the subsystems: in the northern area 1, we have a lower N:Si slope, indicating a higher uptake of silicate. It supports the fact that diatoms are dominant in the northern subsystem, although they are found over the whole IPUS. [*Alvarez-Salgado et al.,* 2002] suggested that the different composition of microplankton populations in the subpolar and subtropical North Atlantic provinces may explain the difference found in the regression slopes. Considering the findings from sections 5 and 3 together, it reinforces the fact that ENAWsp imposed their signature in the northern IPUS during this survey. The rest of the domain is driven by ENAWst characteristics, along with the influence of the northern waters advected at the surface by the upwelling current. The intercept of the regression line gives additional information: silicate (see Fig. 14) and phosphate (not shown) were still measurable (respectively 0.25 and 0.1 µmol/l) whereas the nitrate concentrations had fallen below the limit of detection. This may suggest that the PP over the shelf of the IPUS is limited by Nitrate. It has already been mentioned by [*Castro et al.,* 2000, *Joint et al.,* 2001a, *Alvarez-Salgado et al.,* 2002].

5.5. A possible scenario.

To sum-up the variability along the NS section, we propose a scenario explaining the bio-physical context. We had the onset of an intense upwelling forced by strong favourable northernly winds prior to the section period. The northern sysytem (north of 41.6°N) was characterized by cold, dense, rich nutrient ENAWsp waters highly mixed. The ecosystem responded primarily by a nano- and picoplankton community rapidly replaced by a more efficient diatoms dominated population. High mixing and maybe terrestrial inputs (low salinity/low temperature) were unfavourable to zooplankton small individuals development. Low export is observed in this region probably linked with intense subsurface current. The surface waters are strongly advected southward by the upwelling current and enter the central area (40.3° to 41.6°N). Here, the relatively calm weather (low winds) led to stratified waters which promote phytoplankton growth organized around a SCM. Below 40 m, another water mass coming from the south is present with different phyto- and zooplankton communities. Moreover, the occurrence of mesoscale structures induce a marked spatial variability of the ecosystem. A strong export and remineralization take place in this shallow region, leading to constant fuelling of nutrients from below and high regenerated production. We also note a strong influence of biogeo-

39

chemical processes at the sediment interface, influencing the whole water column, probably related to internal-waves. This is a transitional system, influenced by the northern waters that are being transformed along their drift, and the subsurface ENAWst waters. At around 40.2°N, we found a hot spot characterized by a well developed upwelling ecosystem with large phytoplancton cells and large zooplankton individuals. At the same time, further south, in less advantageous environment (less nutrients), a more stable ecosystem exists where diverse size cells and species are found. The communities here are far different from those found at the northern tip of the IPUS. Although upwelling pulses drive the main variability of the chlorophyll a by providing significant nutrient concentrations on the shelf, a high influence of the water column stability on nutrients inputs and mixing rates in the surface layer was found. It will in turn shape the community structures and the vertical repartition of both zoo- and phytoplankton. Stratification and homogenizing phases alternate, superimposing on the more global upwelling variability, confirming findings from [*Alvarez-Salgado et al.,* 2003]. Finally, we also note a strong coupling between zooplankton and phytoplankton communities, in terms of size fraction, ecological functioning and species composition.

6. Selected highlight: the cross-shore variability.

Here we use East-West sections 1 and 2, performed at 41° and 40°N respectively, to study the cross-shore variability of the physical and biogeochemical characteristics in the IPUS. Note that section EW1 (41°N) was performed between August 21th and 22th, when northerlies were intense ($\simeq$ 15 m/s), whereas section EW2 (40°N) was done with weak decreasing northerlies ($<$ 5 m/s).

Physical sections are depicted on Fig. 15 for both transects. Other sections for transect EW1, namely temperature and density, were already presented in [*Rossi et al.,* 2010]. Chlorophyll a concentration for both sections are presented in Fig. 16 along with a contouring of the minimum of dissolved oxygen concentration over the shelf ($<$ 200 µmol/kg). [*Rossi et al.,* 2010]already analysed the upwelling dynamics: the coastal upwelling is associated with cold (13°C and below) and dense waters ($\sigma_\theta >$ 27) that were brought over the shelf and reached the surface at the coast. The lighter surface waters ($\sigma_\theta \simeq$ 26) are pushed offshore (further than 9.7°W) by the Ekman drift associated with the Northern winds. Figure 3 in [*Rossi et al.,* 2010] also reveals a dome of dense waters penetrating into the surface layers at around 9.25°W, slightly onshore the continental margin, that they associated to a secondary upwelling. They also noted the presence of very dense and cold waters ($\sigma_\theta \simeq$ 27 and $<$ 12.5°C) lying on the seabed inshore the edge of the shelf break below this secondary upwelling. They

40
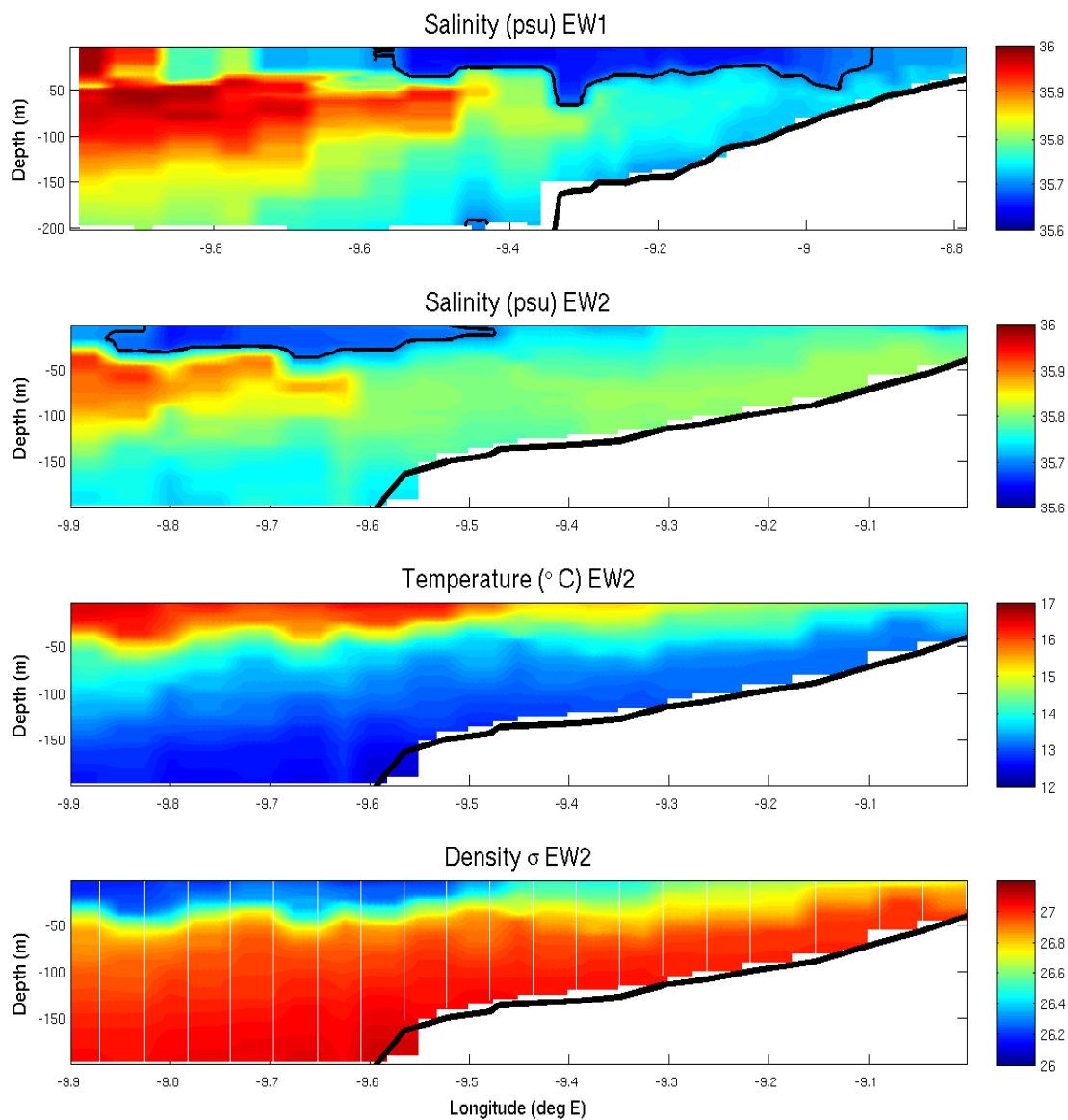
Figure 15: Longitude versus depth sections of CTD sensors for both EW transects: first panel is for EW1 at 41°N and last three panels are for EW2 at 40°N. 2 first panels are salinity (psu or g salt /kg of water), third is temperature (°C), fourth is density (σ_θ). The black lines in the salinity sections contour the WIBP plume (< 35.7). The white dotted lines indicate the measurement positions; the thick black line represents the observed bathymetry.

41
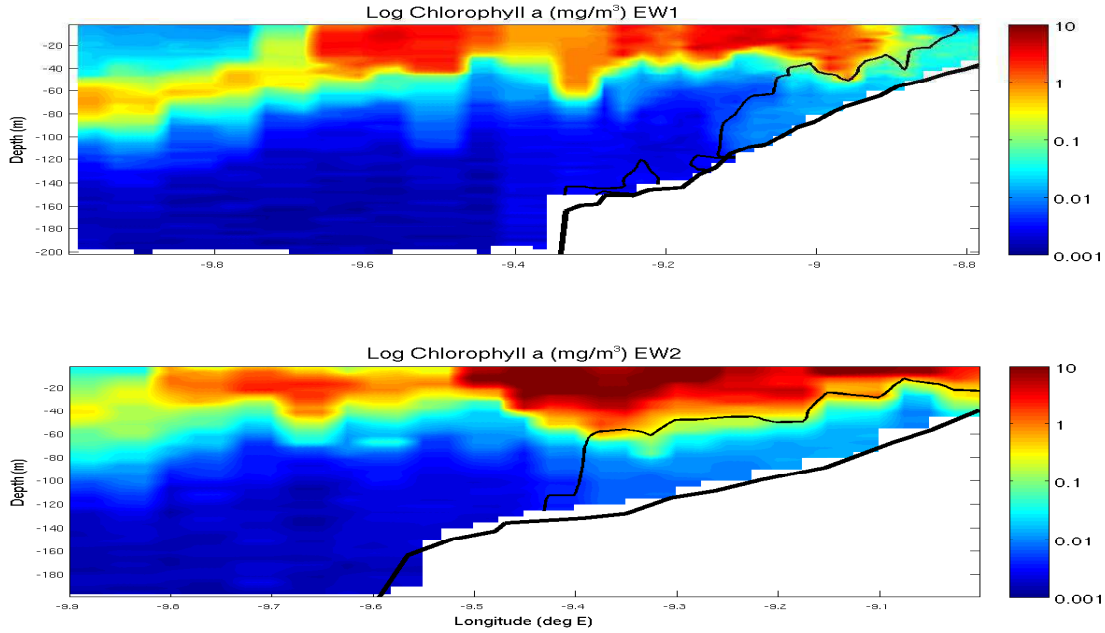
Figure 16: Latitude versus depth sections of chlorophyll *a* concentrations (from fluorometer converted in mg/m^3) for both EW transects: the first panel is for EW1 at 41°N, second is for EW2 at 40°N. Black lines on the sections indicate the isoline of the minimum of dissolved oxygen concentration (< 200 µmol/kg). The thick black lines represent the observed bathymetry.

are the coldest and densest (12.295°C and 27.089) waters that have been freshly upwelled over the shelf. On Fig. 15, similar observations can be done but after a relaxation of the northern winds and associated Ekman pumping. The coastal upwelling decreased in intensity and freshly upwelled waters only reach 14°C at the coast, whereas coldest and densest shelf waters are characterized by $\sigma_\theta \simeq$ 26.45 and < 13°C. The lighter surface waters ($\sigma_\theta < 26.2$) were also pushed offshore and are a sign of an ancient upwelling pulse. On the salinity profiles of EW1 (panel 4 on Fig. 15), ENACWst can be identified by the red patch offshore, whereas ENACWsp were present below 200 m and further north. The black contour represents the WIBP which was present between 8.9 and 9.55°W. Interestingly, it is observed again on the southern section between 9.5 and 9.88°W. The thickness of the WIBP layer ($\simeq$ 30 − 40 m) is maintained during its southwestward drift. However the width of this tongue of less saline water had decreased, from $\simeq$ 70 to $\simeq$ 40 km . These dynamics of the WIBP are described in details by [*Otero et al.,* 2008].

    [*Rossi et al.,* 2010] analyzed the signature in the chlorophyll *a* concentrations

42

and concluded on the presence of several upwelling fronts that have been advected offshore. On Fig. 16 several fronts are observed (local maxima in chlorophyll, associated with previous physical analysis). The ancient upwelling front associated with the lighter waters and located far offshore the coast is characterized by high chlorophyll concentrations ($1 - 5$ mg/m^3) and is located between $9.45°$ and $9.7°$W along EW1. A succession of upwelling fronts is also observed on section EW2 at $40°$N (Fig. 16). The current upwelling is characterized by high chlorophyll a concentrations ($1 - 10$ mg/m^3) between 9 and $9.2°$W, then comes the former one between 9.25 and $9.5°$W supporting the highest chorophyll concentrations (> 10 mg/m^3). Finally the most ancient one is found offshore between 9.65 and $9.8°$W characterized by moderate chlorophyll a content ($1 - 5$ mg/m^3). It has drifted offshore further south when comparing sections EW1 and EW2. Between the two former local maxima, moderate concentrations are observed ($1 - 5$ mg/m^3), associated with a SCM ($\simeq 20$ m) instead of a surface maximum. The ecosystem seems to respond specifically to intense transient upwelling pulses, with a peak of biological activity in the mixed layer, intersected by moderate activity at the SCM in between. These successive changes in the chlorophyll a concentration patterns are surely linked to changes in the planktonic communities. Shelf waters (between 8.9 and $9.3°$W) at $41°$N support high chlorophyll content ($1 - 10$ mg/m^3) but it is lower than the shelf waters of section EW2 (upper panel of fig. 16) where chlorophyll a reaches concentrations up to 10 mg/m^3. The very high wind surface mixing, confirmed by low values of buoyancy frequency (not shown) may be a factor explaining lower concentrations at $41°$N than at $40°$N. Restratification after an intense upwelling pulse allow larger phytoplankton cells to grow and to use more efficiently nutrients brought to the euphotic layer. Considering the findings from previous Section 5, although the general nitrate gradient is supposed to be positive poleward, coastal stations of EW2 also beneficiated of the very high remineralization processes taking place at the inner shelf bottom providing higher nutrients concentration to the surface.

On the nutrient sections of section EW2 (not shown), we can track the nutrient depletion of surface waters along the cross-shore gradient. Nutrient values within the mixed layer ($\simeq 10$ to 40 m) are around 10 µmol/l for nitrate, 1 µmol/l for phosphate and 6 µmol/l for silicate from 9 to $9.25°$W. Then, for the former upwelling front, they decrease to $2 - 5$ µmol/l $0 - 0.4$ µmol/l and $1 - 2$ µmol/l for nitrate, phosphate and silicate respectively. Finally, westward of $9.6°$W, the nitrate concentration are below the detection level, whereas there remains low quantities of silicate ($0.3 - 0.7$ µmol/l) and phosphate (0.1 µmol/l) reinforcing the fact that Nitrate is the limiting factor for PP also in surface waters off the shelf [*Joint et al.,* 2001a, *Castro et al.,* 2000]. The mean nutrient concentration of waters below 150 m at the slope (offshore) are about

43

2/3 of what is found ot the bottom of the inner shelf. This is true for the three types of nutrient measured and along transects EW1 and EW2. It seems to indicate that remineralization processes account for about 1/3 of the nutrient available for surface coastal ecosystem.

It is worth noting that the minimum of oxygen concentration ($<$ 200 µmol/kg) is found on the shelf bottom and is particularly well correlated with the highest surface concentrations of phytoplankton (see black isolines on Fig. 16). The shelf break upwelling and its local chlorophyll maximum already documented by [*Rossi et al.,* 2010] have a signature with low oxygen concentrations between 9.2 and 9.3°W. It is a sign of intense remineralization by the microbial life due to sinking of dead cells, particles, fecal fellets, constituting the POM. The area of minimum dissolved oxygen on the bottom is concomitant with a maximum of turbidity (not shown). Resuspension processes from the sediment by tidal currents and internal waves seem to play a key role.

On Fig. 17, we report HPLC pigments composition of phytoplankton and zooplankton biomass for section EW2 only. The successive pulses of biological activity are symbolized by the 3 peaks on the total chlorophyll a content from HPLC at 9.1, 9.4 and 9.65°W, coinciding with maxima in the fluorometer derived profile. The global size repartition of phytoplankton along the section at 40°N revealed that shelf samples (east of 9.4°W, symbolizing the two most recent upwelling fronts) are dominated by microphytoplankton ($\simeq$ 90 %) in the surface and sub-surface layers. From 9.4°W to 9.6°W, surface samples remain dominated by the micro- fraction, whereas in subsurface, nano- and picoplankton communities increase. Then, around 9.6°W, in the transition between the ancient and recent fronts, both surface and subsurface samples reveal a quite equilibrated composition: 50 % of micro- and 25 % of nano- and 25 % of picophytoplankton. The sample inside the ancient front at 9.75°W, show in fact a size composition very close to the one from the coastal fronts. Although it has a lower chlorophyll a content, it is strongly dominated by microphytoplankton as the coastal front. Focussing on the pigments composition, all peaks of chlorophyll a are coinciding with high values of fucoxanthin and peridinin: diatoms and dinoflagellates dominate the micro-phytoplankton population. The maximum of fucoxanthin and peridinin is found slightly offshore the coastal front. These populations of large cells are known to have a slower development and seem to appear after a light time lag as compared to the immediate coastal upwelling as already mentioned by [*Tilstone et al.,* 2003, *Joint et al.,* 2001b, *Ras et al.,* 2008]. Chlorophyll b concentrations are high close to the coast suggesting an immediate response of green algae. Zeaxanthin as well as alloxanthin has also moderate values at the coast, attesting the presence of crytophytes, as well as cyanobacteria and

44
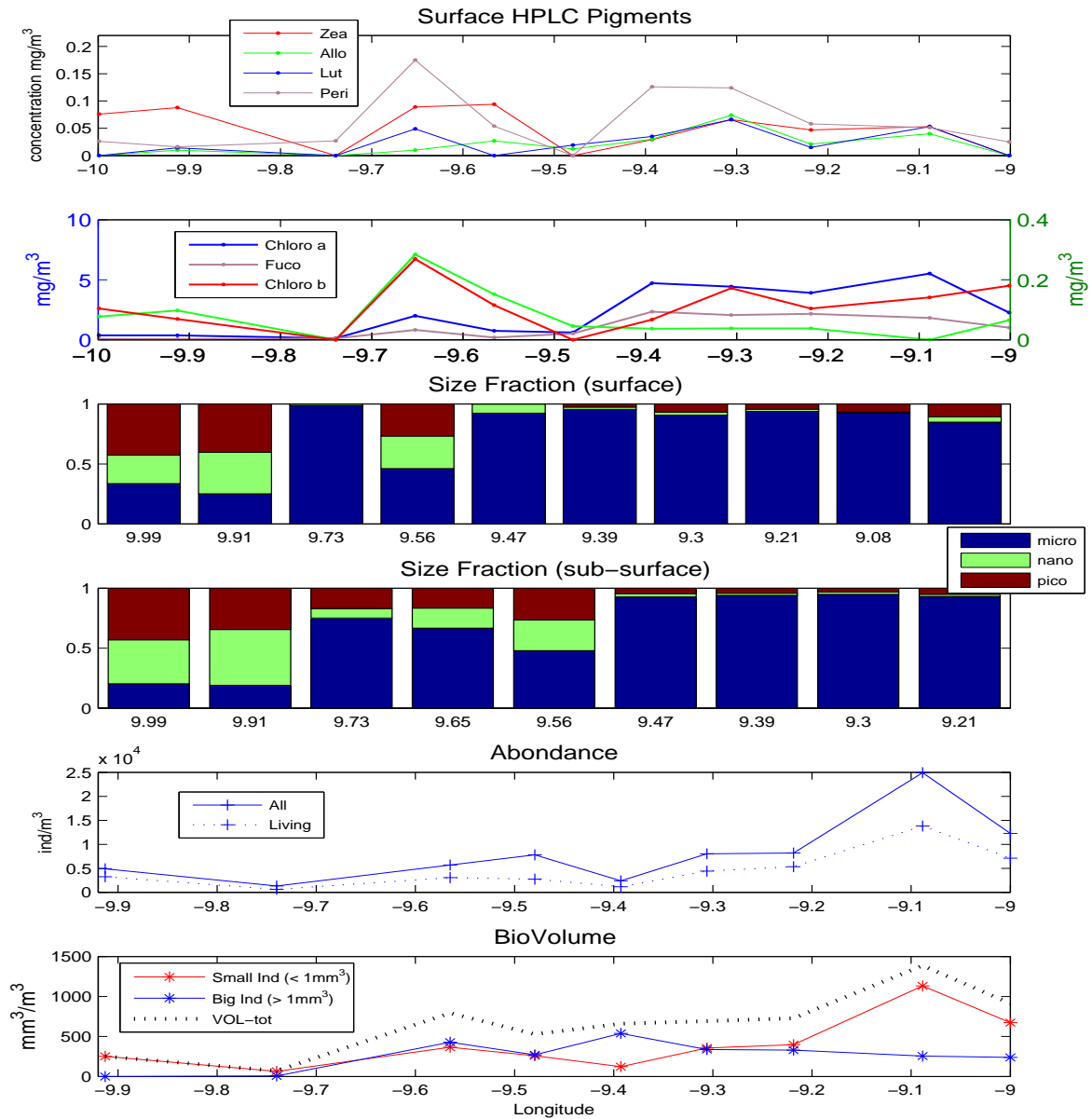
Figure 17: All data presented here are for the EW2 section at 40°N. Phytoplankton pigments concentration (from HPLC) are displayed on the two upper panels. On the second panel, chlorophyll a and fucoxanthin (blue and pink lines respectively) are related to the y-axis on the left (blue), whereas chlorophyll b and 19-hexanoyloxyfucoxanthin (red and green lines respectively) to the y-axis on the right (green). The size fractions of phytoplankton are plotted on panels 3 and 4; zooplankton abundance (from Zooscan) and biovolume are on the two lower panels.

45

prochlorophytes in the most recent upwelling front. When moving offshore from the second to the ancient front, peridinin increases as compared to fucoxanthin. This suggests that dinoflagellates predominate over diatoms when nutrient concentrations decreased along the westward drift. This alternance between diatoms and dinoflagellates populations has been described in a lagrangian experiment following a water mass offshore by [*Joint et al.,* 2001a]. Lutein and zeaxanthin symbolising cyanobacteria and prochlorophytes, are present from the coast to the offshore waters. They reach high values inside the ancient front between 9.55° and 9.7°W. At the same location, a peak of 19-hexanoyloxyfucoxanthin indicate a population of haptophytes. The two samples west of 9.9°W are characterized mainly by zeaxanthin, showing the importance of nano- and picoplankton (cyanobacteria and prochlorophytes) communities offshore (oligotrophic area). For the zooplankton biomass, we have the highest biomass at the coast, decreasing when moving offshore (Fig. 17). In the coastal front, small individuals of zooplankton dominate the community. This observation may explain that phytoplankton biomass does not show a coastal maximum because of intense microzooplankton grazing pressure. Copepods (fig. not shown) represent 70 to 80 % of the community over the shelf. In the two most coastal samples, we found few large larvae of Crustaceans and Gastropods, associated with Bivalves, Appendicularia, Doliolidae and Echinodermata larvae. Then large individuals become dominant from 9.3° to 9.5°W, where the maximum phytoplankton biomass is observed. In this area, Oithona Copepods, Chaetognaths and Bryozoans become dominant, along with Bivalves and Appendicularians. They must feed on the large diatoms and dinoflagellates that are very abundant, which allow an efficient transfer of energy along the foodweb. The last offshore station has low biomass of small zooplankton individuals. Being very different from the coastal and transitional waters, the offshore oligotrophic ecosystem is roughly composed of 50 % of small copepods and 50 % of Cladocera. The difference between living and all objects lines in the fifth panel of fig. 17 allow to estimate the export of organic materials (fecal pellets and particulate organic matter) to the seabed. The maximum difference ($\simeq 1200$ particles $/m^3$) is observed at the coastal stations where intense grazing by microzooplankton occur. Significant quantities of non-living particles ($\simeq 300$ - 500 particles $/m^3$) are found in the water column until 9.6°W.

Finally, the IPUS area reveals a strong cross-shore gradient, driven by the transient upwelling pulses that provide nutrient rich waters to the euphotic zone, being advected southward and offshore by the upwelling surface drift. The recent upwelled waters first support a rapid response of small phytoplankton as cryptophytes, cyanobacteria and prochlorophytes, almost immediately followed by microphytoplankton (dinoflagellates and diatoms). At the coast, the zooplankton popu-

46

lation is mainly composed by numerous small copepods and few large individuals. They impose a high grazing pressure on the phytoplankton and the ecosystem here is highly dynamic and productive (strong export). Then, when moving offshore, phytoplanktonic populations evolve, dinoflagellates dominate slowly diatoms, whereas in the subsurface waters nano- and picoplankton communities increase. There few large zooplankton species are found. The core of an ancient front was sampled and revealed that the size fractionated community within these waters was not evolving much (mainly microplankton), supporting the idea of advection of a coastal ecosystem offshore. However, the species composition was quite different both in zoo- and phytoplankton populations, suggesting that the ecosystem adapts itself to the changing conditions (less nutrients, increasing temperature and salinity). As mentioned previously, a strong coupling between zoo- and phytoplankton community exists. Size distribution for both trophic levels was often almost concomitant in space and time. Offshore waters have a completely different composition from a physical and biogeochemical point of view, as compared to the coastal and transitional waters. The numerous small scale physical structures advecting coastal productive upwelling offshore are then expected to have a strong impact on the open ocean waters.

7. Selected highlight: a filament study.

In order to better assess the importance of filamental structures in the IPUS, one of this mesoscale structure was intensively sampled during leg 2 of the survey. Northern winds have drastically decreased as compared to leg 1, but they were still imposing a light offshore Ekman drift in the surface layer. The relatively calm conditions were adequate for filaments development and tracking. Using real-time acquisition of satellite data, we focussed our study on filament that initiated around 40.3°N and started elongating offshore almost zonally (see SST from MODIS Aqua on fig. 18). A transect was made inside the filament (September 6 and 7) from the coast to the west: physical and biogeochemical data from this section are presented on Figures 18 and 19. Then several transects were performed crossing the structure from one side to another, as it can be seen on the satellite images (Fig. 18). We will concentrate our analysis on the North/South section done at 10.6°W on September, 8. Data from CTD sensors and LADCP currents are displayed on Figure 20.

The filament dimensions are roughly 2° in length ($\simeq$ 170 km) for a coastal base of almost 1° ($\simeq$ 100 km), getting slimmer offshore 1/4° ($\simeq$ 25 km). The tip of the filament has a mushroom shape, quite typical of these mesoscale structures. On Fig. 18, a low salinity lens is marked by the black contour (< 35.7 psu). This surface layer has lower temperature ($\simeq$ $16 - 18$°C) than surrounding ($\simeq$ $18 - 19$°C) and offshore

47
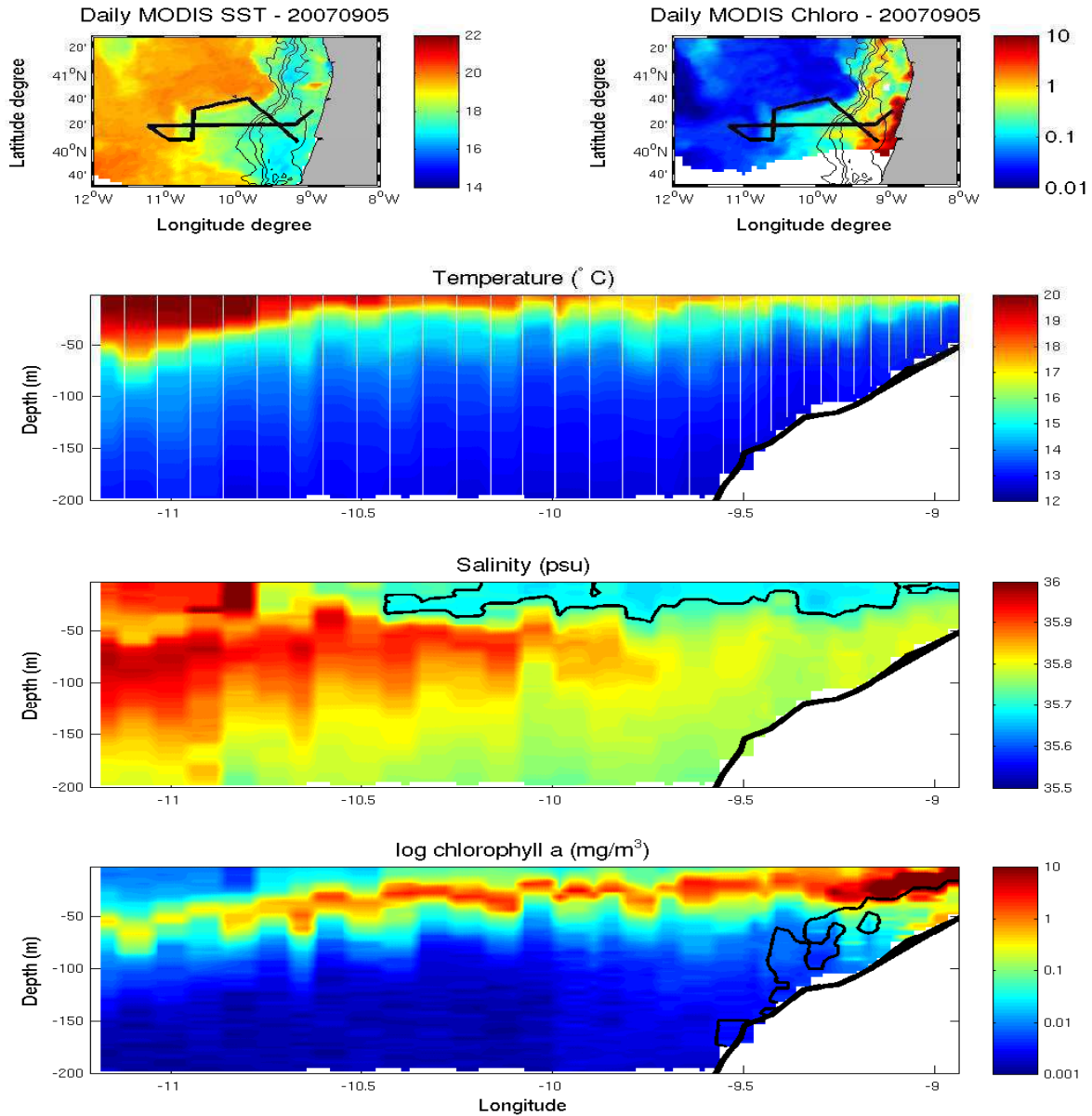
Figure 18: Two upper vignettes: SST (°C) and chlorophyll a concentration (mg/m^3) from MODIS Aqua over the central IPUS on the 05/09/2007. The black thick lines superimposed represent the filament network performed. Three lower panels: longitude versus depth sections of CTD sensors for the EW transect inside the filament (temperature in °C, salinity (psu) and chlorophyll a concentrations from the fluorometer converted in mg/m^3). The black line in the chlorophyll a section indicates the minimum of dissolved oxygen concentration ($<$ 200 μmol/kg). The black line in the salinity section contours the WIBP plume ($<$ 35.7 psu). The white vertical lines indicate the measurement positions; thick black lines represent the observed bathymetry.

48

waters ($> 20°$C, see Fig. 18). The density section (not shown) reveals slightly lighter waters associated with this surface layer constituting the filament. It is composed of the WIBP mixed with freshly coastal upwelled waters that are being advected inside the filament, reaching 10.75°W. [*Peliz et al.,* 2002] already suggested that waters that feed the filaments may have their origin in the low coastal salinity waters of the WIBP. Our observations confirmed that they may provide a buoyant input to the filaments which creates a preferential 'conduit' for exchanges between coastal and offshore waters.

Chlorophyll *a* concentrations inside the filament are relatively high as compared to surrounding waters. On Fig. 18, chlorophyll *a* concentrations are comprised between 1 and 5 mg/m^3 until 10.6°W, whereas they were around 0.5 mg/m^3 at 10°W offshore the previous EW sections (see Fig. 16). Over the continental margin the phytoplankton is almost equally distributed within the mixed layer (down to 50 m), whereas a SCM appears around 9.6°W.

Looking at Figure 19, similar cross-shore gradients in the phyto- and zooplankton populations are observed, as detailed in Section 6. Exceptionally, few additional pigments as phaeophorbide *a*, chlorophyllide *a*, prasinoxanthin and divinyl *a* were measured [1]. They give new information about the functioning of the phytoplankton communities. The coastal sites were already under stratified conditions after the last upwelling pulse, which corresponds to a mature ecosystem dominated by large cells. Diatoms and dinoflagellates, associated with large zooplankton individuals, were dominant until 9.5°W. Phaeophorbide *a* and chlorophyllide *a* are a sign of senescence of diatoms populations and of grazer fecal pellets, respectively. These pigments are found in high concentrations at the coast (panel 5 of Fig. 19), where large zooplankton grazors feed on large phytoplankton. Both pigments concentrations decrease when moving offshore, but chlorophyllide *a* stay significant. Its values inside the filament is slightly larger than the last station done outside the filament, attesting the fact that the filament is a preferential place for a dynamical ecosystem and energy transfer within the foodweb. The relative proportion of microphytoplankton is around 80 % over the shelf, whereas it is reduced to 30 % or less west of 9.5°W. West of 9.5°W the community appears to be dominated by nanoplankton which reaches 50 % in the surface waters and even more in the subsurface SCM, whereas picoplankton

---

[1]These additional pigments were measured only on a subset of the total samples. We performed a double sampling for 16 stations and subset samples were analysed by two different laboratories to intercalibrate our measurements. On the common pigments that both labs had measured, the agreement was very good. For instance, chlorophyll *a*, fucoxanthin and 19-Hexanoyloxyfucoxanthin concentrations were correlated with a R^2 of 0.91, 0.96 and 0.94, respectively.

49
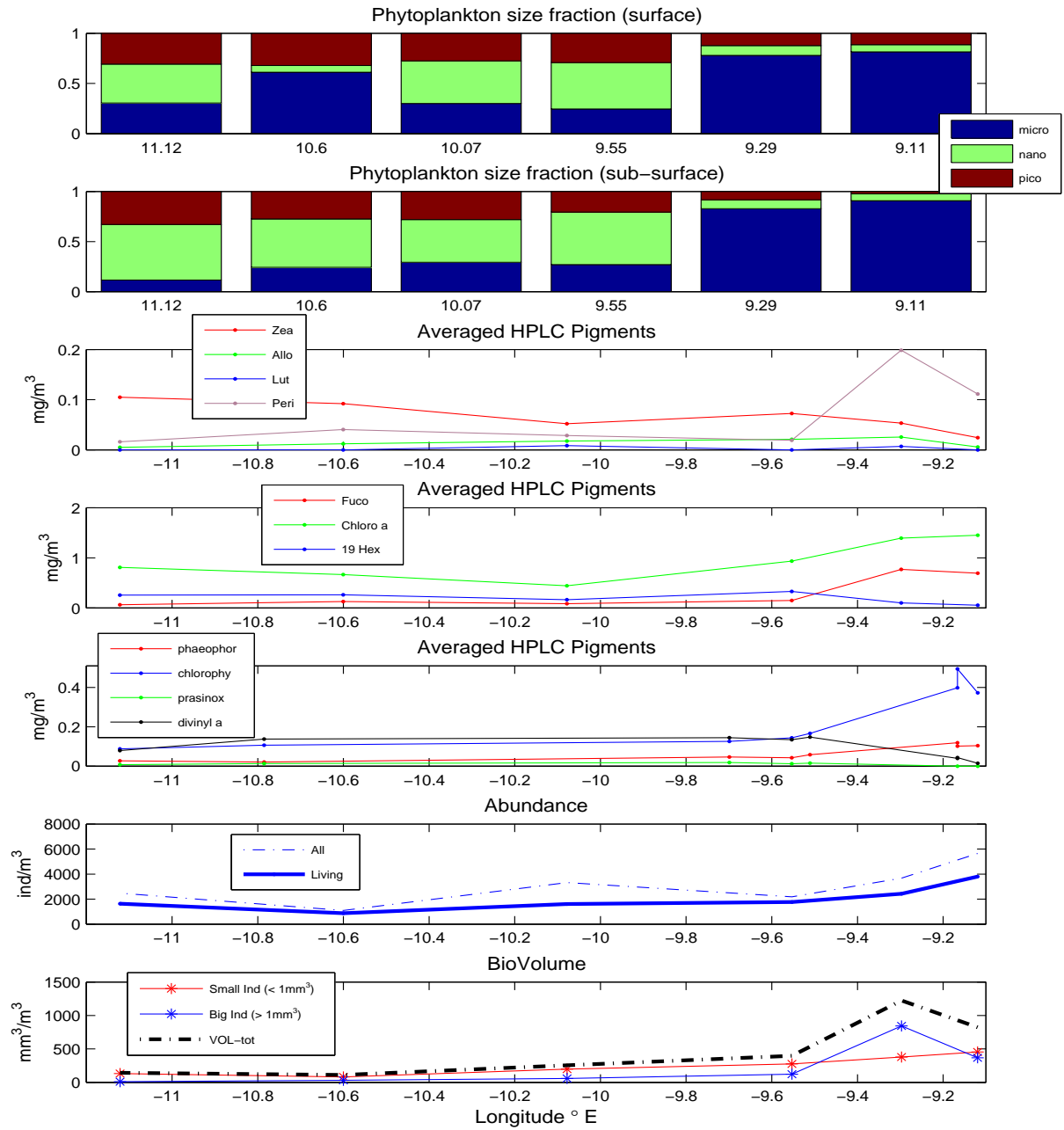
Figure 19: Phytoplankton size fraction (surface and subsurface) on the two upper panel, phytoplankton pigments concentration (from HPLC) averaged over 2 depths (surface and subsurface) on panels 3, 4 and 5. Zooplankton abundance (from Zooscan) and biovolume on the three bottom panels for the EW transect inside the filament at $\simeq 40.3°$N.

50

only reach around 25 %. Zeaxanthin, 19-hexanoyloxyfucoxanthin and praxinoxan-thin are increasing when moving offshore, attesting the presence of cyanobacteria, prochlorophytes, prymnesiophytes and prasinophytes. These pico- and nanophyto-plankton dominate the community when nutrients concentrations (especially nitrate) are decreasing offshore inside the filament. A noticeable difference between the sample outside the filament (at 11.12°W) and those inside is the proportion of micro-phytoplankton: they are still more abundant in the filament than in the open ocean, being brought from the rich coastal waters within the filament. More details on the zooplankton grazing in a filament are given in [*Fileman and Burkill,* 2001]. As expected, zooplankton communities are dominated by small individuals westward of 9.5°W. However, looking at panel 6 of Fig. 19, the difference between the number of all and living objects is quite high ($\simeq$ 1000 particles /m^3) until far offshore (10.4°W). It also supports the idea of an active ecosystem within the filament intensively pro-ducing POM, as compared to the low values ($<$ 300 particles /m^3) observed offshore on the previous EW transects.

Now we focus on the NS section crossing the filament at 10.6°W (Fig.20). The filament from 40.3° to 40.45°N is clearly identified by extrema in the tempera-ture/salinity/chlorophyll a/AOU sections, both at the surface and subsurface. A minimum of temperature is observed at the surface, while a deflection of the thermo-cline is also noticeable in the subsurface (from 50 to 40 m). The core of the filament is characterized by a minimum of salinity (35.57 psu) until $\simeq$ 50 m that lies on a sub-surface salinity maximum ($>$ 35.9 psu from 50 to 100 m). This cross-section does confirm the low buoyancy of the water constituting the filament suggested by [*Peliz et al.,* 2002]. The chlorophyll a reveals a significant surface concentration in-side the filament (0.1 mg/m^3) as compared to outside ($<$ 0.05 mg/m^3). The SCM followed the thermocline movement and is situated at around 35 m between 40.3° - 40.45°N, against 50 m outside. It matches with a maximum of Coloured Dissolved Organic Matter content as indicated by the black contouring and a minimum in the AOU (-15 μmol/kg symbolizing a strong oxygen production by PS). The signature in the AOU is also detectable until 150-200 m where we reach a maximum ($>$ 40 μmol/kg) suggesting that the product of this relatively high surface biological pro-duction is also exported deeper in the water column and remineralized. The currents derived from LADCP allow us to calculate roughly the offshore transport induced by the filament. We defined it from 40.3° to 40.45°N having an extension in the vertical of 50 m. We estimated a westward transport due to the filament of 0.16 Sv. This estimation is quite low, but still within the range of the observations of few filaments summarized by [*Sanchez et al.,* 2008]. The transport is computed at the top of the filament which explains that it is relatively lower than other larger structure sampled

51
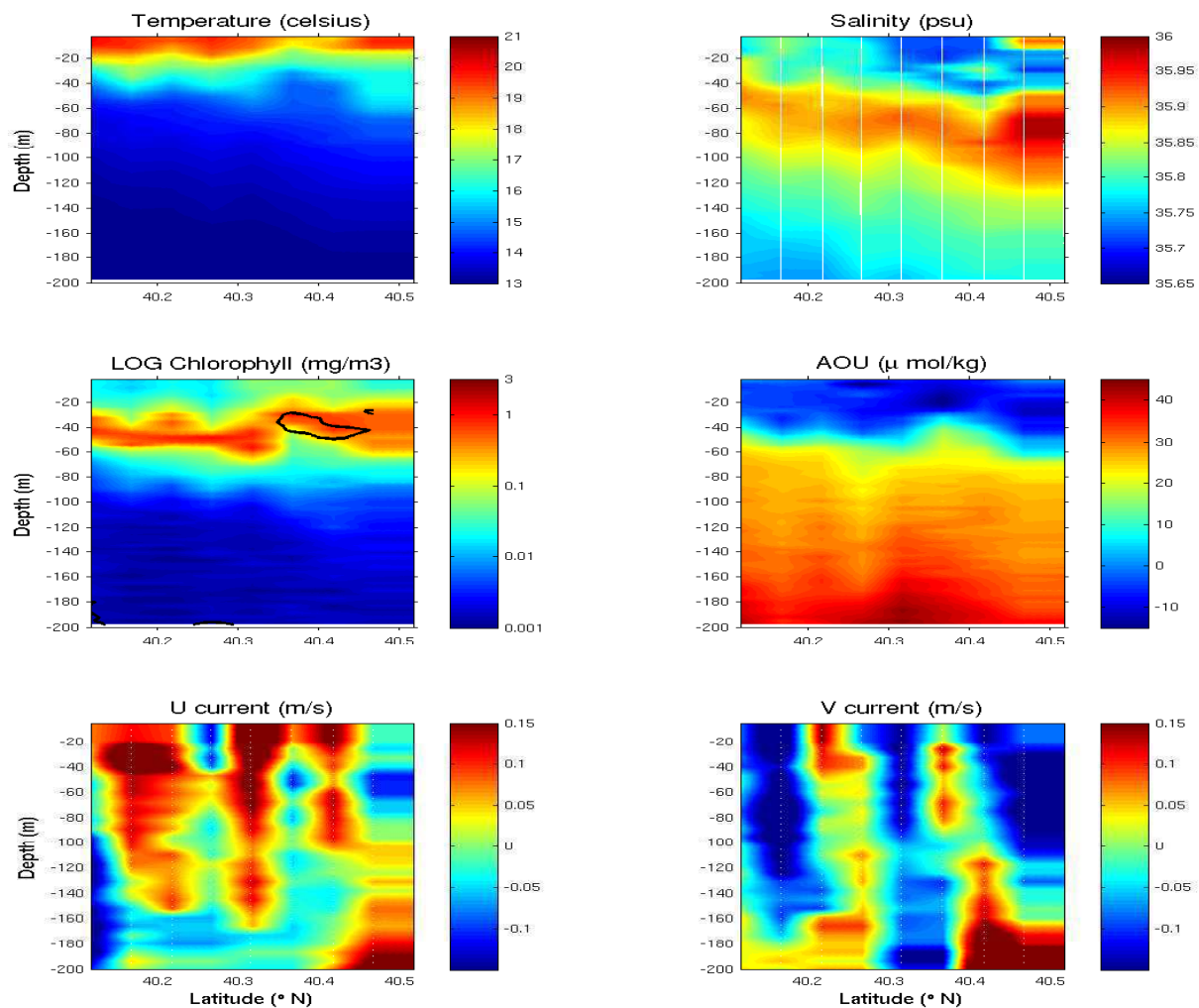
Figure 20: All data presented here are from the NS transect crossing the filament at 10.6°W. Four first panel are latitude versus depth sections of CTD sensors. First panel is temperature (°C), second is salinity (psu), third is chlorophyll *a* concentrations from the fluorometer (converted in mg/m³) and fourth is AOU (μmol/kg). Black line on the chlorophyll *a* profil indicate the maximum of Colored Dissolved Organic Matter, from the second fluorometer. The white dotted lines indicate the measurement positions. Two lower panels are cross-shore (lower left) and along-shore (lower right) velocities (m/s) from LADCP. On the lower left red color indicates current directed to the west, while blue color to the east. On the lower right panel, red color represents current to the north while blue color to the south.

52

in [*Sanchez et al.,* 2008]. By multiplying the westward velocities by the chlorophyll content, we obtained a flux of chlorophyll through the filament which is around 0.016 mg m^{-2} s^{-1}. Integrating this value over the filament vertical surface (50 m for 0.15° of latitude), we found that around 82.5 g/s of chlorophyll *a* are transported within the filament. It is in very good agreement with the flux of 70.7 g/s calculated by [*Garcia-Munõz et al.,* 2005] in the Canary upwelling system. To have a very rough estimate of the role of such structures on the cross-shore transport of coastal water masses, we extrapolated our results. If we consider that westward velocities were similar at the initiation of the filament at the coast ($\simeq$ 0.11 m/s), along with chlorophyll concentrations from the coastal areas ($\simeq$ 5 mg/m^3), integrated over the dimension deduced from satellite images (100 km width for a thickness of 50 m), we found that more than 2.75 kg s^{-1}of chlorophyll *a* can be exported from the coast to the open ocean by the filament. Of course, it is a very rough estimation since all variables, namely the width, velocities and chlorophyll *a* concentration are time and space dependent. More reliable estimation of offshore transport of biogeochemical properties are given in [*Alvarez-Salgado et al.,* 2001, *Garcia-Munõz et al.,* 2005, *Alvarez-Salgado et al.,* 2007].

The complete current section through the filament is also used to understand the physical background behind the offshore drift of such structure. We clearly detect a strong surface cyclonic eddy with negative (-0.1 m/s at 40.25°N) and positive velocities (> 0.15 m/s at 40.3°N) southward of the filament. A subsurface anticyclonic dipole is observed northward of the filament: positive velocities of 0.1 m/s located at 40.43°N from the surface until 80 m associated with negative velocities of -0.1 m/s at 40.45°N (40-60 m). On both sides of the filament, a cyclonic eddy southward and an anticyclonic one northward, advect coastal upwelled waters offshore. Inside the filament, at 40.375°N, a counter jet ($\simeq -0.1$ m/s eastward) is observed and may be related to a subsurface compensation of surface westward flow. Several observations as those from [*Garcia-Munõz et al.,* 2005] mentionned these recirculating gyres on each side of a filament. [*Meunier et al.,* 2010] studied trapped filaments formation due to topographic effect and they also described in their simulations the occurrence of these two mesoscale eddies associated with the formation of a trapped filament.

The filament sampled under calm weather conditions provides us a nice picture of these ubiquitous features of the world EBUS. Its formation and maintenance is driven by the physics and the interactions with other mesoscale structures such as eddies. Although relatively isolated from outside, the coastal ecosystems embedded inside the filament evolve and respond to the water masses changes. Particularly, the decrease in nutrients consumed by the biology leads to changes in both zoo- and phytoplankton

53

communities. Because it is initiated close to the coast and then drifting offshore, it plays a major role in the cross-shelf exchange of organic matter and in the local carbon cycling as shown in [*Alvarez-Salgado et al.,* 2001, *Garcia-Munõz et al.,* 2005, *Alvarez-Salgado et al.,* 2007].

8. Conclusion and perspectives.

This paper presents a multidisciplinary field survey of the northern and central Iberian Peninsula Upwelling System (IPUS) performed in August/September 2007. The strong northerlies were favourable to upwelling development and a strong physical response was observed both on satellite and *in-situ* data, with temperature at the coast dropping below 13°C. The ecosystem showed also a strong response with chlorophyll *a* concentration higher than 10 mg/m³ along the coast. A general analysis of the water masses revealed the complex hydrography of this continental margin and its general biogeochemical functioning. The circulation pattern was briefly studied and emphasized the important role of mesoscale features such as eddies and filaments that contributed to the highly variable shelf circulation. The north-south variability was studied on a coastal transect, showing the heterogeneity of this coastal upwelling. We defined three different subsystems, having particular physical characteristics as well as ecosystem responses. The most intense upwelling was found at the northern tip of the peninsula, where a diatoms dominated population grew under high nutrient supplies and low zooplankton predation. The coastal freshwater intputs appeared to have a significant effect on the physics and biology in this area. The central area was characterized by very high remineralization activity over the shelf, which compensated the relatively low nutrients inputs from deep waters. In this area, northern water masses and associated ecosystems are advected while changes in their communities are observed, whereas a subsurface saline water mass is coming from the south. There the phytoplankton community is diverse and productive and supports the highest zooplankton biomass. Then the southern subsystem appear to be a well developed upwelling set-up where the stability of the water column associated with previous nutrient inputs supports a productive ecosystem. The cross-shore variability is also studied and a strong gradient of physical as well as biological variables is observed. The near shore area was highly dynamical and was dominated by relatively small phytoplankton under control by microzooplankton grazing. After a short decay, large cells of diatoms and dinoflagellate appeared, associated with large zooplankton individuals. One of the recurrent observation was also the tight coupling observed in several zones between the primary and secundary productions and communities. The shelf ecosystems were exported offshore with filaments, eddies or simple Ekman drift. Changes in the species composition occured, but some

54

characteristics remained. The tracking of a filament during the survey allowed us to quantify better their importance in terms of coast/open ocean exchange. They were responsible for a significant transport since they extended far offshore the favourable areas for biological production. The transitional area contrasted strongly with the poor ecosystem found offshore. This descriptive paper allowed us to analyse the main physical patterns observed during the survey that shaped the ecosystem functioning, from nutrient cycling to zooplankton biomass. Of course, further investigations need to be done, along with specialists from the oceanographic community, to better investigate this nice data set. A more fine sampling strategy, associated with real-time acquisition of high resolution satellite maps, may be a future good strategy to assess this mesoscale variability.

9. Acknowledgements.

55

References

[*Alvarez et al.,* 2008] Alvarez I., M. Gomez-Gesteira, M. deCastro and J.M. Dias. Spatiotemporal evolution of upwelling regime along the western coast of the Iberian Peninsula. Journal of Geophysical Research, vol. 113, C07020, doi:10.1029/2008JC004744, 2008.

[*Alvarez-Salgado et al.,* 2001] Alvarez-Salgado, X.A., M.D. Doval, A.V. Borges, I. Joint, M. Frankignoulle, E.M.S. Woodward and F.G. Figueiras. Off-shelf fluxes of labile materials by an upwelling filament in the NW Iberian Upwelling System. Progress in Oceanography, 51, 321-337, 2001.

[*Alvarez-Salgado et al.,* 2002] Alvarez-Salgado, X.A., S. Belosoa, I. Joint, E. Nogueira, L. Chou, F.F. Perez, S. Groom, J.M. Cabanas, A.P. Rees and M. Elskens. New production of the NW Iberian shelf during the upwelling season over the period 1982-1999. Deep-Sea Research I, vol. 49, 17251739, 2002.

[*Alvarez-Salgado et al.,* 2003] Alvarez-Salgado, X.A., F.G. Figueiras, F.F. Perez, S. Groom, E. Nogueira, A.V. Borges, L. Chou, C.G. Castro, G. Moncoiffe, A.F. Ríos, A.E.J. Miller, M. Frankignoulle, G. Savidge and R. Wollast. The Portugal coastal counter current off NW Spain: new insights on its biogeochemical variability. Progress in Oceanography, vol. 56, 281321, 2003.

[*Alvarez-Salgado et al.,* 2007] Alvarez-Salgado, X.A., Arístegui, J., Barton, E.D., Hansell, D.A., Contribution of upwelling filaments to offshore carbon export in the subtropical Northeast Atlantic Ocean. Limnology and Oceanography, 52, 1287-1292, 2007.

[*Aminot and Kerouel.,* 2007] Aminot A. and R. Kerouel. Dosage automatique des nutriments dans les eaux marines : méthodes en flux continu. Ed. IFREMER, Méthodes d'analyse en milieu marin, Brest (France), 2007.

[*Barbosa et al.,* 2001] A.B. Barbosa, A.B., H.M. Galvao, P.A. Mendes, X.A. Alvarez-Salgado, F.G. Figueiras and I. Joint. Short-term variability of heterotrophic bacterioplankton during upwelling off the NW Iberian margin. Progress in Oceanography, vol. 51, 339359, 2001.

[*Batteen et al.,* 2007] Batteen, M.L., Martinho, A.S., Miller, H.A. and McClean, J.L., A Process-Oriented Study of the Coastal Canary and Iberian Current System. Ocean Modelling, vol. 18, 1-36, 2007.

56

[*Batten et al.,* 2001] Batten S.D., Fileman E. and E. Halvorsen. The contribution of microzooplankton to the diet of mesozooplankton in an upwelling filament off the north west coast of Spain. Progress in Oceanography, vol. 51, 385-398, 2001.

[*Blanco-Bercial et al.,* 2006] Blanco-Bercial L., F. Alvarez-Marques and J.A. Cabal. Changes in the mesozooplankton community associated with the hydrography off the northwestern Iberian Peninsula. ICES Journal of Marine Science, vol. 63, 799-810, 2006.

[*Borges and Frankignoulle,* 2001] Borges A.V. and M. Frankignoulle. Short-term variations of the partial pressure of CO_2 in surface waters of the Galician upwelling system. Progress in Oceanography, vol. 51, 283302, 2001.

[*Castro et al.,* 2000] Castro C.G., F.F. Perez, X.A. Alvarez-Salgado and F. Fraga. Coupling between the thermohaline, chemical and biological fields during two contrasting upwelling events off the NW Iberian Peninsula. Continental Shelf Research, vol. 20, 189-210, 2000.

[*Castro et al.,* 2006] Castro C.G., M. Nieto-Cid, X.A. Alvarez-Salgado and F.F. Perez. Local remineralization patterns in the mesopelagic zone of the Eastern North Atlantic, off the NW Iberian Peninsula. Deep-Sea Research I, vol. 53, 19251940, 2006.

[*Cabal et al.,* 2008] Cabal J., G. Gonzlez-Nuevo and E. Nogueira. Mesozooplankton species distribution in the NW and N Iberian shelf during spring 2004: Relationship with frontal structures. Journal of Marine Systems, vol. 72, 1-4, 282-297, 2008.

[*Cermeno et al.,* 2006] Cermeno P., E. Maranon, V. Perez, P. Serret, E. Fernandez, C.G. Castro. Phytoplankton size structure and primary production in a highly dynamic coastal ecosystem (Ría de Vigo, NW-Spain): Seasonal and short-time scale variability. Estuarine, Coastal and Shelf Science, vol. 67, 251-266, 2006.

[*Fileman and Burkill,* 2001] Fileman E. and P. Burkill. The herbivorous impact of microzooplankton during two short-term Lagrangian experiments off the NW coast of Galicia in summer 1998. Progress in Oceanography, vol. 51, 361383, 2001.

[*Fiúza et al.,* 1982] Fiuza, A., Macedo, M., and M. Guerreiro. Climatological space and time variation of the Portuguese coastal upwelling. Oceanologica Acta 5, 3140, 1982.

57

114

[*Garcia and Gordon,* 1992] Garcia H.E. and L.I. Gordon. Oxygen Solubility in Seawater: Better Fitting Equations. Limnology and Oceanography, Vol. 37, No. 6, 1307-1312, 1992.

[*Garcia-Munõz et al.,* 2005] García.Munõz, M., J. Arístegui, J.L. Pelegrí, A. Antoranz, A. Ojeda and M. Torres. Exchange of carbon by an upwelling filament off Cape Ghir (NW Africa). Journal of Marine Systems, vol. 54, 83-95, 2005.

[*Gasparini,* 2007] Gasparini, S. Plankton Identifier: a software for automatic recognition of planktonic organisms. http://www.obs-vlfr.fr/~gaspari/Plankton_Identifier/index.php, 2007.

[*Gordon et al.,* 1995] Gordon L.I., Jennings J.C., Ross A.R. and J.M. Krest. A suggested protocol for continuous flow automated analysis of seawater nutrients (phosphate, nitrate, nitrite, and silicic acid) in the WOCE hydrographic program and the Joint Global Ocean Fluxes Study. OSU College of Oceanography Descriptive Chemistry, Oceanography Group Technical Report 93-10, 1995.

[*Gorsky et al.,* 2010] Gorsky, G., Ohman, M.D., Picheral, M., Gasparini, S., Stemmann, L., Romagnan, J.-B., Cawood, A., Pesant, S., García-Comas, C. and F. Prejger. Digital zooplankton image analysis using the ZooScan integrated system. Journal of Plankton Research, in press, 2010.

[*Grosjean et al.,* 2004] Grosjean, P., Picheral, M., Warembourg, C. and Gorsky, G. Enumeration, measurement,and identification of net zooplankton samples using the ZOOSCAN digital imaging system. ICES J. Mar. Sci., 61, 518-525, 2004.

[*Halvorsen et al.,* 2001] Halvorsen, E., A.G. Hirst, S.D. Batten, K.S. Tande and R.S. Lampitt. Diet and community grazing by copepods in an upwelled filament off the NW coast of Spain. Progress in Oceanography, vol. 51, 399-421, 2001.

[*Haynes and Barton,* 1990] Haynes, R. and E.D. Barton. A poleward flow along the Atlantic coast of the Iberian peninsula. Journal of Geophysical Research, vol. 95, 1142511441, 1990.

[*Haynes et al.,* 1993] Haynes, R., Barton, E.D. and Pilling, I. Development, Persistence, and Variability of Upwelling Filaments. Journal of Geophysical Research, vol. 98, 22681-22692, 1993.

[*Joint et al.,* 2001a] Joint, I., Inall, M., Torres, R., Figueiras, F.G., Alvarez-Salgado, X. A., Rees, A. P., and E.M.S, Woodward. Two Lagrangian experiments in the

58

Iberian upwelling system: tracking an upwelling event and an off-shore filament. Progress in Oceanography, vol. 51, 221-248, 2001.

[*Joint et al.,* 2001b] Joint, I., Rees, A.P., and E.M.S. Woodward. Primary production and nutrient assimilation in the Iberian upwelling in August 1998. Progress in Oceanography, vol. 51, 303-320, 2001.

[*Joint et al.,* 2002] Joint, I., S.B. Groom, R. Wollast, L. Chou, G.H. Tilstone, F.G. Figueiras, M. Loijens and T.J. Smyth. The response of phytoplankton production to periodic upwelling and relaxation events at the Iberian shelf break: estimates by the ^{14}C method and by satellite remote sensing. Journal of Marine Systems, vol. 32, 219238, 2002.

[*Labasque et al.,* 2004] Labasque T., C. Chaumery, A. Aminot and G. Kergoat. Spectrophotometric Winkler determination of dissolved oxygen: re-examination of critical factors and reliability. Marine Chemistry, Vol. 88, issues 1-2, 53-60, 2004.

[*Lorenzo et al.,* 2005] Lorenzo, L.M., B. Arbones, G.H. Tilstone and F.G. Figueiras. Across-shelf variability of phytoplankton composition, photosynthetic parameters and primary production in the NW Iberian upwelling system. Journal of Marine Systems, vol. 54, 157173, 2005.

[*Meunier et al.,* 2010] Meunier, T., Rossi, V., Morel, Y. and X. Carton. Influence of a bottom topography on an upwelling current: generation of long trapped filaments. Submitted to Ocean Modelling, 2010.

[*Minas et al.,* 1986] Minas H.J., M. Minas and T.T. Packard. Productivity in upwelling areas deduced from hydrographic and chemical fields. Limnology and Oceanography, vol. 31, 6, 1182-1206, 1986.

[*Motoda,* 1959] Motoda, S. Devices of simple plankton apparatus. Memoirs. Faculty of Fisheries. Hokkaido University 7, 73-94, 1959.

[*Otero et al.,* 2008] Otero, P., M. Ruiz-Villarreal and A. Peliz. Variability of river plumes off Northwest Iberia in response to wind events. Journal of Marine Systems, vol. 72, 1-4, 238-255, 2008.

[*Pauly and Christensen,* 1995] Pauly, D., and Christensen, V. Primary production required to sustain global fisheries. Nature, 374, 255-257, 1995.

59

[*Peliz et al.,* 2002] Peliz A., T.L. Rosa, A.M.P. Santos and J.L. Pissarra. Fronts, jets, and counter-flows in the Western Iberian upwelling system. Journal of Marine Systems, vol. 35, 6177, 2002.

[*Peliz et al.,* 2005] Peliz, A., Dubert, J., Santos, A., Oliveira, P.B., and Le Cann, B. Winter upper ocean circulation in the Western Iberian Basin - Fronts, Eddies and Poleward Flows: an overview. Deep Sea Research I, 52, 621-646, 2005.

[*Quaresma et al.,* 2007] Quaresma, L.S., J. Vitorino, A. Oliveira and J. da Silva. Evidence of sediment resuspension by non-linear internal waves on the western Portuguese mid-shelf. Marine Geology, vol. 246, 123-143, 2007.

[*Queiroga et al.,* 2007] Queiroga H., T. Cruz, A. dos Santos, J. Dubert, J.I. Gonzalez-Gordillo, J. Paula, A. Peliz and A.M.P. Santos. Oceanographic and behavioural processes affecting invertebrate larval dispersal and supply in the western Iberia upwelling ecosystem. Progress in Oceanography, vol. 74, 174191, 2007.

[*Raimund et al.,* 2010] Raimund, S., Vernet M., Rossi V., Morel Y., Garçon V., Quack B. and P. Morin. Distribution of Volatile Halogenated Organic Compounds in the Iberian Peninsula Upwelling System. Submitted to JGR or Marine Chemistry, 2010.

[*Ras et al.,* 2008] Ras J., Claustre H. and J. Uitz. Spatial variability of phytoplankton pigment distributions in the Subtropical South Pacific Ocean: comparison between in-situ and predicted data. Biogeosciences, vol. 5, 353-369, 2008.

[*Relvas et al.,* 2007] Relvas, P., Barton, E.D., Dubert, J., Oliveira, P.B., Peliz, A., da Silva, J.C.B., and Santos, A.M.P. Physical oceanography of the western Iberia ecosystem: Latest views and challenges. Progress in Oceanography, 74, 149-173, 2007.

[*Resende et al.,* 2007] Resende, P., U.M. Azeiteiro, F. Goncalves and M.J. Pereira. Distribution and ecological preferences of diatoms and dinoflagellates in the west Iberian Coastal zone (North Portugal). Acta Oecologica, vol. 32, 224235, 2007.

[*Ribeiro et al.,* 2005] Ribeiro, A.C., A. Peliz, and A.M.P. Santos. A study of the response of chlorophyll-a biomass to a winter upwelling event off Western Iberia using SeaWiFS and in situ data. Journal of Marine Systems, vol. 53, 87107, 2005.

60

117

[*Roed and Shi,* 1999] Roed, L. P., and X. B. Shi. A numerical study of the dynamics and energetics of cool filaments, jets and eddies off the Iberian Peninsula. Journal of Geophysical Research, 104(C12), 29817-29841, 1999.

[*Rossi et al.,* 2009] Rossi, V., López C., Hernández-García E., Sudre J., Garçon V., and Morel Y. Surface mixing and biological activity in the four Eastern Boundary Upwelling System. Nonlinear Processes in Geophysics, 16, 557-568, 2009.

[*Rossi et al.,* 2010] Rossi, V., Morel, Y. and V. Garçon. Effect of the wind on the shelf dynamics: Formation of a secondary upwelling along the continental margin. Ocean Modelling, vol. 31, 3-4, 51-79, 2010.

[*Sanchez et al.,* 2008] Sanchez, R.F., P. Relvas, A. Martinho, and P. Miller. Physical description of an upwelling filament west of Cape St. Vincent in late October 2004, Journal of Geophysical Research, Vol. 113, C07044, doi:10.1029/2007JC004430, 2008.

[*Santos et al.,* 2004] Santos, A.M.P., A. Peliz, J. Dubert, P.B. Oliveira, M.M. Angelico and P. Ré. Impact of a winter upwelling event on the distribution and transport of sardine (Sardina pilchardus) eggs and larvae off western Iberia: a retention mechanism. Continental Shelf Research, vol. 24, 149165, 2004.

[*Santos et al.,* 2007] Santos A.M.P., A. Chícharo, A. dos Santos, T. Moita, P.B. Oliveira, A. Peliz and P. Re. Physical-biological interactions in the life history of small pelagic fish in the Western Iberia Upwelling Ecosystem. Progress in Oceanography, vol. 74, 192209, 2007.

[*Sharples et al.,* 2009] Sharples, J., C.M. Moore, A.E. Hickman, P.M. Holligan, J.F. Tweddle, M.R. Palmer, and J.H. Simpson. Internal tidal mixing as a control on continental margin ecosystems. Geophysical Research Letters, vol. 36, L23603, doi:10.1029/2009GL040683, 2009.

[*Tilstone et al.,* 2003] Tilstone, G.H., F.G. Figueiras, L.M. Lorenzo, B. Arbones. Phytoplankton composition, photosynthesis and primary production during different hydrographic conditions at the Northwest Iberian upwelling system. Marine Ecology Progress Series, vol. 252, 89104, 2003.

[*Torres and Barton,* 2007] Torres, R. and E., Barton. Onset of the Iberian upwelling along the Galician coast. Continental Shelf Research, vol. 27, 1759-1778, doi:10.1016/j.csr.2007.02.005., 2007.

61

[*Varela et al,* 2005] Varela, R.A., G. Roson, J.L. Herrera, S. Torres-Lopez and A. Fernandez-Romero. A general view of the hydrographic and dynamical patterns of the Rías Baixas adjacent sea area. Journal of Marine Systems, vol. 54, 97-113, 2005

[*Vandromme et al.,* 2010] Vandromme, P., Stemmann L., Garcia-Comas, C., Colbert, S., Berline, L., Picheral, M., Gasparini S., Guarini, J.M. and G. Gorsky. Assessing the properties of net collected and automatically classified zooplankton size spectra before their use in models or ecological studies. Journal of Plankton Research, in review, 2010.

[*Van Heukelem and Thomas,* 2001] Van Heukelem, L. and C.S. Thomas. Computer-assisted high performance liquid chromatography method development with applications to the isolation and analysis of phytoplankton pigments. Journal of Chromatography A, 910, 31-49, 2001.

[*Wooster et al.,* 1976] Wooster, W., Bakun, A., and D. McLain. The seasonal upwelling cycle along the eastern boundary of the North Atlantic. Journal of Marine Research 34 (2), 131-141, 1976.

62

3.2   Résumé de l'article 1 (français).

Dans cet article, les données physiques et biogéochimiques récoltées lors de la campagne MOUTON 2007 sont présentées et analysées de façon descriptive. Cette campagne a eu lieu dans la zone centrale et nord de l'upwelling de la Péninsule Ibérique, du 14 Août au 9 Septembre 2007. Les objectifs sont d'étudier la variabilité spatio-temporelle à mésoéchelle de l'upwelling et sa biogéochimie, en relation avec les processus physiques. Ces données pourront également être destinée à valider des sorties de modèles couplés.

Les données recueillies proviennent de stations bathysonde équipée de plusieurs appareils de mesure. Nous disposions en plus d'une sonde Conductivity Temperature Depth (CTD), qui mesure la pression, la température et la conductivité (salinité et densité) de l'eau, de deux fluorimètres (qui mesurent respectivement la concentration en chlorophylle a et le CDOM Coloured Dissolved Organic Matter), de capteurs optiques, ainsi qu'une sonde d'oxygène dissous. De plus, la bathysonde et la coque du bateau étaient équipés d'un Acoustic Doppler Current Profiler (ADCP) qui enregistre les composantes horizontales des courants dans la colonne d'eau. Des échantillons d'eau ont aussi été récoltés à différentes profondeurs à l'aide de 12 bouteilles Niskin pour réaliser des mesures biogéochimiques. Les pigments chlorophylliens ont été analysés par HPLC (High Performance Liquid Chromatography), l'oxygène dissous titré par la méthode Winkler, le CDOM et les matières en suspension sont estimés à partir de filtrations. Les biomasses de zooplancton ont été également suivies par la réalisation de traits verticaux à l'aide d'un filet WPII à certaines stations CTD. Les conditions météorologiques sur zone étaient très favorables au développement d'un upwelling avec des forts vents de nord avant et pendant la campagne. Les cartes satellites de température de surface et de couleur de l'océan révèlent un fort upwelling, avec des températures de moins de 13°C à la côte, associé à une réponse élevée de l'écosystème planctonique avec des concentrations de chlorophylle a supérieures à 10 mg/m3.

En première partie, les principales masses d'eau présentes et leurs caractéristiques générales biogéochimiques ont été décrites à l'aide de toutes les données récoltées. Ensuite, la circulation complexe ayant lieu sur le plateau est décrite et révèle notamment l'importance des structures à mésoéchelle tels les tourbillons sur cette marge continentale.

La section nord-sud de 39°à 42.8°N est ensuite étudiée en détail et permet de séparer la zone côtière en trois sous provinces, chacune caractérisée par un fonc-

tionnement physique et biogéochimique particulier. A l'extrême nord de la zone, les eaux ENACWsp (Eastern North Atlantic Central Water of subpolar origin) upwellées supportent une production biologique importante dominée par des diatomées, sous une faible pression de broutage due à de faibles biomasses de gros individus de zooplancton. Le domaine central est quant à lui sous l'influence d'eau ENACWst (sub-tropical) upwellée, moins favorable (plus pauvre en nutriment), mais enrichie par des processus intenses de reminéralisation et de remise en suspension de nutriments sur le plateau peu profond. De plus, on note la présence de la Western Iberian Buoyant Plume (WIBP) dans la couche de surface qui, advectée du nord (Rias) par les courants d'upwelling, contient des écosystèmes du nord en évolution constante. Plus au sud, on observe une masse d'eau de subsurface provenant du sud qui diminue les processus de reminéralisation et contient relativement peu de nutriment pour une production modérée et une forte pression de broutage. Entre ces deux sous provinces, les concentrations maximales de chlorophylle a sont observées, causées par de faibles biomasses de zooplancton et une colonne d'eau stable en surface mais toujours enrichie en nutriments.

Le gradient côte – large est analysé à l'aide des sections est-ouest réalisées à 40°et 41°N à quelques jours d'intervalle, sous des conditions de vent contrastées. La physique semble répondre aux pulses successifs d'upwelling, marqués par des fronts de température associés à des maxima locaux de chlorophylle a, entrecoupés de période de relaxation/stratification. La zone très côtière contient des petites espèces de nano- et picophytoplancton, controlées par un intense broutage par du petit zooplancton. Au niveau du plateau se trouve le phytoplancton de plus grosse taille tel que des diatomées et dinoflagellés en interaction avec du gros zooplancton. Puis, au large dans les anciens fronts d'upwelling, on trouve des cyanobactéries et des prochlorophytes qui peuvent tirer avantage des concentrations réduites de nutriments.

L'export de masses d'eau côtières via une structure filamenteuse à 40.3°N est investigué et révèle un écosystème relativement productif au sein du filament comparé aux eaux environnantes. Des espèces typiques des zones côtières se retrouvent advectées vers le large et peuvent bénéficier pendant un laps de temps de conditions favorables à leur développement. Bien que de nombreux changements des communautés planctoniques aient lieu durant l'export, les biomasses à l'extrémité du filament sont significativement différentes de l'écosystème du large.

Ce papier descriptif démontre la forte influence de l'hydrodynamique de la zone sur la biogéochimie et sur l'écosystème en général. Une des premières radiales

quasi-synoptique le long de la côte a permis de différencier trois sous provinces ayant un fonctionnement spécifiques. On a aussi décrit la présence des eaux ENACWst au nord de la zone avec une réponse spécifique de l'écosystème, liée notamment aux fortes conditions d'upwelling rencontrées. Un couplage significatif entre les communautés de phytoplancton et zooplancton en terme de taille a aussi été mis en évidence. L'étude du filament a enfin confirmé l'importance qualitative et quantitative de tels processus sur les échanges côte-large.

3.3   Perspectives and other study derived from the survey.

The huge amount of data of great quality as revealed by the previous chapter foster us to look for collaborations in order to make the most of the survey. Below are presented two ongoing studies concerning all data, or a subset only, collected during MOUTON 2007.

Stefan Raimund and Marc Vernet from Roscoff were onboard the RV Pourquoi Pas? to collect Volatile Halogenated Organic Compounds (VHOC). Their sampling strategy was included in the biogeochemical sampling I organized onboard. Then Stefan and colleagues finished the analyses on land to study for the first time these chemicals in the IPUS. Stefan and I are now trying to explain the VHOC distributions by others environmental data, while we are collaborating with other co-authors to write the paper.

The second study concerns the zooplankton samples I collected onboard, and that were analysed by different methods on land. I did the dryweight analyses and I worked in close collaboration with taxonomists (Denis Altukhov and Alexandra Goubanova, Ukrain). I then started to perform the zooscan analyses myself, that were then finalized by two trainees that I co-supervised with Lars Stemman. Finally, Jean-Baptiste Romagnan used his taxonomic knowledges to sort all images created by the Zooscan. This very complete dataset will be analysed by Jean-Baptiste and I, in relation with the environmental context deducted from my previous analyses.

3.3.1   Distribution of Volatile Halogenated Organic Compounds in the Iberian Peninsula Upwelling System.

Water samples taken in the Iberian Peninsula Upwelling System revealed that spatial distribution of halocarbons are related to sea surface temperature. Varia-

tions in sea surface temperatures can be explained by convection and advection processes; two typical processes in upwelling systems. Statistical methods showed distinct similarities between three different clusters of VHOCs. In those clusters were usually halocarbons with the same halogens (bromocarbons, iodocarbons and chlorocarbons). Those groups were reflected in correlations patterns between VHOCs (Volatile Halogenated Organic Compounds) and environmental variables. Typical correlation patterns indicated that bromocarbons might have a phytoplanktonic source in the open ocean. Iodocarbons showed correlation patterns which were discussed to indicate a bacteria-related source in the open ocean. This idea is supported by the fact, that highest concentrations of iodocarbons were found off shore.

Furthermore it was shown that bromocarbon concentrations of near shore water samples were elevated several hours after high tide. This fact and the observed concentration gradient (lower values towards the open ocean) led us to conclude, that the main source of bromocarbons is located in the upwelling and that water masses with elevated bromocarbon concentrations are translocated westwards .

The postulated high concentrations of VHOCs were not found during the campaign. In the upwelling, only weak correlations with marker pigments for phytoplankton were encountered. Hence we reject the idea that upwelling regions might be hot spots for VHOC formation due to diatoms. However the upwelling induced nutrient supply might have some effects on shore line macroalgae beds. We suggest that further studies between the shore line and the upwelling might contribute to a better understanding of sources within the upwelling areas.

See annex A for further details.

3.3.2 Zooplankton communities and size spectra in the Iberian Peninsula Upwelling System.

A complete description of the zooplankton data is currently being performed with Ecologists from Laboratoire d'Océanographie de Villefranche/Mer and Biologists from the Institute of Biology of the Southern Seas, Sevastopol, Ukraine. The previous paper highlights the high variability of the hydrodynamical conditions along zonal and meridional gradient, both from a physical and biological point of view. This study will focus on the zooplankton dataset, and aims at describing the func-

tioning of the secondary producers, namely the zooplankton, along with the general hydrodynamical and biogeochemical context.

We will benefit of a complete and complementary dataset, since we have biomass estimation from dry-weight measurements, from biovolumes and abundances (Zooscan), as well as manual countings for a few stations. Moreover, the Zooscan data allow us to have an estimation of the size of each object. We can then study these populations using the theory of the size spectra: they represent abundances of individuals separated in size classes. It is an indication of the community composition and of the efficiency of energy transfer through the food chain. Moreover, each object has also been sorted out to the genus level or even species level when possible, using a specific sofware (*Gasparini* [2007]). We can then study the species composition of the community from the Zooscan data, but also using the few samples where Biologists identified the individuals manually. This is a great opportunity to better assess the zooplankton functioning and dynamics in this upwelling area (Romagnan, Rossi et al., 2010, in prep.).

Chapter 4

Punctual small scale physical processes observed during MOUTON 2007 and their academic studies.

As mentioned in the previous chapter, this multidisciplinary study generated a huge amount of data, both of physics and biogeochemistry. In Chapter 3, we presented the general context of the survey, and we detailed the spatial variability of the ecosystem, responding to hydrodynamical changes. In this chapter, observations were used to focus on one mechanism, a secondary upwelling front along the continental margin, that I then studied in detail using numerical modelling (Article No. 2).

A simulation from the study presented in Article No. 2 (section *3.2 Numerical results for a 3D configuration: impact of the along-shore shelf extension*) revealed an interesting filamentation process. This promising observation initiated further work that was done in collaboration with Thomas Meunier from Brest (Laboratoire de Physique des Océans). Thomas, Yves, and I designed the research lines of this work. The MICOM code I used in the Article No. 2 was transfered to Thomas who made the changes to perform all simulations presented in the following. I was then

involved in the writing process with other co-authors. Article No. 3 investigates a new theory for generation of long trapped filaments.

Contents

4.1 Article 2: Effect of the wind on the shelf dynamics: formation of a secondary upwelling along the continental margin, Rossi *et al.*, Ocean Modelling, 2010.

Reference : Rossi, V., Y. Morel and V. Garçon. 2010. Effect of the wind on the shelf dynamics: formation of a secondary upwelling along the continental margin, Ocean Modelling, vol. 31, 3-4, p 51-79, doi:10.1016/j.ocemod.2009.10.002.

Effect of the wind on the shelf dynamics: Formation of a secondary upwelling along the continental margin

V. Rossi [a,*], Y. Morel [b], V. Garçon [a]

[a] Laboratoire d'Études en Géophysique et Océanographie Spatiales, CNRS, 18 Avenue Edouard Belin, 31401 Toulouse Cedex 9, France
[b] Service Hydrographique et Océanographique de la Marine, (SHOM), 42 av Gaspard Coriolis, 31057 Toulouse, France

ARTICLE INFO

ABSTRACT

In this paper, the authors study the influence of the wind on the dynamics of the continental shelf and margin, in particular the formation of a secondary upwelling (or downwelling) front along the shelf break.

Observations during the MOUTON2007 campaign at sea along the Portuguese coast in summer 2007 reveal the presence of several upwelling fronts, one being located near the shelf break. All upwellings are characterized by deep cold waters close to or reaching the surface and with high chlorophyll concentrations. Simplified numerical models are built in order to study a possible physical mechanism behind this observation. First, a simple shallow water model with three distinct layers is used to study the formation of secondary upwelling fronts. We show that the physical mechanism behind this process is associated with onshore transport of high potential vorticity anomalies of the shelf for upwelling favorable conditions. Sensitivity studies to bottom friction, shelf width, continental slope steepness, shelf "length" are analysed in terms of potential vorticity dynamics. In particular bottom friction is analyzed in detail and we find that, even though bottom friction limits the barotropic velocity field, it enhances the cross-shore circulation, so that no steady state is possible when stratification is taken into account. Bottom friction accelerates the onshore advection of high potential vorticity, but also drastically reduces its amplitude because of diabatic effects. The net effect of bottom friction is to reduce the secondary upwelling development. Based on similar mechanisms, previous results are then extended to downwelling favorable conditions. Finally a more realistic configuration, with bottom topography, wind forcing and stratification set up from observations, is then developed and the results confronted to the observations. Simulations overestimate the velocity amplitude but exhibit good agreement in terms of density ranges brought over the shelf and general isopycnal patterns.

The application and extension of the results to more general oceanic regions is discussed and we conclude on the influence of such process on the dynamics of wind driven circulation over a shelf.

© 2009 Elsevier Ltd. All rights reserved.

1. Introduction

Upwelling systems are characterized by high productivity of plankton and pelagic fish. Their contribution to the world ocean productivity, up to 17% of the global fish catch (Pauly and Christensen, 1995), while representing only 0.5% of the total surface of the world ocean, identifies them as major biological and socio-economical areas.

The Iberian Peninsula Upwelling System (IPUS) is part of the four main wind driven eastern boundary upwelling zones. The MOUTON07 campaign at sea aimed at studying its physical and biogeochemical properties. The collected *in situ* data revealed a special pattern on a cross-shore section: apart from the typical coastal upwelling front, a secondary upwelling appears at the edge of the shelf near the continental margin. Such secondary upwellings along the shelf break have already been observed in other areas (Hart and Currie, 1960; Bang and Andrews, 1974 in the Benguela current; Huyer, 1976 in Oregon and North-West Africa; Dickson et al., 1980 in European shelves; Barth et al., 2004 over the Atlantic Bight) but to our knowledge it has not been documented for the IPUS area up to now. These shelf break processes are also of biological interest since they can enhance the primary production in the vicinity of the dome where deep rich nutrient waters are being upwelled into the euphotic zone. In the following, "secondary upwelling" will always refer to the upwelling of bottom water near the shelf break.

Wind driven upwellings, and particularly the Eastern Boundary Upwelling systems, are regional processes mostly driven by the

* Corresponding author. Tel.: +33 561 333 007; fax: +33 561 253 205.
E-mail addresses: vincent.rossi@legos.obs-mip.fr (V. Rossi), yves.morel@shom.fr (Y. Morel), veronique.garcon@legos.obs-mip.fr (V. Garçon).

local wind stress which generates currents in the frictional Ekman layer. Near a coast in the northern hemisphere, an along-shore wind oriented with the coast to its left produces offshore transport in the surface Ekman layer. Boundary conditions imply divergence of this current near the coast which generates an upwelling. The influence of bottom friction or a variable bottom topography on these upwelling systems and on the formation of secondary upwellings, in particular associated with a shelf-break, have been studied since the early 70s. It is well known that bottom friction has important effects on the shelf circulation and many authors have studied its effect (see Smith, 1968; Garvine, 1971, 1973). Hsueh and O'Brien (1971) or Hsueh and Ou (1975) showed its equivalence with the wind stress and its ability to generate upwelling when it acts on a pre-existing current. When it is associated to a wind driven upwelling, the bottom friction is known to equilibrate the surface wind stress and the surface and bottom Ekman layers connect into a steady cross-shore circulation. Among others, Hill and Johnson (1974), Johnson and Killworth (1975), Lill (1979) or Janowitz and Pietrafesa (1980) calculated analytical solutions for

this steady state with complex topographies including a shelf and a margin. They showed that at the shelf break the variations of the velocity field induce an upwelling. This has been recently revisited in Estrade et al. (2009) who calculated new solutions of the Ekman currents over variable topographies. They showed that the shallowest part of the shelf, where the surface and bottom Ekman layer merge, acts as a kinematic barrier and that the upwelling occurs at the offshore edge of this area. As a result, in regions where the shelf is shallow, upwellings are located far offshore of the coast, at the shelf break. All these papers however concentrate on homogeneous flows (or weakly stratified flows for which the density can be considered as a passive scalar).

O'Brien and Hurlburt (1972) were among the first to study the effect of stratification on the development of a coastal upwelling. They performed two layer numerical simulations above a flat bottom and showed that a baroclinic jet was formed at the coast. Another important difference with the homogeneous case is that they found no steady state in their numerical results. They explained the formation of this jet by conservation of potential vorticity: they
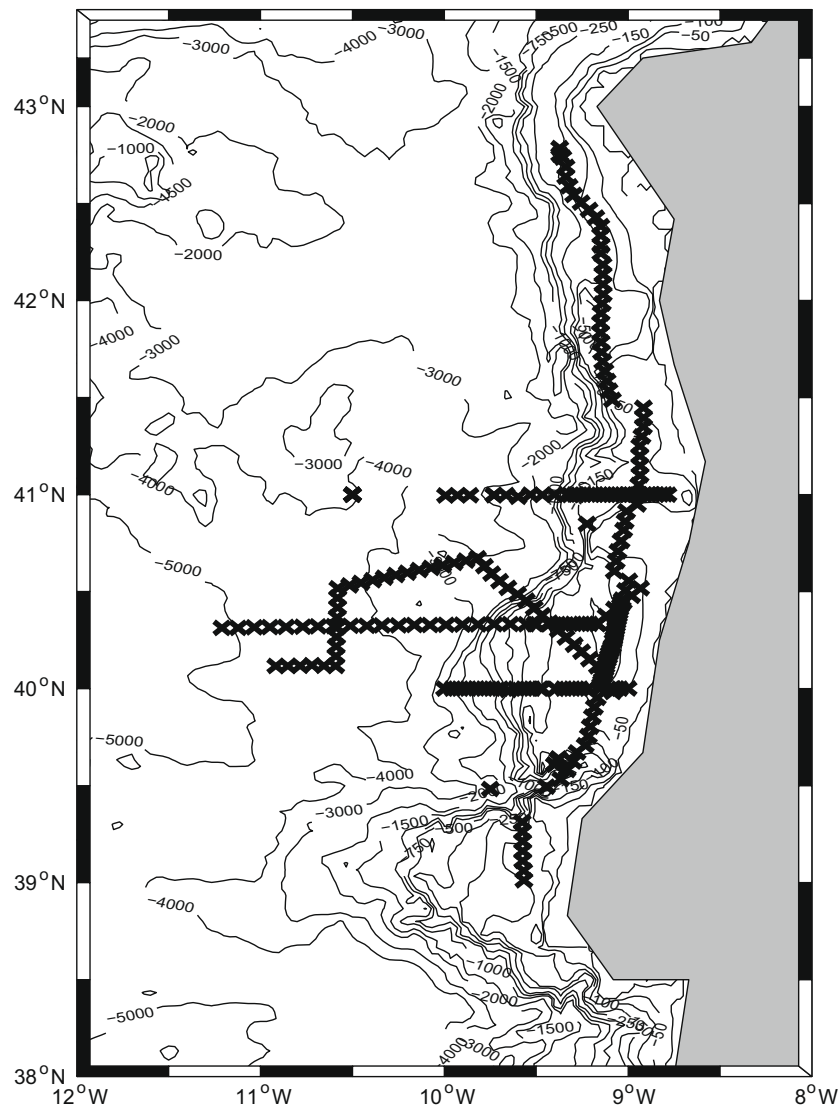
Fig. 1. Overview of the MOUTON07 oceanographic campaign offshore the Iberian peninsula. Crosses indicate the position of CTD stations; contours represent the bathymetry.

assumed the potential vorticity was not changed during the upwelling development, so that vorticity anomalies develop to compensate the stretching effect due to the upwelling development. As the stretching is of opposite sign in the upper and lower layers, the vorticity and velocity field are baroclinic and concentrated in the region of upwelling. The same authors also studied the case of a varying bottom topography in particular with an extended shelf and a margin. They found that a secondary upwelling develops at the shelf break and invoked potential vorticity conservation to explain this phenomenon. They however did not detail their argument or further investigate this effect.

Millot and Crépon (1981) studied *in situ* observations of current and temperature variations along the coasts of the Gulf of Lions. They analysed high frequency oscillations of the surface current, occurring mainly at the inertial frequency, and showed they were generated by transient gusts of wind. To do so they developed an analytical model linearizing the 2D equations for a two layers and a flat bottom configuration. They calculated the early stages of the dynamics generated by a wind on a shelf and, even though they focused on the oscillatory part, their results confirmed those from O'Brien and Hurlburt (1972) and provided a useful analytical

model for the development of an adiabatic upwelling. This model has been extended recently by Morel et al. (2006) while studying the modification of PV field of coastal upwelling and downwelling currents. They calculated the solution of the non-linear equations assuming that PV is not modified and that the along-shore velocity is in geostrophic equilibrium (a well verified hypothesis that only leads to filter the inertia-gravity waves). They showed that, if no dissipation processes are taken into account, only the barotropic part of the circulation keeps increasing while the baroclinic part is limited to a value reached when the layer outcrops. The outcropping front however keeps moving offshore.

The influence of stratification on upwellings has also been recently studied from observations by Lentz (2001), who analyzed observations taken on the Carolina shelf in winter and summer and showed the strong modifications of the Ekman circulation picture when stratification exists. Lentz and Chapman (2004) extended the model obtained for a homogeneous ocean to a stratified one and found approximate steady state solutions. When comparing their analytical results to numerical ones they however found that the steady state assumption was questionable.
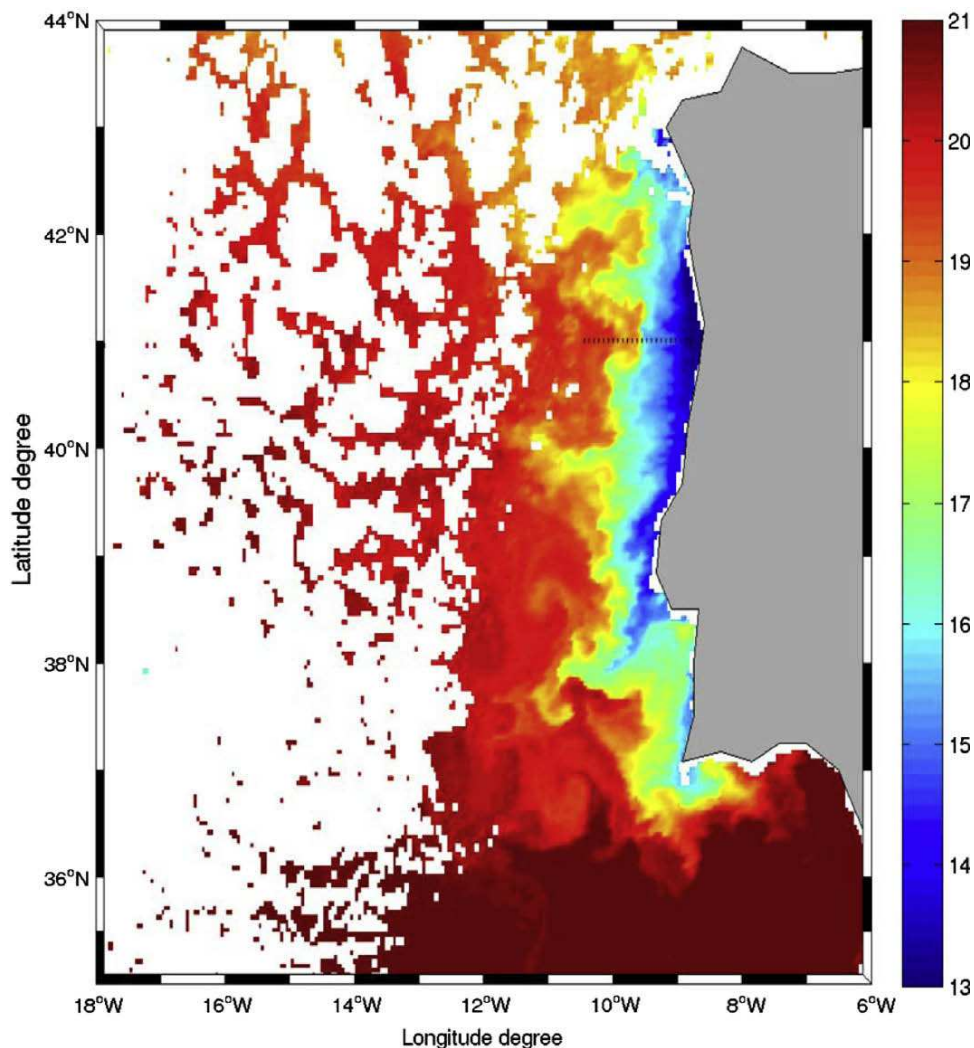
Fig. 2. Sea surface temperature (in Celsius degrees) on August, 21th from MODIS Aqua. The dotted line at 41°N represents the position of the section analyzed in this paper.
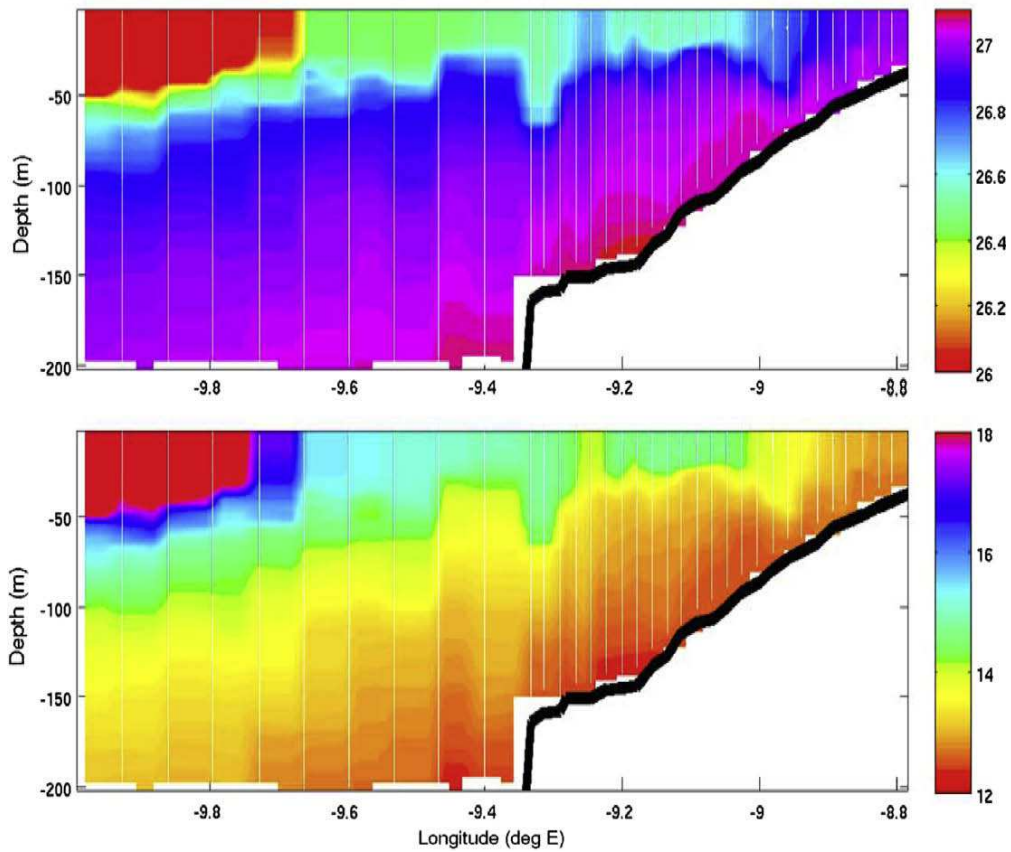
Fig. 3. Potential density (top) and temperature (in Celsius degrees, bottom) sections from *in situ* data along 41°N. The white lines indicate the CTD casts; the thick black line represents the measured bathymetry. Data were interpolated using elliptic interpolation schemes. Note that the resolution of the CTD casts was higher over the shelf than offshore.
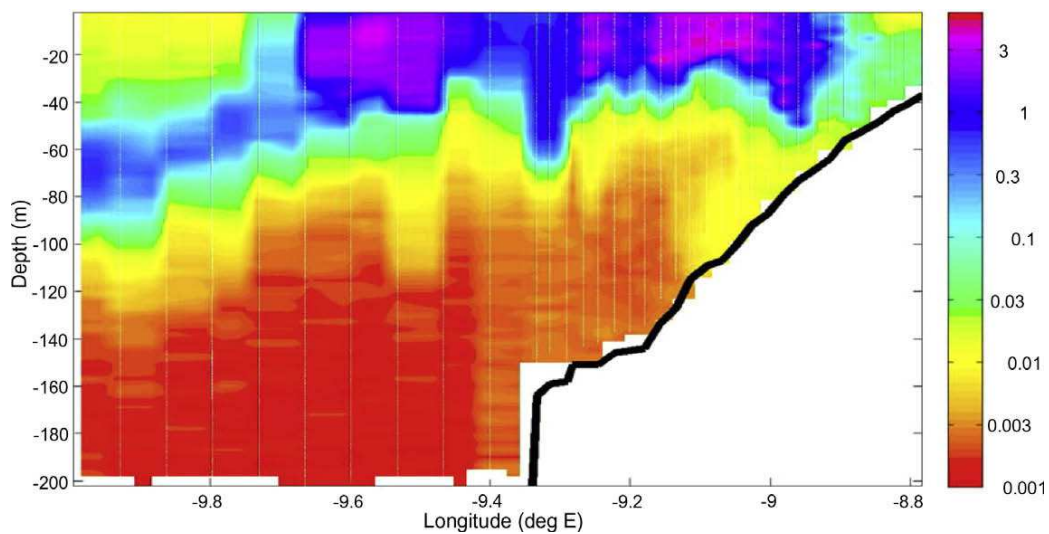
Fig. 4. Chlorophyll *a* section from the *in situ* fluorometer along 41°N (in mg/m³ displayed as a logarithmic scale). The white lines indicate the CTD casts; the thick black line represents the observed bathymetry.

The equilibration of upwelling systems and the mechanism responsible for the generation of (secondary) shelf break upwellings are thus issues that have received some attention. Even though recent studies using realistic modeling for both the physical and biogeochemical components of upwelling systems at high resolution (see for instance Gibbs et al., 2000, Marchesiello et al.,
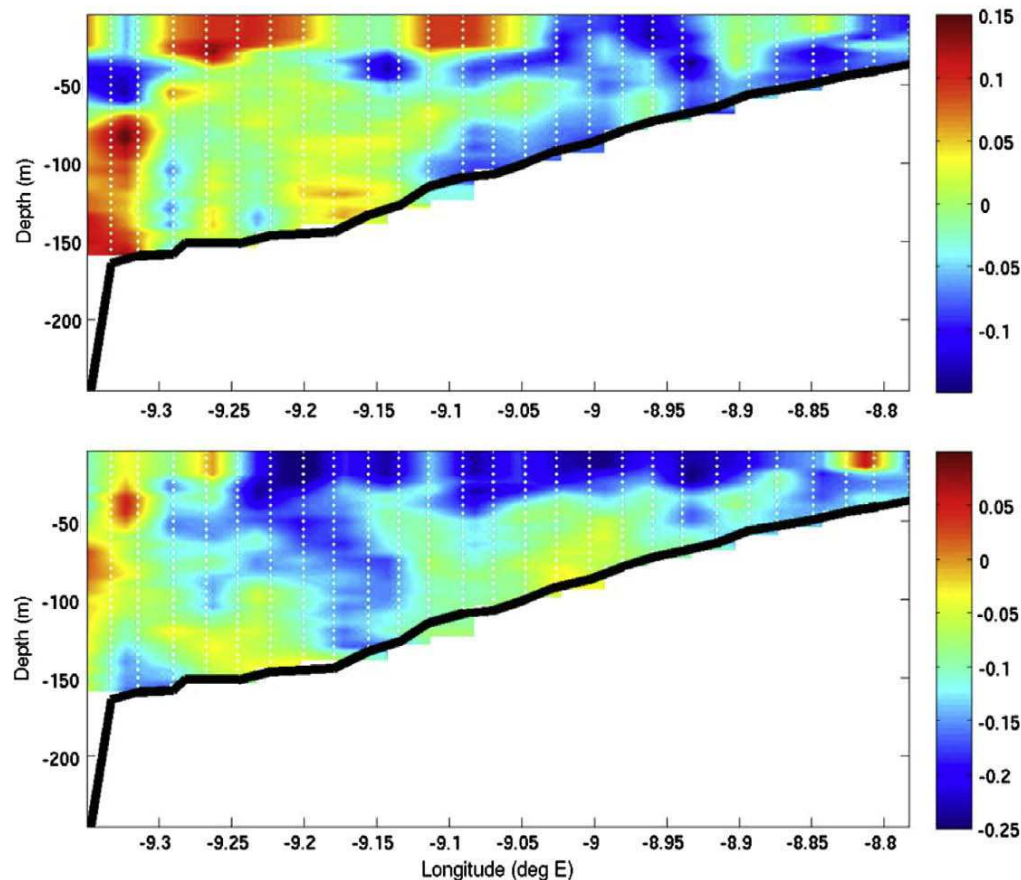
Fig. 5. Cross-shore (upper panel) and along-shore (lower panel) velocities (m/s) from LADCP along the 41°N section. On the upper panel red color indicates current directed to the west, while blue color to the east. On the lower panel, red color represents current to the north while yellow-green-blue colors to the south. The white dotted lines indicate the measurement positions; the thick black line represents the observed bathymetry. (For interpretation of color mentioned in this figure the reader is referred to the web version of the article.)

2000, Marchesiello et al., 2003, Penven et al., 2006 and Gruber et al., 2006) have yielded new insights on the upwelling equilibration (or other processes such as instability of the upwelling front), these issues are still not fully elucidated.

Previous works have then identified two mechanisms responsible for the development of upwellings:

- the frictional circulation developed in surface and bottom Ekman layer whose divergence creates upwellings, a mechanism that has received most attention;
- a more adiabatic analysis associated with PV conservation, which has been less studied and which will be developed below.

In this paper we concentrate on the generation of secondary upwellings and focus on adiabatic processes associated with PV analysis. In the second section we describe the secondary upwelling observed on the IPUS system and the numerical and theoretical tools we will use throughout the study. Some basic physical principles are also exposed. Numerical results showing the development of secondary upwelling close to a shelf break are analysed in Section 3 and their sensitivity to several parameters such as the bottom friction is also discussed. This brings some new elements concerning the possibility to equilibrate an upwelling system with bottom friction. Even though it is not the primary subject of this study, 3D simulations are also performed to confirm

the ability of the adiabatic process to generate secondary upwellings. These numerical results and sensitivity studies are then extended to downwelling cases. In the fourth section, we analyse the simulations from a more realistic model tempting to fit the observations. All these results are summarized in the last section where the application to other oceanic regions and more generally the role of the wind on the dynamics of an extended shelf are also discussed.

2. Observational evidences and tools

2.1. Observations of a secondary upwelling: the MOUTON 2007 cruise at sea

As mentioned above, the Iberian shelf is known as an important wind driven eastern boundary upwelling area, characterized by quasi-permanent intense upwelling conditions and high biological productivity. An along-shore southward wind stress establishes during summer and creates surface Ekman current directed to the west. A strong upwelling is usually generated during this favourable upwelling season, with a coastal jet flowing equatorward. A poleward counter-current, thought to be density gradient driven, is also observed just above the slope during most of the year, intensified in winter (Peliz et al., 2005). The general
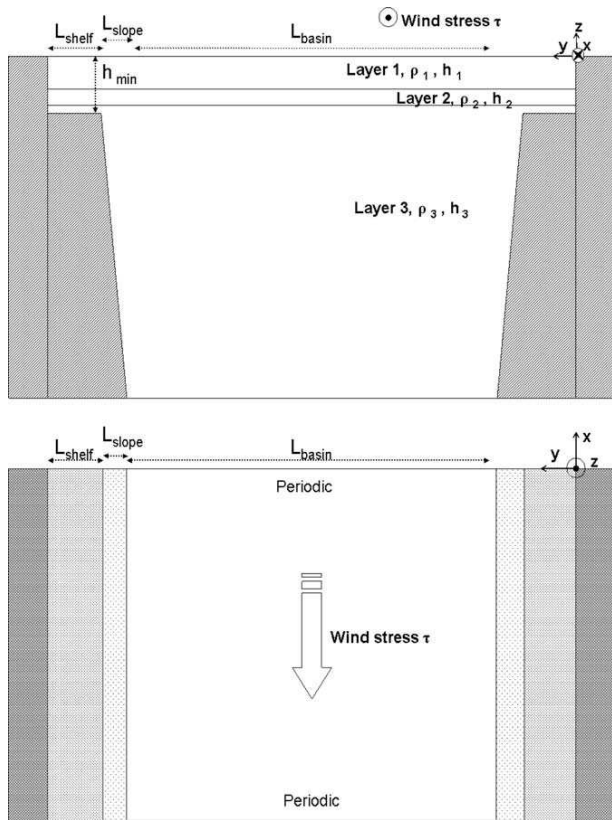
Fig. 6. Schematic representation of the academic model configuration (side view on the upper panel, top view on the lower panel).

Fig. 7. Schematic representation of PVA^d inversion principle (upper panel a): a positive (respectively negative) PVA^d within a layer is associated with a squeezing (resp. a stretching) of the layer thickness. The lower panel b is a schematic representation of the cross-shore circulation generated by the wind (Ekman drift superimposed on a barotropic mode generated because of the coast) and PVA^d generation mechanism applied to our configuration: the advection of a fluid column by the barotropic onshore current generates a negative PVA^d at the shelf-edge associated with a stretching of layer thickness and leading to the formation of a secondary upwelling at shelf break.

circulation patterns over the area are quite complex with strong seasonal variations (see Relvas et al., 2007).

The MOUTON07 cruise was conducted along the western coast of the Iberian Peninsula (mainly Portuguese coast), onboard the research vessel "Pourquoi-Pas?" (see Fig. 1). The cruise was divided in two legs during which the upwelling area above Lisboa was surveyed: the first one took place from August 11th to August 26th, the second from August 30th to September 14th 2007. Physical and biological data were gathered along East-West and North-South transects or repeatedly at fixed points.

The observational area extends from 38 to 42°N and from the coast to almost 3 degrees offshore (11°W). Data from the Quikscat scatterometer and onboard wind measurements reveal that after 2 days of moderate southerly winds (August, 13−14th), upwelling favorable wind conditions prevailed during the first part of the cruise with intense northerly wind (10–25 m/s) blowing during 2 weeks, from August, 15th to August, 26th with temperatures near the coast dropping to less than 13 °C. Fig. 2 shows a satellite image of sea-surface temperature (SST) on 21th of August, where the upwelling is clearly visible.

Observations were made using a Conductivity-Temperature-Depth (CTD) instrument, a Lowered Acoustic Doppler Current Profiler (LADCP) and other biogeochemical sensors. The sampling was adjusted to 24 scans per second and the lowering speed of the CTD was about 0.5 m/s. The CTD casts were limited to the upper 200 m (or above when the bathymetry was shallower) due to the maximum bearable depth of operation of some biogeochemical sensors. Data processing included removal of spurious values by low pass filtering.

Table 1
Parameters names and corresponding values for the 2D configuration reference experiment (see Fig. 6 for schematic representation) and for the 3D configuration experiment.

Parameters	Reference experiment	3D experiment
L_{shelf}	60 km	60 km
L_{slope}	60 km	60 km
L_{basin}	760 km	180 km
h_{min}	100 m	100 m
Δx	1000 m	2000 m
W_{shelf}	–	500 km
τ_x	0.4 Nm^{-2}	0.4 Nm^{-2}
τ_y	0 Nm^{-2}	0 N m^{-2}
f	0.9×10^{-4} s^{-1}	0.9×10^{-4} s^{-1}
C_d	0	0

Fig. 3 shows the temperature and density sections along 41 °N. The transect started at the coast on August, 21th at 10 a.m. and ended on August, 22th at 3 p.m. It clearly shows the coastal upwelling associated with cold (13 °C and below) dense water ($\sigma_\theta > 27$) brought over the shelf and reaching the surface at the coast. The lighter surface waters ($\sigma_\theta \simeq 26$) are pushed offshore (further than 9.7°W) by the Ekman drift associated with the pres-
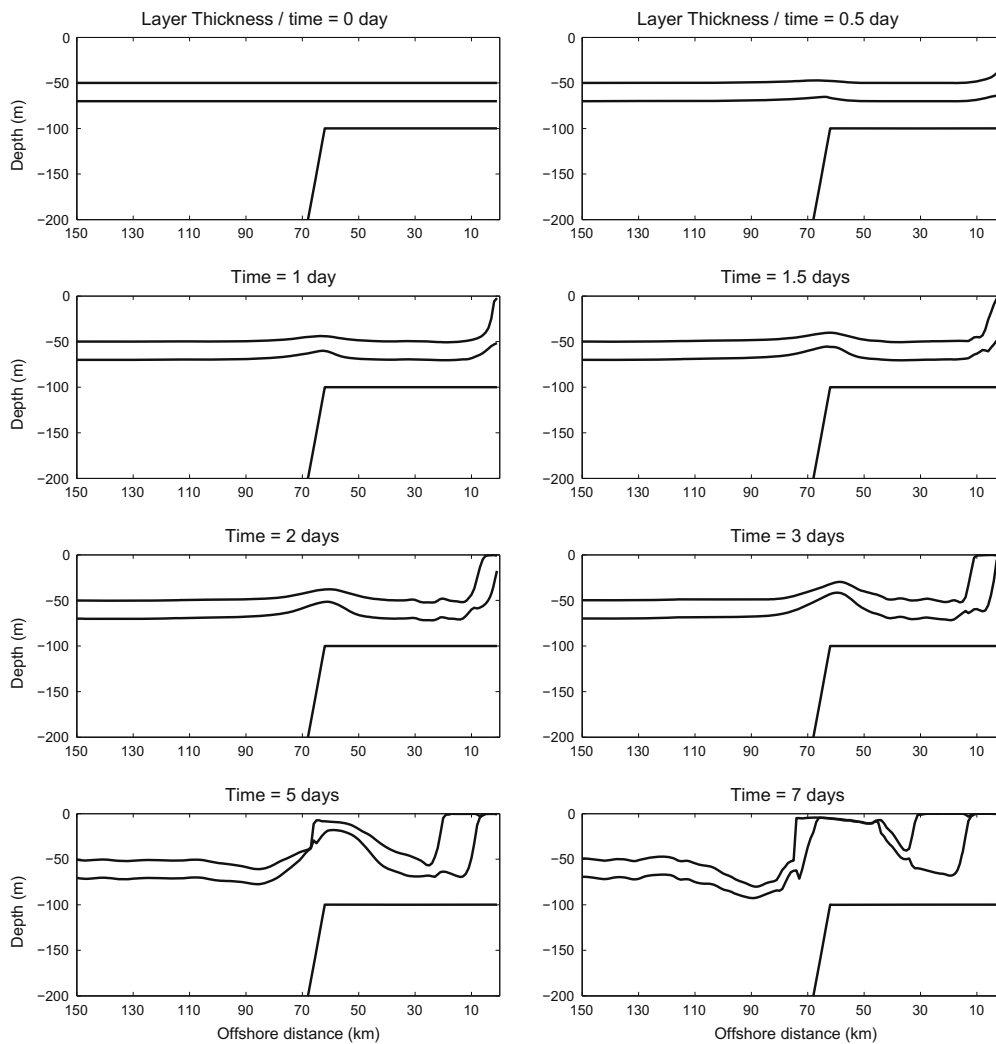
Fig. 8. Cross-section of the layer interfaces at different times for the reference run. Notice the development of the secondary upwelling in the vicinity of the shelf-break and also the continual offshore progression of the coastal upwelling front.

ence of intense Northern winds that started about 9 days before the observation. Fig. 3 also reveals a dome of dense waters penetrating into the surface layers ($\sigma_\theta \simeq 26.75$, for a density of the surrounding waters of 26.5) between the shelf break and 9°W with a strong intrusion around 9.25°W, slightly inshore of the continental margin. We associate this front to a secondary shelf break upwelling phenomenon. Note also the presence of very dense and cold waters ($\sigma_\theta \simeq 27$ and a temperature <12.5 °C) lying on the seabed inshore of the edge of the shelf break below this secondary upwelling. It constitutes the coldest and densest waters that have been upwelled over the shelf characterized by a temperature of 12.295 °C and a potential density of 27.089. To determine the origin of these waters, we used a deeper CTD cast performed at 41°N/ 10.5°W (offshore end of the section) which reached 2000 m below the surface by using another CTD cage. We found that the deepest upwelled waters over the iberian shelf come from a depth of 250 m below the sea surface. This result from the *in situ* data contrasts with the smaller depths commonly mentioned in previous studies (see for instance Chhak and Di Lorenzo, 2007) and used as a reference for nutrients concentration (Walsh, 1991). Finally, also notice

the smaller scale variations of the vertical position of the seasonal thermocline, typical of internal gravity waves.

Fig. 4 shows the chlorophyll *a* concentration estimated from fluorometer data which were converted after calibration using laboratory HPLC analysis. The most ancient upwelling front associated with the lighter waters is located far offshore. It is characterized by high chlorophyll concentrations ($1-5$ mg/m^3) between 9.45° and 9.7°W. Surface layers are restratified by atmospheric fluxes and mixing and deep waters are however still continuously upwelled and advected toward the coast. As a consequence, at 8.9°W there exists a more recent upwelling front that also originates from the coast. Between these two upwelling fronts, close to the shelf break (9.25°W), there exists an additional -secondary- upwelling front. All fronts are associated with high chlorophyll contents ($1-10$ mg/m^3) due to their richness in nutrients, whose intensity and extension are variable. In particular the secondary upwelling at 9.25°W identified above presents chlorophyll concentrations with a well defined local maximum at the same location where it reaches around 3 mg/m^3. The biological signature of the shelf break front confirms that this feature is not only a transient pro-
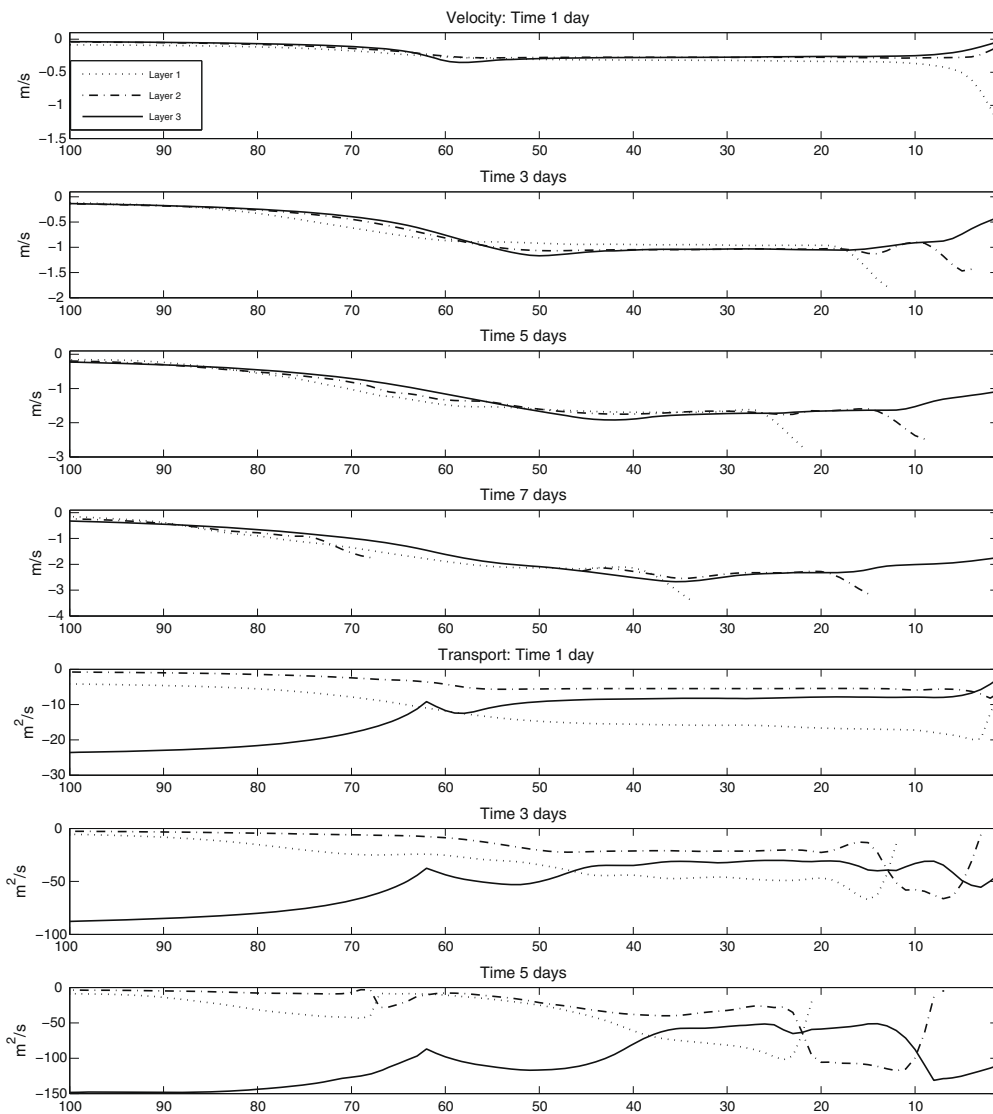
Fig. 9. Spatial structure of the along-shore velocities (four upper panels) and the along-shore transport (three lower panels) for the reference run at different times. The dotted line is layer 1 (surface), the dashed-dotted line is layer 2 and the plain line is layer 3.

cess, associated with internal waves for instance, since it supports phytoplankton growth of the order of the main front one, a typical feature of upwelling systems.

The current section from LADCP is presented in Fig. 5 with cross-shore velocities in the upper panel and along-shore velocities in the lower one. The error estimate is around 5 cm/s for this section. Note that the data exhibited much larger errors offshore of the shelf break because of rough oceanic conditions and had to be discarded. High frequency processes can alter the synopticity of the present current section, and spoil the signature of the upwelling. Tidal currents are however expected to be very weak because the tide coefficient was very low (about 40) during the transect which yields to currents of a few cm/s in this area. Actually, currents exhibit the typical signature expected for an upwelling phenomenon: the along-shore velocities are mostly negative (southward), intensified at the surface; the cross-shore velocities are mostly positive (westward or offshore) at the surface and neg-

ative (onshore) below. Note also a light intensification of both cross and along-shore currents in the vicinity of the shelf, around 9.25°W. Small scale features with alternating signs also superimpose on this general upwelling pattern. They are generally correlated with the small scale variations of the thermocline position mentioned above and are probably associated with inertial gravity waves.

To summarize, the observations presented above show that:

- the dynamical signatures (in particular the along-shore velocity) of the upwelling extend over the whole shelf and are not restricted to the frontal areas.
- apart from an ancient front, located offshore of the shelf break, and the newly developed one near the coast, there exists a secondary front above the shelf break that seems to be permanent and associated with significant biological activity. This has not been reported for the IPUS before.
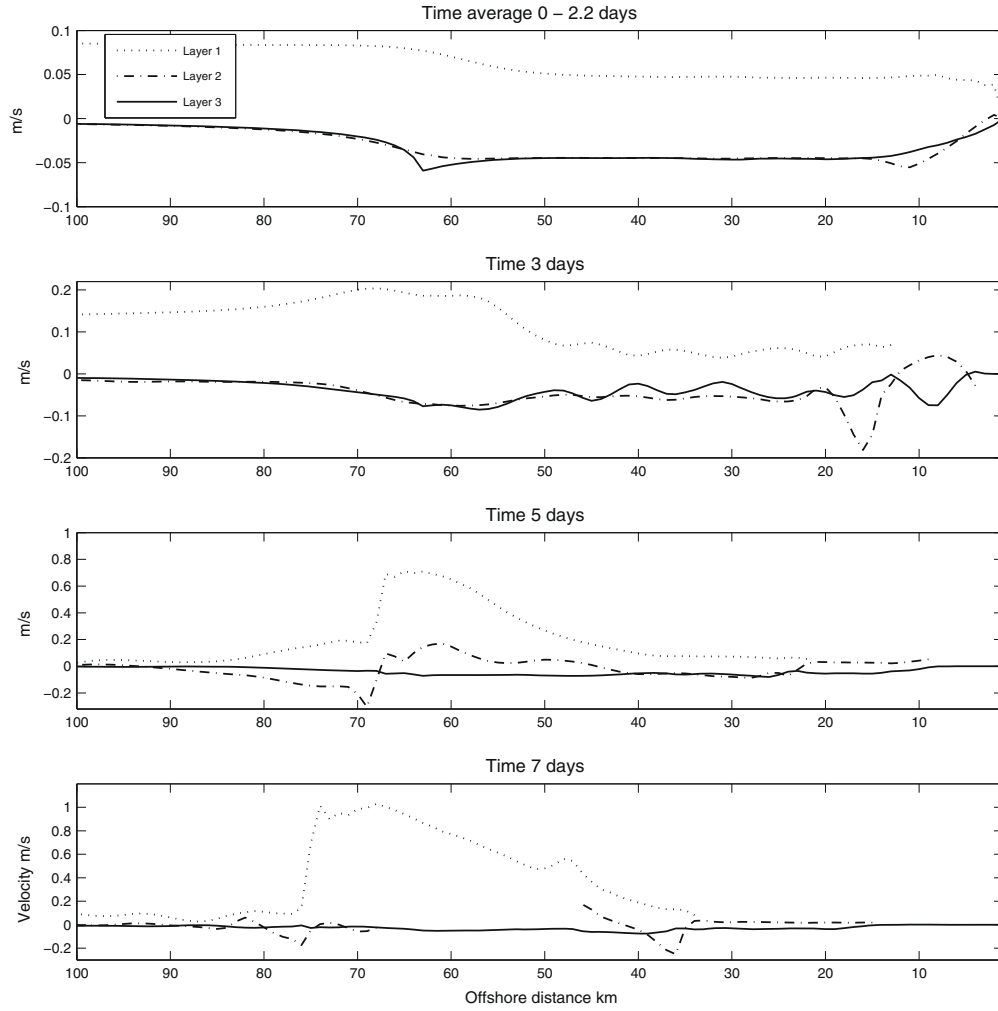
Fig. 10. Spatial structure of the cross-shore velocities for the reference run at different times. The dotted line is layer 1 (surface), the dashed-dotted line is layer 2 and the plain line is layer 3. In panel one, a time average was made over 3 periods of the inertial oscillations (at 41°N, it is 3×18.25 h $\simeq 2.2$ days).

In the following, we concentrate on the dynamics of this secondary upwelling.

2.2. Academic model and configuration

We concentrate on adiabatic effects and motions mostly in geostrophic equilibrium for which the dynamics is governed by potential vorticity evolution (see section below). We thus use a shallow water model, derived from MICOM (or Miami Isopycnic Coordinate Ocean Model, see Bleck and Boudra, 1986, Bleck and Smith, 1990, Bleck et al., 1992, Herbette et al., 2003 and Winther et al., 2007) with N distinct vertical layers of constant density. The dynamics in each layer $k = 1, \ldots, N$ (from top to bottom) is governed by the equations:

$$
\begin{aligned}
&\partial_t u_k + (\mathbf{u}_k \cdot \nabla) u_k - f v_k = -\partial_x \mathcal{M}_k + F_x + T_x \\
&\partial_t v_k + (\mathbf{u}_k \cdot \nabla) v_k + f u_k = -\partial_y \mathcal{M}_k + F_y + T_y \\
&\partial_t h_k + \nabla \cdot (h_k \mathbf{u_k}) = 0
\end{aligned}
\tag{1}
$$

where $\mathbf{u}_k = (u_k, v_k)$ and h_k are the horizontal velocity field and layer thickness of layer k. $f = 0.9 \times 10^{-4}$ s^{-1} the Coriolis parameter, assumed to be constant here. $\mathcal{M}_k$ is the Montgomery potential related to h_k according to:

$$
\mathcal{M}_k = g h_T + \sum_{i=1}^{i=N} g h_i + \sum_{i=1}^{i=k-1} \frac{\rho_i - \rho_k}{\rho_o} g h_i
\tag{2}
$$

where g is the acceleration due to gravity. ρ_k is the density in layer k, ρ_0 a reference density.

Finally, $\mathbf{F} = (F_x, F_y)$ represents the explicit numerical viscosity (see Winther et al., 2007) and $\mathbf{T} = (T_x, T_y)$ the effect of the wind forcing or bottom friction which depends on surface and bottom stresses $(\tau_{\mathbf{x}}, \tau_{\mathbf{y}})$: the frictional forcing is the vertical derivative of a stress, assumed to be equal to a parameterized stress at the boundary and linearly decreasing to zero over a critical thickness $thkbot = 10$ m (see Bleck and Smith, 1990). For instance, if layer 1 is deeper than $thkbot$ then the wind forcing acts only on layer 1 with $\mathbf{T} = (T_x, T_y) = (\tau_{\mathbf{x}}/(\rho_1 \times h_1), \tau_{\mathbf{y}}/(\rho_1 \times h_1))$. The wind will be along-shore ($T_y = 0$) constant and imposed at $t = 0$ over the whole domain. The bottom stress follows a quadratic law and is given by:

$$
\vec{\tau} = -\rho C_d |\vec{\mathbf{u}}| \vec{\mathbf{u}},
\tag{3}
$$

where C_d will be varied from 0 to 0.01.

The SST snapshot (Fig. 2) does not exhibit 3 dimensional effects in the observed area, such as a southward along-shore extension of a cold filament initiated further north, and we thus believe the secondary upwelling can be represented with a 2D configuration.
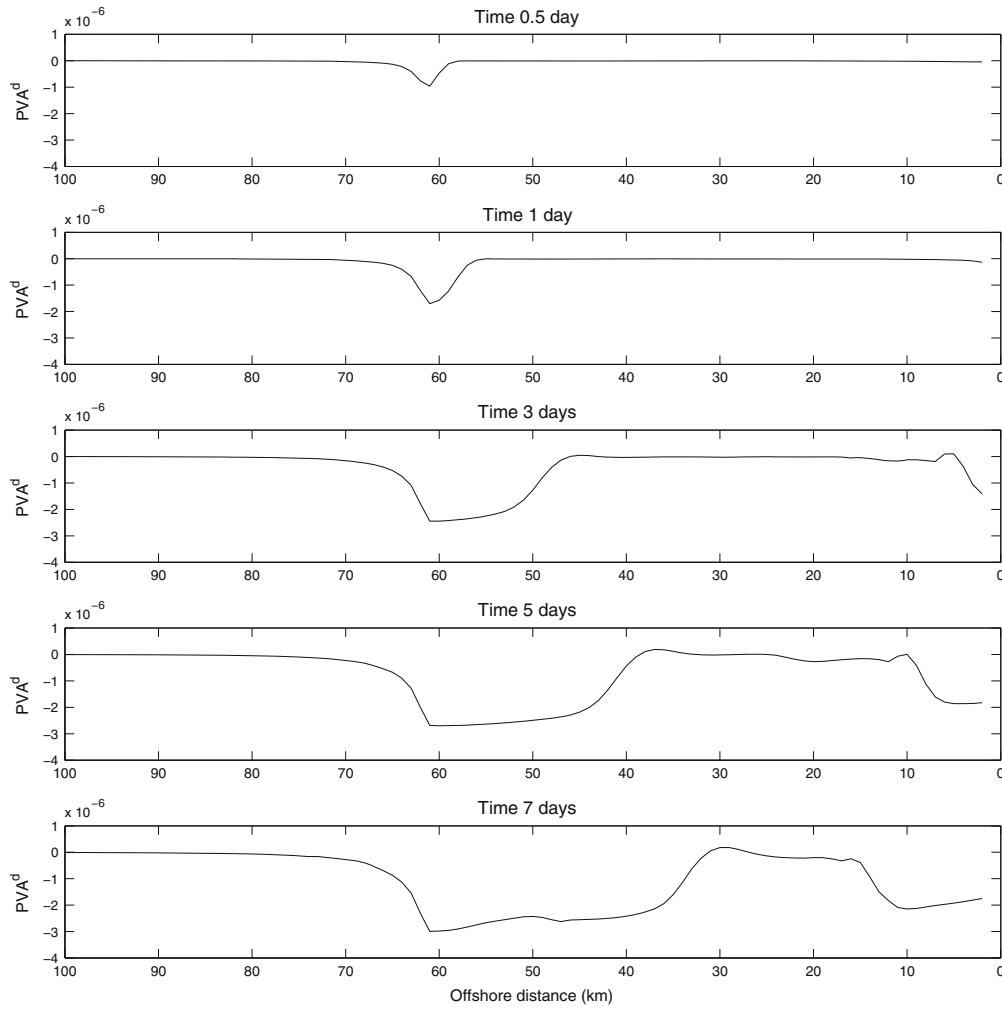
Fig. 11. Spatial structure of PVA^d in layer 3 for the reference run at different times. Notice the strong negative anomaly developing between 40 and 60 km.

In the observations presented above we can identify three components that seem to be of importance for the generation of a secondary upwelling: the wind, an extended continental shelf and the continental margin. These will be retained in all configurations selected in this paper. We will first consider three layers and concentrate on cross-shore variations. Fig. 6 represents the associated 2D configuration used in the next chapter. The upper layer represents the well mixed surface layer and is 50 m thick at rest, corresponding to the typical thickness of a mixed layer in the Atlantic Ocean in summer. A thin (20 m thickness at rest) intermediate layer is used to represent the thermocline and finally the lower layer represents the deep layers (reaching up to 1100 m off the shelf). The bottom topography represents a flat shelf and a deep area with respective total depths $h_{min} = 100$ m and 1100 m, separated by a continental margin whose length (and slope) L_{slope} can be varied. The extension of the shelf, L_{shelf}, and the length of the deep flat basin, L_{basin}, are also variable. Finally, the full domain is symmetric in order to model both upwelling and downwelling favorable conditions (see Fig. 6).

2.3. Potential vorticity

Potential vorticity (PV) is a quantity which depends on vorticity and stratification and is conserved for each fluid parcel for adia-

batic evolutions. PV is also related to the velocity field which can then be calculated by inverting the PV field under the assumption of (cyclo-)geostrophic equilibrium. PV conservation and invertibility are key properties that helped understand and interpret many geophysical fluid processes (McWilliams and Gent, 1980; Hoskins et al., 1985; McIntyre and Norton, 1990). In this paper, our numerical results will be analysed in terms of PV evolution which is written for each isopycnic layer k:

$$PV_k = \frac{\zeta_k + f}{h_k} \tag{4}$$

where $\zeta_k = \partial_x V_k - \partial_y U_k$ is the relative vorticity.

In the presence of a variable bottom topography, the PV of the lower layer is not zero at rest. In order to invert the PV and calculate the velocity (and layer thickness fields), it is then useful to introduce another quantity, the dynamical potential vorticity anomaly, PVA^d (see Herbette et al., 2005), defined for each layer k as:

$$PVA_k^d = \left[\frac{\zeta_k + f}{h_k} - \frac{f}{h_{k.rest}} \right] = \frac{1}{h_k} \left[\zeta_k - \frac{f(h_k - h_{k.rest})}{h_{k.rest}} \right] \tag{5}$$

where $h_{k.rest}$ is the kth layer thickness at rest and can vary with the position. Note that, contrarily to PV, PVA^d is not conserved following a fluid parcel, it is a local measure of the difference between

the PV and the PV at rest, and can be inverted to calculate the geostrophic velocity and thickness for all layers.

The presence of a PVA_k^d pole in a layer k is indeed associated with a circulation extending to all layers but intensified in layer k (Hoskins et al., 1985) and to variations of layer thicknesses to ensure geostrophic equilibrium. A positive PVA_k^d pole in a layer k is associated with a squeezing of the kth layer and stretching of the adjacent layers. A negative PVA_k^d pole in a layer k is associated with a stretching of the kth layer and squeezing of the adjacent layers (see Fig. 7a).[1]

When the PV at rest varies, the conservation of PV implies a readjustment of PVA^d when fluid parcels are displaced adiabatically through this background gradient. As a result, the fluid column can be stretched or squeezed (associated with a geostrophic current), depending on the sign of the PVA^d that is generated.

2.4. Basic physical interpretations

If we hypothesize that the motion is two-dimensional ($\partial_x = 0$), that there is no bottom topography variation, that $T_y = 0$, and if we neglect viscosity ($F_x = F_y = 0$), Eq. (1) can be written:

$$\partial_t u_k + v_k \partial_y u_k - f v_k = T_x$$
$$\partial_t v_k + v_k \partial_y v_k + f u_k = -\partial_y \mathcal{M}_k \qquad (6)$$
$$\partial_t h_k + \partial_y (h_k v_k) = 0$$

When there is no coast, the steady state solution of the equations consists in a velocity field concentrated in the upper layer oriented to the right of the wind and with a magnitude given by $v_1 = -T_x/f = -\tau_x/(\rho_1 f h_{1.rest})$: the Ekman drift. When a coast is taken into account, a boundary condition is imposed on the cross-shore velocity field, $v_k(y = 0) = 0$. At the boundary, the wind stress (and the bottom friction when it is significant) can thus only be balanced by the along-shore acceleration and we get:

$$\partial_t u_k(y = 0) = T_x(y = 0), \qquad (7)$$

which yields

$$u_k(y = 0) = T_x(y = 0)t. \qquad (8)$$

As a result, the along-shore velocity increases linearly with time at the coast, until additional processes equilibrate the upwelling development. Bottom friction and an along-shore pressure gradient (the term $-\partial_x \mathcal{M}_k$ neglected in the 2D configuration considered here) are two mechanisms that can efficiently compensate the wind stress effect and limit the along-shore current (see O'Brien and Hurlburt, 1972; Garvine, 1973; Lentz and Chapman, 2004; Chapman and Lentz, 2005 and Lathuilière, 2008).

As shown in Morel et al. (2006), if T_x is considered constant, PV is not modified. PV is initially constant within a layer (starting from rest and flat isopycnals), and it keeps the same initial value during the evolution, so that $PVA_k^d = 0$, which yields:

$$\zeta_k = -\partial_y u_k = f \frac{(h_k - h_{k.rest})}{h_{k.rest}}. \qquad (9)$$

Together with the geostrophic equilibrium this imposes a strong constraint on the spatial structure of the along-shore current. As shown in Morel et al. (2006), the along-shore current is given by a sum of barotropic and baroclinic modes with specific cross-shore structures:

$$u_k = \sum_m U_m^k(t) exp(-y/R_m), \qquad (10)$$

Fig. 12. Position of the isopycnal interfaces at different times calculated from the inversion of the PVA^d given in Fig. 11 for the secondary shelf break upwelling.

where m is the mode index and R_m is its associated deformation radius.

Eq. (8) then yields:

$$u_k = \sum_m T_m^k t exp(-y/R_m), \qquad (11)$$

where T_m is the projection of T_x on mode m and T_m^k its component in layer k.

The cross-shore structure of the upwelling current can thus be entirely inferred from PV conservation and the assumption of nearly geostrophic equilibrium.

The barotropic mode has no vertical variations and is associated with the external radius of deformation $R_e = \sqrt{gH}/f$ where H is the total water depth (see Millot and Crépon, 1981; Morel et al., 2006). For typical oceanic depth, R_e is large (several hundreds of kilometers at least). This contrasts with baroclinic modes for which the internal radius reaches a few tens of kilometers at most in the deep ocean and a few kilometers at most on a shelf. In addition, the projection of the wind acceleration T_x on the barotropic mode is simply $T_{barot}^k = T_0 = \tau_x/\rho_1 H$, where H is the total water depth. Thus, for an extended shelf far from the coast, all baroclinic modes rapidly vanish and there only remains the barotropic mode:

$$u_k = u_{barot} = \tau_x t \, exp(-y/R_e)/\rho_1 H. \qquad (12)$$

The cross-shore current is the addition of the Ekman drift (solution far from the coast) and barotropic and baroclinic modes with

---

[1] Close to a boundary, Kelvin currents (Kelvin waves having infinite wavelength) can spoil this general property. This property is however verified when the PVA^d pole is located further than an internal radius of deformation from a boundary.
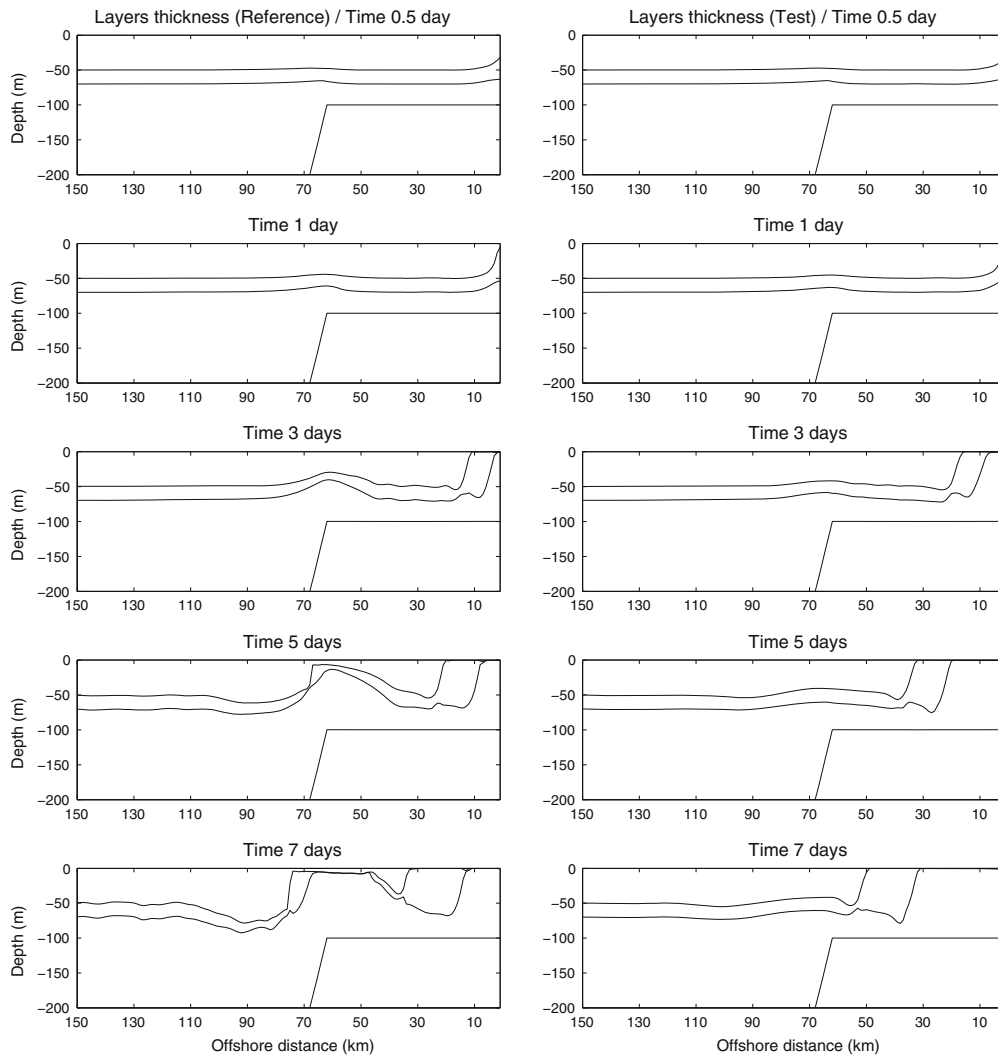
Fig. 13. Cross-section of the layer interfaces at different times for the test with $C_d = 3.10^{-3}$ (right panel) compared to the reference experiment (left panel).

the same spatial structures varying with the external and internal radii of deformation: $v_m = V_m^0 exp(-y/R_m)$ where V_m^0 is the amplitude. V_m^0 is calculated so that, at the coast, it exactly compensates the Ekman drift projected on the vertical structure of the mode.

Thus as showed in Fig. 7b, for an extended shelf, far from the coast all baroclinic modes rapidly vanish and there only remains the Ekman drift and the compensating barotropic mode that varies very smoothly.[2]

The projection of the Ekman drift on the barotropic mode is also obvious and yields $V_{barot}^0 = h_{1.rest}T_x/(fH) = \tau_x/(\rho_1 fH)$. As a result, the cross-shore velocity field far from the coast is a superimposition of the Ekman drift and the compensating barotropic mode: there thus exists opposite sign velocities below the Ekman layer.

When there exists bottom topography variations associated with a continental margin, low PV fluid parcels from the deep ocean are advected onto the shelf by the barotropic cross-shore current. This creates negative PVA[d] which stretches the bottom

layer, and generates upwelling in this area (see Fig. 7b). This mechanism was already mentioned by O'Brien and Hurlburt (1972) and we are going to study its impact in more details.

3. Results

3.1. Numerical results for the 2D three layers configuration

3.1.1. Model and parameters

In the present section, we consider the three layers configuration described in Fig. 6 and we define a reference experiment with specific parameters. Sensitivity studies are then carried out to evaluate the influence of several parameters: bottom friction, shelf width, shelf slope, wind stress variations. The total width of the basin is set to $2 \times L_{shelf} + 2 \times L_{slope} + L_{basin} = 1000$ km so as to avoid interactions between the upwelling and downwelling areas while keeping a reasonable calculation time (preliminary tests have showed that some differences appear for a total width of 500 km, whereas with a total width of 2000 km the differences are very small). Δx represents the horizontal resolution.

For the reference experiment, the parameters are given in Table 1.

---

[2] When the rigid lid approximation is made, the external radius is infinite and the barotropic eigenmode thus compensates the net (vertically integrated) Ekman flow. There thus exists a cross-shore barotropic velocity extending over the whole basin that compensates the net Ekman transport.

Fig. 14. Spatial structure of the along-shore velocities at different times for the simulation with $C_d = 3.10^{-3}$ (black lines) versus reference experiment (grey lines) for the surface layer (dotted lines) and the bottom layer (plain lines).

3.1.2. Reference run

Fig. 8 represents the layer interface for the reference experiment on the upwelling favorable side at different times. Starting from rest and flat interfaces, a coastal upwelling is initiated with a rising of the layer interfaces that is already visible after 0.5 day of upwelling favourable wind. Simultaneously, a secondary upwelling is also developing at the shelf break but at a lower rate than the coastal one. Both the coastal and (secondary) shelf break upwellings keep developing throughout the simulation, respectively moving offshore and onshore. The secondary one becomes quite strong after 2–3 days and the first interface, associated with the base of the mixed layer, reaches its maximum elevation (10 m below the sea surface) after about 6 days. The interfaces are then flattened below the surface and the coastal upwelling eventually absorbs the secondary upwelling (see day 7). At the coast, the lower interface outcrops after about three days of simulation. Note also that internal waves are present in the simulation: generated near the outcropping region they propagate offshore. Their wavelength is about 10 km and their amplitude reaches 10 m.

The four upper panels of Fig. 9 represent the evolution of the along-shore current u. As expected from theory and many previous studies (see for instance O'Brien and Hurlburt, 1972; Gill and Clarke, 1974; Millot and Crépon, 1981), the along-shore wind stress generates a southward flow intensified in the upper layers near the coast at the beginning of the simulation and in the vicinity of the outcropping region when the upwelling is well developed (notice the two peaks in the upper layers around 12 and 3 km at day 3, associated with the outcropping of the first and second layers, respectively). A strong barotropic current is however also developing that keeps growing if no dissipative processes are taken into account, as it is the case in this reference experiment. The maximum amplitude of the baroclinic velocity is roughly given by $f \times R_d \simeq 0.5$ m/s (see Morel et al., 2006). The barotropic velocity is given by $\simeq \tau/(\rho \times h_{min}) \times \text{time}_{second} \simeq 0.35 \times \text{time}_{day}$ and keeps increasing as long as the wind stress is applied. It becomes as strong as the baroclinic velocity on the shelf after 2 days and reaches more than 2 m/s after 7 days. As seen above, the signature of the baroclinic velocity is confined near the upwelling front whereas the barotropic velocity extends over the whole shelf. It however rapidly decreases over the continental margin as the total depth rapidly increases. The signature of the secondary upwelling is less important and its associated baroclinic amplitude reaches about 0.2 m/s. Notice that, contrarily to the coastal upwelling, the current is intensified in the lower layer for the secondary upwelling. Despite its weaker velocity signature, the secondary upwelling effect is quite important in terms of transport as the intensification of the coastal upwelling is concentrated in the shallow upper layers whereas the secondary upwelling extends over
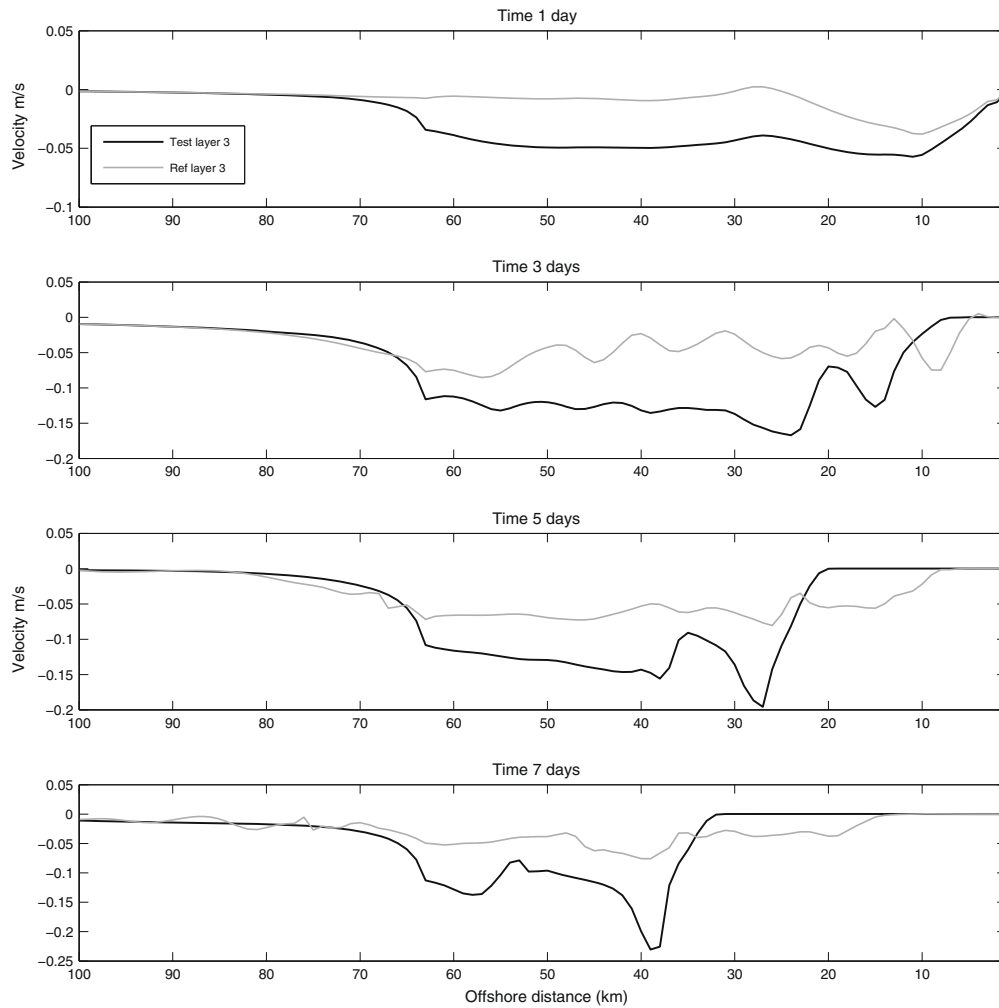
Fig. 15. Spatial structure of layer 3 cross-shore velocities at different times for the simulation with $C_d = 3.10^{-3}$ (black line) compared to the reference experiment (grey line).

the inflating lower layer. The three lower panels of Fig. 9 show the evolution of the along-shore transport. Notice the transport associated with the secondary upwelling becomes as strong as the coastal upwelling one after 2 days.

Fig. 10 represents the evolution of the cross-shore current v. As expected from previous studies, the velocity is offshore in regions and layers where the wind forcing acts, and onshore otherwise. The evolution of the cross-shore velocity is however strongly influenced by inertial oscillations whose magnitude is as strong as the mean currents (see Millot and Crépon, 1981; for instance at 1 day of our simulation, the velocity reaches a minimum and is close to zero over most of the domain, even in the upper layer). To get rid of this influence, a time average over 3 periods of inertial oscillations was done on the first panel of Fig. 10. Notice also that, as the development of the secondary upwelling squeezes the upper layer near the shelf break, the offshore velocity is strongly increased in this region to maintain the net flux imposed by the wind forcing.[3]

---

[3] The velocity increase is probably partly associated with the simplified configuration we have used here. When the surface layer thickness, which mimics the mixed layer, diminishes because of the upwelling development, the net cross-shore velocity over this layer is increased to maintain the same transport. In nature, vertical mixing would homogenize the surface water and lead to an increase of the surface layer thickness. This could drastically reduce the increase we observed in the simplified academic configuration considered.

Other remarkable phenomena on this figure are the signatures of the gravity waves that are quite clear at day 3.

Fig. 11 represents the PVA^d at different times. A strong negative pole appears in the bottom (third) layer in the vicinity of the shelf break. It grows and moves onshore. This modification of the PV structure gives rise to the development of a current in geostrophic equilibrium with modified layer depths. Indeed, Fig. 12 represents the position of the isopycnic levels resulting from the inversion of the PVA^d given in Fig. 11 (assuming PVA$^d = 0$ in the upper layers) under the assumption of geostrophic equilibrium (and with no baroclinic current at the coast). Notice the good agreement with the structure given in Fig. 8, except for the coastal upwelling not represented: the PVA^d generation in the third layer seems to explain most of the secondary upwelling signature. This proves that the upwelling developing at the shelf break is associated with the adiabatic advection of low PV columns from the deep ocean onto the shelf, as already argued by O'Brien and Hurlburt (1972).

As explained in Thomas (2005) and Morel et al. (2006), PV is also modified in the surface and thermocline layers. Indeed, even if the wind is constant, the wind forcing varies along isopycnic levels when their vertical position varies (as is the case for upwelling or downwelling processes). As predicted in both studies, this effect leads to the development of negative PVA^d near the shelf
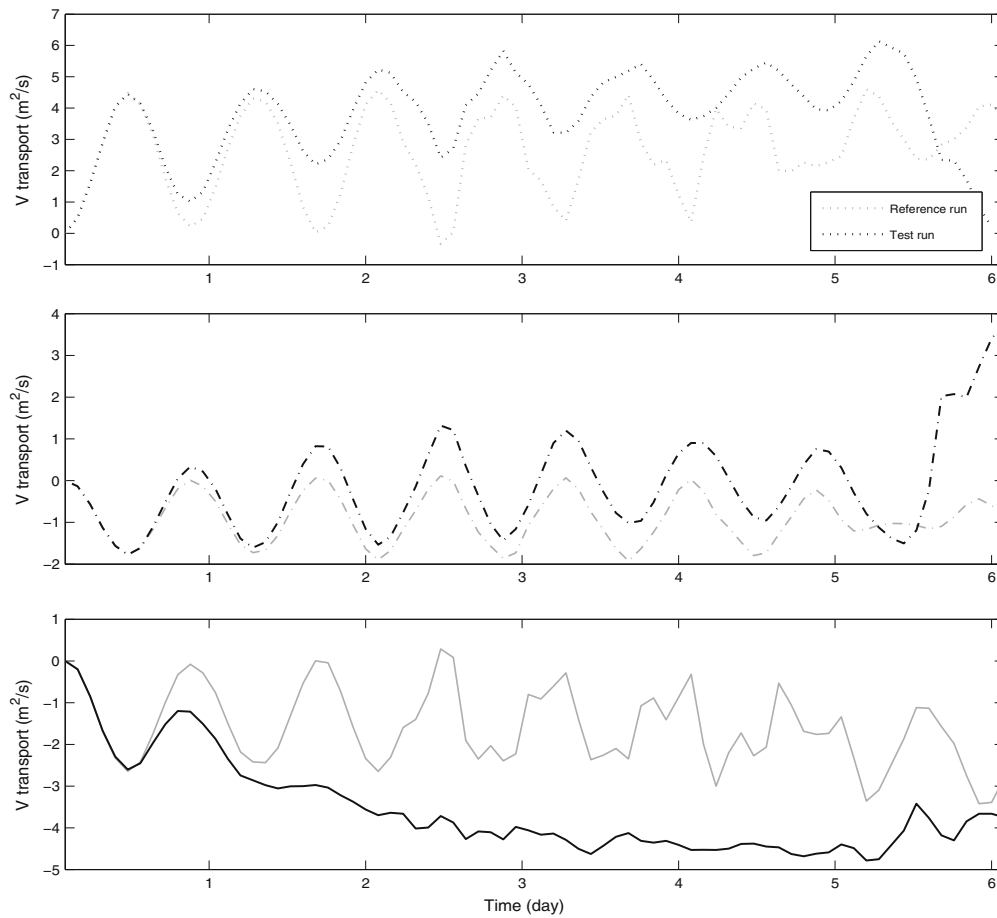
Fig. 16. Temporal evolution of cross-shore transport at mid-shelf (40 km offshore) for the simulation with $C_d = 3.10^{-3}$ (black line) versus the reference experiment (grey line). The upper panel represents the surface layer, the middle one layer 2, and the lower panel layer 3.

break upwelling front. This has two consequences on the present results:

- This process acts in the frontal region and modifies the PV in the lower layer when it is affected by the wind forcing. It explains the negative PVA[d] that extends from the upwelling front to the coast from day 3 (see Fig. 11).
- It also plays a role on the development of the secondary upwelling. Indeed, the upper layer PV is modified in this region because of this process. This explains the underestimation of upward motions of the interfaces in Fig. 12 in the last days and shows that adiabatic advection of low PV in the lower layer is not the only process that has to be invoked to explain the secondary upwelling in details.[4] It remains however the main one in this reference experiment.

---

[4] Notice that as the interfaces bend upward and downward in the secondary upwelling region, both positive PVA[d] is created on the inshore side and negative PVA[d] on the offshore side. Looking more precisely at Fig. 8, we observe an asymmetry of the interface slope which is steepened at the offshore edge of the shelf break but flattened on the inshore side, a difference that can be explained by the latter opposite sign PVA[d] creation.

3.1.3. Impact of bottom friction

We have investigated the effect of bottom friction on the configuration presented above. In the reference experiment where $C_d = 0$, we have seen that no stationary solution is reached, the barotropic velocity increasing linearly with time and the upwelling front continually moving offshore. The vertical extension over which the bottom stress is distributed is 10 m. Fig. 13 compares the evolution of the layer interfaces between the reference run (the left panels are reproduced from Fig. 8) and the same configuration except for $C_d = 3.10^{-3}$. As for the reference run, we can observe the development of both the coastal and shelf break upwelling. There are however two striking differences in comparison with the reference run. First, the offshore progression of the coastal upwelling is drastically increased: after 7 days of simulation, the lower interface outcrops at 25 km from the coast whereas in the reference run the distance was only 15 km. Second, the secondary upwelling is far less developed in comparison with the reference experiment: in the reference run, the first interface rises up to 5 m below the surface after 7 days, whereas with bottom friction it stays about 30 m below. Bottom friction thus increases the rate of development of the coastal upwelling and decreases the amplitude of the secondary upwelling, which are not intuitive results. This can be explained by the influence of the bottom friction on the cross-shore circulation and on the lower layer PV evolution.

First let us remember that, on the shelf, the circulation induced by the development of the upwelling is mostly along-shore, barotropic and constant (away from the outcropping region and shelf

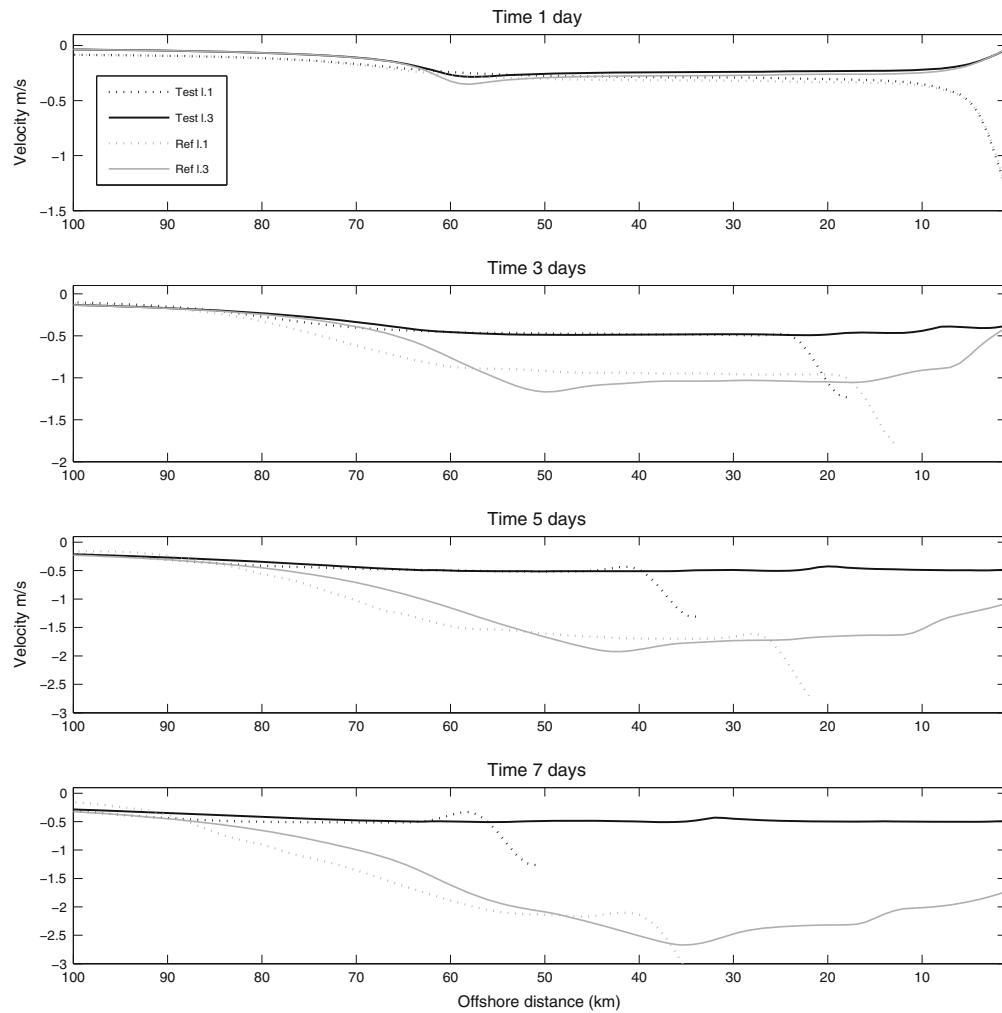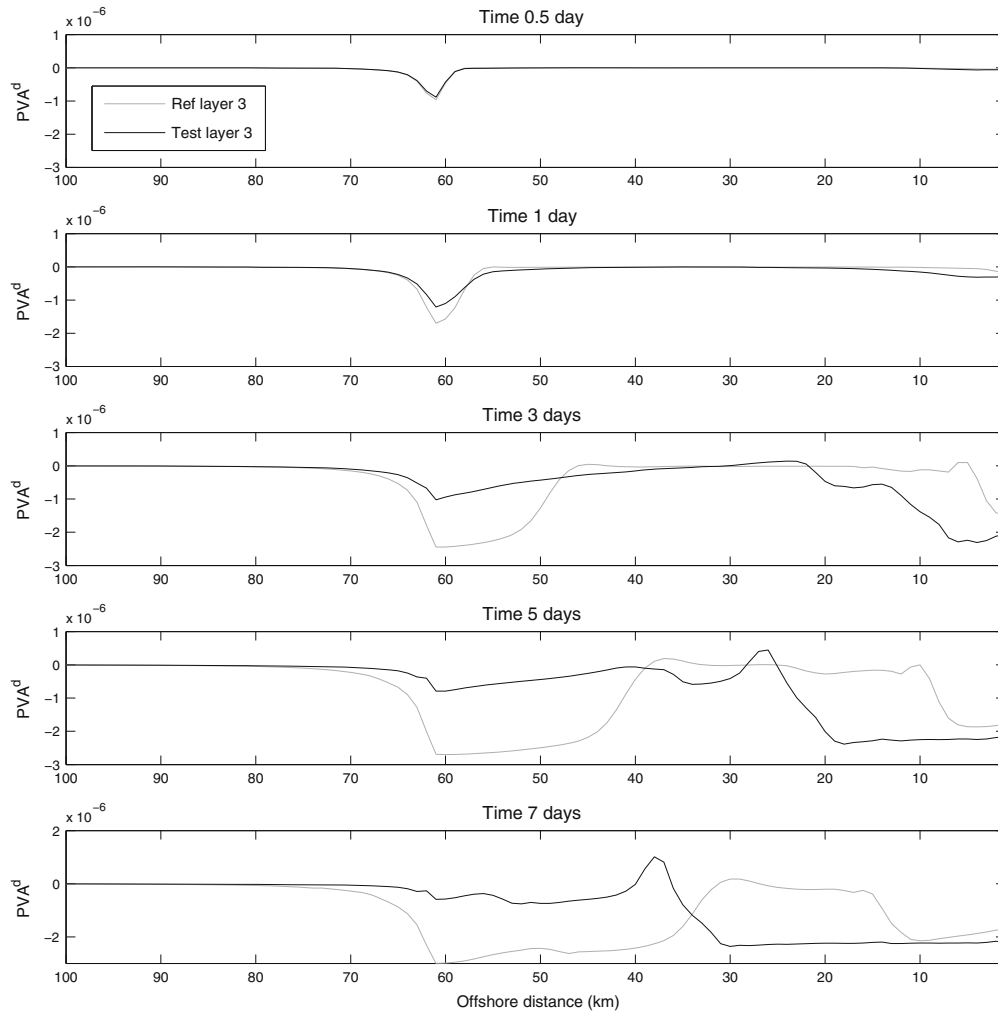**Fig. 17.** Spatial structure of PVA^d in layer 3 at different times for the simulation with $C_d = 3.10^{-3}$ (black line) versus the reference experiment (grey line).

break, see Fig. 9). The bottom stress on the shelf is thus mostly along-shore, constant and opposite to the surface wind stress and applied to the lower layer numbered 3. Far enough from the coast, the barotropic circulation dominates and the bottom stress is:

$$\tau_x^{bottom} = -\rho C_d |u_{barot}| u_{barot}. \tag{13}$$

It increases with the barotropic along-shore current (see Eq. 12) until it equilibrates the surface wind stress τ_x^{wind}. This is the case when:

$$|u_{barot}| = |\tau_x^{wind}/\rho C_d|^{1/2}. \tag{14}$$

Eq. (12) also yields an estimate of the duration of the transition stage, before equilibrium between bottom and surface stress is reached:

$$t_{eq} = H\sqrt{\frac{\rho}{\tau C_d}}. \tag{15}$$

In the present case, Eqs. (14) and (15) predict a maximum (barotropic) along-shore current of $u_{max} = 0.36$ m/s and a transition duration of about $t_{eq} = 1.1$ day, in good agreement with the numerical results which show that a maximum velocity of 0.4 m/s is reached after about 1.5 days (see Fig. 14).

As far as the cross-shore circulation is concerned, in the frictionless case, a compensating transport develops which is mostly associated with the barotropic mode and is thus distributed over the whole water column. Equivalently to the surface stress, bottom friction is also associated with a bottom Ekman drift, whose strength is given by $v_{barot}^3 = -\tau_x^{bottom}/(\rho_3 fh_3)$. At equilibrium, the surface and bottom Ekman drift exactly compensate so that the resulting transport is now concentrated in the bottom layer and is thus stronger than the fritionless case. Fig. 15 indeed shows the cross-shore velocity in the third layer after 5 days for the reference experiment and the experiment with a bottom friction $C_d = 3.10^{-3}$. It is about twice the reference one over the shelf. This accelerates the transport of PV in the lower layer when friction is taken into account.

The vanishing of the barotropic mode also reinforces the progression of the coastal upwelling front in the surface layer. When both the surface and bottom stresses are considered, the resulting cross-shore circulation pattern is an enhancement of both the surface and bottom cross-shore currents. Thus, although the along-shore barotropic mode is now limited, the surface and bottom fronts move offshore and onshore even faster and no steady state is reached.

Notice that as in the equilibrium state, the bottom Ekman transport exactly compensates the surface (wind generated) one, the

143
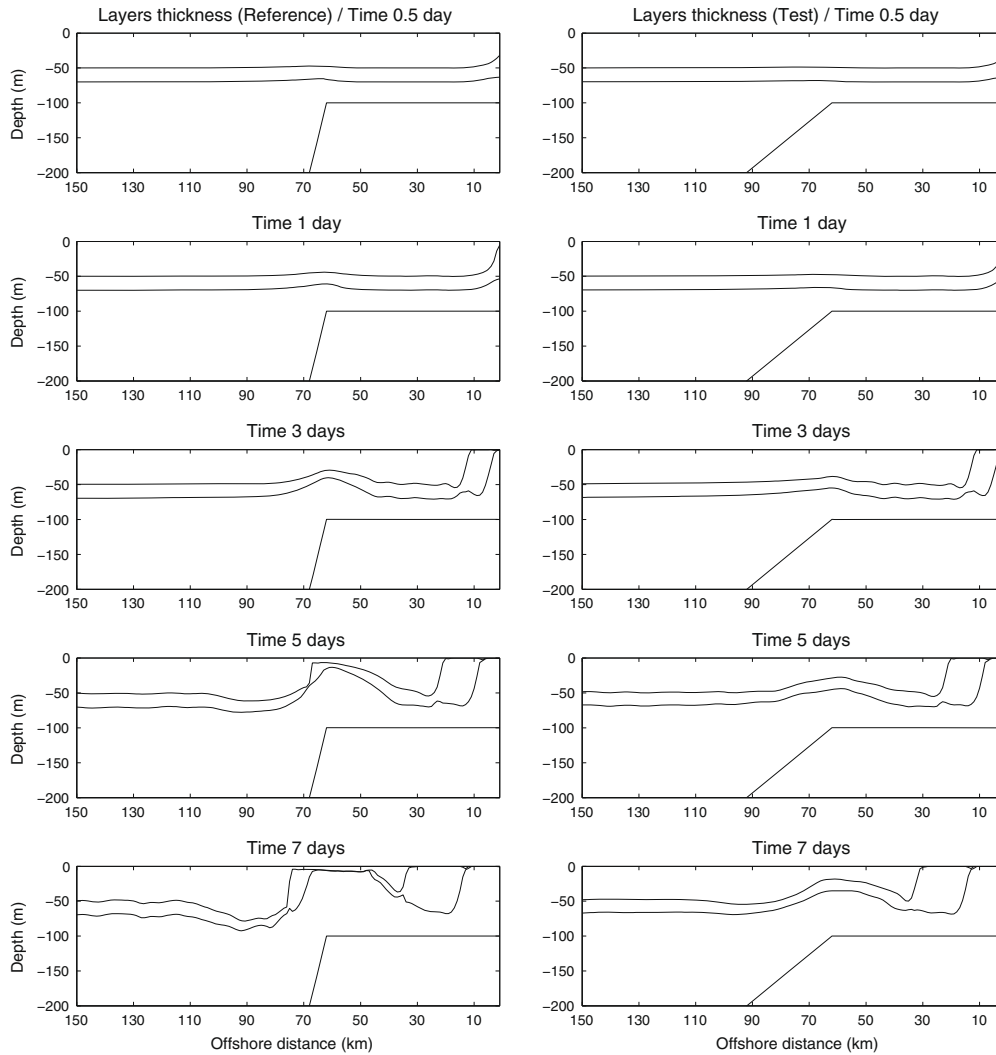
Fig. 18. Cross-section of the layer interfaces at different times for a simulation with $L_{slope} = 300$ km (right panel) versus the reference experiment (left panel).

cross-shore circulation at equilibrium does not depend on the bottom friction coefficient C_d in the present configuration. However, the duration of the transition phase and the maximum along-shore current are proportional to $C_d^{-1/2}$. In addition, also notice (see below) that the rate of modifications of PV proportional to C_d has a strong impact on the development of the secondary upwelling. The solutions strongly depend on the choice of C_d if the duration of the transition phase is lower or of the order of the time period during which the wind is applied. We have tested different values for C_d between 0 and 0.01. The case presented here ($C_d = 3.10^{-3}$) reaches the upper limit of the admitted physical values for this parameter. It thus allows to underline its effect while remaining physically relevant.

The temporal evolution of the cross-shore transport in the middle of the shelf (40 km offshore of the coast, see Fig. 16), confirms a significant increase of the offshore transport in the surface layer and onshore transport in the bottom layer, after about 1 day. Also note the stronger dissipation of the oscillations associated with inertia-gravity waves (as already found by Webster, 1985). Finally notice the abrupt damping of the upper layer cross-shore transport and its strong increase in the second layer after about 6 days, which is simply associated with the vanishing of the upper layer

when the outcropping front reaches 40 km (this happens after about 7.5 days in the reference experiment). In the area where the bottom layer reaches the surface (between the coast and the outcropping front) the bottom layer is subject to both the surface and bottom stress which equilibrates so that the cross-shore velocity is almost null in this region (see Fig. 15).

As far as the shelf break upwelling is considered, as it is associated with the generation of PVA^d by advection of high PV from the deep ocean, the effect has to be sought among the mechanisms that act on the development of this PVA^d. Two mechanisms can be identified. First, we have seen that bottom friction accelerates the cross-shore advection which should increase the generation of PVA^d and in turn the secondary upwelling. Second, bottom friction is a diabatic effect and can thus modify the lower layer PV itself. Following Morel et al. (2006), we can evaluate the impact of bottom friction on the modification of PV. As shown in Morel et al. (2006), the PVA evolution equation in each layer is:

$$\frac{dPV_k}{dt} = \frac{1}{h_k} rot(\vec{\tau}_k / h_k). \tag{16}$$

For the bottom layer, the right hand side term is associated with the bottom stress. Given the bottom friction dependency on the current,
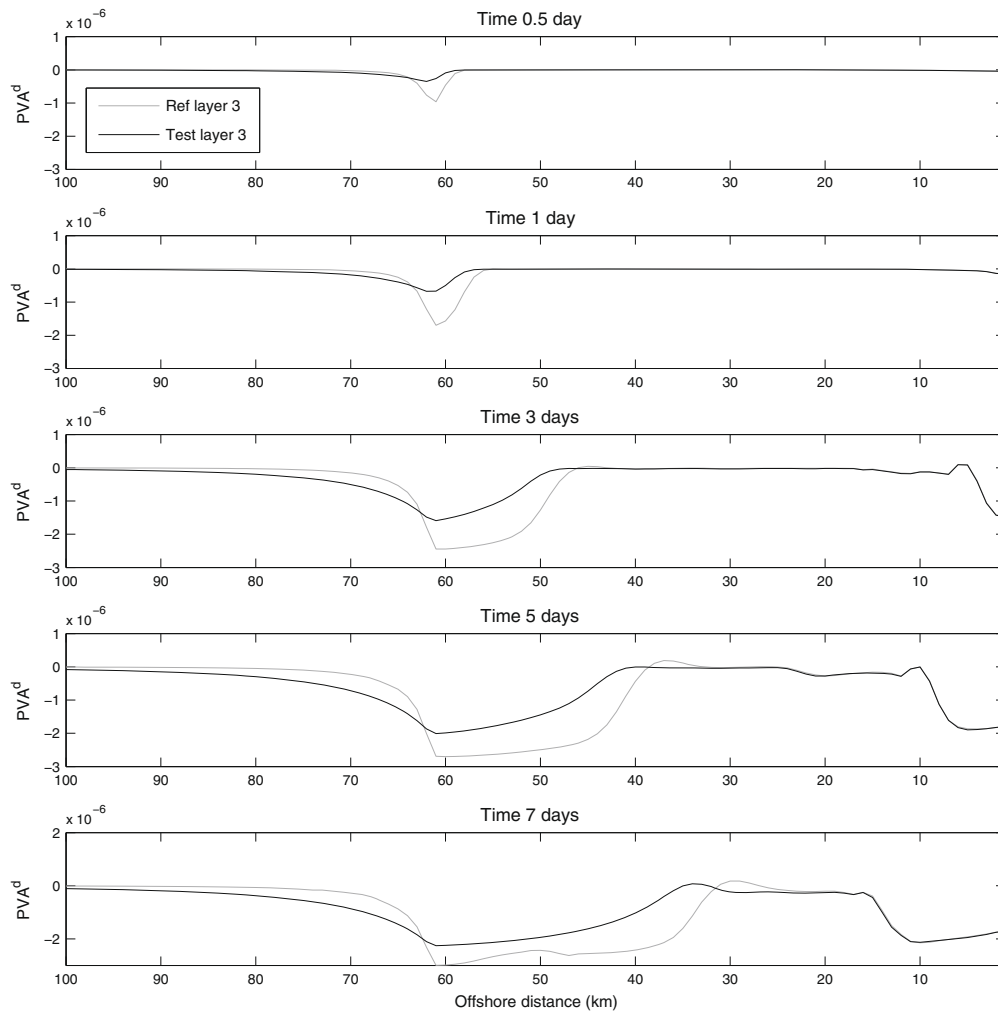
Fig. 19. Spatial evolution of PVA^d in layer 3 at different times for the run with $L_{slope} = 300$ km (black line) versus the reference experiment (grey line).

as we consider a 2D configuration and as the current is mostly along-shore and negative, the latter equation can be written:

$$\frac{dPV_k}{dt} = -\frac{1}{h_k}\partial_y(\tau_x/\rho h_k) \simeq -\frac{1}{h_k}\partial_y(-C_d\bar{u}\bar{u}/h_k) = -\frac{1}{h_k}\partial_y(C_d u^2/h_k) \tag{17}$$

In the vicinity of the shelf-break u^2 and $1/h_k$ decrease, so that the right hand side term is strongly positive. As the PVA^d created by the adiabatic circulation is negative, this proves that bottom friction acts so as to diminish the (negative) strength of the PVA^d and in turn the strength of the secondary upwelling. The two mechanisms identified above thus compete to modify the PVA^d in the vicinity of the shelf-break. Fig. 17 shows the evolution of the PVA^d in the third layer for both the reference experiment and the experiment with bottom friction. It shows that the PVA^d develops further inshore but is also dramatically reduced when bottom friction is taken into account. This is consistent with the observed reduction of the secondary upwelling and proves that the diabatic effect has a much higher influence than the acceleration of the cross-shore circulation on the evolution of the PVA^d. Finally also notice that a negative PVA^d is created near the coast and extends offshore following the outcropping front. This particular feature has been already explained above in the reference run analysis.

To summarize we have found that bottom friction:

- Balances the wind stress and allows the barotropic velocity to rapidly reach an equilibrium value over the shelf.
- Accelerates the cross-shore velocities in both the surface and bottom Ekman layers, which increase the offshore progression of the coastal upwelling front and onshore progression of the deep layers. As a result, no steady state is reached for the baroclinic circulation if no additional processes are taken into account.
- Diminishes the strength of the secondary upwelling by strongly modifying the PVA^d of the deep layers when they are advected above the shelf.

3.1.4. Impact of the margin slope

As the secondary upwelling is associated with high PV brought from the continental margin on the shelf, we can expect an influence of the steepness of the slope on its development, and we here investigate the effect of this parameter. The steepness of the slope is modified using the parameter L_{slope} (increasing L_{slope} decreases the slope steepness). Fig. 18 compares the position of the layer interfaces at different times for the reference experiment and an experiment where L_{slope} has been multiplied by 5 (so that the slope
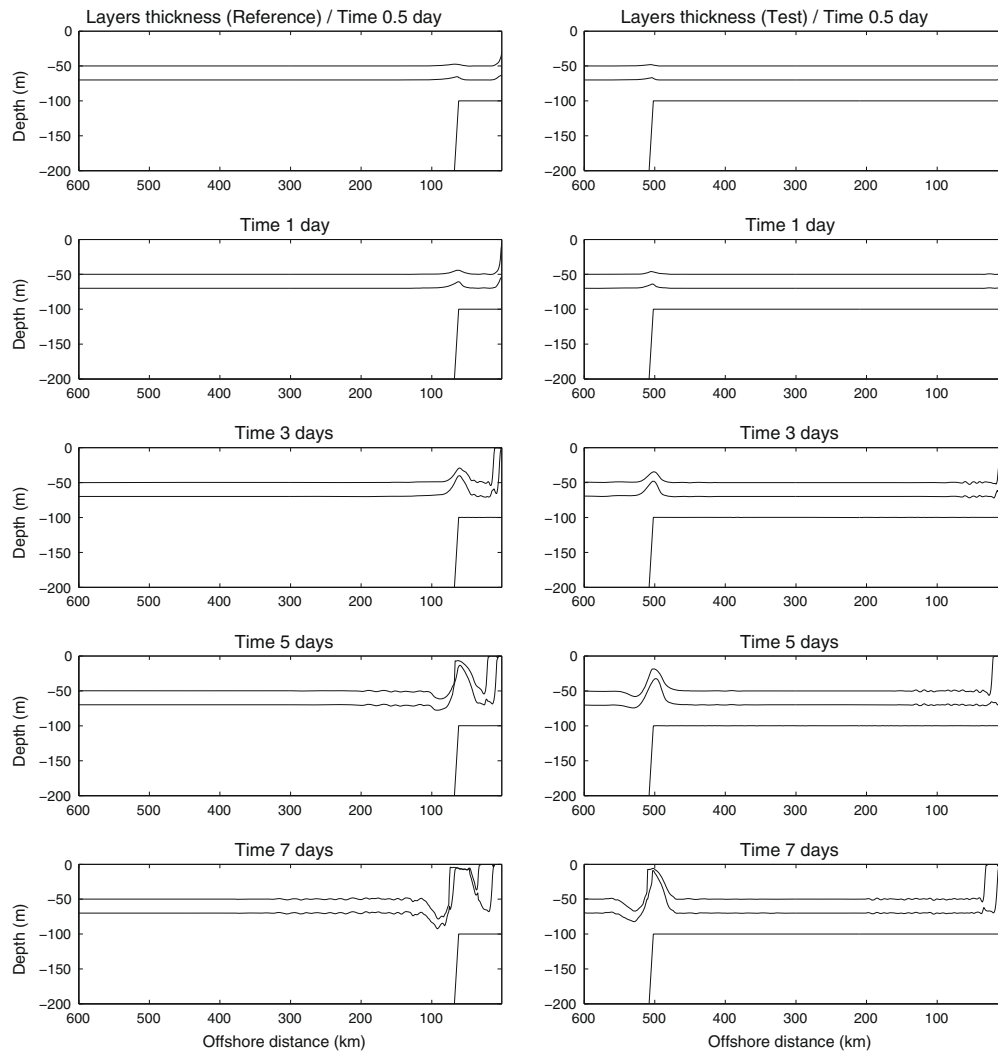
Fig. 20. Cross-section of the layer interfaces at different times for a simulation with $L_{shelf} = 500$ km (right panel) versus the reference experiment (left panel).

steepness is divided by 5). The coastal front evolutions are similar in both experiments, but, as already found in Janowitz and Pietrafesa (1980), the development of the secondary upwelling is much slower with the smoother slope: after 5 days, the first interface remains about 30 m below the reference run with the new slope. Fig. 19 compares the evolution of the lower layer PVA[d] for the reference experiment and the new slope and shows that when the slope steepness diminishes, the rate of PVA[d] generation also diminishes. The explanation is straightforward: as the wind stress is not modified, the cross-shore transport in the lower layer is the same in both the reference and new slope experiment. The cross-shore velocity is thus not strongly modified on the shelf or in the deep ocean and the advection rate is thus not modified. For a given PV value above the slope, fluid parcels are located much further from the shelf-break for the smooth slope. As a result, after a fixed time period, the fluid parcels advected on the shelf have much lower PVA[d] strength with the smooth slope.

3.1.5. Impact of the shelf width

We here investigate the influence of the shelf width and change the shelf extension L_{shelf} from 10 km to 500 km ($L_{shelf} = 60$ km for the reference experiment). When $L_{shelf} = 10$ km, the coastal and secondary upwelling almost immediately merge to obtain a unique front: it is as if there was no shelf. This is not surprising and the case of wide shelves is more interesting. Fig. 20 shows the position of the interfaces for the widest shelf we have tested ($L_{shelf} = 500$ km) and compares it to the reference experiment. The coastal upwelling is not affected by the length of the shelf whereas the secondary upwelling front seems to be slightly diminished: after 5 days of simulation, the first interface reaches 10 m below the surface in the reference run against only 20 m in the test run (10 m below the reference run). Fig. 21 represents the PVA[d] in the third layer for different times and three variable shelf widths. At any time we clearly see that the anomaly responsible for the secondary upwelling is reduced when the width of the shelf is increased. The explanation behind this is that the cross-shore circulation generated by the wind is mostly barotropic, diminishing exponentially from the coast with a characteristic length given by the external radius of deformation $R_e = \sqrt{gH}/f$ (where H is the total depth of the fluid). On the shelf we have $R_e \simeq 300$ km and in the deep ocean $R_e \simeq 1000$ km. When the bottom topography varies, it is not obvious to evaluate a "mean" radius of deformation giving the rate at which the barotropic circulation diminishes but Figs. 20 and 21 indicate that it is close to $R_e \simeq 1000$ km. The
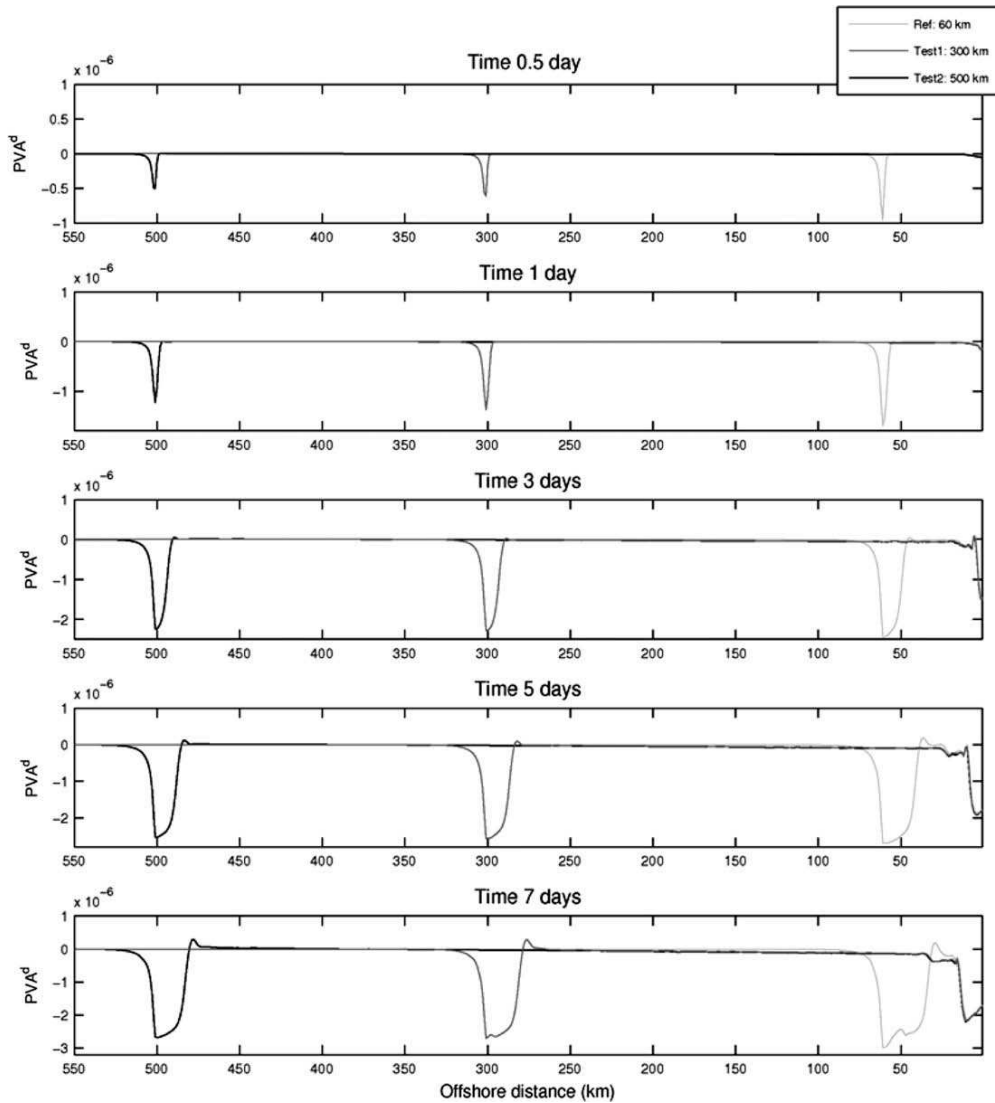
Fig. 21. Spatial evolution of PVA^d in layer 3 for simulations with $L_{shelf} = 500$ km (black) and $L_{shelf} = 300$ km (dark grey) and the reference experiment (light grey).

striking result is in fact that the damping of the secondary upwelling is low, so that even with very wide shelves, we can expect the wind to generate upwellings/downwellings along continental slopes.

3.1.6. Impact of high frequency wind forcing

Upwelling processes are driven by the wind, which suggests that the characteristics of the forcing should influence its formation and development. Millot and Crépon (1981) and Webster (1985) showed that a wind forcing on a shelf generates inertial oscillations and inertia-gravity waves generated in the transient phase of the geostrophic adjustment process. As noticed previously, internal waves are generated in the reference run whose wavelength is around 10 km. We test here a sinusoidal forcing of the form:

$$\tau_x = \tau_x^{mean} + \Delta_\tau \sin\left(2\pi \frac{time}{T}\right) \qquad (18)$$

where $\tau_x^{mean} = 0.4$ N/m^2 (same average forcing as previous runs); *time* is the model time in days; we varied $\Delta_\tau = 0.1$–0.6 N/m^2 and

the period of the sinusoid $T = 0.01$–0.5 day^{-1} (corresponding to time period of half an hour to 12 h). The different high frequency forcing runs did not show any significant differences in the interfaces positions, neither among velocities or transports in any direction as compared to the reference run and we decided not to go further in this study. Our results thus showed that when no diabatic processes are considered, the high frequency variability of the wind stress has no effect on the mean circulation.

3.2. Numerical results for a 3D configuration: impact of the along-shore shelf extension

We have seen that the secondary upwelling only exists when the shelf width is greater than the internal radius of deformation. As in realistic configuration the shelf width varies when moving along-shore, we may wonder if the secondary upwelling still exists if the region, over which the shelf width is greater than the internal radius, has a limited extension along-shore. In the previous 2D experiments this extension is indeed unlimited. A complete 3D analysis is beyond the scope of this study, but, as a first step, we
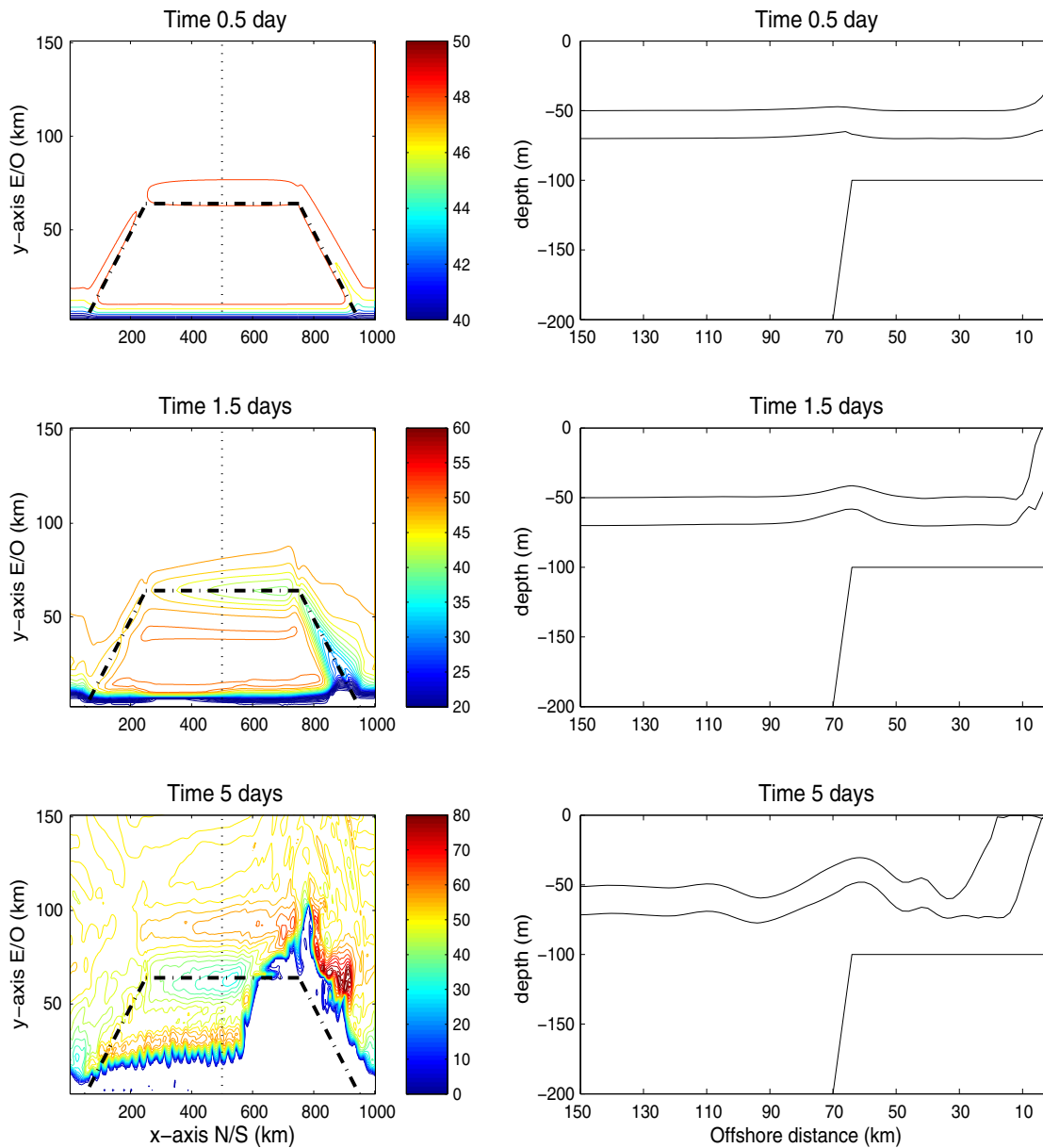
Fig. 22. On the left panels, contours of the surface layer thickness in meters (initial thickness 50 m) at different times for the 3D simulation on the left panels. The dashed-dotted line represents the shelf extension. On the right panels, corresponding cross-sections of the layer interfaces at different times at the middle of the shelf ($x = 500$ km, marked by the slight dotted line).

have extended our results to a 3D configuration. We added a new parameter for the along-shore extension of the shelf called W_{shelf}. Several tests were carried out with different W_{shelf} and basin dimensions revealing some complex 3D effects that will not be studied here. In Fig. 22 we present results for a specific configuration where only the upwelling side is kept, we have chosen $L_{shelf} + L_{slope} + L_{basin} = 300$ km in the cross-shore (y) direction and 1000 km in the along-shore (x) direction. Periodic boundary conditions are imposed along-shore. For this 3D configuration, the old and new parameters are given in Table 1, while the stratification stayed unchanged.

The formation of the secondary upwelling along the shelf break is clearly visible for this simulation. As in the 2D case, its intensity (upward displacement of isopycnal interfaces) is growing with time (see Fig. 22 left panels). A cross-section at the middle of the shelf confirms the formation of the secondary shelf break upwelling (see Fig. 22 right panels) and shows that after 5 days of simulation, layer three reaches 30 m below the sea surface which is less than the reference run (see Fig. 8) but still significant. Moreover, the secondary upwelling amplitude is much higher on the upwind side of the shelf along the shelf break. This is in fact not surprising as in this area the margin is no longer parallel to the main (along-shore) flow. Cross-margin advection is then drastically increased and so is PVA[d]. This effect is different from the one studied in Pringle (2002) who concentrated on the steady state upwelling generated by a wind, a bottom friction for a homogeneous flow with a
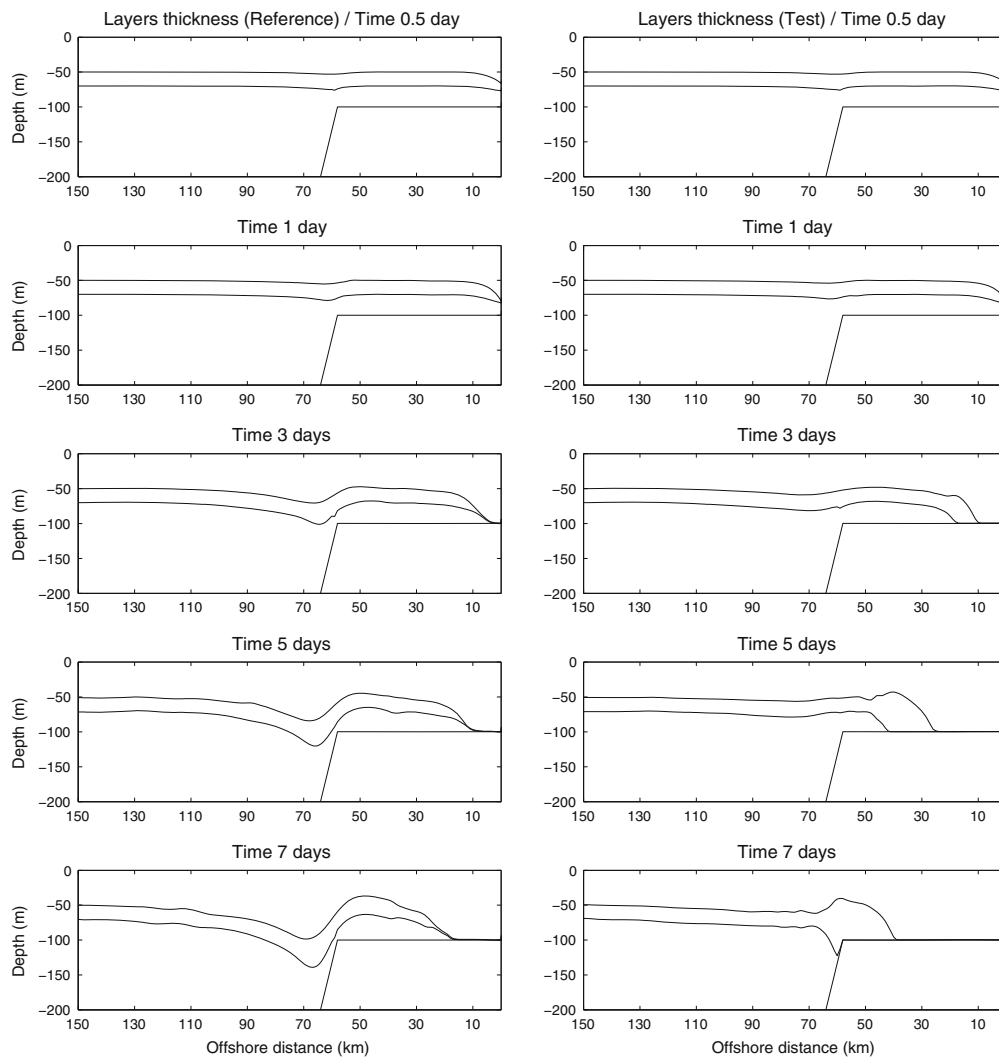
Fig. 23. Cross-section of the layer interfaces at different times for the test with $C_d = 3.10^{-3}$ (right panel) compared to the reference experiment (left panel) for the case of a downwelling current.

topography similar to the present one. In his case, the upwelling depends on the bottom friction.

Finally, also note the formation of instabilities along the coastal upwelling front and the complex structures in the area where the shelf widens ($x = 700$–900 km): the coastal upwelling extends much further offshore in this region forming a filament extending seaward after 5 days. This seems to show that a bottom topography transverse to the shore is able to generate and trap upwelling filaments, an interesting process linked with PVA[d] anomaly creation, that will not be further studied here but encouraged additional work.

3.3. Extension to downwelling conditions from the 2D three layers configuration

By using the 2D three layers configuration, the previous results are extended to downwelling favorable conditions. In the left panel of Fig. 23 we have represented the interface evolution for the 2D reference experiment but on the downwelling side (same wind stress strength but opposite direction). In this case, the primary coastal downwelling is also accompanied by a secondary one, this time developing over the shelf break.

The mechanisms for the formation of this secondary front are similar to the upwelling side: the development of the coastal downwelling generates an offshore barotropic current which extends over hundreds of kilometers covering the entire shelf; high PV columns are then advected offshore over the continental margin where the PV is initially much lower; this generates positive PVA[d] (see grey lines in Fig. 24) and a circulation in geostrophic equilibrium for which isopycnic levels are deflected downward (left panel of Fig. 23). The amplitude of the downwelling is similar to the upwelling one: comparison between the interface displacements, velocity field and PVA[d] intensity of the downwelling and upwelling show very close results (compare left panels of Fig. 23 and grey line of the lower panel in Fig. 24 respectively with Figs. 8 and 11). After 3 days of simulation, the vertical displacement of the first interface (upward for upwelling and downward for downwelling current) is 21 m in both cases, while the PVA[d] reaches
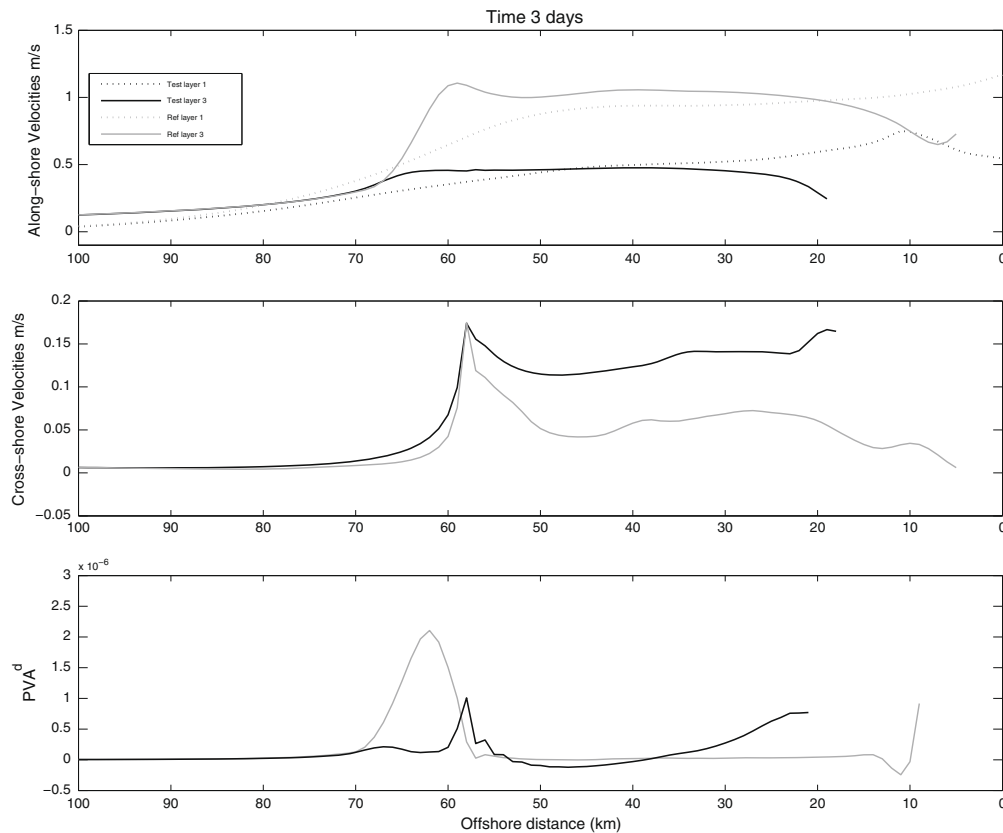
Fig. 24. Diagnostics for the downwelling current. Upper panel: spatial structure of the along-shore velocities after 3 days of simulation with $C_d = 3.10^{-3}$ (black lines) versus reference experiment (grey lines) for the surface layer (dotted lines) and the bottom layer (plain lines). Middle panel: spatial structure of layer 3 cross-shore velocities after 3 days of simulation with $C_d = 3.10^{-3}$ (black line) compared to the reference experiment (grey line). Lower panel: spatial structure of PVA^d in layer 3 after 3 days of simulation with $C_d = 3.10^{-3}$ (black line) versus the reference experiment (grey line).

2.45×10^{-6} for the upwelling against 2.1×10^6 for the downwelling case.

Similar effects are also found for the influence of bottom friction: the adiabatic cross-shore circulation is strengthened whereas the secondary downwelling is damped because bottom friction drastically diminishes PVA^d (see Figs. 23 and 24).

4. Application to the MOUTON *in situ* data: 2D numerical results for a realistic configuration

In the following, we use a more realistic configuration to simulate the *in situ* structure described in the second section. To do so, we increased the number of layers and fitted the configuration to the observations coming from the MOUTON campaign. The initial stratification comes from the deeper CTD cast made at 41°N/ 10.5°W reaching 2000 m below the surface. As shown in Fig. 25, we chose 15 layers with a density interval of $\Delta\rho/\rho = 0.14$. Following the previous results, the forcing used is an average of the wind measured on the research vessel. The bathymetry is taken from the depth measurements performed onboard along the transect. To restrain our attention to the processes studied in the previous simplified 3 layers configuration, the other parameters used in this simulation are the same as for the 2D reference run. In particular, we did not include additional processes such as vertical mixing, which probably also play an important role. The simulations last 7 days, the observations have been performed between day 5 and 6.

Figs. 26 and 27 present current and density sections for a case without bottom friction ($C_d = 0$). Figs. 28 and 29 are the same but for $C_d = 3.10^{-3}$.

Some patterns in both cross and along-shore velocities are qualitatively reproduced (compare Figs. 5–26 and 28). For the cross-shore circulation, the surface offshore flow which extends over the first 40 m, its intensification in the vicinity of the shelf break and the onshore sub-surface current, are represented. As far as the along-shore velocities are concerned, the main southward flow with its intensification in the mixed layer is represented, but its amplitude is strongly overestimated for the simulation without bottom friction. Even though the discrepancy is much reduced, the amplitude is still overestimated for the simulation with $C_d = 3.10^{-3}$. The general pattern is however more realistic in this case: as in the observations the maximum velocities are located between the coast and the shelf break and diminish in the bottom Ekman layer, whereas they are close to the coast when $C_d = 0$ and do not vary vertically below the thermocline.

Note also that in these realistic simulations internal waves are more numerous and present higher amplitude in comparison with the 3 layer ones. During their offshore propagation, these internal waves have noticeable influence on the interface positions and also on the velocity field. Their associated small scale variations are more visible when bottom friction is low or neglected (see Fig. 26).

The density sections presented in Figs. 27 and 29 exhibit similar general patterns and compare well with the observations (Fig. 3): the lighter layer outcrops quite far offshore and the deep layers have been advected onshore up to the coast. The secondary

upwelling is much reduced in the simulation with $C_d = 3.10^{-3}$ and only visible very close to the shelf break. It is much clearer in the case without bottom friction for which lighter waters still extend over most of the shelf as it is the case in the observations. Even the internal wave signature on the density field seems in better agreement with the observations without bottom friction, the case with $C_d = 3.10^{-3}$ leading to too smooth and parallel interface positions. To conclude, day 6 of the run without friction shows a good agreement with the observed one for the density section: dense waters are upwelled up to the coastal area, the isopycnal dome of dense waters (secondary upwelling front) isolates a water mass of intermediate density in the middle of the shelf, the lighter front and strongly stratified waters extend far offshore (9.4°W).

A noticeable difference with the observations for both numerical simulations is that the modeled interfaces stay flat offshore 9.4 °W in both realistic runs whereas the observed isopycnal levels exhibit a large scale slope extending from 10°W to the coast. This pattern was also found for other E/W sections performed during the campaign. This can be the remains of previous upwellings (the upwelling season generally begins in early July in this area). The *in situ* profile indeed also depends on past oceanic and atmospheric conditions. Before the campaign, Quikscat data reveal 10 days of moderate northerly winds, immediately followed by a short inversion to southern winds (between August, 13th and 14th). The numerical results only simulate the intense upwelling phase and started from an ocean at rest, neglecting the initial state associated with these pre-existing events. Alternatively, this difference can be due to variations of the wind stress over the area, leading to Ekman pumping and large scale variations in the vertical position of the pycnocline. This process was studied in Capet et al. (2004) and they showed that nearshore winds variations have to be taken in account for realistic modeling, which was not the case in the present study.

5. Discussion and conclusion

5.1. Summary and discussion of the results

Motivated by *in situ* observations of a shelf break upwelling phenomenon, we studied the effect of the wind on the shelf circulation for a shelf extending farther offshore than the internal deformation radius. We focused on the adiabatic mechanism based on PV dynamics proposed by O'Brien and Hurlburt (1972) which we detailed. We used 2D configurations with 3 layers to illustrate and evaluate its ability to explain secondary shelf break upwellings and the sensitivity of this process to several parameters. We have shown that:

- For a reference run without bottom friction, the secondary shelf-break upwelling is very intense and rapidly develops. It is mostly explained by adiabatic advection of low PV and creation of negative PVA[d] on the shelf. This secondary upwelling keeps increasing until it is absorbed by the coastal upwelling when it moves offshore.
- Bottom friction has three effects on this picture. First it rapidly equilibrates the wind stress and drastically limits the along-shore barotropic velocity. Second, it enhances the cross-shore Ekman circulation and, keeping the upwelling from reaching a steady state, it accelerates both the offshore propagation of the coastal upwelling front and the advection of deep waters onto the shelf. Finally, it strongly modifies the PV in the lower layer so as to diminish the PVA[d] strength, overcoming the effect of advection enhancement and leading to a reduction of the secondary upwelling.
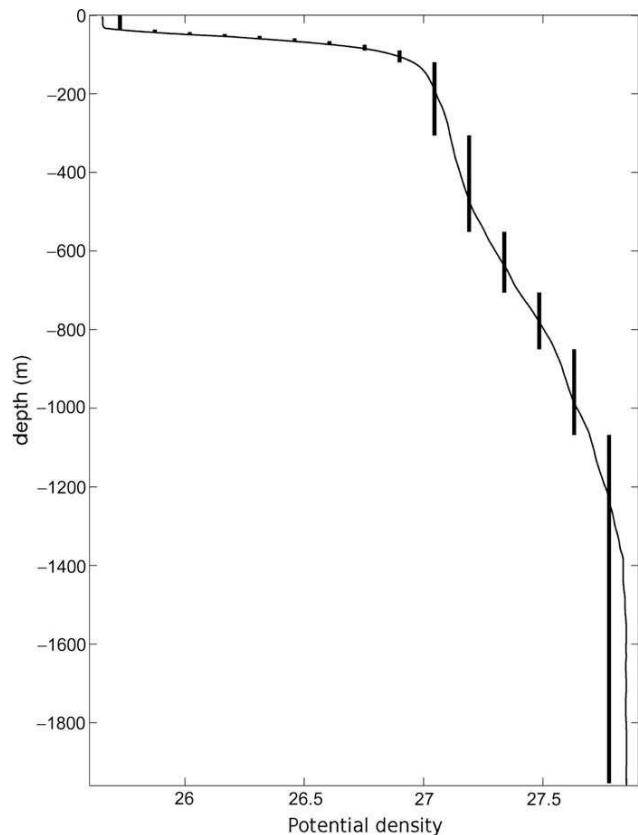
Fig. 25. *In situ* and numerical potential density profiles: the black line represents the smoothed density profile from the CTD cast at 41°N/10.5°W. The black segments represent a discretization in 15 layers of this profile (for each layer, the density is given on the *x*-axis and the layer thickness by the length of the associated black solid segment).

- The secondary upwelling increases with increasing margin slopes.
- The secondary upwelling is not sensitive to high frequency temporal variations of the wind stress and very weakly to the shelf width.
- The secondary upwelling is still present in 3D configuration for which the along-shore extension of the shelf is limited but comparable to the barotropic deformation radius.
- In the 3D case, the mechanism is enhanced over some areas where the shelf is no longer parallel to the coast as the cross-margin advection and PVA[d] creation rate are drastically increased.
- The 3D test also revealed that bottom topography plays an important role for the development of mesoscale feature from upwelling systems. In particular it could be a major factor for the generation of long filaments extending offshore. Since the formation of these filaments were up to now supposed to be associated to capes or coastal variations (see Roed and Shi, 1999), this original observation was an opportunity for us to initiate further work.
- The previous results can be easily transposed to downwelling currents.
- More realistic 2D results show similarities with the observations but also some discrepancies in particular for the along-shore velocity amplitude.
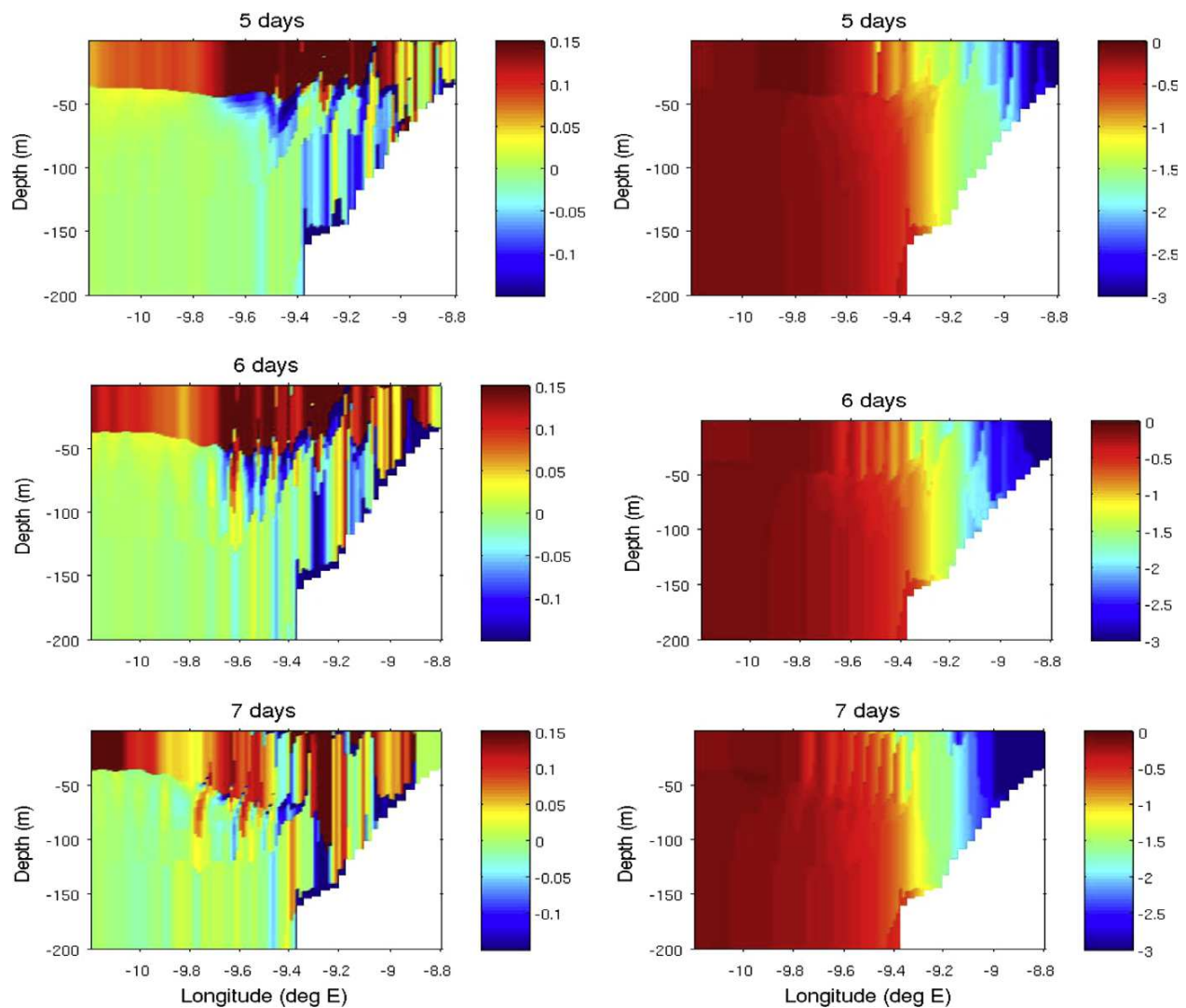
Fig. 26. Current profiles (m/s) at different times for the realistic run without bottom friction $C_d = 0$. Cross-shore currents are represented on the left panel, and along-shore currents on the right panel.

It is thus difficult to demonstrate that the observed shelf break upwelling is associated to the PVA[d] generation process presented previously. Indeed, the *in situ* profile is a snapshot of an area where many 3D physical processes and their interactions result in complex circulation and characteristics. There exists significant discrepancies in the density or velocity fields showing that our 2D simulations probably neglect important effects such as 3D or diabatic processes, associated with mixing or atmospheric buoyancy fluxes.

To reach better agreements, it seems important to identify and take into account the processes that lead to the equilibration of the upwelling circulation pattern, in particular to keep the upwelling front from continually moving offshore and to reach realistic velocity values. We have shown that bottom friction is not enough: realistic C_d still leads to too strong barotropic currents while increasing the unsteady nature of the upwelling. Vertical mixing can smooth the vertical velocity profile and decrease the maximum values, but it will not modify the net transport in the surface and bottom Ekman layers as long as they do not overlap. Its impact on the equil-

ibration of the upwelling circulation is thus probably moderate. As a result, we believe 3D effects have to be taken into account. For instance, barotropic/baroclinic instabilities radiate energy off the main front limiting its offshore propagation (see Marchesiello et al., 2003). Alternatively, as mentioned above, an along-shore pressure gradient can also act so as to equilibrate the circulation. Using satellite observations Colas et al. (2008) have indeed shown that a longshore pressure gradient indeed plays a significant role in the equilibration of the upwelling current. Recent realistic 3D upwelling simulations with high resolution regional models embedded within coarser resolution ones yield quite realistic results (Marchesiello et al., 2003; Penven et al., 2006; Gruber et al., 2006). Thus, taking into account the fact that upwelling systems are included in and fed by more general large scale gyres, is probably important to explain the observed equilibrated state. Notice that, at first order, a longshore pressure gradient would not modify the cross-shelf circulation and would only limit the strength of the barotropic along-shore current. In nature, the effect of bottom friction is thus probably more limited than in the experiments we
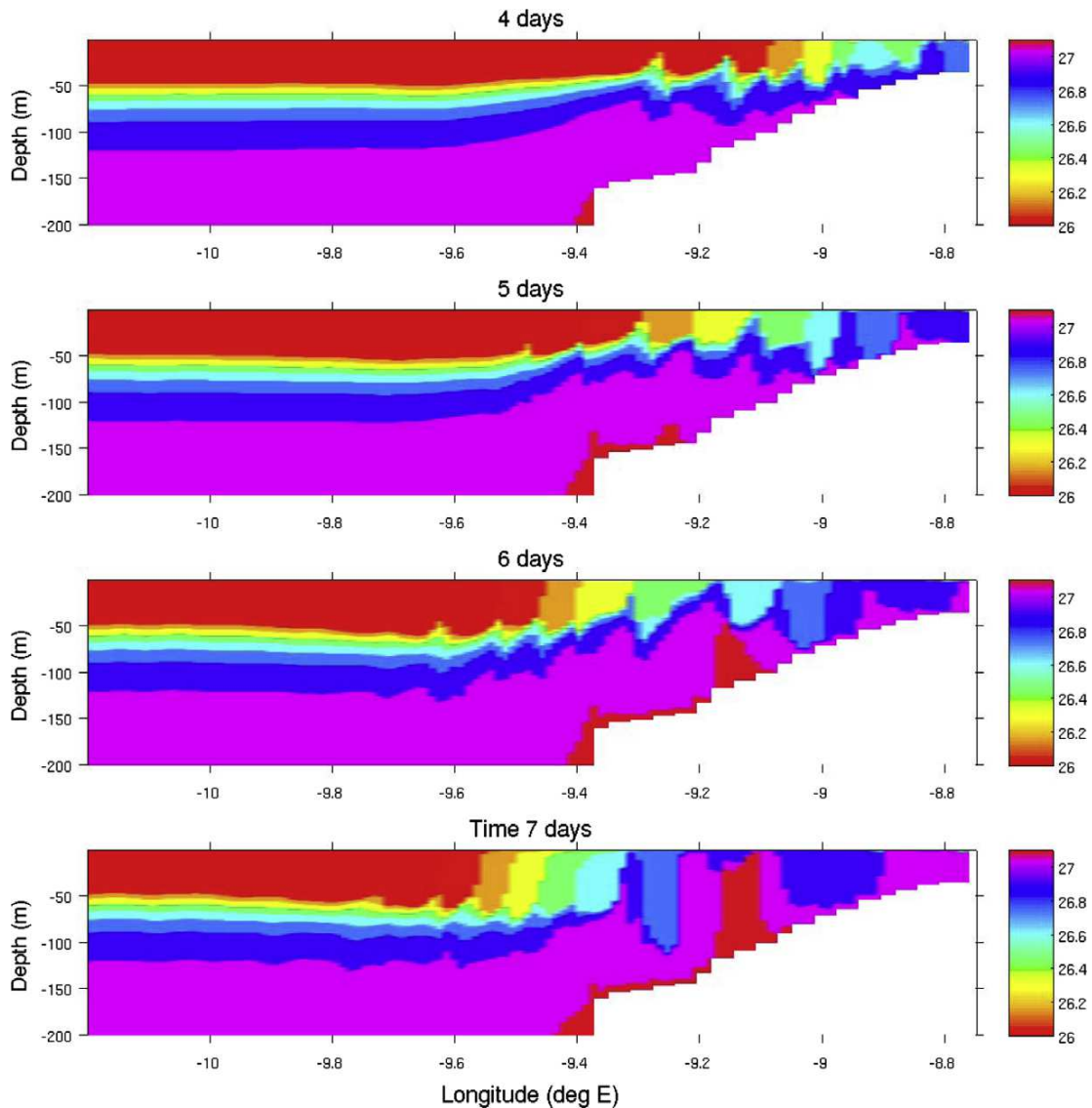
Fig. 27. Density profiles at different times for the realistic run without bottom friction $C_d = 0$. Note that the color bar is identical to the one in Fig. 3. (For interpretation of the references to color in this figure legend, the reader is referred to the web version of this paper.)

have presented. This could explain the fact that, in our realistic experiments, the frictionless solution best fits most observations at sea, despite its unreasonable longshore velocity magnitude.

We have however shown that, when a coastal upwelling initiates, adiabatic advection of dense water from the margin onto the shelf acts as a low PV source and generates negative PVA^d which can in turn develop upwellings and biological activity near the shelf break. This mechanism certainly also plays a role in nature.

5.2. Extension to wind driven circulation on a shelf and perspectives

As a concluding remark, we would like to mention that the processes studied here are also of interest for the general wind driven circulation on an extended shelf.

First, even in regions where no strong permanent winds exist a weak mean wind is able to generate a cross-shore circulation that, when its effect is accumulated over long time periods, can generate

significant PVA^d and currents in the shelf break area. Seasonal modification of the mean winds could then explain seasonal reversal of margin currents even when the margin is far from the coast. Seasonal current reversals have been observed along the bay of Biscay margin for instance (see Colas, 2003; Friocourt et al., 2007).

Second, strong transient winds can also generate significant PVA^d and currents on the shelf and in the shelf break area. The geostrophic circulation established by the processes studied here will indeed be maintained even when the wind has stopped and will slowly dissipate in regions where the water depth is larger than the Ekman layer, if no strong opposite winds follow. As a result, the upward displacement of the thermocline could last long enough to generate phytoplankton blooms along the shelf break, a feature that has also been observed along the bay of Biscay margin.

Then, let us mention again that for wide shelves, a few kilometers away from the coast, the circulation associated with the wind boils down to surface and bottom Ekman circulation, superimposed on a mainly along-shore barotropic circulation. This
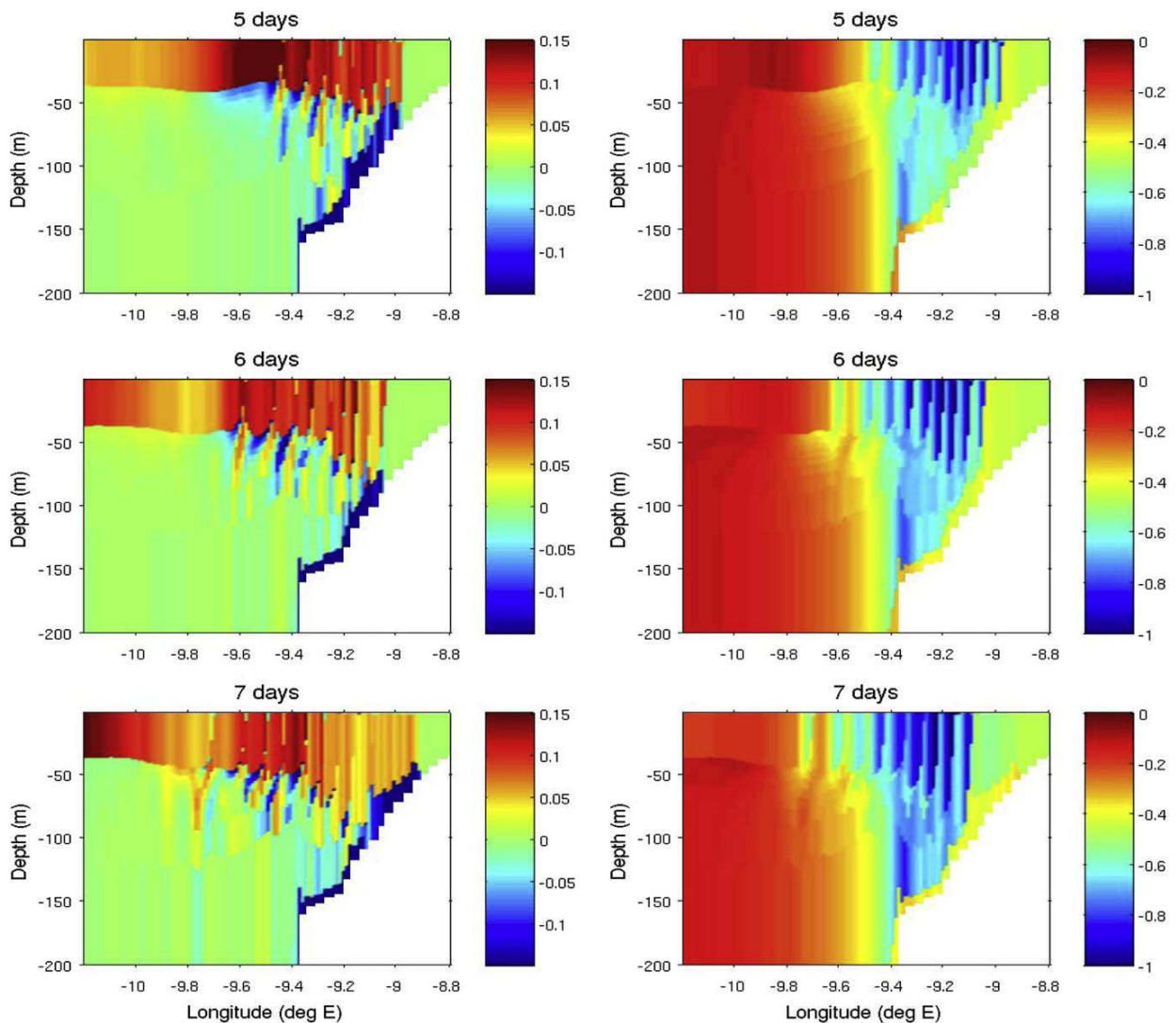
Fig. 28. Current profiles (m/s) at different times for the realistic run with bottom friction $C_d = 3.10^{-3}$. Cross-shore currents are represented on the left panel, and along-shore currents on the right panel.

barotropic circulation can be much stronger than the Ekman drift (up to 10 cm/s or so if the wind blows long enough) and extends over the whole shelf, even for wide shelves. As a result the circulation associated with a wind is not confined within a narrow region near the coast, where the (baroclinic) upwelling develops. Noticeable currents are found up to the shelf break and can in turn have an effect on the deep/coastal ocean exchange. We have however only studied simple configurations and the extension of our results to spatially varying winds, complex shorelines and bottom topography is however not straightforward.

We also noticed from onboard observations and from the analysis of a 2 months time series of satellite SST images (not shown) that strong air-sea coupling occurs above the Iberian peninsula upwelling region. Indeed in Fig. 2 clouds are present almost exclusively above the warm water (>20 °C) offshore the coastal upwelling, a permanent feature observed onboard throughout the first leg of the campaign where strong northerly upwelling favourable wind occurred. In fact, in such a situation, surface latent heat fluxes are enhanced over warm areas offshore and this forms high convective clouds. In this case, the sky was often clear above the upwelling area, where cold temperatures inhibited atmospheric convection. On the other hand, when the northern wind stops, a typical sea breeze summer regime takes place. In the morning, warm and humid air masses are moved onshore above cold newly upwelled waters. This led to condensation and the formation of low clouds and fog. This is a sign of strong ocean/atmosphere coupling which may be of interest to understand the local climate conditions.

Non-linear effects (such as non-linear internal waves, the interactions between outcropping layer interfaces and the surface wind stress, the development of instabilities, etc.) are known to be of importance in upwelling areas. Recently Liang and Robinson (2009) studied the influence of some of these effects on the Californian upwelling system. Their methodology could be applied to study the influence of such nonlinear processes on the development of the secondary upwelling, whose signatures are indeed clearly visible in our 2D and 3D simulations.

Finally, the processes detailed here are important for multidisciplinary modeling studies since they could enhance the primary production occurring in the euphotic zone, and also directly

154
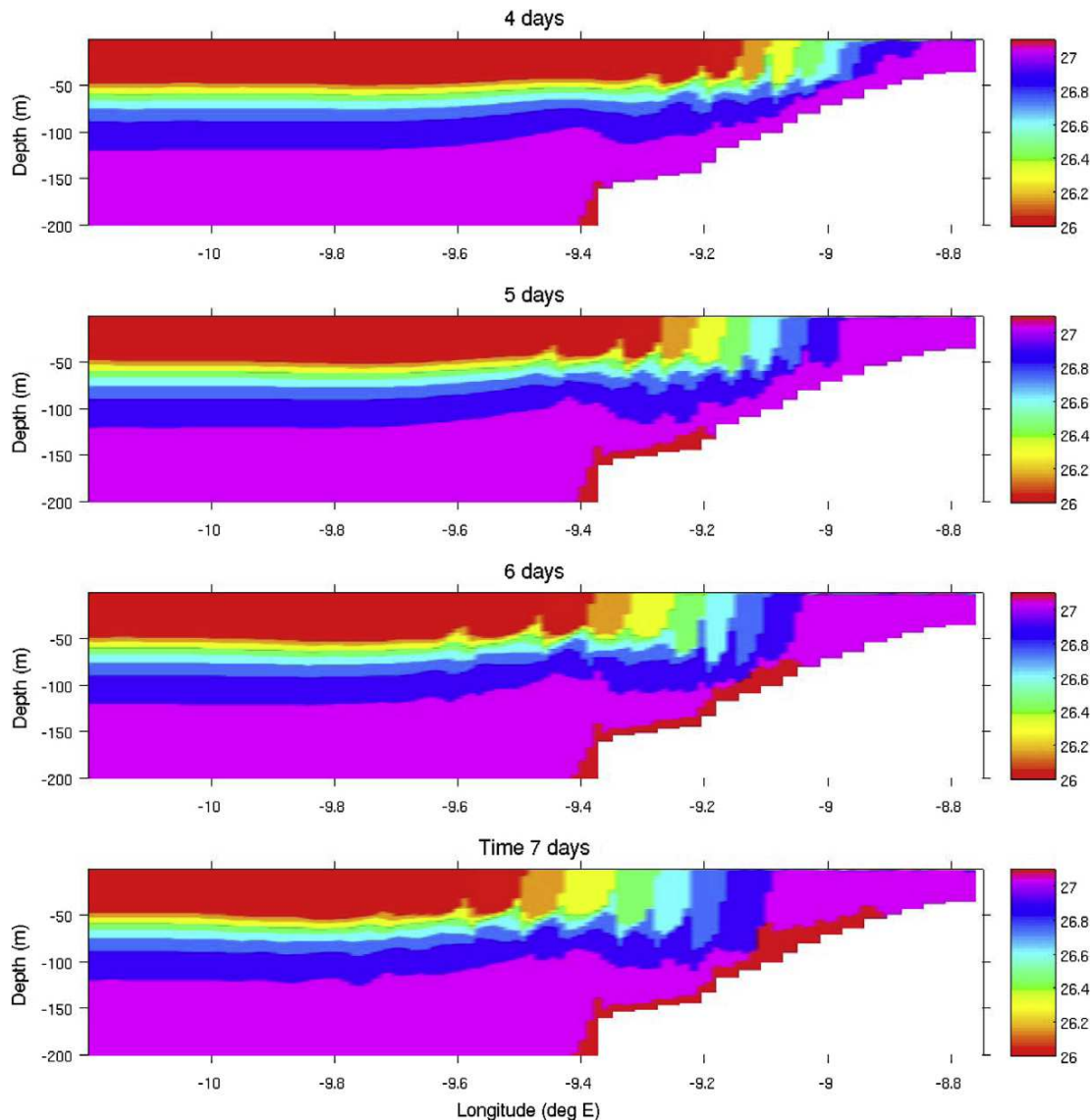
Fig. 29. Density profiles at different times for the realistic run with bottom friction $C_d = 3.10^{-3}$. Note that the color bar is identical to the one in Fig. 3. (For interpretation of the references to color in this figure legend, the reader is referred to the web version of this paper.)

influence waters exchange between the productive shelf and the open oligotrophic ocean.

References

Bang, N.D., Andrews, W.R.H., 1974. Direct current measurements of a shelf-edge frontal jet in the southern Benguela system. Journal of Marine Research 32, 407–421.

Barth, J.A., Hebert, D., Dale, A.C., Ullman, D.S., 2004. Direct observations of along-isopycnal upwelling and diapycnal velocity at a shelfbreak front. Journal of Physical Oceanography 34, 543–565.

Bleck, R., Boudra, D., 1986. Wind driven spin-up in eddy-resolving ocean models formulated in isopycnic and isobaric coordinates. Journal of Geophysical Research 91, 7611–7621.

Bleck, R., Smith, L., 1990. A wind driven isopycnic coordinate model of the North and equatorial Atlantic Ocean: model development and supporting experiments. Journal of Geophysical Research 95, 3273–3285.

Bleck, R., Rooth, C., Hu, D., Smith, L., 1992. Salinity driven thermocline transients in a wind and thermocline forced isopycnic coordinate model of the North Atlantic. Journal of Physical Oceanography 22, 1486–1505.

Capet, X., Marchesiello, P., McWilliams, J.C., 2004. Upwelling response to coastal wind profiles. Geophysical Research Letters 13, L13–311. doi:10.1029/2004GL020123.

Chapman, D.C., Lentz, S.J., 2005. Acceleration of a stratified current over a sloping bottom, driven by an alongshelf pressure gradient. Journal of Physical Oceanography 35, 1305–1317.

Chhak, K., Di Lorenzo, E., 2007. Decadal variation in the Californian current upwelling cells. Geophysical Research Letters 34, L12604.

Colas, F., 2003. Circulation et dispersion Lagrangiennes en Atlantique Nord-Est. PhD Thesis, Université de Bretagne Occidentale, UBO, Brest, France.

Colas, F., Capet, X., McWilliams, J.C., Shchepetkin, A., 2008. 1997-1998 El Nino off Peru: a numerical study. Progress in Oceanography 79, 138–155.

Dickson, R.R., Gurburtt, P.A., Pillai, V.N., 1980. Satellite evidence of enhanced upwelling along the European continental shelf. Journal of Physical Oceanography 10, 813–828.

Estrade, P., Marchesiello, P., Colin De Verdière, A., Roy, C., 2009. Cross-shelf structure of coastal upwelling: a two-dimensional extension of Ekman's theory and a mechanism for inner shelf upwelling shut down. Journal of Marine Research 66, 589–616.

Friocourt, Y., Levier, B., Speich, S., Blanke, B., Drijfhout, S., 2007. A regional numerical ocean model of the circulation in the Bay of Biscay. Journal of Geophysical Research 112, C09008. doi:10.1029/2006JC003935.

Garvine, R.W., 1971. A simple model of coastal upwelling dynamics. Journal of Physical Oceanography 1, 169–179.

Garvine, R.W., 1973. The effects of bathymetry on the coastal upwelling of homogeneous water. Journal of Physical Oceanography 3, 47–56.

Gibbs, M.T., Marchesiello, P., Middleton, J.H., 2000. Observations and simulations of a transient shelfbreak front over the narrow shelf at Sydney, southeastern Australia. Continental Shelf Research 20, 763–784.

Gill, A.E., Clarke, A.J., 1974. Wind-induced upwelling, coastal currents and sea level changes. Deep-Sea Research 21, 325–345.

Gruber, N., Frenzel, H., Doney, S.C., Marchesiello, P., McWilliams, J.C., Moisan, J.R., Oram, J., Plattner, G.K., Stolzenbach, K.D., 2006. Eddy-resolving simulation of plankton ecosystem dynamics in the California current system. Deep-Sea Research I 53. doi:10.1016/j.dsr.2006.06.005.

Hart, T.J., Currie, R.I., 1960. The Benguela current. Discovery Reports 31, 127–297.

Herbette, S., Morel, Y.G., Arhan, M., 2003. Erosion of a surface vortex by a seamount. Journal of Physical Oceanography 33 (8), 1664–1679.

Herbette, S., Morel, Y.G., Arhan, M., 2005. Erosion of a surface vortex by a seamount on the beta plane. Journal of Physical Oceanography 35 (11), 2012–2030.

Hill, R.B., Johnson, J.A., 1974. A theory of upwelling over the shelf break. Journal of Physical Oceanography 4, 19–26.

Hoskins, B., McIntyre, M., Robertson, W., 1985. On the use and significance of isentropic potential vorticity maps. Quarterly Journal of the Royal Meteorological Society 111, 877–946.

Hsueh, Y., O'Brien, J.J., 1971. Steady coastal upwelling induced by an along-shore current. Journal of Physical Oceanography 1, 180–186.

Hsueh, Y., Ou, H.W., 1975. On the possibilities of coastal, mid-shelf, and shelf break upwelling. Journal of Physical Oceanography 5, 670–682.

Huyer, A., 1976. A comparison of upwelling events in two locations: Oregon and North-West Africa. Journal of Marine Research 34, 531–546.

Janowitz, G.S., Pietrafesa, L.J., 1980. A model and observations of time-dependent upwelling over the mid-shelf and slope. Journal of Physical Oceanography 10, 1574–1583.

Johnson, J.A., Killworth, P.D., 1975. A bottom current along the shelf break. Journal of Physical Oceanography 5, 185–188.

Lathuilière C., 2008. Echanges côte-large et propriétés biogéochimiques dans les régions d'upwelling de bord Est. PhD Thesis, Université de Paris VI, UPMC, Paris, France.

Lentz, S.J., 2001. The influence of stratification on the wind-driven cross-shelf circulation over the North Carolina shelf. Journal of Physical Oceanography 31, 2749–2760.

Lentz, S.J., Chapman, D.C., 2004. The importance of nonlinear cross-shelf momentum flux during wind-driven coastal upwelling. Journal of Physical Oceanography 34, 2444–2457.

Liang, X.S., Robinson, A.R., 2009. Multiscale processes and nonlinear dynamics of the circulation and upwelling events off monterey bay. Journal of Physical Oceanography 39, 290–313.

Lill, C.C., 1979. Upwelling over the shelf break. Journal of Physical Oceanography 9, 1044–1047.

Marchesiello, P., Gibbs, M.T., Middleton, J.H., 2000. Simulations of coastal upwelling on the Sydney continental shelf. Marine and Freshwater Research 51, 577–588.

Marchesiello, P., McWilliams, J.C., Shchepetkin, A., 2003. Equilibrium structure and dynamics of the California current system. Journal of Physical Oceanography 33, 753–783.

McIntyre, M., Norton, W., 1990. Dissipative wave-mean interactions and the transport of vorticity or potential vorticity. Journal of Fluid Mechanics 212, 403–435.

McWilliams, J.C., Gent, P.R., 1980. Intermediate models of planetary circulations in the atmosphere and the ocean. Journal of Atmospherical Sciences 37, 1657–1678.

Millot, C., Crépon, M., 1981. Inertial oscillations on the continental shelf of the gulf of lions - observations and theory. Journal of Physical Oceanography 11, 639–657.

Morel, Y.G., Darr, D.S., Talandier, C., 2006. Possible sources driving the potential vorticity structure and long-wave instability of coastal upwelling and downwelling currents. Journal of Physical Oceanography 36, 875–896.

O'Brien, J.J., Hurlburt, H.E., 1972. A numerical model of coastal upwelling. Journal of Physical Oceanography 2, 14–26.

Pauly, D., Christensen, V., 1995. Primary production required to sustain global fisheries. Nature 374, 255–257.

Peliz, A., Dubert, J., Santos, A., Oliveira, P.B., Le Cann, B., 2005. Winter upper ocean circulation in the Western Iberian Basin – Fronts, Eddies and Poleward Flows: an overview. Deep Sea Research I 52, 621–646.

Penven, P., Debreu, L., Marchesiello, P., McWilliams, J.C., 2006. Evaluation and application of the ROMS 1-way embedding procedure to the central california upwelling system. Ocean Modelling 12, 157–187.

Pringle, J.M., 2002. Enhancement of wind-driven upwelling and downwelling by alongshore bathymetric variability. Journal of Physical Oceanography 32, 3101–3112.

Relvas, P., Barton, E.D., Dubert, J., Oliveira, P.B., Peliz, A., da Silva, J.C.B., Santos, A.M.P., 2007. Physical oceanography of the western Iberia ecosystem: latest views and challenges. Progress in Oceanography 74, 149–173.

Roed, L.P., Shi, X.B., 1999. A numerical study of the dynamics and energetics of cool filaments, jets and eddies off the Iberian Peninsula. Journal of Geophysical Research 104(C12) (29), 817–841.

Smith, R.L., 1968. Upwelling. Oceanographic and Marine Biology Annual Review, vol. 6. Allen and Unwin, London. pp. 11–46.

Thomas, L.N., 2005. Destruction of potential vorticity by winds. Journal of Physical Oceanography 35, 2457–2466.

Walsh, J.J., 1991. Importance of continental margins in the marine biogeochemical cycling of carbon and nitrogen. Nature 350, 53–55.

Webster, I., 1985. Frictional continental shelf waves and the circulation response of a continental shelf to wind forcing. Journal of Physical Oceanography 15, 855–864.

Winther, N.G., Morel, Y.G., Evensen, G., 2007. Efficiency of high order numerical schemes for momentum advection. Journal of Marine Systems 67 (1–2), 31–46.

4.2 Résumé de l'article 2 (français).

Cet article est basé sur une observation particulière provenant de la campagne MOUTON 2007. La section est-ouest à 41°N en densité et en température a révélé, outre l'arrivée d'eau dense et froide à la côte suivant le processus classique d'upwelling, la présence d'eau plus dense et froide en surface, au niveau de la rupture de pente entre le plateau continental et le talus. Il a été proposé de nommer ce phénomène front secondaire d'upwelling de marge continentale, ou secondary shelf-break upwelling. La signature de ce front secondaire, ainsi que celui à proximité de la côte, marquée par des concentrations de chlorophylle a supérieures aux eaux environnantes, atteste de la pérennité d'une telle structure. Les courants observés sont aussi analysés afin d'estimer la circulation associée à cette structure hydrodynamique. Il apparaît à l'issue de ces observations que ce front ne provient pas d'effets en trois dimensions. Il est aussi particulièrement lié aux vents qui forcent l'upwelling et à la topographie de la marge continentale (plateau étendu et cassure abrupte au niveau du talus). Ainsi, afin de mieux comprendre la formation de cette structure, un modèle numérique hydrodynamique académique est utilisé en deux dimensions. L'upwelling est modélisé par trois couches, reproduisant respectivement la couche de mélange, la thermocline et l'océan profond, au sein d'un bassin orienté est-ouest. A chaque extrême, une marge continentale classique est modélisée par un talus avec une forte pente, puis un plateau plat et étendu. Un vent plein nord constant est appliqué afin de forcer la circulation de l'upwelling. Une simulation de référence est réalisée et analysée en terme de Vorticité Potentielle (VP), grandeur physique conservative (dans le cas simple d'une circulation adiabatique) qui dépend de la stratification et du champ de courant présent. L'expérience de référence a bien simulé le développement de ce front secondaire d'upwelling au dessus de la marge continentale, ainsi que les courants associés. Elle nous permet d'avancer l'explication suivante : l'advection vers la côte par les courants barotropes d'upwelling d'une colonne d'eau initialement au milieu du bassin (VP faible) vers le plateau (VP forte) entraîne la création d'une anomalie de VP négative au niveau de la rupture de pente du plateau, qui par réaction (principe d'équilibre géostrophique et d'inversion de la VP) provoque un bombement des isopycnes sus-jacents, aboutissant ainsi à ce front localisé en surface au dessus de la jonction plateau – talus.

Plusieurs simulations ont ensuite permis d'étudier la sensibilité de ce phénomène à plusieurs paramètres du modèle. Parmi ceux-ci, nous pouvons retenir l'effet du frottement sur le fond qui freine la circulation méridienne barotropique mais intensifie les courants zonaux baroclines. Dans le même temps,

cet effet de frottement diabatique diminue drastiquement la VP des couches profondes, résultant ainsi de façon globale en une diminution de l'intensité du front secondaire. Ce processus étant lié à la topographie, il a aussi été montré une corrélation positive entre l'intensité du front secondaire et l'importance de la rupture de pente entre le talus et le plateau. Une simulation en trois dimensions basée sur le même modèle a permis de montrer que l'extension du plateau le long de la côte ne modifie pas la formation de front secondaire. Cette expérience a aussi mis en évidence une formation de filaments mésoéchelle qui seront étudiés par la suite. Enfin, ces résultats ont été également étendus à la situation inverse, où un vent opposé provoquerait un phénomène de downwelling côtier et secondaire au niveau de la marge continentale.

Finalement, une configuration semi-réaliste 2D a été construite en considérant la stratification observée pendant MOUTON 2007, la géométrie de la marge continentale de la section considérée, ainsi que le forçage de vent mesuré pendant la campagne. Malgré une surestimation des vitesses, les sorties simulées montrent un bon accord avec les profils observés, ce qui renforce nos hypothèses et confirme le rôle d'un tel processus dans l'océan réel. Ce travail basé sur des observations a permis de comprendre, à l'aide d'un modèle simple, un phénomène physique qui semble avoir lieu dans toutes les zones d'upwelling. Cette étude a aussi permis de faire progresser nos connaissances sur la circulation complexe qui a lieu sur n'importe quelle marge continentale possédant un plateau étendu et forcé par le vent.

4.3 Article 3: Influence of a bottom topography on an upwelling current: generation of long trapped filaments, Meunier, Rossi *et al.*, in revision, Ocean Modelling.

Reference : Meunier T., Rossi, V., Y. Morel and X., Carton. Influence of a bottom topography on an upwelling current: generation of long trapped filaments, in revision, Ocean Modelling.

Influence of a bottom topography on an upwelling current : generation of long trapped filaments

T. Meunier[*,a], V. Rossi[b], Y. Morel[c], X. Carton[a]

[a]*Laboratoire de Physique de l'Océan, Université de Bretagne Occidentale, 46 avenue Legorgeu, 29200 Brest, France*
[b]*Laboratoire d'Études en Géophysique et Océanographie Spatiale, CNRS, Observatoire Midi-Pyrénées, 14 avenue Edouard Belin, 31400 Toulouse, France*
[c]*Service hydrographique et océanographique de la marine, (SHOM), 42 av Gaspard Coriolis, 31057 Toulouse, France*

Abstract

In this paper, the authors investigate the influence of bottom topography on the formation and trapping of long upwelling filaments. They use a 2-layer shallow water model on the f-plane. A wind forced along-shore current, associated with coastal upwelling along a vertical wall, encounters a promontory of finite width and length, perpendicular to the coast.

In the lower layer, topographic eddies form, which are shown to drive the formation of a filament on the front. Indeed, as the upwelling current and front develop along the coast, the along shore flow crosses the promontory, re-arranging the potential vorticity structure and generating intense vortical structures : water columns with high potential vorticity initially localized upon the promontory are advected into the deep ocean, forming cyclonic eddies, while water columns from the deep ocean with low potential vorticity climb on the topography forming a trapped anti-cyclonic circulation. These topographic eddies interact with the upper layer upwelling front and form an elongated, trapped and narrow filament.

Sensitivity tests are then carried out and it is shown that :

- baroclinic instability of the front does not play a major role on the formation of long trapped filaments;

- increasing the duration of the wind forcing increases the upwelling current and limits the offshore growth of the filament;

- modifying the promontory characteristics (width, length, height and slopes) has strong impact on the filament evolution, sometimes leading to a multipolarisation of the potential vorticity anomaly structure which results in much more complicated patterns in the upper layer (numerous shorter and less coherent filaments). This shows that only specific promontory shapes can lead to the formation of well defined filaments;

- adding bottom friction introduces a slight generation of potential vorticity in the bottom layer over the promontory, but does not significantly alter significantly the formation of the filament along the outcropped front in the present configuration;

- modifying the stratification characteristics, in particular the density jump between the layers, has only a weak influence on the dynamics of topographic eddies and on filament formation;

1

- the influence of capes is also modest in our simulations, showing that topography plays the major role in the formation of long and trapped upwelling filaments.

Key words: Eastern boundary, Mesoscale dynamics, Upwelling/Downwelling, Topographic flows, Upwelling filaments, Potential vorticity

1. Introduction

Long trapped filaments of cold water are ubiquitous features along upwelling fronts. They sometimes extend hundreds of kilometers offshore and have been shown to play a major role in the offshore transport of recently upwelled coastal water ([*Kostianoy and Zatsepin,* 1996]) and in feeding the oligotrophic offshore waters with nutrients and organic materials ([*Alvarez-Salgado et al.,* 2007] and more particularly over the Iberian peninsula upwelling [*Alvarez-Salgado et al.,* 2001]). They are thus important physical features for eastern boundary upwelling ecosystems.

Figure 1 shows a set of satellite images of the Iberian peninsula on the 09/05/2009 (column 1), 09/05/2005 (column 2).The images on the first row are the Sea Surface Temperature (SST) and on the second row the Chlorophyll-a concentration (Sea Surface Color). Long, trapped and recurrent filaments are observed on SST and chlrophyll maps off Cape Finisterre (43°N), São Vicente (37°N) and the Estremadura promontory (between 38.5 and 39.5°N). However on all maps, another tongue of cold upwelled water pointing offshore also clearly arises from the upwelling front just South of the Estremadura promontory.

In-situ and remotely sensed data have provided some desriptions of upwelling filaments (see for instance [*Brink,* 1983]; [*Flament et al.,* 1985]; [*Washburn and Armi,* 1988]; [*Strub et al.,* 1991]; [*Navarro-Pérrez and Barton,* 1998]; [*Barton,* 2001]), and many numerical and theoretical studies have focused on their dynamics. [*Haynes et al.,* 1993] used satellite data of the West-Iberia upwelling system to show that large filaments were often closely related with capes, but noted the repeated occurrence of two large filaments at two different locations corresponding with a straight coastline. They assumed that those filaments were related with unstable meanders of the jet, but their stationarity remained unexplained.

One of the first process studies on upwelling filament dynamics was performed by [*Haidvogel et al.,* 1991]. Their model was able to reproduce cold filaments along the upwelling front. They concluded from a set of sensitivity cases, including removal of the coastline geometry and the bottom topography, that the presence of large capes along the coast, was necessary to the generation of upwelling filaments. [*Marchesiello et al.,* 2003] studied the equilibrium structure of the California current system and conducted different sensitivity tests. They showed that mesoscale variability was intrinsic to the current and not due to the variability of the forcing. On the contrary of [*Haidvogel et al.,* 1991], they showed that even in the case of a straight coastline and a flat bottom, upwelling filaments and eddies still occurred, but with no preferential location, confirming the conclusions of [*Roed and Shi,* 1999], that instability induced filaments
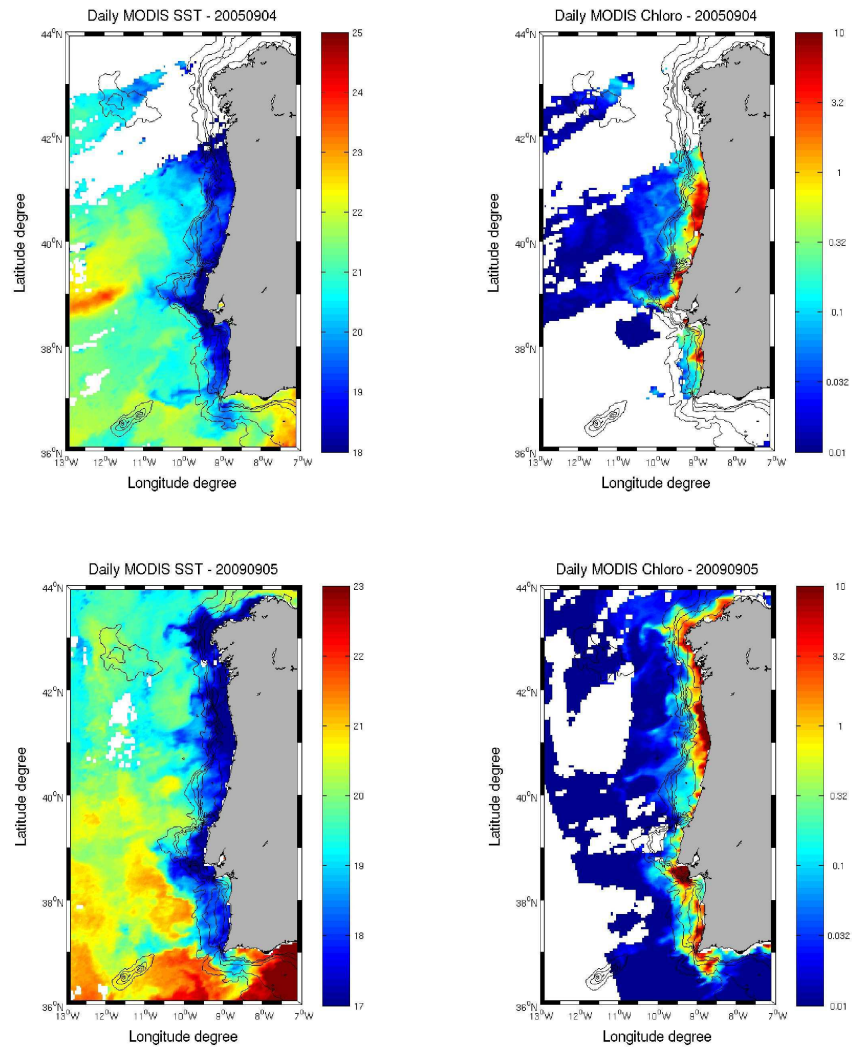
Figure 1: Sea Surface Temperature (first row) and Chlorophyl distribution (second row) situation off the West Iberian coast during three distinct upwelling episodes (09/05/2009 on the first column, 09/05/2005 on the second column and 09/04/2001 on the third column).

3

and eddies could happen in the absence of coastal irregularities. Removing only the topography, [*Marchesiello et al.,* 2003] concluded that a standing wave could be generated at the cape, in agreement with results from a numerical study of [*Batteen,* 1997] who noted anchorement of filaments at coastline irregularities, while [*Roed and Shi,* 1999] only noted a weak anchoring of the meander. [*Ikeda,* 1981] and [*Ikeda,* 1989] showed using two-layer quasigeostrophic models, that unstable meanders of a buoyancy driven coastal jet would move downstream by a combined effect of propagation and advection, so that some physical process had to be involved in the anchoring of filaments at the capes as observed by [*Marchesiello et al.,* 2003].

Recently [*Batteen et al.,* 2007] conducted a process oriented study of the Northern Canary Current System (NCCS) and revisited the upwelling instability and filamentation problem in this region. They modified the bottom topography, boundary conditions and wind forcing and found that :

- the flat bottom experiment shows many of the typically observed features of the NCCS;

- adding the bottom topography shows that topography has an important role in intensifying and trapping the equatorward current near the coast, in weakening the subsurface poleward current, and in intensifying eddies off the capes of Iberia;

- the flat bottom experiment produces anticyclonic meanders near cabo Roca and Cabo São Vincente, but not off Figueira da Foz;

- the beta effect plays an important role on the formation of the subsurface meander off cabo Roca.

To summarize, four main source have been identified to explain the generation of filaments along upwelling fronts :

- the frontal or baroclinic instability of the front;

- the effect of capes;

- the planetary beta effect;

- bottom topography.

Upwelling filaments have also been classified into different types (see [*Strub et al.,* 1991]), but one important distinction is wether they are trapped or not. Because the trapping of filaments always happens at the same locations, we believe that the observed long trapped upwelling filaments are associated with topographic features and we chose to focus on this aspect in the present study. Again, different studies ([*Ikeda,* 1989, *Capet and Carton,* 2004]) concluded that topographic irregularities were destabilization source for upwelling fronts, but the effect of bottom topography on the development of trapped filaments has not received a lot of attention, in particular the details of the mechanism is not clear and its sensitivity to different parameters remains to be studied.

[*Stern and Chassignet,* 2000] showed, using both a $1_{1/2}$ and a three-layer isopycnic model, that intrinsic instability was not sufficient to generate detrainment of fluid and eddy-separation from the jet. They concluded that, to generate a blocking wave and detrain water, there was a need for a downstream variation in jet transport, and noted that this variation could happen in the case of alongshore varying topography, but did not investigate further on this point.

4

[*Viera and Grimshaw,* 1994] studied the evolution of a potential vorticity front over an iso-
lated topography, using a $1_{1/2}$ layers quasi geostrophic model, and showed, that a linearly
stable jet associated with a potential vorticity front could produce large and pinched off me-
anders when interacting with bottom topography. [*Herbette et al.,* 2003] have shown that a
seamount could interact with a surface intensified eddy and generate filaments (or even split
the eddy). Finally, while studying the generation of secondary upwelling fronts along continen-
tal slopes [*Rossi et al.,* 2009] found, in one of the experiment with a promontory (see fig. 22 in
[*Rossi et al.,* 2009]), that a bottom topography could trap upwelled waters and even observed the
formation of a trapped filament extending offshore.

Therefore, in the present paper, we study the evolution of an upwelling front in the presence
of an along shore varying topography, in the form of cross-shore coastal promontories. We focus
on the formation and trapping of long filaments extending offshore and we base our approach on
the ppotential vorticity analysis used in the papers quoted in the previous paragraph. The outline
of the paper is the following :

- in section 2 (Model and tools), we describe the numerical model and recall some basic prin-
  ciples relating potential vorticity (thereafter *PV*) and potential vorticity anomalies (there-
  after *PVA*) to the dynamics;

- in section 3 (Reference experiment), we present a first simulation that illustrates the devel-
  opment of a long filament. In particular we describe how the generation of *PVA* by the
  displacement of water columns above the promontory can generate a permanent filament
  trapped downstream of the promontory;

- in section 4 (Sensitivity study), we study the sensitivity of this mechanism to different
  regimes and parameters : stable and unstable cases, wind forcing duration, promontory
  height, width and length, stratification, bottom friction;

- in section 5 (Conclusion), we sum up and discuss our results.

2. Model and tools

2.1. Equations and model

The model used is an adiabatic version of MICOM (Miami Isopycnic Coordinate Ocean
Model) ([*Bleck and Boudra,* 1986]; [*Bleck and Smith,* 1990];[*Bleck et al.,* 1992]) modified to in-
clude a fourth order scheme in the non-linear advection terms and a biharmonic diffusion
operator to improve the PV dynamics ([*Winther et al.,* 2007, *Morel and McWilliams,* 2001,
Herbette et al., 2003]). This model solves the shallow water equations which, for the two-layer
configurations considered here, can be expressed as :

$$\partial_t \mathbf{u_k} + (\mathbf{u}_k.\nabla)\mathbf{u}_k + f_0 \mathbf{k} \times \mathbf{u}_k = -\nabla \mathcal{M}_k + F_k + T_k^w, \qquad (1)$$
$$\partial_t h_k + \nabla.(\mathbf{u}_k h_k) = 0, \qquad (2)$$

where k is the layer number (here, $k = 1$ for the top layer and $k = 2$ for the bottom one),
$\mathbf{u}_k = (u_k, v_k)$ is the horizontal velocity, $f_0 = 10^{-4} s^{-1}$ is the Coriolis parameter (considered
constant here), h_k is the thickness of the isopycnal layer k, T_k^w represents the wind forcing, and

5
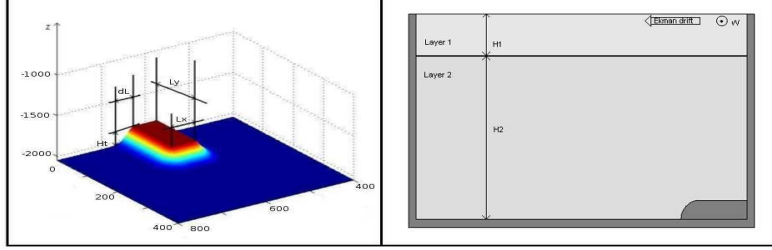
Figure 2: a : Details of the promontory : It is centered on $x = 300km$. Lx and Ly are respectively the length and width of its flat top, Ht its height, and dL is the typical length of its Gaussian sloping sides. b : Model configuration at rest : a shallow surface layer of depth H_1 and density ρ_1 lies over a bottom layer of depth H_2 and density ρ_2. The numerical domain is a periodic zonal channel with vertical walls and a flat bottom.

F_k contains the frictional and viscosity terms (horizontal diffusion is associated with a biharmonic operator with a viscosity that depends on the velocity modulus and deformation tensor, see [*Winther et al.,* 2007]). Finally, $\mathcal{M}_k$ is the Montgomery potential (pressure along an isopycnal surface), which can be written :

$$\mathcal{M}_k \quad = \quad \sum_{i=1}^{2} g\, h_i + \sum_{i=1}^{k-1} \frac{\rho_i - \rho_k}{\rho_k} g\, h_i, \tag{3}$$

where ρ_i is the density of the isopycnic layer i and g is the gravity acceleration.

2.2. Configuration and parameters

The configuration is a periodic zonal channel on an f-plane, with vertical side walls on the northern and southern boundaries. The bottom is flat except near the southern boundaries in the middle of the domain where there exists a promontory. As shown in figure 2, the promontory is composed of a flat plateau of variable height H_t, length Ly and width Lx, rounded at its offshore edge, and surrounded by a Gaussian slope of a variable extension dL (figure 2). To represent a mid latitude summer thermocline, the surface layer depth at rest $H_1 = 50$ m and the bottom layer depth away from the promontory is $H_2^\infty = 2000$ m for most experiments. The upper layer density is fixed to $\rho_1 = 1000\ kg/m^3$, the water column stratification is defined by the reduced gravity $g' = g(\rho_2 - \rho_1)/\rho_1$. Unless stated otherwise (when testing the sensitivity to the stratification characteristics) $g' \simeq 0.01$.

$R_d = \sqrt{g' H_1 H_2/(H_1 + H_2)}/f_0$ is the Rossby radius of deformation, and $R_d \simeq 7\ km$ ($H_1 = 50$ m, $H_2^\infty = 2000$ m, $f_0 = 10^{-4}\ s^{-1}$ and $g' = 1^o/_{oo}$) for most of the experiments presented below.

The parameters corresponding to the various simulations presented below can be found in table 6.

6

164

2.3. Potential vorticity and potential vorticity anomaly

For the shallow water model used here, the potential vorticity for each isopycnic layer is defined as :

$$PV_k = \frac{f_0 + \zeta_k}{h_k}, \tag{4}$$

where $\zeta_k = \nabla \times \mathbf{u}_k = \partial_x v_k - \partial_y u_k$ is relative vorticity in layer k, and h_k is the layer thickness. In the absence of diabatic process, PV is conserved for each fluid particle. PV is also related to the velocity field that can then be calculated by inverting the PV field under the assumption of (cyclo-)geostrophic equilibrium. PV conservation and invertibility are key properties which helped understand and interpret many geophysical fluid processes ([*McWilliams and Gent,* 1980], [*McIntyre and Norton,* 1990], [*Hoskins et al.,* 1985], see also [*Morel et al.,* 2006, *Rossi et al.,* 2009] for applications to upwelling dynamics).

PV is finite at rest and in order to invert it and to calculate the velocity, we use the potential vorticity anomaly (*PVA*) which is defined in each layer k as the difference between the local *PV* and a reference *PV* for a state at rest (no current and flat isopycnals) (see [*Herbette et al.,* 2003, *Herbette et al.,* 2005, *Rossi et al.,* 2009]) :

$$PVA_k = H_k (PV_k - PV_k^{ref}) = H_k \left(\frac{f_0 + \zeta_k}{h_k} - \frac{f_0}{H_k}\right) = \frac{H_k}{h_k}\left(\zeta_k - f_0 \frac{\delta h_k}{H_k}\right), \tag{5}$$

where $H_k(x, y)$ is the layer thickness at rest, and $\delta h_k = h_k - H_k$. Notice that we have also multiplied the *PV* difference by the layer thickness at rest so that *PVA* is proportional to the vorticity, which makes it easier to analyze. *PVA* contains the dynamical signal associated with the PV field and the geostrophic velocity field can be inferred from the *PVA* field. Notice that, as H_k is a function of position, contrary to *PV*, *PVA* is not conserved for each particle in the presence of a variable bottom topography. It is however directly related to the circulation. The presence of a *PVA* pole in a layer k is indeed associated with a circulation extending to all layers but intensified in layer k ([*Hoskins et al.,* 1985, *Rossi et al.,* 2009]) : a positive *PVA* pole being associated with a cyclonic circulation, a negative one with an anticyclonic circulation.

As shown in [*Verron and Le Provost,* 1985, *Herbette et al.,* 2003], when a current develops above a seamount, two opposite sign eddies appear : an anticyclone trapped above the topographic feature associated with the displacement of low PV water columns from the deep ocean upon the seamount and a cyclone associated with the advection of high PV water columns off the topography. Figure 3) describes this process which is adiabatic and relies on the advection of PV and the formation of PVA poles. It also shows that between the two opposite sign eddies a strong jetlike current is formed.

2.4. Previous results and general upwelling characteristics

[*Morel et al.,* 2006] found an exact analytical solution for the geostrophic circulation of a 2-D configuration with a flat bottom and a constant wind forcing T^w. In practice, $T^w = \tau^w/(\rho_1 h_1)$ (where τ^w is the surface wind stress) is not constant but, with the approximation $T^w = \tau^w/(\rho_1 H_1)$, the following formulas provide a good evaluation for the position of the outcropping front and velocity field as a function of the wind stress intensity and the duration of the wind forcing. It is then possible to obtain a stationary basic state current with the desired characteristics by limiting the forcing to a chosen period for a given wind stress intensity.

7
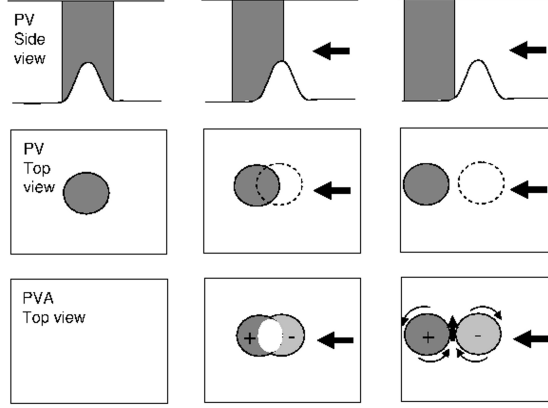
Figure 3: Schematic view of the development of a topographic dipole when a current develops above a seamount. The initial PV structure (top panels for the side view and middle panels for the top view) is associated with high PV above the seamount and lower PV in the deeper ocean; the fluid is initially at rest and the PVA (lower panels) is null. The current exchanges the position of low and high PV water columns which forms positive and negative PVA. An anticyclonic circulation develops above the topography whereas a cyclonic circulation is associated with the high PV water columns detaching from the seamount. The current is intensified between the opposite sign eddies.

The distance of the outcropping front from the coast is :

$$Y(t) \quad = \quad min\{0, -\frac{T^w}{f(1 + \delta)}(t - t_0)\} \tag{6}$$

$$t_0 \quad = \quad \frac{fR_d(1 + \delta)}{T^w} \tag{7}$$

and the alongshore velocity field in both layers is given by :

if $y < Y(t)$

$$U_1 \quad = \quad U_c \exp\frac{y}{R_d} + U_b(t), \tag{8}$$

$$U_2 \quad = \quad -\delta U_c(t) \exp\frac{y}{R_d} + U_b(t), \tag{9}$$

if $y \geqslant Y(t)$

$$U_1 \qquad undefined, \tag{10}$$

$$U_2 \quad = \quad -f\delta(y - Y(t)) - \delta U_c(t) \exp\frac{Y}{R_d} + U_b(t). \tag{11}$$

where $\delta = H_1/H_2$, t_0 is the time necessary for the lower layer to outcrop at the coast ($y = 0$). $U_b(t)$ and $U_c(t)$ are the temporal evolution of the barotropic and baroclinic components respectively and can be written as :

if $t < t_0$

$$U_b \quad = \quad \frac{\delta T^w}{1 + \delta}t \tag{12}$$

$$U_c \quad = \quad \frac{T^w}{1 + \delta}t \tag{13}$$

8

166

176   if $t \geqslant t_0$

$$U_b \quad = \quad \frac{\delta T^w}{1 + \delta} t \qquad\qquad (14)$$

$$U_c \quad = \quad f R_d \exp \frac{-Y(t)}{R_d} \qquad\qquad (15)$$

177   Notice that the maximum current is reached at the outcropping front (for $t \geqslant t_0$) and is given
178   by:

$$
\begin{aligned}
U_1^{max} \quad &= \quad f R_d + \frac{\delta T^w}{1 + \delta} t \\
&= \quad (1 + \delta) f R_d + \delta f |Y(t)| \qquad\qquad (16)
\end{aligned}
$$

179   Notice that the barotropic mode is spatially constant and only the cross shore spatial structure
180   of the baroclinic mode varies as $\exp \frac{y}{R_d}$. In addition, the amplitude of the baroclinic component
181   of the velocity field is limited whereas the barotropic one grows linearly with time (until other
182   processes such as bottom friction become non-neglegible).
183   The wind stress corresponding to a 30 knots wind (15 m/s) is $\tau^w \simeq 0.2 N/m^2$ and thus we get
184    $T^w \simeq 4.\ 10^{-6}\ m/s^2$ (for $H_1 = 50\ m$). Then, the previous formulas show that it takes about
185    $t_o \simeq 2$ days for the outcropping front to be generated and after 10 days of wind forcing, the front
186   is located $Y \simeq 35\ km$ offshore and the maximum velocity at the front is about $U_1^{max} \simeq 70\ cm/s$.
187   The barotropic velocity, and the velocity field in the deep layer over most of the domain, are
188    $U_b \simeq 8\ cm/s$. The characteristics of the upwelling found in the numerical simulations presented
189   below are in very good agreement with these analytical results.

190   **3. Reference experiment**

191   The wind forcing was kept constant $T^w = \tau^w/(\rho_1 H_1)$ in the reference simulation that we
192   present here.
193   Figure 4 shows the evolution of the *PVA* in the upper layer superimposed on the shape of the
194   promontory for the reference experiment (see table 6). During the upwelling development, the
195   upper layer vanishes close to the coast and is replaced by deep waters that reach the sea surface.
196   This area is associated with an infinite *PVA* in the upper layer (see [*Bretherton,* 1966]) and is thus
197   delimited by a strong *PVA* gradient that we use to trace the upwelling front and the development
198   of the upwelling filaments (it is qualitatively comparable to the sea surface temperature front).
199   The strong *PVA* gradient associated with the upwelling front becomes evident on the third
200   day of the experiment. It is accompanied by an intense baroclinic surface intensified jet super-
201   imposed on a spatially constant barotropic westward flow. The influence of bottom topography
202   is noticeable after 4 days, when the front begins to form a small meander on the western (down-
203   stream) side of the promontory. The initial topographical meander keeps on growing offshore
204   downstream of the promontory. After 12 days of simulation, it starts to roll up anticyclonically
205   around the promontory. At day 16, another branch appears, growing offshore but partly rolling
206   up cyclonically. The meander has then become a thin and elongated filament, surrounded by
207   two counter-rotating recirculations.Its length is about 200 km and its width about 100 km near
208   the coast and 20 km near the tip. It is similar to the 'squirts', observed in all major upwelling
209   systems. After 28 days, the filament is still growing offshore and is about 220 km long, but its
210   offshore edge has rolled up cyclonically. As shown on Fig. 4, the filament continues to grow

9
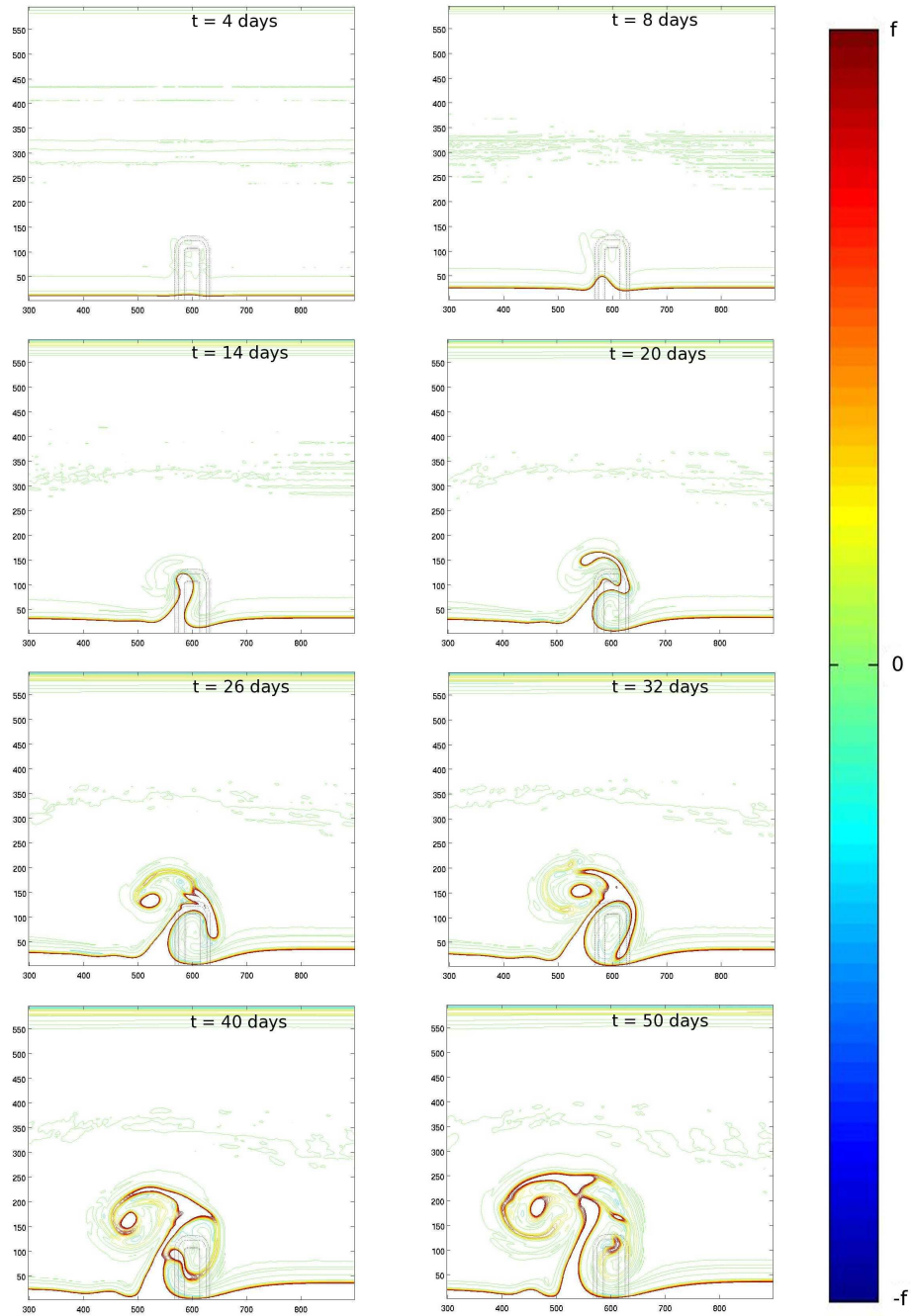
10

Figure 4: Evolution of the PVA in the upper layer for the reference experiment at $t = 4, 8, 14, 20, 26, 32, 40, 50$ days. The thick red line represents the $PVA = +f$ contour and is a good marker of the upwelling front. The axis are labelled in km.
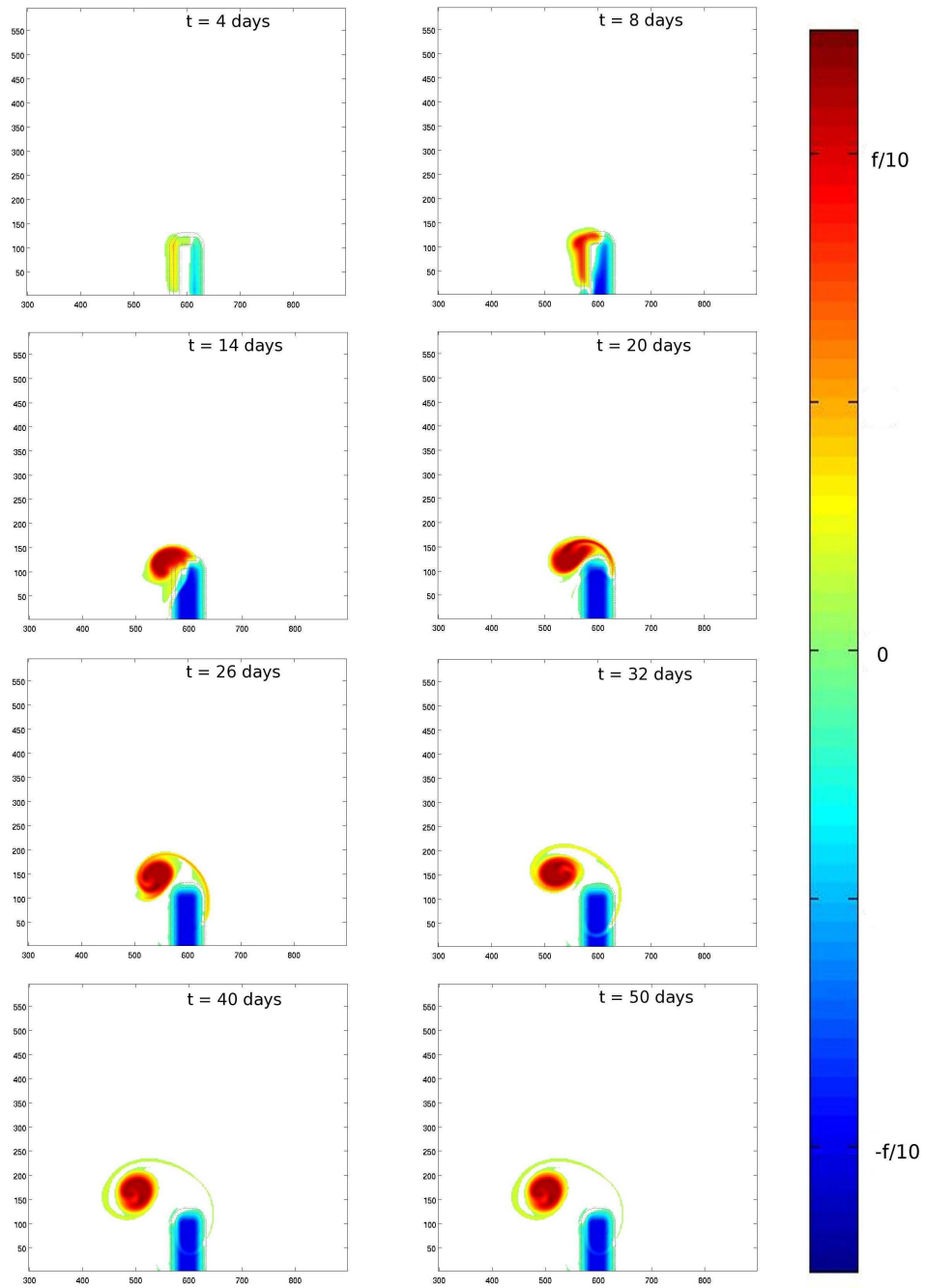
11

Figure 5: Evolution of the PVA in the bottom layer for the reference experiment at $t = 4, 8, 14, 20, 26, 32, 40, 50$ days. The generation of PVA is visible in the first 10 days. It is then advected from day 10 to day 50.
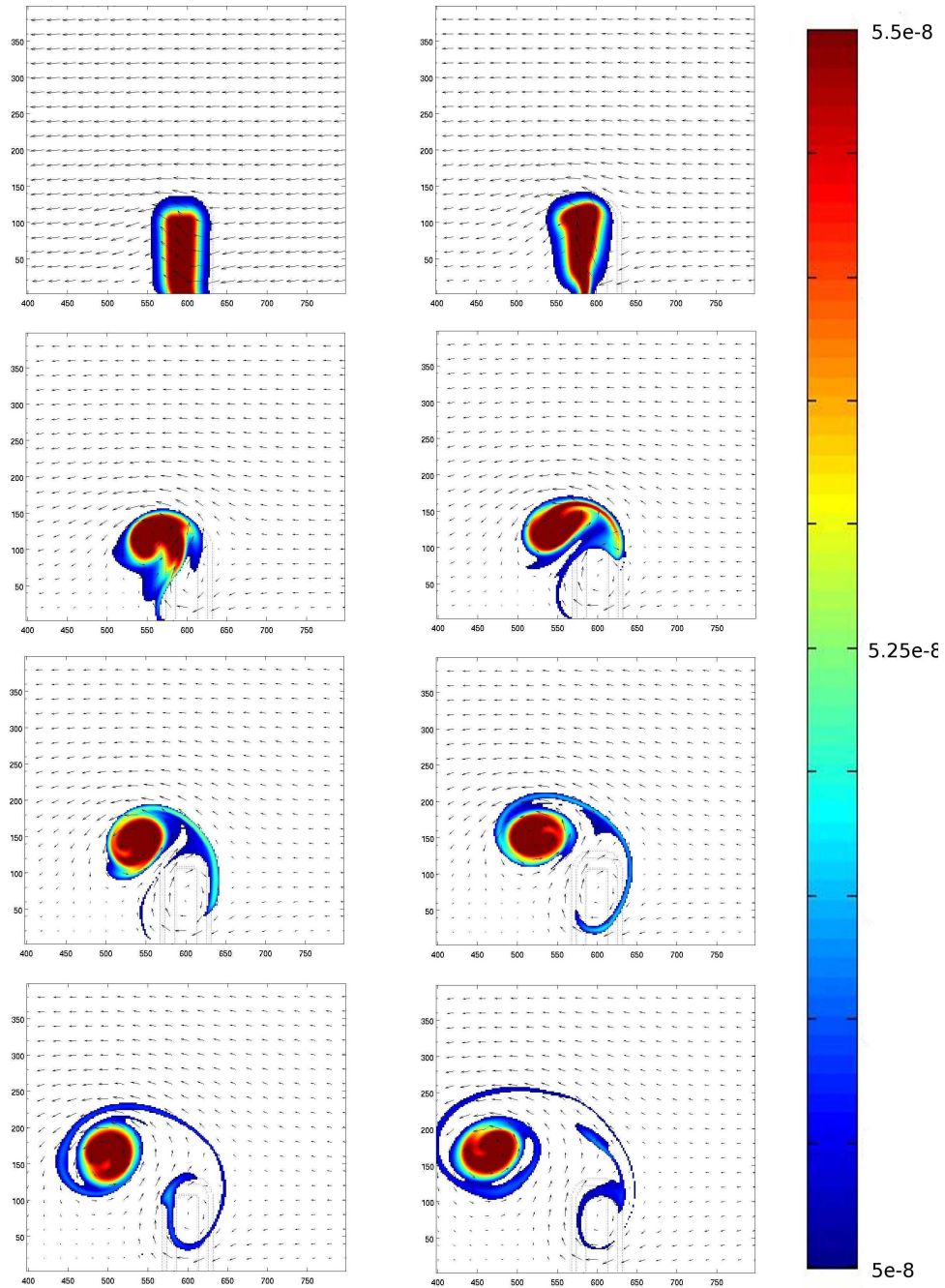
12

Figure 6: Evolution of the bottom layer absolute potential vorticity for the reference experiment superimposed on the velocity field. The high *PV* pool is visible on the promontory. Note that potential vorticity is strictly conserved and is only advected by the current. Comparison with Fig. 5 also shows that the anticyclonic and cyclonic circulations are associated with the negative and positive PVA poles that develop because of bottom topography, as expected.

211 until the end of the simulation (it is about 230 km long after 50 days), corresponding to a mean
212 growth rate of about 5 km per day for the whole life cycle, consistent with the observed mean
213 value found by [*Kostianoy and Zatsepin,* 1996]. But the growth rate of the filament is variable
214 during the life cycle, with higher initial growth rates of up to 12 *km day*$^{-1}$ (i.e. 14 *cm s*$^{-1}$) after
215 10 days, then decreasing untill the end of the experiment.

216 The formation of the filament is very similar to the erosion process of a surface vortex by
217 a seamount studied in [*Herbette et al.,* 2003]. As already explained above, the origin of these
218 counter-rotating eddies can indeed be inferred from the *PV* and *PVA* evolution in the lower
219 layer. Indeed, as shown in [*Morel et al.,* 2006, *Rossi et al.,* 2009] a barotropic westward current
220 is generated during the upwelling development. The baroclinic circulation opposes this current
221 in the upper layer, but its extension is of the order of the first internal radius of deformation
222 (about 7km here) which is quite small. As a result, water columns move westward over most of
223 the lower layer. As the dynamics is adiabatic here, the initial *PV* field is simply advected and
224 the positive anomaly associated with the promontory moves downstream (see Fig. 6) replaced
225 by lower *PV* water columns coming from deeper region. Figure 5 shows that it creates opposite
226 sign *PVA* (see also [*Herbette et al.,* 2003]): high *PV* water columns coming from the promontory
227 move in regions with lower *PV* at rest, forming a positive *PVA* downstream of the promontory,
228 while low *PV* water columns move upon the promontory, which is associated with high *PV* at
229 rest, forming a negative *PVA* that is being trapped above the promontory. As shown in Fig. 6,
230 this topographic *PVA* dipole is associated with cyclonic and anticyclonic circulations extending
231 over the whole water column. An offshore jetlike current develops between the two opposite sign
232 PVA poles, which forms the filament.

233 After 7 days both positive and negative *PVA* reach a maximum modulus of $\pm 0.1f$, the nega-
234 tive *PVA* obviously remains trapped above the topography, maintaining offshore currents on the
235 western side of the promontory which reach about 40 *cms*$^{-1}$. But the high *PVA* pole is strongly
236 deformed and propagates offshore and westward under the combined effect of advection and in-
237 teraction with bottom topography. The topographic β-drift of a *PVA* pole along the slope of the
238 promontory scales -in the quasi-geostrophic approximation- as $U_{drift} = \beta_t R_d^2$, with $\beta_t = f_0 \alpha / H_2$
239 where $\alpha = H_t/dL$ is the characteristic slope of the promontory, and R_d^2 is the square of the Rossby
240 radius. For the reference experiment, U_{drift} is found to be about 2.5 *cms*$^{-1}$. The barotropic ve-
241 locity field associated with a PVA pole in the lower layer can be scaled using the circulation
242 theorem :

$$U^- \simeq C/2\pi l \tag{17}$$

$$C = \int\int_P PVA \, \frac{h_2}{H_{tot}} \, dS \tag{18}$$

$$\simeq \int\int_P PVA \, dS \tag{19}$$

243 where *C* is the circulation or total PVA reservoir inside a domain *P*, *l* is the distance from the
244 center of the PVA pole, $H_{tot} = H_1 + H_2$ and *dS* is the surface element. If we assume that all water
245 columns above the promontory have been replaced by water columns coming from the deeper
246 ocean, the negative PVA forming above the promontory is given by :

$$PVA = -\frac{f \, H_p(x, y)}{H_2^\infty} \tag{20}$$

13

171

where $H_p(x, y)$ is the the promontory height.

The total circulation associated with the negative *PVA* of the promontory, over the domain *P* is then

$$C \quad = \quad -\frac{f}{H_2} \int \int_P H_p(x, y) dS \tag{21}$$

$$\simeq \quad -\frac{f}{H_2} H_t \left[L_x \, L_y + dL \, (L_x + L_y/2) \right] \tag{22}$$

For the positive pole, the calculations are similar : the PVA reservoir, and thus circulation, is exactly the opposite of the negative one above the promontory (water columns are exchanged between the deep ocean and the promontory). As the effect of both PVA poles superimposes, the maximum barotropic current between both poles is thus roughly given by :

$$U_{max}^{jet} \quad \simeq \quad 2C/2\pi l \tag{23}$$

$$C \quad \simeq \quad \frac{f}{H_2} H_t \left[L_x \, L_y + dL \, (L_x + L_y/2) \right] \tag{24}$$

where *l* is the mid distance between both pole centers.

When both PVA poles are well developed, $l \simeq 30$ km and $U_{max}^{jet} \simeq 36$ *cm/s*, which is the order of magnitude of the maximum offshore current observed downstream of the promontory (40 *cm/s*). These modelled velocities are in very good agreement with what have been observed in-situ in the IPUS area and also in other upwelling regions (see [*Sanchez et al.,* 2008]).

Notice that the estimation of U_{max}^{jet} or U^- is only correct in the case of circular *PVA* structures, or far enough from the structure so that shape effects become neglegible. Here, this is obviously not verified, but, using this simple scaling can give us a good insight of the order of magnitude of the velocity associated with the topographic *PVA* pole development and its sensitivity to the promontory characteristics.

In summary, an anticyclonic circulation is generated and trapped above the promontory by advection of low *PV* over the topography, forming a negative *PVA* pole. A cyclonic circulation also forms because of advection of high *PV* from the promontory into a deeper environment. This forms a trapped topographic dipole associated with a strong offshore current that generates the filament and its well known 'squirt' or 'mushroom' shapes (see [*Strub et al.,* 1991]). The strength of the current depends on the total PVA reservoir of the promontory.

Finally, notice that, even though the initial topographic cyclone slowly separates from the trapped anticyclone, because of the outcropping and vanishing of the upper layer, the meander and filament are themselves also associated with an equivalent high *PVA* (see [*Bretherton,* 1966]) reinforcing and maintaining a cyclonic circulation on the downstream side of the negative *PVA* pole.

4. Sensitivity experiments

To strengthen the physical relevance of the mechanism described above and to assess the respective importance of the various parameters and characteristics of the configuration, a set of sensitivity tests was performed. Here we focused on the stability of the front, the forcing duration time, of the promontory characteristics (width, length, height and slopes), of the stratification and of bottom friction. For comparison of the various model output, we take as a reference time the $t = 42$ days (6 weeks) output, and use the *PVA* maps as a qualitative indicator of the efficiency of the model configuration to produce long, coherent and trapped filaments.

14

4.1. The stability of the front

The reference run showed that the sole presence of the topography allowed the development of a long filamentary structure reaching as far as 230 km offshore. However, mixed barotropic-baroclinic instability is a well known feature of upwelling currents [*Shi and Roed,* 1999] and has sometimes also been referred to as the main process for filament formation [*Haidvogel et al.,* 1991]. It is thus important to evaluate the relative influence of topography and intrisic instability on the development of the long filament.

Baroclinic instability can only develop when there exists opposite sign potential vorticity gradients or *PVA* (see [*Charney and Stern,* 1962]). The outcropping front is associated with positive *PVA*. As shown by [*Morel et al.,* 2006], negative *PVA* is generated along the upwelling front (see Fig. 7 below) because as isopycnic surfaces bend upward they enter the region influenced by the wind stress. A wind stress curl then exists along isopycnic levels which has been shown to necessarily form negative *PVA* (the formation of negative *PVA* by the wind has also been studied in [*Thomas,* 2005]). In the simple 2-layer configuration used here, this effect is associated with the fact that $T^w = \tau^w/(\rho_1 h_1)$ varies with the layer depth h_1.

In the reference experiment, the possibility of the flow to become baroclinically unstable has thus been suppressed by modifying the distribution of the wind forcing : $T^w = \tau^w/(\rho_1 H_1)$ provides a constant wind stress so that the upwelling still develops but the dynamics remains adiabatic and the PV field is conserved. As a result, no negative PVA is formed along the front and no baroclinic instability can develop.

In the present test, we use the actual wind forcing $T^w = \tau^w/(\rho_1 h_1)$. Figures 7 and 8 show the evolution of the *PVA* in the upper layer and in the lower layer respectively. In comparison with the reference experiment (see Fig. 4 and 5), negative PVA is develops along the upwelling front. This negative PVA strip interacts with the positive PVA associated with the outcropping forming new small-scale meanders, with wavelengths of 30 km after 10 days (notice the association of the small upwelling front meanders with small negative PVA poles). These small-scale meanders are associated with baroclinic (or sometimes called frontal) instabilities ([*Barth,* 1989 a, *Barth,* 1989 b, *Morel et al.,* 2006, *Capet and Carton,* 2004, *Killworth,* 1980]) but are neither trapped nor forming long filaments. They indeed propagate along the upwelling front, re-enter the domain on the eastern side and only very slowly develop after their initial growing. After 5 weeks of experiment, their offshore extension is less than 50 km (from the front).

The impact on the main filament is also minor: the positive and negative *PVA* poles still develop in the bottom layer and their time evolution is not significantly modified. The surface filament is very similar to the one observed in the stable case and it extends as far offshore. The only noticeable difference, apart from the absence of the small amplitude meanders along the front, is that the topographic filament is here truncated by the small scale eddies and also appears slightly larger at its base. This proves that, at least in our simplified configuration, intrisic baroclinic instability has little influence on the formation of the long filament and that the main mechanism is associated with topography, as described above.

The stable front configuration is also of particular interest because the dynamics is adiabatic and *PV* is conserved following fluid parcels in all layers and can be used as a tracer. For this reason, and because we have shown that no substantial difference existed in the formation of the filament, we keep the stable front configuration as our reference experiment for the following sensitivity tests that will thus be carried with the modified and constant wind forcing.

15
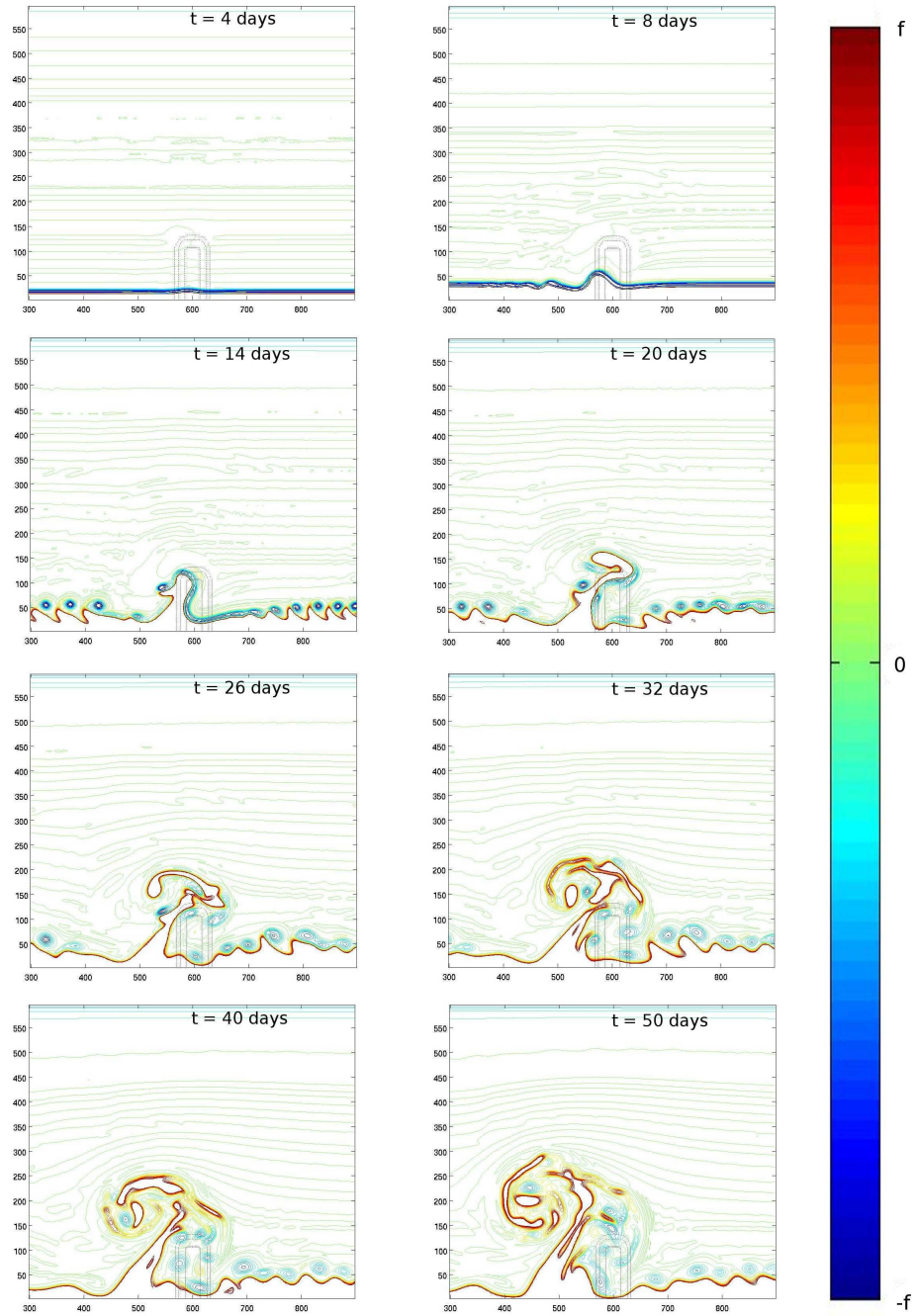
16

Figure 7: Evolution of the *PVA* in the upper layer for the unstable experiment at $t = 4, 8, 14, 20, 26, 32, 40, 50$ days. Notice the additional smaller meanders, but the formation of the large filament is the same as in Fig. 4.

174
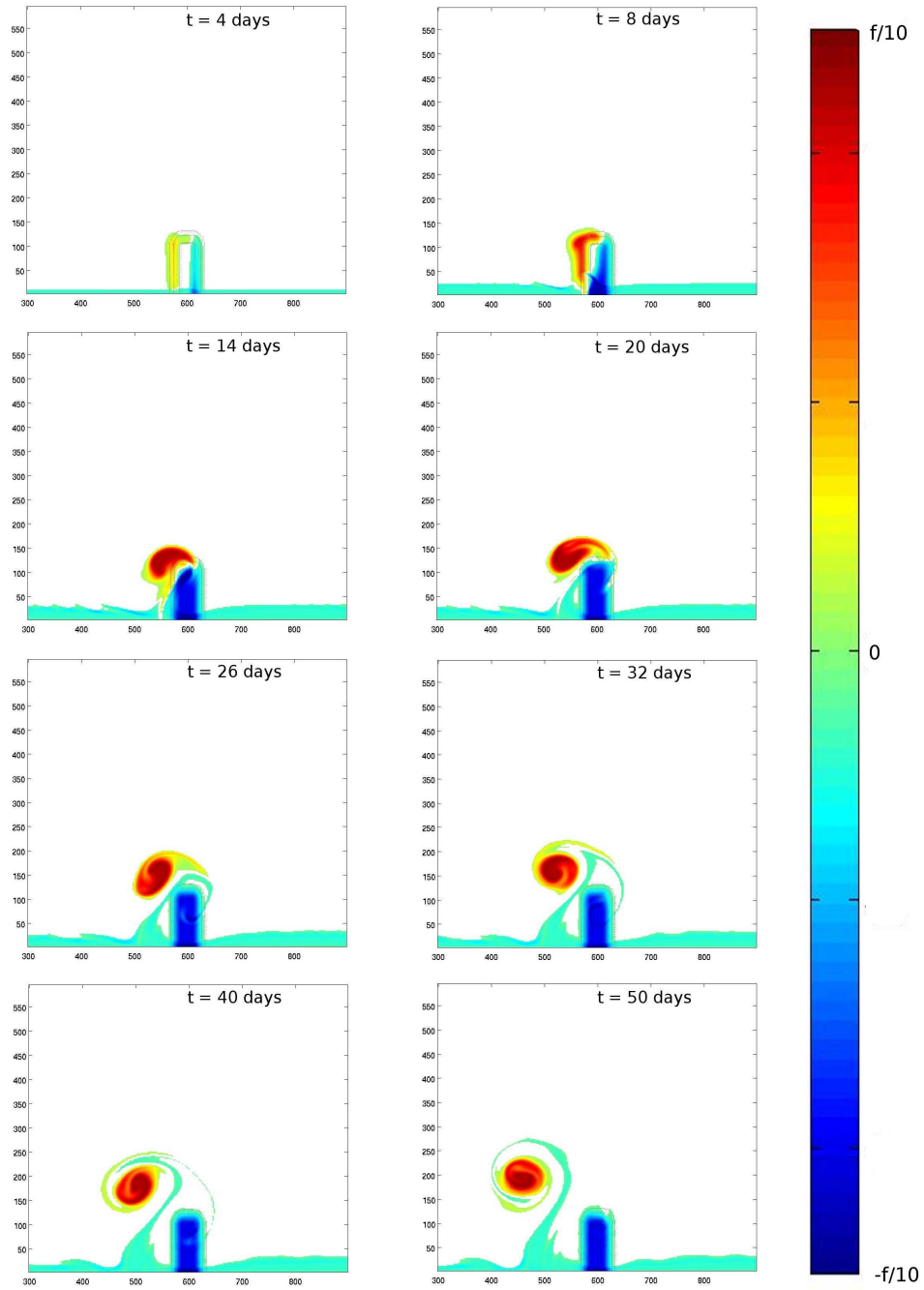
17

Figure 8: Evolution of the PVA in the bottom layer for the unstable experiment at $t = 4, 8, 14, 20, 26, 32, 40, 50$ days.

4.2. The influence of the stratification characteristics

In addition to the reference experiment ($g' = 0.01$, $H_1 = 50$ m), six additional experiments were performed to evaluate the influence of the stratification characteristics on the dynamics of the topographic filament : 3 experiments varying g' (0.005, 0.02 and 0.03), and 3 experiments varying H_1 (25, 100, and 200 m). It may seem redundant to vary both parameters (as they both influence the Rossby radius) but we finally found out that their respective influence on the upwelling front evolution is quite different.

Figure 9 represent the upper layer PVA after 42 days for different values of g' and shows only modest modification of the filament. This is not entirely suprising as the density jump mostly influences the baroclinic currents in the vicinity of the front via the Rosbby radius of deformation. Topographic eddies are formed and influence the dynamics through the barotropic circulation, which is not modified. In addition, the position of the upwelling front is also only slightly affected by a modification of g' : the offshore displacement is not modified and only the initial time at which the outcropping front forms depends on this parameter.

Varying H_1 (Fig. 10) does not modify the lower layer dynamics either (see the similarities of the *PVA* structure in the lower layer after 42 days on the right panels of Fig. 10). However, since it also plays a role in the strength of the wind forcing ($T^w = \tau^w/(\rho_1 H_1)$), it strongly modifies the position of the upwelling front, which forms later and extends more slowly for deeper thermoclines (larger H_1). The differences in the filament evolution with different H_1 is thus the result of the time lag between the upwelling front evolution associated with H_1 and the distribution of the topographic eddies when the outcropping first forms. As a result, the advective effect of the topographic eddies on the upwelling front is in general simply delayed. The time period necessary for the upwelling front to be formed is $t_o \simeq 0.7, 2, 6$ and 16 days for $H_1 = 25, 50, 100$ and 200 m respectively. As a result, for the duration of the wind forcing considered here (10 days), varying H_1 does not strongly modify the filament except for the deepest thermocline (here associated with the case $H_1 = 200m$) for which the upwelling front is not formed and no filament is then visible (see Fig. 10 lower panel). Interestingly, the final offshore extent has close values for the all other experiments.

Finally notice that the experiment where g' is varied and the experiment where H_1 is varied have different Rossby radius of deformation : $R_d = 5, 7, 10, 14$ km, for $H_1 = 25, 50, 100, 200$ m respectively (or $g' = 0.005, 0.01, 0.02$ and 0.03 respectively). This underlines again that the important mechanisms for the filament development is the barotropic circulation and the formation of the upwelling front. In our configuration the development of the filament is mainly controlled by the bottom layer *PVA* evolution which is almost insensitive to R_d.

4.3. The forcing duration time

We here study the effect of a variation of the wind forcing duration time. As seen above, the wind forcing acts both on the offshore front position and the velocity strength, especially the one of the barotropic current.

Figure 11 shows the *PVA* front after 42 days of experiments in the upper layer for forcing durations of 10 (reference experiment), 20, 30, and 40 days. There still exists a trapped filament that extends far offshore downstream of the promontory, but its characteristics drastically depend on the forcing duration : it becomes thicker and bends downstream when the wind blows for a long time.

In fact, increasing the wind forcing duration does not substantially modify the formation of the *PVA* in the bottom layer but induces stronger barotropic current directed downstream. This

18
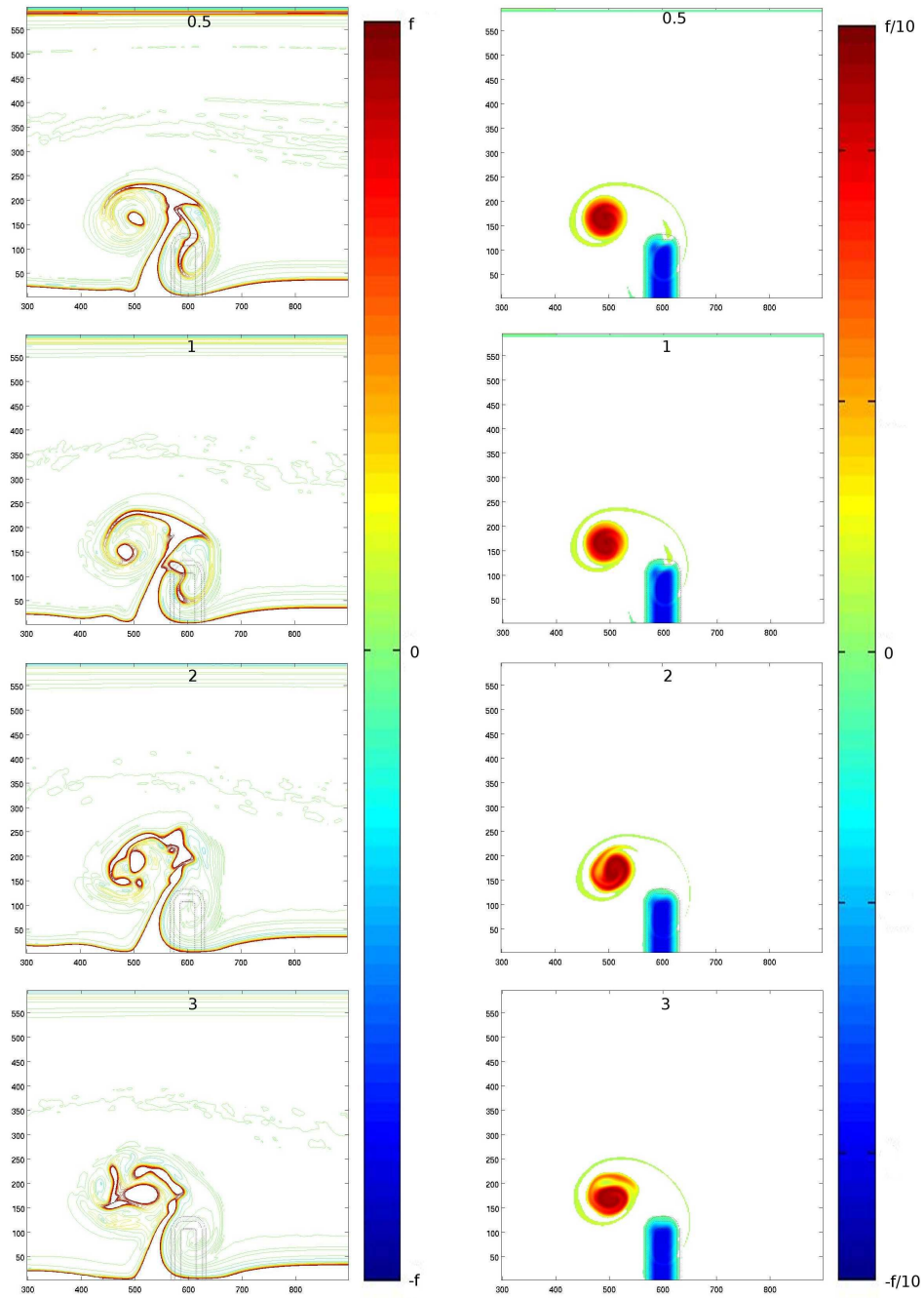
Figure 9: Maps of PVA in the upper (left hand panel) and bottom (right hand panel) layers at $t = 42$ days for the $\delta\rho = 0.5, 1, 2$ and $3 kgm^-3$ experiments.
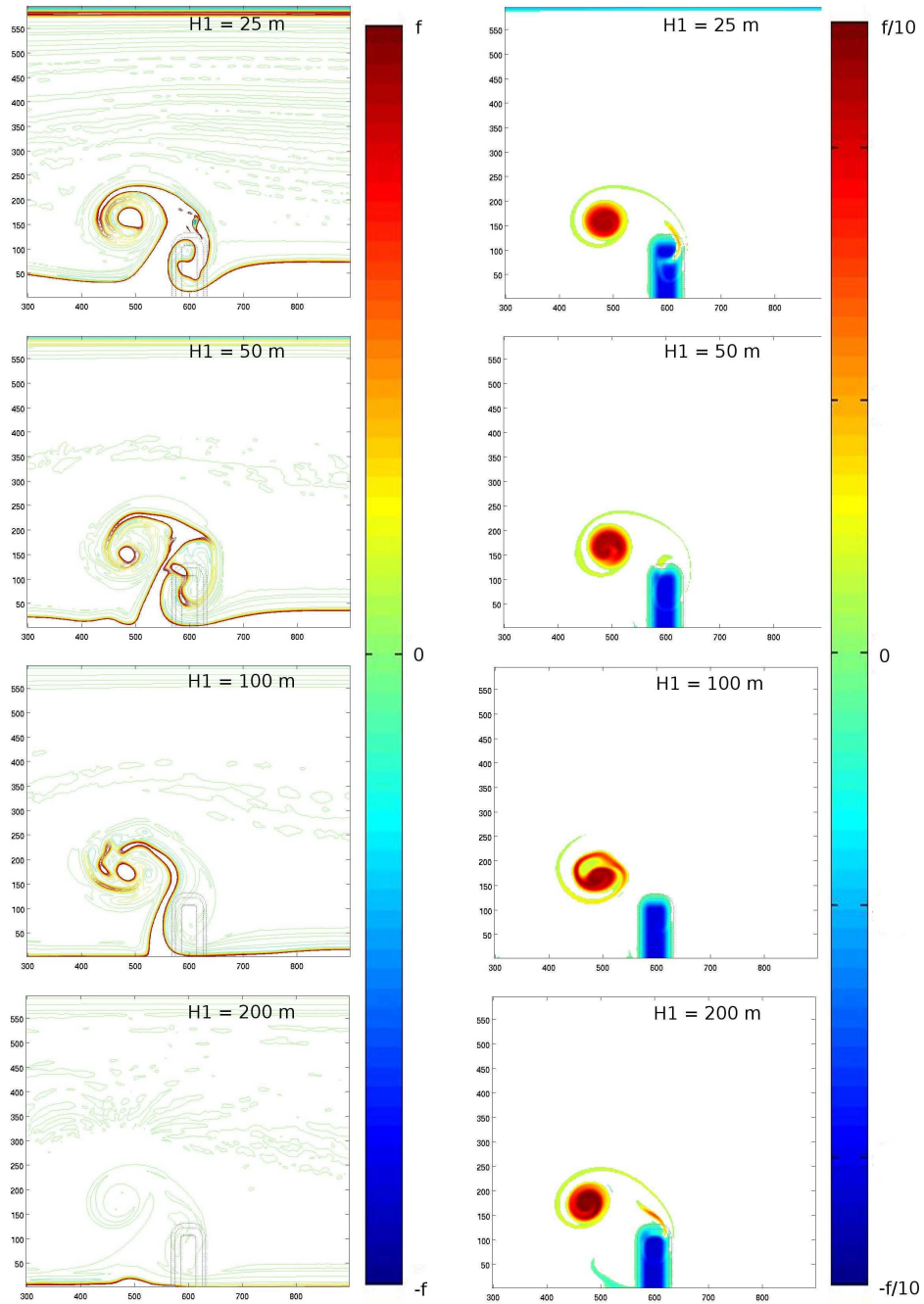
Figure 10: Maps of *PVA* in the upper (left hand panel) and bottom (right hand panel) layers at $t = 42$ days for the $H_1 = 25, 50, 100, 200m$ experiments.
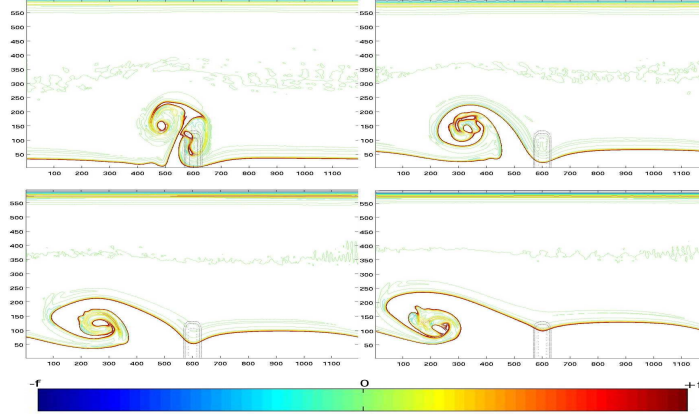
Figure 11: Maps of PVA in the upper layer at $t = 42$ days for the 10, 20, 30 and 40 days of wind forcing cases.

intensifed upwelling can mask the topographic circulation and the offshore jet. In addition, as the barotropic current increases, the positive pole becomes quickly advected downstream and only shortly interacts with the negative *PVA* pole on the topography. As a result, the upper layer *PVA* front rolls up cyclonically around the bottom layer positive *PVA* pole and is entrained downstream, giving it a breaking wave like shape. When increasing the forcing duration time, the distance from the front and jet to the coastal wall increases, while the offshore distortion of the front is less obvious, since its initial position almost reaches the offshore edge of the promontory (see the 40 day forcing case).

Notice that according to Eq. 13 and 15 the maximum barotropic velocity is roughly given by $U_b^{max} \simeq 8, 6.10^{-3} t_d$, where t_d is the duration time of the wind forcing in days. We thus get $U_b^{max} \simeq 8, 6\ cm/s$ for 10 days and $U_b^{max} \simeq 34, 4\ cm/s$ for 40 days, which is stronger than the offshore advection associated with the topographic eddies. Notice such barotropic currents are far beyond what is observed, at least offshore the continental shelf, and that in practice, bottom friction keeps the barotropic velocity from reaching such values.

4.4. The promontory height

As the main process proposed here for the development of an upwelling filament is the generation of topographic *PVA* in the bottom layer associated with the existence of a promontory, it is important to detail how the shape and size of the latter can affect *PVA* generation and thus filamentation. The maximum *PVA* and the strength of the topographic eddies are proportional to the height of the promontory which is thus a key parameter.

Six experiments were carried out with different promontory heights : H_t = 50, 100, 300, 500, 1000 and 1500 m, to be compared with the 200 m of the reference experiment. Figure 12 shows

21

the upper and lower layer *PVA* field after 42 days for the 50, 200, 500, and 1500 m experiments. For small topographies (Ht = 50 m), the filament forming in the upper layer along the front has a much smaller offshore extension, is less pinched off and its tip is advected downstream. In fact, the effect is the same as for the influence of the forcing duration discussed above: the topographic circulation becomes much smaller than the upwelling current (the offshore current is about 10 *cm s*$^{-1}$ for Ht = 50 m, to be compared with the reference experiment where it is about 40 *cm s*$^{-1}$). The positive *PV* pole is quickly advected downstream and the offshore current is masked by the upwelling current giving the filament a breaking wave shape and limiting its offshore extension.

The H_t = 500 and H_t = 1500 m experiments (see Fig. 12 left panels) show that after 42 days of experiment, the filament is also much reduced in comparison with the reference experiment (100 km for H_t = 1500*m*, and 140 km for H_t = 500 m). The limiting factor for large H_t is associated with the difficulty for water columns to climb on or leave the topography. Indeed, most of the positive and negative *PVA* in the bottom layer remains trapped on the slope (see Fig. 12 right panels). As a result, instead of forming two strong opposite sign *PVA* poles that locally reinforce the offshore circulation, *PVA* of both signs mix on the promontory evolving into a complex pattern of multiple small poles with few coherence. The overall integrated *PVA* and circulation associated with the topographic eddies is then much reduced. In fact, as already found by [*Herbette et al.,* 2003] in the case of a vortex interaction with a seamount, the topographic circulation can not be much stronger than the background velocity and the *PVA* creation is limited. Figure 13 shows the maximum extent of the filament for the 7 experiments. Similarly to [*Herbette et al.,* 2003]'s optimum value of seamount height for vortex erosion, there exists an optimal promontory height for the filament extension which corresponds here to the reference experiment : H_t = 200 m.

4.5. The promontory width

Three experiments were carried out to test the sensitivity of the filament formation to the width of the promontory (parameter Lx). We tested Lx = 0 km (Gaussian ridge), 20 km (reference experiment), 50, and 100 km (see Fig. 14). This parameter mostly affects the PVA reservoir and strength of the circulation associated with the topographic eddies. The evolution of *PVA* in the bottom layer for small Lx exhibits similarities with the reference experiment, with a generation of negative *PVA* on the upstream part of the promontory in the first week of experiment, fully invading it after 10 days, and a generation of positive *PVA* downstream of the ridge, quickly evolving into a cyclonic vortex detaching from the offshore edge of the ridge. In fact, in the case of small L_x, most of the *PVA* reservoir is contained along the promontory slope, not above the plateau, and the results are then obviously not sensitive to this parameter in this case.

Increasing L_x increases the PVA reservoir and the potential strength of the topographic eddies. The Lx = 50 km and 100 km cases show a strong rolling up of the positive PVA and of the filament around the promontory. The *PVA* structure also exhibits a multipolar structure and the filament has multiple branches that do not extend very far offshore. In fact, strong topographic eddies leads to complex non linear interactions between the opposite sign *PVA* poles. The position and shape of the negative PVA is fixed and remains trapped above the promontory, whereas the positive one is advected and deformed by the total velocity field that develops in the lower layer. The latter effect is a combination between the barotropic circulation associated with the upwelling development, which is spatially constant, and the anticyclonic eddy, which varies spatially and can induce strong deformations. When the PVA reservoir increases, the effect of the negative PVA pole dominates the positive PVA pole and filament dynamics which are advected

22
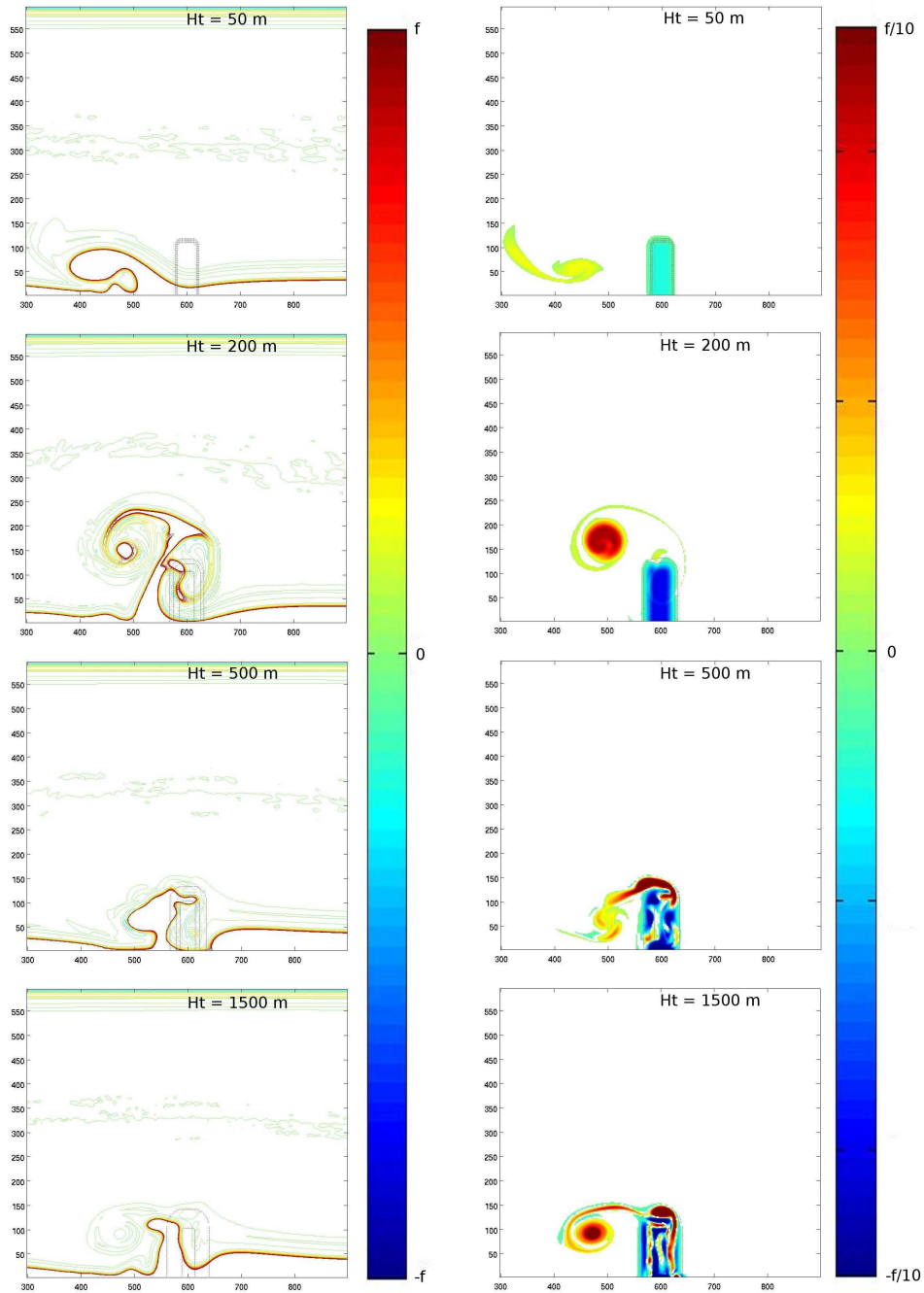
Figure 12: Maps of *PVA* in the upper (left hand panel) and bottom (right hand panel) layers at $t = 42$ days for the $H_t = 50, 200, 500$ and $1500 m$ experiments.
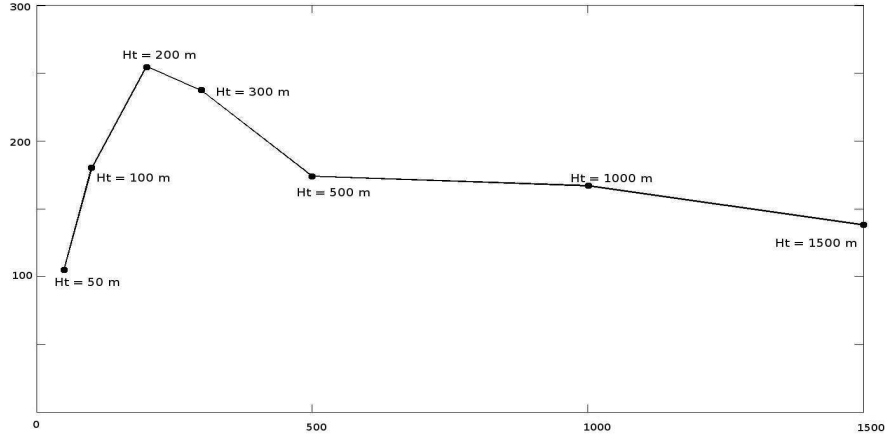
Figure 13: Offshore extent of the filament after 50 days of experiment for the $Ht = 50, 100, 200, 300, 500, 1000$ and $1500m$ cases. The x axis is time (days) and the y axis is offshore distance (kms).

anticyclonically around the promontory and deformed. This greatly reduces the total length of the filament.

As a result, the width of the promontory also plays an important role in the development of a coherent filament structure in the upper layer and again, there exists an optimum value for the width of the promontory. This is shown in Fig. 15 where the offshore extension of the topographic filament is plotted for various choices of L_x. The optimum value is $L_x = 20$ km (reference experiment) for the present configuration.

4.6. The side slopes

In order to evaluate the importance of topographic β-effect in the offshore displacement of the positive PVA, three experiments were performed with different margin lengths for the promontory : $dL = 0$, 10, 20 (reference experiment) and 40 km. This parameter acts on the PVA reservoir (with close similarities with L_x) but also on the topographic slope and β-effect. The previous choices for dL corresponds to slopes $tan\alpha = \infty$, 2.10^{-2}, 10^{-2}, 5.10^{-3} respectively.

Figure 16 shows upper and lower layer PVA maps at $t = 42$ days for the different margin lengths. As could be expected, the influence of dL is similar to L_x : above a critical value, the total circulation is dominated by the negative PVA pole and the filament wraps around the promontory. Despite very different values for the topographic slope and β-effect, the similarities between Fig. 16 and 14 are striking.

This confirms that the topographic β-effect has a minor impact on the dynamics, and that the important parameter in the generation of coherent and trapped filaments is the total amount of PVA over the promontory.

24
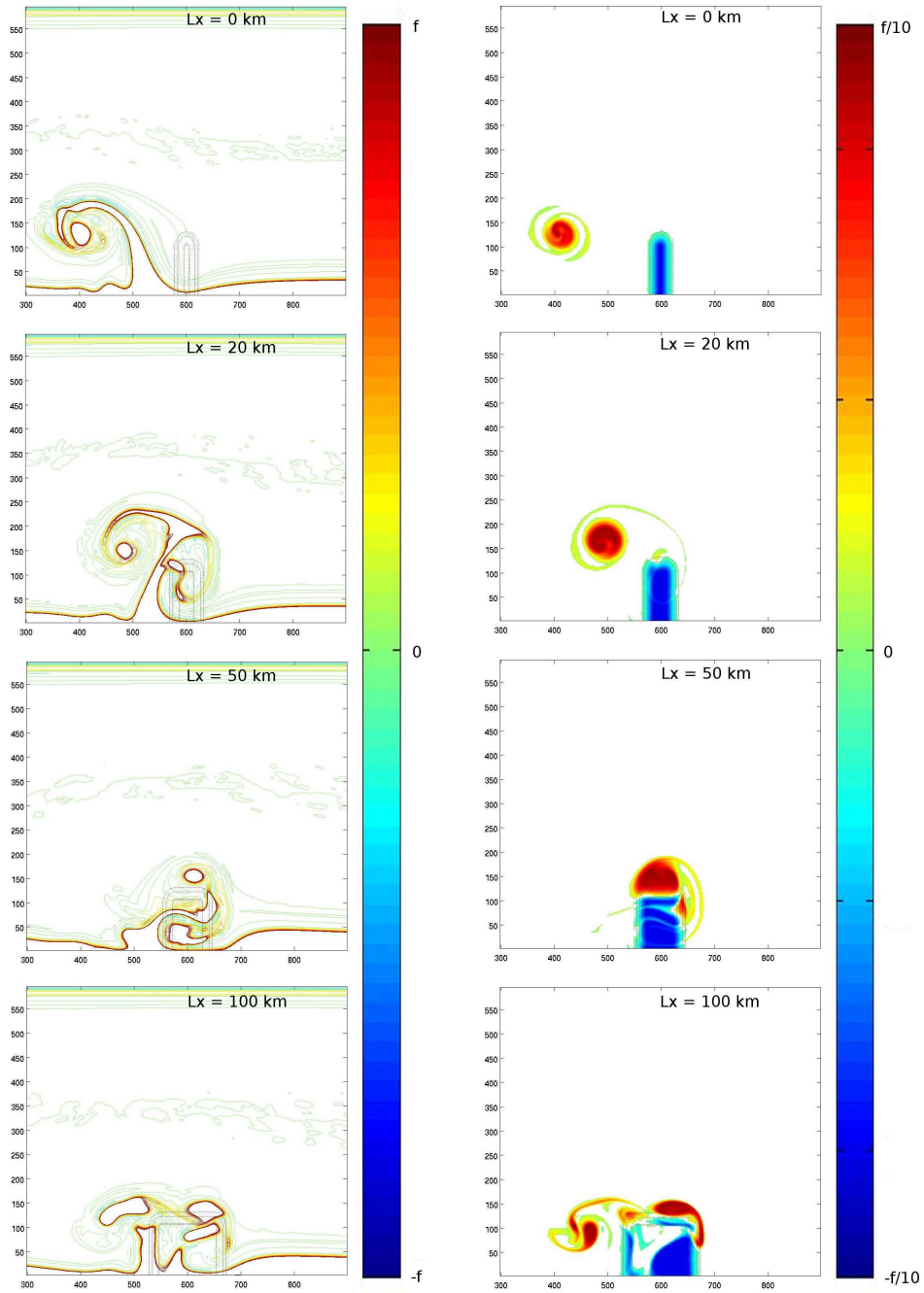
Figure 14: Maps of *PVA* in the upper (left hand panel) and bottom (right hand panel) layers at $t = 42$ days for the $Lx = 0, 20, 50$ and $100km$ experiments.
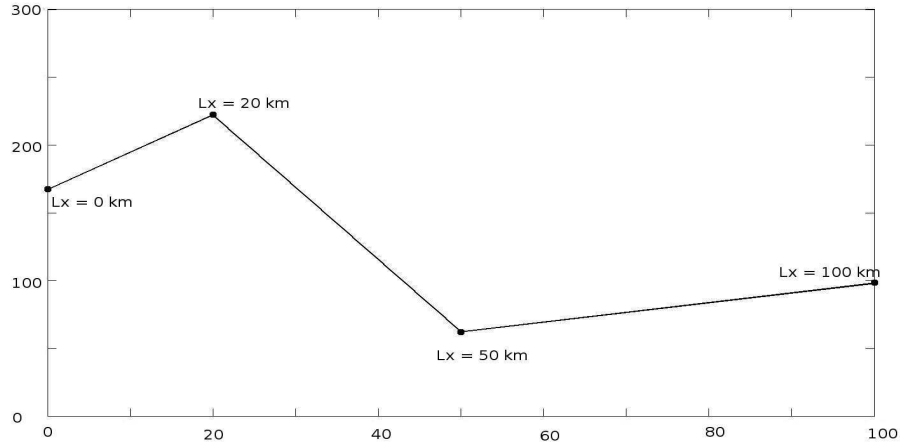
Figure 15: Offshore extent of the filament after 50 days of experiment for the $Lx = 0, 20, 50$ and $100km$ cases cases. The x axis is time (days) and the y axis is offshore distance (kms).

4.7. The promontory length

As discussed above, anisotropy in the shape of the promontory can also modify the structure and strength of the topographic circulation. The sensitivity of the results to the promontory length Ly was thus studied with $Ly = 50$ km, $Ly = 100$ km (reference experiment), $Ly = 150$ km and $Ly = 200$ km.

Figure 17 shows the structure of the *PVA* after 42 days in both layers and for the different L_y. The offshore extension of the bottom layer negative *PVA* pole obviously follows L_y and also drives the length of the filament which always extends further than the promontory. The $Ly = 200km$ case shows that there exists a maximum length of the filament over which it breaks, so that very long promontories are not necessarily the most efficient ones. This is underlined in Fig. 18 which shows the maximum offshore extension of the filament as a function of L_y. The optimal value is here around 150 km. Another particular feature for long promontories ($Ly = 200$ km), is that the filament no longer rolls up around the positive *PVA* pole as it drifts far offshore, its base is much wider and its offshore shape much thinner.

4.8. Bottom friction

Two experiments were performed adding a bottom friction term to the reference configuration. Figure 19 shows the *PVA* in the upper layer (left hand panel) and the *PV* in the bottom layer at $t = 42days$ (right hand panel) for the Cd = 0, 3 10−3, and 5 10^{-3} Nm^{-2} cases. The formation and evolution of the filament in the upper layer is unchanged by the addition of the bottom friction. The effect of friction is only visible in the *PV* of the bottom layer: As the positive *PV* reservoir that has left the promontory to form the positive *PVA* pole gets eroded, new higher *PV* is generated over the promontory, resulting in weakening the negative *PVA* pole.

26

184
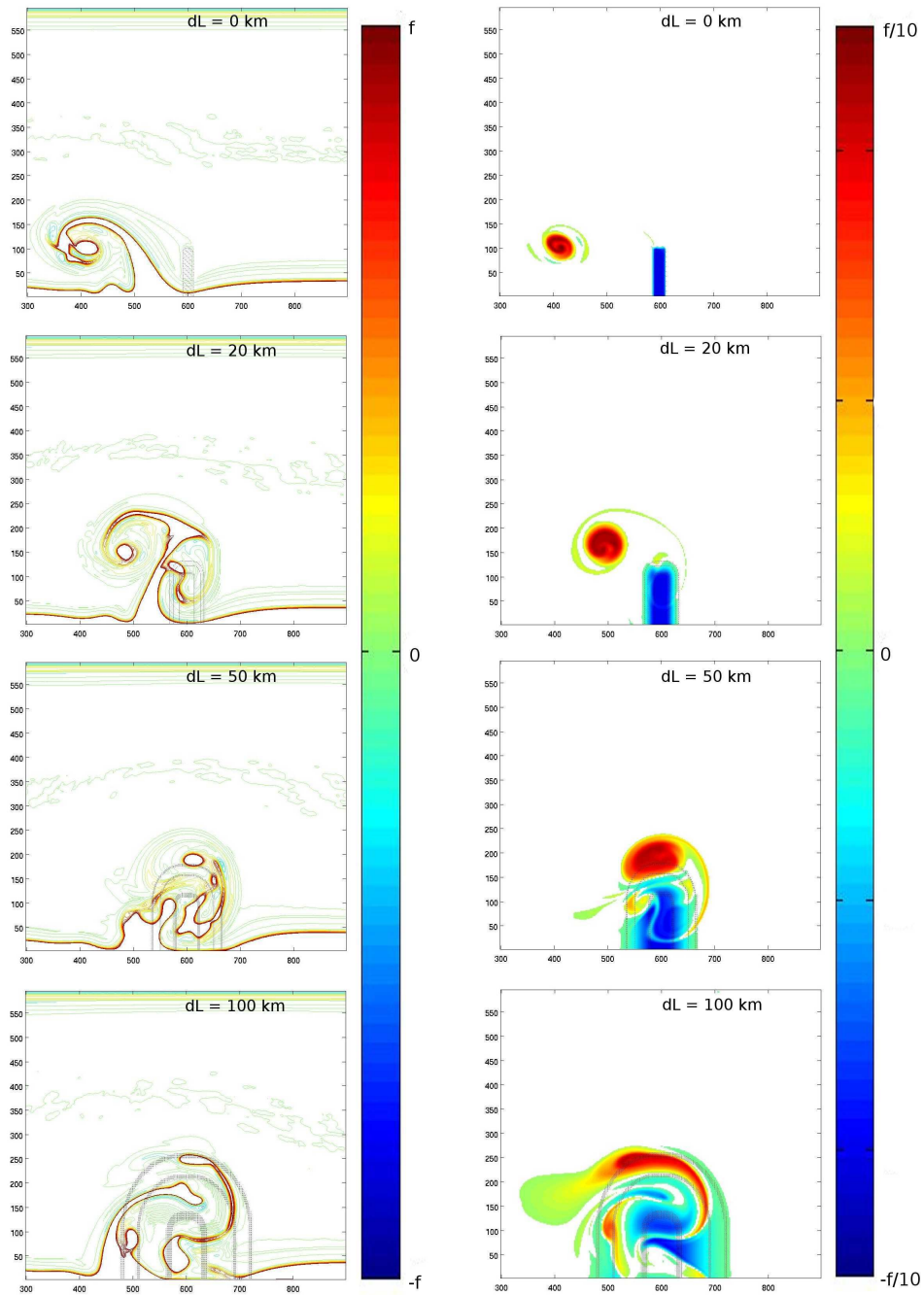
27

Figure 16: Maps of *PVA* in the upper (left hand panel) and bottom (right hand panel) layers at $t = 42$ days for the $dL = 0, 20, 50$ and $100km$ experiments.
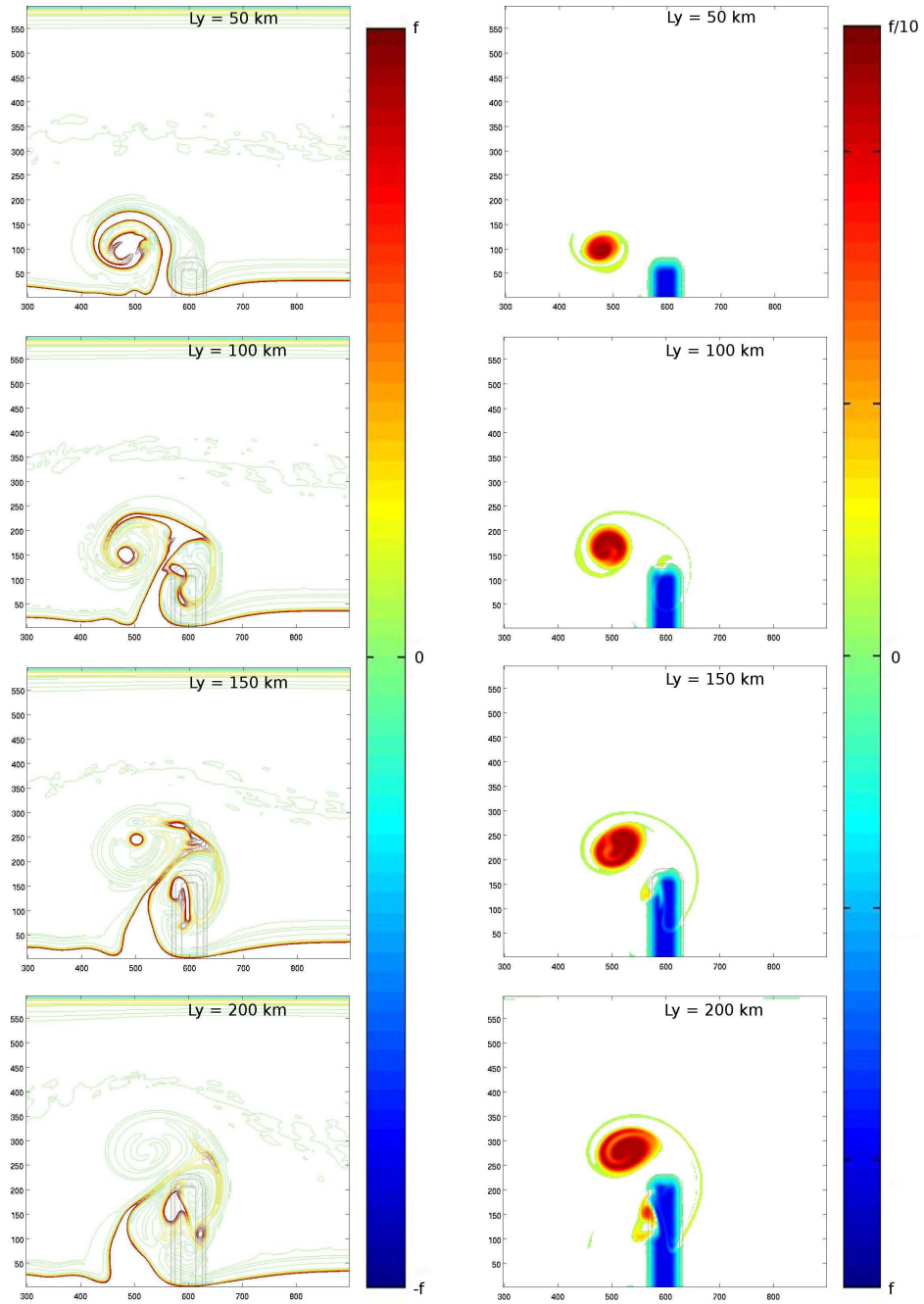
Figure 17: Maps of *PVA* in the upper (left hand panel) and bottom (right hand panel) layers at $t = 42$ days for the $Ly = 50, 100, 150$ and $200 km$ experiments.
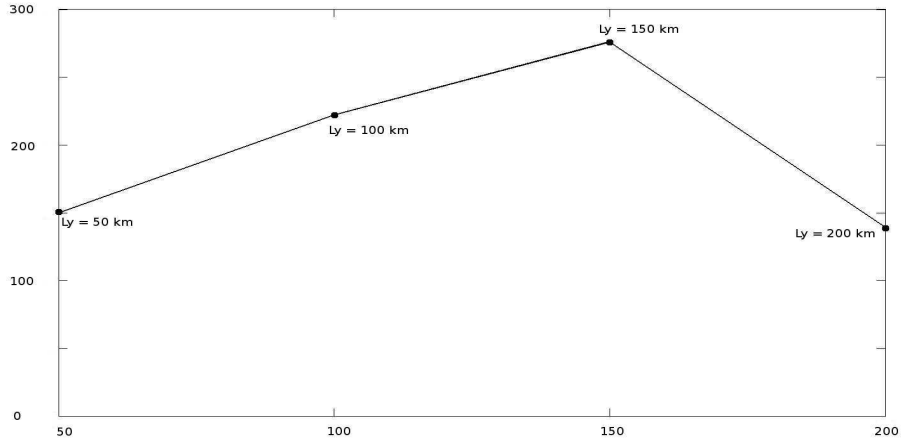
Figure 18: Offshore extent of the filament after 50 days of experiment for the $Ly = 50, 100, 150$ and $200 km$ cases cases. The x axis is time (days) and the y axis is offshore distance (kms).

As a result, bottom friction leads to a relaxation of the circulation and to a new state of rest, which allows new topographic eddies and front filamentation to occur if the wind starts blowing again.

4.9. Combined influence of a cape and topography

Finally, complementary experiments including a cape or a cape superimposed on a larger promontory and a canyon where performed in order to compare the impact of the coastline geometry with the topographic process proposed here. Upwelling filament dynamics have sometimes been associated with capes triggering ([*Strub et al.,* 1991]), but most capes have large promontory-like undersea extends like Cabo Roca, Cabo Finisterre and the Estremadura promontory on the western Iberian coast.

The upper two panels in Fig. 20 show the *PVA* in the upper (left hand side) and bottom (right hand side) layer for two sizes of capes, both having the same Gaussian shape. Viscosity induces increased diabatic effects near boundaries which results here in the development of a layer of positive PVA. The presence of a cape allows this PVA to detach from the coast and wrap into a positive PVA pole. This process generates a cyclonic vortex downstream of the cape that in turn induces an offshore displacement of the outcropped front for small capes (cape 1 is 50 km long and 25 km wide), and in the generation of a thin filament parallel to the coast for the larger capes (cape 2 is 100 km long and 100 km wide). Superimposing the first cape with the reference promontory (third panel) leads to a long and thin filament pointing offshore and developing downstream of the cape. This combination of cape and promontory seems to be particularly efficient to generate the filament, because the cape alters the anticyclonic circulation on the promontory, so that the filament keeps on growing offshore instead of rolling up around the promontory.

29

187
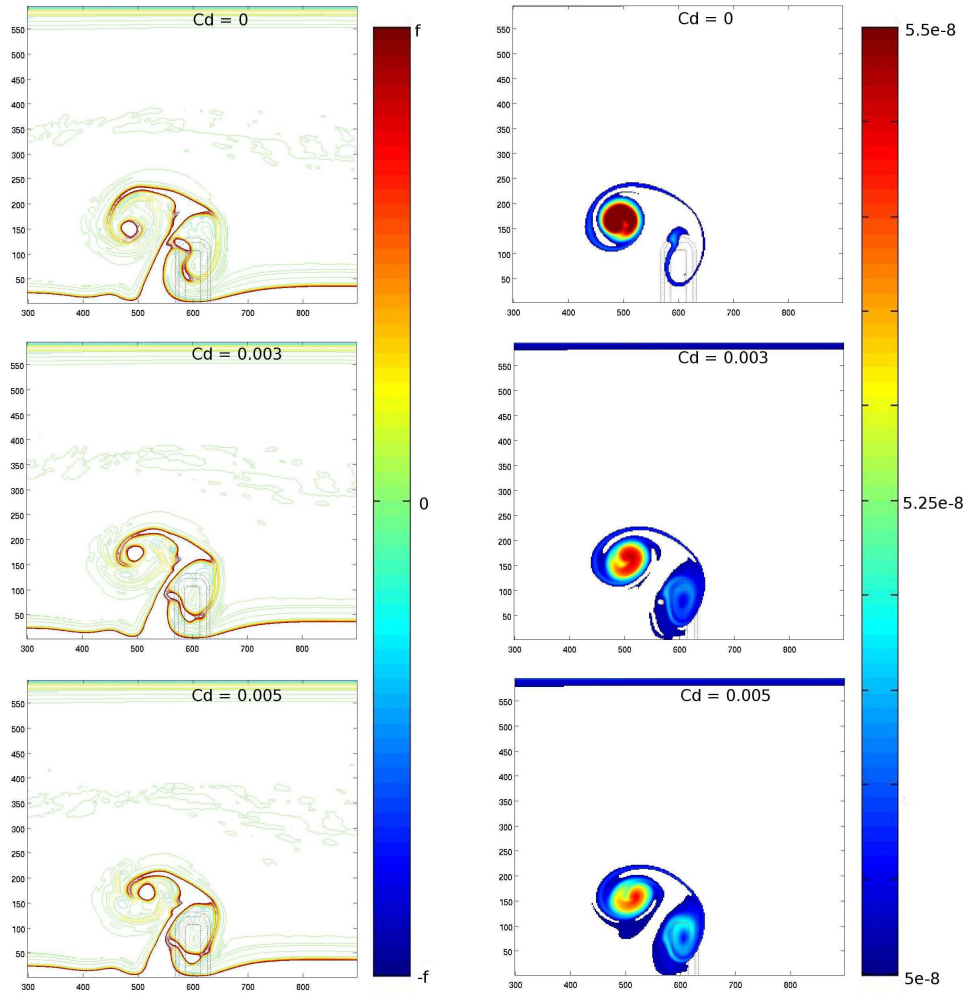
Figure 19: Maps of *PVA* in the upper (left hand panel) and bottom (right hand panel) layers at $t = 42$ days for the $C_d = 0, 3.10^{-3}$ and 5.10^{-3} Nm^{-2} experiments.

The lower panels in Fig. 20 show the effect of a canyon having the same shape as the reference promontory. Such a configuration generates a cyclonic circulation above the promontory and an anticylonic one downstream. As a result, the jetlike current between both eddies is now directed shoreward and can not generate a filament. However, the cyclonic circulation induces an offshore current upstream of the canyon that, even though associated with a much weaker current than the promontory case, can advect the upwelling front offshore. This is observed on Fig. 20 where a filament forms in the upper layer upstream of the canyon. Also notice that the upwelling front disapeared downstream of the promontory. There probably also exists an optimal shape of the canyon for the development of the filament, but this is beyond the scope of the present study and we simply conclude that canyons can also play an important role in the formation of trapped and long upwelling filaments.

5. Conclusion

5.1. Generation of long trapped filament by topographic effect

In this paper, we have studied the formation of long trapped upwelling filaments which are ubiquitous features in all major upwelling systems. We focused on the effect of bottom topography using an idealized two-layer configuration with a wind forcing that generates an upwelling front along a vertical coastal wall in the presence of a transverse promontory or ridge. The physical process studied is based on the formation of PVA when the upwelling current interacts with the bottom topography. At rest, in the bottom layer, the promontory is a positive potential vorticity anomaly pool, because the ambient potential vorticity is stronger over the promontory than in the rest of the domain. As the upwelling current sets up, this high potential vorticity gets advected downstream of the promontory by the alongshore current, and is replaced by lower potential vorticity water, generating a negative potential vorticity anomaly (*PVA*) over the promontory, and a positive potential vorticity anomaly downstream. The positive *PVA* is advected offshore by the trapped negative pole current field, and evolves into a cyclonic vortex eventually advected downstream. The negative *PVA* induces an anticyclonic circulation anomaly that remains trapped above the topography and, if it is strong enough, will modify the mean upwelling current. This produces a geostrophic offshore flow on the downstream side of the promontory which is able to distort the upwelling front and then forms a meander. The latter finally evolves into a thin filaments that grows offshore, and that may be sometimes slightly rolling up around the topographic eddies. The barotropic part of the circulation plays the main role in the latter process.

Then, we evaluated the influence of baroclinic instability on the formation of the meanders generated by topographic effects using stable and unstable configurations. The modelled stable current is able to generate a very large and stationary filament when interacting with topography whereas baroclinic instabilities of the jet produce additional numerous shorter meanders quickly propagating downstream that have a weak influence on the topographic filament development. The characteristics of the meanders and filaments associated with baroclinic instability are sensitive to the stratification and, as found in some previous studies (see [*Haidvogel et al.,* 1991, *Strub et al.,* 1991]), long filament can also emerge in this case, but the trapping of the filament and their development at identical locations can only be explained by topographic effects. The Southern North-West African upwelling system, offshore of Mauritania is a good example of the multiplicity of dynamics of the upwelling filaments : Recent satellite and in-situ observations (SOLAS-ICON cruise, unpublished yet) showed a whole range of filaments with different sizes, shapes and behaviour. The intrinsic instability of the upwelling

31
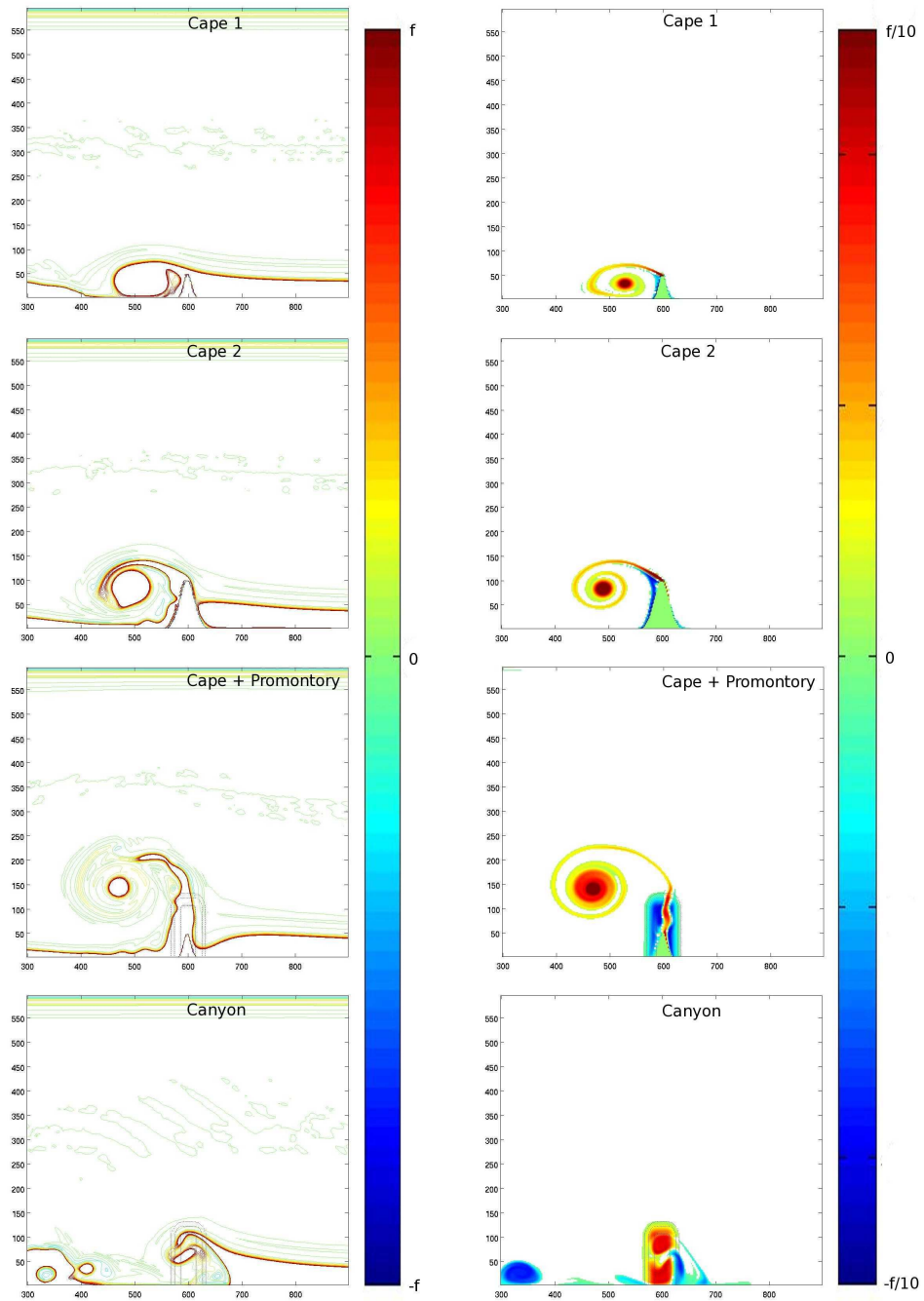
Figure 20: Maps of *PVA* in the upper (left hand panel) and bottom (right hand panel) layers at t = 42 days for the two capes experiments (panels 1 and 2), the cape over the promontory experiment (panel 3) and the canyon experiment (panel 4).

front generates pinched off meanders, developing and propagating all along the front, whereas a quasi permanent filament associated with an anticyclonic eddy is found over the Cape Blanc promontory.

We have also found that the deviation of the upwelling current by a cape and the generation of vorticity by the viscous boundary layer generate a cyclonic pool of cold water downstream of the cape rather than a long offshore filament. Thus, at least for the simplified configurations used in the present paper, the process involved in the generation of upwelling filaments at capes is rather associated with the submarine promontories that generally exist in their continuity, modifying the potential vorticity structure of the current as explained above.

The topographic eddies are generated by the barotropic circulation associated with the upwelling development. Their advective effect on the upwelling front as well as the formation of filaments are again associated with their barotropic vorticity. The process thus mainly involves the barotropic circulation. As a consequence, modifying the stratification does not strongly modify the mechanism we have identified, nor the generation of topographic filaments as long as the upwelling front is formed.

Increasing the duration of the wind forcing induces a further extension of the upwelling front, and intensifies the strength of the upwelling barotropic current but not of the topographic eddies. The cyclonic eddy detaching from the topography is thus advected further dowstream which, together with the change in the upwelling front extension, modify the characteristics of the filament. In our case the filament width increases and bends downstream when applying wind forcing for a longer time. Let us note that increasing the duration of the wind forcing also increases the source of diabatic *PV* generation (see [*Morel et al.,* 2006]) and thus the instability of the current. This was not investigated in the present paper, but we expect that, as a result, the relative importance of the unstable structure increases as the forcing lasts longer, so that a greater part of the offshore transport can be attributed to the instability of the jet in this case. This should however not change our conclusions on the trapping of long upwelling filaments.

Sensitivity tests to the shape of the topographic feature have shown that the width, height, length and slope of the topography are important parameters for the process. Multipolarisation of the *PVA*, decreasing the coherence and the length of the surface filaments, can occur in the case of a too wide or too tall promontory. The height of the promontory controls the available *PVA* pool, so that a too small promontory can not produce a large stationary filament, but neither can a very tall promontory above which flows and *PVA* can barely form. There exists optimal values of the topography characteristics to maximize the offshore extension of the filament. In other words, the formation of long trapped upwelling filaments by topographic features is a selective process and is restricted to some height, width, slope and length ranges.

5.2. Discussion and perspectives

The two-layer adiabatic model we have used is however very simplified and in nature, many other parameters and many additional processes, that have not been studied here, can influence the development of topographic eddies and formation of upwelling filaments, among which :

- the existence of an extended shelf and a continental slope ;

- the existence of a more complex and realistic large scale circulation (presence of a deep poleward undercurrent) associated with or preceeding the upwelling development;

- the influence of a more complicated stratification and of the specific dynamics of the mixed layer or the influence of mixing in general;

33

- the influence of the planetary β effect;

- the influence of bottom friction.

The beta effect seems of particular importance as it strongly influences the dynamics of eddies and induces westward propagation. We can thus imagine, for Eastern boundary upwellings, that any localized source of vortices such as bottom topography, but also capes, could favor the offshore development of filaments : indeed the cyclonic vortex developing downstream of a cape would be advected westward entraining upwelled cold waters and forming a localized filament instead of a circular patch as observed in the present study.

Another interesting subject is the influence of bottom friction. We have found here that its influence was weak, but this was expected since we considered a deep ocean. Bottom friction would obviously plays a stronger role than observed here for upwelling developing above shallow areas (corresponding to extended shelves). As its effect is to reduce the currents in the bottom layers, we expect this would limit the strength of the upwelling barotropic velocity and downstream transport.However, meanwhile it would also renew the reservoir of positive PVA above the promontory. As a result, after a period of relaxation of the winds, despite the fact that the initial positive PVA moved away from the topography, the same mechanism could be repeated for a new upwelling event.

However, even though these processes can have a strong influences on the result and their effect is worth investigating, we believe that they would not substantially modify our main result : the bottom topography plays a key role on the formation of the long upwelling filaments, whatever the direction of the current and details of the topography, *PVA* has to form when the flow passes over topography, developing a trapped circulation whose signature extends over the entire water column and influences the upper layer dynamics advecting water parcels offshore.

Finally, more in situ observations of early stage development of upwelling filaments are needed to confirm our results and the main influence of the barotropic circulation associated with topographic eddies. This implies a deep and extended mapping of the circulation.

6. Acknowledgements

34

References

[*Alvarez-Salgado et al.,* 2001] Alvarez-Salgado, X.A., M.D. Doval, A.V. Borges, I. Joint, M. Frankignoulle, E.M.S. Woodward, F.G. Figueiras, Off-shelf fluxes of labile materials by an upwelling filament in the NW Iberian Upwelling System. Progress in Oceanography, 51, 321-337, 2001.

[*Alvarez-Salgado et al.,* 2007] lvarez-Salgado, X.A., Arstegui, J., Barton, E.D., Hansell, D.A., Contribution of upwelling filaments to offshore carbon export in the subtropical Northeast Atlantic Ocean. Limnology and Oceanography, 52, 1287-1292, 2007.

[*Bang and Andrews,* 1974] Bang, N.D., and Andrews, W.R.H., Direct current measurements of a shelf-edge frontal jet in the southern Benguela system, Journal of Marine Research, 32, 407-421, 1974.

[*Barth,* 1989 a] Barth, J.A. Stability of a coastal upwelling front 1. Model developing and a stability theorem, Journal of Geophysical Research, Vol. 94, 10844-10856, 1989.

[*Barth,* 1989 b] Barth, J.A. Stability of a coastal upwelling front 2. Model results and comparison with observations, Journal of Geophysical Research, Vol. 94, 10857-10883., 1989.

[*Barth,* 1994] Barth, J.A. Short-wavelength instabilities on coastal jets and fronts, Journal of Geophysical Research, Vol. 98, 16095-16115, 1994.

[*Barton,* 2001] Barton, E.D., M.E Inall, T,J, Sherwin and R. Torres., Vertical structure, turbulent mixing and fluxes during Lagrangian observations of an upwelling filament system off Northwest Iberia, Progress in Oceanography, Vol. 51, 249-267, 2001.

[*Barton,* 2004] Barton, E.D., Aristegui, J., Tett, T. and Navarro-Pérrez, E., Variability in the Canary Islands Area of Filament-Eddy Exchanges, Progress in Oceanography, Vol. 62, 71-94, 2004.

[*Batteen,* 1997] Batteen, M.L., Wind-forced modeling studies of currents, meanders, and eddies in the California Current system Journal of Geophysical Research-Oceans, Vol 102, C1, 985-1010, 1997.

[*Batteen et al.,* 2007] Batteen, M.L., Martinho, A.S., Miller, H.A. and McClean, J.L., A Process-Oriented Study of the Coastal Canary and Iberian Current System, Ocean Modelling, vol. 18, 1-36, 2007.

[*Bleck and Boudra,* 1986] Bleck., R. and Boundra, D., Wind driven spin-up in eddy-resolving ocean models formulated in isopycnic and isobaric corrdinates, Journal of Geophysical Research, vol. 91, 7611-7621, 1986.

[*Bleck and Smith,* 1990] Bleck., R. and Smith, L., A wind driven isopycnic coordinate model of the North and equatorial Atlantic Ocean: Model development and supporting experiments Journal of Geophysical Research, vol. 95, 3273-3285, 1990.

[*Bleck et al.,* 1992] Bleck., R., Rooth, C., Hu, D., and Smith, L., 1992. Salinity driven thermocline transients in a wind and thermocline forced isopycnic coordinate model of the North Atlantic. Journal of Physical Oceanography, vol. 22, 1486-1505.

[*Brink,* 1983] Brink, K.H., The near-surface dynamics of coastal upwelling, Progress in Oceanography, vol. 12, 223-257, 1983.

[*Bretherton,* 1966] Bretherton, F.P., Critical layer instability in baroclinic flows, The Quarterly Journal of the Royal Meteorological Society, vol. 92, 325-334, 1966.

[*Capet and Carton,* 2004] Capet, X.J. and Carton, X.J. Nonlinear Regimes of Baroclinic Boundary Currents, Journal of Physical Oceanography, vol. 34, 14001409, 2004.

[*Charney and Stern,* 1962] Charney, J.G. and Stern, M.E., On the Stability of Internal Baroclinic Jets in a Rotating Atmosphere, Journal of the Atmospheric Sciences, vol. 19, 159172, 1962.

[*Dewey et al.,* 1991] Dewey, R.K., Moum, J.N., Paulson, C.A., Caldwell, D.R. and Pierce, S.D., Structure and Dynamics of a Coastal Filament, Journal of Geophysical Research, vol. 96, 14885-14907, 1991.

[*Flament et al.,* 1985] Flament, P., Armi, L. and Washburn, L., The Evolving Structure of an Upwelling Filament, Journal of Geophysical Research, vol. 90, 11765-11778, 1985.

[*Garvine,* 1971] Garvine, R.W., A simple model of coastal upwelling dynamics, Journal of Physical Oceanography, 1, 169-179, 1971.

[*Garvine,* 1973] Garvine, R.W., The effects of bahtymetry on the coastal upwelling of homogeneous water, Journal of Physical Oceanography, 3, 47-56, 1973.

[*Gill and Clarke,* 1974] Gill, A.E. and A.J., Clarke, Wind-induced upwelling, coastal currents and sea level changes, Deep-Sea Research, vol. 21, 325-345, 1974.

[*Haidvogel et al.,* 1991] Haidvogel, D.B., Beckmann, A. and HedStrm, K.S., Dynamical Simulations of Filament Formation and Evolution in the Coastal Transition Zone, Journal of Geophysical Research, vol. 96, 15017-15040, 1991.

[*Haynes et al.,* 1993] Haynes, R., Barton, E.D. and Pilling, I. Development, Persistence, and Variability of Upwelling Filaments, Journal of Geophysical Research, vol. 98, 22681-22692, 1993.

[*Herbette et al.,* 2003] Herbette, S., Morel, Y.G. and Arhan, M., Erosion of a surface vortex by a seamount, Journal of Physical Oceanography, vol. 33, (8):1664-1679, 2003.

35

683 [*Herbette et al.,* 2005] Herbette, S., Morel, Y.G. and Arhan, M., Erosion of a surface vortex by a seamount on the beta
684 plane, Journal of Physical Oceanography, vol. 35, (11):2012-2030, 2005.
685 [*Hoskins et al.,* 1985] Hoskins, B., McIntyre, M. and W. Robertson, On the use and significance of isentropic potential
686 vorticity maps, Quarterly Journal of the Royal Meteorological Society, vol. 111, 877-946, 1985.
687 [*Ikeda,* 1981] Ikeda, M., Meanders and Detached Eddies of a Strong Eastward-Flowing Jet Using a Two-Layer Quai-
688 Geostrophic Model, Journal of Physical Oceanography, vol. 11, 526-540, 1981.
689 [*Ikeda,* 1989] Ikeda, M., Lygre, K. and Sandven, S., A Process Study of Mesoscale Meanders and Eddies in the Norwe-
690 gian Coastal Current, Journal of Physical Oceanography, vol. 19, 20-35 1989.
691 [*Killworth,* 1980] Killworth, P.D., Barotropic and baroclinic instability in rotating stratified fluids, Dynamics of Atmo-
692 sphere and Ocean, vol. 4, 143-184, 1980.
693 [*Kostianoy and Zatsepin,* 1996] Kostianoy, A.G. and Zatsepin, A.G., The West African coastal upwelling filaments and
694 cross-frontal water exchange conditioned by them, Journal of Marine Systems, vol. 7, 349-359, 1996.
695 [*Lentz and Chapman,* 2004] Lentz, S.J. and D.C., Chapman, The importance of nonlinear cross-shelf momentum flux
696 during wind-driven coastal upwelling, Journal of Physical Oceanography, 34, 2444-2457, 2004.
697 [*Marchesiello et al.,* 2003] . Marchesiello, P., J. C. McWilliams and A. Shchepetkin, Equilibrium structure and dynam-
698 ics of the California Current System. J. Phys. Oceanogr., 33, 753-783, 2003.
699 [*McIntyre and Norton,* 1990] McIntyre, M., and W. Norton, Dissipative wave-mean interactions and the transport of
700 vorticity or potential vorticity, Journal of Fluid Mechanics, vol. 212, 403-435, 1990.
701 [*McWilliams and Gent,* 1980] McWilliams, J.C., and Gent, P.R., 1980. Intermediate models of planetary circulations in
702 the atmosphere and the ocean. Journal of Atmospherical Sciences, vol. 37, 1657-1678.
703 [*Morel and McWilliams,* 2001] Morel, Y. and McWilliams, J., Effects of Isopycnal and Diapycnal Mixing on the Sta-
704 bility of Oceanic Currents, Journal of Physical Oceanography, vol. 31, 2280-2296, 2001.
705 [*Morel et al.,* 2006] Morel, Yves, G., Darr, D. S. and C. Talandier, Possible sources driving the Potential Vorticity struc-
706 ture and long-wave instability of coastal upwelling and downwelling currents Journal of Physical Oceanography,
707 vol. 36, 875-896, 2006.
708 [*Navarro-Pérrez and Barton,* 1998] Navarro-Pérrez, E. and Barton, E.D., The Physical Structure of an Upwelling Fil-
709 ament off the North-West African Coast during August 1993, South African Journal of Marine Science, vol. 19,
710 61-73, 1998.
711 [*O'Brien and Hurlburt,* 1972] O'Brien, J.J. and Hurlburt, H.E., A numerical model of coastal upwelling, Journal of
712 Physical Oceanography, vol. 2, 1972.
713 [*Pringle,* 2002] Pringle, J.M., Enhancement of wind-driven Upwelling and Downwelling by alongshore bathymetric
714 variability, Journal of Physical Oceanography, 32, 31013112, 2002.
715 [*Relvas et al.,* 2007] Relvas, P., Barton, E.D., Dubert, J., Oliveira, P.B., Peliz, A., da Silva, J.C.B. and A.M.P. Santos,
716 Physical oceanography of the western Iberia ecosystem: Latest views and challenges, Progress in Oceanography,
717 74, 149-173, 2007.
718 [*Rossi et al.,* 2009] Rossi, V., Morel, Y. and Garcon, V., Effect of the wind on the shelf dynamics: Formation of a
719 secondary upwelling along the continental margin, Ocean Modelling, 2009, doi : 10.1016/j.ocemod.2009.10.002.
720 [*Roed and Shi,* 1999] Roed, L. P., and X. B. Shi, A numerical study of the dynamics and energetics of cool filaments,
721 jets and eddies off the Iberian Peninsula. Journal of Geophysical Research, 104(C12), 29817-29841, 1999.
722 [*Sanchez et al.,* 2008] R. F. Sanchez, P. Relvas, A. Martinho, and P. Miller, Physical description of an upwelling fil-
723 ament west of Cape St. Vincent in late October 2004, Journal of Geophysical Research, Vol. 113, C07044,
724 doi:10.1029/2007JC004430, 2008.
725 [*Shi and Roed,* 1999] X. B. Shi and Roed, L. P., Frontal Instabilities in a Two-Layer, Primitive Equation Ocean Model,
726 Journal of Physical Oceanography, Vol. 29, 948-968, 1999.
727 [*Stern and Chassignet,* 2000] M.E. Stern and E.P. Chassignet, Mechanism of eddy separation from coastal currents ,
728 Journal of Marine Research, Vol. 58, 269-295, 2000.
729 [*Strub et al.,* 1991] Strub, T.P., Kosro, P.M., and Huyer, A., The nature of the cold filaments in the California Current
730 System, Journal of Geophysical Research, vol. 96, 14743-14768, 1991.
731 [*Thomas,* 2005] Thomas, L.N., Destruction of potential vorticity by winds, J. Phys. Ocean., vol. 35, 2457-2466, 2005.
732 [*Verron and Le Provost,* 1985] Verron. J. and Le Provost, C., A numerical study of quasi-geostrophic flow over topog-
733 raphy, J. Fluid Mech., vol. 154, 231-252, 1985.
734 [*Viera and Grimshaw,* 1994] Viera, F. and Grimshaw, R., Topographic Forcing of Coastal Mesoscale Phenomena: Fil-
735 amentation, Vortex Formation, and Eddy Detachment, Journal of Physical Oceanography, vol. 24, 1433-1448,
736 1994.
737 [*Washburn and Armi,* 1988] Washburn, L. and Armi, L., Observations of Frontal Instabilities on an Upwelling Filament,
738 Journal of Physical Oceanography, vol. 18, 1075-1092, 1988.
739 [*Winther et al.,* 2007] Winther, N.G., Morel, Y.G. and Evensen, G., Efficiency of high order numerical schemes for
740 momentum advection, Journal of Marine Systems, vol. 67 (1-2), 31-46, 2007.

36

δt_t	δt_c	δx	N_x	N_y	N_{days}	ν	T_x	f	$H_2 + H_1$
5 s	200 s	2000 m	601 pts	301 pts	50 days	0.3 $m^2 s^{-1}$	-0.2 Nm^{-2}	10^{-4} s^{-1}	2050 m

Experiment	$d\rho$ (kgm^{-3})	Cd	H_1 (m)	Forcing duration (days)	H_t (m)	L_x (km)	L_y (km)	dL (km)
Ref	1	0	50	10	200	20	100	20
Inst	1	0	50	10	200	20	100	20
Notopo frc 10	1	0	50	10	0	0	0	0
Notopo frc 20	1	0	50	20	0	0	0	0
Notopo frc 30	1	0	50	30	0	0	0	0
Notopo frc 40	1	0	50	40	0	0	0	0
Cd 3e-3	1	3.10^{-3}	50	10	200	20	100	20
Cd 5 e-3	1	5.10^{-3}	50	10	200	20	100	20
frc time 20	1	0	50	20	200	20	100	20
frc time 30	1	0	50	30	200	20	100	20
frc time 40	1	0	50	40	200	20	100	20
H_t 50	1	0	50	10	50	20	100	20
H_t 100	1	0	50	10	100	20	100	20
H_t 300	1	0	50	10	300	20	100	20
H_t 500	1	0	50	10	500	20	100	20
H_t 1000	1	0	50	10	1000	20	100	20
H_t 1500	1	0	50	10	1500	20	100	20
L_x 0	1	0	50	10	200	0	100	20
L_x 50	1	0	50	10	200	50	100	20
L_x 100	1	0	50	10	200	100	100	20
L_y 50	1	0	50	10	200	20	50	20
L_y 150	1	0	50	10	200	20	150	20
L_y 200	1	0	50	10	200	20	200	20
dL 0	1	0	50	10	200	20	100	0
dL 10	1	0	50	10	200	20	100	10
dL 40	1	0	50	10	200	20	100	40
H_1 25	1	0	25	10	200	20	100	20
H_1 100	1	0	100	10	200	20	100	20
H_1 200	1	0	200	10	200	20	100	20
$d\rho$ 0.5	0.5	0	50	10	200	20	100	20
$d\rho$ 2	2	0	50	10	200	20	100	20
$d\rho$ 3	3	0	50	10	200	20	100	20

37

4.4   Résumé de l'article 3 (français).

Cet article est focalisé sur l'interaction entre un bombement topographique et une circulation d'upwelling. Suite à l'observation de processus de filamentation dans la simulation en trois dimensions présentée dans Rossi et al., 2010, nous avons initié cette étude basée sur des outils de modélisation similaires. Cette étude a été menée par Thomas Meunier dans le cadre de sa thèse.

Les filaments sont des structures couramment observées dans les zones d'upwelling et plusieurs mécanismes ont déjà été proposés pour expliquer leur formation (déstabilisation du courant barocline d'upwelling, effet beta, effet des caps et autres irrégularités de la ligne de côte et effet de la topographie). Cependant, certains filaments observés sur des images satellites ne peuvent s'expliquer par les théories antérieures. Ces filaments dits piégés présentent des dimensions importantes et se développent à des endroits préférentiels de la côte.

Nous avons donc étudié un upwelling idéalisé sous l'influence d'un vent favorable qui impose rapidement la mise en place de la circulation barotrope et barocline typique d'upwelling. Lorsque la circulation parallèle à la côte rencontre le promontoire, placé perpendiculairement à la côte, il se crée une modification du champ de VP sur le promontoire et aux abords de celui-ci dans la couche du fond, associée à des tourbillons topographiques. En particulier, la montée d'une colonne d'eau du bassin sur le plateau provoque une anomalie de VP négative sur le plateau associée à un tourbillon anticyclonique piégé. D'autre part, les colonnes d'eau initialement sur le promontoire sont advectées vers le bassin créant une anomalie de VP positive et une circulation cyclonique. Ces deux structures tourbillonnaires interagissent avec la couche superficielle et le front d'upwelling, créant ainsi un fin filament allongé piégé sur le promontoire. Cette nouvelle théorie et les caractéristiques des filaments piégés simulés sont en accord avec les observations satellitaires mentionnées précédemment. Ensuite, afin de mieux comprendre ce mécanisme, des tests de sensibilité sont réalisés. Nous avons montré que les instabilités baroclines ou les caps côtiers incriminés précédemment par d'autres auteurs, ne jouent pas de rôle significatif dans ce mécanisme. L'ajout d'un frottement sur le fond diminue légèrement les courants simulés, mais ne modifie pas l'occurrence d'un filament ni son analyse qualitative et permet le renouvellement du processus. Bien que le développement de filament soit ralenti, la modification de la stratification n'a pas non plus montré d'effet important, attestant de l'importance de la circulation barotrope dans notre configuration. Cependant, une augmentation de la durée du

forçage de vent aurait tendance à diminuer le développement du filament piégé par modification du champ de courant. Les caractéristiques géométriques du promontoire ont aussi une influence notable sur les structures filamentaires observées. La hauteur du promontoire gouverne le réservoir de VP et ainsi l'intensité des anomalies de VP, tandis que les autres paramètres comme les pentes et la largeur du promontoire peuvent créer une subdivision des structures aboutissant à plusieurs filaments moins cohérents. Il existe donc dans l'océan réel des dimensions particulières optimales de promontoire pour la formation de filaments, qui seront ainsi piégés sur cette zone.

Bien que des filaments soit souvent observés en face de caps, il semblerait que ce soit la topographie sous-jacente (promontoire) très souvent associée, plutôt que le cap lui-même, qui génère des anomalies de VP en interaction avec le courant et ainsi crée le filament piégé. Cependant, d'autres effets qui n'ont pas été considérés ici, tels que la circulation océanique globale, une topographie d'un plateau réaliste, l'influence du mélange, etc... peuvent aussi jouer un rôle. Cette étude a permis de démontrer sans ambiguïté l'effet important de la topographie sur la formation de filaments dans une zone d'upwelling.

Chapter 5

Biological activity and mesoscale horizontal stirring in the surface ocean of the 4 Eastern Boundary Upwelling Systems: a comparative study.

In the previous chapter, two physical processes occurring at mesoscale, namely filamental structures formation and a secondary upwelling front, were studied using numerical modelling. Their characteristics and their physical signature have been investigated, while we also mentioned the large influence they should have on the biology, especially in this coastal productive area. *Alvarez-Salgado et al.* [2007] and references therein already showed the large influence of a singular filament on the offshore export. Others (*Oschlies and Garçon* [1998, 1999]; *McGillicuddy et al.* [2003]) concentrated on the positive effect of mesoscale eddies on the production in the open ocean using global modelling studies. Since filaments and mesoscale eddies are ubiquitous features of upwelling areas, an interesting issue is to have an idea of their global average effect, as compared to the Ekman transport, on the planktonic ecosystem. This issue has not been addressed up to now and to do so, we used satellite data for estimating the surface currents and determining chlorophyll concentrations, comparing each EBUS. A recent tool applied to oceanographic data set, the FSLE detailed in Chapter 2, are computed to estimate horizontal stirring of these areas. Two articles are presented below and summarize our findings.

These two studies were led by myself and done in close collaboration with spanish colleagues, C. López and E. Hernández-García, for the use of the FSLE. In addition to challenging oceanographic perspectives, these studies also stimulated further work dealing with the method itself, as detailed in the *Conclusions* section.

Contents

5.1 Article 4: Comparative study of mixing and biological activity of the Benguela and Canary upwelling systems, Rossi *et al.*, 2008 Geophysical Research Letters

Click Here for Full Article

Comparative study of mixing and biological activity of the Benguela and Canary upwelling systems

V. Rossi,[1] C. López,[2] J. Sudre,[1] E. Hernández-García,[2] and V. Garçon[1]

[1]   We present a comparative study of the horizontal mixing properties, from satellite derived data of the surface velocity field, of the two eastern boundary Canary and Benguela upwelling systems, based on a Finite Size Lyapunov Exponents analysis. Each area can be subdivided into two subsystems attending to their mixing activity values. These coincide nicely with distinct biological signatures. When investigating links with chlorophyll as a proxy for biological activity in these two upwelling systems, results show that surface horizontal stirring and mixing vary inversely with chlorophyll standing stocks. Ekman-transport induced upwelling exhibits a positive correlation with chlorophyll. These two findings are complementary since spatial structure in plankton distributions results from both dynamics of the $3D$ turbulent medium and of the marine ecosystem. **Citation:** Rossi, V., C. López, J. Sudre, E. Hernández-García, and V. Garçon (2008), Comparative study of mixing and biological activity of the Benguela and Canary upwelling systems, *Geophys. Res. Lett.*, *35*, L11602, doi:10.1029/2008GL033610.

1.   Introduction

[2]   Eastern boundary upwelling zones constitute a major contribution to the world ocean productivity. They include the Canary and Benguela upwelling systems (hereafter CUS and BUS, respectively), located along the African coast symmetrically with respect to the Equator. Both areas are characterized, among other features, by a significant equatorward alongshore advection, physical forcings by local and large scale winds, a high sub- and mesoscale activity, seaward extension beyond the continental shelf of the boundary current and an intense biological activity via filament formation.

[3]   The aim of this work is to make a comparative study of these two upwelling systems, focussing on their mesoscale activity and the interaction between marine surface hydrodynamics and biological processes (similar studies in other upwelling systems can be consulted [e.g., see *Chase et al.*, 2007].

[4]   The basic inputs to our analysis are satellite data of the marine surface, including velocity field and chlorophyll concentration. We quantify horizontal transport processes by the well-known technique of the Finite Size Lyapunov Exponents (FSLE) [*Aurell et al.*, 1997], which is specially

suited to study the stretching and contraction properties of transport in geophysical data [*d'Ovidio et al.*, 2004]. The calculation of the FSLE goes through computing the time, τ, at which two fluid parcels initially separated at a distance δ_0, reach a final separation δ_f. At position $\mathbf{x}$ and time t the FSLE is given by $\lambda\,(\mathbf{x},\ t,\ \delta_0,\ \delta_f) = \frac{1}{\tau}\log\frac{\delta_f}{\delta_0}$. In a typical snapshot of the FSLE [see e.g. *d'Ovidio et al.*, 2004, Figure 1] the maximum values organize in lines which are a good approximation for the areas of maximal convergence, if they are calculated for the backwards-in-time dynamics, which is the one performed all along this work. In work by *d'Ovidio et al.* [2004, also, Comparison between Eulerian diagnostics and finite-size Lyapunov exponents computed from altimetry in the Algerian basin, submitted to Deep Sea Research, 2008] and *Lehahn et al.* [2007] the adequacy of the FSLE to characterize horizontal mixing and transport structures in the upper ocean has been demonstrated, as well as its usefulness, when correlating with distributions of tracers such as temperature or chlorophyll, despite the strong intrinsic dynamics of these tracers. In particular, it is discussed that FSLEs, because of the averaging effect produced by computing them by integrating over trajectories which extend in time and space, are rather robust against noise and uncertainties in the velocity data. Here we have checked this explicitly by considering a random perturbation of the velocity field at every spatial point at any time. The error obtained in our computations of averages of FSLEs ranges between 0.3% and 2.8% for multiplicative perturbations of the velocity field of 5% and 10%, respectively. In addition, spatial averages of FSLEs can define a measure of mixing in a given spatial area, the larger this average the larger the mixing activity. Inverses of FSLEs values give estimations of mixing times. We will use the FSLEs as an analyzer tool to highlight differences and similarities between the CUS and BUS. Finally, we quantify the amount of Ekman-transport induced upwelling and find a positive correlation with chlorophyll standing stocks. We discuss how vertical and horizontal processes may lead to the observed chlorophyll distributions.

2.   Data
2.1.   Computation and Analysis Areas

[5]   Our study focuses on the transitional area of exchange processes between the shelf and offshore in the open ocean. Among these processes, sub- and mesoscale structures such as filaments contribute to the offshore export of organic matter produced in the very coastal upwelling [*Mackas et al.*, 2006]. These filaments in the fluctuating boundary between the upwelling and the edge of the oligotrophic subtropical gyres play a key role in the modulation of the carbon balance by seeding the inner ocean. The role of this

---

[1]LEGOS/CNRS, Toulouse, France.
[2]Instituto de Física Interdisciplinar y Sistemas Complejos, Universitat de les Illes Balears, Palma de Mallorca, Spain.
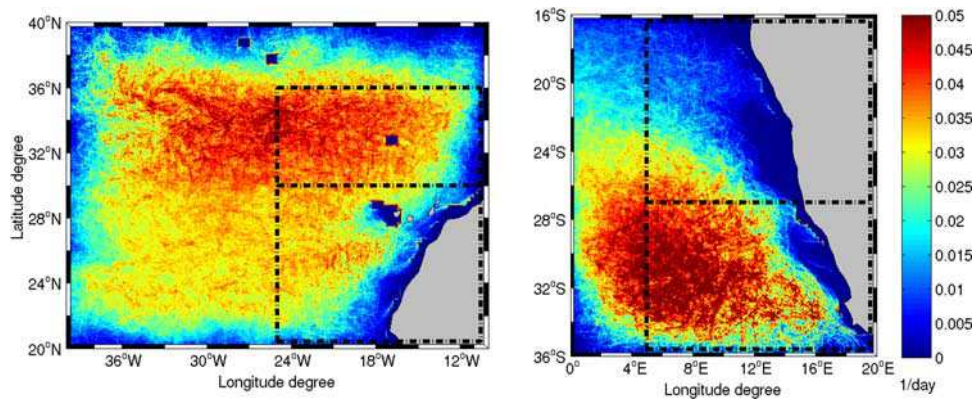
Figure 1. Time average over the period June 2000–June 2005 of the FSLEs (left) for the CUS and (right) for the BUS. The boxes denote the analysis areas of our study. The central horizontal line in each plot divides the two subregions.

moving transitional area, at the border of the gyre, westward of the maximum extension of the chlorophyll filaments, must be considered. To investigate the island effect from the Canary Archipelago and to have, at the same time, a similar analysis area for CUS and BUS, we have adapted the areas from *Mackas et al.* [2006], by approximating them to the best fitting rectangle whose lateral sides are meridionally oriented. In Figure 1, the analysis areas are shown delimited by the dashed lines ($25–10°W$, $20–36°N$ for CUS and $5–20°E$, $16–36°S$ for BUS). We used the full geographical areas shown in Figure 1 to make our numerical computations. Note that the computation areas are larger than the analysis ones, considering the fact that particles may leave the area before reaching the fixed final distance δ_f. In addition, several tests with different shapes and area selections (not shown) lead to similar results.

2.2. Velocity and Wind Stress Data

[6] The weekly global $1/4°$ resolution product of surface currents developed by *Sudre and Morrow* [2008] has been used. The surface currents are calculated from a combination of wind-driven Ekman currents, at 15 m depth, derived from Quickscat wind estimates, and geostrophic currents computed from time variable Sea Surface Heights. These SSH were calculated from mapped altimetric sea level anomalies combined with a mean dynamic topography from *Rio et al.* [2005]. These weekly velocity data, which are then interpolated linearly to obtain a daily resolution, depend on the quality of their sources as the SSH fields and the scatterometer precision. However, they were validated by *Sudre and Morrow* [2008] with different types of in situ data such as Lagrangian buoys, ADCP, and current-meter float data. In both areas, zonal and meridional components show an average correlation with for e.g. Lagrangian buoy data, between 0.52 and 0.76. The Ekman transport U_E along the East-West direction was computed using the formula $U_E = T_y/(f\rho)$ where T_y is the meridional wind stress (obtained from the scatterometer Quickscat weekly wind estimates), ρ is the density of seawater and f is the Coriolis parameter.

2.3. Chlorophyll Data

[7] A 5 year long time series from June 2000 to June 2005 of ocean color data is used. Phytoplankton pigment concentrations are obtained from monthly SeaWiFS (Sea-viewing Wide Field-of-view Sensor) products of level 3 binned data, generated by the NASA Goddard Earth Science (GES)/Distributed Active Archive Center (DAAC) with reprocessing 5.1. The bins correspond to grid cells on a global grid, with each cell approximately 9 by 9 km.

3. Results

3.1. Horizontal Mixing Properties

[8] In Figure 1 we draw the time average (covering the period June 2000 – June 2005) of the FSLE computed for the CUS and BUS. Following *d'Ovidio et al.* [2004] the prescribed length-scales in our analysis are $\delta_0 = 0.025°$ and $\delta_f = 1°$ so that we focus on the mesoscale horizontal features. Choosing a slightly different value of δ_f does not alter qualitatively our results (see caption of Figure 2). For both the CUS and BUS, two different subsystems, according to their mixing activity, can be defined: north and south of $30°N$ for the CUS, and north and south of $27°S$ (latitude of the intense Lüderitz upwelling cell) for the BUS. Comparing both zones, the most clear distinction is that while in the BUS the subdivision in two areas of activity is rather evident, in the CUS this is not so sharp. Note also that the imaginary division line passes north of the Canary Archipelago.

[9] A further detailed comparison between the different subsystems follows by considering the averages of the FSLEs over the analysis areas. Results indicate similar values for the horizontal mixing times in the most active subsystems of both regions, ranging from 26 to 40 days. On the contrary, the least active subsystem in the Canary has much larger values for the FSLEs than the least active one in the BUS. While in the CUS the mixing times are in the range $37–56$ days, in the BUS this is $53–90$ days.

[10] *Waugh et al.* [2006] found a close relationship between the mean FSLE and the mean eddy kinetic energy (EKE) in the Tasman Sea. We have confirmed that a geographical subdivision similar to the one in Figure 1 is obtained from EKE. However, a clear relationship between these two quantities does not appear. Indeed, the Eulerian diagnostic EKE calculated for a given day only considers the corresponding snapshot of the velocity field and can not catch any temporal variability whereas the FSLE Lagrangian method does. Thus a robust relationship between EKE and FSLE is not expected when velocity fields are highly
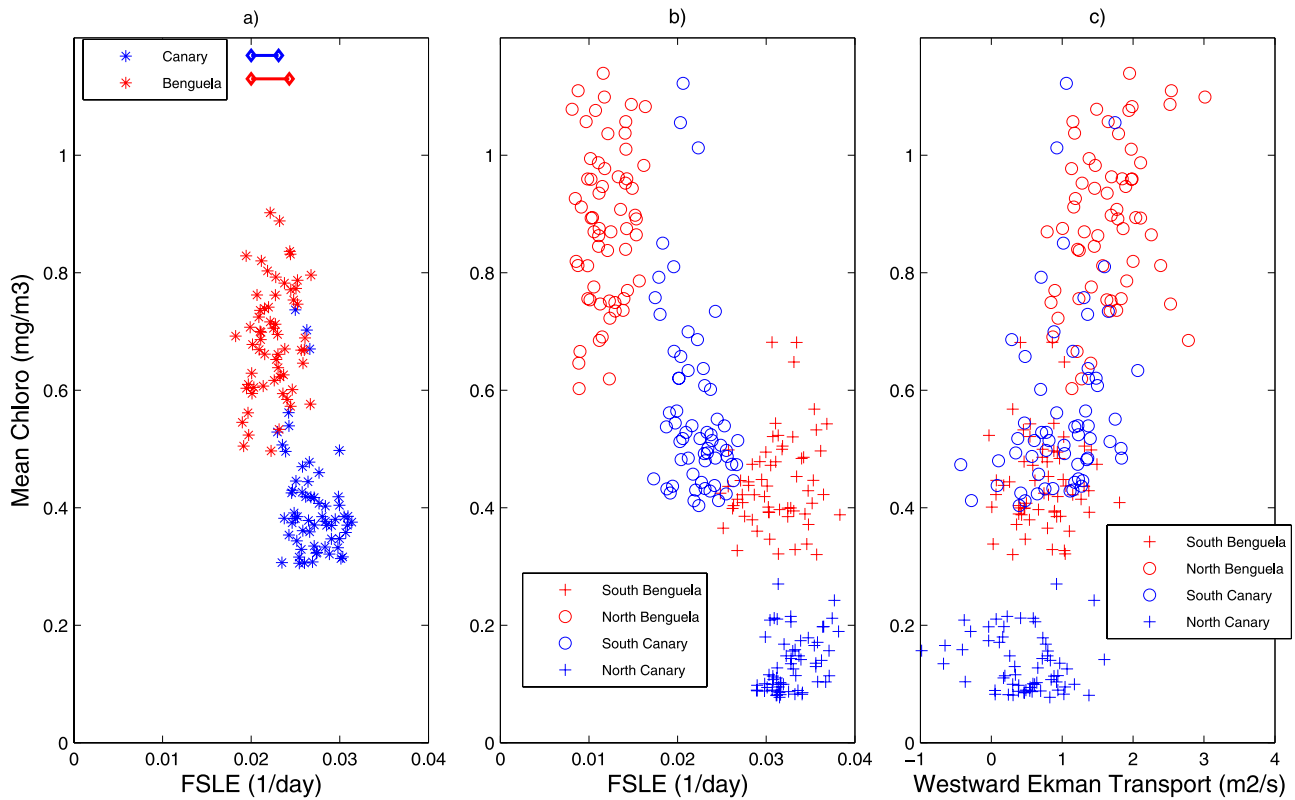
Figure 2. (a) Monthly-mean chlorophyll concentrations versus FSLE for the whole area: blue asterisks for CUS and red for BUS. Each horizontal bar represents the spatial averaged standard error of a FSLE mean for each domain, BUS (red) and CUS (blue). These errors were calculated at each grid point from temporal FSLE means over the 5 years time series. (b) Same for the different subregions as denoted in the legend. (c) Same as Figure 2b but for monthly-mean chlorophyll concentrations vs Ekman transport. The correlation coefficient for all the data in a) is $R^2 = -0.62$. This coefficient changes to -0.53, and -0.66, when changing δ_f to $\delta_f = 0.8°$ and $\delta_f = 1.2°$, respectively. If we consider the different subregions in b), the correlation coefficient is $R^2 = -0.83$. For $\delta_f = 0.8°$ and $\delta_f = 1.2°$, it becomes -0.80 and -0.85, respectively.

variable. A detailed study of the relation between FSLE and Eulerian measurements is given by d'Ovidio et al. (submitted manuscript, 2008).

3.2. Biological Activity

[11] We study here the correlation of the FSLEs (horizontal mixing) with chlorophyll concentration data. Hovmöller plots of the surface chlorophyll distribution in both the BUS and CUS (not shown here) reveal the existence of two spatial zones with very distinct degree of chlorophyll in each upwelling system. The lines separating them (around 30°N for CUS and 27°S for BUS) coincide with those obtained from the FSLE analysis.

[12] If one plots spatial averages of chlorophyll concentration versus spatial averages of FSLE, over the entire analysis area (Figure 2a) and over each subsystem (Figure 2b), for each month from June 2000 to June 2005, a negative correlation between FSLEs and chlorophyll concentration emerges. For both areas, the subsystems with more mixing activity are the ones poorer in chlorophyll. This is in the line of *Gruber et al.* [2007] findings of meso and sub-mesoscale processes associated to reduced biological activity in coastal upwelling systems. We note that theoretical studies in idealized settings, in which nutrients reach plankton only by lateral stirring, display also negative correlation between

mixing and biomass (although mixing and productivity may be positively correlated) [*Tél et al.*, 2005; *Birch et al.*, 2007].

[13] Upwelling areas are definitely affected by water vertical movements and velocities which are not captured by the surface analysis provided by FSLEs. Thus, the vertical part of the physical forcing will be taken in consideration in the following. Moreover, we examine the influence of Ekman transport which brings nutrients from the coast and can also play a very relevant role in the chlorophyll signature.

[14] First we evaluate the horizontal divergence of the surface velocity field: $\Delta(x, y, t) \equiv \partial_z v_z = -(\partial_x v_x + \partial_y v_y)$. Negative (positive) values of Δ indicate upwelling (downwelling) areas because it signals surface spatial points where fluid parcels diverge (converge). Figure 3 shows the average value of Δ over the period June 2000–June 2005 for the CUS and BUS. The blue color of the Δ field in the coastal areas indicates the presence of upwelling processes there. Note that in the coastal zones of the Benguela, the well known upwelling cells Cape Frio, Walvis Bay and Lüderitz in the northern subsystem appear clearly, being more intense than the southern cells, in agreement with *Monteiro*'s [2008] estimates of the northern system accounting for 80%, on average, of the total upwelled flux over the whole BUS.
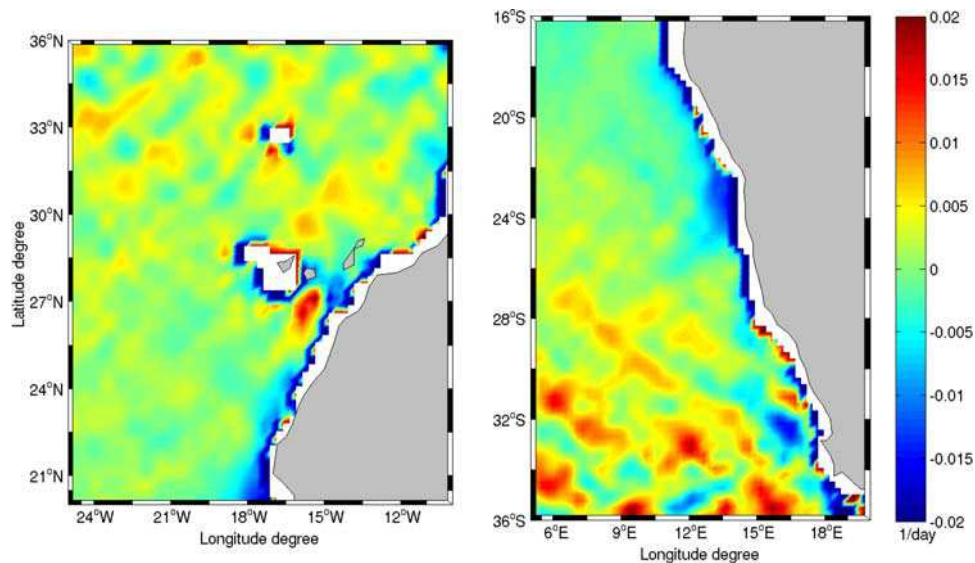
Figure 3. Temporal average value of the field $\Delta\,(x,\,y,\,t) \equiv \partial_z\,v_z = -(\partial_x\,v_x + \partial_y\,v_y)$ over the period June 2000–June 2005 for (left) CUS and (right) BUS. The blue color indicates upwelling areas whereas red signals downwelling ones.

Concerning the CUS (Figure 3, left) one can see a slight blue-color predominancy (enhanced upwelling) in the southern subregion.

[15] When we compute the Ekman transport we observe that the northern region of the BUS, richer in chlorophyll, is characterized by a higher offshore transport. In the CUS, both sub-areas have high values for the offshore transport very close to the coast, with similar values in the southern and northern subregions. Further from the coast, the highest westward transport in the southern CUS area coincides again with the highest chlorophyll content. Figure 2c shows spatial averages of chlorophyll concentration vs averages of Ekman transport over each subsystem. Negative values of the average from June 2000 to June 2005 indicate an offshore transport to the east, whereas positive ones indicate a transport to the west. A positive correlation appears confirming the effect of Ekman-transport induced upwelling on biological productivity. This finding is not incompatible with the distinct clustering (Figures 2a and 2b) since horizontal currents are strongly related to the vertical circulation. Creation of sub- and mesoscale surface chlorophyll structures results from the full 3D turbulent motion of the ocean.

4. Summary and Conclusions

[16] The distribution of FSLEs computed over a 5 year period with state of the art velocity fields derived from multiple sensors (altimeter, scatterometer) allowed us to compute horizontal stirring rates in the surface ocean of two major eastern boundary upwelling systems of the Atlantic ocean: the Canary and Benguela systems. A clear subdivision within each system appeared according to the mixing activity, coinciding with distinct levels of chlorophyll richness.

[17] Previous studies have suggested that eddies tend to enhance biological productivity in the open ocean, particularly in low nutrient environments. Finding a negative correlation between horizontal mixing and chlorophyll standing stocks suggests that this may not apply to upwelling regions. Comparing Figures 1 and 3 shows that areas characterized by high FSLE are correlated with intense vertical movements (downwellings as well as upwellings), whereas the areas with low FSLE are mainly dominated by upwards vertical velocities (upwellings). *Lehahn et al.* [2007] recently showed that vertical motions associated with eddies are more precisely located close to the lines of high FSLE. Regions of high FSLE averages indicate a high occurrence of intense eddies which modify the three dimensional mean flow. The nutrient Ekman pumping, dominant process in upwelling areas, weakened and the fueling of nutrients toward the surface decreased.

[18] Another possible explanation may rest upon the fact that upwelling from deeper waters and offshore Ekman transport of nutrients are important mechanisms for surface-waters enrichment. In the areas where the Ekman drift dominates over mesoscale activity, like in the northern BUS and southern CUS, a large dispersion of fluid particles, i.e., large values of FSLEs, does not occur. This would also indicate that the horizontal turbulent mixing of nutrients in surface waters is a second-order effect for biomass enhancement as compared to the vertical mechanisms.

[19] Other factors may of course influence the phytoplanktonic biomass. *Chase et al.* [2007] for instance showed in the upwelling system of the U. S. West Coast that there is a link between chlorophyll concentration and iron availability through river inputs and shelf deposition/re-suspension processes. In our two systems BUS and CUS exhibiting a larger shelf than that of the U.S. West coast, the very low river runoff can not deliver any major iron input to the inner shelf. Moreover, high dust deposition occurs leading to non-limiting iron concentration in both systems [*Jickells et al.*, 2005; *Mackas et al.*, 2006]. Consequently we did not consider these controls as primary factors in our analysis. Further work should investigate the robustness of the relationship found in our two systems when examining FSLEs versus production. Still much needs to be done to fully understand how plankton distributions are controlled

by the interplay between their turbulent medium and the non-linear processes of their ecology. However FSLEs lead to a clear clustering of subsystems suggesting that one may use these simple Lagrangian diagnostics as integrated and comparative indices for characterizing horizontal dynamical features in all eastern boundary upwellings.

References

Aurell, E., G. Boffetta, A. Crisanti, G. Paladin, and A. Vulpiani (1997), Predictability in the large: An extension of the concept of Lyapunov exponent, *J. Phys. A Math Gen.*, *30*, 1–26.

Birch, D. A., Y.-K. Tsand, and W. R. Young (2007), Bounding biomass in the Fisher equation, *Phys. Rev. E*, *75*, 066304, doi:10.1103/PhysRevE.75.066304.

Chase, Z., P. G. Strutton, and B. Hales (2007), Iron links river runoff and shelf width to phytoplankton biomass along the U. S. West Coast, *Geophys. Res. Lett.*, *34*, L04607, doi:10.1029/2006GL028069.

d'Ovidio, F., V. Fernández, E. Hernández-García, and C. López (2004), Mixing structures in the Mediterranean Sea from finite-size Lyapunov exponents, *Geophys. Res. Lett.*, *31*, L17203, doi:10.1029/2004GL020328.

Gruber, N., H. Frenzel, P. Marchesiello, J. C. McWilliams, T. Nagai, and G.-K. Plattner (2007), On the role of eddies for coastal productivity and carbon export to the open ocean, *Geophys. Res. Abstr.*, *9*, 07743.

Jickells, T. D., et al. (2005), Global iron connections between desert dust, ocean biogeochemistry, and climate, *Science*, *308*, 67–71.

Lehahn, Y., F. d'Ovidio, M. Lévy, and E. Heyfetz (2007), Stirring of the northeast Atlantic spring bloom: A Lagrangian analysis based on multi-satellite data, *J. Geophys. Res.*, *112*, C08005, doi:10.1029/2006JC003927.

Mackas, D., P. T. Strub, A. C. Thomas, and V. Montecino (2006), Eastern ocean boundaries pan-regional view, in *The Sea*, vol. 14a, *The Global Coastal Ocean: Interdisciplinary Regional Studies and Syntheses: Pan-Regional Syntheses and the Coasts of North and South America and Asia*, edited by A. R. Robinson and K. H. Brink, chap. 2, pp. 21–60, Harvard Univ. Press, Cambridge, Mass.

Monteiro, P. M. S. (2008), Carbon fluxes in the Benguela Upwelling system, in *Carbon and Nutrient Fluxes in Continental Margins: A Global Synthesis*, edited by K. K. Liu et al., chap. 2.4, Springer, New York, in press.

Rio, M.-H., P. Schaeffer, F. Hernández, and J.-M. Lemoine, (2005), The estimation of the ocean Mean Dynamic Topography through the combination of altimetric data, in-situ measurements and GRACE geoid: From global to regional studies. paper presented at GOCINA Workshop, Cent. Eur. de Geodyn. et de Seismol., Kirchberg, Luxembourg.

Sudre, J., and R. Morrow (2008), Global surface currents: A high resolution product for investigating ocean dynamics, *Ocean Dyn*, in press.

Tél, T., A. de Moura, C. Grebogi, and G. Karolyi (2005), Chemical and biological activity in open flows: A dynamical system approach, *Phys. Rep.*, *413*, 91–196.

Waugh, D., E. Abraham, and M. Bowen (2006), Spatial variations of stirring in the surface ocean: A case study of the Tasman Sea, *J. Phys. Oceanogr.*, *36*(3), 526–542.

_____

V. Garçon, V. Rossi, and J. Sudre, LEGOS/CNRS, Toulouse, F-31401 CEDEX 9, France. (veronique.garcon@legos.obs-mip.fr)

E. Hernández-García and C. López, Instituto de Física Interdisciplinar y Sistemas Complejos IFISC, Campus Universitat de les Illes Balears, E-07122 Palma de Mallorca, Spain.

5.2   Résumé de l'article 4 (français).

Dans cet article une analyse comparative est réalisée entre le mélange horizontal de surface et l'activité biologique associée dans les deux zones d'upwelling de bord Est (EBUS) de l'océan Atlantique, les upwellings du Benguela et des Canaries. Le calcul des FSLE (Finite-Size Lyapunov Exponents), décrit au Chapitre 1, est basé sur des courants horizontaux provenant de produits satellitaires (altimétrie et diffusiométrie). Il permet ici d'étudier le mélange horizontal à mésoéchelle de l'océan de surface au sein des 2 EBUS. Des données mensuelles de concentration de chlorophylle a issues du satellite SeaWiFS sont utilisées comme indicateur de l'activité biologique sur la période Juin 2000 – Juin 2005. Une comparaison de l'activité de mélange dans les deux zones étudiées, nous amène à les diviser en deux sous-systèmes qui présentent des niveaux de turbulence bien distincts. La même distinction se retrouve sur des diagrammes Hovmöller temps/latitude de la teneur en chlorophylle a de surface, les zones les plus riches en chlorophylle étant associées aux sous-systèmes présentant les FSLEs les plus faibles. Le mélange horizontal de surface est ainsi corrélé négativement aux stocks de chlorophylle a. Afin de mieux comprendre les mécanismes impliqués dans cette relation négative, le transport d'Ekman et les vitesses verticales (estimées à partir de l'incompressibilité du champ de vitesse 2D) sont étudiés. La corrélation positive, déjà mentionnée dans des travaux antérieurs, entre la concentration de chlorophylle a et le transport d'Ekman vers l'ouest est confirmée, tandis que les sous-systèmes les plus turbulents sont caractérisés globalement par de moindres mouvements verticaux dirigés vers la surface (ceux favorables à la biologie). L'activité mésoéchelle, comme les tourbillons qui modifient le champ de vitesses en 3 dimensions, semble ainsi diminuer l'apport dans la zone euphotique de nutriments en freinant globalement les courants d'upwelling dirigés vers la surface. Bien que la dynamique intrinsèque de l'écosystème (non considérée dans cette étude) joue un rôle important sur la chlorophylle a, des études théoriques ont déjà mis en évidence un effet négatif du mélange sur les biomasses phytoplanctoniques simulées. Ce résultat original contraste avec l'effet positif connu qu'ont ces structures sur l'écosystème oligotrophe du large.

5.3 Article 5: Horizontal stirring and biological activity in the surface ocean of the four Eastern Boundary Upwelling Systems, Rossi *et al.*, 2009 Nonlinear Processes in Geophysics

Reference : Rossi, V., C. López, J. Sudre, E. Hernández-García, Morel Y. and V. Garçon. 2009. Horizontal stirring and biological activity in the surface ocean of the four Eastern Boundary Upwelling Systems, Nonlinear Processes in Geophysics, 16, p 557-568.

**Nonlinear Processes
in Geophysics**

Surface mixing and biological activity in the four Eastern Boundary Upwelling Systems

V. Rossi[1,2], **C. López**[2], **E. Hernández-García**[2], **J. Sudre**[1], **V. Garçon**[1], **and Y. Morel**[3]

[1]Laboratoire d'Études en Géophysique et Océanographie Spatiale, CNRS, Observatoire Midi-Pyrénées, 14 avenue Edouard Belin, Toulouse, 31401 Cedex 9, France
[2]Instituto de Física Interdisciplinar y Sistemas Complejos IFISC (CSIC-UIB), Campus Universitat de les Illes Balears, 07122 Palma de Mallorca, Spain
[3]Service Hydrographique et Océanographique de la Marine, (SHOM), 42 avenue Gaspard Coriolis, 31057 Toulouse, France

Abstract. Eastern Boundary Upwelling Systems (EBUS) are characterized by a high productivity of plankton associated with large commercial fisheries, thus playing key biological and socio-economical roles. Since they are populated by several physical oceanic structures such as filaments and eddies, which interact with the biological processes, it is a major challenge to study this sub- and mesoscale activity in connection with the chlorophyll distribution. The aim of this work is to make a comparative study of these four upwelling systems focussing on their surface stirring, using the Finite Size Lyapunov Exponents (FSLEs), and their biological activity, based on satellite data. First, the spatial distribution of horizontal mixing is analysed from time averages and from probability density functions of FSLEs, which allow us to divide each areas in two different subsystems. Then we studied the temporal variability of surface stirring focussing on the annual and seasonal cycle. We also proposed a ranking of the four EBUS based on the averaged mixing intensity. When investigating the links with chlorophyll concentration, the previous subsystems reveal distinct biological signatures. There is a global negative correlation between surface horizontal mixing and chlorophyll standing stocks over the four areas. To try to better understand this inverse relationship, we consider the vertical dimension by looking at the Ekman-transport and vertical velocities. We suggest the possibility of a changing response of the phytoplankton to sub/mesoscale turbulence, from a negative effect in the very productive coastal areas to a positive one in the open ocean. This study provides new insights for the understanding of the variable biological productivity in the ocean, which results from both dynamics of the marine ecosystem and of the 3-D turbulent medium.

1 Introduction

Although they represent only a very small fraction of the total surface of the world's ocean, the Eastern Boundary Upwelling Systems (EBUS) are the most productive regions of the world due to their important coastal biological productivities which support large commercial fisheries, up to 20% of the global fish catch (Pauly and Christensen, 1995). They include the Canary (CUS) and the Benguela upwelling systems (BUS) in the Atlantic Ocean and the Peru/Chile (or Humboldt HUS) and California upwelling systems (CalUS) in the Pacific Ocean. Under the action of wind from quasi-stationary high pressure cells over the subtropical ocean basins, a surface uprising of deep cold water rich in nutrients occurs over continental shelves almost all year long. This process explains the high primary production in these regions which constitutes the base of a highly dynamical and rich food chain. Roughly, the intensity of coastal upwelling is modulated by the force and direction of the wind, by the local topography and by the ambient oceanic characteristics.

These EBUS are spatially and temporally heterogeneous from both a physical and biological point of view. The development of diverse structures such as intense fronts, coastal plumes in retention areas, offshore filaments and eddies interplays with the complex spatial distribution of phytoplankton. This mesoscale and sub-mesoscale oceanic turbulence is known to strongly modulate the structure, biomasses and rates of marine ecosystems, since it can stimulate the primary productivity (McGillicuddy et al., 1998; Oschlies and Garçon, 1998), affect plankton community composition (Owen, 1981; Kang et al., 2004; Mackas et al., 2005) and play a significant role in exchange processes in the transitional area between the productive coastal zone and the oligotrophic open ocean by transporting organic matter and marine organisms from the coast to the open ocean (Moore et al., 2007). This latter mechanism, i.e. the large coastal

Published by Copernicus Publications on behalf of the European Geosciences Union and the American Geophysical Union.

209

productivity and its export to the inner ocean via filament formation, identifies them as key regions in the global marine element cycles, such as carbon and nitrogen (Mackas et al., 2006).

While sharing common bio-physical characteristics, their biological productivity is highly variable and governed by diverse factors and their interaction, which are still poorly understood. Several previous comparative studies investigated these major environmental factors and leading physical processes that may control it. When considering all EBUS together, Carr and Kearns (2003) showed that phytoplankton productivity results from a combined effect of large-scale circulation and local factors. Patti et al. (2008) suggested that several driving factors, as nutrients concentration, light availability, shelf extension and among others a surface turbulence proxy from a wind-mixing index, must be taken into account when investigating the phytoplankton biomass distribution. Globally, their statistical study pointed out that all these factors are playing a role whereas they are acting at different levels on the productivity. It is then highly relevant to consider an original Lagrangian measure of mixing for comparative approach among EBUS.

The aim of this study is first to quantify and compare the mixing activity in the EBUS using the technique of the Finite-Size Lyapunov Exponents. The spatial distribution and the temporal evolution of the mixing and stirring activity is analysed. The link between turbulence and chlorophyll concentration (as a proxy for biological activity) is then investigated, leading to propose some underlying mechanisms behind the relationship revealed. Finally, we discuss previous comparative approaches performed among these EBUS with new insights from the present mixing analysis.

2 Methods

The basic ingredients of our comparative analysis are satellite data of the marine surface including a two dimensional velocity field and chlorophyll concentration data as a proxy for biological activity and a specific numerical tool employed to analyze these data. We quantify horizontal transport processes by the Lagrangian technique of the Finite Size Lyapunov Exponents (FSLEs) (Aurell et al., 1997), which is specially suited to study the stretching and contraction properties of transport in geophysical data (d'Ovidio et al., 2004). The calculation of the FSLE goes through computing the time, τ, at which two fluid particles initially separated by a distance δ_0 reach a final separation distance δ_f, following their trajectories in a 2 D velocity field. At position x and time t the FSLE is given by: $\lambda\,(x, t, \delta_0, \delta_f) = \frac{1}{\tau} \log \frac{\delta_f}{\delta_0}$. We are in fact considering the four neighbors of each gridpoint and we selected the orientation of maximum separation rate (fastest neighbor to reach the final separation distance). The equations of motion that describe the horizontal evolution of particle trajectories are computed in longitudinal

and latitudinal spherical coordinates (ϕ, θ, measured in degrees; δ_0 and δ_f are also measured in degrees): $\frac{d\phi}{dt} = \frac{u(\phi, \theta, t)}{R \cos \theta}$, $\frac{d\theta}{dt} = \frac{v(\phi, \theta, t)}{R}$. u and v represent the eastward and northward components of the surface velocity field, and R is the radius of the Earth. Numerical integration is performed by using a standard fourth-order Runge-Kutta scheme with an integration time step of $dt=1$ day. Spatiotemporal interpolation of the velocity data is achieved by bilinear interpolation. We follow the trajectories for 300 days, so that if τ gets larger than 300 days, we define $\lambda=0$. FSLEs depend critically on the choice of two length scales: the initial separation δ_0 and the final one δ_f. d'Ovidio et al. (2004) argued that δ_0 has to be close to the intergrid spacing among the points x on which FSLEs will be computed, which is $\delta_0=0.025°$. On the other hand, since we are interested in mesoscale structures, δ_f is chosen equal to $1°$, implying a separation distance of about 110 km close to the equator. In this respect, the FSLEs represent the inverse time scale for mixing up fluid parcels between the small-scale grid and the characteristic scales of eddies in these upwelling areas. Choosing slightly different values for δ_f does not alter qualitatively our results, the main pattern and averages remain the same. To sum up, maps of FSLE are computed monthly for the period June 2000 to June 2005 on all points of a latitude-longitude grid with a spacing of $\delta_0=0.025°$. An alternative tool to FSLE is the Finite-Time Lyapunov exponents (Haller, 2001; Beron-Vera et al., 2008) but we expect that similar results would be obtained by this last technique for the present spatial and temporal scales. This is so because we use a value of δ_0 smaller than the typical structures in the velocity field, so that FSLE is close to the value of the local Lyapunov exponent and thus of the FTLE at large times (Aurell et al., 1997; Artale et al., 1997). The time integration of the particle trajectories can be performed in two different ways: forward or backward in time. In a typical snapshot of the backwards-in-time dynamics, the maximum values of FSLE organize in lines which are a good approximation for the areas of maximal convergence. On the other hand, FSLE calculated with the forward-in-time integration exhibit large values in the regions of maximal divergence. The line-shaped regions of maximal convergence (divergence) approximate the so-called unstable (stable) manifolds of the hyperbolic trajectories in the flow (Boffeta et al., 2001; Koh and Legras, 2002; d'Ovidio et al., 2004). As a consequence, these ridges, i.e. lines of maximum separation or convergence rates, move with the flow as if they were material lines and thus delineate fluid domains with quite distinct origin and characteristics. Although it would be good to have for ridges in FSLEs some rigorous analysis, of the type of Shadden et al. (2005) for ridges in FTLEs, putting it in a firmer mathematical basis and identifying its limits of validity, there is ample numerical and theoretical evidence confirming this behavior (Koh and Legras, 2002; Lehahn et al., 2007; d'Ovidio et al., 2009). We focus in this work on the backward-in-time dynamics since FSLEs' lines have a

Nonlin. Processes Geophys., 16, 557–568, 2009 www.nonlin-processes-geophys.net/16/557/2009/

210

clear interpretation as fronts of passive scalars driven by the flow (d'Ovidio et al., 2009). These lines strongly modulate the fluid motion since when reaching maximum values, they act as transport barriers for particle trajectories thus constituting a powerful tool for predicting fronts generated by passive advection, eddy boundaries, material filaments, etc. In a different set of papers (d'Ovidio et al., 2004, 2009; Lehahn et al., 2007; Rossi et al., 2008), the adequacy of FSLE to characterize horizontal mixing and transport structures in the marine surface has been demonstrated as well as its usefulness when correlating with tracer fields like temperature or chlorophyll. Related Lagrangian diagnostics (FTLEs) have even been used to understand harmful algae development (Olascoaga et al., 2008). In addition, spatial averages of FSLEs can define a measure of horizontal mixing in a given spatial area, the larger this spatial average the larger the mixing activity. Following these studies, we will use in this work the FSLE as an analysis tool of the horizontal mixing activity of the surface ocean and will highlight similarities and differences both at a hydrodynamic and biological level.

We study the transitional area of exchange processes between the shelf and offshore in the open ocean. The filaments in the fluctuating boundary between the upwelling and the edge of the oligotrophic subtropical gyres play a key role in the modulation of the carbon balance by seeding the inner ocean. To consider the role of this moving transitional area, we chose as analysis areas coastal strips of 8 degrees (in the meridional direction) in each system. However we used the full geographical areas to make our numerical computations. Note that the computation areas are larger than the analysis ones, considering the fact that particles may leave the area before reaching the fixed final distance δ_f. In addition, several tests with different shapes and area selections (not shown) exhibit similar results.

3 Satellite data

A five year long time series from June 2000 to June 2005 of ocean colour data is used. Phytoplankton pigment concentrations (chlorophyll-a) are obtained from monthly SeaWiFS (Sea viewing Wide Field-of-view Sensor) products[1], generated by the NASA Goddard Earth Science (GES)/Distributed Active Archive Center (DAAC). The bins correspond to grid cells on a global grid, with approximately 9 by 9 km.

The weekly global $1/4°$ resolution product of surface currents developed by Sudre and Morrow (2008) has been used. The surface currents are calculated from a combination of wind-driven Ekman currents, at 15 m depth, derived from Quikscat wind estimates, and geostrophic currents computed from time variable Sea Surface Heights. These SSH were calculated from mapped altimetric sea level anomalies combined with a mean dynamic topography from Rio et al.

(2004). These weekly velocity data, which are then interpolated linearly to obtain a daily resolution with a 0.025° intergrid spacing, depend on the quality of their sources as the SSH fields and the scatterometer precision. However, they were validated with different types of $insitu$ data such as Lagrangian buoys, ADCP and current meter float data. In our four areas, zonal and meridional components show respectively an average correlation coefficient (R^2) with for e.g. Lagrangian buoy data of 0.64 and 0.57.

We analyse satellite data which are two-dimensional fields. We are also interested in the third dimension and the influence of vertical movements in upwelling, which are known to be relatively intense. To perform this, we propose to compute the Ekman transport and the divergence of the velocity field from the available data. The Ekman transport was calculated using $U_E = \frac{T_y}{f\rho}$, where T_y is the meridional wind stress (obtained from the Quikscat scatterometer weekly wind estimates), ρ is the density of seawater and f is the Coriolis parameter. We also look at the vertical dimension by quantifying the horizontal divergence of the surface velocity field, using the incompressibility assumption: $\Delta(x, y, t) \equiv \partial_z V_z = -(\partial_x V_x + \partial_y V_y)$. This calculation gives an estimate of the mean vertical velocities over the whole period. Negative (positive) values of Δ indicate upwelling (downwelling) areas because they signal surface spatial points where fluid parcels diverge (converge).

4 Results

4.1 Comparative study of the mixing activity

4.1.1 Spatial distribution of the mixing properties from FSLEs

In Fig. 1 we draw the time average (covering the period June 2000–June 2005) of the FSLEs computed for the four EBUS. For all areas, two different subsystems, according to their mean mixing activity, can be defined. The zonal limits are as follows: 30° N for the Canary (CUS) and the California upwelling system (CalUS), 27° S for the Benguela (BUS) and 25°S for the Humboldt (HUS). Comparing these four upwelling zones, a distinction appears in both upwellings of the Southern Hemisphere where the limit between subsystems is clearly marked while in areas of the Northern Hemisphere it is not so sharp. Note also that the imaginary division lines are usually associated with particular topographic or hydrographic features: for the CUS, the line passes north of the Canary archipelago, the offshore HUS limit coincides with the Nazca Ridge and the BUS limit matches the latitude of the intense Lüderitz upwelling cell. The dark blue areas (FSLE value below 0.005 day^{-1}) located close to the coast indicate some retention zone since the mixing time is very large or infinite (the computation of FSLE gives zero when particles move toward the coast).

---

[1] We used the level 3 binned data with reprocessing 5.1. See http://oceancolor.gsfc.nasa.gov for further details.
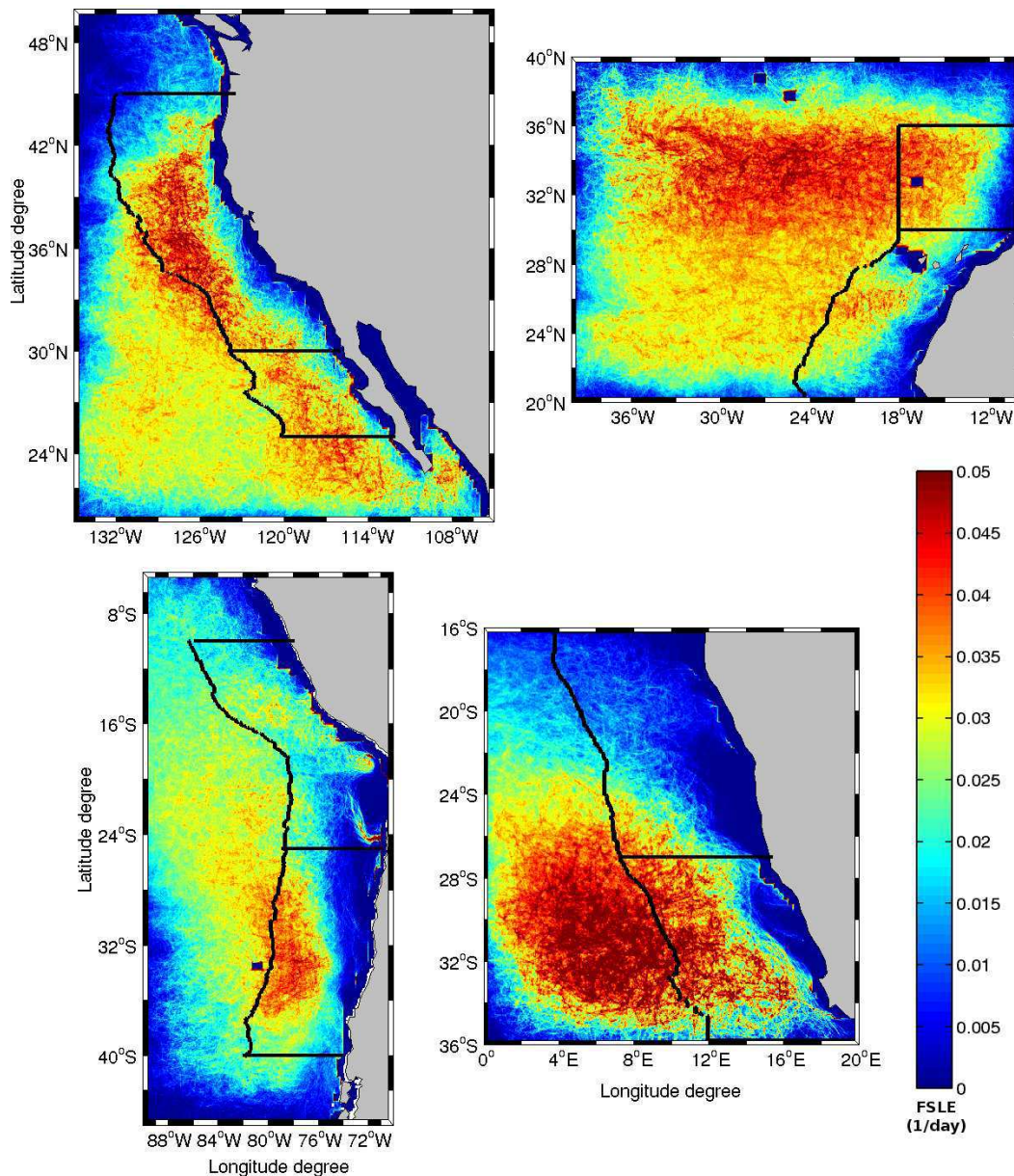
Fig. 1. Time average over the period June 2000–June 2005 of the FSLEs for the CalUS (upper left), the CUS (upper right), the HUS (lower left), and the BUS (lower right). Black lines indicate the analysis area as 8 degrees coastally oriented strips and the corresponding subdivisions.

To further quantify the variations in the stirring we examine the probability density functions (PDF) of FSLEs. These distributions are calculated for the FSLEs' time average normalized by the mean values from all grid points within each area (Fig. 2a). For all regions except the BUS (red line), the PDFs have a similar shape: their distributions are broad and slightly asymmetric, with a peak at low mixing activity and a quite long tail of high mixing. However the width and peak values vary depending on the considered system. The PDF of the BUS exhibits a particular asymmetric shape: we can observe one high peak in the low FSLEs values (around half of the spatial mean value, corresponding to ~0.008 day^{-1}) and a bump standing in moderate values of FSLEs (between 2 to 3 times the mean value, corresponding to 0.03–0.04 day^{-1}). Considering the very distinct PDFs of FSLEs between both BUS subsystems (as compared to the HUS) we can associate the high peak of low FSLEs to the northern subsystem, whereas the moderate FSLEs' bump constitutes a signature of the intense mixing in the southern subsystem constantly fed by numerous and powerful Agulhas rings. Note also that

Nonlin. Processes Geophys., 16, 557–568, 2009   www.nonlin-processes-geophys.net/16/557/2009/

212

the CalUS exhibits a thinner and higher peak as compared to the others, indicating that the mean mixing is moderate and quite homogeneous over the entire analysis area (high occurrence of values close to 1, meaning many values are found around the spatial mean). Waugh and Abraham (2008) showed that the PDFs of FTLEs (for Finite-Time Lyapunov Exponents) have a near-universal distribution in the global open surface ocean since they are reasonably well fit by Weibull distributions following: $P(\lambda) = \frac{b}{a} \left(\frac{\lambda}{a} \right)^{b-1} \exp(\frac{-\lambda^b}{a^b})$, with $a = \bar{\lambda}/0.9$ and $b = 1.6-2.0$. We expected a similar behavior for FSLEs because of the close relation among these quantities. We confirmed that normalized PDFs computed over the upwelling areas are quite well fitted by a Weibull distribution with parameters close to those proposed by these authors, except for the BUS. In Fig. 2b, the normalized PDFs of FSLEs from the CUS and HUS are quite well modeled by a Weibull distribution with parameter $b = 2.2$ whereas the PDFs' from CalUS (Fig. 2c) fits better a Weibull distribution with parameter $b = 3.4$ related with the higher and thinner peak around the average. The particular shape of the PDF of normalized FSLEs over the BUS indicates again that mixing in this upwelling system is much more heterogeneous.

4.1.2 Temporal evolution of the mixing intensity along the period 2000–2005

A more detailed comparison between the different subsystems can be performed by calculating the time evolution of the spatial averages over the analysis area of each of the four upwellings (Fig. 3a) and each subsystem (Fig. 3b and c). First of all we can sort each area according to their global averaged mixing activity. The mixing in the CalUS appears to be the most vigorous one (spatial average over the whole period: 0.025 day^{-1}), followed by the CUS (0.021 day^{-1}), and finally the HUS (0.019 day^{-1}) and BUS (0.017 day^{-1}) which presents the lowest mixing activity. A strong annual signal is observed in the time evolution of the mixing in the Humboldt, Canary and California upwelling systems. The five peaks of high mixing, corresponding to the five years of data, reflect the seasonal variability of the surface wind. In each hemispheric winter, the sea surface exhibits a more turbulent behaviour due to stronger winds. The last year of these time series reveals a somewhat different pattern of mixing, with a double peak for both upwellings of the Northern Hemisphere, suggesting that 2005 might be a particular year. In fact, this event has been already documented by Schwing et al. (2006) who studied the large-scale atmospheric forcing that contributed to these unusual physical oceanic conditions and the associated ecosystems responses. Note that both systems of the Northern Hemisphere oscillate in phase and are out of phase with the Southern Hemisphere systems. Periods of minimum turbulence values, for instance in the HUS, occur from March through May and coincide with the upwelling relaxation period, linked with the coastal wind regimes. A similar observation may be done for
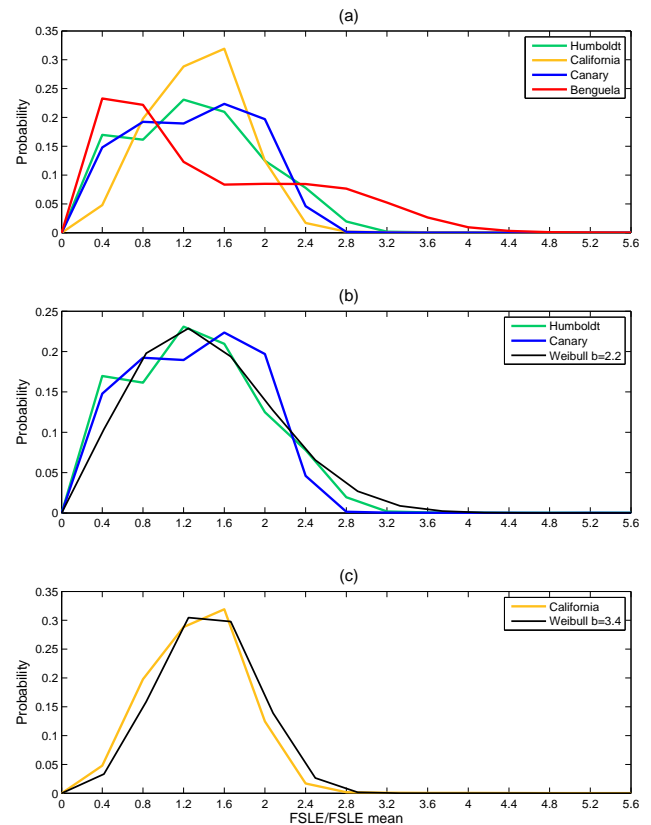
Fig. 2. (a) Normalized Probability Density Function calculated over the FLSEs time average of Fig. 1 for each EBUS (whole analysis area, i.e. 8 degrees coastal strip). Panels **(b)** and **(c)** same as in (a) for three of the PDFs fitting a Weibull distribution.

the BUS: the minimum mixing values during austral summer/autumn coincide with the upwelling relaxation period. Despite the fact that a high variability of the mixing is observed in all systems, the Benguela exhibits the strongest interannual variability of the mixing among all four EBUS. Note also an increasing trend of the mixing in the CalUS over these five years, confirmed by the computation of FSLE anomalies (not shown), suggesting a long-term change linked with global climate change (Bograd et al., 2009, and references therein). In all four regions, the difference of horizontal mixing activity is clear between tropical and temperate subsystems which showed the maximum of mixing (Fig. 3b and c). This observation can be explained by the intensification of large scale atmospheric forcing at mid-latitudes. When going away from the relatively calm equator, the intensity of the trade winds is increased in the gyre, associated to the presence of jet streams and increased pressure gradient. As already mentioned, this difference is more pronounced in areas of the Southern Hemisphere than of the Northern one. In Fig. 1, one can see a weak predominance of red colour in the temperate subsystem of the CalUS (north), suggesting
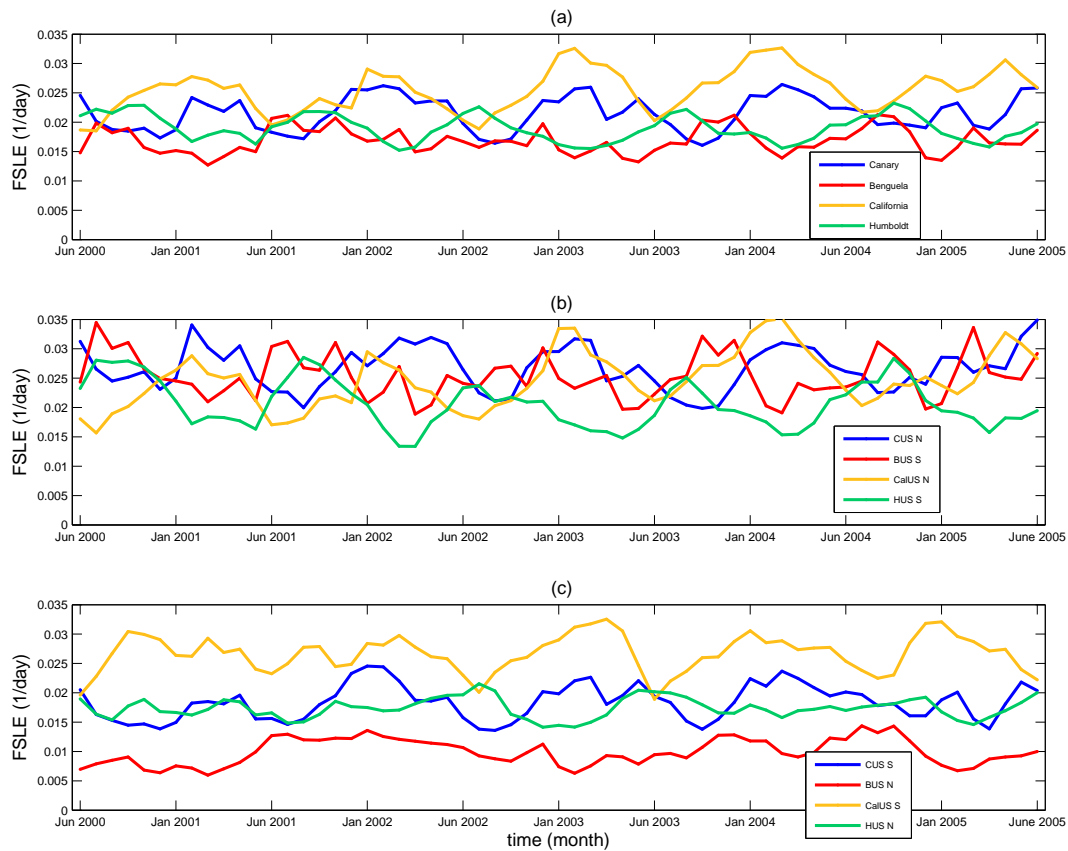
Fig. 3. **(a)** Spatial average versus time of the backward FSLEs. Spatial averages are computed over the analysis areas (8 degrees coastal strip): Canary (blue), Benguela (red), California (yellow) and Humboldt (green); **(b)** Same as in (a) but for the most temperate subsystems; **(c)** Same as in (a) but for the tropical subsystems.

it might be the most turbulent one. However the picture is more complex due to the particular temporal evolution of their mixing activity. Initially slightly less active than the southern one, the northern subsystem exhibits a positive tendency of increase, whereas the former is characterized by a flat long term pattern. As a consequence, the temperate subsystem becomes more turbulent than the tropical one at around year 2003. These different behaviors of the northern and southern CalUS subsystems were recently studied by Bograd et al. (2009) using newly developed upwelling index. Finally, the CalUS is quite particular as compared to the others since its horizontal mixing activity is more homogeneous: when averaging it over space and time in each subsystem, the FSLE means are very comparable, the southern one being slightly higher. Comparing these four upwelling zones, one can note that in the most turbulent temperate subsystems the values of the FSLEs are quite similar: within the range 0.018–0.04 day^{-1}, i.e., horizontal mixing times between 40 and 90 days. On the contrary, the least active tropical subsystems (excluding Southern California) are characterized by FSLE ranges from 0.003–0.025 day^{-1} equivalent

to horizontal mixing times from 65 to 530 days. Again on Fig. 3b and c, the mixing activity of the four subsystems from the Northern Hemisphere seems to vary in phase and shows a minimum during the boreal summer/autumn. On the other hand, in the BUS and HUS, the most turbulent temperate systems exhibit a visible annual cycle, with a minimum occurring during the austral summer/autumn, whereas the least active tropical ones show a high non linear variability and no obvious trend. Note that the northern BUS shows the smallest mixing activity of all areas.

The high spatio-temporal variability of the surface mixing revealed from FSLEs may strongly modulate the biological components of these complex and dynamic ecosystems. Next we proceed to investigate the correlation between horizontal mixing with the biological activity in our regions of interest.

4.2 Relationship with the biological activity

Now we study the relationship between the FSLEs and surface chlorophyll concentration estimated from space. First we performed Hovmöller plots of the surface chlorophyll

Nonlin. Processes Geophys., 16, 557–568, 2009 www.nonlin-processes-geophys.net/16/557/2009/

214
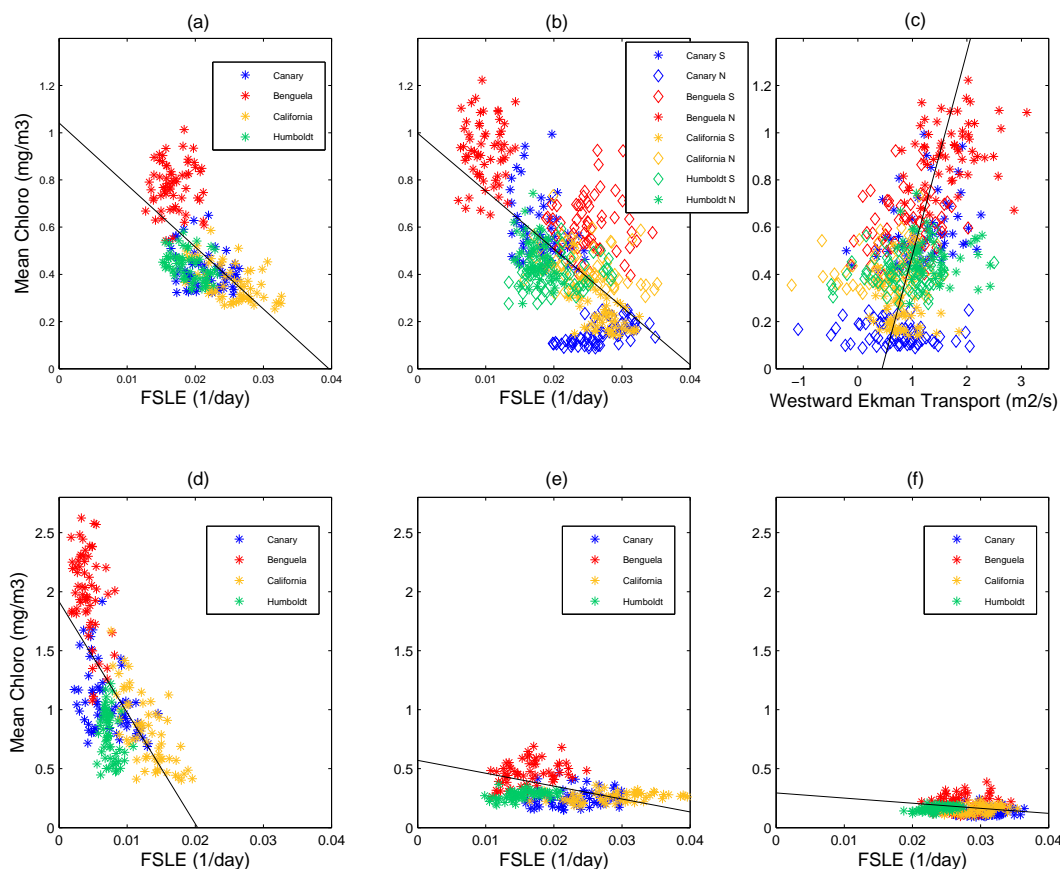
Fig. 4. Chlorophyll-*a* versus backward FSLEs, both averaged over the analysis areas (8 degrees coastal strips) for: **(a)** Whole analysis areas (R^2=0.38); **(b)** Same as in (a) but per subsystem (R^2=0.43); **(c)** Same as in (b) but for chlorophyll-*a* versus westward Ekman transport per subsystem (R^2=0.21; for visual improvement, the regression line has been obtained with the opposite order, x-axis versus y-axis); **(d, e, f)** Same as in (a) but for three successive strips oriented along the coast, **(d)** 2° from the coast, **(e)** within the 2° to 5° coastally oriented strip and **(f)** within the 5° to 9° coastally oriented strip.

distribution in the four upwellings by averaging the chlorophyll concentration along lines of constant latitude within the analysis areas for our five years of study (not shown). In each upwelling system, a clear distinction appears between two different zones, a southern one and a northern one, characterized by a very distinct degree of chlorophyll richness. In fact, the limits of the subsystems observed in the chlorophyll concentration Hovmöller plots coincide with the previous latitutinal limits deduced from FSLEs (around 30° N for CUS and CalUS, 27° S for BUS and 25° S for HUS). We also noticed that the poorest subsystem in chlorophyll matches the most turbulent one and vice-versa; this remark stands for the four EBUS. The spatial averaged chlorophyll over each analysis area (8° degrees coastal strips) reveals that the BUS admits the highest chlorophyll-*a* content (0.78 mg/m^3), followed by the HUS (0.43 mg/m^3), CUS (0.42 mg/m^3) and CalUS (0.36 mg/m^3). This ranking is just the opposite as the one based on the mixing activity of the surface ocean.

If one plots spatial averages of FSLE versus spatial averages of chlorophyll concentration, over the entire analysis area and over each subsystem (Fig. 4a and b), for each month from June 2000 to June 2005, a negative correlation between FSLEs and chlorophyll concentration emerges. For all four areas, the subsystems with the highest mixing activity are the poorest in chlorophyll. Note on Fig. 4a that each upwelling system is characterized by a clear clustering, with an exception of the CalUS which presents a more widespread distribution. The same observation is valid for each subsystem on Fig. 4b. Although these EBUS present common features, they seem also to have particular functioning revealed by these clusters. When considering only the most turbulent subsystems of each EBUS, the correlation is rather clear (R^2=0.75, not shown) suggesting that the higher the mixing activity is, the stronger the inverse relationship is between surface chlorophyll and mixing. The inhibiting effect of stirring revealed by the negative correlation seems to occur above a certain value – a turbulence threshold – and might act differently depending on the system. Following similar

www.nonlin-processes-geophys.net/16/557/2009/ Nonlin. Processes Geophys., 16, 557–568, 2009

215

calculations of spatial means over strips oriented along the coast (see Fig. 4, three lower panels d, e, and f), we observe a high negative correlation at the coast, decreasing when shifting to offshore strips, and even becoming flat when approaching the oligotrophic gyre further offshore. This finding obtained from an analysis over the four EBUS seems to indicate a variable response of the biology to physical stirring, valid in such diverse areas widespread over the world ocean.

Upwelling areas are definitely affected by water vertical movements and velocities, through uplift of rich nutrients water and 3-D turbulence, which are not captured by our previous analysis. We will also examine the influence of Ekman transport which creates pumping of nutrients and carries them from the deep layer to the coastal surface waters where light is not limiting. Vertical velocities and Ekman transport, which can both play a very relevant role in the chlorophyll signature detected from space, will be considered in the following.

We evaluated the horizontal divergence, Δ, of the surface velocity field and averaged it over the period June 2000–June 2005 at each point of the CUS, BUS, CalUS and HUS (not shown). The negative values of the Δ field in the coastal areas indicates the presence of upwelling events. We noticed that in the coastal zones of the BUS, the well known upwelling cells Cape Frio, Walvis Bay and Lüderitz in the northern subsystem appear clearly, being more intense than the southern cells, in agreement with Monteiro (2009) estimates of the northern subsystem accounting for 80%, on average, of the total upwelled flux over the whole BUS. The intense upwelling cells spread along the Peru/Chile coast are also visible, whereas the area above $15°$ S is mainly characterized by negative velocities which represent the equatorial upwelling. When averaging the temporal mean of the Δ field over the analysis area of each subsystem, representing a measure of the mean vertical velocities averaged over space and time, we confirm that the less (most) horizontally stirred system is associated with negative (positive) mean vertical velocities indicating predominance of upwelling phenomena (downwelling, respectively). This stands for the BUS, HUS and CUS since their less turbulent systems are respectively characterized by $\overline{\Delta}_{nBUS} = -0.0036\,\mathrm{day}^{-1}$, $\overline{\Delta}_{nHUS} = -0.002\,\mathrm{day}^{-1}$ and $\overline{\Delta}_{sCUS} = -0.0016\,\mathrm{day}^{-1}$ whereas their most turbulent exhibit positive means ($\overline{\Delta}_{sBUS} = 0.0012$, $\overline{\Delta}_{sHUS} = 2.2 \times 10^{-4}\,\mathrm{day}^{-1}$ and $\overline{\Delta}_{nCUS} = 8.7 \times 10^{-4}\,\mathrm{day}^{-1}$). For the CalUS, the distinction of two different subregions is not so clear, as compared to the others, confirmed by the very close negative average $\overline{\Delta}_{nCalUS} = -8 \times 10^{-4}\,\mathrm{day}^{-1}$ and $\overline{\Delta}_{sCalUS} = -1 \times 10^{-3}\,\mathrm{day}^{-1}$. It seems that areas dominated with upward processes are restricted to the very coastal areas whereas the offshore waters are dominated by downward ones. The global averages of Δ over the whole domain reveal negative values (upwelling) and give the following ranking: the most intense upward velocities are found in the BUS, followed by the CalUS, then comes the HUS and finally the CUS.

To complete the analysis, we have calculated the Ekman transport U_E along the E-W direction. Not surprisingly, its spatial distribution (not shown) is particularly linked to the spatial distribution of chlorophyll: high chlorophyll contents are often associated with intense Ekman transport, indicating high upwelling intensity. Indeed the northern regions of the BUS and HUS, the richest in chlorophyll and presenting the minimum mixing activity, are characterized by the highest offshore transport. In the CUS, both sub-areas have high values for the offshore transport very close to the coast, with similar values in the southern and northern subregions. Further from the coast, the highest westward transport in the southern CUS area coincides again with the highest chlorophyll content. The same analysis may be done for the CalUS with a less marked difference in the offshore southern subsystem. Figure 4c represents the spatially averaged westward Ekman transport U_E versus spatial averages of chlorophyll concentration, over each subsystem from June 2000 to June 2005 (one point per month). Negative values indicate an Ekman transport to the east, whereas positive ones indicate an offshore Ekman transport to the west. A positive correlation appears confirming the effect of Ekman-transport induced upwelling on biological productivity. This finding is not surprising and compatible with previous results (Thomas et al., 2004) since horizontal currents are strongly related to the vertical circulation. A global average of Ekman transport over space (analysis areas) and time reveals similar ranking deduced from the chlorophyll content, except a shift between CUS and HUS. The BUS has the highest ($-1.33\,\mathrm{m}^2/\mathrm{s}$), then come the CUS ($-1.07\,\mathrm{m}^2/\mathrm{s}$) and HUS ($-1.01\,\mathrm{m}^2/\mathrm{s}$) and finally the CalUS ($-0.7\,\mathrm{m}^2/\mathrm{s}$).

5 General discussion

Divisions of each area into two subsystems, based on different levels of temporal averaged horizontal stirring rates, are quite consistent with limits deducted from different criteria in other studies (Carr and Kearns, 2003; Mackas et al., 2006; Monteiro, 2009). We also proposed a ranking of horizontal mixing that gives new insights as compared to the classification made by Patti et al. (2008) based simply on a wind-mixing index. Systems from the same hemisphere seem to exhibit a similar behaviour with a dominant annual cycle when studying the temporal evolution of their spatially averaged horizontal mixing activity. The study from PDFs confirmed the statistical structure of these Lagrangian diagnostics already documented by Waugh and Abraham (2008). They showed that PDFs of FTLEs (Finite-Time Lyapunov Exponents, comparable to FSLEs) computed over the global surface ocean may be reasonably modelled by two kinds of distributions: in weak strain regions they are well fitted by Rayleigh distributions whereas for large-strain regions PDFs are better fitted by a general Weibull distribution. Since most of the regions under study reveal a quite nice fitting to a

Nonlin. Processes Geophys., 16, 557–568, 2009 www.nonlin-processes-geophys.net/16/557/2009/

216

Weibull distribution, with slightly different parameters values as indicated in Waugh and Abraham (2008), they can be considered as large-strain regions. The PDF of normalized FSLEs over the BUS shows a particular distribution, indicating that the mixing activity over this system is quite unique. The ranking in terms of chlorophyll content is the same than the one proposed by Cushing (1969), linking chlorophyll content and higher trophic level production. Carr (2001) and Carr and Kearns (2003) compared the EBUS depending on their primary productivity estimated from remote sensing and found also the same ranking, except for a switch between the HUS and CUS. The temporal variations of the chlorophyll stocks and their coupling with Ekman transport was studied in details by Thomas et al. (2004) over the four EBUS and more precisely over the CUS by Lathuilière et al. (2008). We globally confirmed that chlorophyll stocks are positively correlated with westward Ekman transport intensity.

When investigating the link of FLSEs with biological data, the scatterplots reveal a negative correlation between horizontal mixing activity and chlorophyll concentration in upwelling areas. This negative effect is in line with Lachkar et al. (2009) who showed that strong eddy activity acts as an inhibiting factor for the biological productivity in coastal upwelling systems. They confirmed that the CUS and CalUS appear to be the most contrasting systems of the 4 EBUS, in terms of biological productivity and mixing activity as well. Patti et al. (2008) also mentioned a negative correlation between turbulence, calculated as the cube of wind speed, and logarithm of the chlorophyll-a concentration for the BUS; however this finding did not hold for the other areas showing a positive relationship. We note that theoretical studies in idealized settings, in which nutrients reach plankton only by lateral stirring, display also negative correlation between mixing and biomass (although mixing and productivity may be positively correlated) (Tél et al., 2005; Birch et al., 2007; McKiver and Neufeld, 2009). In the following we propose some mechanisms to explain this inverse relationship, as compared to the open ocean and other low nutrient environments, where several studies showed that eddies and turbulent mesoscale features tend to rather enhance biological productivity (McGillicuddy et al., 1998; Oschlies and Garçon, 1998).

In our case, we focussed on very productive areas where the high biological productivity is maintained by a large nutrient supply from deep waters driven by Ekman pumping. Horizontal turbulent mixing of nutrients in surface waters, which was significant in the oligotrophic areas, is now a second order effect as compared to the vertical mechanisms (nutrient Ekman pumping) in the most productive subsystems. McKiver and Neufeld (2009), lay the emphasis on a ratio between the biological ecosystem timescale (inverse of the growth rate) and the flow timescales. When increasing the ratio, corresponding to an increase of turbulence, they indicate a negative effect on the phytoplankton mean concentration as it is the case in our study. The localized pulses of nu-

trients are rapidly being dispersed by intense mixing before being used efficiently by the phytoplankton to grow. Similar processes were documented in a theoretical modeling study from Pasquero et al. (2005). When associating an upwelling of nutrient with coherent vortices, they find a lower primary productivity than without vortices. They explained this observation by the trapping properties of eddies and the limited water exchange between the vortex cores and the surrounding waters. Eddies are able to trap and export offshore rich coastal waters which are not being used efficiently by the phytoplankton, resulting in a lateral loss of nutrients of the coastal upwelling. We also observed that areas characterized by high FSLEs are correlated with intense vertical movements (downwellings as well as upwellings), whereas the areas with low FSLEs are mainly dominated by upward vertical velocities (upwellings). Lehahn et al. (2007) recently showed that vertical motions associated with eddy are more precisely located close to the lines of high FSLEs. Regions of high FSLE averages indicate a high occurrence of intense eddies which modify the three dimensional mean flow. The nutrient Ekman pumping, dominant process in upwelling areas, is weakened and the fuelling of nutrients toward the surface decreased. A significant stirring revealed by high FSLEs may decrease the Ekman transport induced upwelling leading to weaker surface chlorophyll stocks.

In the scope of previous works concentrating in the open ocean, and considering Fig. 4 (3 lower panels), we suggest the possibility of a variable response of the phytoplankton to the mesoscale oceanic turbulence. This changing behavior, represented by the high negative correlation at the coast decreasing when moving offshore, may be explained when considering the different dominant processes in the areas of interest. In very coastal areas, intense biological productivity is supported by the intensity of Ekman induced upwelling of nutrients. However, a high turbulence caused by eddies may induce an offshore lateral loss of nutrients and may decrease the vertical fuelling of surface waters from nutrients Ekman pumping, thus leading to a negative effect on biological production. Then, when moving offshore in the transitional area between the very coastal upwelling and the oligotrophic gyre, the moderate production regime relies on the offshore export of coastal rich waters. In this case, the turbulent mixing of nutrients may have a minor influence on moderate productivity, from the compensation of weak positive and negative effects. Then, in the open ocean where the biological productivity is weak and limited by very low nutrient concentrations, the resultant effect of horizontal mixing on phytoplankton growth becomes positive. The phytoplankton development is being promoted by eddies which induce vertical velocities and an upward flux of nutrients toward the very depleted surface waters (McGillicuddy et al., 1998; Oschlies and Garçon, 1998).

Other factors are of course influencing at different levels the biological productivity in the ocean, more particularly in these highly variable areas. Several studies tried to iden-

tify the main factors among the four EBUS. Carr and Kearns (2003) distinguished different types of factors and discussed which ones control primary productivity. Oxygen concentrations and displacement of the thermocline symbolized the large-scale upwelling intensity; the local forcings were represented by quantities such as Photosynthetically Available Radiation, offshore transport and SST gradient, but the authors omitted the turbulence. They showed that large-scale circulation patterns are responsible for the main differences between EBUS. Then, the local forcings, and their combination with large-scale factors, explain the weaker variations. If we would consider only the nutrient concentration and Ekman pumping intensity (from their study) on one hand, and the turbulence from FSLEs (from our study) on the other hand, we can easily explain differences among EBUS without taking into account all other factors. Here we argue that adding our turbulence data from FSLEs to nutrients concentration and Ekman transport intensity allow us to simply obtain similar results, suggesting the fact that the turbulence effect is important to be considered. Patti et al. (2008) studied the factors driving the chlorophyll content and they found that nutrient local concentrations, mainly governed by local upwelling intensity (Ekman pumping), explain the main differences between very productive areas (HUS and BUS) as compared to the other two (CalUS and CUS). These processes act as first order factors whereas the continental shelf width appears to be the key secondary order factor explaining the difference between HUS and BUS, also mentioned by Carr and Kearns (2003). The mixing from FSLEs can also explain the main differences observed since the CalUS and CUS admit the highest surface mixing activity. Moreover, the highest chlorophyll content observed in the northern Benguela coincides again with the minimum of mixing measured by FSLEs. The BUS appears to be the most productive system since the Ekman pumping over a large width shelf is maximum and associated with the lowest mixing. Patti et al. (2008) also discussed other factors such as light limitation, solar cycle, presence of retention areas, etc., concluding that they should act at different levels, in different areas. It is also well known that micronutrient availability and alternative biogeochemical processes such as N_2 fixation or denitrification may also play a role in nature. However, the variability among all these factors over all areas is too large to identify trivial patterns. Consequently we did not consider these controls as primary factors in our analysis.

6 Conclusions

The distribution of FLSEs computed from multi-sensor velocity fields over a 5 year period allowed us to make a comparative study of the mixing activity in the four eastern boundary upwelling systems. Each area was divided into two subsystems showing different levels of temporal averaged horizontal stirring rates. When studying the temporal

evolution of their spatially averaged mixing, we proposed a ranking in terms of horizontal mixing intensity for all four EBUS. We also found that the more vigorous mixing occurs in subsystems further away the equator explained by the intensification of large scale atmospheric forcing at higher latitudes. Systems from the same hemisphere seem to exhibit a similar behavior with a dominant annual cycle. The PDF computations of FSLEs reveal the statistical structure of these Lagrangian diagnostics. When investigating the link of FSLEs with biological data, the subdivisions detected from FSLEs' maps appeared to be also visible on chlorophyll concentration Hovmöllers suggesting that these two quantities are linked. The scatterplots revealed a negative correlation between horizontal mixing activity and chlorophyll concentration in upwelling areas. We then confirmed that chlorophyll stocks are positively correlated with westward Ekman transport intensity over the four EBUS. It thus seemed that the horizontal turbulent mixing of nutrient is a second order effect as compared to the vertical mechanisms. After estimating the mean vertical velocities from incompressibility assumption, we proposed another explanation: the regions of high FSLEs are characterized by occurence of intense eddies and their verticals velocities associated. This will modify the whole 3-D flow and lead to a global decrease of the nutrient Ekman pumping (supported by low Ekman transport). We finally suggest the possibility of a variable response of the phytoplankton to the sub/mesoscale oceanic turbulence depending on the distance to the coast. This changing behavior is represented by the high negative correlation at the coast decreasing when moving offshore. It may be explained when considering the different areas and their associated dominant bio-physical processes. We then discuss the effect of others factors not considered here, and compare our approach to all previous comparative works.

Further work should investigate the robustness of the relationship found in our four systems when examining FSLEs versus biological stocks. Still much needs to be done to fully understand how plankton distributions are controlled by the interplay between their turbulent medium and the non-linear processes of their ecology. Coupled modelling approaches appear to be the only way to consider all these factors simultaneously. Besides a better understanding of the interactions between biological and physical processes, these coupled modelling studies will allow us to investigate and determine the respective effect of abiotic and biotic factors.

Although dealing with other scales of study may lead to different conclusions, chaotic stirring and turbulence in the ocean play a very important role by influencing biological processes at any scale. The negative effect of horizontal stirring on biological productivity in upwelling areas shown here needs to be considered when trying to estimate the carbon-pump efficiency on a global scale since upwelling areas shelter more than 20% of the global biological productivity (Ryther, 1969; Cushing, 1969; Chavez and Toggweiler, 1995). The global estimation of CO_2 fluxes at the ocean-atmosphere

Nonlin. Processes Geophys., 16, 557–568, 2009   www.nonlin-processes-geophys.net/16/557/2009/

218

interface will gain in accuracy when considering this effect through, for instance, a spatial parameterization of turbulence.

Edited by: A. Turiel
Reviewed by: A. M. Tarquis and two other anonymous referees

The publication of this article is financed by CNRS-INSU.

References

Artale, V., Boffetta, G., Celani, A., Cencini, M., and Vulpiani, A.: Dispersion of passive tracers in closed basins: Beyond the diffusion coefficient, Phys. Fluids, 9, 3162–3171, 1997.

Aurell, E., Boffetta, G., Crisanti, A., Paladin, G., and Vulpiani, A.: Predictability in the large: an extension of the concept of Lyapunov exponent, J. Phys. A, 30, 1–26, 1997.

Beron-Vera, F. J., Olascoaga, M. J., and Goni, G. J.: Oceanic mesoscale eddies as revealed by Lagrangian coherent structures. Geophys. Res. Lett., 35, L12603, doi:10.1029/2008GL033957, 2008.

Birch, D. A., Tsand, Y. K., and Young, W. R.: Bounding biomass in the Fisher equation, Phys. Rev. E, 75, 066304, 2007.

Boffetta, G., Lacorata, G., Redaelli, G., and Vulpiani, A.: Detecting barriers to transport: A review of different techniques, Phys. D, 159, 58–70, 2001.

Bograd, S. J., Schroeder, I., Sarkar, N., Qiu, X., Sydeman, W. J., and Schwing, F. B.: Phenology of coastal upwelling in the California Current, Geophys. Res. Lett., 36, L01602, doi:10.1029/2008GL035933, 2009.

Carr, M. E.: Estimation of potential productivity in Eastern Boundary Currents using remote sensing, Deep-Sea Res. II, 49, 59–80, 2001.

Carr, M. E. and Kearns, E. J.: Production regimes in four Eastern Boundary Current Systems, Deep-Sea Res. II, 50, 3199–3221, 2003.

Chavez, F. P. and Toggweiler, J. R.: Physical estimates of global new production: The upwelling contribution, in: Upwelling in the Ocean: Modern Processes and Ancient Records, John Wiley and Sons Ltd., 313–320, 1995.

Cushing, D. H.: Upwelling and fish production, in FAO Fisheries Technical Papers, 84, 1–40, 1969.

d'Ovidio, F., Fernández, V., Hernández-García, E., and López, C.: Mixing structures in the Mediterranean Sea from finite-size Lyapunov exponents, Geophys. Res. Lett., 31, L17203, doi:10.1029/2004GL020328, 2004.

d'Ovidio, F., Isern-Fontanet, J., López, C., Hernández-García, E. and García-Ladona, E.: Comparison between Eulerian diagnostics and Finite-Size Lyapunov Exponents computed from Altimetry in the Algerian basin, Deep-Sea Res. I, 56, 15–31, 2009.

Haller, G.: Lagrangian structures and the rate of strain in a partition of two dimensional turbulence, Phys. Fluids, 13, 3365–3385, 2001.

Kang, J., Kim, W., Chang, K., and Noh, J.: Distribution of plankton related to the mesoscale physical structure within the surface mixed layer in the southwestern East Sea, Korea, J. Plankton Res., 26(12), 1515–1528, 2004.

Koh, T. and Legras, B.: Hyperbolic lines and the stratospheric polar vortex, Chaos, 12, 382–394, 2002.

Lachkar, Z., Gruber, N., and Plattner, G. K.: A comparative study of biological productivity in Eastern Boundary Upwelling Systems using an Artificial Neural Network, Biogeosciences Discus., submitted, 2009.

Lathuilière, C., Echevin, V., and Lévy, M.: Seasonal and intraseasonal surface chlorophyll-*a* variability along the northwest African coast, J. Geophys. Res., 113, C05007, doi:10.1029/2007JC004433, 2008.

Lehahn, Y., d'Ovidio, F., Lévy, M., and Heyfetz, E.: Stirring of the Northeast Atlantic spring bloom: a Lagrangian analysis based on multisatellite data, J. Geophys. Res., 112, C08005, doi:10.1029/2006JC003927, 2007.

Mackas, D., Tsurumi, M., Galbraith, M., and Yelland, D.: Zooplankton distribution and dynamics in a North Pacific Eddy of coastal origin: II. Mechanisms of eddy colonization by and retention of offshore species, Deep-Sea Res. II, 52, 1011–1035, 2005.

Mackas, D., Strub, P. T., Thomas, A. C., and Montecino, V.: Eastern Ocean Boundaries Pan-Regional View, in: The Sea, Chapter 2, p 21–60, edited by: Robinson, A. R. and Brink, K. H., Harvard Press Ltd., 2006.

McGillicuddy J., Robinson A., Siegel D., Jannasch H., Johnson R., Dickey T., McNeil, J., Michaels, A., and Knap, A.: Influence of mesoscale eddies on new production in the Sargasso Sea, Nature, 394, 263–266, 1998.

McKiver, W. J. and Neufeld, Z.: The influence of turbulent advection on a phytoplankton ecosystem with non-uniform carrying capacity, Phys. Rev. E., 79, 061902, 2009.

Monteiro, P. M. S.: Carbon fluxes in the Benguela Upwelling system, in: Carbon and Nutrient Fluxes in Continental Margins: a Global Synthesis, chapter 2.4, edited by: Liu, K. K., Atkinson, L., Quiñones, R. and Talaue-McManus, L., to appear (October), 2009.

Moore, T., Matear, R., Marra, J., and Clementson, L.: Phytoplankton variability off the Western Australian Coast: Mesoscale eddies and their role in cross-shelf exchange, Deep-Sea Res. II, 54, 943–960, 2007.

Olascoaga, M. J., Beron-Vera, F. J., Brand, L. E., and Kocak, H.: Tracing the early development of harmful algal blooms with the aid of Lagrangian coherent structure, J. Geophys. Res., 113, C12014, doi:10.1029/2007JC004533, 2008.

Oschlies, A. and Garçon, V.: Eddy-induced enhancement of pri-

mary production in a model of the North Atlantic Ocean, Nature, 394, 266–268, 1998.

Owen, R. W.: Fronts and Eddies in the sea: mechanisms, interactions and biological Effects, in: Fronts and Eddies in the Sea, p 197–233, edited by: Owen, R.W., Academic Press, London, 1981.

Patti, B., Guisande, C., Vergara, A.R., Riveiro, I., Barreiro, A., Bonanno, A., Buscaino, A., Basilone, G., and Mazzola, S.: Factors responsible for the differences in satellite-based chlorophyll *a* concentration between the major upwelling areas, Est. Coast. Shelf Sc., 76, 775–786, 2008.

Pasquero, C., Bracco, A., and Provenzale, A.: Impact of the spatiotemporal variability of the nutrient flux on primary productivity in the ocean, J. Geophys. Res., 110, C07005, doi:10.1029/2004JC002738, 2005.

Pauly, D. and Christensen, V.: Primary production required to sustain global fisheries, Nature, 374, 255–257, 1995.

Rio, M.-H. and Hernández F.: A mean dynamic topography computed over the world ocean from altimetry, in-situ measurements, and a geoid model, J. Geophys. Res., 109, C12032, doi:10.1029/2003JC002226, 2004.

Rossi, V., López, C., Sudre, J., Hernández-García, E., and Garçon, V.: Comparative study of mixing and biological activity of the Benguela and Canary upwelling systems, Geophys. Res. Lett., 35, L11602, doi:10.1029/2008GL033610, 2008.

Ryther, J. H.: Photosynthesis and fish production in the sea, Science, 166, 72–76, 1969.

Schwing, F. B., Bond, N. A., Bograd, S. J., Mitchell, T., Alexander, M. A., and Mantua, N.: Delayed coastal upwelling along the U.S. West Coast in 2005: A historical perspective, Geophys. Res. Lett., 33, L22S01, doi:10.1029/2006GL026911, 2006.

Shadden, S. C., Lekien, F., and Marsden, J. E.: Definition and properties of Lagrangian coherent structures from finite-time Lyapunov exponents in two-dimensional aperiodic flows, Phys. D, 212, 3–4, 271–304, 2005.

Sudre, J. and Morrow, R.: Global surface currents: a high resolution product for investigating ocean dynamics, Ocean Dyn., 58(2), 101–118, 2008.

Tél, T., de Moura, A., Grebogi, C., and Karolyi, G.: Chemical and biological activity in open flows: A dynamical system approach, Phys. Rep., 413, 91–196, 2005.

Thomas, C. A., Strub, T. P., Carr, M. E., and Weatherbee, R.: Comparisons of chlorophyll variability between the four major global eastern boundary currents, Int. J. Rem. Sens., 25, 7, 1443–1447, 2004.

Waugh, D. W. and Abraham, E. R.: Stirring in the global surface ocean, Geophys. Res. Lett., 35, L20605, doi:10.1029/2008GL035526, 2008.

5.4 Résumé de l'article 5 (français).

Cet article est une extension de l'article précédent avec une approche et des outils similaires mais aussi incluant d'autres zones géographiques ainsi que des diagnostics originaux. Il présente une étude comparative régionale entre les quatre EBUS (océan Atlantique : Benguela et Canaries ; océan Pacifique : Californie et Humboldt) du mélange horizontal de surface en relation avec l'activité biologique. Le mélange horizontal est estimé à partir du calcul des FSLEs, basé sur des courants de l'océan de surface en 2 dimensions. La distribution spatiale des FSLEs est étudiée à partir de moyennes temporelles de 2000 à 2005 et à partir de leur Probability Density Function (PDF) ou densité de probabilité. Cette première analyse nous a notamment permis de diviser chaque EBUS en deux différents sous-systèmes, sur la base de l'intensité de leur mélange horizontal moyen. Alors que ces subdivisions correspondent à des structures topographiques spécifiques à chaque EBUS qui influent sur leur circulation, les fonctions de densité de probabilité des FSLEs de 3 EBUS peuvent être toutes modélisées par une distribution de type Weibull. Ensuite, grâce à une moyenne spatiale calculée au cours des 5 années de l'étude, la variabilité temporelle interannuelle et saisonnière du mélange horizontal est décrite. Un classement des 4 EBUS en fonction de l'intensité moyenne de leur mélange horizontal est aussi proposé. Alors que 3 des EBUS paraissent avoir un fonctionnement et une organisation assez similaires, l'upwelling de Californie apparaît assez singulier. Ensuite, la relation entre cette activité de mélange et les concentrations de chlorophylle a déduites du capteur satellitaire SeaWiFS est investiguée. Chaque sous-système caractérisé par une intensité du mélange spécifique présente également une signature distincte en chlorophylle a. Une corrélation négative globale est mise en évidence entre le mélange horizontal et la teneur en chlorophylle a, sur l'ensemble des 4 EBUS, ainsi que sur leurs sous-systèmes pris séparément. Un calcul similaire, mais réalisé au sein de bandes successives orientées parallèlement à la côte, permet de montrer une évolution de la réponse du phytoplancton au mélange horizontal. La relation fortement négative dans la première bande côtière, diminue lorsque l'on se déplace de bande vers l'océan ouvert, pour devenir nulle (voire positive en accord avec la bibliographie) dans le gyre oligotrophe. Suivant la méthode développée par Rossi et al., 2008, le transport d'Ekman et les vitesses verticales (incompressibilité du champ de vitesse 2D) sont investigués. La corrélation positive entre la chlorophylle a et le transport d'Ekman vers l'ouest est confirmée, tandis que les sous-systèmes les plus turbulents de 3 EBUS sont encore caractérisés globalement par de moindres mouvements verticaux dirigés vers la surface

(ceux favorables à la biologie). Ces résultats originaux sont discutés à la vue de la bibliographie abondante sur ces thématiques, puis des hypothèses sont proposées afin d'expliquer les mécanismes de cette réponse variable du phytoplancton à la turbulence mesoéchelle de surface. L'activité physique mésoéchelle comme les tourbillons semble ainsi diminuer l'apport de nutriments global à la côte en freinant les forts courants d'upwelling dirigés vers la surface, qui normalement supportent une forte production biologique. Un deuxième mécanisme serait l'export vers le large par les tourbillons des nutriments pas encore exploités par le phytoplancton côtier. Ensuite, dans la zone de transition, les processus mésoéchelle ont une influence très limitée (compensation des effets positifs et négatifs) sur des systèmes dont la productivité repose sur les caractéristiques de masses d'eau côtières advectées. Dans l'océan ouvert, où la production de surface est fortement limitée par de très faibles concentrations de nutriments, ces processus mésoéchelle et leurs vitesses verticales associées favorisent la croissance du phytoplancton en augmentant significativement l'apport de nutriments en surface. Afin de confirmer ces explications, la conclusion mentionne le besoin d'utiliser des outils de modélisation en trois dimensions qui permettront de considérer simultanément tous les facteurs qui influent sur la production biologique de ces zones d'importance.

Chapter 6

Conclusions and perspectives.

6.1 Conclusions

The objectives of this study were numerous but centered around a general scientific overarching question: the influence of the physical processes on the regional ecosystem at mesoscales in coastal upwellings.

The use of several and complementary tools was necessary to assess the various mechanisms occurring at these scales.

First, the use of *in-situ* data from the MOUTON 2007 survey allowed us to study the high variability of the biogeochemistry of this area, strongly linked to its physical environment. The general hydrography was analyzed and revealed the presence of several water masses with different biogeochemical characteristics driven by both the large scale and local circulation, itself forced by local upwelling events. Then, we divided the central and northern IPUS (Iberian Peninsula Upwelling System) into three different biogeochemical provinces with their specific dominant processes.

- The most intense upwelling was found at the northern tip of the peninsula, where a diatoms dominated population grew under high nutrient supplies from ENACWsp (Eastern North Atlantic Central Waters from subpolar origin) and low zooplankton grazing predation.

- The southern end of our surveyed area was characterized by quite low nutrient concentrations related to the source waters (ENACWst, from subtropical origin) and due to lower upwelling strength. The planktonic communities were

223

here composed of a mix of species typical of both oligotrophic and eutrophic waters.

- The central subsystem was influenced by a surface layer coming from the north and a subsurface water mass coming from the south. This resulted in an heterogenous system, where numerous mesoscale features were observed, creating a few hot spots of high biological productivity. The very high reminer-alization activity over the shelf, associated to resuspension processes provided high nutrient inputs thus supporting the productivity of these hot spots.

We also studied the cross-shore gradient from East-West transects and from the sampling of a filament. The coastal upwelling was characterized by a high productivity that is exported offshore by mesoscale features. At the near shore area, a community of dinoflagellates and cyanobacteria developed, under the control of microzooplankton grazing. It became a diatoms-dinoflagellate dominated ecosystem over the shelf under the upwelling relaxation period. Then the Coastal Transition Zone was clearly a transition between the very productive coastal upwelling and its associated community and the oligotrophic ecosystem found offshore. Data from the filament allowed us to assess its impact in terms of cross-shore exchanges of biological material, and to better understand its physical structure.

We confirmed the strong influence of physical mesoscale processes on the plank-tonic ecosystem and the need to better understand the hydrodynamical part before studying coupled effects. In the same dataset, we observed a secondary upwelling front located at the discontinuity between the slope and the shelf. To understand the mechanisms behind this observation, we built a simplified 2D numerical model and the simulation successfully reproduced the secondary upwelling at the shelf break. This frontal structure is caused by the eastward advection (from barotropic upwelling currents) of deep water columns onto the shelf. The abrupt change in depth creates a negative anomaly of Potential Vorticity, that generates an up-ward displacement of isopycnals. A reduction of the secondary front was observed when adding a bottom friction because it strongly reduced the PV of offshore water columns. We concluded on several implications that can be of interest for any shelf circulation forced by the wind.

In the latter study, a 3D simulation revealed a filamentation process occurring when the along-shore upwelling current interacts with an extended promontory. This was further investigated with collaborators and we proposed and analysed a new mechanism for filament formation associated to bottom topography using a

similar 2D numerical model. The alongshore current encounters a promontory and creates anomalies of potential vorticity in the lower layer. As a consequence, cyclonic and anticyclonic circulation patterns develop and interact with the upwelling front in the upper layer. This generates a long trapped filament in the vicinity of the promontory. This process is sensitive to the shape of the promontory but very slightly to the wind forcing, coast line irregularities and baroclinic instabilites.

In Chapter 5, we used satellite data associated with a lagrangian tool (FSLE for Finite-Size Lyapunov Exponent) to study the offshore export of upwelled waters and the importance of horizontal mixing in relation to the biological activity over the four EBUS. Satellite data provided a good coverage over space and time and allowed us to initiate a comparative study between these zones. First we studied the spatio-temporal variability of the horizontal mixing showing similarities as well as discrepancies between the four areas. It allowed us to divide latitudinally each area into two subsystems that present a distinct averaged mixing activity. Surprisingly, each subsystem revealed also a particular chlorophyll a content, proxy of the biological activity. When investigating the link between horizontal surface mixing and chlorophyll content, a negative relationship was shown. The negative effect of the horizontal turbulence was strong at the coast and decreased when moving offshore. It seemed related to a diminution of vertical velocities of the coastal upwelling, as well as a lateral loss of nutrient being exported in moving eddies. Horizontal mixing induced by eddies thus has a negative effect on the phytoplankton in coastal upwellings (*Rossi et al.* [2008, 2009]), whereas a positive effect stands for the open ocean.

6.2   Perspectives

This study highlights the necessity to study coastal areas and EBUS since they shelter a large part of the global primary productivity, more than 20 % (*Pauly and Christensen* [1995]), and productive marine ecosystems. They are also areas where a major part of the commercial fisheries, as well as other human recreational activities, take place. Since the coastal circulation appears to be very complex, these zones are natural laboratories to study mescoscale processes and their influence on a productive ecosystem. Moreover, their highly dynamical biogeochemical cycling related to emission of some greenhouse gases and the occurrence of Oxygen Minimum Zones (OMZs) place them are at the heart of current issues associated with climate change.

6.2.1 Mesoscale variability of the Iberian Peninsula Upwelling System.

Concerning the biogeochemical variability of the IPUS, the ongoing work about the zooplankton dataset will give new insights of the functioning of the ecosystem. Collecting data at sea is a costly process that has to be well prepared. From Chapters 3 and 4, it clearly appears that the determination of the sampling strategy is crucial to answer a scientific question. It may be great for a future survey to concentrate our effort on a few transects, determined by real-time acquisition of high resolution satellite maps, while performing finer (high resolution) sampling. Moreover, additional variables such as primary productivity (from incubation experiments) as well as bacterial community composition and bulk activity (using genomics methods) should be monitored to better assess the nutrient and plankton budgets in this area. The sampling of a dynamical structure observed during the survey might be tracked by a smaller coastal boat, equipped with a set of biogeochemical sensors mounted on a Seasoar for instance, to ensure a complete spatial coverage of the structure with a high reactivity.

The shallow shelf and associated processes whithin or at the sediment interface seemed to play a key role on the biogeochemical cycles of the central area and have to be better understood. We propose to survey some chemical as well as biogeological variables related to these processes, both in the water column and in the sediments. Apart form the classical oceanographic survey (currents, hydrography...), one could measure the Particulate Organic Matter and Dissolved Organic Matter, along with planktonic and microbial communities within the water column until the seabed to assess its biogeochemical functioning. The second approach could focus on the benthic communities, performing sediment sampling cores and using labelling techniques to monitor in the lab the bacterial activity within the sediment. Since this continental margin is also influenced by sediment river discharge, a surveillance of the river flow and particulate content may be desirable. It will allow a better understanding of remineralization and sediment / water column interactions.

We also showed that nitrate was the limiting factor of PP in this area. Another direction may be to monitor all chemical species involved in the complex nitrogen cycle that characterized upwelling areas, to really understand the nitrogen cycle. In the same direction, we can wonder if hypoxic areas might occur in this mid-latitude upwelling. Although source waters are better oxygenated than in the tropical ocean, the future expansion of OMZs in the global ocean may change their properties.

The deep origin of upwelled waters at the northern tip of the IPUS was also among the most surprising results. We indeed found waters originally coming from ~ 350 m whereas typical upwelled waters are coming from ~ 200 m. Further investigations have to be performed to explain this observation. It could include the monitoring of local atmospherical conditions (wind) that drive the upwelling, surveying the shelf and offshore waters under contrasting upwelling events, but also using modelling techniques to understand which factors can create such a strong Ekman pumping (ocean / atmosphere interactions).

Concerning the physical part, ponctual observations of a structure along with numerical tools allowed us to investigate particular mechanisms such as the formation of a secondary upwelling front along the continental margin or a filamentation process. But high resolution data of such structure are lacking to confirm and detail our findings. A more intense mapping of the subsurface circulation over the shelf from moored ADCP, associated with coastal HF radars that provide the surface flow, during for longer period, may be great opportunities to better understand the shelf circulation.

Moreover, we studied in details the physical and biogeochemical functioning of a filamental structure in the IPUS and the significant offshore transport of a productive ecosystem has been shown. The study of this single structure, associated with the high occurrence of such filaments all year long in the EBUS, leads us to propose to evaluate the global role of mesoscale filamental structures on the metabolic balance of the whole northern Atlantic oligotrophic gyre (see *Alvarez-Salgado et al.* [2007]). We propose first to better quantify the variability of their characteristics by installing two "coastal observatories" in the IPUS and the Canary Upwelling System, over the shelf at two precise locations favouring the formation of such filaments. A constant monitoring will be performed: observations can be continuously collected using moored buoys equipped with biogeochemical and physical sensors, as well as radar HF for the surface circulation. Additionally, Gliders (that since recently contain also both physical and biogeochemical sensors) could be deployed every month within a filamental structure to survey the coastal transition zone and this particular dynamical structure elongating offshore. In a second step, a 3D coupled modelling study at high resolution (resolving the mesoscale to allow filamental formation) might be initiated to extrapolate our results to the whole oceanic basin.

The model used in *Rossi et al.* [2010] was built to concentrate on adiabatic effect and motions mostly in geostrophic equilibrium. It did not include the mixed layer dynamics, although observations revealed that the upper ocean stratification

and characteristics are highly dependant on the transient guts of wind measured onboard. We propose here to study the influence of a high frequency wind forcing on the mixed layer dynamics using a numerical model. We suspect an important influence on the thickness of the mixed layer and in turn changes in the buoyancy of the surface layer and its dynamics.

A few simulations, not shown in the paper by *Rossi et al.* [2010], revealed a particular behavior of the vertically averaged cross-shore transport using oscillatory wind stress. Small positive and negative alternations of cross-shore velocities were observed over the whole modelled basin, symbolizing the compensation of surface offshore flow by subsurface onshore flow. However, under particular forcings the transport oscillations generated at the center of the basin were resonance-excited. It showed significant oscillations (velocities $\simeq 1$ m/s) which we related to a basin oscillation caused by the propagation of Poincaré waves. This physical process has to be studied since it appears poorly documented and might play a role in the horizontal mixing and renewal time of the shelf waters of a closed basin.

6.2.2 Inhibiting effect of mesoscale turbulence from FSLE on the surface chlorophyll in the EBUS: toward an identification of effective processes.

From Chapter 5, several interrogations remain concerning the underlying processes behind the negative correlation between surface chlorophyll and horizontal mixing showed by *Rossi et al.* [2008, 2009]). When considering that the spatial structure in plankton distributions results from both dynamics of the turbulent medium and of the marine ecosystem, a multidisciplinary modelling study has to be initiated. The perspectives presented here were only tackled during this thesis but need further development.

a - An academic modelling of the Benguela Upwelling System.

Based on an academic coupled modelling study, we will investigate how plankton concentrations at the surface are controlled by the interplay between the physical mixing processes and the intrinsic biological dynamics. The idea is to use a simple biological model that is being coupled to the velocity field derived from satellite in 2 dimensions. We would like to simulate the difference of phytoplankton content observed in the two subsystems described by *Rossi et al.* [2008, 2009]. We

chose the Benguela upwelling area since the two subsystems revealed the most constrasting picture, both in term of horizontal mixing and biological activity, in order to understand the processes behind the negative relationship in a simple 2D framework. The biological model is derived from *Sandulescu et al.* [2008] and describes the interaction of a three-level trophic chain in the mixed layer of the ocean, including: phytoplankton P, zooplankton Z and dissolved inorganic nutrient N. Only horizontal transport is explicitly taken into account in the 2D flow from satellite, the upwelling being modeled as a source term in the nutrient equation. The nutrient supply due to vertical mixing (a term in the reaction equation) mimics the upwelling. It is very low offshore the shelf and high in the nutrient-rich coastal upwelling. Nutrients are consumed by the phytoplankton according to a Holling type II functional response and recycled of a part of all dead organic matter. The phytoplankton grows upon the consumption of the nutrients, but its concentration is decreased due to grazing by zooplankton and natural mortality. The grazing enters as a growth term for the zooplankton concentration with an efficiency factor. Zooplankton mortality is assumed to be quadratic. Additional details can be found in *Oschlies and Garçon* [1999]. The coupling of the biological and the hydrodynamic model yields an advection-reaction system, as it was described in a general case in Chapter 2. We add also an eddy diffusion process acting on plankton and nutrient concentrations (adding a diffusion coefficient) to incorporate the small-scale turbulence, which is not explicitly taken into account by the velocity field used. This study initiated during my stay at IFISC (CSIC/UIB, Palma de Mallorca, Spain) is currently being continued by Ismael Hernandez-Carrasco (IFISC).

b - Toward a 3D realistic coupled modelling of the IPUS using HYCOM.

The objective here is to model the IPUS in a realistic configuration with a regional version of HYCOM and a biological model embedded. We will use the physical model HYCOM (for HYbrid Coordinate Ocean Model, *Bleck* [2002] and see http://www.hycom.org/). Coordinate surfaces in this model adhere to isopycnals wherever this does not violate minimum layer thickness requirements; elsewhere, coordinate surfaces are geometrically constrained. It is a primitive-equation model containing 5 prognostic equations, two for the horizontal velocity components, a mass continuity or layer thickness tendency equation, and two conservation equations for a pair of thermodynamic variables, such as salt and temperature. These primitive equations have been described in Chapter 2. External forcings will include river run-off, latent heat fluxes, precipitation and evaporation. Since we are

interested in mesoscale processes, we might select high frequency forcing. Initial conditions and boundary conditions will use MERCATOR fields for physical variables.

Concerning the biological part, as a first step, we will use a NPZD model already embedded in the source code. It contains 4 compartments, namely the dissolved organic Nitrogen, Phytoplankton, Zooplankton and Detritus. In Chapter 3 (Article No. 1), we documented strong North-South as well as cross-shore gradient in terms of planktonic communities. Another outcome of this study was the strong coupling observed between phytoplankton and zooplankton size distribution. Considering these findings, we may split the N and P boxes into 2 different size classes, representing the large and small individuals, characterized by a different set of biological parameters. Since we also showed in Article 1 that the IPUS is nitrogen limited, we may plan to detail the nitrogen cycle as a third step. It will be performed by dividing the Nitrogen box into several chemical species such as ammonium NH_4^+, nitrite NO_2^- and nitrate NO_3^-. Some studies (*Alvarez-Salgado et al.* [1997]; *Joint et al.* [2001] suggested urea as an important source of nitrogen for the phytoplankton. A box of Dissolved Organic Nitrogen would be added to the biological model and the parameterization of fluxes between DON and phytoplankton setted with care.

The model outputs will be compared to the *in-situ* data collected during MOUTON 2007, in order to better estimate the biological parameters, as well as the reliability of the physics and external forcings.

Although a physical version of the code already exists for the IPUS, a huge amount of modelling work remains to be done before obtaining a workable version of the coupled model. A first step could be to pursue the 2D model developed in chapter 4 to include biogeochemical variables.

We will focus our investigations on the modification of the vertical velocity field by eddies, the possible presence of subduction processes offshore, and the horizontal transport from the coast to the open ocean they induce. Extending these interrogations to a global scale, a spatial parameterization of turbulent processes may be done to properly assess their role on the global biogeochemical budget.

c - Extension of the Finite Size Lyapunov exponents theory.

Another concern derived from *Rossi et al.* [2008, 2009] deals with the lagrangian tool, namely the FSLE. It is based on the 2D turbulence theory, whereas we clearly identified that vertical velocities are crucially important for the biological processes. We would like to know if the 2D structures (Lagrangian Coherent Structures) revealed by the Lyapunov computation are in fact associated with significant vertical velocities underneath. It might be articulated along two research lines: (i) can we extend the Local Lyapunov calculation to 3D flow ? (ii) what is the difference between LCS revealed by the forward and backward in time calculation (see Discussion of *TewKai et al.* [2009]) ? There exist relations that link the horizontal velocities (that are measured quite accurately) to the vertical components, but these methods present significant errors (see for instance *Isern-Fontanet et al.* [2008]; *Klein and Lapeyre* [2009]). In general, it is still a great challenge to evaluate mesoscale vertical velocities in the ocean.

6.2.3   General perspectives.

Annex B (*TewKai et al.* [2009]) showed that mesoscale structures as revealed by the FSLE have also a strong impact on marine top predators population and their behavior. It clearly emphasizes the fact that mesoscale processes affect the whole ecosystem. It pointed out the need to work in close collaboration with other field such as Ecology and Fishery science, that have a direct impact on humans food supply and coastal management.

All future perspectives detailed above may be summarized in three topical questions, which are of course already considered by a large part of the oceanographic community:

What are the limitation and driving factors of the primary production of EBUS ?

What processes link PP and higher trophic levels of interest for human food supply ?

What might their future hold in a global climate change context ?

6.3 Conclusions et perspectives (français)

6.3.1 Conclusions (français).

Les objectifs de cette étude étaient multiples mais centrés autour d'une thématique générale : l'influence des processus physiques sur l'écosystème régional à mésoéchelle dans les upwellings côtiers. L'utilisation d'outils divers et variés était nécessaire pour aborder les nombreux mécanismes impliqués.

Dans un premier temps, l'analyse des données in-situ provenant de la campagne MOUTON 2007 nous a permis d'étudier la grande variabilité biogéochimique de l'upwelling de la péninsule Ibérique (IPUS), fortement lié à son environnement physique. Le contexte hydrographique général a été analysé et a montré, sous l'influence de la circulation globale et locale (évènement d'upwelling et phénomènes à mésoéchelle locaux), la présence de nombreuses masses d'eau ayant des caractéristiques biogéochimiques particulières. La région côtière a été divisée en trois sous-provinces biogéochimiques :

- L'upwelling le plus intense est observé au nord de la zone, où une population dominée par des diatomées se développe grâce à des forts apports de nutriments par les eaux ENACWsp (Eastern North Atlantic Central Water d'origine subpolaire) upwellées, et en lien avec de faibles biomasses de zooplancton.

- La zone sud est quant à elle caractérisée par de moindres concentrations de nutriments, en lien avec la masse d'eau ENACWst (d'origine tropicale) upwellée, qui supporte un écosystème contrasté, constitué d'un assortiment d'espèces typiques de zones eutrophe et oligotrophe.

- Le système central est influencé en surface par une masse d'eau advectée du nord, tandis qu'une seconde masse d'eau provient du sud en subsurface. Cette zone hétérogène où de nombreuses structures à mésoéchelle sont observées présente certains hot spots avec une forte productivité biologique, soutenus par d'intenses processus de reminéralisation et de remise en suspension de nutriments à l'interface du sédiment.

Le gradient contrasté côte-large a été également mis en évidence à partir de l'analyse détaillée de sections Est-Ouest. La zone très côtière est caractérisée par une communauté de dinoflagellés et cyanobactéries contrôlées par un fort broutage du microzooplancton. Au cours de sa dérive vers le large, sous des conditions de

relaxation de l'upwelling, une domination de diatomées apparaît et coexiste avec les dinoflagellés. Plus au large, des cyanobactéries et prochlorophytes dominent les communautés, mais présentent des concentrations significativement plus importantes que l'écosystème du large. L'upwelling côtier est caractérisé par une forte production exportée vers le large au sein de structures à mésoéchelle, tel le filament qui a été étudié. Nous avons également estimé le transport induit par le filament et progressé sur la compréhension de sa structure physique.

L'état physique de l'IPUS influence fortement son fonctionnement biogéochimique et doit être étudié en détail. Nous avons observé sur une radiale Est-Ouest un front secondaire d'upwelling localisé au niveau de la marge continentale. Pour mieux comprendre cette structure, nous avons construit un modèle numérique simple en 2D qui a bien reproduit le phénomène à la rupture de pente entre le talus et le plateau continental. L'advection par le courant barotrope d'upwelling vers la côte de colonnes d'eau du bassin océanique sur le plateau crée une anomalie de vorticité potentielle (VP) liée au changement abrupt de profondeur. Elle génère en réaction un bombement des isopycnes sus-jacentes expliquant le front d'upwelling secondaire. Une réduction du front a été observée avec l'ajout d'un frottement sur le fond, lié à une érosion de la VP des colonnes d'eau du large. Cette étude a permis également de documenter les circulations océaniques complexes de marge continentale forcées par le vent.

Une simulation de l'étude précédente a révélé un processus de filamentation dû à l'interaction du courant parallèle à la côte avec une structure topographique. Avec des collaborateurs, nous avons utilisé un modèle numérique similaire à celui de l'étude précédente afin de proposer l'explication suivante : lorsque le courant d'upwelling parallèle à la côte rencontre un promontoire topographique, une anomalie de VP est créée en sub-surface et entraîne la mise en place de circulations cyclonique et anticyclonique de part et d'autre du promontoire. En interaction avec la couche de surface, un long filament s'étire vers le large, piégé sur le promontoire. Ce processus est apparu sensible à la forme du promontoire, mais peu au forçage du vent, aux instabilités baroclines ainsi qu'aux irrégularités de la ligne de côte.

Dans le Chapitre 5, nous utilisons des données satellites et un outil lagrangien (Exposants de Lyapunov à taille finie : Finite Size Lyapunov Exponents- FSLE) qui nous permettent de comparer l'activité de mélange de l'océan de surface et l'export des masses d'eau upwellées en lien avec l'activité biologique des 4 zones d'upwelling de bord Est (EBUS). L'analyse spatio-temporelle du mélange horizontal

révèle des ressemblances et des spécificités entre les quatre EBUS. Parmi les caractéristiques communes, les quatre zones ont été divisées en deux sous-systèmes séparés latitudinalement et caractérisés par une intensité moyenne du mélange bien distincte. Chaque sous-système est aussi caractérisé par une signature en chlorophylle de surface particulière. Nous mettons en évidence une relation négative entre le mélange horizontal de surface et les concentrations en chlorophylle dans les quatre zones. Sûrement causé par une diminution des vitesses verticales d'upwelling et une perte latérale de nutriments induits par les tourbillons à mésoéchelle, cet effet négatif de la turbulence à mésoéchelle sur l'écosystème planctonique est très significatif à la côte et diminue lorsqu'on se déplace vers l'océan ouvert. La turbulence horizontale induite par les tourbillons dans l'océan côtier a ainsi un effet inhibiteur sur la production biologique des upwellings, alors qu'un effet positif existe dans l'océan ouvert.

6.3.2 Perspectives (français).

Cette étude a mis en évidence le besoin crucial d'étudier les zones d'importance que sont les upwelling de bord Est. L'approche pluridisciplinaire est nécessaire et a permis d'évaluer la forte influence qu'ont les processus physiques à mésoéchelle sur l'écosystème planctonique. Ces zones sont aujourd'hui au cœur des débats pour les processus biogéochimiques complexes qui s'y déroulent et pour leur interaction avec le changement global du climat.

L'étude déjà initiée en collaboration ayant pour but d'étudier les biomasses de zooplancton, la composition en espèces et les spectres de taille du zooplancton en lien avec l'environnement, va permettre de progresser sur la compréhension de la variabilité de l'écosystème de l'IPUS. Une campagne étant un processus coûteux, il est apparu important de bien définir la stratégie de collecte de données. Pour une éventuelle prochaine campagne, on pourrait concentrer nos efforts sur quelques sections, déterminées par acquisition simultanée de cartes satellites, où la résolution des mesures serait plus fine. Il faudrait également rajouter des variables biogéochimiques, telles l'estimation de la production primaire (incubation), l'évaluation des biomasses microbiennes et de leur activité globale (par techniques génomiques) pour mieux comprendre son fonctionnement biogéochimique. On peut imaginer également disposer d'un bateau côtier plus petit, plus réactif et équipé d'un Seasoar pour permettre un échantillonnage haute fréquence efficace d'une structure à sub-mésoéchelle.

Les processus à l'interaction du sédiment se sont révélés d'une grande importance sur le cycle biogéochimique de l'IPUS. Nous proposons ici une étude pluridisciplinaire de la colonne d'eau mais aussi du sédiment. D'une part, on pourrait, en plus des variables classiques, mesurer les particules en suspension et dissoutes, associées aux biomasses planctoniques et microbiennes, dans la colonne d'eau jusqu'au sédiment. D'autre part, des carottes de sédiment pourraient être prélevées afin d'étudier les communautés benthiques et d'estimer leur activité par techniques de marquage radioactif au laboratoire. Les débits des rivières et leur charges sédimentaires semblent aussi jouer un rôle important et seront suivis, ce qui permettra une compréhension accrue des processus biogéochimiques à l'interface sédiment / colonne d'eau.

La limitation en nitrate du plateau a été démontrée mais son cycle est encore méconnu. Il s'agirait ici de mesurer les espèces chimiques impliquées dans les processus complexes qui peuvent avoir lieu dans une zone d'upwelling et sur le fond qui présente parfois une déplétion en oxygène. Dans ce contexte, on peut se demander si l'intensification des OMZ ne pourrait pas créer l'apparition d'une telle zone sur ce plateau continental.

L'origine profonde des eaux upwellées au nord de la zone reste un phénomène inexpliqué. On pourrait ainsi mesurer des variables atmosphériques locales, liées à l'intensité de l'upwelling, étudier la colonne d'eau sur et en dehors du plateau, et en parallèle utiliser des outils de modélisation pour comprendre quels facteurs peuvent expliquer une origine si profonde des eaux upwellées.

Pour les processus physiques, nous avons pu observer un processus ponctuel (formation du front secondaire d'upwelling par exemple) puis l'étudier à partir d'un modèle. Cependant on manque cruellement de données à plus haute résolution de telles structures pour ensuite valider complètement nos résultats. Une solution serait d'équiper une zone d'intérêt d'une marge continentale avec des ADCP fixés sur une bouée, couplés à des radars côtiers haute fréquence. Ceux-ci fourniraient une bonne couverture temporelle des courants de la colonne d'eau et de la surface, respectivement, et permettraient ainsi de mieux comprendre la circulation d'une marge continentale.

Nous avons aussi étudié en détail la structure physique et biogéochimique d'un filament dans l'IPUS, révèlant ainsi l'export associé significatif vers le large d'un écosystème productif. Cet export important au sein de la structure échantillonnée, associé à la formation continue de filaments toute l'année dans les EBUS nous

amène à proposer en perspective d'évaluer le rôle global des filaments à mésoéchelle sur la balance métabolique du gyre oligotrophe de l'océan Atlantique Nord. Pour cela, nous proposons la mise en place de 2 observatoires côtiers dans l'IPUS et dans l'upwelling des Canaries, localisés tout deux à un site préalablement choisi de formation privilégiée de filaments. Une surveillance permanente des structures sera assurée par un mouillage fixe équipé de capteurs physiques et biogéochimiques, couplé à un radar HF pour observer la circulation de surface. Additionnellement, des Gliders aussi équipés de capteurs physiques et biogéochimiques seront déployés périodiquement au sein de la structure s'élongeant vers le large. Dans un second temps, l'extrapolation des résultats à l'impact global de tels filaments à l'échelle du bassin sera réalisée grâce à une étude de modélisation couplée 3D à haute résolution.

Le modèle utilisé dans *Rossi et al.* [2010] fut construit pour étudier les effets adiabatiques d'une circulation supposée en équilibre géostrophique, sans tenir compte des effets de la couche de mélange. Or les observations ont révélé un fort impact des modifications de vents à haute fréquence sur la stratification et l'épaisseur de la couche de mélange dans l'IPUS. En utlisant un autre type de modèle, on peut donc proposer d'étudier la dynamique de la couche de mélange en réponse à un forçage de vents variable à haute fréquence.

Des simulations omises de l'article *Rossi et al.* [2010] ont montré une alternance positive et négative du transport perpendiculaire à la côte forcé par un vent oscillatoire. Nous avons identifié des ondes de Poincaré, qui se propagent depuis le centre du bassin, et qui peuvent être excitées par une certaine forme de forçage. Cela peut constituer une piste de recherche qui semble peu documentée et qui joue un rôle sur le mélange des eaux du plateau avec celles du large.

A partir du Chapitre 5 (*Rossi et al.* [2008, 2009]), plusieurs interrogations se posent. Nous avons proposé des hypothèses pour expliquer la relation inverse entre mélange horizontal et concentration de chlorophylle dans les zones d'upwelling. Pour éclaircir ce phénomène, des outils de modélisation sont nécessaires. Une approche en 2D concerne le couplage des courants issus de télédétection spatiale avec un modèle simple NPZ et permettra de reproduire la différence entre les sous-systèmes et peut être identifier un mécanisme. La deuxième concerne la mise en place d'une maquette du modèle HYCOM en 3D couplé avec un module biogéochimique. Ce sera l'occasion de tester et évaluer dans un cadre réaliste nos hypothèses sur le rôle des tourbillons qui diminueraient les vitesses verticales associées aux phénomènes d'upwelling et induiraient à la fois une perte latérale de nutriments.

D'autres questionnements provenant du Chapitre 5 concernent l'outil lagrangien utilisé, les FSLE. Bien que cet outil soit basé sur la théorie de la turbulence en 2 dimensions, ce sont bien les vitesses verticales qui sont importantes pour la biologie. Les deux axes sont : (i) Peut-on étendre le calcul des Lyapunov locaux (FSLE ou FTLE) à une circulation en trois dimensions ? (ii) Quelles sont les vitesses verticales associées aux LCS (Lagrangian Coherent Structures) déduites du calcul 2D des FSLE ? Les structures calculées en forward ou backward in time sont-elles comparables ?

Enfin, l'Annexe B présente un article (*TewKai et al.* [2009]) qui montre la corrélation entre le comportement de prédateurs marins supérieurs, les grandes frégates, et les LCS de l'océan de surface mises en évidence par les FSLE. Cela démontre clairement la forte influence de ces phénomènes à méso- et sub mésoéchelle sur les écosystèmes et leur structuration, à tous les niveaux trophiques. Les études en collaboration avec des écologistes et des biologistes sont donc fortement recommandées.

Enfin, nous pouvons résumer ces perspectives autour de trois questions générales :

Quels sont les facteurs qui contrôlent la production primaire des EBUS ?

Quelles sont les interactions entre l'écosystème planctonique et les échelons supérieurs exploités ?

Quel sera le futur comportement de ces zones sous l'influence du changement global du climat ?

Bibliography

Abraham, E., The generation of plankton patchiness by turbulent stirring, *Nature*, *1998*, 577–580, 1998.

Alvain, S., C. Moulin, Y. Dandonneau, H. Loisel, and F. Breon., Instruments and Methods: A species-dependent bio-optical model of case I waters for global ocean color processing., *Deep-Sea Res. Pt I*, *53*, 917–925, 2006.

Alvarez-Salgado, X., C. Castro, F. Perez, and F. Fraga, Nutrient mineralization patterns in shelf waters of the Western Iberian Upwelling, *Cont. Shelf Res.*, *17*, 1247–1270, 1997.

Alvarez-Salgado, X., J. Aristegui, E. Barton, and D. Hansell, Contribution of upwelling filaments to offshore carbon export in the subtropical Northeast Atlantic Ocean, *Limnol. Oceanogr.*, *52*, 1287–1292, 2007.

Aminot, A., and R. Kerouel., *Dosage automatique des nutriments dans les eaux marines : méthodes en flux continu.*, Ed. IFREMER ed., Brest (France), 2007.

Arístegui, J., and M. Montero, Temporal and spatial changes in plankton respiration and biomass in the Canary Islands region: the effect of mesoscale variability, *J. Marine Syst.*, *54*, 65–82, 2005.

Arístegui, J., E. Barton, P. Tett, María, F. M. M. G.-M. noz, G. Basterretxea, A. Cussatlegras, A. Ojeda, and D. deArmas, Variability in plankton community structure, metabolism,and vertical carbon fluxes along an upwelling filament (Cape Juby, NW Africa), *Prog. Oceanogr.*, *62*, 95–113, 2004.

Aristegui, J., et al., The influence of island-generated eddies on chlorophyll distribution: a study of mesoscale variation around Gran Canaria, *Deep-Sea Res. Pt I*, *44*, 71–96, 1997.

Aurell, E., G. Boffetta, A. Crisanti, G. Paladin, and A. Vulpiani., Predictability in the large: an extension of the concept of Lyapunov exponent., *J. Phys. A*, *30*, 1–26, 1997.

Bakun, A., Global climate change and intensification of coastal ocean upwelling, *Science*, *247*, 198–201, 1990.

Barreira, L., and Y. Pesin, vol. 23, University Lecture Series ed., American Mathematical Society, 2002.

Barton, E., and J. Arístegui, The Canary Islands Coastal Transition Zone - Upwelling, Eddies and Filaments, *Prog. Oceanogr.*, *62 (2-4)*, 67–69, 2004.

Barton, E., et al., The transition zone of the Canary Current upwelling region, *Prog. Oceanogr.*, *41 (4)*, 455–504, 1998.

Behrenfeld, M., et al., Satellite-detected fluorescence reveals global physiology of ocean phytoplankton, *Biogeosciences*, *6*, 779–794, 2009.

Birch, D., W. Young, and P. Franks, Thin layers of plankton: Formation by shear and death by diffusion, *Deep-Sea Res. Pt I*, *55*, 277–295, 2008.

Bleck, R., An oceanic general circulation model framed in hybrid isopycnic-Cartesian coordinates., *Ocean Model.*, *37*, 55–88, 2002.

Boffetta, G., A. Celani, and M. Vergassol, Inverse energy cascade in two-dimensional turbulence: Deviations from Gaussian behaviour, *Phys. Rev. E*, *61*, r29–r32, 2000.

Boffetta, G., G. Lacorata, G. Redaelli, and A. Vulpiani, Detecting barriers to transport: A review of different techniques, *J. Phys. D*, *159*, 58–70, 2001.

Brewin, R., S. Sathyendranath, T. Hirata, S. Lavender, R. Barciela, and N. Hardman-Mountford., A three-component model of phytoplankton size class for the Atlantic Ocean, *Ecol. Model.*, *in press*, 2010.

Brink, K., and T. Cowles, The Coastal Transition Zone Program, *J. Geophys. Res.*, *14*, 637–647, 1991.

Capet, X., P. Klein, B. Hua, G. Lapeyre, and J. McWilliams, Surface kinetic energy transfer in surface quasi-geostrophic flows, *J. Fluid Mech.*, *604*, 165–174, 2008a.

Capet, X., J. McWilliams, M. Molemaker, and A. Shchepetkin, Mesoscale to Submesoscale Transition in the California Current System. Part I: Flow Structure, Eddy Flux, and Observational Tests, *J. Phys. Oceanogr.*, *38*, 29–43, 2008b.

Carr, M., et al., A comparison of global estimates of marine primary production from ocean color., *Deep-Sea Res. Pt II*, *53*, 741–770, 2006.

Castro, C., X. Alvarez-Salgado, F. Figueiras, F. Perez, and F. Fraga, Transient hydrographic and chemical conditions affecting microplankton populations in the coastal transition zone of the Iberian upwelling system (NW Spain) in September 1986, *J. Mar. Res.*, *55*, 321–352, 1997.

Checkley, D., and J. Barth, Patterns and processes in the California current system, *Prog. Oceanogr.*, *83*, 49–64, 2009.

Chisholm, S., Stirring times in the Southern Ocean., *407*, 685–686, 2000.

Coble, P., Marine Optical Biogeochemistry: The Chemistry of Ocean Color, *Chem. Rev.*, *107*, 402–418, 2007.

Danabasoglu, G., J. McWilliams, and P. Gent, The Role of Mesoscale Tracer Transports in the Global Ocean Circulation, *Science*, *264*, 1123–1126, 1994.

Demarcq, H., Trends in primary production, sea surface temperature and wind in upwelling systems (1998-2007), *Prog. Oceanogr.*, *83*, 376–385, 2009.

Denman, K., et al., *Couplings Between Changes in the Climate System and Biogeochemistry*, Cambridge University Press ed., Cambridge, United Kingdom and New York, NY, USA., 2007.

Dickey, T., Emerging ocean observations for interdisciplinary data assimilation systems, *J. Marine Syst.*, *40-41*, 5–48, 2003.

d'Ovidio, F., V. Fernández, E. Hernández-García, and C. López, Mixing structures in the Mediterranean Sea from finite-size Lyapunov exponents., *Geophys. Res. Lett.*, *31*, L17 203, 2004.

d'Ovidio, F., J. Isern-Fontanet, C. López, E. Hernández-García, and E. García-Ladona, Comparison between Eulerian diagnostics and Finite-Size Lyapunov Exponents computed from Altimetry in the Algerian basin, *Deep-Sea Res. Pt I*, *56*, 15–31, 2009.

Falkowski, P., D. Zieman, Z. Kolber, and P. Bienfang, Role of eddy pumping in enhancing primary production in the ocean, *Nature*, *352*, 55–58, 1991.

Franklin, D., A. Poulton, M. Steinke, J. Young, I. Peeken, and G. Malin, Dimethyl-sulphide, DMSP-lyase activity and microplankton community structure inside and outside of the Mauritanian upwelling, *Prog. Oceanogr.*, *83*, 134–142, 2009.

Fréon, P., M. Barange, and J. Arístegui, Eastern Boundary Upwelling Ecosystems: Integrative and Comparative Approaches : Integrative and comparative approaches, *Prog. Oceanogr.*, *83*, 1–14, 2009a.

Fréon, P., F. Werner, and F. Chavez, *Conjectures on future climate effects on marine ecosystems dominated by Small Pelagic Fish*, Cambridge University Press ed., Cambridge, United Kingdom and New York, NY, USA., 2009b.

Fréon, P., et al., Functional group biodiversity in eastern boundary upwelling ecosystems questions the wasp-waist trophic structure, *Prog. Oceanogr.*, *83*, 97–106, 2009c.

Garçon, V., A. Oschlies, S. Doney, D. McGillicuddy, and J. Waniek, The role of mesoscale variability on plankton dynamics in the north atlantic, *Deep-Sea Res. Pt II*, *48*, 2199–2226, 2001.

Gasol, J., L. Alonso-Sáez, L. Vaqué, F. Baltar, M. Calleja, C. Duarte, and J. Arístegui, Mesopelagic prokaryotic bulk and single-cell heterotrophic activity and community composition in the NW Africa–Canary Islands coastal-transition zone, *Prog. Oceanogr.*, *83*, 189–196, 2009.

Gasparini, S., Plankton Identifier: a software for automatic recognition of planktonic organisms., *http://www.obs-vlfr.fr/~gaspari/Plankton_Identifier/index.php*, 2007.

Gordon, L., J. Jennings, A. Ross, and J. Krest., A suggested protocol for continuous flow automated analysis of seawater nutrients (phosphate, nitrate, nitrite, and silicic acid) in the WOCE hydrographic program and the Joint Global Ocean Fluxes Study., 1995, oceanography Group Technical Report 93–10.

Gorsky, G., et al., Digital zooplankton image analysis using the ZooScan integrated system., *J. Plankton Res.*, *in press*, 2010.

Grosjean, P., M. Picheral, C. Warembourg, and G. Gorsky, Enumeration, measurement,and identification of net zooplankton samples using the ZOOSCAN digital imaging system., *ICES Mar. Sc.*, *61*, 518–525, 2004.

Gruber, N., H. Frenzel, S. Doney, P. Marchesiello, J. McWilliams, J. Moisan, J. Oram, G. Plattner, and K. Stolzenbach., Eddy-resolving simulation of plankton ecosystem dynamics in the California Current System, *Deep-Sea Res. Pt I*, *53*, 1483–1516, 2006.

Hernández-Carrasco, I., E. Hernández-García, C. López, and A. Turiel., How reliable are Finite-Size Lyapunov Exponents for the assessment of ocean dynamics?, *Chaos*, *submitted*, 2010.

Heukelem, L. V., and C. Thomas., Computer-assisted high performance liquid chromatography method development with applications to the isolation and analysis of phytoplankton pigments., *J. Chromatogr. A*, *910*, 31–49, 2001.

Holland, W., the Role of Mesoscale Eddies in the General Circulation of the Ocean—Numerical Experiments Using a Wind-Driven Quasi-Geostrophic Model, *J. Phys. Oceanogr.*, *8*, 363–392, 1978.

Isern-Fontanet, J., G. Lapeyre, P. Klein, B. Chapron, and M. Hecht, Three-dimensional reconstruction of oceanic mesoscale currents from surface information, *J. Geophys. Res.*, *113*, C09 005, 2008.

Jansen, E., et al., *Paleoclimate*, Cambridge University Press ed., Cambridge, United Kingdom and New York, NY, USA., 2007.

Johnson, K., et al., Observing Biogeochemical Cycles at Global Scales with Profiling Floats and Gliders, *Oceanography*, *22 (3)*, 216–255, 2009.

Joint, I., A. Rees, and M. Woodward, Primary production and nutrient assimilation in the Iberian Upwelling in August 1998, *Prog. Oceanogr.*, *51 (2-4)*, 303–320, 2001.

Karolyi, G., A. Pentek, I. Scheuring, T. Tel, and Z. Toroczkai, Chaotic flow: The physics of species coexistence, *P. Natl. Acad. Sci. USA*, *97*, 13 661–13 665, 2000.

Keeling, R., A. Körtzinger, and N. Gruber., Ocean Deoxygenation in a Warming World, *Annu. Rev. Mar. Sci.*, *2*, 199–229, 2010.

Klein, P., and G. Lapeyre, The Oceanic Vertical Pump Induced by Mesoscale and Submesoscale Turbulence, *Annu. Rev. Mar. Sci.*, *1*, 351–375, 2009.

Koh, T., and B. Legras, Hyperbolic lines and the stratospheric polar vortex, *Chaos*, *12*, 382–394, 2002.

Koné, V., E. Machu, P. Penven, V. Andersen, V. G. con, P. Fréon, and H. Demarcq., Modelling the primary and secondary productions of the southern Benguela upwelling system: A comparative study through two biogeochemical models, *Global Biogeochem. Cy.*, *19*, 2005.

Kostadinov, T., D. Siegel, and S. Maritorena, Global variability of phytoplankton functional types from space: assessment via the particle size distribution, *Biogeosciences Discuss.*, *7*, 4295–4340, 2010.

Labasque, T., C. Chaumery, A. Aminot, and G. Kergoat., Spectrophotometric Winkler determination of dissolved oxygen: re-examination of critical factors and reliability., *Mar. Chem.*, *88 (1-2)*, 53–60, 2004.

Lagerloef, G., G. Mitchum, R. Lukas, and P. Niiler, Tropical Pacific near-surface currents estimated from altimeter, wind, and drifter data, *J. Geophys. Res.*, *104*, 23 313–23 326, 1999.

Lapeyre, G., and P. Klein, Impact of the small-scale elongated filaments on the oceanic vertical pump, *J. Mar. Res.*, *64*, 835–851, 2006.

Lehahn, Y., F. d'Ovidio, M. Lévy, and E. Heyfetz, Stirring of the Northeast Atlantic spring bloom: a Lagrangian analysis based on multisatellite data, *J. Geophys. Res.*, *112*, C08 005, 2007.

Lévy, M., P. Klein, and A. Tréguier, Impact of submesoscale physics on production and subduction of phytoplankton in an oligotrophic regime, *J. Mar. Res.*, *59*, 535–565, 2001.

Lewis, M., E. Horne, J. Cullen, N. Oakey, and T. Platt., Turbulent motions may control phytoplankton photosynthesis in the upper ocean, *Nature*, *311*, 49–50, 1984.

López, C., Z. Neufeld, E. H.-G. E., and P. Haynes, Chaotic advection of reacting substances: plankton dynamics on a meandering jet, *Phys. Chem. Earth Pt B*, *26*, 313–317, 2001.

Lyapunov, A., The general problem of the stability of motion, *Int. J. Control*, *55 (3)*, 531–534, 1992.

Mahadevan, A., and A. Tandon, An analysis of mechanisms for submesoscale vertical motion at ocean fronts, *Ocean Model.*, *14*, 241–256, 2006.

Mahadevan, A., L. Thomas, and A. Tandon, Comment on *Eddy/Wind Interactions Stimulate Extraordinary Mid-Ocean Plankton Blooms*, *Science*, *320*, 448b, 2008.

Martin, A., Phytoplankton patchiness: the role of lateral stirring and mixing, *Prog. Oceanogr.*, *57*, 125–174, 2003.

McGillicuddy, D., A. Robinson, D. Siegel, H. Jannasch, and R. Johnson, Influence of mesoscale eddies on new production in the sargasso sea, *Nature*, *394*, 263–266, 1998.

McGillicuddy, D., L. Anderson, S. Doney, and M. Maltrud, Eddy-driven sources and sinks of nutrients in the upper ocean: result from a $0.1°$ resolution model of the north atlantic, *Global Biogeochem. Cy.*, *17*, 1035, 2003.

McGillicuddy, D., L. Anderson, N. Bates, T. Bibby, and K. Buesseler, Eddy/wind interactions stimulate extraordinary mid-ocean plankton blooms, *Science*, *316*, 1021–1026, 2007.

McKiver, W., and Z. Neufeld, Influence of turbulent advection on a phytoplankton ecosystem with nonuniform carrying capacity, *Phys. Rev. E*, *79 (6)*, 061 902, 2009.

Mitchell, J., H. Yamazaki, L. Seuront, F. Wolk, and H. Li., Phytoplankton patch patterns: Seascape anatomy in a turbulent ocean, *J. Marine Syst.*, *69*, 247–253, 2008.

Moore, T., R. Matear, J. Marrac, and L. Clementson., Phytoplankton variability off the Western Australian Coast: Mesoscale eddies and their role in cross-shelf exchange, *Deep-Sea Res. Pt II*, *54*, 943–960, 2007.

Motoda, S., *Devices of simple plankton apparatus.*, Faculty of Fisheries. ed., Hokkaido University, Japan., 1959.

Ohde, T., H. Siegel, J. R. mann, and M. Gerth., Identification and investigation of sulphur plumes along the Namibian coast using the MERIS sensor, *Cont. Shelf Res.*, *27*, 744–756, 2007.

Oschlies, A., Can eddies make ocean desert blooms?, *Global Biogeochem. Cy.*, *16 (4)*, 1106–1117, 2002.

Oschlies, A., and V. Garçon, Eddy-induced enhancement of primary production in a model of the north atlantic ocean, *Nature*, *394*, 266–269, 1998.

Oschlies, A., and V. Garçon, An eddy-permitting coupled physical-biological model of the north-Atlantic, sensitivity to advection numerics and mixed layer physics, *Global Biogeochem. Cy.*, *13*, 135–160, 1999.

Pasquero, C., A. Bracco, and A. Provenzale, Impact of the spatiotemporal variability of the nutrient flux on primary productivity in the ocean, *J. Geophys. Res.*, *110*, 2005.

Paulmier, A., and D. Ruiz-Pino., Oxygen minimum zones (OMZs) in the modern ocean, *Prog. Oceanogr.*, *80 (3-4)*, 113–128, 2009.

Paulmier, A., D. Ruiz-Pino, and V. G. con, The oxygen minimum zone (OMZ) off Chile as intense source of CO2 and N2O, *Cont. Shelf Res.*, *28 (20)*, 2746–2756, 2008.

Pauly, D., and V. Christensen, Primary production required to sustain global fisheries, *Nature*, *374*, 255–257, 1995.

Perruche, C., P. Riviére, P. Pondaven, and X. Carton, Phytoplankton competition and coexistence: Intrinsic ecosystem dynamics and impact of vertical mixing, *J. Marine Syst.*, *81*, 99–111, 2010.

Ras, J., H. Claustre, and J. Uitz., Spatial variability of phytoplankton pigment distributions in the Subtropical South Pacific Ocean: comparison between in-situ and predicted data., *Biogeosciences*, *5*, 353–369, 2008.

Relvas, R., J. Luis, and A. Santos, Importance of the mesoscale in the decadal changes observed in the northern Canary upwelling system, *Geophys. Res. Lett.*, *36*, L22 601, 2009.

Rio, M., P. Schaeffer, F. Hernandez, and J. Lemoine, The estimation of the ocean Mean Dynamic Topography through the combination of altimetric data, in-situ measurements and GRACE geoid: from global to regional studies, in *Proceedings of GOCINA workshop*, 2005.

Rodríguez, J., M. Moyano, and S. Hernández-León, The ichthyoplankton assemblage of the Canaries–African coastal transition zone: a synthesis, *Prog. Oceanogr.*, *83*, 314–321, 2009.

Rossi, V., C. López, J. Sudre, E. Hernández-García, and V. Garçon, Comparative study of mixing and biological activity of the Benguela and Canary upwelling systems., *Geophys. Res. Lett.*, *35*, L11 602, 2008.

Rossi, V., C. López, E. Hernández-García, J. Sudre, V. Garçon, and Y. Morel, Surface mixing and biological activity in the four Eastern Boundary Upwelling System., *Nonlinear Proc. Geoph.*, *16*, 557–568, 2009.

Rossi, V., Y. Morel, and V. Garçon, Effect of the wind on the shelf dynamics: formation of a secondary upwelling along the continental margin, *Ocean Model.*, *31 (3-4)*, 51–79, 2010.

Rykaczewski, R., and D. Checkley, Influence of ocean winds on the pelagic ecosystem in upwelling regions, *P. Natl. Acad. Sci. USA*, *105*, 1965–1970, 2008.

Sandulescu, M., C. López, E. Hernández-García, and U. Feudel, Biological activity in the wake of an island close to a coastal upwelling, *Ecol. Complex.*, *5*, 228–237, 2008.

Sangra, P., et al., The Canary Eddy Corridor: A major pathway for long-lived eddies in the subtropical North Atlantic, *Deep-Sea Res. Pt I*, *56*, 2100–2114, 2009.

Shchepetkin, A., and J. McWilliams, The Region Ocean Model System (ROMS): A split-explicit, free-surface, topography-following-coordinate oceanic model, *Ocean Model.*, *9*, 347–404, 2005.

Shillington, F., L. Hutchings, T. Probyn, H. Waldron, and W. Peterson, Filaments and the Benguela frontal zone: offshore advection or recirculating loops ?, *S. Afr. J. Mar. Sci.*, *12*, 207–218, 1992.

Solomon, S., et al., *Technical Summary*, Cambridge University Press ed., Cambridge, United Kingdom and New York, NY, USA., 2007.

Stramma, L., G. Johnson, J. Sprintall, and V. Mohrholz., Expanding Oxygen-Minimum Zones in the Tropical Oceans, *Science*, *320*, 655–657, 2008.

Stramski, D., R. Reynolds, M. Kahru, and B. Mitchell, Estimation of Particulate Organic Carbon in the Ocean from Satellite Remote Sensing, *285*, 239–242, 1999.

Strub, P., Kosro, P.M., and H. A., The nature of the cold filaments in the California Current System, *J. Geophys. Res.*, *96*, 14,743–14,768, 1991.

Sudre, J., and R. Morrow, Global surface currents: a high resolution product for investigating ocean dynamics,, *Ocean Dynam.*, *58 (2)*, 101–118, 2008.

TewKai, E., V. Rossi, J. Sudre, H. Weimerskirch, C. López, E. Hernández-García, F. Marsac, and V. Garçon., Top marine predators track Lagrangian coherent structures, *P. Natl. Acad. Sci. USA*, *106*, 8245–8250, 2009.

Vandromme, P., L. Stemmann, C. Garcia-Comas, S. Colbert, L. Berline, M. Picheral, S. Gasparini, J. Guarini, and G. Gorsky., Assessing the properties of net collected and automatically classified zooplankton size spectra before their use in models or ecological studies., *J. Plankton Res.*, *in prep.*, 2010.

Wunsch, C., and R. Ferrari., Vertical mixing, energy, and the general circulation of the oceans., *Annu. Rev. Fluid Mech.*, *36*, 281–314, 2004.

Annexe A : Distribution of Volatile Halogenated Organic Compounds in the Iberian Peninsula Upwelling System.

.1 Article 6: Distribution of Volatile Halogenated Organic Compounds in the Iberian Peninsula Upwelling System, Raimund, Vernet, Rossi *et al.*, 2010 to be submitted to Journal of Geophysical Research.

Distribution of Volatile Halogenated Organic Compounds in the Iberian Peninsula Upwelling System

1 Introduction

Volatile Halogenated Organic Compounds (VHOCs) are trace gases that can influence atmospheric chemistry. These gases are climatically active and potentially a major source of reactive halogens. VHOCs may contribute to 20-35% of stratospheric bromine; essentially by the short-lived polyhalogenated compounds CH_2Br_2 and $CHBr_3$ (Pfeilsticker et al. 2000). Bromine may contribute up to 30 % of ozone depletion in the troposphere and lower stratosphere (Salawitch et al. 2005; Yang et al. 2005). World oceans, via the marine-atmosphere boundary layer have been suggested to be the largest source of nonanthropogenic VHOCs to the atmosphere. In contrast to anthropogenic halocarbons, VHOC with natural sources are characterized as short-lived compounds with life-times in the range of minutes (e.g. diiodomethane) to about a one year (chloromethane) (Law and Sturges 2006). The transport of these gases to the lower stratosphere results from large-scale ascent in the tropics and rapid deep convection. Thus, the role of VHOCs for stratospheric ozone depleting is depending on various factors: (1) the ozone depleting potential of the gas itself (life-time, halogen, and breakdown products), (2) saturation level in the boundary layer, (3) location of the source (distance to deep convection) and (4) seasonal aspects.

In the last two decades the magnitude of oceanic formation and emissions of certain halocarbons has been estimated in several studies (e.g. Class and Ballschmiter 1988; Lobert et al. 1997; King et al. 2002; Quack et al. 2004; Quack et al. 2007b; Carpenter et al. 2009). Generally, halocarbon concentrations are higher in the coastal regions than in the open ocean. Brominated and iodinated compounds have mainly biological sources in coastal regions. Biological sources are related to macroalgae (Laturnus 2001), phytoplankton (Hill and Manley 2009) or bacteria (Amachi 2008). Furthermore abiotic processes are an additionally source for marine VHOCs. Among these processes, photochemical production in surface waters (Richter and Wallace 2004) and anthropogenic discharge (Quack and Wallace 2003) are most important. Anthropogenic discharge is the strongest source for the long-lived chlorinated halocarbons.

Biological function and production of halocarbons still remain unclear. It has been proposed that vanadium-dependent haloperoxidases (vHPOs) are the crucial enzymes for the formation of polyhalogenated compounds (Leblanc et al. 2006). Triggered by H_2O_2, vHPOs are able to oxidize halides (bromide and iodide primarily) leading to the halogenations of organic substrates. Macroalgae are claimed as the most effective producer for various iodo- and bromocarbon and might contribute up to 70% of global bromoform emissions (Carpenter and Liss 2000). Seaweed incubation experiments have demonstrated, that macroalgae produce various halocarbon, and that formation is highly species-dependent (Nightingale et al. 1995; Carpenter et al. 2000). Since macroalgae distribution is restricted to coastal regions, halocarbons have highly localized sources. Compared to macroalgae production, phytoplankton produce relatively less VHOCs. However, global phytoplanktonic emissions can become significant considering the large size of the open oceans. Beside eukaryotic phytoplankton (mainly diatoms), marine bacteria (e.g. *Prochlorococcus*) might play an important role in the understanding of global halogen budget (Smythe-Wright et al. 2006).

Upwelling systems are characterized by high primary production, predominantly by diatoms. In laboratory experiments it could be shown that some diatoms synthesise bromoperoxidase and iodoperoxidase, two key enzymes for the formations of halocarbons. It was demonstrated that cultures of marine diatoms produce various brominated and iodinated compounds (Moore et al. 1996). Hence it can be assumed that upwelling regions are potentially hot spots for halocarbon formation.

Halocarbon distribution in upwelling systems has been poorly studied. Recently, Carpenter et al. (2009) and Quack et al. (2007a; 2007b) observed elevated dibromomethane and bromoform concentrations in the Mauritanian upwelling. Both studies hypothesised that biological sources like diatom abundance or macro algae beds were the major source for brominated halocarbons. However, underlying factors for VHOC distribution patterns remain poorly understood.

Upwelling systems are well suited to investigate the formation of halocarbons by different phytoplankton groups, especially due to the absence of macroalgae. However, advection and convection of water masses into the upwelling may eliminate possible relations between VHOC concentrations and phytoplankton biomass: (1) convection elevates cold, nutrient rich waters and may reduce VHOC concentration in surface waters, (2) advection transports VHOC-rich coastal waters towards the upwelling (Carpenter and Liss 2000), (3) advection from the upwelling to the open ocean influences VHOC levels and (4) floating macro algae may cause increased VHOC levels far from the coast line (Moore and Tokarczyk 1993).

In this work, halocarbon distributions were investigated in the Iberian Peninsula Upwelling System during a campaign along the coast off Portugal, which took place in summer 2007 (August 11th to September 14th) within the framework of the *Modélisation océanique d'un théâtre d'opérations navales* (MOUTON) program on the French research vessel *Pourquoi pas*.

Here we present spatial, vertical and temporal distribution of VHOCs in the Iberian upwelling system in summer 2007. Environmental variables are analysed for their possible influence on the VHOC distribution. Different potential sources four different VHOC groups are identified.

2 Method

2.1.1 Study Area

The study area extended from 39.1 to 42.8°N and 8.9 to 11.1°W. In this area we sampled 69 stations along three different transects and four additional 30-hours stations (see Figure 1).
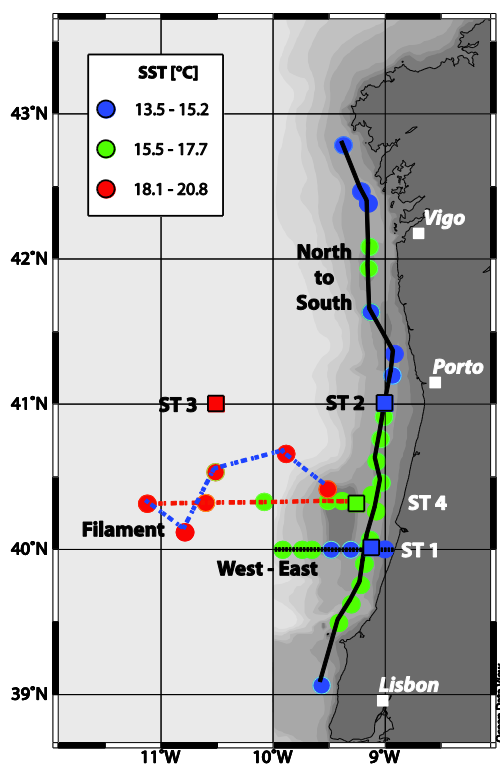
Figure 1. Mouton campaign 2007 in the Iberian Peninsula Upwelling System.

Tracks and 30-hours stations were grouped by sea surface temperature. Dots represent position of a CTD-station. Lines reflect tracks of the cruise (solid line: north to south track within the upwelling; dotted black line: west to east track

The Iberian Peninsula Upwelling System is the northern extent of the Canary Upwelling. It ranges from about 36°N to about 46°N and from the Iberian coast to roughly 24°W (Perez et al. 2001). During summer north/northwesterly tradewinds generate a southward flow, which results in an offshore Ekman transport. This Ekman transport is responsible for the upwelling of cold and nutrient enriched waters from 100-300 m depth to the surface along the coastline (Smyth et al. 2001). Upwelling events are usually strongest in the north of the Iberian Peninsula Upwelling system (off Cap Finisterre) and are often related to westward flowing advections. These so called filaments are bands of cold and less salty waters which can reach as far as 100 km westward (Coelho et al. 2002).

Samples were taken using a 12-bottle CTD rosette (10-L-Niskin bottles). At each station, up to five samples were collected at different levels of the water column: surface, upper thermocline, maximum of chlorophyll, lower thermocline and bottom depth. Samples were taken to determine VHOC concentrations, pigment composition and nutrient levels. Physical variables and meteorological data were recorded simultaneously.

Various sea surface temperature (SST) satellite images revealed that the strength of upwelling off the Iberian Peninsula shows intense fluctuation on multiday dimensions. The main sampling took place between August 14th and 25th with high wind velocity and a resulting strong upwelling. Sampling in a filament and 30h stations took place during calm weather conditions between September 4th and 9th with moderate upwelling.

2.1.2 Physical variables and pigment analysis

Physical variables were recorded simultaneously by the CTD rosette and meteorological sensors of the vessel. Oxygen values were calibrated by independent sampling and Winkler titration. Pigments were analysed using a HPLC technique described by Wright et al. (1991). A HPLC system was used from THERMO spectrasystem equipped with a C18 (CLI) inverse column. One litre of sample was filtered at -200mbar onto a 25 mm GF/F filter. Filters were stored at -196°C in liquid nitrogen. Extraction of pigments was conducted with cold methanol (-20°C) for 12 hours. Detection limits range between 0.002 µg/mL for Chl b, Chl $c2$ and Alloxantin and 0,013 µg/mL for beta-Caroten. Pigments identification and quantification was done by comparing retention times and peaks areas and adsorption spectra obtained using certified standard solutions from DHI Group, Denmark.

Samples for nutrient analysis were taken in 125 ml polyethylene bottles, pre-treated with hydrochloric acid and deionised water, and finally rinsed with the sea water to analyse. These bottles have been kept at -20°C in darkness until the analysis were carried out. For nutrient analysis a semi-automated system was used (TECHNICON, autoanalyser II). The following nutrients were determined:

- Silicic acid ($Si(OH)_4$): following the protocol of Fanning and Pilson (1973).
- Nitrate (NO_3^-) and nitrite (NO_2^-): as described by Bendschneider and Robinson (1952) and Wood et al. (1967). Firstly, nitrite concentrations were determined. Then, nitrate was reduced to nitrite and finally the nitrite concentration was measured. The difference between both gives the nitrates concentration.
- Phosphate(PO_4^{3-}): as defined by Murphy and Riley (1962).
-

2.1.3   Analysis of volatiles

VHOCs were analysed using a purge-and-trap technique and GC-ECD (Chrompack CP 9000) modified after Pruvost et al. (1999). The purge-and-trap-loop was altered and Valco valves were replaced by highly saltwater resistant Swagelok models. Sampling devices were modified according to Bulsiewicz et al. (1998). These new sampling devices (30 ml) were highly gastight; leak tests showed tightness for over a week. In contrast to Bulsiewicz, sampling devices were directly connected to the Niskin bottle and to the purge-and-trap-loop respectively via Swagelok miniature quick connectors. The connector between Niskin-bottle and sampling device comprises a filter element with 15 μm pore size, to remove larger particles. Samples were stored in the dark at 4°C and finally analyzed within four hours after sampling.

Volatiles were extracted by purging with ultra-pure nitrogen for 20 min at a flow of 90 ml min^{-1}. Purging took place at ambient temperature in a purge chamber, which contained a glass frit (Pyrex 4). The gas flow was dried downstream using a condenser (held at 2 °C) and a magnesium perchlorate trap.

Volatiles were concentrated in a stainless steel capillary tube (150 cm) at -78°C and subsequently injected into a gas chromatographic column by thermodesorption (100°C, backflush). Separation of the compounds was performed using a capillary column (fused silica megabore DB-624, 75 m, 0.53 mm id, 3 mm film thickness, J & W Scientific, flow: 6 ml min^{-1} ultra pure nitrogen) and a temperature program (10 min at 70°C, rising for 8 min to 150°C and stable for 7 min at 150°C). Quantification of volatiles was performed by external liquid standards (EPA 624 mix standards, AccuStandard; iodoethane, dibromomethane, chloroiodomethane, diiodomethane, bromoiodomethane Carlo Erba). Liquid standards were diluted in seawater and treated like a normal sample.

Table 1 shows the studied VHOC and gives the detection limits for each of them.

Table 1. Volatile Halogenated Organic Compounds determined in the Iberian Peninsula Upwelling System.

VHOC	Abbr.	Molecular formula	LoD [pmol L^{-1}]
Idoethane	IE	CH_3CH_2I	0.1
Chloroform	CF	$CHCl_3$	0.58
Methyl chloroform	MC	CH_3CCl_3	0.1
Tetrachloromethane	TCM	CCl_4	0.05
Trichloroethylene	TCE	C_2HCl_3	0.1
Dibromomethane	DBM	CH_2Br_2	0.09
Bromodichloromethane	BDCM	$CHBrCl_2$	0.11
Chloroiodomethane	CIM	CH_2ClI	0.03
Perchloroethene	PCE	$CCl_2=CCl_2$	0.06
Dibromochloromethane	DBCM	$CHBr_2Cl$	0.07
Bromoiodometahane	BIM	CH_2BrI	0.15
Bromoform	BF	$CHBr_3$	0.43
Diiodomethane	DIM	CH_2I_2	0.09

* LoD: Limit of Detection.

2.1.4 Data analysis

Multivariate methods such as principal component analysis (PCA) or cluster analysis are useful statistical tools to simplify complex data set by reducing the number of potential correlations between variables (Mudge 2007, see there detailed information about statistical methods). In order to determine physical, chemical and biological variables, which could explain the distribution of VHOC we attempt to visualize possible groupings in our dataset. In a first step, a cluster analysis was performed in order to estimate a possible clustering within the dataset. Various variables were treated with a K-means-cluster analysis, including time of the day, water temperature, sea surface temperature (SST), salinity, density, bottom depth, sampling depth and Chlorophyll *a* concentration.

In a second step, a PCA was carried out in order to evaluate similarities between variables of our data set. Here, we computed a PCA for a data set of normalized VHOC values. As a result of the PCA, similarities between the sampling stations formed distinct clusters. Hence we estimated the factor, which might be causal for this clustering. For that, we combined results from the cluster analysis with the PCA. It appeared that SST was the crucial factor.

Consequently in a third step variable correlation matrices were performed for each SST-cluster. Data were analyzed performing one-way and factorial ANOVA with subsequent post-hoc Tukey's honestly

significant difference method for unequal sample size. For the comparison of only two data sets, paired t-tests were performed.

Pearson correlation cross tables were calculated in order to determine the extent to which two variables show linear proportionality to each other. For all statistical tests and techniques *Statistica* (Release 8.0) and *Primer E* (Release 5) were used.

Detailed information about multivariate exploratory techniques (such as PCA or cluster analysis) are given by Legendre (1998), whereas Sokal and Rohlf (1995) gives a comprehensive introduction about univariate analysis (such as ANOVA or Pearson correlations).

3   Results

3.1.1   Upwelling during the campaign and sampling strategy

Sampling strategy (for results see Figure 1) was defined by evaluating satellite images (Figure 2). Both Chl-*a* concentration- and SST-images indicated a proceeding upwelling and phytoplankton bloom along the coast of Portugal.
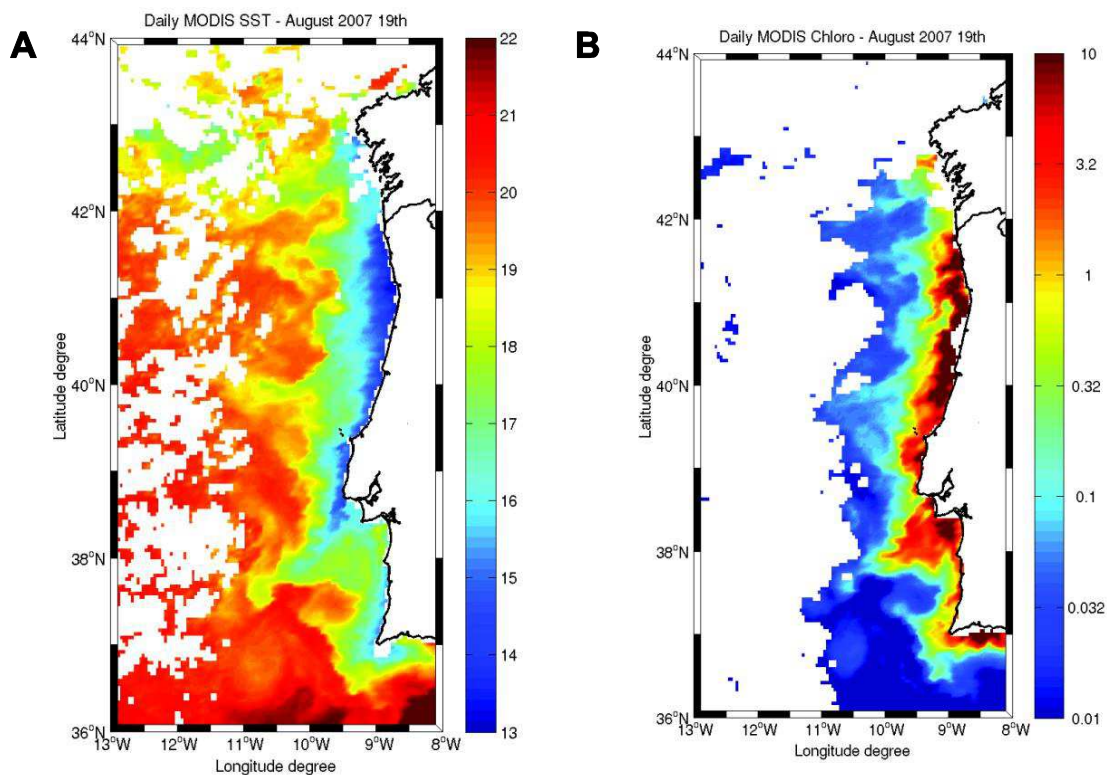
Figure 2. Satellite image of sea surface temperature (SST) and Chl-*a* concentration on August 19th 2007.

The north-to-south track followed a 100 m bottom depth isoline and was located within the upwelling. This track was chosen in order to investigate VHOC concentrations within the maximum of phytoplankton density. The west-to-east track followed 40°N degree of latitude from the open ocean toward the upwelling. This track was chosen to investigate differences between coastal influenced upwelled waters and nutrient depleted open ocean waters. A distinct offshore filament was sampled heading westwards at 40.4°N. This track was completed by sampling outside the filament heading eastwards. Additionally, samples were taken at four 30 h stations (ST 1 – 4). Station 1 (40°N, 9.1°W) and 2 (41°N, 9°W) were located within the upwelling. Station 3 (41°N, 10.5°W) was a reference point in the open ocean. Station 4 (40.3°N, 9.2°W) was located just outside the upwelling.

Satellite images indicated that sea surface temperature decreased in the first two weeks of the campaign compared to the previous weeks, indicating that upwelling took place before the start of the campaign. A satellite sea-surface temperature image taken on August 19th showed clear upwelling conditions occurring in the studied area (Figure 2, A). Distinctive upwelling took place along the Iberian Peninsula from Cap Finisterre to 37°N with highest convection about 41°N. A clear temperature gradient is visible from the open ocean (around 21°C) towards the coast (less than 15°C). Filaments were visible at 37.5°N, 40°N and 41.5°N. These cold water bands extend from the Iberian coast up to 12°W and are characterised by temperatures significantly lower than the surrounding water masses. Satellite images of Chl-*a* concentrations indicated a phytoplankton bloom along the Iberian Peninsula (see Figure 2, B). Concentrations were highest near the coastline (more than 3.5 µg/L) and low in the open ocean (two orders of magnitude lower). Coupled to upwelling and advection, a meandering structure of the phytoplankton density is clearly visible all along the coast. During the last week of the campaign, upwelling conditions were still evident although wind velocity decreased (less than 10 m/s) and sea surface temperatures increased by several degrees along the coast.

3.1.2 Spatial distribution of selected VHOCs

Sea surface concentrations for selected VHOC measured during the MOUTON campaign are presented in Figure 3.
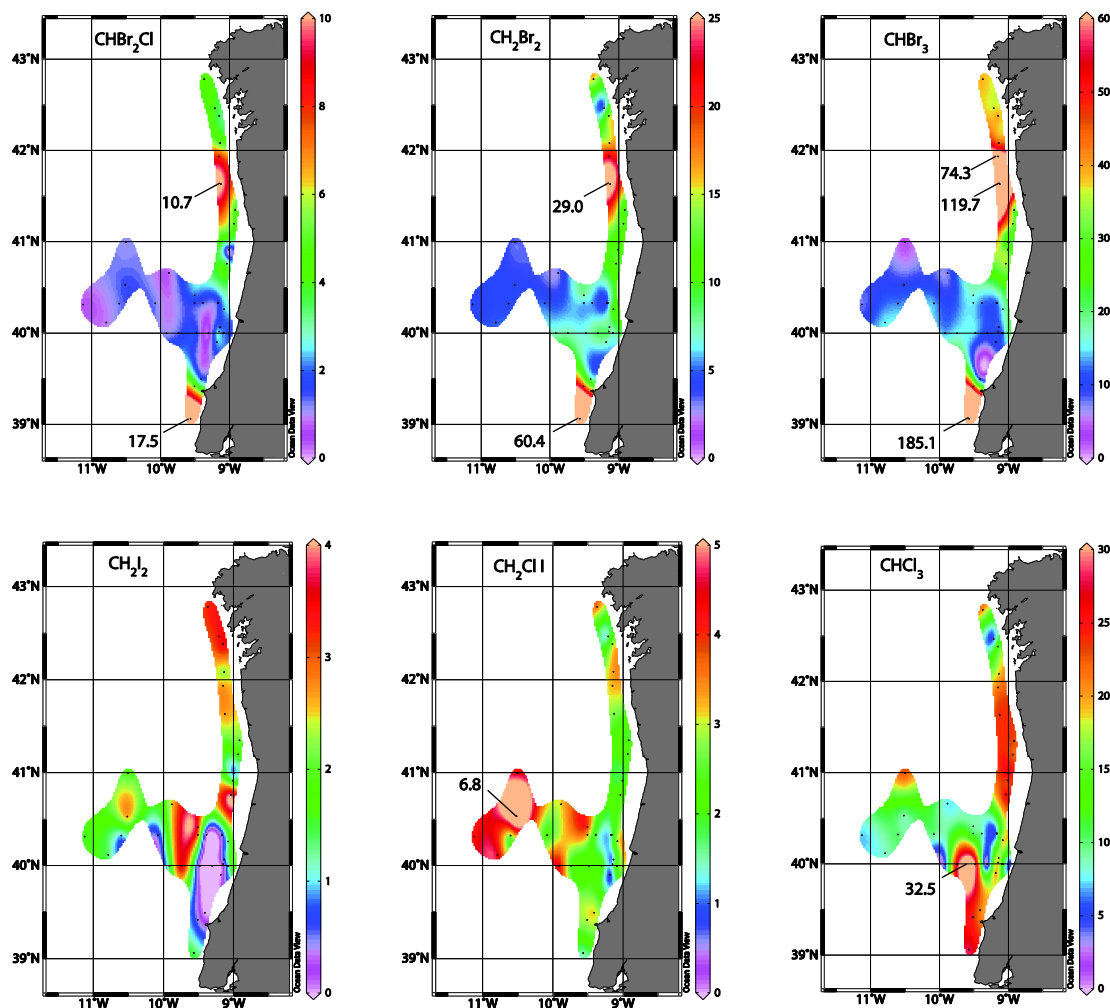
Figure 3. Seasurface values of selected VHOCs.

Dibromochloromethane (CHBr$_2$Cl), dibromomethane (CH$_2$Br$_2$), bromoform (CHBr$_3$), chloroform (CHCl$_3$), chloroiodomethane (CH$_2$ClI) and diiodomethane (CH$_2$I$_2$) in pmol L^{-1}. Colour scales with different concentration range. Stations with values out of scale are labelled.

Generally, concentrations of brominated compounds were high along the coast and low in the filament and in the open ocean. The highest values were found between 41°N and 42°N and around 39.5°N (185.1 pmol L^{-1} for bromoform, 60.4 pmol L^{-1} for dibromomethane and 17.5 pmol L^{-1} for dibromochloromethane).

Concentrations of iodated compounds were about the same range than dibromochloromethane (surface mean of 2.7 pmol L^{-1} for chloroiodomethane and 1.5 pmol L^{-1} for diiodomethane). The highest surface concentrations of chloroiodomethane were recorded in the open ocean far from the coastline (up to 6.8 pmol L^{-1}). Other sampling sites with elevated chloroiodomethane values were

located in the upwelling at 42°N and at the northernmost station (4.5 pmol L^{-1}). Diiodomethane levels were elevated in open ocean waters (up to 4.2 pmol L^{-1}) and at two stations near the coast.

Chloroform levels were the highest among the chlorinated compounds (surface mean of 16.9 pmol L^{-1}). Values were elevated in the upwelling between 40.5 and 42° N (up to 23.9 pmol L^{-1}) and south of 40°N. The highest chloroform concentration was recorded at the junction between upwelling and intermediate water masses at 40°N (32.5 pmol L^{-1}). Concentrations were low in the open ocean and in the filament structure.

3.1.3 SST as grouping variable

In order to evaluate VHOC distribution patterns we performed cluster analyses and a principal component analysis (PCA). The result of the PCA was used to visualize relationships among studied VHOCs and their sampling sites (Figure 4).
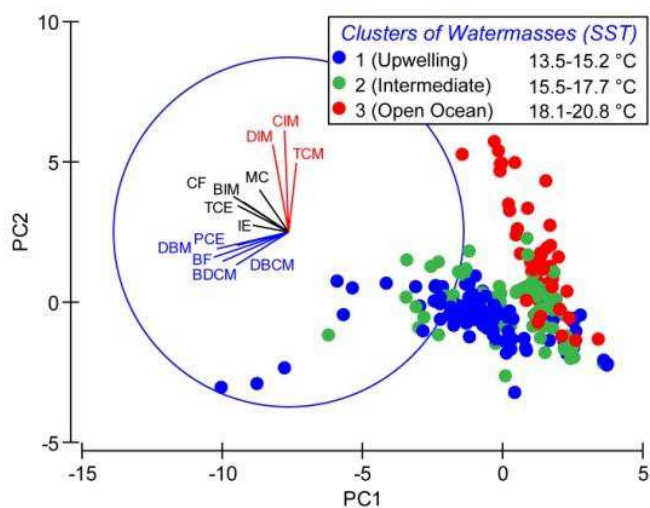
Figure 4. Principal Component Analysis (PCA) of all normalized VHOC data.

Similarities among VHOC are plotted as vectors, while similarities between the sampling sites are plotted as dots. Samples are grouped by SST-clusters. For abbreviations of VHOC see Table 1. Correlations to the principal component PC1 (x-axis) explain 32 % of the data and correlations to the principal component PC2 (y-axis) explain about 17% of all data.

Diiodomethane, chloroiodomethane and tetrachloromethane are best explained by PC2 and show high similarities among themselves. Dibromomethane, bromoform, dibromochloromethane, bromodichloromethane and perchloroethene formed a second cluster, which is related to PC1. A

third cluster is composed of iodoethane, bromoiodomethane, 1,1,2-trichlorethene, methyl chloroform and chloroform. This group however is not well explained by the PCA model. Because of the marginal vector length of perchloroethene and tetrachloromethane, correlations to PC1 and PC2 are low.

Figure 4 illustrates clear similarities between various samples sites. Here we found that sample sites form three clusters. In order to demonstrate the underlying feature of this data spreading, we overlaid the plot with results of a cluster analysis. From the studied physical variables sea surface temperature (SST) was determined as a factor that could best explain the distribution pattern of the sampling sites. Other variables (e.g. salinity or chlorophyll a) did not reflect the clustering of the sampling sites. SST values form three clusters and reflected different water masses: The *upwelling water mass* reflect stations with a SST-mean of 14.5 °C (see also Figure 1). These stations were located were close to the coast of the Iberian Peninsula. *The Intermediate water mass* attributed stations with a SST-mean of 16.4°C. Those stations were located either close to the coast line (aged upwelled waters) or in the filament (cold waters mixed with open ocean waters). The *Open ocean water mass* featured a SST-mean of 19.7°C. All stations were located in the far off Iberian coast.

3.1.4   Relationship Between the Compounds

Similarities between VHOCs were shown in the PCA model (see Figure 4). In order to evaluate correlations in-between gases, we calculated Pearson correlations matrices. In Figure 5 we present those correlations of three representative halocarbons to all other VHOCs. Brominated compounds are well correlated among each other in all water masses. Highest correlations were found between dibromomethane and bromoform in intermediate water masses. Clear correlations between iodated compounds were remarkable between chloroiodomethane and diiodomethane in the open ocean and less articulated in intermediate water masses. In the upwelling however, no significant correlations were found among iodated compounds. Correlations between chlorinated compounds were weak. The highest correlations were visible between methyl chloroform and chloroform in the upwelling.
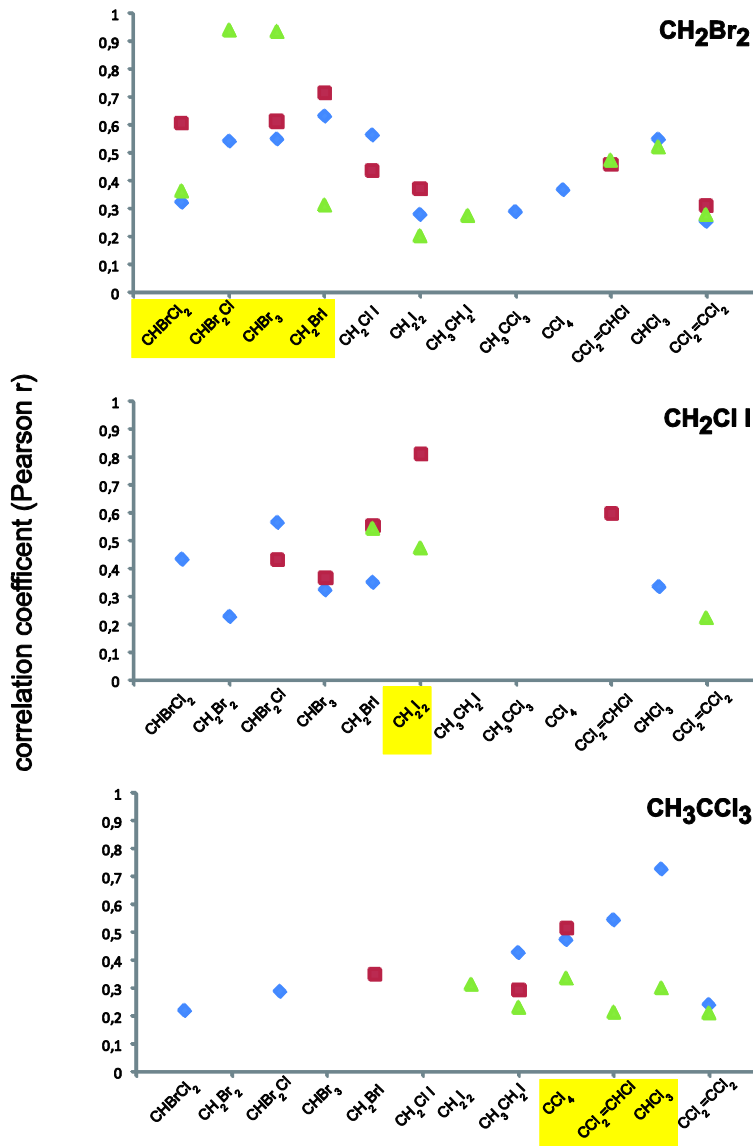
Figure 5. Results of cross-tabulation tables of Pearson r correlation coefficients (selected VHOCs against all VHOCs).

Significant (p<0.05) correlations of three representative VHOC to all other VHOCs. The correlation cross table were calculated for all samples. Data are clustered in three different water masses: Upwelling (blue), intermediate water (green) and open ocean (red). Remarkable correlations are indicated in yellow.

3.1.5   Vertical distribution of VHOCs compared to environmental parameters

Based on the three water mass types (as defined above), we studied the vertical distribution of VHOCs and environmental parameters in each water mass. Figure 6 shows the distribution of representative halocarbons and synoptic data. Sampling depth was a highly significant factor for most variables. More detailed information is given in Table 2, Table 3 and Table 4. There, VHOCs and environmental variables are grouped by different water mass and depth (mean values of all samples from surface to thermocline and samples below the thermocline).
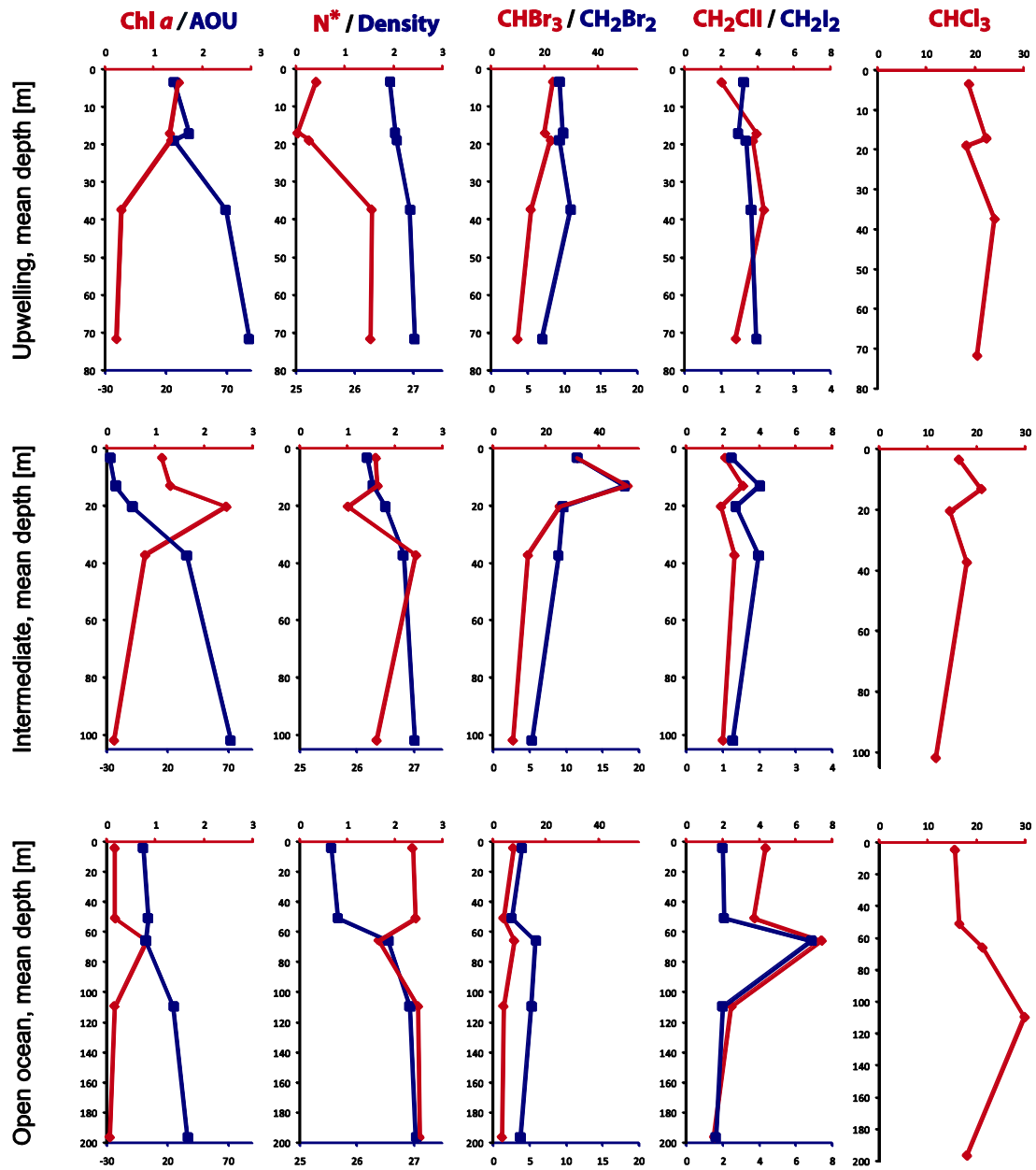
Figure 6 Depth profiles of chlorophyll *a* [µg L⁻¹], AOU [µmol L⁻¹], N*[µmol L⁻¹], density [σ] and selected VHOC [pmol L⁻¹] in the three defined water masses at five depth.

Row 1: Upwelling waters. Row 2: Intermediate waters. Row 3: Open ocean waters. Values expressed as mean of samples of surface, upper thermocline, maximum of chlorophyll, lower thermocline and bottom. Red lines use primary x-axis (above, red). Blue lines refer to secondary x-axis (below, blue). Note: CIM concentration at open ocean province had different scale from the other provinces.

In the upwelling, σ-values showed a deep mixing without a clear pycnocline (Figure 6, row 1). Maxima of Chl-*a* were observed in the first 20 m (1.5µg L-1) and reached very low values in the deeper layer below 40 m. The apparent oxygen utilisation (AOU) was negatively correlated to Chl-*a*: values were low near the surface and in the Chl-*a* maximum whereras AOU-values increased with depth. N* (a linear combination of nitrate and phosphate; see (Gruber and Sarmiento 1997)) is a benchmark for the marine nitrogen cycle. Low N*-values reflect a nitrate loss whereas high values indicate nitrogen fixation. In the upwelling, N* showed the same pattern as AOU: the lowest values were found in surface waters and in the Chl-*a* maximum. Bromocarbons showed no clear peak in the water column. While dibromomethane did not vary significantly with depth, bromoform concentrations were significantly lower in the deeper layer compared to the upper layer (factor 2.4, p= 0.001). Variations of chloroiodomethane, diiodomethane and chloroform did not vary significantly with depth in the upwelling.

In the intermediate water mass (Figure 6, row2), the water column was weakly stratified (pycnocline at about 20 m). However, a clear Chl-*a* maximum was recorded at 20-m depth and corresponded to a minimum N*-value. AOU values were significantly elevated below the pycnocline. For all gases, maximum values were measured just above the Chl *a* maximum. Values of brominated compounds were up to 6.7 times higher here compared to the deeper layer values. Iodated compounds and chloroform showed maxima just above and below the Chl-*a* maximum. However variations of diiodomethane and chloroform did not vary significantly with depth.

In the open ocean (Figure 6, row3), the water column was clearly stratified. The pycnocline (66 m) corresponded with the Chl-*a* maximum. N*-values were in average 1.5 times higher in the upper layers of the open ocean compared to the upper layer in the identified intermediate water mass, indicating a lower loss of nitrogen in the open ocean. At the Chl-*a* maximum however, N* values were significantly lower, in average 1.5 times than in all other water layers. Brominated compounds showed no clear maxima throughout the water column. Concentrations were low compared to coastal waters (about 3 times lower for the surface concentrations). However, bromocarbon concentrations were significantly higher at the Chl-*a* maximum. Iodinated compounds showed maximum values at the Chl-*a* peak. Values were 2-5 times higher there compared to all other depth, and 2.7 – 3.2 times higher compared with the coastal waters. Chloroform showed a maximum concentration below the pycnocline (2 times higher compared to surface waters).

Table 2. Mean values of 13 VHOC in pmol/L and DBM/BF- ratio in the Iberian Upwelling. Data grouped by sampling depth (Cluster 1: surface to maximum of chlorophyll; Cluster 2: below maximum of chlorophyll) and SST (Cluster SST1: *Upwelling*, T < 15.3 ; Cluster SST2: *Intermediate*, 15.4 > T < 18°C; Cluster SST3: *Open Ocean*, T>18.1°C).

	Surface to Thermocline				Below Thermocline			
	Entire Data	Upwelling	Intermediate	Open Ocean	Entire Data	Upwelling	Intermediate	Open Ocean
CH_3CH_2I	1.12	1.14	1.33	0.73	0.88	1.31	0.65	0.56
$CHCl_3$	17.81	19.24	16.14	18.54	18.36	21.9	13.9	20.96
CH_3CCl_3	4.92	4.57	5.48	4.46	5.18	5.42	5.18	4.73
CCl_4	5.86	3.66	6.12	8.81	3.4	2.34	3.27	5.72
C_2HCl_3	8.59	8.67	8.8	8.11	7.39	8.1	7.64	5.5
CH_2Br_2	9.18	9.42	11.48	4.77	6.89	8.59	6.61	4.18
$CHBrCl_2$	2.44	3.45	2.51	0.76	2.28	2.98	2.34	0.8
CH_2ClI	2.97	2.04	2.15	5.84	1.94	1.73	2.22	1.76
$CCl_2=CCl_2$	1.73	2.27	1.6	1.13	1.88	2.39	1.65	1.4
$CHBr_2Cl$	2.79	3.22	3.27	1.32	2.04	2.77	1.83	1.07
CH_2BrI	1.67	2.08	1.37	1.55	1.72	2.06	1.82	0.84
$CHBr_3$	22.19	21.68	31.09	7.36	9.26	11.93	9.54	3.48
CH_2I_2	2.21	1.62	1.41	4.52	1.71	1.91	1.53	1.72
$CH_2Br_2/CHBr_3$	0.41	0.43	0.37	0.65	0.74	0.72	0.69	1.2

Table 3. Physical and chemical variables in the Iberian Upwelling region. Data grouped by sampling depth and SST

(*Upwelling waters,* 13.5-15.2°C; *Intermediate waters,* 15.5 – 17.7°C; *Open Ocean waters,* 18.1-20.8°C).

	Surface to Thermocline				Below Thermocline			
	Entire Data	Upwelling	Intermediate	Open Ocean	Entire Data	Upwelling	Intermediate	Open Ocean
SST [°C]	16.38	14.46	16.37	19.66	16.38	14.46	16.37	19.66
Salinity [PSU]	35.74	35.68	35.69	35.92	35.76	35.76	35.77	35.76
Temp [°C]	15.56	14.16	15.71	17.48	13.04	12.93	13.2	12.89
Oxygen [mL/L]	245.37	224.2	264.66	239.58	198.92	183.39	198.91	230.0
AOU [$\mu mol\ L^{-1}$]	4.71	32.91	-15.43	1.18	63.99	80.14	63.16	33.73
Turbidity [NTU]	0.37	0.65	0.35	-0.01	0.12	0.16	0.14	-0.03
Nitrate [μmol/L]	3.14	7.35	1.59	0.37	10.48	12.5	10.05	8.08
Silicate [μmol/L]	1.76	3.13	1.06	1.27	4.71	5.82	4.53	3.25
Phosphate [μmol/L]	0.3	0.62	0.19	0.08	0.72	0.86	0.69	0.53
N* [μmol/L]	1.14	0.19	1.34	2.07	1.89	1.57	1.85	2.52

Table 4. Mean values of marker pigments in the Iberian Upwelling region. Data grouped by sampling depth and SST

(*Upwelling,* 13.5-15.2°C; *Intermediate,* 15.5 – 17.7°C; *Open Ocean,* 18.1-20.8°C).

	Surface to Thermocline				Below Thermocline			
	Entire Data	Upwelling	Intermediate	Open Ocean	Entire Data	Upwelling	Intermediate	Open Ocean
chla	1466.93	1774.72	1584.17	577.78	457.66	550.0	426.88	no data
chlb	115.21	101.82	122.25	111.39	33.94	30.13	35.21	no data
chlc2	172.1	233.48	178.96	52.61	42.09	72.25	32.04	no data
chlc3	100.14	90.95	112.52	71.11	38.19	43.63	36.38	no data
fuco	708.24	907.86	797.26	86.17	251.38	329.13	225.46	no data
but	35.15	18.8	35.71	58.67	9.56	8.63	9.88	no data
perid	83.48	87.71	96.76	30.44	28.63	29.38	28.38	no data
hex	114.37	64.1	117.06	183.17	27.5	11.63	32.79	no data
diadino	96.82	102.12	113.93	28.67	30.5	34.13	29.29	no data
allo	20.01	21.7	22.92	7.17	6.38	12.88	4.21	no data
lut	11.24	12.68	13.73	0.28	5.69	1.88	6.96	no data
zea	44.33	32.9	40.55	75.33	7.81	7.75	7.83	no data
caro	40.93	52.34	42.78	16.72	10.88	6.38	12.38	no data

3.1.6 Temporal and tide factors in the upper layers

Diurnal and tidal variations of VHOC concentrations were investigated by calculating ANOVAs of all samples taken in the upper layers (sea surface to thermocline). Again, the data set was divided into the three different water masses.

In order to investigate the factor time, samples were sorted by the sampling time and divided in four groups: night, day, and intermediates. All samples taken in between 2h after sunset and 2h before sunrise were defined as "night samples". All samples taken in between 2h after sunrise and 2h before sunset were defined as "day samples". Intermediate times were defines as morning or evening samples. Results of the ANOVAs indicate that the factor time has significant effects (Figure 7) on bromocarbons. In the upwelling, values were significantly higher after sunset (factor 1.5 to 1.8; p-values between 0.002 and 0.055) and stayed rather low during the rest of the day. Intermediate waters showed higher concentrations between dusk and night, compared to the period between dawn and daytime (factor 1.8 to 2.1). Diurnal variations of bromocarbons in the open ocean were less clear. Variances for dibromomethane and dibromochloromethane are small (factor 1.1 and 1.2) and statistically not significant. Bromoform however showed a significantly elevated concentration during night-time (factor 2, p = 0,05). Time of the day showed no significant influence on iodocarbons and chloroform (data not shown).
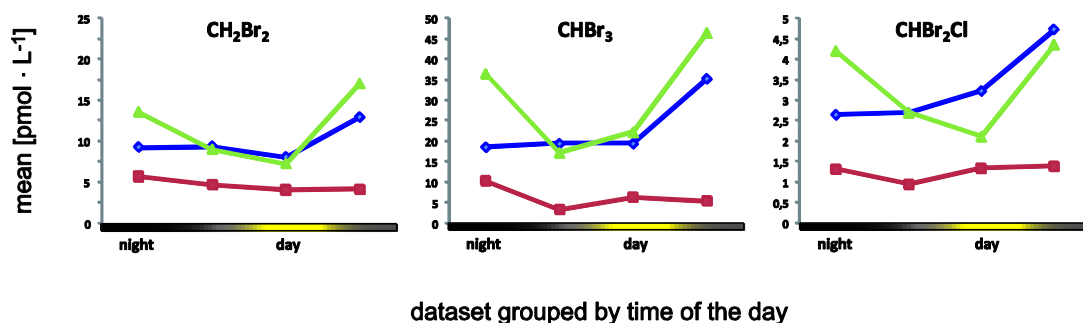
Figure 7. Influence of time of the day to bromocarbons.

Mean values of four different times of the day (night, day, and intermediates) for samples from the surface to the thermocline. Night and day were defined as two hours before sunrise and sunset, respectively.

In order to investigate the factor tide, samples were sorted by the sampling time and divided in four groups: high tide, low tide, incoming mid tide and outgoing mid tide. Sampling times were compared with tide tables, provides by SHOM (*Service hydrographique et océanographique de la marine*) for

different places along the Iberian coast. Figure 8 illustrates clear effects of tide on VHOC levels within the upwelling. Upwelling values of brominated compounds were significantly elevated when water flowed back from the coast to the open ocean. In intermediate water masses the effect is still noticeable but statistically less significant. Similarly to brominated compounds chloroform and iodated compounds showed elevated concentrations in the upwelling during the outgoing tide. In intermediate water masses however, values of chloroiodomethane and diiodomethane were significantly elevated at incoming tide. Generally, in intermediate water masses, effects are noticeable and are not significant in the open ocean.
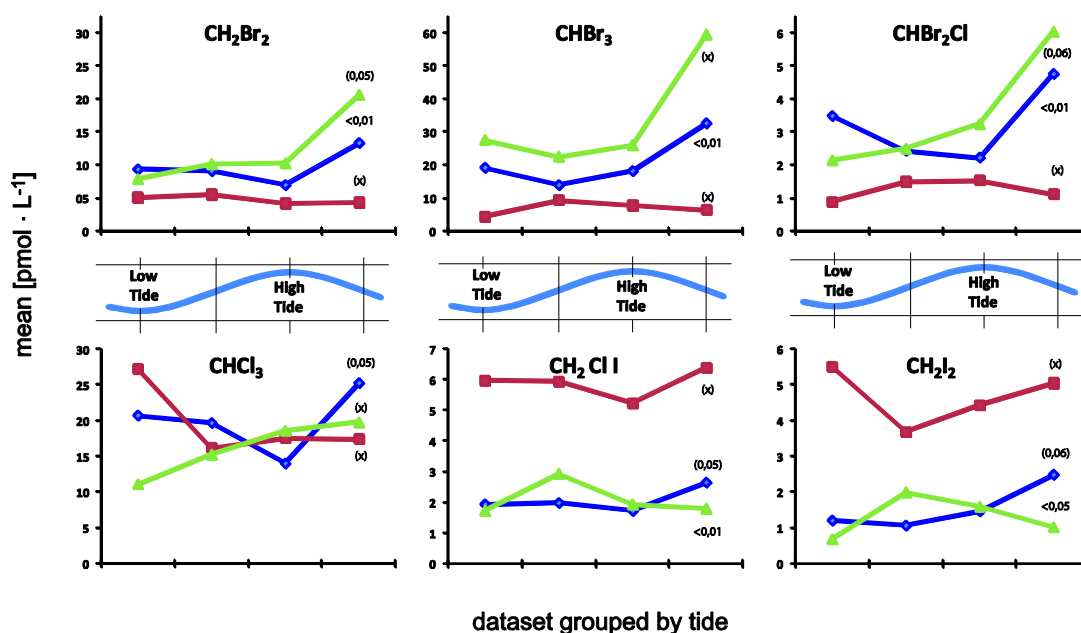
Figure 8. Influence of tide to selected VHOCs in the upper layers.

Blue lines: in the upwelling. Green lines: intermediate waters. Red line: open ocean. Mean- and p-values are plotted against four tidal steps (low tide, incoming mid tide, high tide, outgoing mid tide). Non-significant effects are expressed as (x). Significant levels are expressed in parentheses (p-values).

4   Discussion

This is the first study of volatile halogenated organic compounds in the Iberian Upwelling, and presents a comprehensive number of brominated, iodated and chlorinated volatiles in an upwelling system. Our data show that multivariate effects are causal for the distributions of VHOCs. Here we

present evidence for different VHOCs sources, which are each causal for the production of a certain group of VHOCs. This study demonstrates for the first time the effect of tide on VHOCs distribution.

4.1.1 Comparison to other studies

Although a wide range of marine regions were investigated for VHOC levels, only a few studies focused on upwelling regions: Class and Ballschmiter (1988) measured bromocarbons and tetrachloromethane near the West African coast (25°N 16°W). The Mauritanian Upwelling was investigated by Quack et al. (2007b) between 17.0 and 20.5 °N in April/March 2005 and by Carpenter et al. (2009) between 16 and 35°N in May/June 2007. Both studies were focused on bromoform and dibromomethane and found similar mean values (see Table 5).

Our values however, were about a factor 2 higher than data reported for the Mauritanian Upwelling, and were rather similar to coastal water values reported for the African Upwelling.

The only study which studied various VHOC along the Iberian Peninsula, were restricted to the shoreline and did not measured in the upwelling(Martinez et al. 2002). These authors focused on monitoring different anthropogenically produced VHOCs and reported results as class distribution and maximum values. Consequently these results give a broad representation for nonnatural coastal inputs of chlorinated volatiles but are less comparable to our results.

Table 5. Comparison of VHOC concentrations in different regions. Mean values in pmol · L^{-1}.

	African Coastal Upwelling	Mauritanian Upwelling	African Coastal Upwelling	North east Atlantic	English Channel	Irish Sea	Antarctic waters	Portugal coast
	25°N 16°W (03/1985)	17-20.5°N 16-19°W (04-05/2005)	16-35°N 14-24°W (05-06/2007)	53-59°N 7-13°W (06-07/2006)	50°N 4°W (2002-2004)	53°N 4°W (2004-2005)	70-72°S 9-11°W (12/2003)	(1999-2000)
	Class and Ballschmiter 1988	Quack et al. 2007	Carpenter et al. 2009		Archer et al. 2007	Bravo-Linares and Mudge 2009	Carpenter et al. 2007	Martinez et al. 2002
CH$_3$CH$_2$I					1.5 [f]	9.5 [g]		
CHCl$_3$						141.77 [g]		167.53 [x]
CH$_3$CCl$_3$						0.92 [g]		12.22
CCl$_4$	6.5 [a]					3.4 [g]		117 [x]
C$_2$HCl$_3$						2.64 [g]		98.94 [x]
CH$_2$Br$_2$	5.77 [a]	4.9 [a]	3.4 [c]	1.1 [e]		5.45 [g]		
		5.8 [b]	3 [d]	1.9 [f]				
			1.4 [e]	15.6 [g]				
CHBrCl$_2$	6.1 [a]					5.06 [g]		
CH$_2$ClI					10.8 [f]	0.91 [g]	0.7 [g]	
CCl$_2$=CCl$_2$						13.13 [g]		78.41 [x]
CHBr$_2$Cl	9.6 [a]					17.3 [g]		
CH$_2$BrI					1.2 [f]		0.8 [g]	
CHBr$_3$	23.74 [a]	10.7 [a]	11.5 [c]	3.4 [e]		214.23 [g]	56.7 [g]	

			9 [b]		14.4 [d]		6.7 [f]	
					3.5 [e]		68.3 [g]	
CH_2I_2						2.5 [f]	2.71 [g]	4.2 [g]

* [a] depth 0-12m; [b] depth 14-50m; [c] upwelling; [d] Canaries; [e] open ocean; [f] shelf and far coast; [g] coastal; [x] coastal and river, not specified, maximum values.

Based on various oceanic data, production of VHOCs has highly localized sources. Saturations are highest in littoral zones, mainly in macro-algae beds. Furthermore, seawater concentrations vary greatly with seasons (Archer et al. 2007) and hence comparisons of different studies might be challenging. Contrary to the assumptions of a strong phytoplankton production in upwelling regions, we report values intermediate between coastal and open ocean values.

4.1.2   On the different origin of VHOCs

Results from the principal component analysis (see Figure 4) showed similarities between three sample sites and between VHOCs. It was shown that sample sites cluster in three groups: upwelling, intermediate water masses, and open ocean. Moreover we showed high similarities between VHOCs indicating similar sources for three different groups: (1) bromocarbons, (2) two iodocarbons (chloroiodomethane and diiodomethane) and (3) the remaining VHOCs (mostly chlorocarbons).

Similarities between VHOCs (Figure 4) and correlations among them (Figure 5) indicated common sources for brominated compounds. Highest correlations between brominated compounds (seeFigure 5, row 1) were recorded in samples with the highest concentrations (intermediate water masses). In intermediate water masses correlations to other gases were not significant or negligibly low. Hence for this region it can be assumed that bromoform, dibromomethane and dibromochloromethane do have the same origin. Contrary to intermediate water masses, correlations between brominated compounds were less pronounced in the open ocean and the upwelling. Thus an additional and more compound-specific source (and/or sink) can be assumed for both water masses.

Dibromomethane/bromoform ratios were calculated by several authors (Carpenter and Liss 2000; Quack et al. 2007b; Carpenter et al. 2009; Jones et al. 2009). Dibromomethane/bromoform slopes were found to be lower in coastal regions and are caused by different sources: macroalgae-produced bromocarbons cause a lower slope whereas slopes are higher in phytoplankton-dominated regions. Our results supported these findings (Table 2).

Iodocarbons (Figure 5, row 2) show clear correlations among each other: the highest correlation was observed between chloroiodomethane and diiodomethane in open ocean waters, a region where the highest concentrations were measured for both gases. Hence both halocarbons do have the same origin and this origin is located in the open ocean. In a recent study it was shown that both compounds can be formed in the presence of dissolved iodine, dissolved organic matter and ozone (Martino et al. 2009).

The correlations of chlorocarbons (Figure 5, row 3) did not show clear patterns. For example, we present correlations of methyl chloroform to all other VHOCs. The highest correlations (methyl chloroform and chloroform) were observed in the upwelling whereas just one significant correlation was observed in the open ocean. Consequently, a common source for chlorinated volatiles might be connected to the shoreline. Martinez et al. (2002) reported a high coastal input of anthropogenic chlorocarbons at several places in Portugal.

4.1.3   Evidence for phytoplanctonic production of VHOCs

Correlations between different VHOC groups and chlorophyll (fluorescence sensor) were found for brominated and iodated compounds (see Figure 9). Moreover, we found a good correlation between both VHOC groups and both biological markers N* and AOU. These correlations were clearly visible for the open ocean and less pronounced in the upwelling or in intermediate water masses. These results indicate that the formation of brominated and iodated compounds was usually coupled to photosynthetically produced oxygen and nitrogen loss; both caused by phytoplankton activity. The absence of strong correlations in the upwelling and intermediate water could have two explanations: either the main source for brominated and iodated compounds was non-biological or, and more likely, the formation of those compounds was locally separated. Main sources of bromo- and iodocarbons are likely coastal zones of the Iberian Peninsula. Water masses are transported westwards containing elevated concentrations of those compounds.
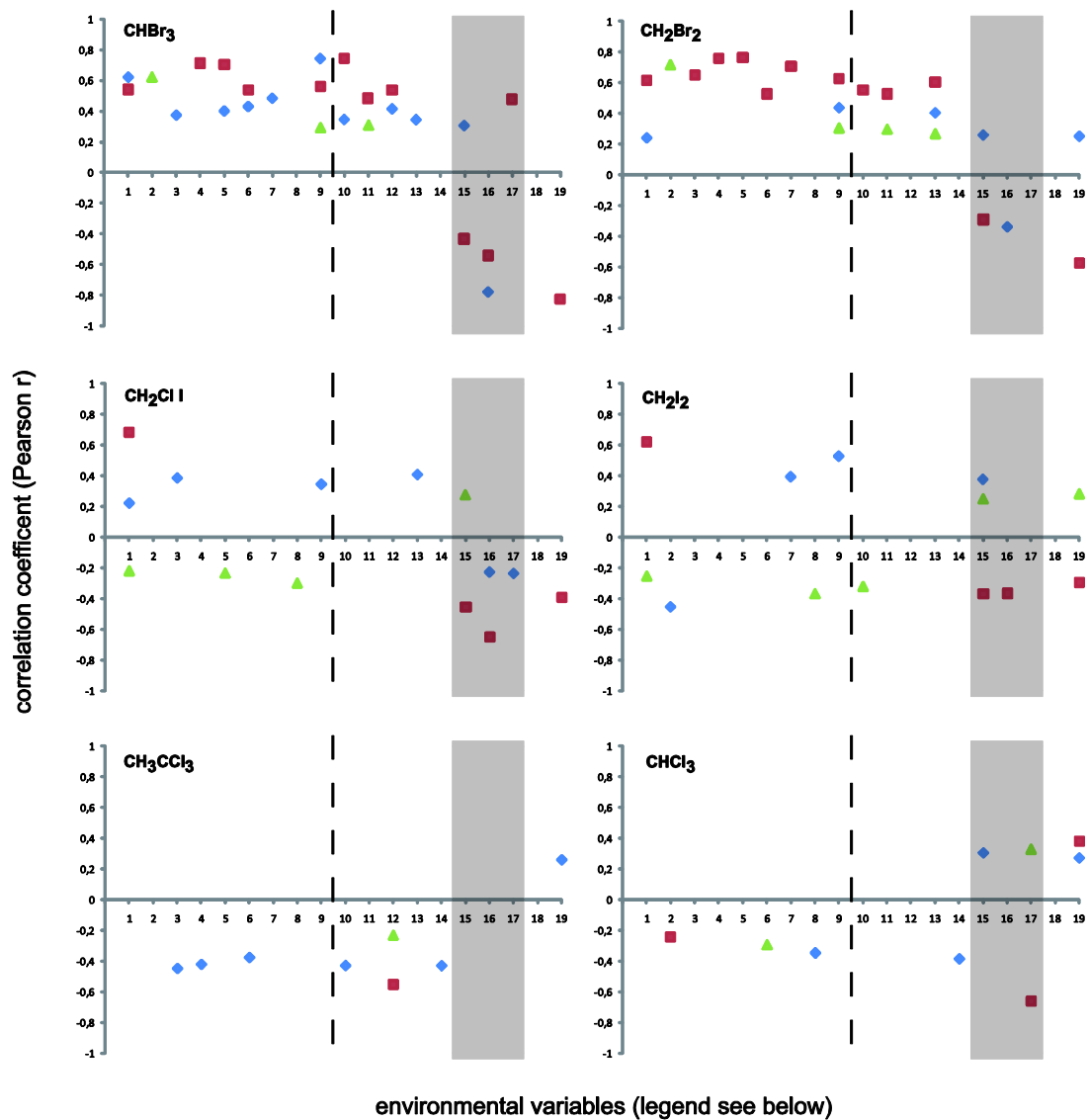
Figure 9. Results of cross-tabulation tables of Pearson r correlation coefficients for selected VHOCs to environmental variables.

Data are clustered into three provinces: Upwelling (blue), Mixed water (green) and Open Ocean (red). Dashed line separate photosynthetic pigments and photoprotective pigments. Grey marks other biological marker. Variables 1-9: photosynthetic pigments (fluorimeter, chl a, chl b, chl c2, chl c3, fuco, but, per, hex). Variables 10-14: photoprotective pigments (diadino, allo, lut, zea, caro). Variables 15-17: N*, AOU, CDOM. Variables 18-19: PAR, lighttransmission.

Correlations to various marker pigments were strong for brominated compounds mainly in the open ocean (Figure 9). Bromoform showed additionally weak correlations in the upwelling. The diversity of correlated pigments emphasise the involvement of different phytoplankton groups in the formation of bromocarbons. Fucoxanthin (Diatoms), Chl-*b* (green algae and prochlorophytes) as well as hexaxanthin and Chl-*c3* (prymnesiophytes) showed the highest correlations to bromocarbons.

Iodated compounds did not correlate to marker pigments in samples with high iodocarbons concentrations (open ocean waters). Weak correlations to Chl-*b* (linked to prochlorophytes) and hex were observed in the upwelling. Chloroiodomethane and diiodomethane likely have a biological origin, since they often correlate with biological markers (fluorescence, N* and AOU). Since phytoplankton is likely not a source for iodocarbons and at the same time N* and AOU correlations suggest a biological origin, it can be assumed, that bacteria are involved in the formation of those VHOCs. This assumption is in agreement with results by (Amachi 2005) who showed formation of both iodated compounds by distinct groups of marine bacteria. As mentioned above, both iodocarbons might have additionally natural but non-biological sources (Martino et al. 2009).

Sun radiation (here expressed as PAR) did not correlate with the measured VHOC in any region. Thus a hypothesis of photolytic formation of iodated compounds might be only a minor source. Light transmission values correlate negatively with bromoform, dibromomethane, chloroiodomethane and diiodomethane in the open ocean. Since plankton has a negative effect on light transmission, plankton abundance may be the cause for elevated bromo- and iodocarbon concentrations.

Chlorinated compounds did not correlate to biological markers (Chl-*a*, N* or AOU). Correlations to marker pigments were weak or negative. Hence it can be assumed that main sources of chlorocarbons are of non-biological origin.

According to all correlations, brominated compounds were produced by microalgae in the open ocean. In the upwelling and in intermediate water masses this formation pathway is masked by strong external sources. Iodocarbons seem to have a bacterial origin and are mainly produced in the open ocean. Due to higher coastal concentrations and missing correlations to biological markers, the main source of chlorinated compounds might be anthropogenic in origin. Since no correlation to radiation exposure were observed, photochemical formation might be a minor source for VHOC in the Iberian upwelling.

4.1.4 Near shore production: main source for brominated compounds in the upwelling?

We found the highest concentrations of bromocarbons in near-shore samples. This finding is in agreement with other studies. Carpenter et al. (2009) found a concentrations gradient in the order coastal region > upwelling > shelf > open ocean. We found lower dibromomethane/bromoform-ratios in near shore waters compared to oceanic waters. A different bromocarbon origin (phytoplankton dominated in open ocean and macroalgae dominated near coast) might be a reason for different ratios.

This is the first study which highlighted the influence of tide to offshore VHOC concentrations. We found strong effects for polybrominated compounds in the upwelling and no effects in the open ocean. Since concentrations are elevated with outgoing tide, it can be assumed that enriched waters are transported westwards thus highlighting the effect of tide on VHOC distribution. Hence, high near shore concentrations can be explained by a translocated macroalgae production.

In the Iberian area elevated concentrations of brominated compounds in the upwelling might be due to near shore production transported westward via a combination of tide and Ekman transport whereas open ocean concentrations could be explained by phytoplankton.

The effect of tide and lateral transport to iodated compounds is weak and unclear. Concentrations are elevated at outgoing midtide in the upwelling and at incoming midtide in the intermediate waters. In the open ocean no statistically significant effect was observed. Thus the production of iodocarbons is less restricted to the coast and a phytoplankton production off shore can be assumed.

Our results show increased bromocarbon concentration after sunset and comparable low concentrations after sunrise. Generally halocarbons are reported to show elevated concentrations with an increase of irradiance (Ekdahl et al. 1998; Marshall et al. 1999; Wang et al. 2009). Since we assume that brominated compounds in the upwelling have a coastal source, it is likely that irradiance increased coastal macroalgae production.

5   Conclusion

Water samples taken in the Iberian Peninsula Upwelling System revealed that spatial distribution of halocarbons are related to sea surface temperature. Variations in sea surface temperatures can be explained by convections and advection processes; two typical processes in upwelling systems.

Statistical methods showed distinct similarities between three different clusters of VHOCs. In those clusters were usually halocarbons with the same halogens (bromocarbons, iodocarbons and chlorocarbons). Those groups were reflected in correlations patterns between VHOCs and environmental variables. Typical correlation patterns indicated that bromocarbons might have a phytoplanktonic source in the open ocean. Iodocarbons showed correlation patterns which were discussed to indicate a bacteria-related source in the open ocean. This idea is supported by the fact, that highest concentrations of iodocarbons were found off shore.

Furthermore it was shown that bromocarbon concentrations of near shore water samples were elevated several hours after high tide. This fact and the observed concentration gradient (lower values towards the open ocean) led us concludes, that the main source of bromocarbons is located in the upwelling and that water masses with elevated bromocarbon concentrations are translocated westwards .

The postulated high concentrations of VHOCs were not found during the campaign. In the upwelling, only weak correlations with marker pigments for phytoplankton were encountered. Hence we reject the idea that upwelling regions might be hot spots for VHOC formation due to diatoms. However the upwelling induced nutrient supply might have some effects on shore line macroalgae beds. We suggest that further studies between the shore line and the upwelling might contribute to a better understanding of sources within the upwelling areas.

6   References

Amachi, S. (2005). "Microbial Influences on the Mobility and Transformation of Radioactive Iodine in the Environment." Journal of Nuclear and Radiochemical Sciences **6**(1).

Amachi, S. (2008). "Microbial Contribution to Global Iodine Cycling: Volatilization, Accumulation, Reduction, Oxidation, and Sorption of Iodine." Microbes and Environments **23**(4): 269-276.

Archer, S. D., L. E. Goldson, et al. (2007). "Marked seasonality in the concentrations and sea-to-air flux of volatile iodocarbon compounds in the western English Channel." Journal of Geophysical Research-Oceans **112**(C8): -.

Bendschneider, K. and R. J. Robinson (1952). "A New Spectrophotometric Method for the Determination of Nitrite in Sea Water." Journal of Marine Research **11**(1): 87-96.

Bulsiewicz, K., H. Rose, et al. (1998). "A capillary-column chromatographic system for efficient chlorofluorocarbon measurement in ocean waters." Journal of Geophysical Research-Oceans **103**(C8): 15959-15970.

Carpenter, L. J., C. E. Jones, et al. (2009). "Air-sea fluxes of biogenic bromine from the tropical and North Atlantic Ocean." Atmospheric Chemistry and Physics **9**(5): 1805-1816.

Carpenter, L. J. and P. S. Liss (2000). "On temperate sources of bromoform and other reactive organic bromine gases." Journal of Geophysical Research-Atmospheres **105**(D16): 20539-20547.

Carpenter, L. J., G. Malin, et al. (2000). "Novel biogenic iodine-containing trihalomethanes and other short-lived halocarbons in the coastal East Atlantic." Global Biogeochemical Cycles **14**(4): 1191-1204.

Class, T. H. and K. Ballschmiter (1988). "Chemistry of Organic Traces in Air .8. Sources and Distribution of Bromochloromethanes and Bromochloromethanes in Marine Air and Surfacewater of the Atlantic-Ocean." Journal of Atmospheric Chemistry **6**(1-2): 35-46.

Coelho, H. S., R. J. J. Neves, et al. (2002). "A model for ocean circulation on the Iberian coast." Journal of Marine Systems **32**(1-3): 153-179.

Ekdahl, A., M. Pedersen, et al. (1998). "A study of the diurnal variation of biogenic volatile halocarbons." Marine Chemistry **63**(1-2): 1-8.

Fanning, K. A. and M. E. Q. Pilson (1973). "Spectrophotometric Determination of Dissolved Silica in Natural Waters." Analytical Chemistry **45**(1): 136-140.

Gruber, N. and J. L. Sarmiento (1997). "Global patterns of marine nitrogen fixation and denitrification." Global Biogeochemical Cycles **11**(2): 235-266.

Hill, V. L. and S. L. Manley (2009). "Release of reactive bromine and iodine from diatoms and its possible role in halogen transfer in polar and tropical oceans." Limnology and Oceanography **54**(3): 812-822.

Jones, C. E., K. E. Hornsby, et al. (2009). "Coastal measurements of short-lived reactive iodocarbons and bromocarbons at Roscoff, Brittany during the RHaMBLe campaign." Atmospheric Chemistry and Physics **9**(22): 8757-8769.

King, D. B., J. H. Butler, et al. (2002). "Predicting oceanic methyl bromide saturation from SST." Geophysical Research Letters **29**(24): -.

Laturnus, F. (2001). "Marine macroalgae in polar regions as natural sources for volatile organohalogens." Environmental Science and Pollution Research **8**(2): 103-108.

Law, C. S. and W. T. Sturges (2006). Halogenated Very Short-Lived Substances. World Meteorological Organization Global Ozone Research and Monitoring Project - Report No. 50.

Leblanc, C., C. Colin, et al. (2006). "Iodine transfers in the coastal marine environment: the key role of brown algae and of their vanadium-dependent haloperoxidases." Biochimie **88**(11): 1773-1785.

Legendre, L. (1998). Numerical ecology, Elsevier Science.

Lobert, J. M., S. A. YvonLewis, et al. (1997). "Undersaturation of CH3Br in the Southern Ocean." Geophysical Research Letters **24**(2): 171-172.

Marshall, R. A., D. B. Harper, et al. (1999). "Volatile bromocarbons produced by Falkenbergia stages of Asparagopsis spp. (Rhodophyta)." Limnology and Oceanography **44**(5): 1348-1352.

Martinez, E., I. Llobet, et al. (2002). "Patterns and levels of halogenated volatile compounds in Portuguese surface waters." Journal of Environmental Monitoring **4**(2): 253-257.

Martino, M., G. P. Mills, et al. (2009). "A new source of volatile organoiodine compounds in surface seawater." Geophysical Research Letters **36**: -.

Moore, R. M. and R. Tokarczyk (1993). "Volatile Biogenic Halocarbons in the Northwest Atlantic." Global Biogeochemical Cycles **7**(1): 195-210.

Moore, R. M., M. Webb, et al. (1996). "Bromoperoxidase and iodoperoxidase enzymes and production of halogenated methanes in marine diatom cultures." Journal of Geophysical Research-Oceans **101**(C9): 20899-20908.

Mudge, S. M. (2007). "Multivariate statistical methods in environmental forensics." Environmental Forensics **8**(1-2): 155-163.

Murphy, J. and J. P. Riley (1962). "A Modified Single Solution Method for Determination of Phosphate in Natural Waters." Analytica Chimica Acta **26**(1): 31-&.

Nightingale, P. D., G. Malin, et al. (1995). "Production of Chloroform and Other Low-Molecular-Weight Halocarbons by Some Species of Macroalgae." Limnology and Oceanography **40**(4): 680-689.

Perez, F. F., C. G. Castro, et al. (2001). "Coupling between the Iberian basin - scale circulation and the Portugal boundary current system: a chemical study." Deep-Sea Research Part I-Oceanographic Research Papers **48**(6): 1519-1533.

Pfeilsticker, K., W. T. Sturges, et al. (2000). "Lower stratospheric organic and inorganic bromine budget for the Arctic winter 1998/99." Geophysical Research Letters **27**(20): 3305-3308.

Pruvost, J., O. Connan, et al. (1999). "A sampling device for collection and analysis of volatile halocarbons in coastal and oceanic waters." Analyst **124**(9): 1389-1394.

Quack, B., E. Atlas, et al. (2004). "Oceanic bromoform sources for the tropical atmosphere." Geophysical Research Letters **31**(23): -.

Quack, B., E. Atlas, et al. (2007a). "Bromoform and dibromomethane above the Mauritanian upwelling: Atmospheric distributions and oceanic emissions." Journal of Geophysical Research-Atmospheres **112**(D9): -.

Quack, B., I. Peeken, et al. (2007b). "Oceanic distribution and sources of bromoform and dibromomethane in the Mauritanian upwelling." <u>Journal of Geophysical Research-Oceans</u> **112**(C10): -.

Quack, B. and D. W. R. Wallace (2003). "Air-sea flux of bromoform: Controls, rates, and implications." <u>Global Biogeochemical Cycles</u> **17**(1): -.

Richter, U. and D. W. R. Wallace (2004). "Production of methyl iodide in the tropical Atlantic Ocean." <u>Geophysical Research Letters</u> **31**(23): -.

Salawitch, R. J., D. K. Weisenstein, et al. (2005). "Sensitivity of ozone to bromine in the lower stratosphere." <u>Geophysical Research Letters</u> **32**(5): -.

Smyth, T. J., P. I. Miller, et al. (2001). "Remote sensing of sea surface temperature and chlorophyll during Lagrangian experiments at the Iberian margin." <u>Progress in Oceanography</u> **51**(2-4): 269-281.

Smythe-Wright, D., S. M. Boswell, et al. (2006). "Methyl iodide production in the ocean: Implications for climate change." <u>Global Biogeochemical Cycles</u> **20**(3): -.

Sokal, R. and F. Rohlf (1995). <u>Biometry: the principles and practice of statistics in biological research</u>, WH Freeman.

Wang, L., R. M. Moore, et al. (2009). "Methyl iodide in the NW Atlantic: Spatial and seasonal variation." <u>Journal of Geophysical Research-Oceans</u> **114**: -.

Wood, E. D., Armstron.Fa, et al. (1967). "Determination of Nitrate in Sea Water by Cadmium-Copper Reduction to Nitrite." <u>Journal of the Marine Biological Association of the United Kingdom</u> **47**(1): 23-&.

Wright, S. W., S. W. Jeffrey, et al. (1991). "Improved Hplc Method for the Analysis of Chlorophylls and Carotenoids from Marine-Phytoplankton." <u>Marine Ecology-Progress Series</u> **77**(2-3): 183-196.

Yang, X., R. A. Cox, et al. (2005). "Tropospheric bromine chemistry and its impacts on ozone: A model study." <u>Journal of Geophysical Research-Atmospheres</u> **110**(D23): -.

Annexe B : Influence of the oceanic mesoscale processes on top predators.

.2 Article 7: Top marine predators track Lagrangian coherent structures, Tewkai, Rossi *et al.*, 2009 Proceedings of the National Academy of Sciences of USA

Top marine predators track Lagrangian coherent structures

Emilie Tew Kai[a,1], Vincent Rossi[b], Joel Sudre[b], Henri Weimerskirch[c], Cristobal Lopez[d], Emilio Hernandez-Garcia[d], Francis Marsac[a], and Veronique Garçon[b]

[a]Institut de Recherche pour le Développement, UR 109, Centre de Recherche Halieutique Méditerranéenne et Tropicale, 34203 Sète Cedex, France; [b]Laboratoire d'Etudes en Géophysique et Océanographie Spatiale, Centre National de la Recherche Scientifique, 31401 Toulouse Cedex 9, France; [c]Centre d'Etudes Biologiques de Chizé, Centre National de la Recherche Scientifique, 79360 Villiers en Bois, France; and [d]Instituto de Física Interdisciplinar y Sistemas Complejos, Consejo Superior de Investigaciones Cientificas–Universitat de les Illes Balears, E-07122 Palma de Mallorca, Spain

Meso- and submesoscales (fronts, eddies, filaments) in surface ocean flow have a crucial influence on marine ecosystems. Their dynamics partly control the foraging behavior and the displacement of marine top predators (tuna, birds, turtles, and cetaceans). In this work we focus on the role of submesoscale structures in the Mozambique Channel in the distribution of a marine predator, the Great Frigate-bird. Using a newly developed dynamic concept, the finite-size Lyapunov exponent (FSLE), we identified Lagrangian coherent structures (LCSs) present in the surface flow in the channel over a 2-month observation period (August and September 2003). By comparing seabird satellite positions with LCS locations, we demonstrate that frigatebirds track precisely these structures in the Mozambique Channel, providing the first evidence that a top predator is able to track these FSLE ridges to locate food patches. After comparing bird positions during long and short trips and different parts of these trips, we propose several hypotheses to understand how frigatebirds can follow these LCSs. The birds might use visual and/or olfactory cues and/or atmospheric current changes over the structures to move along these biologic corridors. The birds being often associated with tuna schools around foraging areas, a thorough comprehension of their foraging behavior and movement during the breeding season is crucial not only to seabird ecology but also to an appropriate eco-systemic approach to fisheries in the channel.

frigatebird | finite-size Lyapunov exponent | Mozambique Channel | submesoscale

In the oligotrophic open ocean mesoscale and submesoscale oceanic turbulence, which spans spatiotemporal scales from one to hundreds of kilometers and from hours to weeks, strongly modulates the structure, biomass, and rates of marine pelagic ecosystems. Eddies can stimulate the primary productivity (1, 2), affect plankton community composition (3–5), or play a significant role in exchange processes in the transitional area between the coast and offshore by transporting organic matter and marine organisms from the coast to the open ocean and vice versa (6). In view of the strong influence of eddies on physical and biogeochemical properties, it is not surprising that higher-level predators concentrate around them, where prey can be found. In fact, all investigations on the relationship between eddies and top-predator communities, using satellite imagery observations, have shown strong ties between them (7, 8). Upper predators particularly used the boundary between 2 eddies (9–12). The key point is that interactions between eddies generate strong dynamic interfaces (13) and make them a complex and energetic physical environment. In these interfaces the energy of the physical system is available to biologic processes, increasing the trophic energy of the biologic system (8). Eddies and associated structures therefore have a crucial ecologic significance, especially in tropical and subtropical regions, characterized by low mixing during winter, inferring weak supply of nutrients to the photic zone (11).

Most previous work dealing with the influence of eddies on top-predator distribution show the necessity of concentrating on submesoscale (<10 km) to fully appreciate the role of eddy–eddy interfaces on biologic production (11). Many different studies confirm that submesoscale tracer patches and filaments are strongly related to interactions between mesoscale surface eddies (1, 14). Despite this, studies on top predators using remote sensing have only used sea surface height as an indicator of eddy activity, which does not resolve submesoscale structures such as filaments, where production should be concentrated. In addition, a fundamental question remains: how do top predators find these zones of higher productivity? This is particularly difficult to understand for central-place foragers, such as seabirds, that breed on land but have to make continuous return trips between feeding zones and the colony where they care for their chick or egg. The additional difficulty in the case of eddies is that the location of production zones moves continuously.

In the West Indian Ocean, the Mozambique Channel (MC) can be considered a natural laboratory to study interactions between biologic and physical processes at mesoscale in oligotrophic areas (subtropical region) because of the transient activity of eddies. Indeed, mesoscale dynamics of the MC have been well described by previous works using remote sensing data, modeling, and in situ observations (15–17). Mesoscale activity is dominant in 2 areas, the central part of the MC and south of Madagascar (17, 18). Wei-merskirch et al. (10) have shown the main role of mesoscale eddies on the foraging strategy of Great Frigatebirds. These birds fly hundreds or thousands of kilometers from the colony in a few days and spend their entire foraging trips in flight, being unable to sit on the water or enter the water column. Bird pathways are preferentially associated with eddies in the MC during their long trips and especially with the edge of eddies, avoiding their core (10). However, it is not clear where exactly they forage in the eddy system and whether and how they locate the zones of high production. The aim of the present study is to describe the fine-scale activity occurring at the edge of eddies and other submesoscale structures and to quantify the role of these on a top predator's foraging movements. We also try to understand how and why these predators might locate these structures.

For the physical environment, we have used horizontal velocity fields computed from satellite altimetry products (19). We have applied to them a recently developed Lagrangian technique, the finite-size Lyapunov exponent (FSLE), which allows computing from marine surface velocity field data, mixing activity and coherent structures that control transport at specified scales (20). FSLEs

ECOLOGY

Fig. 1. Argos locations of Great Frigatebirds during long trips (black points) and short trips (red points) in the MC, between August 18 and September 30, 2003. The green point denotes Europa Island.

measure how fast fluid particles separate to a specified distance. Lagrangian coherent structures (LCSs) (e.g., transport barriers, filamental structures, or vortex boundaries) are identified as ridges (locations containing the maximum values) of Lyapunov exponent fields (21–24). Dispersion rates of tracer particles can be calculated by integrating trajectories toward the future (forward) or toward the past (backward), giving rise to 2 different quantifiers, $FSLE_f$ and $FSLE_b$, respectively, containing complementary information (see *Materials and Methods*). Ridges of $FSLE_b$ attract neighboring trajectories, whereas $FSLE_f$ repel them. This is why we call them *attracting* and *repelling* LCSs, respectively. Sometimes, especially for plotting, it is convenient to write $FSLE_b$ and $FSLE_f$ as having negative and positive values, respectively, and expressions such as |FSLE| refer simultaneously to both types of exponents. For the marine top predators, we have used Argos positions of Great Frigatebirds from the colony on Europa Island in the MC during August and September 2003. Additional details are given in *Materials and Methods*.

In this study we test whether seabird positions during their foraging trips are related to dynamic structures. This is performed in different contexts: during short and long trips, day and night, and during the outward part of their foraging trips and the return back to the colony. We finally discuss which foraging strategy these top predators might use to locate prey patches.

Results

Seabird Locations During Trips and FSLE Fields. We compare here the locations of the LCSs identified as ridges in FSLE maps and measured bird positions during August and September 2003. We will see that the latter are not random but correlated with the former.

First, Fig. 1 shows Argos positions of Great Frigatebirds during long trips (black points) and short trips (red points) between August 18 and September 30, 2003. Locations of seabirds during long trips superimposed on FSLEs fields (September 24 to October 6, 2003) are shown in Fig. 2. During the week of September 24, bird 11377 (green circles) is located on high $FSLE_b$ values (the attracting LCSs), as is bird 16255 (blue circles). The positions of bird 8023 (red circles) seem to be linked to fluid repelling structures (the ridges of $FSLE_f$) instead. For bird 8023, at the beginning of travel, the trajectory is rectilinear in the northeast direction and then follows the repelling mushroom-like structures. Foraging patches (triangles), where birds reduce flying speed, seem to exhibit the same distribution as the birds' moving positions. During the week of October 6 the movements of bird 8023 are mostly on repelling structures (Fig. 2D), as during the week of September 24, and perhaps also on some attracting structures. The important point is that any of both types of LCSs is more visited than locations outside. The positions of bird 19827 (magenta circles) are well superimposed on fluid attracting structures (ridges of $FSLE_b$) but not on repelling ones. These 2 examples of the overlay of seabird movement and foraging positions on FSLE fields during long trips show that the locations of birds tend to overlay on LCSs, either on attracting (Fig. 2 A and C) or repelling ones (Fig. 2 B and D).

To put the above observations in quantitative form, we specified a threshold defining a significant presence of LCSs: |FSLE| > 0.1 d^{-1}. It corresponds to mixing times smaller than 1 month. This value is chosen because it is a typical value for Lyapunov exponents in different areas of the globe (14, 20) and because regions where the Lyapunov exponents are larger already have the shape of 1-dimensional lines (see Fig. 2). The distributions of FSLEs in the whole MC and the central part and in areas crossed by seabirds were tested for conformity to the normal distribution using the Kolmogorov-Smirnov (KS) sample test, and they all are clearly non-normal. Histograms of relative frequency of FSLE in the whole MC, the central part, and in areas visited by seabirds are shown in Fig. 3. In the whole MC and the central part, Lagrangian structures detected by |FSLE| > 0.1 day^{-1} represent a minority of locations, occupying ≤30% of the total area. However, in areas crossed by frigatebirds
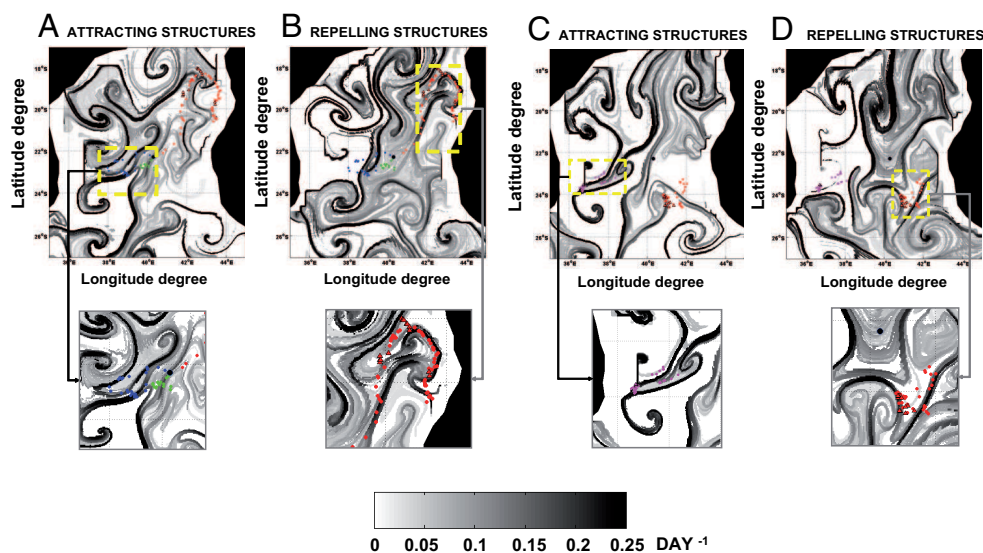
Fig. 2. Overlays of seabird positions on FSLE maps. (*A* and *C*) Backward integration in time for FLSE computation (d^{-1}). (*B* and *D*) Forward integration in time (d^{-1}). *A* and *B*, week of September, 24, 2003. *C* and *D*, week of October, 6, 2003. Circles represent seabird trajectories and triangles foraging patches. Each color represents the tag of a different bird (red, tag 8023; blue, tag 16255; green, tag 11377; magenta, tag 19827).
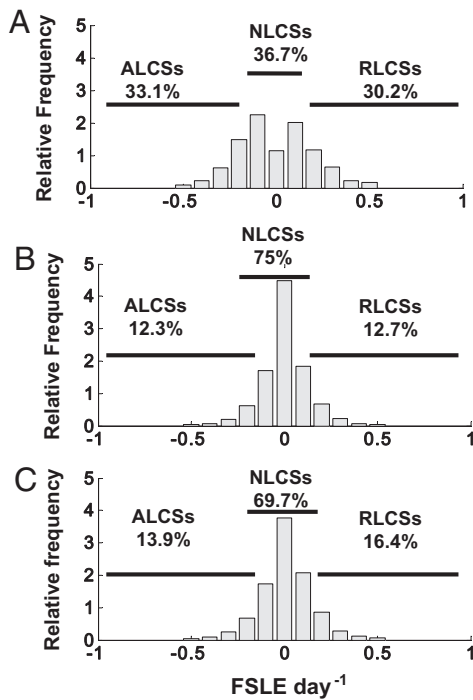
Fig. 3. Histograms of relative frequency of FSLEs with percentage of attracting (ALCSs) and repelling LCSs (RLCSs). Positive values refer to FSLE$_f$ and negative to FSLE$_b$. (*A*) Areas crossed by seabirds (long and short trips); (*B*) in the whole MC; and (*C*) in the central part (16°–24°S/30°–45°E).

>60% of the birds are on LCSs. Five KS 2-sample (KS-2) tests comparing the distributions of FSLEs in the whole MC and in the central part with the distribution of FSLEs on areas visited by seabirds during long and short trips were performed. The tests confirmed that distributions of FSLEs in areas crossed by seabirds are highly different from those found over the whole area and the central part ($P < 0.0001$ for both long and short trips). Distribution patterns provide clear evidence that Great Frigatebirds are not randomly distributed throughout the FSLE range (both backward and forward) and that seabirds move over specific areas rich in

LCSs, despite the area occupied by LCSs being small. Nearly two-thirds of the birds' positions are on LCSs, even though only ≤30% of the whole area or the central part (Fig. 3) contain high |FSLE| and are then occupied by LCSs. These numbers were further checked by χ^2 analyses using the 1-tailed G-test for goodness of fit (log-likelihood ratio), which clearly show that there are significant differences between positions of birds on LCSs and on other structures (Table 1) (G-test, $P < 0.001$); this confirms again that seabird positions are located more on LCSs (|FSLE| > 0.1 day $^{-1}$) than outside during long and short trips, despite the small area occupied by LCSs (Fig. 3). An additional test checking the relationship between bird positions at a given week t and the LCSs computed for that week and for the following weeks, t + 1, t + 2, ... t + 9, is described in the supporting information (SI) *Methods*. The association of bird tracks and LCSs, measured by the significance of a G-test, is highest for the LCSs of week t and decreases with the time lag to the other weeks ($p_{t + 1} = 0.81 > p_{t + 3} = 0.19 > p_{t + 5} = 0.12$) (Table S1).

FSLE Distributions over Different Types of Flights. We performed several statistical tests to determine whether there are statistically significant differences among travel/foraging locations, outgoing/return trips, and day/night flights.

Boxplots of FSLEs on seabird positions during long and short trips are presented in Fig. 4. The range of variation of FSLE is clearly more dispersed during long trips than short trips, and the median between both kinds of trips is similar. Furthermore, distributions are clearly different between long and short trips, as confirmed by a KS-2 test ($P \ll 0.001$). Indeed, 65.9% of seabird positions during long trips and 56% during short trips are on LCSs (Table 1). During long trips, Great Frigatebirds forage during a longer time and so cover a larger range of variation of FSLE values than during short trips. One-tailed G-test for goodness of fit confirms that there is a difference between the number of seabird locations on FSLE ridges and outside the ridges (Table 1) ($G = 30.613, P = 0.001$, df = 10 for long trips; and $G = 32.057, P \ll 0.001$, df = 6 for short trips).

KS-2 tests show that the distribution of the birds between attracting and repelling LCSs displays no statistically significant difference during long trips ($P > 0.05$) but differs during short trips ($P < 0.01$). During short trips birds follow the attracting LCSs more than the repelling ones. The analyses clearly demonstrate that

Table 1. Absolute frequency of seabird positions on LCSs and on no Lagrangian structures for long and short trips per week and result of the G-test for goodness of fit

Week	All trips LCSs: |FSLE| > 0.1 day^{-1}	|FSLE| < 0.1 day^{-1}	Long trips LCSs: |FSLE| > 0.1 day^{-1}	|FSLE| < 0.1 day^{-1}	Short trips LCSs: |FSLE| > 0.1 day^{-1}	|FSLE| < 0.1 day^{-1}
1	38	9	19	7	19	2
2	78	40	55	12	23	28
4	208	85	147	54	61	31
5	167	109	137	84	30	25
6	120	77	89	51	31	26
7	79	55	72	32	7	23
8	53	34	53	34	—	—
9	61	59	61	59	—	—
10	55	31	45	24	10	7
14	35	12	35	12	—	—
15	10	5	10	5	—	—
%	63.7	36.3	65.9	34.1	56.0	44.0
G-test (log-likelihood ratio)						
n	1420		1097		323	
k	11		11		7	
df	10		10		6	
G	28.119		30.613		32.057	
P	0.00173		0.001		0.000	

One-tailed tests. Null hypothesis Ho: Seabird positions share equally LCSs (|FSLE| > 0.1 day^{-1} and on no LCSs. α = 5%.
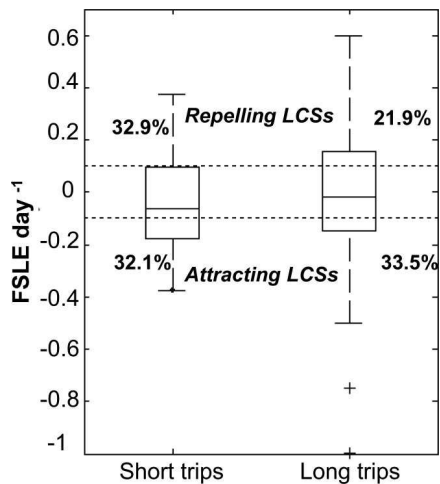
Fig. 4. Box plots of the distribution of FSLEs during short and long trips. The upper and lower ends of the center box indicate the 75th and 25th percentiles of the data; the center of the box indicates the median. Suspected outliers appear in a box plot as individual points (+) outside the box. Dotted lines represent the threshold for detection of LCSs.

seabirds follow the FSLE ridges during their foraging trips, but more during long trips than during short trips. This result emphasizes the probable difference in Great Frigatebird behavior during long vs. short trips.

Boxplots of FSLE show that patterns of distribution of FSLE are not very different between flying and foraging positions (Fig. S1). Distributions of FSLEs are statistically similar for foraging and crossed areas (KS-2 test, $P = 0.29$ for long trips and $P = 0.51$ for short trips) but differ from FSLE distribution in the whole area (KS test, $P < 0.0001$). During long trips 69.6% of seabird positions during flying and 62% during foraging are on LCSs (Fig. S1); these figures are 61.8% and 66.7%, respectively, during short trips. During flying and foraging seabirds split almost equally between repelling and attracting structures (G-test, $P > 0.05$) (Table S2). All of this indicates that seabirds seem to prefer being on ridges of FSLE both for travel and foraging.

We have also investigated differences in seabird distributions in relation to FSLEs between the outward and return parts of the trip (Fig. S2 *A and C*). KS-2 test shows that there is no significant difference of seabird distribution during long trips (KS-2, $P > 0.01$) and during short trips ($P > 0.05$), between the outward and return parts of the trip. For all types of trips (short and long) there is no significant difference of seabird positions, either on repelling or attracting flow structures, during the outward and return parts of the trip (G-test, $P > 0.05$) (Table S3).

Great Frigatebirds feed mainly during daytime (10). We therefore examined whether we could identify differences between day- and nighttime distribution of seabirds. Boxplots of seabird distribution on FSLE between day and night show that patterns of distribution of FSLEs are similar during day and night during short (Fig. S2B) and long trips (Fig. S2D). The range of variation of FSLE during long trips is, however, more dispersed at night than during short trips. KS-2 test shows that there is no significant difference between FSLE distributions visited by birds during day and night ($P > 0.05$ during long or short trips). The probability for the frigatebirds to fly over attracting or repelling structures during day and night is statistically similar (G-test, $P > 0.05$) for long trips but may be different for short trips (G-test, $P = 0.025$) (Table S3). During daytime short trips, seabirds may follow the attracting structures more than the repelling ones.

Discussion

Because eddies affect all stages of the marine ecosystem, they are determinant for the triad "enhancement–concentration–retention"

identified by Bakun (8, 25). From upwelling-driven processes at the center of cyclonic eddies (1, 2), or from other processes at the boundaries between eddies (13), local enrichment and new production have been observed. The cyclic circulation in vortices also produces retention of larvae and other planktonic organisms in their core, whereas concentration occurs in the convergence zones located at the boundary between them, which are detected by FSLEs.

Transport barriers and filament generation by interaction between eddies induce horizontal and vertical biogeochemical and biologic enhancement (13). FSLEs seem very well suited to detect such transport barriers, vortex boundaries, and filaments at meso- and submesoscale (20, 26) and to study the link with the ecologic behavior of marine top predators. However, a word of caution is required about the spatial resolution we used. Indeed, the FSLEs are computed from satellite altimetry products (19), with a spatial resolution of 1/4° interpolated here onto a 1/40° grid. This interpolation might induce some bias in the data. However, FSLEs, because of the averaging effect produced by computing them by integrating over trajectories that extend in time and space, are rather robust against noise and uncertainties in velocity data (26, 27) (see also *SI Methods*). The velocity field used here has been validated, and the correlation with velocities from Lagrangian drifting buoy data in the MC was satisfactory (*SI Methods* and Fig. S3). Furthermore, Argos positioning of birds is not of equivalent quality. Some positions have a margin of error of a few hundred meters, whereas others have an error margin of more than 1 km. Definite improvements would be to reduce interpolation by using an original higher-resolution velocity field and to obtain more precise bird locations.

In the central part of the MC, it is known that the boundary of eddies is very energetic and allows the aggregation of top-predator foraging, especially Great Frigatebirds (10), which preferentially stay in this part of the channel. To date it was believed that Great Frigatebirds used edges of eddies mainly for food because these areas are rich in forage species and associated top predators [especially tuna and dolphins (28)]. Superimposing Great Frigatebird positions on FSLE fields shows that their spatial distribution is linked to eddies and more generally to the different types of LCSs, and not only for foraging but also for traveling. Observations are in agreement with the histograms and KS tests, which demonstrate that seabirds are not randomly distributed in relation to attracting and repelling LCSs.

However, analysis of location of seabirds during long and short trips shows that the percentage of positions on LCSs is different between both kinds of trips (Table 1). During long trips, birds seem to take full measure of the LCSs, whereas on short trips they do not take full advantage of them. This difference between long and short trips is probably due to the behavior of seabirds. During short trips birds have to bring food frequently to their chick, so they feed in areas where prey are easily accessible, close to Europa Island. They used preferentially attracting structures during daytime, probably because these structures are conducive to the aggregation of prey. During long trips birds avoid areas near Europa Island, probably because the foraging yield is less rich than that of more distant waters and/or because of strong interspecific competition near the island (10). However, birds preferentially follow the LCSs in both cases.

In addition, seabirds follow LCSs not only for their foraging but also for their traveling movements. The distributions of FSLEs during the outward and inbound journeys to the colony indicate that they exhibit the same flying behavior before and after their foraging activity. Furthermore, the fact that the distribution of visited FSLEs is identical during day and night indicate that they are able to use these LCSs to move during periods of darkness. Frigatebirds move continuously during day and night at an average altitude of 200 m and never completely stop moving when they forage, but they come to the sea surface to eat only during daytime (10). If they used these structures only for food availability, then the distribution of FSLEs

for areas crossed by birds should be different between day and night. This is not the case. This means that frigatebirds do not go to FSLEs ridges only to forage but that they follow them most of the time as cues to eventually find prey patches there.

It is relatively easy to understand why the attracting LCSs could be places for prey accumulation, given that horizontal flow will make passively advected organisms close to these lines approach them. More puzzling is the role of the repelling LCSs, which are also preferred locations for the frigatebirds. First we should mention that at the vortex edges, lines of the attracting and repelling types are very close and nearly tangent. Thus, it may be the case that birds' positions located at repelling lines are simultaneously also located on attracting ones; in *SI Methods* we explain that a position is said to be on an LCS if it is closer to it than 0.025°. Thus, if the attracting and repelling LCSs are close enough, the same bird position may be attributed to both structures. We have determined that, among the 30.2% of bird positions that were found on repelling coherent structures, 53.7% of these were in fact visiting both structures, and thus the interpretation is that they are associated to vortex edges (or to other structures in which both types of lines are tangent). For the remaining fraction that does not seem to be associated to these edges, we believe that the 3-dimensional dynamics of the flow close to these structures gives the clue for their association to bird positions. Note that FSLE values have been calculated on the basis of the 2-dimensional surface flow, and the FSLE methodology identifies these regions as places of filament and submesoscale structure formation by horizontal advection. But there is growing evidence (29, 30) of strong links between submesoscale structures from different origins and vertical motions. Thus, in an indirect manner, the calculated LCSs may be indicating the places in the ocean where vertical upwelling and/or downwelling of nutrients and organisms could occur. This is obviously important for the birds and may explain why they prefer to fly and to forage on top of them. The role of these LCSs in biologic activity is rather complex and may vary depending on the area and scale of study. For instance, Rossi et al. (31) found an inverse relationship between mixing activity (high FSLEs) and phytoplankton stocks in very productive areas, such as coastal eastern boundary upwelling.

The above arguments linking LCSs and vertical motion can be more easily justified for the attracting LCS case, because the vorticity involved in the interaction between vertical and horizontal motion will also tend to be aligned with these structures (30). But we note that in flows consisting of slowly moving eddies, we are close to the so-called integrable situation in which a large proportion of tangencies between attracting and repelling structures is expected (as indeed observed). As a consequence, it may happen that a bird starts a trip by following an attracting LCS, loses its surface signal, and finds itself on top of a repelling one simply by continuing its previous path in a more-or-less straight way. We stress, however, that all explanations we give to the observed relationship between LCSs and bird paths contain a number of hypotheses that need additional research.

One may ask how frigatebirds "follow" the LCSs during day and night. Several hypotheses can be put forward.

First, because frigatebirds use atmospheric currents, especially to gain altitude by soaring and then glide over long distances (32), we can suppose that the coupling between the ocean and the atmosphere at meso- and submesoscale generates atmospheric currents followed by seabirds. Indeed some investigators (33–36) emphasize the role of local air–sea feedbacks arising from ocean mesoscale features. For example, Chelton et al. (36) showed that an ocean–atmosphere coupling is observed in the California Current System during summer. They conclude that sea surface temperature fronts generated by mesoscale activity (eddies and upwelling) have a clear influence on the perturbation of summertime wind stress curl and divergence. In the MC, mesoscale eddies and their interaction would force the atmosphere and generate air currents favorable to Great Frigatebirds, which might take advantage of the wind to spend the least possible energy in flight.

Second, we cannot exclude that birds may follow visual or, more likely, olfactory cues. Foraging behavior of seabirds is complex and results from a number of behavioral parameters, such as sight, smell (37, 38), memory effect (39), and environmental parameters [chlorophyll concentration (10) or wind speed and direction]. Nevitt et al. (40) suggest that seabirds use olfaction to track high concentrations of odor compounds, such as dimethyl sulfide (DMS), and sight when they locate prey patches. The use of models of odor transport suggests that olfaction plays a role in foraging behavior (40). Structures detected using FSLEs are dynamic and, as mentioned above, may induce vertical mixing favorable to phytoplankton enhancement (41, 42) and their patchy distribution. The grazing of phytoplankton by zooplankton induces the production of DMS (43), which is very attractive for different species of seabirds (44). Even if there is no study on the role of olfaction in Great Frigatebird foraging behavior, we can hypothesize that they use olfaction to detect DMS and productive areas and find food patches. The interaction between the ocean and the atmosphere at submesoscale and wind may allow the dispersion of the DMS or other odors and favor their detection by seabirds that follow LCSs until they see a patch of prey. These LCSs could be viewed as moving habitat facilitating movement of seabirds. Indeed, frigatebirds might use these odorous corridors to move between food patches with efficacy.

Whatever the cue used by frigatebirds to locate and follow these LCSs, our results provide the first evidence that a top predator tracks these FSLE ridges to locate food patches. It allows us to better understand how top predators search prey and why they are able to concentrate precisely at LCSs. Because these structures are mobile, a simple memory is not sufficient for a central-place forager to return to a productive prey area. Predators could thus take a general bearing where eddies are likely to be found (e.g., to the northwest in the MC for a colony located in the central MC) and then move until they cross an FSLE ridge, which they will follow until they encounter a prey patch. Because they are unable to sit on the water, frigates are often in association with subsurface top predators to forage. We can suppose that if frigatebirds track LCSs to locate prey, it is possible that they are associated with tuna schools around foraging areas (10). Thus, understanding the rationale behind their localization is crucial not only in seabird ecology but also in the detection of the presence of tuna schools. This kind of multidisciplinary approach opens up interesting prospects in the management of ecosystems and fisheries and can be useful in the ecosystemic approach to fisheries, especially to better characterize temporary tuna habitats in the MC. Future work is to identify the responsible mechanism by which an aerial predator may spot and follow LCSs.

Materials and Methods

In this part we provide a brief overview of the methodology; further details for each section are given in *SI Methods*.

Great Frigatebirds. Europa (22.3° S, 40.3° E) is 1 of the 2 colonies (with Aldabra) of Great Frigatebirds in the West Indian Ocean. The island is located in the central part of the MC. Great Frigatebirds have the ability to undertake long-range movements out of the breeding season (10), but they behave as central-place foragers when breeding. Their diet is composed essentially of flying fish and Ommastrephid squids (10), but Great Frigatebirds are also kleptoparasites, meaning they can steal prey from others. One of their particularities is that they cannot wet their feathers or dive into the water to feed. They forage mainly through association with tuna and dolphin schools, which bring prey to the surface.

To track movements of frigatebirds, 8 birds were tracked with satellite transmitters and altimeters between August 18 and September 30, 2003, resulting in 1864 Argos positions. The mean time between each position is 0.07 days, with a minimum of 0.001 days and a maximum of 1.1 days. All seabird positions from a given week were collocated on the time and space grid on which the FSLEs were calculated (with 0.025° resolution).

ECOLOGY

LCSs by FSLEs: FSLE Method. Oceanic variability in surface velocities is not probably sensed directly by Great Frigatebirds but rather indirectly via transported substances. This calls for a Lagrangian perspective on the problem. Thus, we quantify horizontal transport processes and LCSs by the Lagrangian technique of FSLE (45), which is specially suited to study the stretching and contraction properties of transport in geophysical data (20). Because of their Lagrangian character, FSLEs describe submesoscale details that cannot be detected by other means, like the inspection of the sea level anomaly maps of the marine surface.

The calculation of the FSLE goes through computing the time, τ, at which 2 tracer particles initially separated at a distance δ_0, reach a final separation distance δ_f, following their trajectories in the marine surface velocity field. At position x and time t the FSLE is given by:

$$\lambda(x, t, \delta_0, \delta_f) = \frac{1}{\tau} \log\left(\frac{\delta_f}{\delta_0}\right).$$

We follow the trajectories for 200 days, so that if τ is larger than this, we define $\lambda = 0$. It is clear that the FSLEs depend critically on the choice of 2 length scales: the initial separation, δ_0, and the final one, δ_f. δ_0 has to be close to the intergrid spacing among the points x on which the FSLEs will be computed (20). In our case we calculate FSLE on all of the points of a latitude–longitude grid with a spacing of $\delta_0 = 1/40° = 0.025°$. On the other hand, because we are interested in mesoscale structures, δ_f is chosen as $\delta_f = 1°$ (i.e., separation of approximately 110 km). In this respect, the FSLE represents the inverse time scale for mixing up fluid parcels between the grid and the characteristic scales of the MC eddies. Maps of FSLE are calculated weekly. An alternative to FSLE is the finite-time Lyapunov exponents (22, 46). At the scales and parameters we are working no significant differences are expected for the locations of LCS by any of the 2 methods.

The time integration of the particle trajectories can be performed in 2 ways: forward and backward in time. For the backward computation, maximum values of FSLE organize in lines that are good approximations of the so-called *unstable manifolds of hyperbolic points*, which for our purposes are lines toward which neighboring fluid trajectories, while escaping from hyperbolic points, approach at long times (20, 23, 24). In consequence they are called attracting LCSs. FSLEs computed integrating trajectories toward the future (i.e., forward) take large values on lines (stable manifolds) from which neighboring trajectories appear to be repelled (repelling LCSs). These lines of maximum separation or convergence rates, or "ridges," delineate fluid domains with quite distinct origin and characteristics. Such lines strongly modulate the fluid motion when reaching maximum values, and they act as transport barriers for particle trajectories, thus constituting a powerful tool for predicting fronts generated by, for example, passive advection, eddy boundaries, and material filaments. Other studies (20, 26, 27, 31, 42) have demonstrated the adequacy of the FSLE to characterize horizontal mixing and transport structures in the marine surface, as well as its usefulness when correlating with tracer fields like temperature or chlorophyll.

1. McGillicuddy J, et al. (1998) Influence of mesoscale eddies on new production in the Sargasso Sea. *Nature* 394:263–266.
2. Oschlies A, Garcon V (1998) Eddy-induced enhancement of primary production in a model of the North Atlantic Ocean. *Nature* 394:266–268.
3. Owen RW (1981) Fronts and eddies in the sea: Mechanisms, interactions and biological Effects. *Fronts and Eddies in the Sea*, ed Owen RW (Academic, London).
4. Kang J, Kim W, Chang K, Noh J (2004) Distribution of plankton related to the mesoscale physical structure within the surface mixed layer in the southwestern East Sea, *Korea J Plankton Res* 26:1515–1528.
5. Mackas D, Tsurumi M, Galbraith M, Yelland D (2005) Zooplankton distribution and dynamics in a North Pacific Eddy of coastal origin: II. Mechanisms of eddy colonization by and retention of offshore species. *Deep-Sea Res II* 52:1011–1035.
6. Moore T, Matear R, Marra J, Clementson L (2007) Phytoplankton variability off the Western Australian Coast: Mesoscale eddies and their role in cross-shelf exchange, *Deep-Sea Res II* 54:943–960.
7. Polovinia J, Howell E, Kobayashi D, Seki M (2001) The transition zone chlorophyll front, a dynamic global feature defining migration and forage habitat for marine resources. *Prog Oceanogr* 49:469–483.
8. Bakun A (2006) Fronts and eddies as key structures in the habitat of marine fish larvae: Opportunity, adaptive response and competitive advantage. *Scientia Marina* 70:105–122.
9. Nel D, et al. (2001) Exploitation of mesoscale oceanographic features by grey-headed albatross *Thalassarche chrysostoma* in the southern Indian Ocean. *Mar Ecol Prog Ser* 217:15–26.
10. Weimerskirch H, Le Corre M, Jaquemet S, Potier M, Marsac F (2004) Foraging strategy of a top predator in tropical waters: Great Frigatebirds in the Mozambique Channel. *Mar Ecol Prog Ser* 275:297–308.
11. Hyrenbach K, Veit R, Weimerskirch H, Hunt G, Jr (2006) Seabird associations with mesoscale eddies: The subtropical Indian Ocean. *Mar Ecol Prog Ser* 324:271–279.
12. Domokos R, Seki MP, Polovinia JJ, Hawn DR (2007) Oceanographic investigation of the American Samoa albacore (*Thunnus alalunga*) habitat and longline fishing grounds. *Fish Oceanogr* 16:555–572.
13. Lima I, Olson D, Doney S (2002) Biological response to frontal dynamics and mesoscale variability in oligotrophic environments: Biological production and community structure. *J Geophys Res* 107:3111.
14. Abraham ER, Bowen MM (2002) Chaotic stirring by a mesoscale surface ocean flow. *Chaos* 12:373–381.
15. De Ruijter WPM, Ridderinkhof H, Lutjeharms R, Schouten M, Veth C (2002) Observations of the flow in the Mozambique Channel. *Geophys Res Lett* 29:1502.
16. Ridderinkhof H, de Ruijter WPM (2003) Moored current observations in the Mozambique Channel. *Deep-Sea Res II* 5:1933–1955.
17. Schouten MW, de Ruijter WPM, van Leeuwen PJ, Ridderinkhof H (2003) Eddies and variability in the Mozambique Channel. *Deep-Sea Res II* 50:1987–2003.
18. Tew Kai E, Marsac F (2009) Patterns of variability of sea surface chlorophyll in the Mozambique Channel: A quantitative approach. *J Mar Syst* 77:77–88.
19. Sudre J, Morrow R (2008) Global surface currents: A high resolution product for investigating ocean dynamics. *Ocean Dyn* 58:101–118.
20. d'Ovidio F, Fernandez V, Hernández-García E, López C (2004) Mixing structures in the Mediterranean Sea from Finite-Size Lyapunov Exponents. *Geophys Res Lett* 31:L17203.
21. Haller G, Yuan G (2000) Lagrangian coherent structures and mixing in two-dimensional turbulence. *Physica D* 147:352–370.
22. Haller G (2001) Lagrangian structures and the rate of strain in a partition of two-dimensional turbulence. *Phys Fluids* 13:3365–3385.
23. Joseph B, Legras B (2002) Relation between kinematic boundaries, stirring and barriers for the Antarctic polar vortex. *J Atmosph Sci* 59:1198–1212.
24. Koh T-Y, Legras B (2002) Hyperbolic lines and the stratospheric polar vortex. *Chaos* 12:382–394.
25. Bakun A (1996) *Patterns in the Ocean: Oceanic Processes and Marine Population Dynamics* (University of California Sea Grant, San Diego, CA, in cooperation with Centro de Investigaciones Biologicas de Noroeste, La Paz, Baja California Sur, Mexico).
26. D'Ovidio F, Isern-Fontanet J, López C, Hernández-García E, García-Ladona E (2009) Comparison between Eulerian diagnostics and Finite-Size Lyapunov Exponents computed from altimetry in the Algerian basin. *Deep-Sea Res I* 56:15–31.
27. Haza A, Poje AC, Özgökmen TM, Martin P (2008) Relative dispersion from a high-resolution coastal model of the Adriatic Sea. *Ocean Modelling* 22:48–65.
28. Jaquemet S, Le Corre M, Weimerskirch H (2004) Seabird community structure in a coastal tropical environment: Importance of natural factors and fish aggregating devices (FADs). *Mar Ecol Prog Ser* 268:281–292.
29. Mahadevan A, Tandon A (2006) An analysis of mechanisms for submesoscale vertical motion at ocean fronts. *Ocean Modelling* 14:241–256.
30. Klein P, Lapeyre G (2009) The oceanic vertical pump induced by mesoscale eddies. *Ann Rev Mar Sci* 1:351–375.
31. Rossi V, Lopez C, Sudre J, Hernandez-Garcia E, Garçon V (2008) Comparative study of mixing and biological activity of the Benguela and Canary upwelling systems. *Geophys Res Lett* 35: L11602.
32. Weimerskirch H, Chastel O, Barbraud C, Tostain O (2003) Frigatebirds ride high on thermals. *Nature* 421:333–334.
33. Xie S (2004) Satellite observations of cool ocean–atmosphere interaction. *Bull Am Meteor Soc* 85:195–209.
34. Chelton D, Schlax MG, Freilich MH, Milliff RF (2004) Satellite measurements reveal persistent small-scale features in ocean winds. *Science* 303:978–983.
35. Seo H, Miller A, Roads J (2007) The Scripps Coupled Ocean–Atmosphere Regional (SCOAR) model, with applications in the eastern Pacific sector. *J Clim* 27:381–401.
36. Chelton D, Schlax MG, Samelson RM (2007) Summertime coupling between sea surface temperature and wind stress in the California Current System. *J Phys Oceanogr* 37:495–517.
37. Nevitt GA (2000) Olfactory foraging by Antarctic procellariiform seabirds: Life at high Reynolds numbers. *Biol Bull* 198:245–253.
38. Nevitt GA, Bonadonna F (2005) Seeing the world through the nose of a bird: New developments in the sensory ecology of procellariiform seabirds. *Mar Ecol Prog Ser* 287:292–295.
39. Davoren GK, Montevecchi WA, Anderson JT (2003) Distributional patterns of a marine bird and its prey: Habitat selection based on prey and conspecific behaviour. *Mar Ecol Prog Ser* 256:229–242.
40. Nevitt GA, Losekoot M, Weimerskirch H (2008) Evidence for olfactory search by wandering albatross, *Diomedea exulans*. *Proc Natl Acad Sci USA* 105:4576–4581.
41. Martin A (2003) Phytoplankton patchiness: The role of lateral stirring and mixing. *Prog Oceanogr* 57:125–174.
42. Lehahn Y, d'Ovidio F, Lévy M, Heyfetz E (2007) Stirring of the northeast Atlantic spring bloom: A Lagrangian analysis based on multisatellite data. *J Geophys Res* 112:C08005.
43. Dacey JWH, Wakeham SG (1986) Oceanic dimethylsulfide: Production during zooplankton grazing on phytoplankton. *Science* 233:1314–1316.
44. Nevitt GA, Veit RR, Kareiva P (1995) Dimethyl sulphide as a foraging cue for Antarctic procellariiform seabirds. *Nature* 376:680–682.
45. Aurell E, Boffetta G, Crisanti A, Paladin G, Vulpiani A (1997) Predictability in the large: An extension of the concept of Lyapunov exponent. *J Phys A* 30:1–26.
46. Beron-Vera FJ, Olascoaga MJ, Goni GJ (2008) Oceanic mesoscale eddies as revealed by Lagrangian coherent structures. *Geophys Res Lett* 35: L12603.

Influence of mesoscale physical processes on planktonic ecosystems in the regional ocean: application to the Eastern Boundary Upwelling Systems.

Abstract

The objectives were numerous but centered on a scientific overarching question: the influence of mesoscale physical processes on planktonic ecosystems in coastal upwellings. The use of several and complementary tools was necessary to assess the various mechanisms occurring at these scales.

First, the variability of the physical and biogeochemical properties of the Iberian Peninsula Upwelling System was studied using in-situ data from the MOUTON 2007 survey. The coastal domain was divided into different biogeochemical provinces: high nutrient concentrations are found in the northern part due to upwelled waters of subpolar origin whereas the southern area was characterized by moderate nutrient concentrations (waters of subtropical origin). The intense cross-shore gradient revealed that the biological activity is associated with the successive upwelling pulses. Data from a filament allowed us to assess its impact in terms of cross-shore exchanges of biological material.

Then, a secondary upwelling front located at the shelf break was observed in these data. We built a simplified 2D numerical model to explain it by the eastward advection from upwelling currents of deep water columns onto the shelf. It creates a negative anomaly of Potential Vorticity (PV) which generates the secondary front. A simulation revealed a filamentation process that was further investigated numerically. The interaction between the alongshore upwelling current and a promontory creates anomalies of PV in the lower layer that generates the development of a long filament trapped in the vicinity of the promontory.

Finally, we used satellite data associated with a lagrangian tool (Finite-Size Lyapunov Exponent) to study the horizontal mixing in relation to the biological activity over the four eastern boundary upwelling zones. We showed a negative relationship between horizontal surface mixing and chlorophyll content, which seems related to a diminution of vertical velocities of the coastal upwelling, as well as a lateral loss of nutrient due to moving eddies. Horizontal mixing induced by eddies thus has an inhibiting effect on the phytoplankton in coastal upwellings, whereas a positive effect stands for the open ocean.

Using diverse and complementary tools allowed us to improve our knowledge of the large influence of physical processes on marine ecosystems in coastal upwelling areas.

Influence des processus physiques à mésoéchelle sur l'écosystème planctonique : application aux zones d'Upwelling de Bord Est.

Résumé

Les objectifs étaient multiples mais centrés autour d'une thématique générale : l'influence des processus physiques à mésoéchelle sur l'écosystème planctonique dans les upwellings côtiers. L'utilisation d'outils variés était nécessaire pour aborder les nombreux mécanismes impliqués.

Dans un premier temps, la variabilité physique et biogéochimique de l'upwelling de la péninsule Ibérique est étudiée grâce aux données in-situ de la campagne MOUTON 2007. La région côtière a été divisée en plusieurs provinces biogéochimiques : des concentrations élevées de nutriments sont observées au nord, dues à l'upwelling des eaux d'origine subpolaire, alors que la zone sud est caractérisée par des concentrations modérées de nutriments (eaux d'origine subtropicale). L'intense gradient côte-large révèle une production biologique fortement liée aux phases successives d'upwelling. La production de l'upwelling côtier est exportée vers l'océan du large au sein de structures à mésoéchelle tel le filament étudié.

Ensuite, un front secondaire d'upwelling au niveau de la marge continentale a été observé dans ces données. Grâce à un modèle numérique en 2D, il a été démontré que cette structure est liée à l'advection par le courant d'upwelling de colonnes d'eau du bassin vers le plateau, créant une anomalie de Vorticité Potentielle (VP). Un bombement des isopycnes sus-jacentes est généré et explique le front d'upwelling secondaire. Une simulation de l'étude précédente a révélé un processus de filamentation qui a été étudié avec un modèle similaire. Le courant d'upwelling parallèle à la côte rencontre un promontoire topographique et crée une anomalie de VP qui entraîne le développement d'un filament piégé sur le promontoire.

Enfin, des données satellites et un outil lagrangien (Finite-Size Lyapunov Exponents) nous permettent de comparer le mélange horizontal de l'océan de surface en lien avec l'activité biologique des quatre zones d'upwelling de bord Est. Nous mettons en évidence une relation négative entre la turbulence de surface et les concentrations de chlorophylle dans les quatre zones. Sûrement causé par une diminution des vitesses verticales d'upwelling et une perte latérale de nutriments induites par les tourbillons à mésoéchelle, cet effet inhibiteur de la turbulence sur l'écosystème planctonique est très significatif à la côte et diminue vers l'océan ouvert.

De par la diversité des outils et des approches, des progrès ont été faits sur la compréhension des effets des processus physiques à mésoéchelle sur les écosystèmes marins dans les upwellings côtiers.

Influence des processus physiques à mésoéchelle sur l'écosystème planctonique : application aux zones d'Upwelling de Bord Est.

Auteur : Vincent ROSSI.
Directeurs de thèse : Véronique Garçon et Yves Morel.
Discipline : Océanographie physique et biologique.
Lieu et date de soutenance : OMP (salle Coriolis) le 15 juin 2010.
Laboratoire : Laboratoire d'Etude en Géophysique et Océanographie Spatiales,
UMR 5566 CNRS/UPS/CNES/IRD, Observatoire Midi-Pyrénées
18 avenue Edouard Belin, 31401 Toulouse Cedex 9, France.

Les objectifs multiples étaient centrés autour d'une thématique générale : l'influence des processus physiques à mésoéchelle sur l'écosystème planctonique dans les upwellings côtiers. L'utilisation d'outils variés était nécessaire pour aborder les nombreux mécanismes impliqués.

La variabilité physique et biogéochimique de l'upwelling de la péninsule Ibérique est d'abord étudiée à partir des données in-situ de la campagne MOUTON 2007. Ensuite, un front secondaire d'upwelling au niveau de la marge continentale a été observé dans ces données, puis expliqué grâce à un modèle numérique en 2D.

Enfin, des données satellites et un outil lagrangien nous permettent de comparer le mélange horizontal de l'océan de surface des quatre zones d'upwelling de bord Est, en lien avec l'activité biologique. Nous mettons en évidence une relation négative entre la turbulence à mésoéchelle et les concentrations de chlorophylle.

De par la diversité des approches, des progrès ont été faits sur la compréhension des effets des processus physiques à mésoéchelle sur les écosystèmes marins dans les upwellings côtiers.

Mots clés : Upwelling de bord Est ; Processus à Mésoéchelle ; Phytoplancton ; Tourbillons ; Filaments ; Exposants de Lyapunov ; Vorticité Potentielle ; Campagne Océanographique ; Modélisation Couplée.